

ABSTRACT

Title of Document: PHASE CHANGE MATERIALS FOR VEHICLE
AND ELECTRONIC TRANSIENT THERMAL
SYSTEMS

Nicholas Robert Jankowski, Doctor of Philosophy, 2020

Directed By: Professor F. Patrick McCluskey,
Department of Mechanical Engineering

Most vehicle operating environments are transient in nature, yet traditional subsystem thermal management addresses peak load conditions with steady-state designs. The large, oversized systems that result are increasingly unable to meet target system size, weight and power demands. Phase change thermal energy storage is a promising technique for buffering thermal transients while providing a functional thermal energy reservoir. Despite significant research over the half century, few phase change material (PCM) based solutions have transitioned out of the research laboratory. This work explores the state of phase change materials research for vehicle and electronics applications and develops design tool compatible modeling approaches for applying these materials to electronics packaging.

This thesis begins with a comprehensive PCM review, including over 700 candidate materials across more than a dozen material classes, and follows with a thorough analysis of transient vehicle thermal systems. After identifying promising materials for each system

with potential for improvement in emissions reduction, energy efficiency, or thermal protection, future material research recommendations are made including improved data collection, alternative metrics, and increased focus on metallic and solid-state PCMs for high-speed applications.

Following the material and application review, the transient electronics heat transfer problem is specifically addressed. Electronics packages are shown using finite element based thermal circuits to exhibit both worsened response and extreme convective insensitivity under pulsed conditions. Both characteristics are quantified using analytical and numerical transfer function models, including both clarification of apparently nonphysical thermal capacitance and demonstration that the convective insensitivity can be quantified using a package thermal Elmore delay metric.

Finally, in order to develop design level PCM models, an energy conservative polynomial smoothing function is developed for Enthalpy and Apparent Capacity Method phase change models. Two case studies using this approach examine the incorporation of PCMs into electronics packages: substrate integrated Thermal Buffer Heat Sinks using standard finite element modeling, and direct on-die PCM integration using a new phase change thermal circuit model. Both show effectiveness in buffering thermal transients, but the metallic phase change materials exhibit better performance with significant sub-millisecond temperature suppression, something improved cooling or package integration alone were unable to address.

PHASE CHANGE MATERIALS FOR VEHICLE AND ELECTRONIC
TRANSIENT THERMAL SYSTEMS

by

Nicholas Robert Jankowski

Dissertation submitted to the Faculty of the Graduate School of the
University of Maryland, College Park, in partial fulfillment
of the requirements for the degree of
Doctor of Philosophy
2020

Advisory Committee:

Professor F. Patrick McCluskey, Chair
Professor Neil Goldsman, Dean's Representative
Professor Hugh Bruck
Professor Jungho Kim
Professor Michael Ohadi

This material was created by a civilian employee of the United States Government as part of his official duties while enrolled for technical training at the University of Maryland. As such it is declared a work of the U.S. Government and is not subject to copyright protection in the United States, excepting certain portions used with permission from other authors or publishers as noted in the text. The views and conclusions contained in this document are those of the author and should not be interpreted as presenting the official policies or position, either expressed or implied, of the U.S. Government.

- Nicholas R. Jankowski
Sensors and Electron Devices Directorate
Army Research Laboratory
U.S. Army Combat, Capabilities, and Development Command
Adelphi, Maryland, U.S.A.
November 13, 2020

Dedication

To my children, Ashleigh, Jeremiah, and Samantha, for reminding me throughout this learning process that there are things in life far more important than the work described in this document. And to my wife, Becky, for being far more patient for a much longer time than I could have managed. I love you all.

Acknowledgements

I would like express my deepest appreciation for everyone who helped me get to and through the doctoral dissertation process. Having taken the scenic route to completion, an extensive list of people have contributed to, supported, and guided my research. First and foremost I am grateful to my advisor, Dr. Patrick McCluskey, for his patience, encouragement, humor, and well-timed motivational kicks. I would also like to thank my committee: Professors Neil Goldsman, Hugh Bruck, Jungho Kim, and Michael Ohadi, for their advice and support in forming and executing this work.

With sadness I include a special word of thanks to Professor Avram Bar-Cohen, a member of my committee until his very recent passing. Dr. Bar-Cohen was a kind, humorous, inspiring man with whom I collaborated both through this work and during his time at DARPA. His guidance helped shape the direction of our thermal program. He will be missed.

My Army Research Laboratory colleagues have been an integral part of this process. Bruce Geil, thank you for hiring me, mentoring me, and introducing me to this technical field. Many thanks to my Compact Power and Thermal Sciences teammates including Drs. Lauren Boteler, Darin Sharar, Adam Wilson, Mike Waits, Brendan Hanrahan, and Andrew Smith for their encouragement in staying focused while juggling academic work and my 'day job'. Last, allow me to express my appreciation to Drs. Paul Barnes and Brian Morgan for mentorship and frank discussion on navigating this process.

Thank you, Dr. Robert Krchnavek, my undergraduate mentor at Rowan University, for first getting me excited about research and convincing me to start down this road. And of course, thanks you Mr. Henry Rowan and family for the gift to the University that

supported my undergraduate degree and created a unique program that shaped my outlook on the engineering field.

I would be remiss in not thanking the volunteer open source software teams behind GNU Octave, GNU Maxima, Elmer, and other scientific tools used here, in addition to the creators of ddrescue and ddrescueview, employed (successfully!) no less than three times since undertaking this process. In addition to acquiring a new hobby, I learned much interacting with and contributing to these developer groups, and their modeling and troubleshooting advice greatly aided my efforts.

Finally, thank you to my wife, my parents, and my children. This long journey did not follow the planned route, but we arrived. Your patience, encouragement, enduring love, and support from beginning to end are what motivated me to try and make you proud.

Table of Contents

Dedication	ii
Acknowledgements	iii
Table of Contents	v
List of Tables	vii
List of Figures	xi
List of Abbreviations	xxi
Chapter 1 – Introduction	1
1.1. Motivation: Transient thermal management for vehicle systems	1
1.2. Scope of work	2
Chapter 2 – Review of thermal phase change and available materials	4
2.1. Thermal energy storage	4
2.2. Utilizing thermal phase change	5
2.3. Thermal phase change materials and properties	8
2.4. Thermal phase change materials summary	40
Chapter 3 – Vehicle applications of phase change materials	42
3.1. The vehicular transient thermal environment	42
3.2. Vehicle application summary and implications for PCM selection	66
3.3. Recommendations for vehicular PCM use	67
Chapter 4 – Power semiconductor devices and thermal packaging	70
4.1. Heat generation in power semiconductor devices	70
4.2. Power semiconductor package thermal transport	72
4.3. Improving power module steady-state thermal resistance	75
4.4. Substrate integrated cooling – fabrication and evaluation	79
4.5. Summary substrate integrated cooling	103
Chapter 5 – Transient heat transfer in power electronics	105
5.1. High rate transient heat transfer – impact on power electronics	105
5.2. Transient heat transfer – thermal circuit approximations	110
5.3. Transient thermal circuit evaluation of power packages	136
Chapter 6 – Electronics integrated phase change materials	174
6.1. Heat transfer - solid-liquid phase change models	175
6.2. Proposed polynomial smoothing functions	187
6.3. Substrate integrated phase change cooling	205
6.4. Phase change integrated SPICE models	276
6.5. Discussion on PCM integrated package design and modeling	329

Chapter 7 – Conclusions	333
7.1. Research Summary	334
7.2. Future Directions	341
7.3. Contributions Summary	348
Appendix A – PCM thermal circuit package study - complete results.....	351
Appendix B – Preliminary investigation of electrical supercooling mitigation in erythritol	366
B.1. Delayed Nucleation Onset and Supercooling	368
B.2. Methods of promoting or inducing nucleation.....	375
B.3. Reducing the Supercooling of Erythritol	386
Appendix C – Preliminary substrate integrated TBHS fabrication	405
C.1. Silicon TBHS substrate fabrication	406
C.2. Ceramic PCM substrate fabrication	417
Appendix D – Complete PCM property tables	421
Bibliography	443

List of Tables

Table 2.1 – Selected pure alkanes and properties	13
Table 2.2 – Selected paraffin waxes	13
Table 2.3 – Properties of fatty acid materials	15
Table 2.4 – Sugar and sugar alcohol PCMs	16
Table 2.5 – Carboxylic acid based PCMs	17
Table 2.6 – Clathrate hydrate materials	18
Table 2.7 – Miscellaneous organic PCMs	18
Table 2.8 – Organic solid-state transition PCMs	20
Table 2.9 – Layered perovskite solid-solid PCMs	22
Table 2.10 – Dialkyl ammonium salt solid-state PCMs	23
Table 2.11 – Salt/water and Salt Hydrate PCM candidates	25
Table 2.12 – Select Salt PCMs	26
Table 2.13 – RoHS non-compliant metallic materials	28
Table 2.14 – Select RoHS Compliant metallic materials	28
Table 3.1 – Common Vehicle Battery Chemistries and Performance Details	54
Table 3.2 – Summary of vehicle PCM applications and temperature requirements	67
Table 3.3 – Vehicle applications and suggested candidate PCMs, sorted by temperature	68
Table 4.1 – Linear thermal equations and electrical circuit equivalents	74
Table 4.2 – Properties of Silicon, Silicon Carbide, and Aluminum Nitride	80
Table 4.3 – AlN saw-cut microchannel cooler dimensions	88
Table 4.4 – AlN stereolithographic microchannel cooler dimensions	89
Table 4.5 – Substrate idealized Poiseuille Numbers	93
Table 5.1 – Power package thermal material properties	138
Table 5.2 – Package layer thermal characteristics	139

Table 5.3 – Thermal Characteristics for each model Case	139
Table 5.4 – Package delay characteristics.....	147
Table 5.5 – Simulated package delay comparison.....	156
Table 5.6 – Relative temperature change from a 5000x h_{eff} increase	160
Table 5.7 – Normalized temperature rise from unit pulse train at $h_{eff} = 10 \text{ kW/m}^2\text{K}$	170
Table 5.8 – Normalized temperature rise from unit pulse train at $h_{eff} = 50 \text{ kW/m}^2\text{K}$	170
Table 5.9 – Normalized temperature rise from unit pulse train at $h_{eff} = 100 \text{ kW/m}^2\text{K}$	170
Table 6.1 – $f(\theta)$ boundary conditions, constant single phase properties	188
Table 6.2 – Enthalpy function polynomial coefficient solution	189
Table 6.3 – Apparent capacity function polynomial coefficient solution.....	190
Table 6.4 – Peak values and function widths of polynomial solutions.....	191
Table 6.5 – Erythritol material properties summary	194
Table 6.6 – Neumann problem simulation parameters	196
Table 6.7 – Silicon TBHS simulation material properties	216
Table 6.8 – Silicon TBHS simulation dimensions and parameter ranges.....	216
Table 6.9 – Silicon TBHS linear thermal performance ratios	230
Table 6.10 – TBHS melting model heat fluxes and time steps.....	231
Table 6.11 – Silicon TBHS best performance temperature suppression values	239
Table 6.12 – Thermal properties used in AlN TBHS model	243
Table 6.13 – AlN TBHS simulation dimensions and parameter ranges	244
Table 6.14 – AlN TBHS linear thermal performance ratios	257
Table 6.15 – AlN TBHS best temperature suppression values.....	267
Table 6.16 – AlN TBHS linear thermal performance ratios	271
Table 6.17 – Minimum geometry AlN-gallium TBHS temperature suppression values	272
Table 6.18 – Melt front locations and melt region midpoints.....	288

Table 6.19 – PCM properties used in the SPICE package model.....	295
Table 6.20 – $T_D/3$ convective sensitivity change with PCM loading	298
Table 6.21 – PCM loaded package thermal suppression comparison	313
Table 6.22 – Gallium loaded package thermal suppression summary.....	318
Table 6.23 – Fast pulse gallium loaded package thermal suppression	320
Table 6.24 –Thermal interface resistances from various electronic materials.....	323
Table B.1 – Effective heterogeneous nucleation materials.....	374
Table B.2 – Materials showing erythritol supercooling mitigation	388
Table B.3 – Pre-test results, no voltage applied.....	397
Table B.4 – Test results, voltage applied.....	398
Table B.5 – Voltage applied, Location summarized results	398
Table B.6 – Post-test results, no voltage applied	399
Table B.7 – Summary of spontaneous and electrically stimulated nucleation	403
Table C.1 – SiTBHS design dimensions	410
Table C.2 – AlNTBHS design dimensions	420
Table D.1 – Paraffins from $n = 10$ to 100.....	421
Table D.2 – Paraffin waxes and blends	422
Table D.3 – Fatty acid materials	422
Table D.4 – Fatty acid blends	423
Table D.5 – Fatty acid derivative materials	424
Table D.6 – Sugar and sugar alcohol materials	424
Table D.7 – Carboxylic acid based materials	425
Table D.8 – Clathrate hydrate materials	425
Table D.9 – Miscellaneous organic materials.....	426
Table D.10 – Miscellaneous organic blends.....	427

Table D.11 – Organic solid-solid transition materials	428
Table D.12 – Layered perovskite solid-solid PCMs	428
Table D.13 – Dialkyl ammonium salt solid-state PCMs	429
Table D.14 – Aqueous and hydrated salt material properties	430
Table D.15 – Hydrated salt blends.....	431
Table D.16 – Pure salts	432
Table D.17 – Salts blends	433
Table D.18 – RoHS non-compliant metallic materials.....	436
Table D.19 – RoHS compliant metallic materials	437
Table D.20 – RoHS compliant Indium Corp. alloys lacking H_f data.....	438
Table D.21 – RoHS non-compliant Indium Corp. alloys lacking H_f data	439
Table D.22 – Commercial organic PCMs.....	440
Table D.23 – Commercial inorganic PCMs.....	442

List of Figures

Figure 2.1 – Solid-to-liquid phase change temperature profiles.....	6
Figure 2.2 – PCM categories as used in this document	12
Figure 2.3 – pentaerythritol, pentaglycerine, and neopentyl glycol binary blend solid-solid transition temperatures and latent heat values	21
Figure 2.4 – Melting/Transition temperature spans of materials in the surveyed PCM literature sorted by median transition temperature.	32
Figure 2.5 – Melting/transition temperature distribution over the surveyed materials.....	32
Figure 2.6 – Median (a) specific and (b) volumetric latent heats for materials up to 250°C.	34
Figure 2.7 – Median (a) specific and (b) volumetric latent heats for materials from 200-1000°C.....	35
Figure 2.8 – I_l PCM figure of merit as proposed by Lu	37
Figure 3.1 – Temperatures seen by various electronics and sensors throughout a standard commercial vehicle	43
Figure 3.2 – Standard drive cycle operating profile information.....	44
Figure 3.3 – (a) Vehicle absorption air conditioning system driven by exhaust waste heat recovery with a PCM thermal buffer, and (b) notional implementation layout.....	52
Figure 3.4 – Cougar MPAV	53
Figure 3.5 - Percent of rated battery power available over the operating temperature range for the General Motors Lithium Ion Voltec battery system.....	55
Figure 3.6 - Engine cooling system with a heat accumulator incorporating a phase change material to thermally buffer the coolant temperature	58
Figure 3.7 – (a) Dual switch module, and (b) internal view of module showing transistor and diode arrays bonded down to substrate and baseplate	59
Figure 3.8 – Range of available exhaust temperatures in a gasoline-fueled passenger vehicle.....	61
Figure 3.9 – (a) p-type and (b) n-type thermoelectric materials and temperature dependent thermoelectric performance	65
Figure 4.1 – (a) Cross-section of a representative power transistor device structure. (b) The electrical resistive components along the device’s conductive path.	71

Figure 4.2 – (a) Representative multi-chip power electronic module (Eupec BSM200GD60DLC). (b) Power module packaging layer stack.	73
Figure 4.3 – Power electronics thermal stack depicting multiple thermal resistance components	75
Figure 4.4 – Simple performance curves showing device temperature rise for packages with a range in values of total thermal resistivity	76
Figure 4.5 – Modified packaging and thermal stack.....	80
Figure 4.6 – Saw-cut aluminum nitride ceramic substrate.	81
Figure 4.7 – Representative packaged and sealed AlN substrate with SiC diode heat source.	83
Figure 4.8 – 3D sketch of microchannel substrate used as the fabrication input file.	85
Figure 4.9 – Fully assembled stereolithographically fabricated AlN microchannel substrate.	85
Figure 4.10 – Diagram of experimental setup for characterization of microchannel substrates.....	86
Figure 4.11 – Mounting block for AlN saw-cut microchannel coolers	89
Figure 4.12 – Flowrate comparisons of the tested saw-cut and STL microchannel substrates.....	92
Figure 4.13 – Measured Poiseuille number (C) for the tested flow conditions	95
Figure 4.14 – Normalized Poiseuille number, C^*	95
Figure 4.15 – Relative developing flow length in each of the tested microchannel substrates.....	97
Figure 4.16 – Relative apparent Poiseuille Number which adds in the effects of entrance, exit, and developing flow losses	98
Figure 4.17 – Energy balance comparing the applied electrical power to the measured increase in fluid heat over (a) 120W range and (b) a close-up of 40W power range	100
Figure 4.18 – Thermal resistance and resistivity of the tested substrate integrated microchannel coolers	102
Figure 5.1 – Hypothetical low duty cycle pulsed thermal profile.....	106
Figure 5.2 – Frequency domain losses profile for high and low thermal inertia electronics	108

Figure 5.3 – Circuit schematic of a representative electrothermal codesign problem.....	112
Figure 5.4 – Discretized one dimensional thermal networks using (a) the finite difference method and (b) the finite element method	114
Figure 5.5 – Finite element equivalent thermal circuit	116
Figure 5.6 – FE equivalent thermal circuit as a symmetric-pi two-port network.....	122
Figure 5.7 – One dimensional insulated bar	124
Figure 5.8 – Normalized two-element approximate temperature profiles at each node..	130
Figure 5.9 – Error in temperature prediction at each node	131
Figure 5.10 – 2-D rectangular finite element equivalent thermal circuit.....	134
Figure 5.11 – Power package configurations used to examine transient behavior.	137
Figure 5.12 – Cauer-type finite difference thermal circuit used in the Rubenstein Elmore delay approximation.....	144
Figure 5.13 – Finite difference thermal circuit refinement for converged Elmore delay approximation.	145
Figure 5.14 – (a) Finite difference and (b) finite element thermal circuit topologies with matched algorithmic and transfer function method Elmore delay	146
Figure 5.16 – Case 4 SPICE thermal circuit representation.	149
Figure 5.17 – Case 1 negative oscillation magnitude for the different layers with increasing mesh refinement	151
Figure 5.18 – Maximum DMP oscillation magnitude for all five Cases with increasing mesh refinement.....	152
Figure 5.19 – Case 1 error accumulation (maximum device temperature relative discrepancy) with time for different values of n	153
Figure 5.20 – Steady-state resistivity of the modeled packages as functions of the backside convection.....	154
Figure 5.21 – Extracted dominant time constant of the modeled packages as functions of the backside convection	155
Figure 5.22 – Peak junction temperature rise under single pulse excitation for Case 1 with varying convection rates and pulse widths	157

Figure 5.23 – Peak junction temperature rise under single pulse excitation for package Cases 2-5 with varying convection rate and pulse widths	158
Figure 5.24 – Relative difference in temperature rise seen by package cases over simulated convection range.....	160
Figure 5.25 – Frequency dependent small signal thermal resistance for each Case over varied convection rates	162
Figure 5.26 – Time domain step response temperature rise for each Case over varied convection rates	164
Figure 5.27 – Time domain pulsed temperature profiles for Cases 1, 3, and 5 with $h_{eff} = 10 \text{ kW/m}^2\text{K}$ subjected to a unit heat pulse train.....	166
Figure 5.28 – Time domain pulsed temperature profiles for Cases 1, 3, and 5 with $h_{eff} = 50 \text{ kW/m}^2\text{K}$ subjected to a unit heat pulse train.....	167
Figure 5.29 – Time domain pulsed temperature profiles for Cases 1, 3, and 5 with $h_{eff} = 100 \text{ kW/m}^2\text{K}$ subjected to a unit heat pulse train.....	168
Figure 5.30 – Time domain 1 ms pulsed temperature profiles for Cases 1, 3, and 5	171
Figure 6.1 – Schematic illustration of the one-dimensional Stefan problem.....	177
Figure 6.2 – Multiple phase front propagation in a one dimensional medium undergoing periodic heating and cooling cycles.....	178
Figure 6.3 – Enthalpy and apparent heat capacity profiles for an abrupt phase transition.	181
Figure 6.4 – Enthalpy and apparent heat capacity profiles for a top-hat phase change approximation.	181
Figure 6.5 – Comparisons of smoothing functions applied to the phase change mushy zone approximation.....	183
Figure 6.6 – Normalized smoothing functions based on a normal distribution.....	186
Figure 6.7 – Homographic smoothing functions used by Yao and Chait, compared to the unit step profile.	187
Figure 6.8 – 3 rd and 5 th order normalized polynomial smoothing functions compared to the standard top-hat profile.	191
Figure 6.9 – One dimensional Neumann melting model	192
Figure 6.10 – Representative analytical solution to the Neumann problem	194

Figure 6.11 – Representative normalized solution to the Neumann melting problem. ...	195
Figure 6.12 – Polynomial fit effective capacity profile for erythritol.....	197
Figure 6.13 – Polynomial fit enthalpy profiles for erythritol.....	197
Figure 6.14 – Numerical approximations of melting front position	199
Figure 6.15 – Normalized P(3) model temperature plotted against normalized Boltzmann coordinate at different time steps.....	200
Figure 6.16 – Melting front location prediction RMSE at $t = 500s$	202
Figure 6.17 – Thermal profile RMSE at $t = 500s$	203
Figure 6.18 – Department of Energy developed TBHS concepts.....	206
Figure 6.19 – Schematic of a substrate integrated thermal buffer heat sink.....	209
Figure 6.20 – Substrate integrated TBHS computational domain	210
Figure 6.21 – Representative finite element meshes used in the TBHS model.....	212
Figure 6.22 – Representative steady-state, non-melting heating profile in a silicon TBHS	217
Figure 6.23 – Steady-state thermal resistivity results for silicon TBHS and equivalent microchannel heat sinks	219
Figure 6.24 – Silicon TBHS normalized thermal resistivity.....	220
Figure 6.25 – Fin efficiency estimates for all silicon TBHS and standard microchannel (non-PCM) heat sink configurations.....	221
Figure 6.26 – Extracted thermal time constants for each silicon TBHS configuration at varying convective rates	223
Figure 6.27 – Estimated solid contribution to silicon TBHS thermal time constant	224
Figure 6.28 – Estimated effective thermal capacitance for each configuration.....	227
Figure 6.29 –Effective thermal capacitance emphasizing convective dependence of PCM impact.....	228
Figure 6.30 – Linear silicon TBHS figure of merit comparisons	229
Figure 6.31 – Extracted threshold melting heat flux values for each silicon TBHS configuration	232

Figure 6.32 – Silicon TBHS simulated melting delay compared to the single-pole melting delay model.....	233
Figure 6.33 – Transient melting temperature map in a representative silicon TBHS.....	235
Figure 6.34 – Representative silicon TBHS melting temperature profiles.....	237
Figure 6.35 – Aggregate (a) absolute and (b,c) microchannel relative silicon-erythritol TBHS temperature suppression	241
Figure 6.36 – Substrate integrated TBHS computational domain (repeated).....	244
Figure 6.37 – Steady-state thermal resistivity results for the AlN TBHS	245
Figure 6.38 – AlN TBHS normalized thermal resistivity values.....	247
Figure 6.39 – Fin efficiency for AlN TBHS substrates	249
Figure 6.40 – Extracted thermal time constants for each AlN TBHS configuration at varying convective rates	250
Figure 6.41 – Estimated solid contributions to AlN TBHS thermal time constant	251
Figure 6.42 – AlN TBHS effective thermal capacitance emphasizing convective dependence of PCM impact	253
Figure 6.43 – AlN TBHS capacitance-resistance figure of merit comparisons.....	255
Figure 6.44 – AlN TBHS thermal time constant-resistance figure of merit comparisons	256
Figure 6.45 – Aggregate AlN TBHS simulated melting delay.....	258
Figure 6.46 – Comparative transient melting temperature maps in LNT and gallium AlN TBHS	260
Figure 6.47 – Aggregate AlN TBHS thermal suppression results for 100 um substrates.....	262
Figure 6.48 – Aggregate AlN TBHS thermal suppression results for 300 um substrates.....	263
Figure 6.49 – Select AlN TBHS melting temperature profiles for $d = 100$ um and $h = 1$ kW/m ² K.....	265
Figure 6.50 – Select AlN TBHS melting temperature profiles for $d = 300$ um and $h = 1$ kW/m ² K.....	266
Figure 6.51 – Select AlN-gallium TBHS transient melting profiles for $d = 100$ um	269

Figure 6.52 – Select AlN-gallium TBHS transient melting profiles for $d = 300 \text{ um}$	270
Figure 6.53 – Simple 1D FEM thermal circuit used for phase change model evaluation	280
Figure 6.54 – PCM thermal circuit melting front estimates	281
Figure 6.55 – PCM thermal circuit interpolated melting front estimates	283
Figure 6.56 – PCM thermal circuit temperature profile estimates for $n = 100$ & 500	285
Figure 6.57 – PCM thermal circuit temperature profile estimates for $n = 1000$ & 5000	286
Figure 6.58 – PCM thermal circuit temperature profile comparison with refined melt front node spacing for $n = 100$ & 500	289
Figure 6.59 – PCM thermal circuit temperature profile comparison with refined melt front node spacing for $n = 1000$ & 5000	290
Figure 6.60 – Thermal circuit prediction of Zivkovic and Fujii phase change center line temperature profile.....	292
Figure 6.61 – Case 5 thermal circuit model with topside PCM block.....	294
Figure 6.62 – Comparison of convection dependent peak junction temperature for Case 5 with topside PCM loading	297
Figure 6.63 – Thermal impedance impact on convective sensitivity in PCM loaded packages.....	298
Figure 6.64 – PCM loaded package temperature step response comparison for $h_{eff} = 100 \text{ W/m}^2\text{K}$	300
Figure 6.65 – PCM loaded package temperature step response comparison for $h_{eff} = 10,000 \text{ W/m}^2\text{K}$	301
Figure 6.66 – PCM loaded package temperature step response comparison for $h_{eff} = 500,000 \text{ W/m}^2\text{K}$	301
Figure 6.67 – Package phase change step responses for Case 1	304
Figure 6.68 – Package phase change step responses for Case 5	305
Figure 6.69 – Close up of melting onset for (a) gallium and (b) LNT during Case 5 phase change step responses	308
Figure 6.70 – Case 5 PCM melt fraction	310

Figure 6.71 – 100 ms, 750 W/cm ² pulsed responses of PCM loaded packages at $h_{eff} = 10 \text{ kW/m}^2\text{K}$	312
Figure 6.72 – 100 ms, 750 W/cm ² pulsed responses of gallium loaded packages at varied convection rates	315
Figure 6.73 – 100 ms, 150 W/cm ² pulsed responses of Gallium loaded packages at varied convection rates	317
Figure 6.74 – High power 1 ms pulsed responses of Gallium loaded packages.....	319
Figure 6.75 – Decrease in PCM thermal buffering due to interface thermal resistance..	324
Figure 6.76 –PCM melt fraction impact of varying interface thermal resistance.....	325
Figure 6.77 –PCM interface thermal resistance impact on 1 ms high power pulses	326
Figure A.1 – Single pulse peak junction temperature comparison for Cases 1 and 2 with topside PCM loading.....	352
Figure A.2 – Single pulse peak junction temperature comparison for Cases 3 and 4 with topside PCM loading.....	353
Figure A.3 – PCM loaded package temperature step response comparison for $h_{eff} = 100 \text{ W/m}^2\text{K}$	354
Figure A.4 – PCM loaded package temperature step response comparison for $h_{eff} = 500 \text{ W/m}^2\text{K}$	354
Figure A.5 – PCM loaded package temperature step response comparison for $h_{eff} = 1 \text{ kW/m}^2\text{K}$	355
Figure A.6 – PCM loaded package temperature step response comparison for $h_{eff} = 5 \text{ kW/m}^2\text{K}$	355
Figure A.7 – PCM loaded package temperature step response comparison for $h_{eff} = 10 \text{ kW/m}^2\text{K}$	356
Figure A.8 – PCM loaded package temperature step response comparison for $h_{eff} = 50 \text{ kW/m}^2\text{K}$	356
Figure A.9 – PCM loaded package temperature step response comparison for $h_{eff} = 100 \text{ kW/m}^2\text{K}$	357
Figure A.10 – PCM loaded package temperature step response comparison for $h_{eff} = 500 \text{ kW/m}^2\text{K}$	357
Figure A.11 – Low power package phase change step response with gallium.....	358

Figure A.12 – Low power package phase change step response with LNT	359
Figure A.13 – Low power package phase change step response with erythritol	360
Figure A.14 – High power package phase change step response with gallium	361
Figure A.15 – High power package phase change step response with LNT	362
Figure A.16 – High power package phase change step response with erythritol	363
Figure A.17 – 100 ms pulsed phase change response of LNT loaded packages	364
Figure A.18 – 100 ms pulsed phase change response of erythritol loaded packages	365
Figure B.1 – Potential effects of supercooling on a thermal protection system	367
Figure B.2 – Variation of the catalytic potency factor.....	373
Figure B.3 – Electrical supercooling reduction electrode set	392
Figure B.4 – Experimental setup for electrically induced nucleation tests.....	393
Figure B.5 – Representative supercooling experiment heating and cooling profile.....	396
Figure B.6 – Nucleation temperatures seen during the erythritol supercooling experiment.....	401
Figure B.7 – Location dependent nucleation accumulation curves for the electrical supercooling mitigation experiment	403
Figure C.1 – Substrate integrated thermal buffer heat sink schematic	405
Figure C.2 – Process for forming a Layer 1 from silicon	408
Figure C.3 – Mask layout for silicon TBHS (SiTBHS) wafer.....	409
Figure C.4 – (a) Photograph of etched 100mm silicon test wafer with (b) a close up of SiTBHS5.....	410
Figure C.5 – Mask layout for SiTBHS serpentine heater array.....	411
Figure C.6 – Photograph of patterned heaters on the backside of fabricated SiTBHS channels.....	412
Figure C.7 – Process of filling and assembling the SiTBHS substrate and manifold	413
Figure C.8 – Photographs of SiTBHS1 (a) after epoxy cap, and STBHS3 (b) during heated melt, (c) water flush, and (d) resolidification	414

Figure C.9 – 3D sketches of the TBHS manifold block415

Figure C.10 – Photographs of AINTBHS_1419

List of Abbreviations

AC	–	Air Conditioning, or Alternating Current
AlN	–	Aluminum Nitride
ARL	–	Army Research Laboratory
C2	–	Command and Control
CAD	–	Computer Aided Design
CAS	–	Chemical Abstracts Service
CO	–	Carbon Monoxide
CPU	–	Central Processing Unit
DBC	–	Direct-Bond Copper (substrate material)
DEVCOM	–	Combat Capabilities Development Command (U.S. Army)
DMP	–	Discrete Maximum Principle
DOD	–	United States Department of Defense
DOE	–	United States Department of Energy
ECU	–	Environmental Control Unit
EHR	–	Exhaust Heat Recovery
EPA	–	United States Environmental Protection Agency
EV	–	Electric Vehicle
FDM	–	Finite Difference Method
FE	–	Finite Element
FEA	–	Finite Element Analysis
FEM	–	Finite Element Method
FOM	–	Figure of Merit
FS	–	Full Scale
FWHM	–	Full Width at Half of Maximum
HC	–	Hydrocarbon
HDPE	–	High Density Polyethylene
HEV	–	Hybrid Electric Vehicle
HEX	–	Heat Exchanger
HTF	–	Heat Transfer Fluid
HVAC	–	Heating, Ventilation and Air Conditioning
IGBT	–	Insulated Gate Bipolar Transistor
IR	–	Infra-red
Li-Ion	–	Lithium Ion (battery chemistry)
LNT	–	Lithium Nitrate Trihydrate
LPG	–	Liquified Petroleum Gas
mol%	–	percentage by molar fraction
MCHH	–	Magnesium Chloride Hexahydrate
MPAV	–	Mine Protected Armored Vehicle
MZW	–	Mushy Zone Width
NiMH	–	Nickel Metal Hydride (battery chemistry)
NPG	–	Neopentyl Glycol
PCM	–	Phase Change Material
PCTES	–	Phase Change Thermal Energy Storage
PDE	–	Partial Differential Equation

PE	–	Pentaerythritol
PG	–	Pentaglycerine
PHEV	–	Plug-in Hybrid Electric Vehicle
ppm	–	parts per million
RC	–	Resistive and Capacitive
Ref	–	Reference
Res	–	Residue (from complex integration)
RMSE	–	Root Mean Squared Error
RoHS	–	Restriction of Hazardous Substances
SEM	–	Scanning Electron Microscope/Micrograph
SiC	–	Silicon Carbide
SPICE	–	Simulation Program with Integrated Circuit Emphasis
SWaP	–	Size, Weight and Power
STL	–	Stereolithography or Stereolithographic
TA&T	–	Technology Assessment & Transfer, Inc.
TAM	–	Trometamol
TBHS	–	Thermal Buffer Heat Sink
TCU	–	Temperature Control Unit
TE	–	Thermoelectric
TEG	–	Thermoelectric Generator
TES	–	Thermal Energy Storage
THF	–	Tetrahydrofuran
TIM	–	Thermal Interface Material
US, USA	–	United States of America
USABC	–	United States Advanced Battery Consortium
VDMOS	–	Vertical Diffusion Metal-Oxide-Semiconductor
wt%	–	percentage by weight
WHR	–	Waste Heat Recovery

Variables/Symbols

AE	–	area enhancement (unitless)
A	–	area [m^2]
AR	–	aspect ratio
C	–	Poiseuille number (unitless) or capacity [F] (electrical) or [J/K] (thermal)
c	–	specific heat capacity [kJ/kgK]
D	–	diameter [m]
E	–	energy, or electrode potential
f	–	frequency [Hz] or friction factor (unitless)
F	–	heat input vector, or nucleation energy
Fo	–	Fourier number, ratio of heat transport to storage capacity (unitless)
g	–	generation (heat) [W/m^3]
h	–	convection coefficient, [W/m^2K], or discretization parameter
H	–	latent heat [kJ/kg] or [MJ/m^3]
$H(s)$	–	complex transfer function
i	–	indexing constant, complex constant, or current [Amps]
I	–	Lu PCM fitness metric

j	–	indexing constant or complex constant
K	–	fluid frictional loss term
\mathbf{K}	–	thermal conductivity matrix
k	–	thermal conductivity [W/mK] or indexing constant
l or L	–	length [meters]
n	–	number
m	–	mass
\mathbf{M}	–	thermal mass matrix
p	–	pressure [Pa or psi]
q	–	heat flow [Watts]
Q	–	volumetric flowrate [m ³ /sec]
R	–	resistance [ohms] (electrical) or [K/W] (thermal)
Re	–	Reynold's number, ratio of inertial to viscous fluid forces
s	–	complex Laplace domain variable
St	–	Stefan number, ratio of sensible to latent heat
T	–	temperature [K or °C]
T_D	–	Elmore delay [s]
T_n	–	Chebyshev polynomial of the first kind
T	–	transmission matrix
t	–	time [s]
u	–	integration parameter
U_n	–	Chebyshev polynomial of the second kind
v or V	–	voltage [V], or volume, [m ³]
w or W	–	width [m]
x	–	position, or location [meters]
Y	–	complex admittance
z	–	complex frequency
Z	–	complex impedance

Greek Symbols

α	–	thermal diffusivity [m ² /s]
δ	–	crystal disregistry [m], or unitless length parameter
η	–	efficiency
γ	–	surface free energy per area [J/m ²]
κ	–	thermal conductivity [W/mK], or curvature [m]
λ	–	mass coupling factor, or arbitrary integration parameter
ν	–	kinematic viscosity [m ² /s]
ρ	–	density [kg/m ³]
θ	–	non-dimensionalized temperature (unitless)
σ	–	surface stress [Pa]
τ	–	time constant [s]
ω	–	circular frequency [rad/s]

Sub- / Superscripts

app	–	apparent
c or C	–	catalyst, cold, cross-section, or crystal

cr	–	critical
conv	–	convective
d	–	diode
e, el	–	element
eff	–	effective
f	–	fusion
fr	–	freezing
H	–	high, hot, or hydraulic
int	–	interfacial
l or L	–	liquid, or low
mc	–	microchannel
M	–	melting
N	–	nucleation
p	–	parallel, pressure, or pulse
q	–	heat
s	–	series, solid, surface
sc	–	supercooled
ss	–	steady-state
t	–	transition
th	–	thermal
v	–	volumetric
"	–	flux (per area)
+	–	developing

Chapter 1 – Introduction

1.1. Motivation: Transient thermal management for vehicle systems

Since the turn of the 21st Century, the United States Army been actively developing the next generation of future ground vehicles with improved system efficiency and capability [1-4]. These systems will have a more complicated power electronics element than current vehicles, whether for managing the required drive-train system or for enabling the use of advanced offensive and defensive payloads. At the same time the U.S. Department of Defense (DOD) issued policies setting increased energy efficiency and fuel economy as immediate priorities for military vehicles as well, putting emphasis on the strategic and operational impact of the military's overall energy usage [5]. System level analyses by both the DOD and the U.S. Department of Energy (DOE) have recognized that improving the management of vehicle heat is critical to achieving higher platform efficiency [6,7]. Depending on operating conditions, typical vehicles reject approximately 65-75% of the fuel's energy as waste heat through the exhaust and radiator, and in current combat vehicles about 10-15% of the useful energy is devoted to running the cooling system [8,9]. In particular, the high power electronics in these new vehicles will require advanced compact thermal management capabilities as designers strive to achieve maximum system power density [10].

While much work has gone into developing advanced cooling technology and improving overall vehicle thermal efficiency, most of those solutions only address the thermal requirement as a steady-state load. In reality, all of these thermal conditions exist as transients over some finite timescale. High power electronics can switch at microsecond to millisecond regimes or be driven continuously for minutes. Engine component temperatures can increase during surges and drop during idle conditions. Under-hood temperatures can be highly dependent on vehicle speed, especially if primary cooling uses intake air. In addition, no matter what the driving profile is for the vehicle, it will likely undergo an ambient-to-operating temperature swing at least once if not several times every day, and vehicle warm-up can be a highly inefficient operating period. Taking all of this into account, the need exists to properly design transient solutions for transient vehicle systems.

Phase change Thermal Energy Storage (TES) has received much attention for non-vehicular applications to load-level, or thermally buffer, transient behavior. Thermal buffering can allow cooling systems to be designed based on total energy, rather than peak power, requirements. Put in other terms, they can be designed for the average, instead of peak, thermal load. This could change the current practice of ‘steady-state thermal overdesign’ and improve the overall vehicle Size, Weight and Power (SWaP) profile.

1.2. Scope of work

This effort focuses on exploring current gaps in mitigating thermal transients in vehicle electronics and power systems. In particular, this work is divided into three general sections:

1. Characterizing potential applications for Phase Change Thermal Energy Storage (PCTES) on vehicles, beginning with a review of available Phase Change Materials (PCMs) and finishing with a full analysis of vehicle transient thermal systems. In particular identifying current limitations to the general design approach, material availability, and research directions related to Phase Change Materials (PCMs) available to buffer transients in vehicle power systems. (Chapters 2-3).
2. Examining approaches to modeling and improving heat transfer in power electronic packages such as those used in vehicle systems, focusing on design level aspects of transient heat transfer as a precursor to incorporating nonlinear thermal components in the models. (Chapters 4-5).
3. Developing design-model compatible techniques for incorporating PCMs as nonlinear elements in transient heat transfer models, including case studies demonstrating use in power electronics packages and cooling structures, and quantifying the performance improvement from PCM integration. (Chapter 6).

Conclusions and recommendations for future work are included in Chapter 7. In addition, early steps toward fabrication and testing of PCM integrated packages and mitigation of hysteresis are presented in Appendices B and C. The full PCM property database produced by the Chapter 2 material investigation is included as Appendix D.

Chapter 2 – Review of thermal phase change and available materials

2.1. Thermal energy storage

When thermal conditions are relatively constant or only slowly changing, it is sound engineering approach to design the thermal management system based on steady-state requirements. However, when a system has a thermal or load profile with substantial periodic or transient events, severe temperature excursions can result that will fall significantly outside of acceptable design margins. The simplest design approach for these thermal conditions would be provide enough cooling capacity to manage the peak thermal condition as steady-state, i.e., as if the maximum load was constantly present. Such a conservative approach can result in significant overdesign depending on the fraction of time that the condition is present, or the duty cycle of a periodic or pulsed system. Along with this overdesign comes associated size, cost, complexity, and reliability concerns.

An alternative to overdesign is to develop a thermal solution that maintains acceptably low steady-state temperatures while providing sufficient thermal capacity to minimize transient temperature rise. The system would absorb the excess heat load for the duration of the transient condition, and then reject the heat at a lower, more system compatible rate. Such Thermal Energy Storage systems have been proposed for numerous industrial, commercial and energy-related applications. A specific form of TES takes advantage of a material's latent heat of phase change to maximize absorbed energy. Unlike single phase absorption, where temperature rises in accordance with the material's specific heat capacity, a Phase Change Material has an approximately isothermal phase front that absorbs energy without sensible temperature rise. Additionally, the latent heat of fusion of many materials is much larger than sensible heat absorption over an equivalent temperature

range. Because of these factors a properly engineered PCM system could maximize energy density while maintaining necessary temperatures for the duration of the transient thermal condition.

2.2. Utilizing thermal phase change

Figure 2.1(a) shows an idealized, lumped mass depiction of temperature rise accompanying energy absorption over a solid-liquid transition. With a constant energy input, a material will warm to the melting temperature, at which point it will begin to transform from solid to liquid. A material not experiencing phase change will continue to heat linearly, following the dashed line in the figure. Additional heat added after reaching the melting temperature serves to drive the phase change process, and additional temperature rise is arrested until full phase change has occurred. Thus, the latent heat absorption that occurs during this change acts as a thermal buffer by limiting temperature rise until the material has fully melted. After this point sensible warming will resume in proportion to the material's liquid-state specific heat capacity.

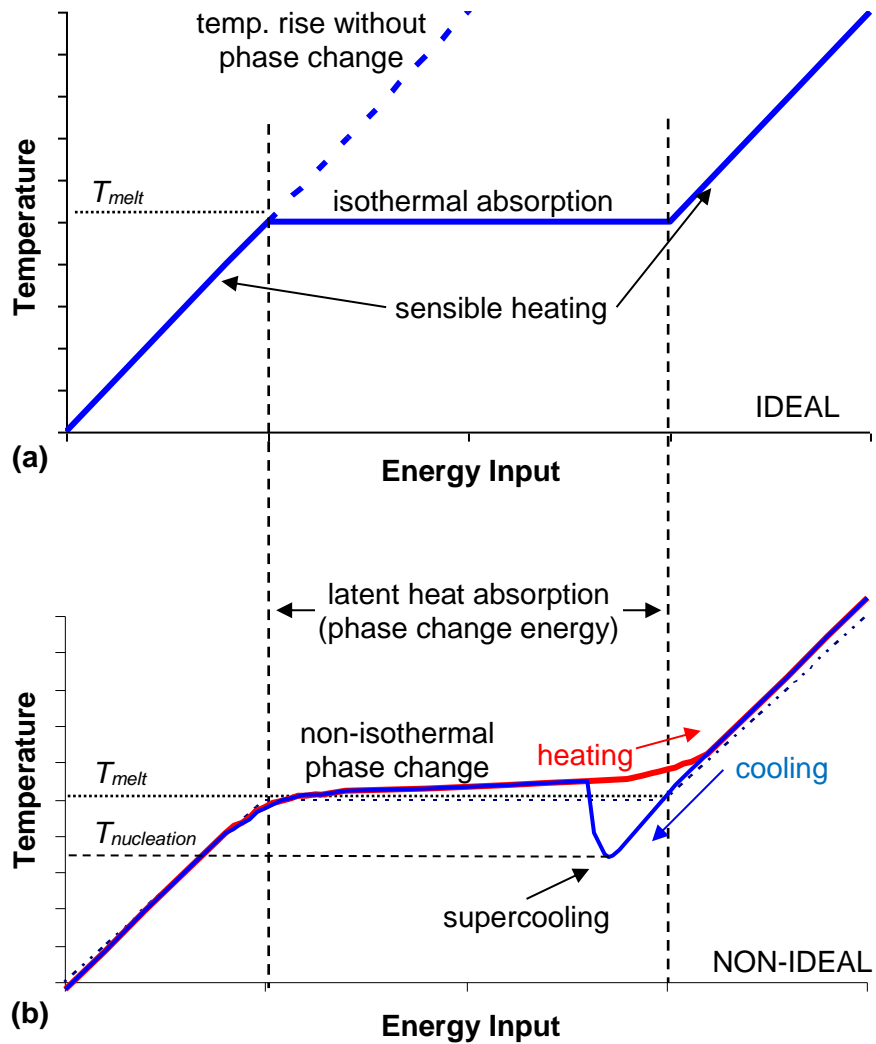


Figure 2.1 – Solid-to-liquid phase change temperature profiles. (a) Ideal, lumped mass profile, and (b) non-ideal profile showing the effects of temperature gradients, broad phase transition, and supercooling.

In reality, several non-ideal factors will affect the phase change profile, some of which are shown in Figure 2.1(b). The entire PCM volume will not usually be isothermal, and phase change will initiate at the hottest surface while other parts of the material continue warming. Thermal gradients will develop where heat is being moved across solid and liquid material to reach the phase front, which will move away from the heat source as

energy is absorbed. This will gradually increase the thermal path-length the heat source and phase front and slow the heat transfer. Additionally, some materials will not have a sharp phase transition at the melting temperature, instead melting over a temperature band. The impact of these changes is to blunt the sharp transitions at the melting temperature, and add a positive slope (small temperature increase) to the phase transition portion of the curve. Finally, some materials experience a hysteresis between the melting and cooling processes, primarily exhibited as supercooling in solid-liquid phase change, where a liquid can cool to temperatures below the nominal melting temperature before nucleation occurs. For energy storage applications, supercooling imposes an additional cooling margin that must be accommodated, decreasing system efficiency. In a thermal protection application, the supercooling concern is whether the system will be sufficiently cooled to guaranty nucleation and full solidification before the next thermal load is expected to occur. Otherwise there will be no latent absorption, liquid will heat sensibly, and temperatures may increase significantly higher than the design limits.

It is worth noting that materials can also undergo a liquid-vapor phase change and that liquid-vapor latent heat can be an order of magnitude larger than for the solid-liquid case (~2,200 kJ/kg versus 305 kJ/kg for water). However, most TES applications restrict themselves to the solid and liquid domains. Handling the heated vapor pressures that develop during liquid-vapor transition can quickly overcomplicate system structural design. Designing to accommodate cyclic pressure changes and allow for vapor overheat can quickly reduce the overall system thermal energy storage density to the point where the liquid-vapor transition loses its appeal [11].

2.3. Thermal phase change materials and properties

One of the difficulties in making use of phase change for TES or thermal buffering is the fact that PCMs have a generally fixed melting temperature. As such, there is no generalized PCM solution, and tailored material selection is required for each specific implementation. This has led the scientific community to identify almost any material with a melting transition as a potential PCM for various applications, with literally hundreds of materials and material combinations being evaluated at any one point in time. The end result of this is a PCM dataset that has become fragmented across a wide range of proceedings, texts, and publications. In fact, the International Energy Agency's *Energy Conservation through Energy Storage Implementing Agreement* working group reported that the lack of a single source for information was hindering scientific development [12]. In response, Zalba et al. compiled one of the more comprehensive material datasets up to that time from data available in the scientific literature that included 173 PCMs and referenced over 230 other reports [13]. The review, however, was limited by the fact that research up to that time focused primarily on materials with melting temperatures below 100°C, with only 28 of the materials melting at higher temperatures. Later reviews expanded the material coverage, including those by Sharma [14], Agyenim [15] and Hailiot [16], primarily between 100°C and 200°C. Later, high temperature PCM studies by Kenisarin [17], Nomura et al. [18], and Gil et al. [19] expanded the general material review all the way up to over 1000°C. In the lower temperature range, reviews by Cabeza, et al. [20], and Oró et al. [21] compiled hundreds of materials from 120°C down to well below freezing temperatures.

While these reviews, especially those occurring since the 2004 Zalba review, appear to be covering the field of PCMs, there still exists the problem of material data fragmentation, and resulting data error propagation, transcription error, and even reference traceability. Some primary material sources, primarily experimental results from meeting and workshop proceedings, have become unavailable, and much of the commercial data retained in the literature is no longer relevant. The remainder of this chapter provides a consolidated overview of material classes and selection criteria for PCMs, followed by a more detailed examination of each class of materials. Full material tables can be found in Appendix D. (Much of the information presented in the remainder of this chapter was originally published in [22].)

2.3.1. Material properties and selection criteria

Earlier PCM reviews, including those by Bentilla [11], Hale [23], Lorsch [24], and Abhat [25], provide comprehensive overviews of the design of latent heat thermal energy storage systems, including material selection, container or heat exchanger considerations, and sample applications. Common to those reviews is the identification of criteria for the selection of a particular PCM. In order of importance, the material must have:

- (a) phase change temperature in the desired operating temperature range
- (b) a high latent heat of fusion to minimize the amount of material
- (c) congruent melting so that the solid and liquid phases maintain composition
- (d) stable and repeatable phase change

Other material factors that may significantly impact design decisions are: toxicity, corrosiveness, cost, percent expansion on melting, and thermal conductivity. The first

three factors are fairly self-explanatory. Material expansion can significantly affect container design or long term reliability when not properly addressed. Whether or not thermal conductivity is a primary concern depends a great deal on how the PCM is being implemented and whether high charge/discharge rates are required. Most common PCMs have very low thermal conductivity, and would generally be called thermal insulators. This directly limits the rate at which the PCM can absorb heat, and is usually overcome using special heat exchangers, heat spreading structures, or high conductivity material additives. Models developed by Lu to create PCM performance metrics gave thermal conductivity the same weighting as latent heat, as they assumed the PCM was a bottleneck in the primary heat removal path [26]. However, several later studies have shown that placing the PCM outside the primary thermal path can allow a properly designed system to take advantage of the PCMs latent heat without severely degrading overall heat removal [27,28].

For the proper modeling or design of a PCM system, sufficient knowledge of material properties is required. At a minimum, a basic energy model requires knowing a PCM's melting temperature ($T_{M,t}$) and latent heat of fusion or transition ($H_{f,t}$). This will permit state modeling of a system where the specifics of geometry and heat transfer are unimportant. For a properly formulated transient model or simulation, the specific heat (c_p), density (ρ), and thermal conductivity (k_{th}) of the material must also be known. Preferably, the latter three properties should be known for both solid and liquid states, as some properties change significantly across a melting transition. Finally, large PCM volumes will be subject to buoyancy and convective forces upon melting and heating, and knowing the liquid state viscosity would be necessary for a high fidelity model. Almost all of these properties vary significantly with temperature, especially close to

the phase change temperature where the material will often be used, so knowledge of property-temperature dependence would complete the high fidelity material data set. This list of ‘necessary’ properties comes to quite a knowledge burden, and unsurprisingly the aforementioned material reviews only contain a portion of it, many containing no more than temperature and latent heat. This places the actual burden on each individual experimentalist to perform validation studies and property measurements for each material used. The compiled dataset here attempts to include as much of the non-temperature dependent material data as is available from the referenced sources.

2.3.2. PCM categories

Figure 2.2 provides a visual layout of the categories that will be used to describe the wide array of previously investigated PCMs. This follows the approach of most prior material reviews that classify materials by chemical type as set forth by Abhat [25], primarily dividing them into organic and inorganic materials and their major subtypes. Solid-state materials, which undergo a phase transformation with significant latent heat below the melting temperature, are broken out into a separate category because of their primary difference in phase change mode. All of these materials classes will be briefly described along with any class-specific material studies and a list of select materials with property data in that class. Where possible, organic materials listed here and in the Appendix include the *CAS Registry Number*¹ to reduce ambiguity, because of the varied and sometimes inconsistent naming of organics in the literature.

¹ *CAS Registry Number is a Registered Trademark of the American Chemical Society*

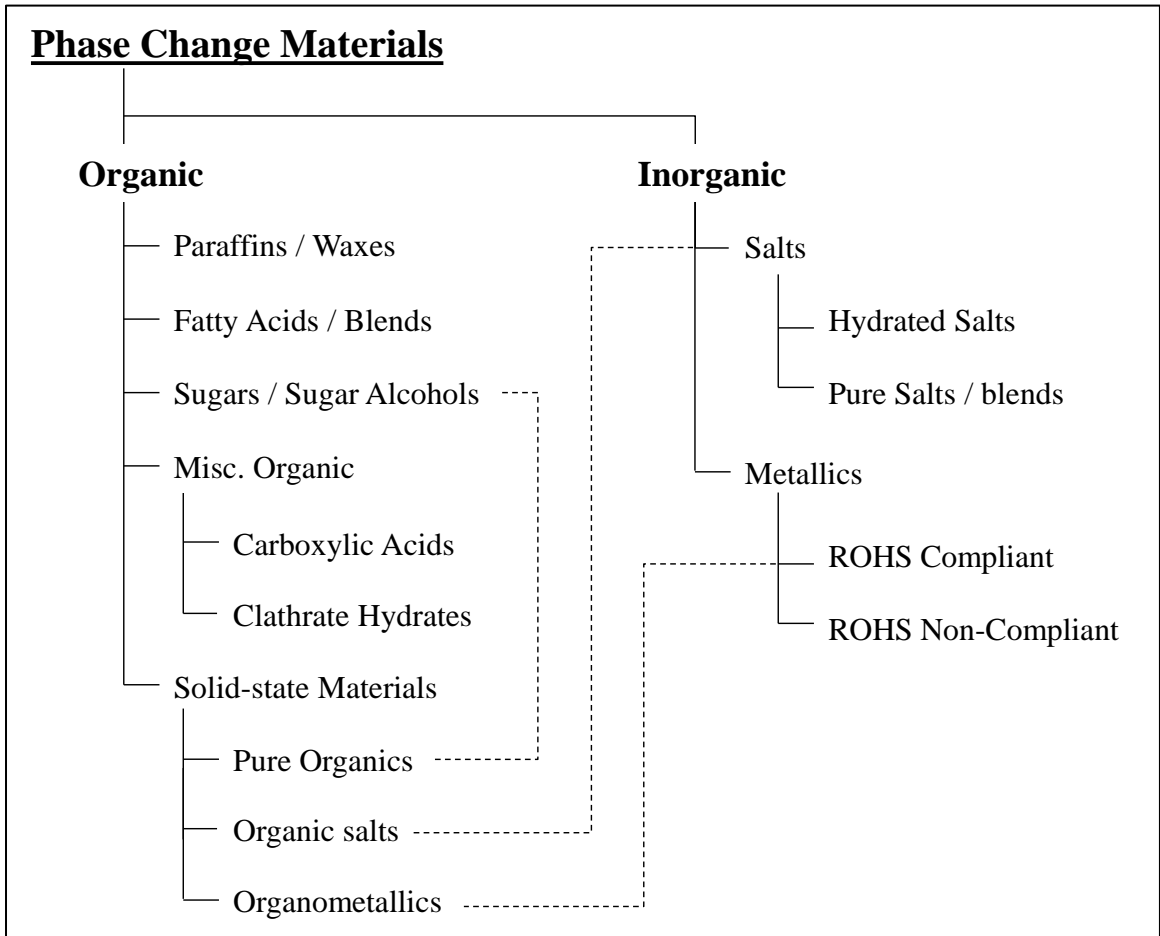


Figure 2.2 – PCM categories as used in this document, primarily split into organic and inorganic materials with dashed lines indicating areas of overlap between distinct sections.

2.3.3. Organic materials

2.3.3.1. Paraffins and paraffin waxes

Paraffins and waxes have been the most studied PCMs due to their availability over a wide range of temperatures for commercial applications, moderate latent heat, chemical compatibility, low toxicity, and relatively low cost. Pure paraffins (alkanes) are defined by a chemical composition of the form C_nH_{2n+2} (also called *n*-alkanes). Both the melting

temperature and latent heat content of the materials generally increase with increasing molecular weight. A paraffin wax is a blend of n-alkanes (typically > 75 wt%) and other hydrocarbon molecules (typically < 25 wt%). It should be noted that most paraffins are found as blends, and the process of obtaining pure, single component alkanes can make their material cost much higher than that of waxes. Additionally, blending alkanes or waxes does allow for tailoring the material to a particular melting range while broadening the phase transition width. A comprehensive study of pure alkanes as phase change materials was performed by Himran, et al., covering a range from C_1 to C_{100} with a melting range of about -183°C to 115°C , and can be found in [29]. Tables 2.1 and 2.2 give thermophysical properties for selections of pure alkanes and waxes, respectively. Full lists of both can be found in Appendix D in Tables D.1 and D.2.

Table 2.1 – Selected pure alkanes and properties

Name	n	CAS #	T_M [°C]	H_f [kJ/kg]	$H_{f,v}$ [J/cm ³]	ρ [kg/m ³]	$k_{th,s}$ [W/mK]	c_p [kJ/kgK]	Ref
Pentadecane	15	629-62-9	10	205-210	157-161	765-768 (l)	--	--	11,23,29
Octadecane	18	593-45-3	27.5-28	243-244	198-211	814-865 (s) 774-780 (l)	0.15-0.36	1.9-2.14 (s) 2.3-2.66 (l)	13,15,23, 29,30
Octacosane	28	630-02-4	61-61.6	252-254	181-189	779-803	--	--	11,23,29
Heptacontane	70	7719-93-9	106	281	235	836	--	--	29
Hectane	100	6703-98-6	115.25	285	241	846	--	--	29

Table 2.2 – Selected paraffin waxes

Name	T_M [°C]	H_f [kJ/kg]	$H_{f,v}$ [J/cm ³]	ρ [kg/m ³]	$k_{th,s}$ [W/mK]	c_p [kJ/kgK]	Ref
Paraffin blend ($n=15-16$)	8	147-153	115-119	751.6-809.5	--	--	24
"Paraffin wax"	32-32.1	251	208	830	0.514 (s), 0.224 (l)	3.26 (s) 1.92 (l)	15
"Medicinal paraffin"	40-44	146	121	830	0.5 (s), 2.1 (l)	2.2 (s) 2.3 (l)	15
"Commercial paraffin wax"	52.1	243.5	197.1	809.5(s) 771(l)	0.15	2.89 (s)	15
Beeswax	61.8	177	168	950	--	--	23

In general, there are a number of pure and blended paraffins with latent heat values that exceed 200 kJ/kg, but most blends do have much lower values. The low density of paraffins significantly reduces their volumetric latent heat values, meaning that more PCM

volume would be required for a specific amount of energy absorption. In addition most paraffins expand by 10-15% on melting, which can complicate container design. Finally, while thermal conductivity data is not available for many paraffins, the available material data shows most pure materials being below 0.25 W/mK, which will significantly reduce energy absorption and discharge rates.

2.3.3.2. *Fatty acids and related materials*

Fatty acids are obtained from naturally occurring vegetable and animal oils, which has increased attention in the materials as a potentially more sustainable PCM option relative to petroleum based paraffins [31]. They are characterized by the general formula $\text{CH}_3(\text{CH}_2)_{(n-2)}\text{COOH}$, and share many characteristics of organic paraffins including low thermal conductivity and significant expansion on melting. They typically have lower latent heat values than paraffins in similar melting ranges while having higher costs. Fatty acids are generally non-toxic, but they have shown the tendency to be mildly corrosive to their storage container [14,32]. While fatty acids are covered in some detail in most PCM reviews, Rozanna et al. performed a specific review of fatty acid materials as sustainable PCMs, covering low melting temperature applications of pure materials and tailored binary mixtures [31]. These materials and their thermal properties are shown in Table 2.3. As with paraffins, blends of fatty acids provide shifted melting temperatures, but at the cost of significantly reduced latent heat. Additionally, derivative products of fatty acids, including alcohols and esters with other compounds, have been investigated. Some have higher latent heats than their base acids, including recently reported fatty acid esters of cetyl and stearyl alcohol [33,34], although they are still generally lower than for comparable paraffins.

Thermal properties for fatty acids, blends, and derivatives of fatty acids can be found in Table D.3, Table D.4, and Table D.5 respectively.

Table 2.3 – Properties of fatty acid materials

Name	Formula	CAS #	T_M [°C]	H_f [kJ/kg]	$H_{f,v}$ [J/cm ³]	ρ [kg/m ³]	$k_{th,s}$ [W/mK]	c_p [kJ/kgK]	Ref
Caprylic acid	CH ₃ (CH ₂) ₆ COOH	124-07-2	16-16.7	148.18-	145.4-	981-1033(s)	0.145-	2.11(s)	31
- octanoic acid				149	153.9	862-901(l)	0.149	1.95(l)	
Capric acid	CH ₃ (CH ₂) ₈ COOH	334-48-5	31.5-32	152.7-	153.3-	1004(s)	0.149-	2.10(s)	31
- decanoic acid				162.83	163.5	853-886(l)	0.153	2.09(l)	
Lauric acid	CH ₃ (CH ₂) ₁₀ COOH	143-07-7	41-44.2	177.4-	178.6-	1007(s)	0.139-	1.76-2.14(s)	13,25,
- dodecanoic acid				211.6	213.1	848-870(l)	0.192	2.15-2.27(l)	31
Elaidic acid	C ₈ H ₁₇ C ₉ H ₁₆ COOH	112-79-8	47	218	185.5 (l)	851(l)	--	--	23
Myristic acid	CH ₃ (CH ₂) ₁₂ COOH	544-63-8	49-58	186.6-	184.7-	990(s)	--	1.59-2.8(s)	23,25,
- tetradecanoic acid				204.5	202.5	844-861(l)		2.16-2.7(l)	31
Pentadecanoic acid	CH ₃ (CH ₂) ₁₃ COOH	1002-84-2	52.5	178	--	--	--	--	14
Palmitic acid	CH ₃ (CH ₂) ₁₄ COOH	57-10-3	55-64	163-	161.2-	989(s)	0.103-	2.06-2.2(s)	13,23,
- hexadecanoic acid				211.8	209.5	845-850(l)	0.172	1.7-2.48(l)	31,32
Stearic acid	CH ₃ (CH ₂) ₁₆ COOH	57-11-4	55-71	186.5-	175.5-	941-965(s)	0.097-	2.07-2.83(s)	13,25,
- octadecanoic acid				210	202.7	839-848(l)	0.172	1.9-2.38(l)	31,32

2.3.3.3. Sugars and sugar alcohols

The majority of sugars and sugar alcohols, also called polyalcohols or polyols, have higher melting temperatures than other organic materials, covering the majority of the 90-200°C melting range. While sugars themselves only have moderate latent heat values, several of the sugar alcohols, primarily xylitol, erythritol, and mannitol, have much higher values than other materials in the same melting temperature range. Detailed phase transition behavior of polyalcohols was reported separately by Talja and Roos [35], and Kaizawa, et al. [36]. They noted that some of the polyalcohols have volumetric latent heat values as much as twice that of other organic materials, as shown in Table 2.4, while still possessing the non-toxic and non-corrosive properties of paraffins. They do, however, still exhibit the typical 10-15% volume expansion on melting typical of organic materials.

Table 2.4 – Sugar and sugar alcohol PCMs

Name	Formula	CAS #	T_M [°C]	H_f [kJ/kg]	$H_{f,v}$ [MJ/m ³]	ρ_s [kg/m ³]	k_{th} [W/mK]	c_p [kJ/kgK]	Ref
Glycerol	C ₃ H ₈ O ₃	56-81-5	17.9	198.7	250 (l)	1260 (l)	--	--	23
Xylitol	C ₅ H ₁₂ O ₅	87-99-0	92.7-94.5	232-263.3	353-400	1520	--	--	35,36,37
Sorbitol	C ₆ H ₁₄ O ₆	50-70-4	95-97.7	110-185	165-278	1500	--	--	35,36,37
Erythritol	C ₄ H ₁₀ O ₄	149-32-6	117-118	315-344	466-509	1480 (s) 1300 (l)	0.733 (s) 0.326 (l)	1.383 (s) 2.765 (l)	35,36,37
Glucose	C ₆ H ₁₂ O ₆	50-99-7	141	174	269	1544	--	--	23
Fructose-D	C ₆ H ₁₂ O ₆	57-48-7	144-145	145	--	--	--	--	16
Isomalt	C ₁₂ H ₂₄ O ₁₁	64519-82-0	145	170	--	--	--	--	16
Maltitol	C ₁₂ H ₂₄ O ₁₁	585-88-6	145-152	173	--	--	--	--	16
Lactitol	C ₁₂ H ₂₄ O ₁₁	585-86-4	146-152	135-149	--	--	--	--	16
Xylose-D	C ₅ H ₁₀ O ₅	58-86-6	147-151	216-280	330-428	1530	--	--	16
Xylose-L	C ₅ H ₁₀ O ₅	609-06-3	147-151	213	326	1530	--	--	16
d-Mannitol	C ₆ H ₁₄ O ₆	69-65-8	165-168	294-341	438-518	1489-1520	--	--	23,37,36
Galactitol	C ₆ H ₁₄ O ₆	608-66-2	188-189	351.8	517	1470	--	--	37

Among sugar alcohols, erythritol has received the most attention as a TES material due to its well positioned melting temperature and high latent heat [37,38]. It has been examined for applications including industrial power cogeneration and off-peak load leveling [37], solar cooking [39,40], and domestic hot water generation [14]. In addition, it was identified by the U.S. Department of Energy as a leading PCM candidate for vehicular power electronics thermal protection [41]. However, materials in this class have been shown to exhibit excessive levels of supercooling, where the material does not resolidify until cooled well below its nominal melting temperature. Chemical [42], mechanical [43], and electrical [44] methods of mitigating supercooling have been studied with some success. Additionally, these organic materials have shown a tendency to decompose at temperatures not too far in excess of their melting temperatures, which creates some concern in long term operation for some applications [36,45].

2.3.3.4. Miscellaneous organic PCMs (solid-liquid)

While the majority of organic PCM study has focused on the previously described categories, it is unsurprising that there are numerous other organic materials that have been

investigated for potential use as PCMs. Of these, certain sub-categories are of interest due to high latent heat values, melting temperatures of particular interest, or other unique properties. Table 2.5 lists a series of carboxylic acid based materials with high volumetric latent heat values at temperatures up to 160°C, but where containment and corrosion might be an issue. Table 2.6 describes a series of clathrate hydrates, ice-like structures that have fairly high latent heat values at low temperatures by shifting upward the melting point of pure ice. Finally, a wide variety of additional organic materials have been investigated for TES including polymers, ketones, phenols, amines and others. Table 2.7 provides a list of those materials with high latent heat values ($H_f > 200\text{kJ/kg}$). The full compiled list of miscellaneous organics and blends can be found in Appendix D as Tables D.7-D.10.

Table 2.5 – Carboxylic acid based PCMs

Name	CAS #	Formula	T_M [°C]	H_f [kJ/kg]	$H_{f,v}$ [MJ/m ³]	ρ_s [kg/m ³]	k_{th} [W/mK]	c_p [kJ/kgK]	Ref
Formic acid	64-18-6	HCOOH	7.8	247	303	1226.7	--	--	23
Acetic acid	64-19-7	CH ₃ COOH	16.7	187	196 (l)	1050 (l)	0.18	2.04 (s) 1.96 (l)	23
d-Lactic acid	10326-41-7	CH ₃ CHOHCOOH	26	184	230	1249	--	--	23
beta-Chloroacetic acid	79-11-8	C ₂ H ₃ ClO ₂	56	147	--	--	--	--	14
Chloroacetic acid	79-11-8	C ₂ H ₃ ClO ₂	56	130	205	1580	--	--	23
Heptadecanoic acid	506-12-7	C ₁₇ H ₃₄ O ₂	60.6	189	--	--	--	--	23
alpha-Chloroacetic acid	79-11-8	C ₂ H ₃ ClO ₂	61.2	130	--	--	--	--	14
Glycolic acid	79-14-1	HOCH ₂ COOH	63	109	--	--	--	--	23
Acrylic acid	79-10-7	CH ₂ =CHCO ₂ H	68	115	--	--	--	--	14
Phenylacetic acid	103-82-2	C ₈ H ₈ O ₂	76.7	102	--	--	--	--	14
Glutaric acid	110-94-1	(CH ₂) ₃ (COOH) ₂	97.5	156	223	1429	--	--	23
Benzoic acid	65-85-0	C ₆ H ₅ COOH	121.7	143	181	1266	--	--	23
Sebacic acid	111-20-6	(HOOC)(CH ₂) ₈ (COOH)	130-134	228	290	1270	--	--	16
Maleic acid	110-16-7	HOOC-CH=CH-COOH	131-140	235	374	1590	--	--	16
Malonic acid	141-82-2	HOOC-(CH ₂)-COOH	132-136	--	--	1620	--	--	16
trans-Cinnamic acid	140-10-3	C ₉ H ₈ O ₂	133	153	191	1250	--	--	16
Chrolobenzoic acid	118-91-2	C ₇ H ₅ ClO ₂	140	164	253	1540	--	--	16
Suberic acid	505-48-6	(CH ₂) ₆ (COOH) ₂	141-144	245	250	1020	--	--	16
Adipic acid	124-04-9	(CH ₂) ₄ (COOH) ₂	151-155	260	354	1360	--	--	16
Salicylic acid	69-72-7	HOC ₆ H ₄ COOH	159	199	287	1443	--	--	23

Table 2.6 – Clathrate hydrate materials

Name	Formula	CAS #	T_M [°C]	H_f [kJ/kg]	Ref
Tetrabutylammonium benzoate 32-hydrate	Bu ₄ NC ₆ H ₅ CO ₂ ·32H ₂ O	--	3.5	--	24
Tetrahydrofuran clathrate hydrate	C ₄ H ₈ O·17.2H ₂ O	18879-05-5	4.4	255	24
Tetrabutylammonium nitrate 32-hydrate	Bu ₄ NNO ₃ ·32H ₂ O	--	5.8	--	24
Trimethylamine semi clathrate hydrate	(CH ₃) ₃ N·10.25H ₂ O	15875-97-5	5.9	239	24
Sulfur dioxide clathrate hydrate	SO ₂ ·6.0H ₂ O	--	7	247	24
Ethylene oxide clathrate hydrate	C ₂ H ₄ O·6.9H ₂ O	--	11.1	--	24
Tetrabutylammonium bromide 32-hydrate	Bu ₄ NBr·32H ₂ O	--	11.7-12.5	193-205	24,46
Sulfur dioxide clathrate hydrate	SO ₂ ·6.1H ₂ O	--	12.1	--	24
Tetrabutylammonium formate 32-hydrate	Bu ₄ NCHO ₂ ·32H ₂ O	--	12.5	184	24
Tetrabutylammonium chloride 32-hydrate	Bu ₄ NCl·32H ₂ O	37451-68-6	14.7-15.7	200.7	24,46
Tetraisoamylammonium formate 40-hydrate	i-Am ₄ NCHO ₂ ·40H ₂ O	--	15-20	--	24
Tetrabutylammonium acetate 32-hydrate	Bu ₄ NCH ₃ CO ₂ ·32H ₂ O	--	15.1	209	24
Di-tetrabutylammonium oxalate 64-hydrate	(Bu ₄ N) ₂ C ₂ O ₄ ·64H ₂ O	--	16.8	--	24
Di-tetrabutylammonium hydrogen phosphate 64-hydrate	(Bu ₄ N) ₂ HPO ₄ ·64H ₂ O	--	17.2	--	24
Tetrabutylammonium bicarbonate 32-hydrate	Bu ₄ NHCO ₃ ·32H ₂ O	--	17.8	--	24
Tetrabutylammonium fluoride 32-hydrate	Bu ₄ NF·32H ₂ O	22206-57-1	24.9-28.3	223.1-240.5	24,46
Tetraisoamylammonium chloride 38-hydrate	i-Am ₄ NCl·38H ₂ O	--	29.8	--	24
Tetrabutylammonium hydroxide 32-hydrate	Bu ₄ NOH·32H ₂ O	147741-30-8	30.2	--	24
Tetraisoamylammonium hydroxide 40-hydrate	i-Am ₄ NOH·40H ₂ O	--	31	--	24
Tetraisoamylammonium fluoride 40-hydrate	i-Am ₄ NF·40H ₂ O	--	31.2	--	24

Table 2.7 – Miscellaneous organic PCMs with $H_f > 200$ kJ/kg

Name	CAS #	Formula	T_M [°C]	H_f [kJ/kg]	$H_{f,v}$ [MJ/m ³]	ρ [kg/m ³]	k_{th} [W/mK]	c_p [kJ/kgK]	Ref
Diethylene Glycol	111-46-6	(HOCH ₂ CH ₂) ₂ O	-10-(-7)	247	296 (l)	1200 (l)	--	--	20
Triethylene glycol	112-27-6	C ₆ H ₁₄ O ₄	-7	247	296 (l)	1200 (l)	--	--	20
Tetrahydrofuran (THF)	109-99-9	(CH ₂) ₄ O	5	280	272	970 (s)	--	--	21
Camphenilone	13211-15-9	C ₉ H ₁₄ O	39	205	--	--	--	--	23
1-Bromodocosane	6938-66-5	C ₂₂ H ₄₅ Br	40	201	--	--	--	--	23
Caprylone	818-23-5	(CH ₃ (CH ₂) ₆) ₂ CO	40	259	--	--	--	--	23
1-Cyclohexyloctadecane	4445-06-1	C ₂₄ H ₄₈	41	218	--	--	--	--	23
8-Heptadecanone	14476-38-1	C ₁₇ H ₃₄ O	42	201	--	--	--	--	23
Cyanamide	420-04-2	HNCNH	44	209	226	1080 (s)	--	--	23
2-Heptadecanone	2922-51-2	C ₁₇ H ₃₄ O	48	218	--	--	--	--	23
3-Heptadecanone	84534-29-2	C ₁₇ H ₃₄ O	48	218	--	--	--	--	23
Camphene	79-92-5	C ₁₀ H ₁₆	50	238	201 (l)	842 (l)	--	--	23
9-Heptadecanone	540-08-9	C ₁₇ H ₃₄ O	51	213	--	--	--	--	23
Hypophosphoric acid	7803-60-3	H ₄ P ₂ O ₆	55	213	--	--	--	--	23
Acetamide	60-35-5	CH ₃ CONH ₂	81	241	280	1159 (s) 999 (l)	--	--	23
Ethyl Lithium	811-49-4	LiC ₂ H ₅	95	389	--	--	--	--	23
High Density Polyethylene	9002-88-4		100-150	200-233	--	--	--	--	13,16
Catechol	120-80-9	C ₆ H ₄ (OH) ₂	104.3	207	283	1370 (s)	--	--	23
Acetanilide	103-84-4	C ₈ H ₉ NO	115-119	152-222	184-269	1210 (s)	--	--	14,23
Succinic anhydride	108-30-5	(CH ₂ CO) ₂ O	119	204	225	1104 (s)	--	--	23
Trometamol (TAM)	77-86-1	H ₂ NC(CH ₂ OH) ₃	132	285	385	1350 (s)	--	--	16
Urea	57-13-6	CO(NH ₂) ₂	133-135	170-258	228-346	1340 (s)	--	--	16
Hydroquinone	123-31-9	C ₆ H ₄ (OH) ₂	172.4	258	351	1358 (s)	--	--	23

2.3.3.5. *Solid-solid transition PCMs*

While all of the aforementioned PCMs make use of the latent heat of fusion for thermal energy storage, there are a number of materials that have distinct solid phases with significant heats of transformation. These solid-solid PCMs, also referred to as solid state, “plastic crystals”, and “dry PCMs”, avoid the engineering difficulty of managing liquid-state containment. This has the additional benefit of reducing settling or phase segregation problems for multi-constituent PCM blends or materials with additives for performance enhancement. Most of the investigated solid-state PCMs are organic materials, primarily consisting of polyalcohols, organometallics and organic salts. It is worth noting that this series of materials does not necessarily include what is typically referred to as form- or shape-stabilized PCMs, where a high melting point material is infused with a low melting point PCM. Numerous combinations comprise that material set, and are not included in this list except for form stabilized high density polyethylene (HDPE) which is included in Table 2.8 as a comparison.

A comprehensive overview of the high melting temperature polyalcohols was conducted by Benson et al., for the U.S. Department of Energy, addressing six different materials and their binary solutions [47]. Those materials plus additional single constituent solid-solid organics are listed in Table 2.8. Properties of binary solid solutions of pentaerythritol, pentaglycerine, and neopentyl-glycol are summarized in Figure 2.3, which demonstrates the ability to tailor the material for any given application over a wide temperature range.

Table 2.8 – Organic solid-state transition PCMs

Name	CAS #	T_i [°C]	H_i [kJ/kg]	T_M [°C]	H_f [kJ/kg]	H_{total} [kJ/kg]	$H_{total,v}$ [MJ/m ³]	ρ_s [kg/m ³]	$c_{p,s}$ [kJ/kgK]	Ref
Neopentane	463-82-1	-133	35.9	-16.54	45.2	81.1	--	--	--	47
Neopentyl alcohol	75-84-3	-31	50.6-53.3	51-55	45.9-46.1	96.5-99.4	--	--	2.79	47,48
Neopentyl glycol	126-30-7	40-48	110.4-131	125-126	44.2-45.3	--	46.8-48.0	1060	--	23,47,48
Diaminopentaerythritol	36043-16-0	68	184	--	--	--	--	--	--	23
Ammediol	115-69-5	78-80	223.9-264	110-112	28-31.7	251.9-295.7	--	--	1.79	23,47,48
Nitroisobutylglycol	77-49-6	79-80	190-201	149-153	28-32	218-233	--	--	--	23,47
Tris(hydroxymethyl) Nitromethane	126-11-4	80-82	149	--	--	--	--	--	--	47
Pentaglycerine	77-85-0	81-89	139-193	197-198	44.6-46	--	51.7-56.1	1160-1220	1.71	23,47,48
Monoaminopentaerythritol	36043-15-9	86	192	--	--	--	--	--	--	23
Tris(hydroxymethyl) acetic acid	2831-90-5	124	205	--	--	--	--	--	--	23
Tris(hydroxymethyl)-aminomethane	77-86-1	131-135	269.9-285.3	166-172	25-27.6	294.9-312.9	--	--	1.80	23,47,48,49
Form-stable HDPE	9002-88-4	133	188	--	--	--	--	960	--	47
Dimethylolpropionic acid	4767-03-7	152-155	287-289	194-197	26.8-27	313.8-316	--	--	--	23,47
Pentaerythritol	115-77-5	182-188	269-303.3	258-260	36.8-37.2	325.8-340.5	452.9-473.3	1390	--	23,47,48,49

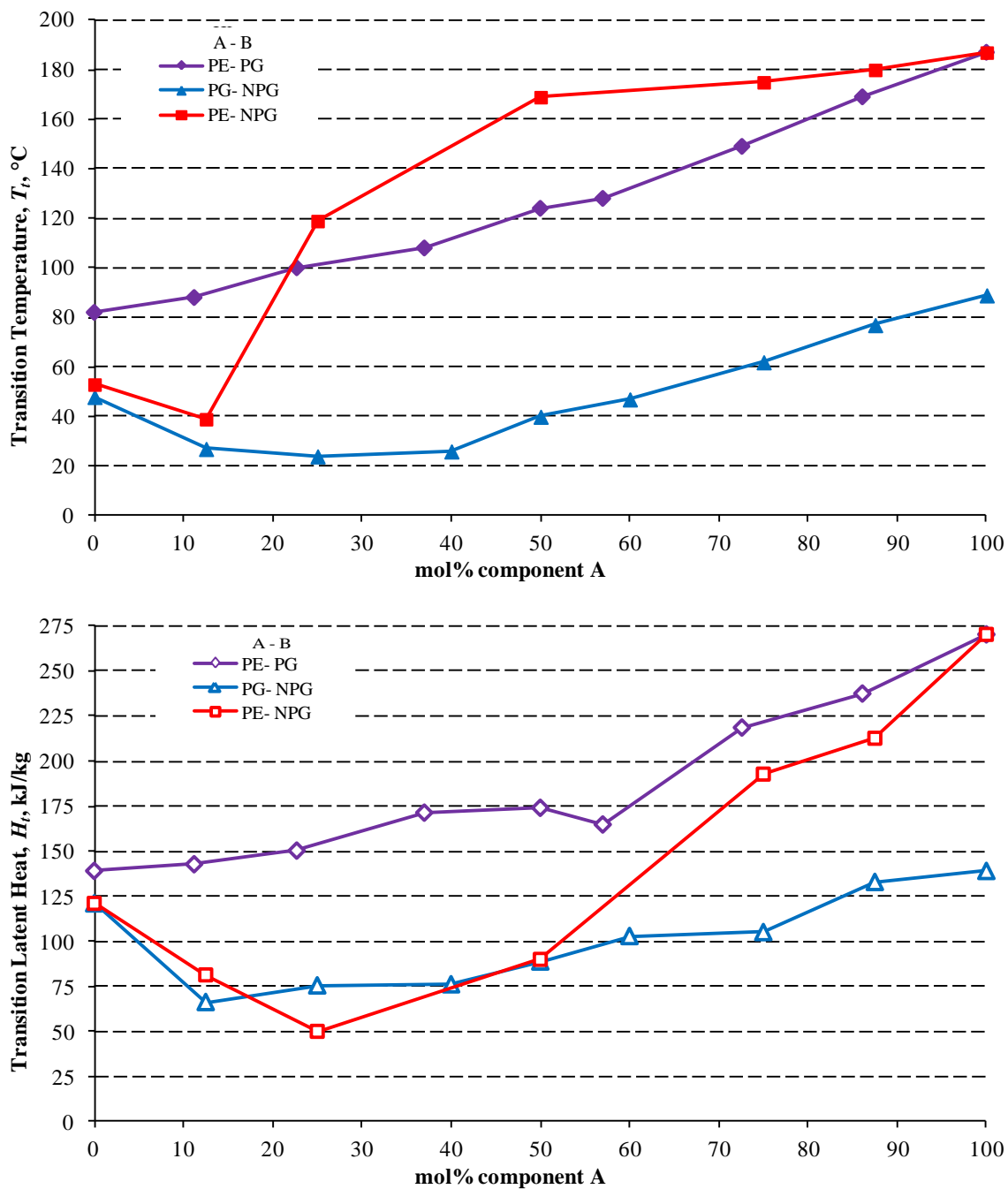


Figure 2.3 – pentaerythritol, pentaglycerine, and neopentyl glycol binary blend solid-solid transition temperatures and latent heat values as a function of the composition as reported by [47].

Properties of a series of organometallic compounds called layered perovskites, represented as $(n\text{-C}_n\text{H}_{2n+1}\text{NH}_3)_2\text{MX}_4$, where M is a metal atom, X is a halogen, and n varies

from 10 to 16, have been characterized in several reports for $X = \text{Cl}$, shown in Table 2.9 (designated in the table as C_nM) [50-52]. Binary mixtures of a number of these materials show behavior similar to the aforementioned polyalcohol blends, with the ability to adjust transition temperature for a $\text{C}_{10}\text{-C}_{16}\text{Co}$ blend from 77-100°C [53].

Table 2.9 – Layered perovskite solid-solid PCMs

Name	CAS #	T_i^a [°C]	H_i [kJ/kg]	$H_{i,v}$ [MJ/m ³]	ρ_s [kg/m ³]	Ref
C_{10}Mn	58675-50-6	32.8	70.3	--	--	50
C_{10}Cu	--	33.8-36.9	62.6	--	--	50
C_{12}Cu	71163-11-6	52.5-63.8	70.2, 147.1 ^a	77.9, 163.5	1111	50,51
C_{12}Mn	75899-75-1	54.1-56.4	80.8	--	--	50
C_{12}Co	56104-91-7	60.7-88.0	92.9	--	--	50
C_{14}Cu	--	69.2-79.5	164.0	194.5	1186	52
C_{15}Cu	--	72.3-87.8	126.4	157.4	1245	52
C_{16}Cu	63643-59-4	72.8-96.0	79.8	--	--	50
C_{16}Mn	53290-99-6	73.1-91.0	104.5	--	--	50
C_{10}Co	56104-89-3	77.7, 82	74.3	--	--	50,53
C_{10}Zn	--	80.1-162.8	100.9	--	--	50
C_{12}Zn	57947-14-5	88.2-156.0	120.2	--	--	50
C_{16}Co	56104-95-1	93.4-164.1	153.8	--	--	50,53
C_{16}Zn	57947-17-8	99.1-160.5	137.5	--	--	50

a – multiple latent heat values represent discrepancy in reported heat release data between sources.

Finally, Steinert, et al., measured solid-solid transition characteristics of a number of dialkyl ammonium salts of the form $\text{C}_{2n}\text{H}_{4n}\text{XNH}_4$, with X being a salt anion, which exhibited solid-solid phase transitions from -2 to 190°C and transition enthalpies up to 186 kJ/kg, shown in Table 2.10 [54]. Many of the materials of these sets exhibit multiple, discrete solid-solid transitions over the ranges shown, with the listed latent heat being the sum over those transitions.

Table 2.10 – Dialkyl ammonium salt solid-state PCMs – from [54]

Name	Formula	T_i [°C]	H_i [kJ/kg]
dioctylammonium iodide	DC ₈ I	-2-6 ^a	58
dioctylammonium hydrogen sulfate	DC ₈ HSO ₄	16-190 ^a	30
dioctylammonium chloride	DC ₈ Cl	21	132
dioctylammonium perchlorate	DC ₈ ClO ₄	23	108
dioctylammonium bromide	DC ₈ Br	30	78
dioctylammonium chlorate	DC ₈ ClO ₃	32	122
dioctylammonium nitrate	DC ₈ NO ₃	45	176
didecylammonium chloride	DC ₁₀ Cl	48	119
dioctylammonium dihydrogen phosphate	DC ₈ H ₂ PO ₄	50-70 ^a	--
didecylammonium chlorate	DC ₁₀ ClO ₃	55.5	154
didecylammonium bromide	DC ₁₀ Br	57	100
didecylammonium nitrate	DC ₁₀ NO ₃	60	179
didodecylammonium chlorate	DC ₁₂ ClO ₃	61.5	159
didodecylammonium perchlorate	DC ₁₂ ClO ₄	62	159
didodecylammonium iodide	DC ₁₂ I	65	80
didodecylammonium chloride	DC ₁₂ Cl	65	123
didodecylammonium nitrate	DC ₁₂ NO ₃	66	185
dioctadecylammonium hydrogen sulfate	DC ₁₈ HSO ₄	70-82 ^a	176
didodecylammonium bromide	DC ₁₂ Br	73	113
didodecylammonium hydrogen sulfate	DC ₁₂ HSO ₄	74-100 ^a	66.5
didecylammonium dihydrogen phosphate	DC ₁₀ H ₂ PO ₄	81	153
dioctadecylammonium chlorate	DC ₁₈ ClO ₃	84-91 ^a	154
dioctadecylammonium perchlorate	DC ₁₈ ClO ₄	88.1	185
didodecylammonium dihydrogen phosphate	DC ₁₂ H ₂ PO ₄	90	183
dioctadecylammonium chloride	DC ₁₈ Cl	91.2	174
dioctadecylammonium iodide	DC ₁₈ I	93	116
dioctadecylammonium nitrate	DC ₁₈ NO ₃	93.5	186
dioctadecylammonium bromide	DC ₁₈ Br	98	135

^a – range in temperatures indicates multiple phase transitions over the range. H_i is total over all transitions.

2.3.4. Inorganic materials

2.3.4.1. Hydrated and aqueous salts

The inorganic PCMs receiving the most attention in the literature are hydrated salts, as they span a melting temperature range similar to paraffins and fatty acids. A hydrated salt is a solution of salt and water that forms a stable crystal with chemical formula $M \cdot n\text{H}_2\text{O}$, where M is the salt molecule and n represents the number of coordinate water molecules in the crystal. Salt hydrates do not melt in the traditional sense. Instead, upon heating a dehydration process occurs where the water molecules come out of the solid solution with an associated latent heat absorption. One drawback to this process is that during dehydration the salt may assume another stable form with a lower n and excess

water, and this new salt hydrate can settle out of solution. This can be an irreversible process, reducing the effective latent heat of a PCM system over time [55].

Early uses of salt hydrates for solar and climate control applications were covered extensively by Lane [56]. These materials generally have higher latent heats, densities, and thermal conductivities than paraffins and fatty acids and are also relatively inexpensive [14]. In addition to the segregation issue described above, significant supercooling and container corrosion is also an issue with salt hydrates. Additional studies have shown that common materials like stainless steel are resistant to corrosion from salts undergoing phase change [57]. More recent studies of polymer materials for lower temperatures [58] and ceramics for higher temperatures [59] suggest that appropriate, lighter weight materials can be found for salt hydrate compatibility. As with the organic materials, blends of hydrated salts permit tailoring melting temperature for a particular application, but usually at reduced effective latent heat. A number of salt hydrates with high latent heat values are listed in Table 2.11 (with pure water included as a reference). A full listing of salt hydrates and salt hydrate blends are available in Appendix D as Table D.14-D.15. Note that also included in this category are aqueous salt mixtures, where the salt mainly serves to lower the freezing temperature of the water, usually with an associated reduction in latent heat. These are quite commonly used in freezing and refrigeration applications.

Table 2.11 – Salt/water and Salt Hydrate PCM candidates, $H_f > 200$ kJ/kg or $H_{f,v} > 300$ MJ/m³

Name	T_M [°C]	H_f [kJ/kg]	$H_{f,v}$ [MJ/m ³]	ρ [kg/m ³]	k_{th} [W/mK]	c_p [kJ/kgK]	Ref
NaCl (22.4 wt%) +H ₂ O	-21.2	222	246.0	1108 (s) 1165 (l)	--	--	20
KCl (19.5 wt%) +H ₂ O	-10.7	283	312.7	1105 (s) 1126 (l)	--	--	20
H ₂ O	0	333- 335	305-307	917 (s) 990-1000 (l)	2.2-2.4 (s) 0.57-0.61 (l)	2.04-2.09(s) 4.18-4.21(l)	13,25, 23,15
Lithium Chlorate Trihydrate (LiClO ₃ ·3H ₂ O)	8.1	253	435.2	1720 (s)	--	--	13
Potassium Fluoride Tetrahydrate (KF·4H ₂ O)	18.5	231- 246	336-358	1439-1455 (s) 1445-1447 (l)	0.608-0.672 (s) 0.479-0.493 (l)	1.41-1.84(s) 2.39-2.68(l)	25,60
Calcium Chloride Hexahydrate (CaCl ₂ ·6H ₂ O)	27.45- 30	161.15- 192	272-346	1682.4-1802 (s) 1496-1620 (l)	1.088 (s) 0.53-0.56 (l)	1.4 (s) 2.2 (l)	13,15, 24,32
Lithium Nitrate Trihydrate (LiNO ₃ ·3H ₂ O)	29.6- 29.9	296	460	1550 (s) 1430 (l)	0.8 (s) 0.56 (l)	1.8 (s) 2.8 (l)	23,61
Sodium Sulfate Decahydrate, Glauber's Salt (Na ₂ SO ₄ ·10H ₂ O)	31- 32.4	251.1- 254	372	1485 (s) 1458-1460 (l)	0.544 (s)	1.93 (s)	13,25, 23
Sodium Carbonate Decahydrate (Na ₂ CO ₃ ·10H ₂ O)	32- 36	246.5- 251	355-362	1440-1442 (s)	--	--	13,23, 32
Calcium Bromide Hexahydrate (CaBr ₂ ·6H ₂ O)	34	115.5- 138	253-303	2194 (s) 1956 (l)	--	--	13,14
Disodium Hydrogen Phosphate Dodecahydrate (Na ₂ HPO ₄ ·12H ₂ O)	35- 40	265- 281	422-427	1507.1-1522 (s) 1442 (l)	0.514 (s) 0.476 (l)	1.69 (s) 1.94 (l)	13,14,25, 23,24
Iron Chloride Hexahydrate (FeCl ₃ ·6H ₂ O)	37	226	--	--	--	--	23
Sodium Thiosulfate Pentahydrate (Na ₂ S ₂ O ₃ ·5H ₂ O)	45- 51.3	200- 217.2	344-376	1720-1730 (s) 1660-1690 (l)	375.756 (s)	1.46 (s) 2.39 (l)	23,25, 24,32
Magnesium Sulfate Heptahydrate (MgSO ₄ ·7H ₂ O)	48.4	202	--	--	--	--	14
Sodium Acetate Trihydrate (Na(CH ₃ COO)·3H ₂ O)	58- 58.4	226-264	--	--	--	--	13
Lithium Acetate Dihydrate (Li(CH ₃ COO)·2H ₂ O)	58- 70	150-377	--	--	--	--	14,23
Sodium Hydroxide Monohydrate (NaOH·H ₂ O)	64.3	227.6-272	385-468	1690-1720 (s)	--	--	13,23
Barium Hydroxide Octahydrate (Ba(OH) ₂ ·8H ₂ O)	78	265.7-301	657	2070-2180 (s) 1937 (l)	1.255 (s) 0.653-0.678 (l)	1.17 (s)	13,23
Ammonium Aluminum Sulfate Hexahydrate (NH ₄)Al(SO ₄)·6H ₂ O	95	269	--	--	--	--	13

2.3.4.2. Fused/molten salts and blends

For high temperature applications, salt-based PCMs provide the largest selection of available materials above 200°C. Salt PCMs, also called fused or molten salts depending on whether they are used primarily in the solid or liquid state, have been characterized with melting temperatures spanning from around 100°C to in excess of 1500°C. A large number of these materials have been investigated for use as PCMs, including a large number of combinations of salt blends. Unfortunately, thermal property data in the PCM literature do not extend beyond melting temperature and latent heat for the majority of these materials, making full evaluation difficult. Salts generally have fairly high density and thermal

conductivity, at least relative to other materials studied thus far, but corrosiveness is a significant concern, and measured melting expansions for different salts vary between 1 and 30% [17]. Table 2.12 lists a set of high latent heat salts up to 600°C. The full list of salts up to 1000°C plus the studied salt blends can be found in Tables D.16 and D.17. Note that latent heat tends to increase with melting temperature, meaning high temperature salts can exceed heat storage density of other materials by as much as 2-3x.

Table 2.12 – Select Salt PCMs up to 600°C with $H_f > 300$ kJ/kg or $H_{f,v} > 450$ MJ/m³

Name	T_M [°C]	H_f [kJ/kg]	$H_{f,v}$ [MJ/m ³]	ρ_s [kg/m ³]	k_{th} [W/mK]	c_p [kJ/kgK]	Ref
Aluminum Chloride (AlCl ₃)	192-192.4	272-280	664-683	2440	--	--	32
Lithium Nitrate (LiNO ₃)	250-254	360-373	857-888	2380	--	--	18,17,32,62
Sodium Nitrate (NaNO ₃)	306-310	172-199	388-450	2257-2261	0.5 (s)	1.1 (s)	18
						1.82 (l)	
Potassium Nitrate (KNO ₃)	330-336	88-266	186-561	2109-2110	0.5 (s)	0.935 (s)	13,63
					0.5 (l)	1.22 (l)	
Sodium Peroxide (Na ₂ O ₂)	360	314	--	--	--	--	32
Lithium Hydroxide (LiOH)	462	875	1269	1450	--	--	18,62
Potassium Perchlorate (KClO ₄)	527	1253	3158	2520	--	--	32.62

2.3.4.3. Metals and alloys

A metallic PCM presents a significantly different engineering challenge for designing thermal energy storage systems. Their high densities and low specific latent heat (kJ/kg) make them unsuitable for large volume or weight sensitive applications. Because of this, metals and alloys have only received cursory attention in the lower temperature PCM review literature, primarily by Hale [23], with Gasanaliyev providing some data on lower temperature Gallium-based metals [64], and Kenisarin providing slightly more focus for high temperatures [17]. Only recently did a review by Ge, et al., address in detail how low melting temperature metallic PCMs can be promising alternatives to traditional organic and inorganic materials due to their unique properties [65]. While the high density creates weight concerns, it does mean that their volumetric latent heat values can be much higher than comparable materials, and the thermal conductivity of most metals is at least one or

two orders of magnitude higher than most other PCMs. This can reduce the need for heat spreaders, ease system design, and may be the key to using PCMs to address high speed transients.

One significant concern for metallic PCMs is the relative toxicity or environmental impact of the constituent metals. The majority of metallic PCMs actually studied for TES or electronics protection were lead based, making them non-compliant with current Restriction of Hazardous Substances (RoHS) directives. This impacts a large number of high latent heat, lower melting temperature metals. Listed in Table 2.13 are PCM candidate metals containing materials (typically lead or cadmium) that render them RoHS non-compliant. Select RoHS compliant metals are listed in Table 2.14. It is worth mentioning that hundreds of low temperature solder formulations exist for both RoHS compliant and non-compliant categories, but very few have been characterized for thermal phase change. Further property measurement of low melting temperature alloys could significantly expand the number of metallic PCM options. A full list of metallic materials can be found in Appendix D, in Tables D.18-D.19, which includes a list of 235 materials from the Indium Corporation low temperature solder database that currently lack sufficient material data for immediate use in thermal applications [66].

Table 2.13 – RoHS non-compliant metallic materials

Formula (Name)	T_M [°C]	H_f [kJ/kg]	$H_{f,v}$ [MJ/m ³]	ρ_s [kg/m ³]	$k_{th,s}$ [W/mK]	$c_{p,s}$ [kJ/kgK]	Ref
Mercury	-38.87	11.4	154.4 (l)	13546	8.34	0.139	65,67
74Ga/22Sn/4Cd	20.2	75.2	449.9	5983	--	--	64
93Ga/5Zn/2Cd	24.6	85.03	511.9	6020	--	--	64
44.7Bi 22.6Pb 19.1In 8.3Sn 5.3Cd	47	36.8	337	9160	15	0.163 (s) 0.197 (l)	66
Bi/Pb/Sn/In ^a	57	29.5	267	9060 (s) 8220 (l)	33.2 (s) 10.6 (l)	0.323 (s) 0.721 (l)	68
47.5Bi 25.4Pb 12.6Sn 9.5Cd 5In	57-65	36	341	9470	15	0.159 (s) 0.188 (l)	66
49Bi 21In 18Pb 12Sn (Cerrow Eutectic)	58	28.9	260	9010	10	0.167 (s) 0.201 (l)	23,66
33Bi/16Cd/51In	61	25	201-251	8040-10040	--	--	23
50Bi 26.7Pb 13.3Sn 10Cd (Wood's metal)	70	32.6-45.8	287-439	9400-9580	18-19	0.146-0.167 (s) 0.167-0.184 (l)	23,66,64
52Bi/26Pb/22In	70	29	234-293	8069-10103	--	--	23
42.5Bi 37.7Pb 11.3Sn 8.5Cd	71-88	34.3	336.483	9810	--	0.146 (s)	66
52Bi 30Pb 18Sn	96	34.7	333	9600	13	0.151 (s) 0.167 (l)	66
55.5Bi 44.5Pb	124-125	20.9	218	10440	4	0.126 (s) 0.155 (l)	23,66
85Pb 10Sb 5Sn	245-255	0.9	9	10360	--	0.15 (s)	66

a – specific formulation unknown

Table 2.14 – Select RoHS Compliant metallic materials up to 600°C

Formula (Name)	T_M [°C]	H_f [kJ/kg]	$H_{f,v}$ [MJ/m ³]	ρ_s [kg/m ³]	$k_{th,s}$ [W/mK]	$c_{p,s}$ [kJ/kgK]	Ref
67Ga-20.5In-12.5Zn	10.7	67.2	415	6170	--	--	64
78.55Ga-21.45In	15.7	69.7	432	6197	--	--	64
82Ga-12Sn-6Zn	18.8	86.5	516	5961	--	--	64
86.5Ga-13.5Sn	20.55	81.9	482	5885	--	--	64
96.5Ga-3.5Zn	25	88.5	526	5946	--	--	64
Gallium	29.8-30	80.3	469	5903 (s) 6093 (l)	33.7 (s) 24 (l)	0.34 (s) 0.397 (l)	23,65,66,67
66.3In 33.7Bi	72	25	200-203	7990-8100	--	--	23,66
60Sn 40Bi	138-170	44.4	361	8120	30	0.18 (s) 0.213 (l)	66
58Bi 42Sn	138.3	44.8	384	8560	19	0.167 (s) 0.201 (l)	66
Indium	156.7	28.47	208	7310	86	0.243	65,66,67
91Sn 9Zn	199	71.2	518	7270	61	0.239 (s) 0.272 (l)	66
46.3Mg 53.7Zn	340	185	851	4600	--	--	65,66,67
96Zn-4Al	381	138	915	6630	--	--	17,64
59Al-35Mg-6Zn	443	310	738	2380	--	1.63 (s) 1.46 (l)	17,64
60Mg-25Cu-15Zn	452	254	711	2800	--	--	17
64.6Al-5.2Si-28Cu-2.2Mg	507	374	1646	4400	--	--	17,64
66.92Al-33.08Cu	548	372	1339	3600	--	--	17,64
87.76Al-12.24Si	557	498	1265	2540	--	--	17,64
46.3Al-4.6Si-49.1Cu	571	406	2257	5560	--	--	17,64
88%Al-12%Si	576	560	1512	2700	160	1.038 (s) 1.741 (l)	17

2.3.4.4. Comments on commercial materials in the literature

The majority of materials described in previous sections were sufficiently generic in description such that the actual material sources should be unimportant. However, decades of PCM literature contain reports on properties and thermal performance of a large number of commercial proprietary materials. While such reporting provides an overview of the range of available materials, the value of such information is tied directly to its age, traceability, and verifiability. This renders much of their continued inclusion in academic literature of little use due frequent invalidation of traceability from corporate/manufacturing changes, lack of a persistent archival reference, or even current unavailability of the products.

Three specific examples were encountered when compiling the materials in this chapter that highlight these problems. First, the paraffin blend P-116 (SunTech P116 or Wax, originally produced by the Sun Oil Company, later Sunoco, Inc.) has been heavily cited in application studies over the past 30 years [25, 29, 69-71], in addition to many of the aforementioned reviews. However, this material has not been commercially produced since 2006, and Sunoco has since sold off its specialty wax product line to another company [Nancy Wright and Jennifer Hall, HollyFrontier Corp., personal communication, January 29, 2013]. Second, no longer available is the TH-series of PCMs from TEAP Energy (Perth, Australia) reported in many reviews but only by citing the corporate website, which was bought by a completely unrelated PCM company sometime around 2009 (PCM Energy P, Ltd., Mumbai, India). It appears TEAP Energy re-incorporated as Phase Change Products Pty, Ltd., and has some similar products, but all previous TH-series references are misleading dead-ends. Finally, Environmental Process Systems, Ltd. (EPS,

Ltd.) still produces PCM solutions, but its oft-cited E-series PCM line is no longer advertised. Its current PCMs appear to be sourced from PCM Products, Ltd. which does provide an extensive material set, but even if the E-series is just rebranded, the material properties cannot be simply traced to those reported for EPS in previous reviews. Material data from all three examples have propagated through material reviews as recently as 2017.

Because material data in archival reports should maintain traceability to the best extent possible, these materials are only included in Appendix D as Tables D.22 and D.23 for historical reference.

2.3.5. Material comparisons

The previous sections have described numerous options for phase change materials from numerous classes over a wide range of temperatures, but stop short of identifying any particular option as being more or less advantageous for use. The primary reason for this is that the wide range of potential PCM applications makes it impossible to state definitively whether a material will even be viable, yet alone optimal, for any particular case. That said, comments can be made about the materials in aggregate that may be useful in guiding future selection decisions. The following subsections compare the different classes based on their available thermal properties.

2.3.5.1. Melting Temperature

The property with the most influence on PCM selection for any particular application is the melting or transition temperature. While an application may be amenable to a small band for melting temperature, this value is generally fixed for any given material. Blending material provide some tunability to this property, but most reviews have shown

that doing so leads to a reduced latent heat (sometimes even below the weight based average). That said, there are numerous materials available over a wide range in temperatures, where the previous sections and the Appendix describe over 800 such materials spanning about 1000°C.

Metallic materials are the only class that spans the full range of these temperatures. Numerous salt hydrates are available below 125°C, with pure salts providing a range of options above 200°C, and organics almost completely span the sub-200°C temperature range. Figure 2.4 depicts the temperature span of surveyed PCMs according to category in order of median material temperature, while Figure 2.5 shows the distribution of surveyed materials over the temperature span. Apparent in the two figures is the abundance of materials in the sub-100°C temperature range, including the variety of material class options available. As previously mentioned, increased thermal analysis of metallic options over the full temperature span could significantly increase the number of viable material options for PCM designers.

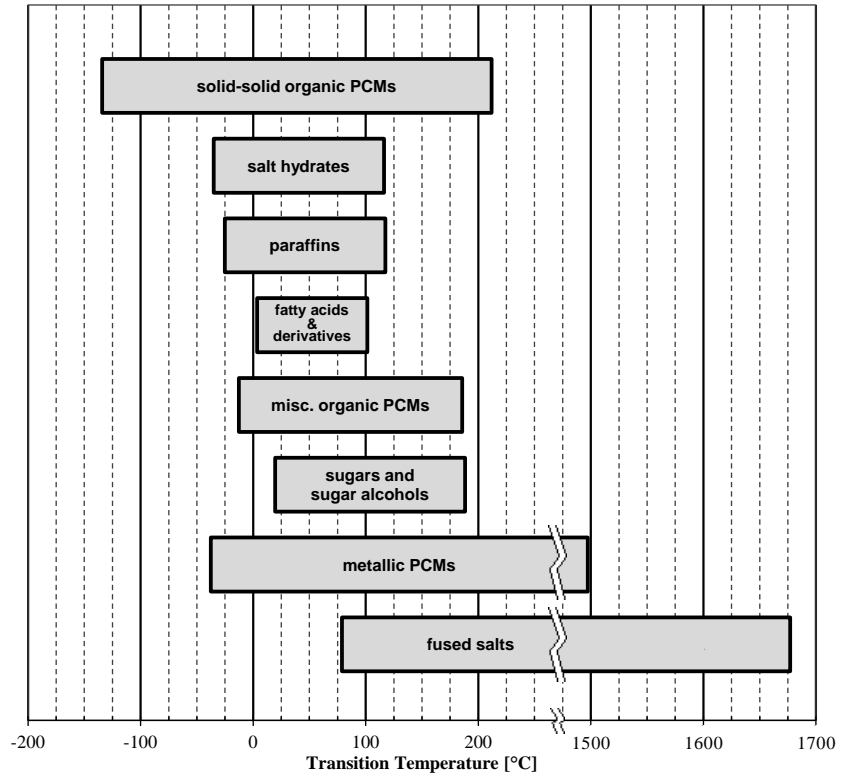


Figure 2.4 – Melting/Transition temperature spans of materials in the surveyed PCM literature sorted by median transition temperature.

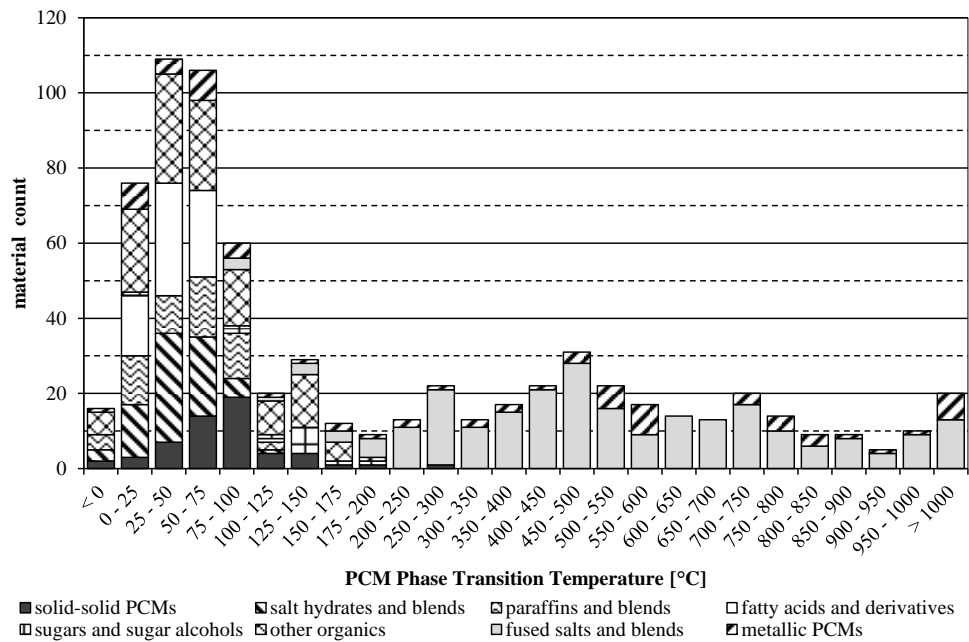


Figure 2.5 – Melting/transition temperature distribution over the surveyed materials

2.3.5.2. Latent heat of fusion

Given several materials to choose from within an acceptable temperature band, the latent heat of melting/solidification will usually serve as the next major selection factor. Historically, the primary measure of fitness for any material has been its specific latent heat value (latent heat per unit mass, e.g., kJ/kg). As a measure of how much energy is required for melting, a higher value generally translates into a lighter, smaller, less expensive packaging solution. Less PCM also reduces the size of the container and any heat spreading solution used to increase heat transfer.

While specific latent heat has been the most common metric, and is often the only one listed in material datasets, volumetric latent heat ($H_{f,v} = H_f \times \rho$, in MJ/m³) can be more useful for certain applications. In addition it may result in a significantly different material evaluation. For example, metallics have been all but ignored for thermal energy storage applications due to their low specific latent heat and high density. Use in a high energy mobile system could result in a prohibitively heavy TES component. However, because of the high density, most metals have a much higher volumetric latent heat than other materials in the same temperature range. In a lower energy, high power system, or one where compact form-factor is important, a higher volumetric latent heat could reduce the space required for PCM, with associated reductions in package/container and heat spreading volume.

Both specific and volumetric latent heats of the materials listed in Appendix D (for which sufficient material property information is available) are shown in Figure 2.6 for melting temperatures up to 250°C. Similarly, Figure 2.7 shows latent heats values for materials up to 1000°C.

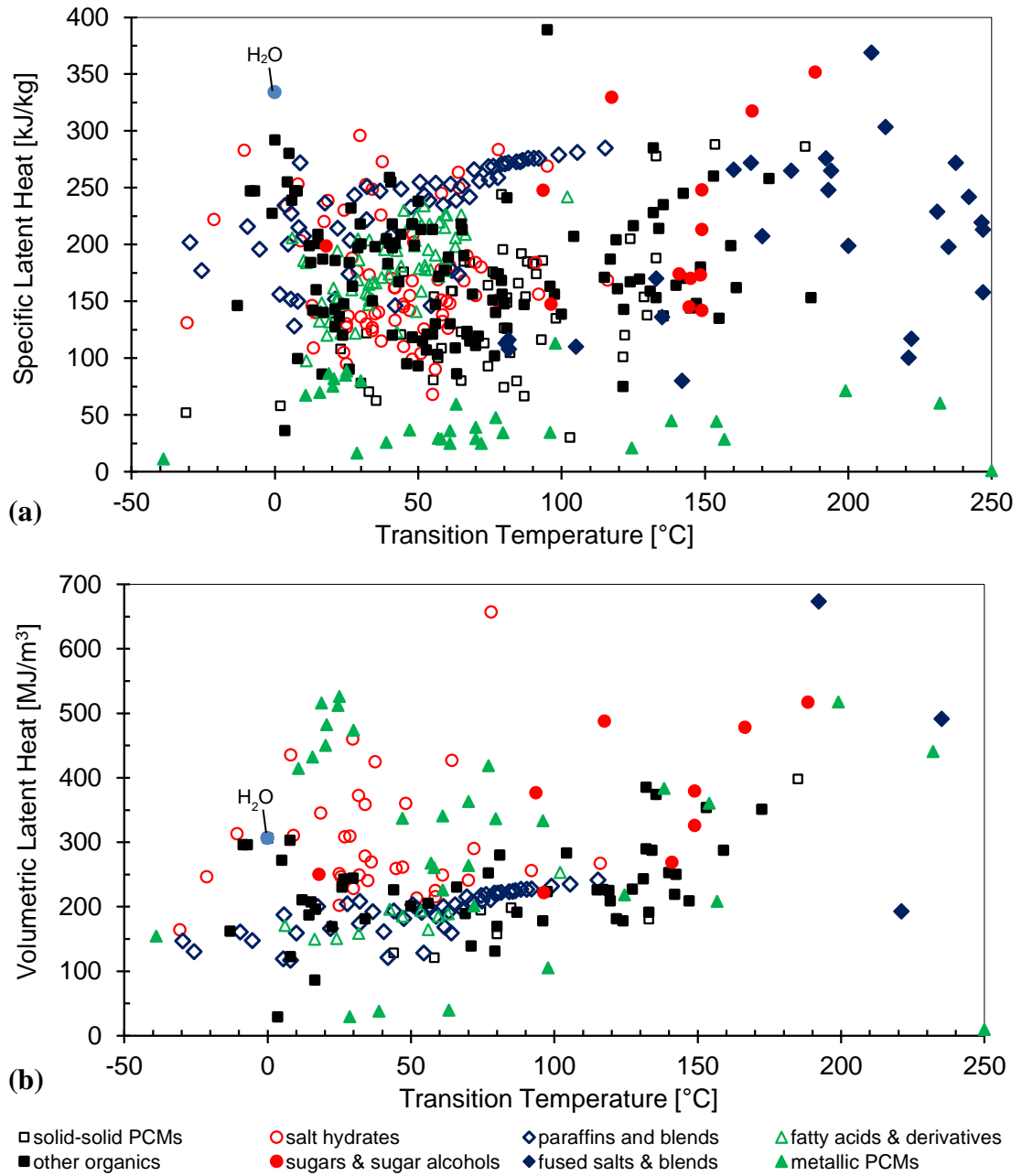


Figure 2.6 – Median (a) specific and (b) volumetric latent heats for materials up to 250°C.

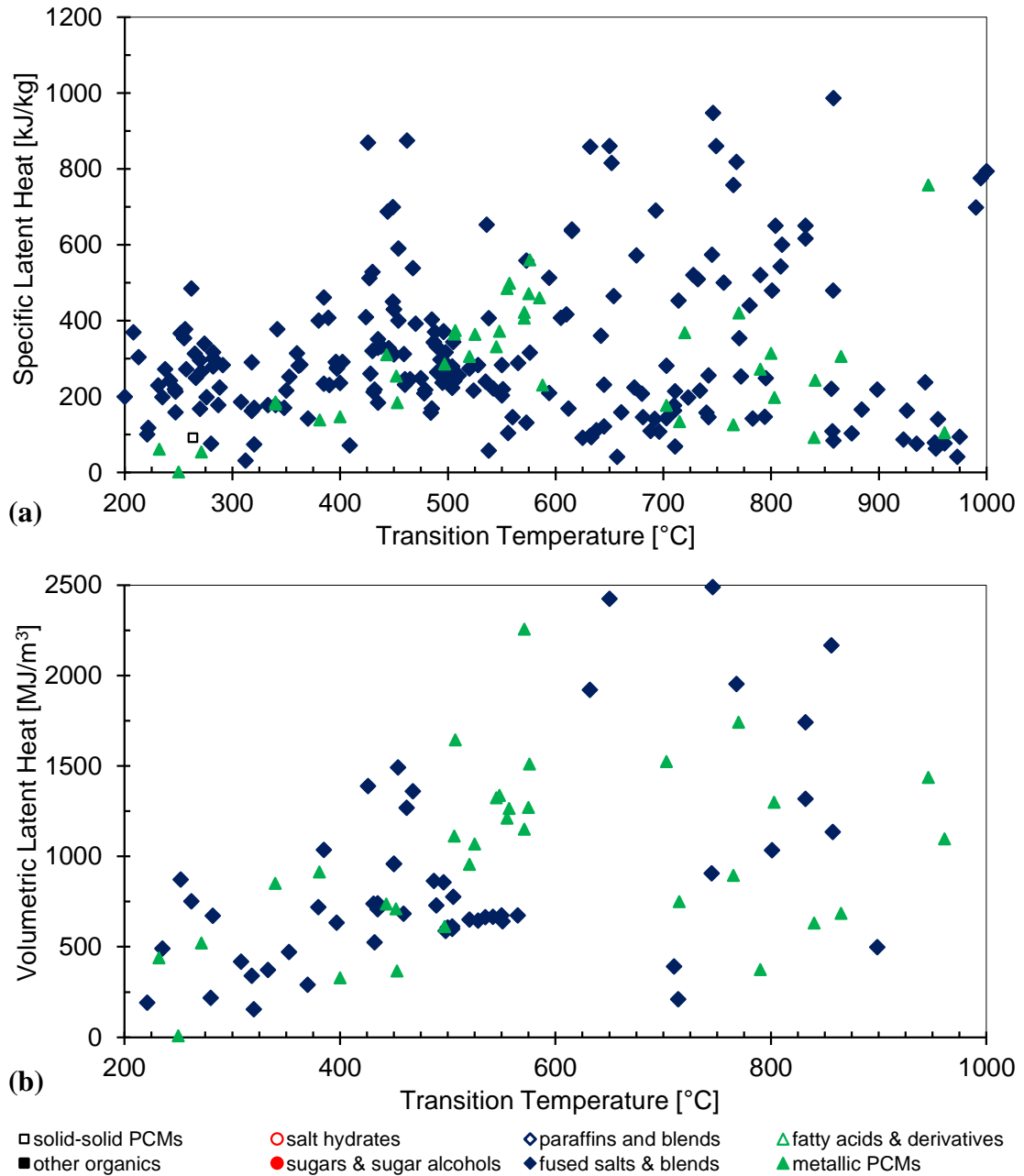


Figure 2.7 – Median (a) specific and (b) volumetric latent heats for materials from 200-1000°C.

It should be noted how Figure 2.6 highlights the inversion that can occur between specific and volumetric latent heat. In Figure 2.6(a), the paraffins are all near the top of the specific latent heat chart for the materials up to about 100°C, whereas the metallic materials are almost all near the bottom. This relationship is nearly reversed in the

volumetric latent heat chart in Figure 2.6(b). Paraffins drop down to the lower-middle of the latent heat range, while salt hydrates and metallics dominate that same temperature range. In particular, a number of Gallium based metals below 30°C become dominant energy density materials despite being near the bottom of the specific latent heat chart.

On the high temperature charts in Figure 2.7, it is fairly clear that only salts and metallics serve as PCMs over this range. While salts appear dominant with respect to specific latent heat, metallics become very competitive with respect to volume. One final point worth mentioning is the significant difference in material count between the specific and volumetric graphs. This highlights the need for more complete material property measurement to better fill out the PCM dataset. It is suspected that there are a large number of high volumetric latent heat materials that have yet to be catalogued, especially with respect to metallic materials.

2.3.5.3. *Composite metrics*

As discussed previously, latent heat is not the only material property of interest to PCM designers. For some applications it is argued that latent heat may not even be the primary design factor. Lu [26] proposed PCM fitness metrics for an electronics thermal protection device. Based on a model of one-dimensional heat conduction through an electronic device material stack, he determined the maximum thermal protection occurs when the following two parameters are maximized:

$$I_1 = \rho H_f k_s \quad (1)$$

$$I_2 = \rho c_p k_s \quad (2)$$

Whether I_1 or I_2 is more important will depend on how wide the operating temperature margin will be. If more energy will be absorbed through sensible heating

above and below the phase change temperature, then I_2 will dominate. Otherwise, a design with narrow temperature margin or large latent heat will have I_1 be the dominant factor. This situation is often represented by the Stephan number, defined as the ratio of sensible to latent heat for an application, or $Ste = c_p \Delta T / H_f$. For most latent heat TES applications, a low Ste situation is generally assumed to be the case. It is readily apparent that I_1 , which consists of volumetric latent heat ($H_{f,v} = \rho H_f$) and thermal conductivity, will inherently favor metallic PCMs and high conductivity salts over other organic and inorganic materials. This was evident in Lu's results, which recommended a tin-zinc alloy for high-temperature semiconductor thermal protection. Unfortunately, the remainder of the materials in Lu's dataset pulled from a proprietary material database and are unavailable for general evaluation. Figure 2.8 shows the values of I_1 for the 100 materials contained in Appendix D with sufficient thermophysical data for calculation.

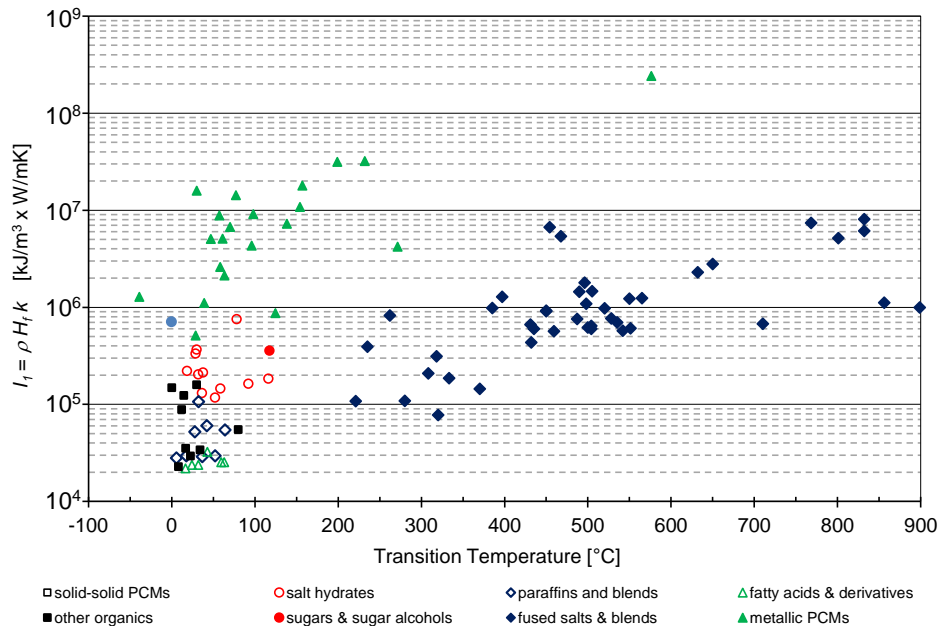


Figure 2.8 – I_1 PCM figure of merit as proposed by Lu applied to the 100 cataloged materials with sufficient thermophysical properties for evaluation.

High thermal conductivity clearly gives metallics the advantage for the I_1 metric, significantly dominating the chart up to $\sim 250^\circ\text{C}$. At higher temperatures salts appear dominant, except for AlSi at 576°C , primarily due to the lack of metals with sufficient property data to include in the analysis. This is unsurprising considering the model that Lu used to produce it. The one-dimensional model placed the PCM directly between the electronic heat source and the heat sink and looked for a solution permitting the maximum heat dissipation within device temperature limits. This gives heat transport and energy storage equal importance, producing the factors above where thermal conductivity dominates. Shao [72] produced a nearly identical PCM figure of merit, with the primary difference being the use of the liquid, rather than solid, thermal conductivity in the metric.

A similar but distinct analysis of PCMs was performed recently by Shamberger [73]. He defined a PCM figure of merit, FOM_q , such that a particular material will absorb heat, q , from a constant temperature reservoir at a rate proportional to this figure of merit. Unlike Lu's I_1 and I_2 parameters, FOM_q is not based simply on material parameters. It also incorporates terms specific to solid and liquid Stephan numbers of the phase change problem. This allows a single metric to evaluate material fitness for a multi-region phase change application, but does require additional effort for materials evaluation.

The definition of FOM_q for a melting one dimensional solid is:

$$FOM_q = \frac{\sqrt{\rho_l c_{p,l} k_l}}{\text{erf}(\lambda)} \quad (3)$$

where λ is the solution to the transcendental equation:

$$\lambda\sqrt{\pi} = \frac{\text{Ste}_l}{\exp(\lambda^2)\text{erf}(\lambda)} - \frac{\text{Ste}_s\sqrt{\alpha_s}}{\sqrt{\alpha_l}\exp(\lambda^2\alpha_l/\alpha_s)\text{erf}(\lambda\sqrt{\alpha_l/\alpha_s})} \quad (4)$$

$$\text{Ste}_{s,l} = c_{p,s,l}|T_m - T_{s,l}|/H_f \quad (5)$$

In the case of a simple solidification, the liquid properties would be replaced by solid properties in (3). This is perhaps more accurate than the Lu metric, which is based only on solid properties, because it better reflects the material state through which heat must be driven when driving the phase change. E.g., while melting the growing liquid film will sit between the heat source and phase front when the series arrangement is used. Thus, it can be seen that use of the Shamberger metric has the promise of better applicability for a particular application and perhaps better accuracy, but it is much less straight forward than the Lu metric, as solving for FOM_q requires first defining temperature bounds, then solving for λ , and finally calculating FOM_q .

Shamberger performed a sensitivity analysis on the parameters in the FOM_q presented above. He confirmed that the primary factors governing the magnitude of FOM_q are $\sqrt{k_l}$ and, in the limit of $\text{Ste}_l \approx 0.5$, also includes $\sqrt{k_l H_{f,v}}$. Thus, both the Lu and Shamberger metrics demonstrate the necessity of a high thermal conductivity in addition to a high *volumetric* latent heat. The ability to get heat to the phase front is just as important as the amount of heat that can be absorbed. Thus, low temperature metal alloys again become dominant amongst the various material classes when heat transfer rate is important, having FOM_q values approximately 10x higher than organics and salt hydrates in the same temperature range.

It is possible that other configurations would lead to alternative arbitrary metrics with different results, but there are two important takeaways from the Lu and Shamberger composite metrics: (1) real heat transfer situations demand material selection based on

more than a single material parameter, and (2) both thermal conductivity and volumetric, rather than specific, latent heat dominate most practical, high rate heat transfer applications.

2.4. Thermal phase change materials summary

The thermal management community has identified hundreds of materials for potential use in Thermal Energy Storage applications, where there is a need to manage a mismatch between times or rates of heat generation and dissipation. Taking advantage of phase change can produce an engineered solution with much higher energy density, but this requires a proper understanding of the available materials and their thermal properties. Consolidating the wide range of materials data from the PCM literature along with material evaluation guidelines allows for identification of high performance material options from across material classes and temperature range. In addition, a number of conclusions can be drawn from the state of PCM material information:

1. Although the primary two PCM parameters are typically melting temperature and specific latent heat, those are far from sufficient for material selection and modeling. The practice of many reviews in limiting themselves to those properties is insufficient for material comparison.
2. Focus on specific, rather than volumetric, latent heat has produced an overestimation of thermal performance of paraffins, despite their low density and thermal conductivities, and practically no investigation of metallic PCMs. This has resulted in many mediocre PCM systems with paraffins and other low temperature organics, with excessive effort given to additives and structures for heat spreading enhancement.

3. Few of the listed materials have ‘complete’ material information, and many materials show significant variation in reported measured values for melting temperature, latent heat, and other properties. While this can be due to accuracy or different measurement techniques between researchers, numerous cases of transcription error (between reviews and primary sources) were also identified. This issue creates the need for individual testing for any serious component or system design, adding to overall cost and effort to produce PCM based systems.
4. Further investigation into metallic and solid-solid PCMs could significantly increase the number of design options for thermal system developers. Both material types impose significantly different design requirements, with metals reducing the need for complex heat spreading structures, and solid-solid PCMs eliminating the complexity of liquid containment.

Chapter 3 – Vehicle applications of phase change materials

Phase Change Materials have been applied to a number of applications in the residential, commercial, industrial, and military sectors. This has included residential and facility climate control [56,74,75], enhancement of power generation and cogeneration [16,76], electrical power grid demand side reduction [77], and electronic component thermal protection [11,26,78-80]. Vehicle applications have been addressed as well, but the treatment has been far less comprehensive, typically addressing individual vehicle components piecemeal or in individual case studies. This chapter will attempt to provide a thorough description of the vehicle as a transient thermal system, including applications for phase change mitigation and case studies where available. (Much of the information presented in this chapter was originally published in [22].)

3.1. The vehicular transient thermal environment

Civilian and military vehicle components are subjected to a wide range of thermal conditions that either are imposed by the external operating environment or are the byproduct of the waste heat from high power components. These components must be able to operate from sub-freezing temperatures to peak temperatures that could reach hundreds of degrees Celsius as shown in Figure 3.1 for a modern commercial vehicle [81].

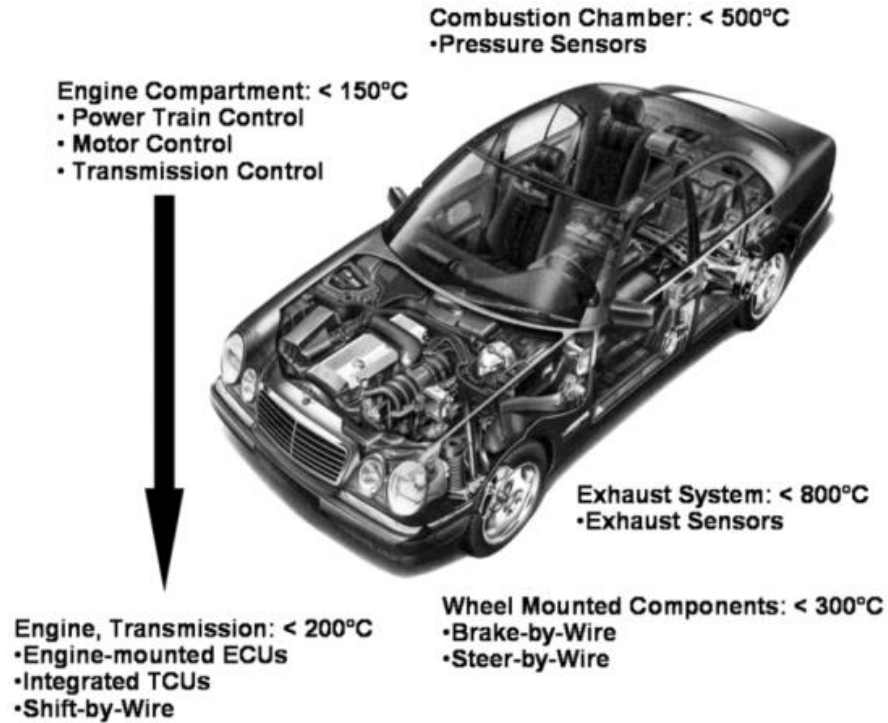


Figure 3.1 – Temperatures seen by various electronics and sensors throughout a standard commercial vehicle, from [81] with permission, © 2004 IEEE.

Additionally, for most cases these temperatures do not represent constant conditions for the vehicle. As shown in Figure 3.2, over any given drive cycle a vehicle can have peak power draws much higher than the average value, with numerous, sudden load changes occurring over the full drive cycle [41,82]. Power surges exceeding 2x the average power draw, but lasting only a few seconds, occur numerous times throughout the US06 drive cycle, and this variation is consistent over numerous drive profiles.

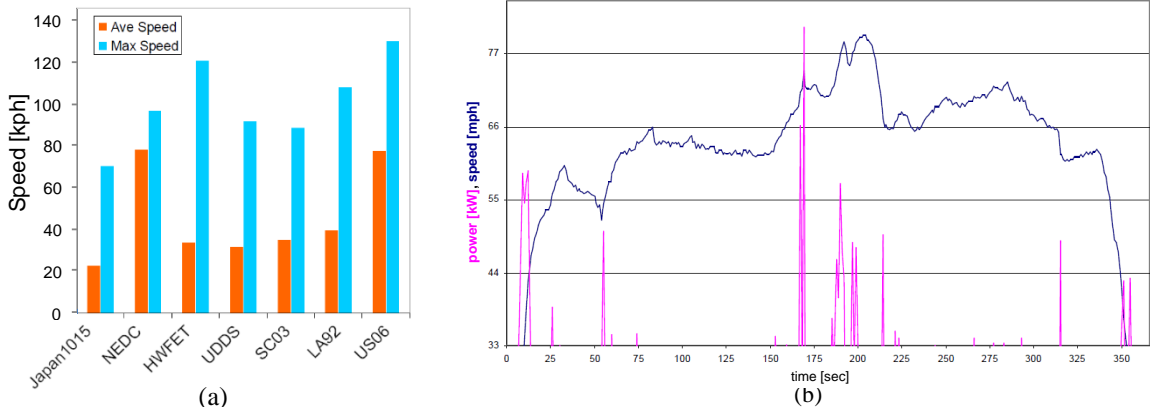


Figure 3.2 – Standard drive cycle operating profile information including (a) average and maximum vehicle speeds under standard driving cycles, and (b) hybrid vehicle speed and excess engine power for the highway portion of the US06 drive profile, adapted from [82] and [41], respectively.

This varying vehicle operation will cause certain power component temperatures to increase during surges and drop during idle, and engine compartment temperatures will be highly dependent on vehicle speed if primary cooling is from intake air. Apart from the driving profile, vehicles will likely undergo an ambient-to-operating temperature swing at least once if not several times every day. Many components are designed for efficient operation at the nominally steady operating temperature, and the vehicle warm-up period can be highly inefficient. In addition, the practice of designing the transient vehicle thermal system according to steady operation conditions will necessarily lead to an oversized thermal system. Designing the engine cooling system to dissipate the peak power shown in Figure 3.2(b), rather than the average power, will result in larger heat exchangers, pumps, radiators, and associated components. Similar statements can be made about vehicle cold start and passenger compartment climate control.

Whatever the transient vehicle thermal conditions, making use of PCM based TES to assist in the thermal management of any particular system requires identifying expected

operating temperature ranges, component temperature limits, and any configuration constraints. From this information, preliminary PCM selection could be based on identifying a melting temperature range for thermal buffering, whether for thermal protection or load leveling, and then selecting a material within that range that maximizes energy storage. The remainder of this chapter will examine vehicle thermal systems or components spanning low ($< 100^{\circ}\text{C}$), mid ($100\text{-}200^{\circ}\text{C}$), and high ($> 200^{\circ}\text{C}$) operating temperature ranges. Thermal conditions for each component will be identified along with examples from prior studies and any particular constraints the application would impose on a PCM.

3.1.1. Low temperature applications, below 100°C

3.1.1.1. Cold start thermal improvement

The higher oil viscosity and decreased combustion efficiency present during vehicle cold start makes it a prime target for thermal improvement. In modern automobiles, the first 1-5km will be driven under inefficient ‘cold engine’ conditions [83]. Many non-PCM studies have demonstrated the thermal benefit of using Exhaust Heat Recovery (EHR) to more quickly bring the engine up to efficient operating temperature. One study by Hyundai Motor Corporation showed that a 2.5% fuel economy improvement could be achieved by preheating both the coolant and gear box oil in a commercial vehicle, with higher savings expected in heavy diesel and hybrid vehicle systems [84]. Another study on cold temperature hybrid vehicle operation showed a 9% fuel economy boost due to EHR [85]. In both cases, however, the cold-start was not eliminated, but only decreased in duration while waiting for the exhaust to warm up the engine.

Attempting to eliminate the cold-start penalty altogether, several groups have used PCMs to maintain component warmth long after engine shut down. Such a PCM would need a melting temperature just high enough to sufficiently warm the component, but low enough to ensure PCM melting even in cooler operating conditions. In addition, a lower PCM temperature reduces environmental heat loss, potentially increasing the time it can maintain component temperature. In a pair of studies by Gumus and Ugurlu, a lower temperature PCM was used to retain heat and improve cold start emissions and efficiency. First, sodium sulfate decahydrate ($T_M \sim 32^\circ\text{C}$) was used on a gasoline engine coolant loop and kept engine temperature about 17°C above ambient after a 12 hour wait, and CO and HC emissions were decreased during startup by about 64% and 15%, respectively [86]. In the second study, sodium phosphate dibasic dodecahydrate ($T_M \sim 36^\circ\text{C}$) was used to keep a liquefied petroleum gas (LPG) engine warm between usage cycles and reduce the usage of a more polluting gasoline combustion stage for cold starts. The PCM kept the engine above LPG evaporation temperature (30°C) for an additional 10 hours relative to the standard system reducing cold start CO and HC emissions by 17% and 29%, respectively [87]. Addressing the issue of diesel fuel component solidification at sub-zero temperatures as described in [88], an unspecified PCM blend ($T_M \sim 70^\circ\text{C}$) was used with a small thermoelectric heater to initiate reflow in a clogged diesel fuel filter [89]. In this case the PCM was not explicitly designed to prevent fuel solidification, but it provided a long duration thermal reservoir for the thermoelectric device to pump heat into the solidified fuel. Finally, in a military heavy vehicle application, the oil pan and filter on a U.S. Army M925 5-ton truck was surrounded by a low temperature PCM (hexadecane, $T_M \sim 18^\circ\text{C}$) keeping the oil warm for over 12 hours after shutdown. This allowed faster cold starts,

improved engine lubrication, and reduced cold-start cranking energy required from the battery by a factor of about 2-6x [90].

3.1.1.2. Sub-ambient refrigeration

Modern society makes extensive use of refrigerated shipping of perishable goods, but on-vehicle refrigeration tends to have reduced efficiency due to system size and weight constraints. It has been proposed in several studies to augment or replace on-board Diesel-driven vapor compression refrigeration systems with a sub-ambient TES system. As many cases of warehouse-to-warehouse shipment have fairly predictable transport times, a PCM-based refrigeration system could permit at-warehouse pre-charging, removing the need for the vehicle to carry the weight of a vapor refrigeration compression system. Warehouse pre-charging could be done with a higher efficiency refrigeration system, and using off-peak electrical power could further reduce operating costs.

There have been a number of analytical and experimental studies into PCM refrigeration systems. In 2003, Simard and Lacroix performed an analytical analysis of PCM refrigeration, including the effects of frost build-up on the heat exchanger [91]. Even in non-ideal conditions, they showed that using a very low temperature PCM ($T_M \sim -43^\circ\text{C}$) a refrigerated truck could provide the equivalent of 3500W of cooling for 8 hours using only 3% of the refrigerated compartment volume for thermal storage. In 2012, Oro investigated the ability of a small amount of PCM ($T_M \sim -21$ to -18°C , again about 3% of container volume) to keep a non-refrigerated container below critical temperatures to simulate a passive storage condition or active refrigeration power failure, showing durations almost twice as long as without a PCM [92]. Taking PCM refrigeration further, Liu, et al [93], and Sharma and Buddhi [94] both experimentally evaluated the ability of a

PCM to maintain a refrigerated van below critical temperatures in the absence of an on-board refrigerator, suggesting use of the warehouse pre-charging approach. Liu developed a proprietary low-temperature PCM ($T_M \sim -26.7^\circ\text{C}$), and showed they could keep frozen goods below 18°C for 10 hours, using a same weight of PCM as a conventional on board refrigerator with half of the energy cost due to off-peak charging. Sharma's work investigated a variety of parameters, such as total PCM mass, PCM placement, and air circulation, and the PCM ($T_M \sim -15.2^\circ\text{C}$) kept the refrigerated space below 5°C for 2-7 hours depending on configuration. Finally, an alternative approach was reported in 2010 by Ahmed et al., where rather than coupling to the refrigeration system, the group investigated using a paraffin-based PCM ($T_M \sim 7^\circ\text{C}$, just above the 4°C compartment temperature) to enhance the chilled compartment wall insulation [95]. Compared to a non-PCM enhanced control trailer, the presence of the PCM reduced the daily peak heat transfer rate by an average of 29%, and total daily heat transfer by 16%.

3.1.1.3. Passenger climate control enhancement

A review of passenger thermal comfort in vehicles concluded that a dominant complicating factor in providing adequate cooling is the transient nature of the passenger compartment thermal/fluid conditions [96]. Commercial vehicles target cabin temperatures of around 25°C regardless of external conditions, while U.S. military systems are specified by MIL-STD-1472F to provide cold air to the cabin at a maximum of 29.5°C [97]. These are steady-state requirements and do not provide any indication of required time to achieve the target temperatures, but it is worth noting that the demand for cool cabin air system can be greatest when the vehicle is least able to provide it, such as when driving at low speeds or idling [98].

Addressing these transient conditions through direct thermal buffering of a vehicle's cabin cooling system has received little attention in the literature, where focus has mainly centered on residential and commercial climate control. A general air conditioning (AC) system improvement review by Chua described PCM integration as a novel improvement to cooling, but any efficiency improvement was highly dependent on matching both thermal conductivity and phase change temperature to expected load profile [99]. In addition, Al-Abidi reviewed a number of approaches and configurations for implementing such a system, with most focus given to off-peak cold storage to achieve "free cooling" during the peak load portion of the day [100]. While actively storing energy would be unlikely in a powered-off vehicle, thermal buffering a vehicle's active cooling system could either provide sufficient cold air during idling periods or reduce the cooling load during start-up after short vehicle-off periods. PCM choice would necessarily differ from facility applications, where ice-storage has received most attention, as too-cold direct air impingement could impact passenger comfort.

It is also worth mentioning the significant amount of facility PCM research over the past few decades examining direct PCM integration with structural material to augment insulating properties with additional thermal capacity. This has mainly focused on wallboard materials, although other construction material demonstrations have shown promising results [101,102]. Material sets would vary significantly for vehicle applications, but a similar design approach could prove worthwhile for a vehicle cabin, and the reader is referred to a comprehensive review of the subject by Tyagi and Buddhi [103].

There have been a few successful demonstrations of passenger climate control thermal buffering. In one case, an airport passenger shuttle cooling system was modified

with a PCM loaded booster tank [104]. PCM characteristics were not specified, but as a surge buffer on the radiator's water-glycol loop it would have required a temperature between the nominal loop temperature and cabin temperature (indicated as 18-22°C in different tests). Previously, the shuttle had suffered from poor cabin cooling due to frequent and prolonged idling periods resulting in long temperature pull down times. During peak cooling system demand, the thermal storage unit was able to provide the equivalent of about half of the required cooling capacity with faster cabin temperature pull-down. This reduced AC energy consumption by 56% relative to available standard AC systems while providing increased passenger comfort. More recently, Delphi Automotive demonstrated a "thermal storage evaporator" for a hybrid vehicle that acts as a PCM buffered air-side heat exchanger for the vehicle cabin [105,106]. Using a small PCM-volume with $T_M \sim 7^\circ\text{C}$, the AC could be turned off and vent temperature maintained below the 15°C comfort limit for 34-42 seconds under high thermal loading conditions, and extended PCM 'charge time' could increase that duration by as much 4x. The company claimed that under certain drive cycles, the technology could reduce HVAC fuel usage by 50% while maintaining passenger comfort [107].

In addition to the cabin cooling requirement, cabin heating could draw 4-6kW from the battery during the start-up period. This significantly decreases useful battery range and lifetime and has a major impact on electric vehicle design, as described in a report on the impact of using a PCM with an electric passenger car in cold climates [108]. The study concluded that battery energy draw over the drive cycle could be reduced by up to 21% by loading the cabin with approximately 5 liters of paraffin ($T_M = 56^\circ\text{C}$). It should be noted

that pre-charging of the PCM during vehicle battery charging was necessary to guarantee a preconditioned cabin.

3.1.1.4. Absorption air conditioning - exhaust side buffering

As the AC system can draw from 12-17% of available engine power in small commercial vehicles, with most of that energy being used to drive the compressor [98], several studies have explored eliminating the electrical cooling load by driving the AC system from reclaimed exhaust heat, primarily through absorption based thermal cycles [109]. A detailed analysis and design of vehicle exhaust driven absorption air conditioning can be found in reports by Lambert and Jones [98,110], and the system concept is shown in Figure 3.3.

Typical refrigeration loop cold and hot side temperatures at steady state can be about 5°C and 60°C, respectively. They showed that the required air conditioning can be provided via recovered exhaust heat even at steady idle, completely eliminating the AC load from the diesel engine. In that design, as well as in [111], energy was recovered from the exhaust by an oil heat exchange fluid with parallel PCM thermal storage in a shell and tube heat exchanger. PCM temperature in both designs was chosen to be just below the designed loop hot-side temperature (~60°C) to keep the oil loop warm enough to decrease start-up time, but not necessarily enough to drive the cycle by itself in the absence of sufficient exhaust heat. However, sufficient energy was stored in the PCM to reduce the initial cooling delay and load-level the cooling system during variable driving conditions. Additionally, high performance absorption systems in non-vehicular applications typically require a higher temperature condensing side, perhaps from 85-95°C. Future development of PCMs for this application could include materials spanning this higher range to enable

higher efficiency systems on vehicles, or perhaps even higher temperatures to permit the PCM to directly drive the adsorption cycle during low temperature exhaust conditions.

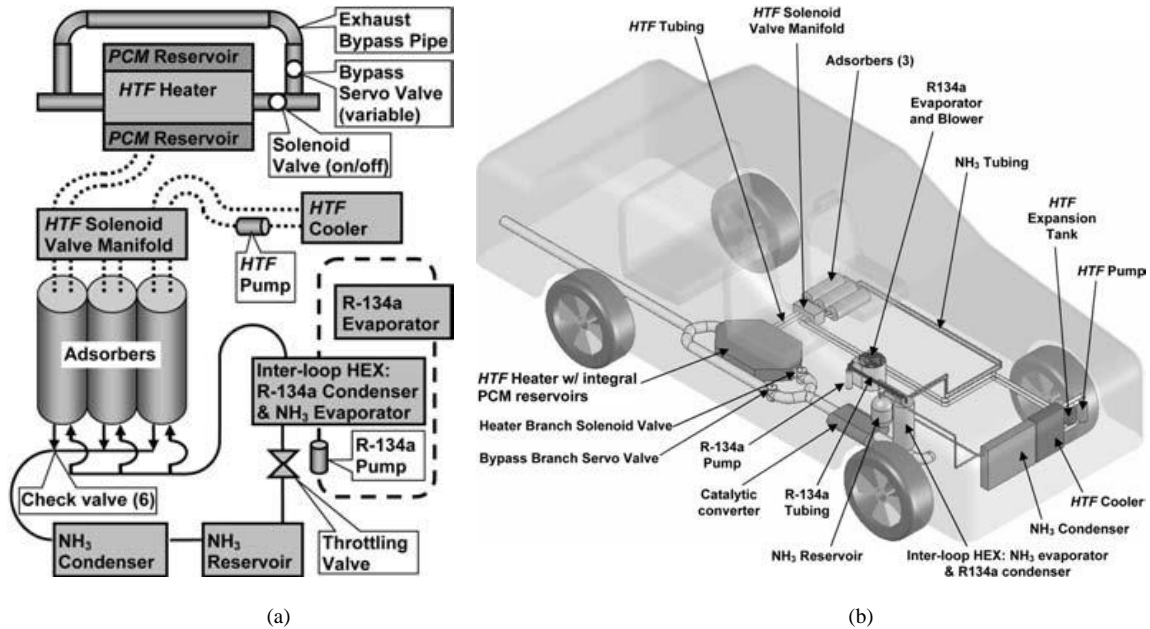


Figure 3.3 – (a) Vehicle absorption air conditioning system driven by exhaust waste heat recovery with a PCM thermal buffer, and (b) notional implementation layout, from [98], with permission.

3.1.1.5. Low temperature electronics thermal protection

Although less common in commercial vehicles, many military vehicles are configured with numerous high power electronic components within the crew cabin. A recent power study of a M2A3 Bradley vehicle detailed several electrical load scenarios with total electrical power ranging from 4 to 10 kW [112]. These loads included Command and Control (C2) computers and displays, radio systems, navigation systems and others, and the total equipment electric load far exceeded the designed personnel heat load (approximately 100-150 W metabolic thermal load per crew member [113]). Most of these systems vent heat to the cabin air after which it must then be rejected through an overburdened, high thermal resistance AC system. Additionally, many electronic systems

being loaded into military vehicles are derived from commercial components with lower maximum temperature limits than militarized hardware, further increasing the cooling challenge.

A recent study modeled two improvements to such a situation on a Cougar Mine Protected Armored Vehicle (MPAV), shown in [114], loaded with C2 equipment. First, a cooling rail architecture was implemented, whereby each electronic system was provided a heat exchanger to a separate liquid cooling loop to avoid passing heat through the cabin air. Second, a PCM was integrated with the heat sink to provide local thermal buffering. Models showed that, with the improved system, components never reached critical temperature (85°C), and the use of the PCM extended operating time by one hour in the case of coolant failure. In this system, the modeled PCM was acetamide embedded within aluminum foam to enhance thermal heat spreading. The acetamide had a melting temperature just below the assumed electronics critical temperature.



Figure 3.4 – Cougar MPAV from [114] with permission, © 2010 IEEE

3.1.1.6. Battery thermal protection

The move toward more complex vehicle electrical architectures including Electric and Hybrid Electric Vehicles (EVs and HEVs) has driven the development of lighter batteries with higher power and energy density. These batteries make up one of the larger cost elements in newer commercial vehicles, and their performance and lifetime are strongly influenced by operating temperature [115,116]. A summary of common vehicle battery technologies, their typical operating temperature ranges and other relevant parameters is given in Table 3.1.

Table 3.1 – Common Vehicle Battery Chemistries and Performance Details [115,117]

Battery Type	Op. Temp Limits [°C]	Typical Energy Storage Efficiency	Energy Density [W-hr/kg]
Lead-acid	-5 – 40	72-78%	~25
Nickel Cadmium	-40 – 50	72-78%	45 - 80
Nickel Metal Hydride	-10 – 40	~90%	~80
Lithium Ion	-30 – 50	~100%	90 - 190

The U.S. Advanced Battery Consortium (USABC) has set standards for commercial hybrid vehicle batteries to be able to operate over the range of -30°C to 52°C, with a future technology goal of -40°C to 85°C [118,119]. For military applications, additional implementation difficulty comes from the wider range of temperature, vibration and shock imposed by the military environment, but a similar set of battery materials and are being explored [120,121]. While Li-Ion technology is meeting the USABC near term goals, optimal battery performance requires operation over a much narrower temperature range. As reported in an overview of the Chevrolet Volt Li-Ion battery system, the available battery output power rolls off very quickly outside of a 20-40°C temperature band, falling to 60% of rated power below 0°C and above ~50°C [122]. Additionally, several battery pack thermal studies have shown that both absolute temperature and temperature uniformity during use can significantly impact battery pack operation and

lifetime [123,124]. Non-uniform heating can occur during rapid discharge creating highly variable pack temperature distributions, and under certain conditions localized temperature excursions can lead to thermal runaway in lithium-based battery packs [125,126]. An in-depth review of battery thermal management requirements and approaches covering these and other concerns was compiled by Rao and Wang [127], and a series of necessary battery thermal control systems have been examined by Pesaran [128]. Most recent commercial HEVs, including the Honda Insight and Toyota Prius, have made use of conditioned cabin air [129], while the recently released Chevrolet Volt Plug-in Hybrid Electric Vehicle (PHEV) has a lower temperature antifreeze loop dedicated to battery thermal control [130].

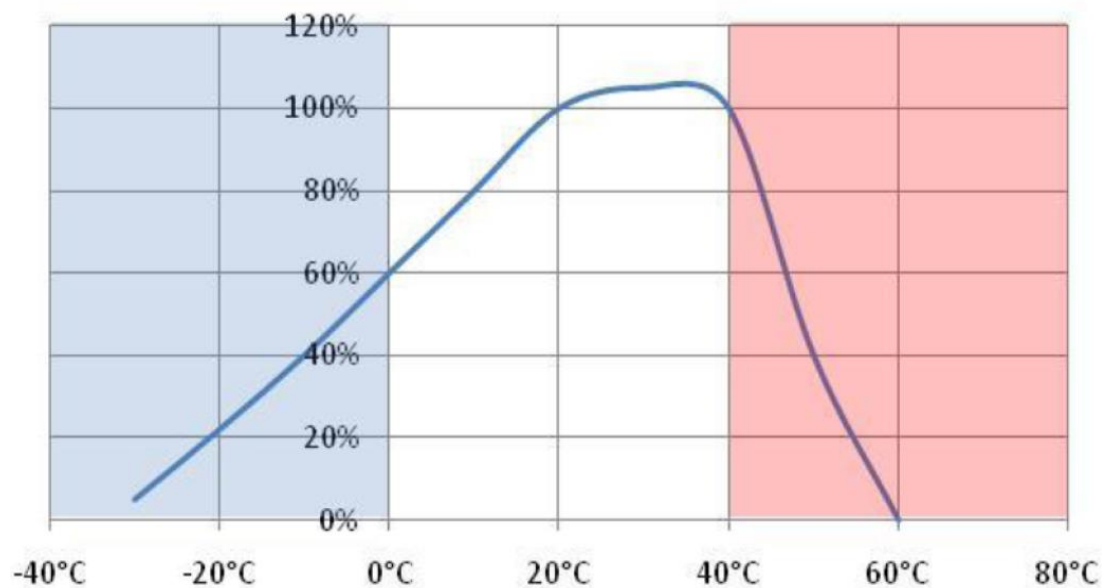


Figure 3.5 - Percent of rated battery power available over the operating temperature range for the General Motors Lithium Ion Voltec battery system showing peak power available from 20-40°C. From [122], with permission from SAE paper 2011-01-1373 Copyright © 2011 SAE International. Further use or distribution is not permitted.

Several investigators have explored using a PCM to augment the battery cooling system. The presence of a PCM, typically paraffin waxes embedded in a metal or carbon

foam, has been shown through both modeling and experiment to decrease peak temperature rise and increase thermal uniformity under high-rate discharge conditions [131,132]. In addition, it was suggested that the thermal capacity of the PCM could both reduce the need for cooling system overdesign and enable higher battery power output at elevated ambient temperatures [133]. The paraffin waxes chosen by the researchers had melting temperatures ranging from 42-56°C, which falls just below the 50-60°C upper temperature limit for NiMH and Li-Ion battery technology. Because significant but predictable battery heating occurs during the recharging cycle of PHEVs, especially for rapid-charging systems [134], incorporating PCM based thermal protection in a vehicle battery pack could play an important role enabling customer-demanded high-rate charging while maintaining battery lifetime and reliability.

3.1.2. Medium temperature applications, between 100 and 200°C

The medium temperature applications are generally related to thermal protection of the under hood drive components, including the engine cooling loop and high-power electronics.

3.1.2.1. Engine coolant loop thermal buffering

Most vehicle engines use an antifreeze coolant loop consisting of an ethylene or propylene glycol and water mix that is pumped to a radiator for heat rejection to maintain temperature between 80-100°C. In some configurations the loop will also cool other engine components (e.g., the transmission or gear-box), while possibly providing some cabin heating [135]. This loop is generally pressurized to maintain the coolant in the liquid phase with the antifreeze boiling temperature being just above 120°C. More complicated

vehicle systems, especially EVs and HEVs, may have one or more additional liquid loops at lower temperatures for cooling electrical components. Because higher cooling loop temperatures decrease the total radiator size for a given heat load, some future civilian and military vehicle designs are targeting a single 100-105°C vehicle coolant loop for all electrical and mechanical components [7,136]. Higher loop temperatures would further decrease radiator size, but such high temperatures can cause performance issues in the engine and reliability issues with elements such as the pump, seals, and hoses [137].

Typically, cooling loop capacity is sized to account for surge and transient loads. Because those peak loads are present for only a fraction of total operating time, design oversizing is reflected in the system pumps, radiators, heat sinks, and other associated hardware. Several studies have looked at shifting some or all of the transient load to a PCM thermal buffer or heat accumulator, using a configuration similar to that shown in Figure 3.6 [137,138]. These studies demonstrated the ability to downsize the cooling system capacity by about 1/3 while staying below maximum engine temperature limits during power surges. Moderate melting temperature materials were investigated, mainly focusing on the polyalcohol erythritol ($T_M \sim 118^\circ\text{C}$), although in [138] it was mentioned that a slightly lower melting temperature PCM would provide more margin for thermal gradients to develop around the cooling system. The melting temperatures of an alternate PCM would have to be above the steady coolant temperature ($\sim 80\text{-}100^\circ\text{C}$ for the primary engine loop, lower temperatures for other loops), but below the loop boiling limit with enough margin for any expected thermal gradients between the loop and critical components.

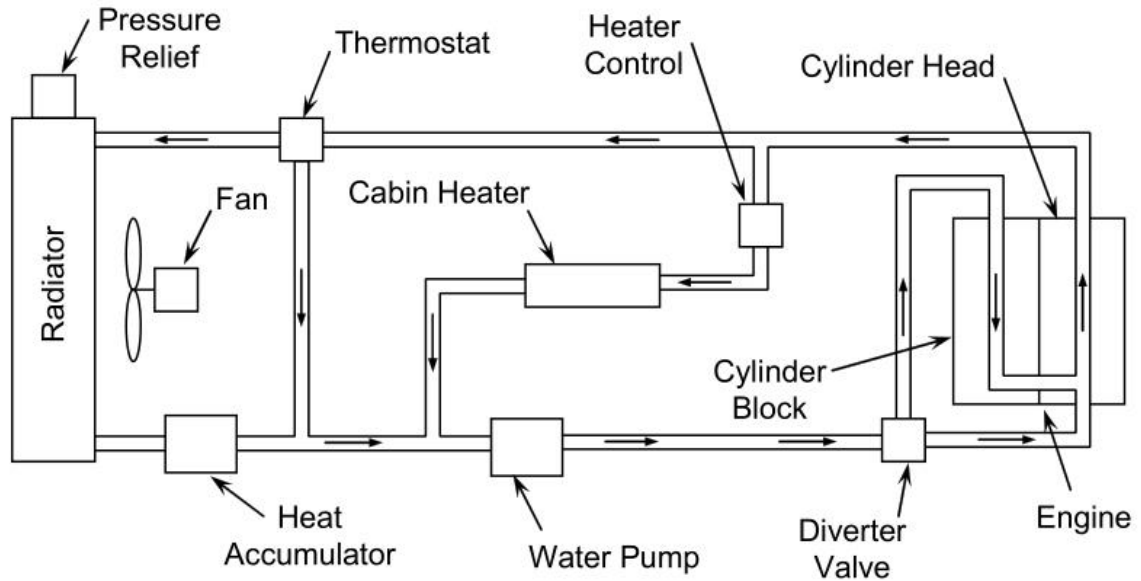


Figure 3.6 - Engine cooling system with a heat accumulator incorporating a phase change material to thermally buffer the coolant temperature, from [137].

3.1.2.2. Vehicle power electronics thermal protection

Increasingly electrified vehicles require more power conversion electronics to move energy to the various vehicle systems, including battery packs, traction motors, and accessory payloads. Core elements of these conversion electronic systems are semiconductor (typically silicon) power transistor and diode array modules that are used as the switching elements, an example of which is shown in Figure 3.7 [139]. While the power conversion efficiency of these components can be high (> 95%), their high power density still creates a challenging thermal management problem. For high power electronics, heat is removed through several packaging layers to a liquid cooled baseplate connected to the vehicle's cooling loop.

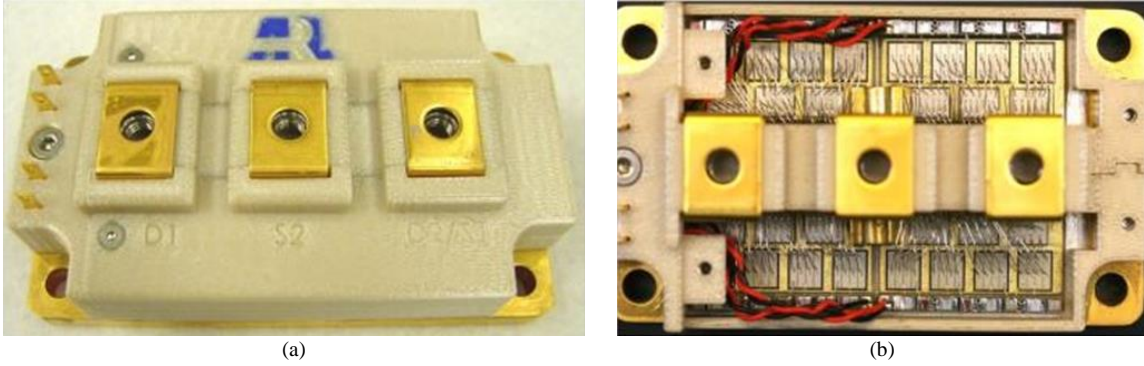


Figure 3.7 – (a) Dual switch module, and (b) internal view of module showing transistor and diode arrays bonded down to substrate and baseplate, from [139].

As mentioned in the previous section, future vehicle designs are targeting a single, high temperature ($> 100^{\circ}\text{C}$) cooling loop for the engine and electronics, which does not provide much margin for silicon devices with typical operating temperature limits of only $125\text{-}150^{\circ}\text{C}$ [81]. As a result, current commercial hybrid vehicles have had to use separate liquid loops for electronics with temperatures around $60\text{-}70^{\circ}\text{C}$ [140]. While semiconductor devices made from wide-bandgap materials, such as silicon carbide and gallium nitride, are being developed with operating temperature limits as high as 400°C , other package material limits keep operation of those devices under 200°C [141]. In addition, while showing significant progress, those semiconductor devices remain cost-prohibitive for widespread commercial adoption, and even military circuit demonstrations are still in the prototyping phase [139,142].

While both DoE and the U.S. Army have been making numerous efforts to reduce overall package thermal resistance [140,143-146], previous studies by the authors [147] and others [148,149] have suggested that the associated material reduction also tends to reduce package thermal capacity which can actually result in higher temperatures under transient loading. Incorporating a PCM into the electronics package to restore thermal

capacity has been shown to significantly slow this temperature rise [11,26,150]. In addition, directly buffering the electronic device creates a shorter thermal path to the PCM than buffering the cooling loop, potentially allowing higher rate transients to be mitigated.

As before with coolant loop thermal buffering, the lower limit for acceptable PCM melting temperature is set by the temperature of the cooling medium, and the upper limit by the limiting temperature of the electronic device. Additional margin must be allowed on both the lower and upper temperature limits to account for the thermal gradient between the PCM and coolant at steady state and between the PCM and device during the transient. Independent DOE and U.S. Army studies have identified erythritol as a candidate PCM for a power electronics thermal buffer heat sink (TBHS) due to both its melting temperature ($T_M = 118^\circ\text{C}$) just below the aforementioned silicon thermal limit and its relatively high latent heat [41,151]. The DOE study also identified the PCM TBHS concept as a key enabler for using silicon electronics on a 105°C cooling loop, while permitting 30-50% reduction in electronics heat sink size and weight relative to a non-PCM baseline.

3.1.3. High temperature applications, above 200°C

The high temperature applications all relate to thermally coupling to the hot engine exhaust for vehicle efficiency improvement. The range of available temperatures, shown for a passenger vehicle in Figure 3.8, provides a number of options for PCM selection and integration with the exhaust system.

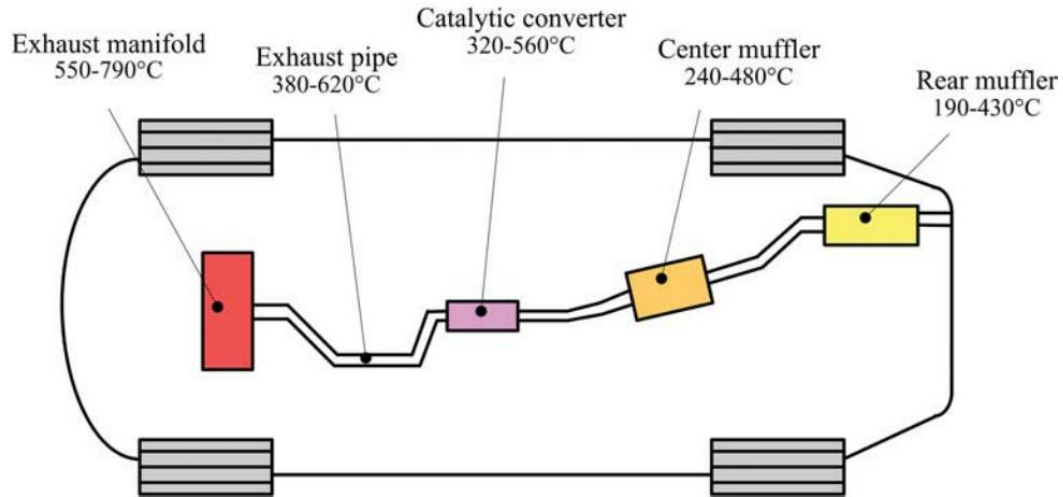


Figure 3.8 – Range of available exhaust temperatures in a gasoline-fueled passenger vehicle, from [8].

3.1.3.1. High temperature exhaust energy storage for cold start improvement

While the cold start improvement efforts described in Section 3.1.1.1 mainly focus on keeping components above ambient conditions in cold environments, the catalytic converter is designed to run at much higher temperatures to burn off polluting compounds from the exhaust stream. Conventional catalysts have light-off temperatures of about 350°C, below which conversion efficiency quickly degrades, but they often operate at higher temperatures for peak performance [152]. Even in warm environments, the catalytic converter will cool quickly resulting in an undesirable cold-start condition on the next use. Studies estimate that 60-80% of certain pollutants emitted during a standard drive cycle occur in the first two minutes while the catalytic converter comes up to temperature [153]. Several advanced emissions controls techniques have been proposed, some of which have included use of a high-temperature PCM to maintain converter temperature over an extended off-time. Reports from Burch, et al., described the use of a high conductivity

aluminum/silicon PCM material ($T_M \sim 580^\circ\text{C}$) and a lower temperature proprietary PCM ($T_M \sim 350^\circ\text{C}$) jacketing the catalytic material on a conventional gasoline engine [154,155]. They found that the lower temperature PCM was more likely to melt completely and had lower losses to ambient than the higher temperature system. It was able to keep converter temperature over 300°C for 24 hours, reducing certain emissions by 84 - 96%. Because the U.S. EPA has estimated that there is less than 24 hours of off-time between 98% of all automobile trips, a thermally buffered catalytic converter could drastically improve overall vehicle emissions [156]. Additionally, future emissions control trends are leading toward lower temperature catalysts (potentially below 200°C) to reduce pollution from large diesel vehicles with lower exhaust temperatures [157], which could open the application to a wider range PCM materials.

3.1.3.2. Exhaust energy thermal buffering for waste heat electrical conversion

A large fraction of fuel energy goes directly out the vehicle exhaust due to combustion process inefficiency, and there has been a lot of interest in reclaiming this energy to improve overall vehicle efficiency. Gasoline engine exhaust peak temperatures can vary from $500 - 900^\circ\text{C}$, while heavy duty vehicles (typically trucks with diesel engines) might only have exhaust temperature peaks from $500 - 650^\circ\text{C}$ [158]. Figure 3.8 highlights the fact that exhaust temperature also varies significantly along the exhaust path. A number of investigators have explored converting that waste heat into electricity, which could augment or even replace the vehicle alternator to help drive the increasing number of vehicle electrical loads.

Little attention has been given to using a PCM thermal buffer to augment electrical conversion of recovered vehicle exhaust energy. However, a recent DoE modeling effort

examined waste heat recovery (WHR) on four vehicle classes, from light cars to heavy trucks, and found that the most limiting condition was insufficient available waste heat during cold starts and intermittent acceleration (city versus highway driving) [159]. These are the same conditions that made thermal buffering an important part of the absorption cooling analysis mentioned in Section 3.1.1.4. In fact, Fu, et al. recently performed a detailed power and temperature mapping of vehicle exhaust as a function of engine speed and load [160], commenting on the energy available for WHR. These maps show that significant variation from the peak design point will occur in real vehicle operation, which can significantly reduce any recovered power and increase the payback period of a WHR system. There have been case studies on hot-side thermal buffering for thermoelectric (TE) [161] and mechanical [162] conversion technologies for other high temperature applications (primarily concentrated solar power generation). They examined using a PCM thermal buffer to maintain a stable hot side temperature, finding that sufficient energy storage allowed for extended operation even after solar input had ceased. As it is likely that there may be significant similarities between TES material sets and heat exchange requirements for vehicle WHR and high temperature, large scale power generation (and in particular solar thermal generation), the reader is referred to a detailed review of the subject by Medrano, et al., in [163]. While source aspects for both TE and mechanical generation technologies are the same, they have unique aspects that affect PCM applicability in either case.

Thermoelectric waste heat recovery: Using a thermoelectric generator (TEG) is one of the most often proposed vehicle heat recovery methods, accomplished by attaching the TEG to a portion of the exhaust pipe at the appropriate temperature for the material. They

are attractive options because they are solid-state and lightweight, potentially providing higher reliability and lower mechanical complexity than other conversion options. A thorough analysis of thermoelectric exhaust heat recovery including the impact of materials and thermal interface conditions can be found in [158], and an overview of recent design techniques can be found in [8,164]. A recent critique of TEG technology identified vehicle waste heat recovery as one of the few power generation applications where thermoelectric usage makes sense relative to more mature conversion technologies, primarily because efficiency of mechanical alternatives significantly decreases at lower power levels [165].

A significant concern with TE materials is that their thermoelectric performance is extremely temperature dependent, as shown in Figure 3.9 [166]. The expected variation in both exhaust heat and temperature means that both the TEG hot side temperature and the magnitude of any thermal gradients will see wide variation over a realistic drive profile (such as that shown in Figure 3.2(b)). This reality means the TEG would likely be off-optimum, operating inefficiently for the majority of its lifetime. A well designed thermal buffer may be able to maintain the material near the optimal performance temperature. For the materials shown, this could fall almost anywhere within the exhaust temperature span, but would likely center around the 400-500°C temperature range. In addition, because of the thermal gradient expected down the length of the exhaust path, a multi-PCM solution might provide for a spatially tailored system with higher efficiency. In any case, decoupling the TEG hot side from the exhaust pipe wall may expand the design space for a TE WHR system.

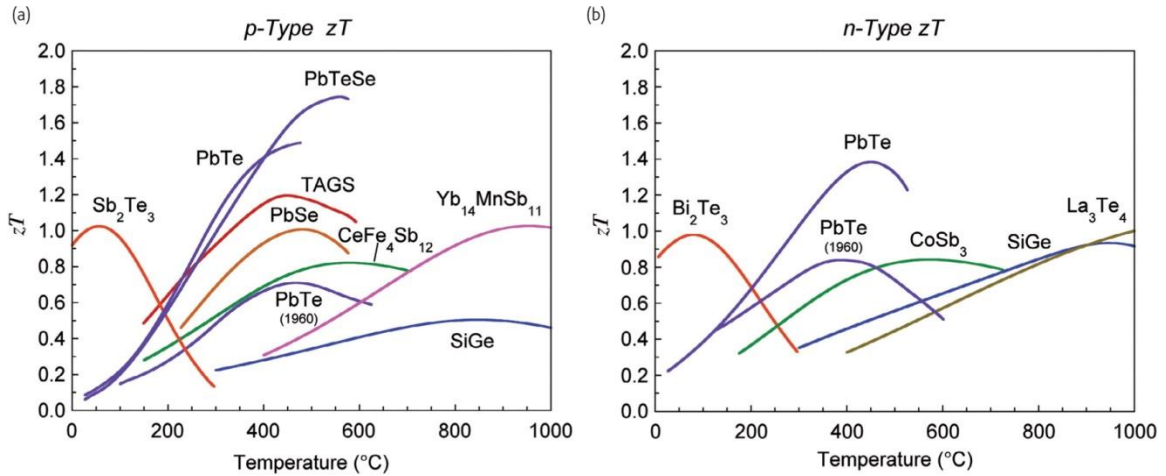


Figure 3.9 – (a) p-type and (b) n-type thermoelectric materials and temperature dependent thermoelectric performance, from [166].

Mechanical waste heat recovery: Using mechanical thermodynamic cycles instead of (or in addition to) TEGs for waste heat recovery has received much attention as well, showing potential total fuel economy improvements near 20% [167,168]. These systems are primarily Rankine based cycles, which are a mature technology that may better tolerate a wider operating temperature span than TEGs, but they are typically used in steady conditions and will be limited in temperature and performance by the chosen working fluid. BMW recently modeled and tested a steam-based Rankine WHR system ($T_{max} = 350^\circ\text{C}$), focusing on the system complexities created by the highly transient exhaust heat exchanger conditions and the potential for resulting system inefficiency or even critical failure [169]. They focused on the need for a complex control system to adjust for high rate transients, but it is possible that a PCM buffering the input could mitigate some of those concerns. In a recent historical review of Rankine cycles for WHR, Sprouse and Depcik [170] indicated that organic fluids are generally chosen over water/steam for cycles with hot side temperatures below 370°C , and there are a significant number of available fluids below

200°C [168]. Thus, despite the fact that storing energy at higher temperature is a major factor in achieving net efficiency improvement [171], the expected variation in exhaust temperature and operating conditions could mandate selecting a lower working temperature working fluid and open the application up to a wide range of potential PCMs.

3.2. Vehicle application summary and implications for PCM selection

The vehicle applications described in this chapter cover a wide range of temperatures, summarized in Table 3.2. The applications are listed with temperature ranges, estimates for desired PCM melting temperature, and comments on the reason for particular temperature selection. As noted the particular melting temperature may depend on whether the PCM is being used for thermal protection or temperature control. As an example, for thermal protection of current battery systems, a buffer temperature of just under 52°C may be appropriate. For optimal performance, however, it may be preferable to attempt to control temperature within a smaller temperature band, perhaps from 20-40°C. Also, it is important to remember that for any particular design a thermal gradient will exist between the PCM and the item being buffered, and PCM choice must allow for some margin between the target and melting temperatures. Finally, all of these applications share the fact that numerous thermo-mechanical factors, beyond those described here, need to be satisfied for successful implementation. These include sufficient heat exchange and heat spreading, maintaining PCM form, containment, and container contact, and staying within vehicle size and weight limits.

Table 3.2 – Summary of vehicle PCM applications and temperature requirements

Application	Temperatures		Likely PCM Temperatures	Comments
	Range	Limit		
Cabin / Payload refrigeration		< 0°C (froz.) <5°C (refr.)	-50–5°C	T_i either just below nominal air temperature if primary cooler, or just above if expected to act as an upper limit buffer during thermal excursions.
Cold start buffering, engine fluids	< 10°C		10-35°C	Lower PCM temperature reduces loss to ambient and insulation requirements
Cabin air conditioning loop		25°C (com) 29.5°C (mil)	5-25°C	Buffering AC cabin fan side of loop, target for PCM is slightly above nominal fluid being buffered: either evaporator refrigerant temperature or vent discharge temperature to ensure charging during normal operation.
Cabin heating		similar	40-70°C	Should melt just below heat exchange temperature, whether charging from electrical cabin heater, engine block, or exhaust gasses.
Vehicle battery pack, current	20-40°C	-30 to 52°C (USABC)	30-40°C (buffer) 50-55°C (protect.)	PCM designed to add thermal inertia either within optimum band to enhance performance, or just below limiting temperature for thermal protection.
Vehicle battery pack, future	est 20-40°C	-40 to 85°C (USABC)	30-40°C (buffer) 65-80°C (protect)	Assumes newer batteries have the same optimal operating point, but higher limiting temperature.
Absorption AC loop from exhaust	60-100°C		55-65°C (current) 85-95°C (high perf.)	Current designs based on conventional AC temps. High perf. numbers estimated for improved absorption loops.
Cabin Electronics		65-85°C	60-80°C	Commercial electronics derate after ~85°C, militarized electronics using COTS impose similar limits.
Cooling loop – Lower temperature	60-80°C		65-85°C	T_i must be greater than nominal loop temperature, but below coolant limit, PRV set point, or component limit.
Higher temperature	100-120°C	< 125°C	110-120°C	Higher temperature loop similar provides less margin for component temperature rise.
Silicon power electronics		125-150°C	110-120°C	Most silicon electronics will operate above 125°C, but are ‘derated’ or run at lower power.
High temp. power electronics		175-200°C	150-175°C	Wide-bandgap electronics can run at hotter than this, but other packaging restrictions limit upper temperature.
Exhaust heat recovery, mechanical		200°C (org) 350°C (H ₂ O)	180-200°C 300-350°C	Available exhaust temperature varies from the engine to the tailpipe. PCM temperature based on working fluid temperature limit.
Exhaust heat recovery, thermoelectric	200-800°C		400-500°C	PCM temp. based on TAGS and PbTe based materials. Higher temperature TE would increase thermal potential.
Cold start buffering, catalytic converter	320-560°C		>300°C	Temperature should be above catalyst light-off temperature. Low-temp catalysts could allow lower T_M .

3.3. Recommendations for vehicular PCM use

Developing future vehicles that are both more energy dense and more efficient will require replacing the traditional thermal system overdesign with intelligent, transient, thermal management methods. The use of thermal buffering can overcome the temporal mismatch between thermal supply and demand commonly found in vehicle systems, with respect to both cooling supply and power generation. Examination of past research into vehicle systems has identified a number of applications with either a transient mismatch or a thermal protection requirement that could benefit from phase change TES. These applications cover the entire range of temperatures present on the vehicle, from near

freezing up to 800°C. A consequence of using a PCM thermal buffer is that a unique material must be used for each system that has a different temperature requirement. Having surveyed over 700 materials from over a dozen material classes in Chapter 2, we can now attempt to match the most promising PCMs to vehicle applications according to likely performance based on material properties. Table 3.3 lists the applications described in this chapter, and provides suggestions on materials which may be worth investigating for future use. It is worth noting that this is limited to materials with known properties, and other materials, especially metallics and solid-state PCMs, may provide a number of alternative options if the material databases are expanded.

Table 3.3 – Vehicle applications and suggested candidate PCMs, sorted by temperature

Application		Material of Interest	Material Class	T _M [°C]
Sub-ambient refrigeration		NaCl or KCl +H ₂ O	aqueous salt	(-21)-(-10)
		Mono/di/tri-ethylene Glycol	organic	(-13)-(-7)
		Tetrahydrofuran	organic	5
Cold start buffering, engine fluids		Gallium-Zinc blends	metallic	10-30
Cabin AC loop, upper limit buffer		Potassium Fluoride Tetrahydrate	Salt hydrate	18.5
Vehicle battery pack, optimal temperature		Lithium Nitrate Trihydrate	salt hydrate	29-30
Vehicle battery pack, thermal protection	Current, T < 52°C	Indalloy 117 (non-ROHS)	metallic	47
	Future, T < 85°C	Barium Hydroxide Octahydrate	salt hydrate	78
Absorption AC loop, exhaust buffering	Current, T ~ 60°C	Sodium Hydroxide Monohydrate	salt hydrate	64
	Future, T > 85°C	Xylitol	sugar alcohol	93-95
Cabin heating		Indalloy 117 (non-ROHS)	metallic	47
		Sodium Hydroxide Monohydrate	salt hydrate	64
Cabin electronics thermal protection		Cerrobend Eutectic (non-ROHS)	metallic	70
		Barium Hydroxide Octahydrate	salt hydrate	78
Cooling loop, upper limit buffering	Low Temp	Barium Hydroxide Octahydrate	salt hydrate	78
		Xylitol	sugar alcohol	93-95
	High Temp	Erythritol	sugar alcohol	117-118
Power electronics thermal protection	Silicon	Erythritol	sugar alcohol	117-118
	High Temp.	Xylose	sugar	147-151
		d-Mannitol	sugar alcohol	168-168
Cold start buffering, catalytic converter	Current, T _c > 350°C	KCl + MgCl ₂ + NaCl	salt blend	385
		Lithium Hydroxide	salt	462
	Future, T _c > 200°C	Lithium Nitrate	salt	250-254
Engine exhaust heat recovery, source buffer	Mechanical	Galactitol	sugar alcohol	188-189
		Aluminum Chloride	fused salt	192
		91Sn,9Zn ^b	metallic	199
	Thermoelectric	Lithium Hydroxide	salt	462
		Potassium Perchlorate	salt	527
	88Al,12Si	metallic	576	

There is, of course, more to successful design than selecting a likely storage material. The steady and transient thermal conditions for the vehicle component must be fully understood, and this information is often unavailable or of poor quality. Not only average and peak temperatures, but also transient duration and frequency needs to be known to set the desired total energy storage requirement and PCM volume. Finally, an often ignored but perhaps be one of the most critical PCM system considerations is how operation will be affected after the PCM storage has been exhausted. In summary, more comprehensive vehicle and component level modeling will be required to understand the large number of internal and external thermal and material parameters in order to successfully implement any PCM-based system.

Chapter 4 – Power semiconductor devices and thermal packaging

The remainder of this report will focus on one particular PCM application described in Chapter 3: thermal protection of power electronic semiconductor devices. These devices have numerous uses both on and off the vehicle, and they create one of the primary thermal challenges in electronic component design. This chapter will provide an overview of power devices and electronic packaging, along with a description of two experimental evaluations of electronics thermal improvements. Specifics on transient thermal aspects of electronic components and packaging, including applications of thermal buffering with PCMs, will be described in following chapters. (Much of the experimental work presented in this chapter were originally published in [144] and [172].

4.1. Heat generation in power semiconductor devices

The silicon transistor has become the standard switch component used in the majority of analog and digital electronics circuits. As briefly mentioned in Chapter 3, for a number of electrical and mechanical reasons devices are being developed using wide-bandgap materials, including silicon carbide and gallium nitride. While these materials might provide for higher temperature and higher speed operation, the general thermal behavior of the devices is similar.

A representative power transistor cross-section is shown in Figure 4.1. Although specific configurations vary, most high power transistors have several features in common that affect their thermal profile. First, most transistor designs have a higher resistance region, commonly called the transistor *junction*, near the top of the device. Heat generated in this region generally must be conducted through the device to the backside contact, where the device is mounted to the circuit board or component package. From this point

heat is removed by conduction or convection according to system design. With respect to Figure 4.1(a) the transistor (a Vertical Diffusion Metal-Oxide-Semiconductor, or VDMOS, transistor), the gate electrode when charged induces the formation of a narrow conductive path, or channel, between the N^+ wells and the N^- region, allowing current to flow from source to drain. Note that the schematic is not to scale. The N^+ region is the device substrate, which actually much thicker than all of the layers above it. The substrate may vary from 200-500 μm , while the remaining layers may only total 1-100 μm , depending on electrical requirements.

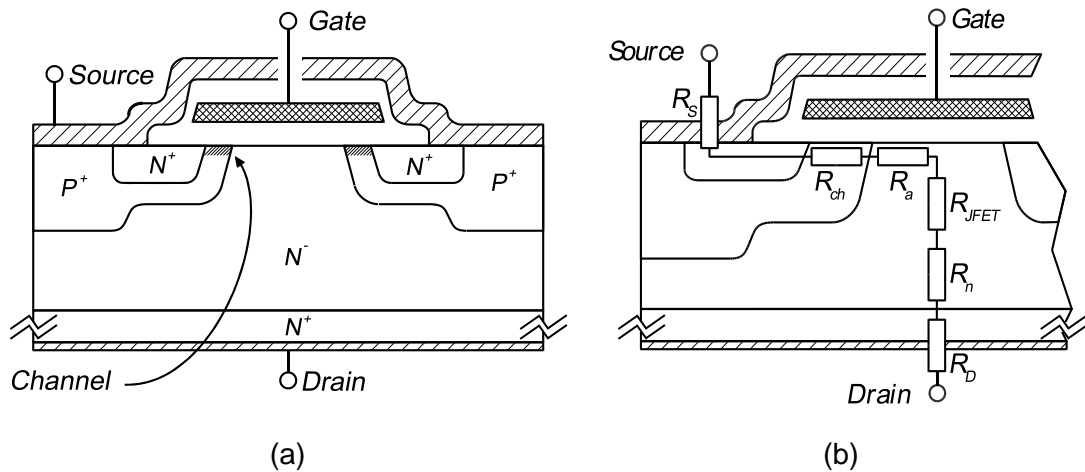


Figure 4.1 – (a) Cross-section of a representative power transistor device structure. (b) The electrical resistive components along the device's conductive path. Note that the figures are not to scale, as the N^+ region at the Drain can be 10-100x thicker than the other layers. Figures adapted from [173,174], with permission under Creative Commons license CC-BY-SA 3.0.

Figure 4.1(b) shows the primary components of electrical resistance along the current path through the device. The power is dissipated in each component via Joule heating can be calculated using:

$$P(t) = i^2(t) \cdot R \quad (6)$$

Where $i(t)$ is the electrical current through the transistor as a function of time, and R is the electrical resistance. Thus, most of the device heat generation occurs in the upper layers of the device, referred to as the device *junction*, where the higher resistance portions of the current path are located. This often permits the assumption to be made that all of the heat generation occurs at the top surface of the device, simplifying device heat transfer models.

4.2. Power semiconductor package thermal transport

Figure 4.2(a) shows a typical high-performance power electronic device module, incorporating a number of semiconductor die assembled into a particular circuit configuration. Figure 4.2(b) shows a cross-sectional sketch of the multiple layers in a typical power module stack. The layers within this package provide electrical interconnection between multiple circuit elements as well as mechanical support for reliable device operation. With respect to the thermal aspects of the package, most power modules are designed with the primary heat removal path through a heat sink at the base. The top of the device is typically kept free for wirebonding or other electrical contact, although there have been a few investigations of using the top side for heat removal as well [175]. All elements between the semiconductor junction and the final heat removal mechanism (whether an air cooled heat sink, liquid cold or chill plate, or other structure) comprise what is referred to as the *thermal stack*. Each piece of that stack contributes to the total thermal impedance of heat flow from the device.

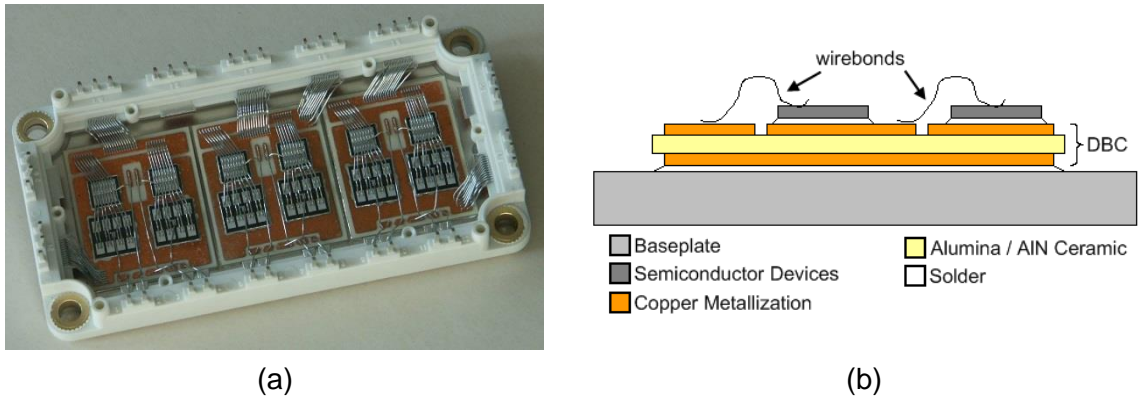



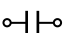
Figure 4.2 – (a) Representative multi-chip power electronic module (Eupec BSM200GD60DLC). (b) Power module packaging layer stack. Not shown in (a) is the electrically (and usually thermally) insulating encapsulant, potting compound, or gel used to fill the remainder of the module package.

Heat flow through and temperature in a linear material is described by the one dimensional heat equation shown in (7), which relates the energy accumulation and generation at any point, x , to the net rate of heat leaving that point:

$$\rho c \frac{\partial T}{\partial t} = k \frac{\partial^2 T}{\partial x^2} + g(x) \quad (7)$$

where ρ , c , and k are material density, specific heat and thermal conductivity, respectively, and $g(x)$ is the heat generation profile in the material. As mentioned earlier, often in electronic device operation heat generation is approximated as a heat flux boundary condition at the top of the device, eliminating $g(x)$. The resulting linear potential energy flow equation is common to numerous disciplines, and results in direct proportions between flow and either spatial or temporal potential gradient. It is often convenient to define thermal proportionality constants in analogous lumped electrical terms of resistance and capacitance. This approach to thermal modeling can be traced back well over half a century [176,177]. The analogy between domains is shown in Table 4.1.

Table 4.1 – Linear thermal equations and electrical circuit equivalents

Thermal Equation	Electrical Equivalent Equation	Equivalent Thermal Proportionality Constant	Standard Circuit Symbol
$q = \frac{kA}{l} \Delta T$	$i = \frac{1}{R} \Delta v$	$R_{th} = l/kA$	
$q = \rho cV \frac{dT}{dt}$	$i = C \frac{dv}{dt}$	$C_{th} = \rho cV$	

Using this analogy, it is possible to show that each layer in Figure 4.2(b) is a component contributing to the total thermal resistance, R_{th} , and thermal capacitance, C_{th} , of the package. Because the relative speed and duration of the electrical functions of these devices are often much faster than the thermal response of the package, often only the steady-state aspects of the device are examined. Additionally, in packages with many large semiconductor devices a 1-dimensional approximation of heat flow can be used. The combination of these assumptions permit the package to be modeled as a 1D thermal resistance chain, as shown in Figure 4.3. The layers generally considered part of the module package, indicated by the dashed box, are traditionally manufactured separately from the heat sink components. Each of these discrete layers contributes to thermal resistance according to its thickness and thermal conductivity. Additionally, it should be noted that there can be some finite contact resistance between each layer, although that component is sometimes lumped into effective resistance of the surrounding layers. Minimizing steady-state temperature rise can then be reduced to minimizing the sum of the thermal resistance components in the stack.

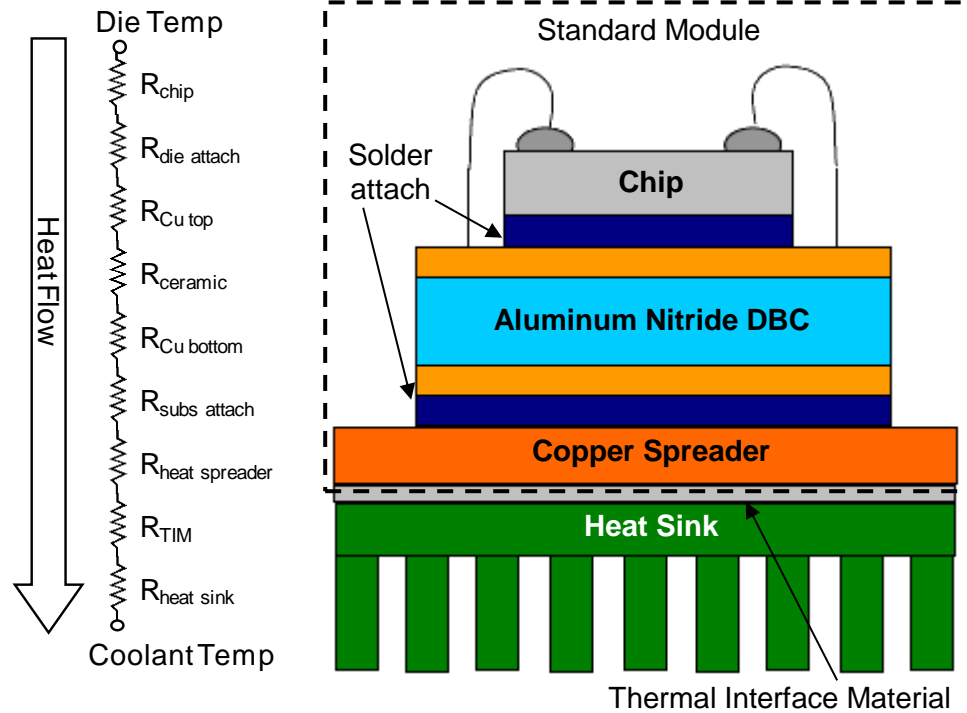


Figure 4.3 – Power electronics thermal stack depicting multiple thermal resistance components (layers not to scale). Dashed box indicates primary thermal module layers, usually manufactured independently from cooling components or heat sinks.

4.3. Improving power module steady-state thermal resistance

Figure 4.4 shows the junction temperature rise in a power package with a range of package thermal resistivities (resistance normalized to device area). With respect to improving steady-state thermal performance, it does not matter which resistances are reduced in the total device stack. The junction temperature will simply be a product of heat flux and total thermal resistance (or resistivity for a 1D, constant area condition), which is given by (8) and (9). Thus, it is sensible for improvement to focus on whichever components of resistance present the largest thermal resistance and the best possibility for reduction in that factor.

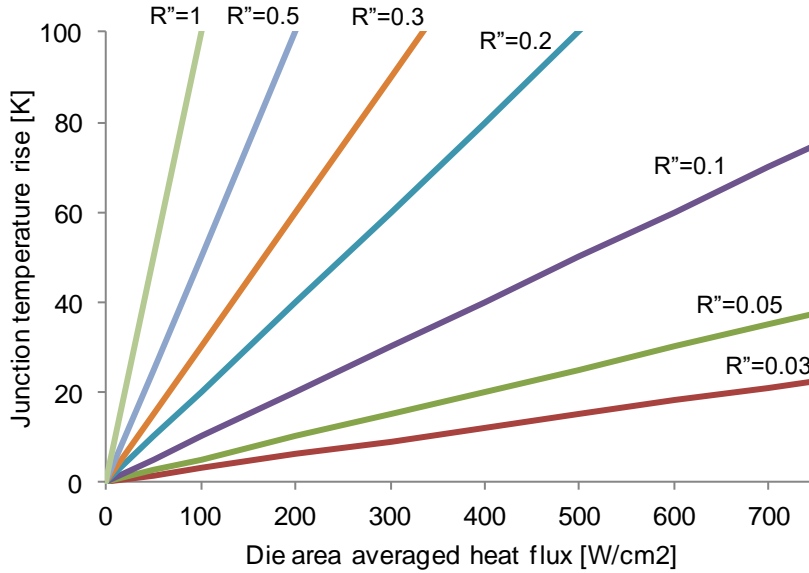


Figure 4.4 – Simple performance curves showing device temperature rise for packages with a range in values of total thermal resistivity (die area averaged, in units of $\text{cm}^2\text{K/W}$).

$$R_{th} = \sum_i \frac{t_i}{k_i A_i} + \frac{1}{h_{eff} A_s} \quad (8)$$

$$R''_{th} = \sum_i \frac{t_i}{k_i} + \frac{1}{h_{eff}} \quad (9)$$

The first terms in (8) and (9) represent the conductive portion of the thermal stack, consisting primarily of the power module itself. Improving the conductive portions of the thermal stack involve either increasing layer thermal conductivity by choosing different materials or thinning the layers to reduce total resistance. (For packages that do not fit the 1-dimensional model well, improvements also can be made by increasing heat spreading between layers.) The second terms represent the total heat sink thermal resistance, including any solid conduction that is not explicitly included in the first terms (such as heat spreading in fins) and fluid convection at the heat removal surface. Heat sink resistance can generally be improved by modifying the cooling mechanism to increase the convection

coefficient, h , or increasing the surface area, A_s . As detailed calculations of heat sink resistance can become quite complicated because it is highly dependent on geometries, fluids, and cooling mechanism, one-dimensional analysis often makes use of an effective convection coefficient, h_{eff} . As described by O'Keefe and Bannion in [178], this is defined as the convection coefficient that would produce the same effective heat removal rate on a flat surface with area equal to the conductive portion of the thermal stack. The effective convection coefficient is related to the actual, average heat transfer coefficient over the wetted surface by

$$h_{eff} = h \cdot AE \cdot \eta \quad (10)$$

where AE is the area enhancement ratio of wetted surface area to cross-sectional area and η is a surface area utilization efficiency term, similar to fin efficiency for an extended surface. For practical forced cooling mechanisms, the value for h_{eff} can vary from as low as $100 \text{ W/m}^2\text{K}$, representing moderate airflow over a finned heat sink, to more than $500,000 \text{ W/m}^2\text{K}$, representing some of the higher reported rates for forced liquid impingement cooling [179].

The thermal resistivities of low performance heat sinks or cold plates can vary quite widely, from about $0.5 - 5 \text{ cm}^2\text{K/W}$ (again, defined as junction temperature rise per unit heat flux at the die). At the same time, reviews of commercial grade and advanced power modules shows that junction-to-case thermal resistivities can be on the order of $0.1 - 0.3 \text{ cm}^2\text{K/W}$ [180,181]. Thus, the dominant factor for thermal improvement has for quite some time been to improve the heat sinking mechanism for the module. Numerous studies have been performed over several decades to address this problem, one of the most

prominent being the seminal work of Tuckerman and Pease demonstrating that microchannel cooling can be a viable high-performance cooling option [182].

Unfortunately, the large flow restriction and resulting pressure drop that these channels impose has made practical system implementation difficult, and temperature nonuniformity over the cooled regions can degrade performance and reduce reliability [183,184]. Estimated limits for maintaining reasonably sized pumps and ancillary components show a need for sub-35 kPa (~5 psi) pressure drops over the cooling device [185]. Modified microchannel designs, including branching [186] and manifolded structures [187,188], have been shown to mitigate some of these problems, and optimization can find acceptable design points [189,190]. The net result shows that microchannel coolers of various designs have demonstrated low thermal resistivity ($< 0.1 \text{ cm}^2\text{K/W}$) and high single-phase heat removal characteristics ($> 700 \text{ W/cm}^2$) [191].

Such low thermal resistivities from using microchannel cooling shift the focus back to the module portion of the stack for overall thermal improvement, as further efforts to increase convective performance approach a ‘diminishing returns’ condition with excessive system cost. The packaging layers, however, have already been optimized to satisfy multiple competing constraints, including high thermal conductivity, low thermal expansion mismatch to the semiconductor device, mechanical strength, and electrical conductance. An alternative to making further adjustments to those layers is to integrate the heat sink function into layers closer to the device. This would have the dual benefit of reducing thermal resistance, and relaxing design constraints on the layers no longer in the thermal path. In addition, by bringing microchannel coolers closer to the heat source, it may be possible to relax the fluidic design constraints, permitting a somewhat lower

convection coefficient while still producing a net reduction in total thermal resistance. The microchannels may be larger diameter, or pumped at lower flowrates, mitigating some of the high pressure drop problems limiting adoption of microchannel systems.

4.4. Substrate integrated cooling – fabrication and evaluation

A number of options are available for integrating module cooling closer to the semiconductor device, from tighter integration with the baseplate all the way to bringing the coolant directly into device contact. While the latter case would provide the lowest potential thermal resistance by completely eliminating any additional material from the thermal stack, it also removes any isolation between the electrical components and the coolant. Vehicle coolants (such as water or ethylene glycol based antifreezes) are generally conductive, creating a potential electrical shorting path. Dielectric coolants (which are primarily fluorocarbons or refrigerants) that could avoid the conductance problem have generally worse cooling performance, and have been shown to reduce convection under similar conditions by 50% or more [192]. As such, an integration point that preserves electrical isolation and enables use of arbitrary coolants is desired.

For the standard power module stack described in Figure 4.3, the device substrate is the aluminum nitride (AlN) direct-bond-copper (DBC) layer. As AlN is a high thermal conductivity dielectric material, the DBC is the closest layer to the device that would still provide electrical isolation, supposedly on the order of 50 V/ μm [193]. Integrating the heat sink function into the ceramic substrate would provide a significantly reduced thermal stack, as shown in Figure 4.5. While there still might be additional package layers or components around those shown, they would be removed from the thermal stack and would have less influence on device thermal performance.

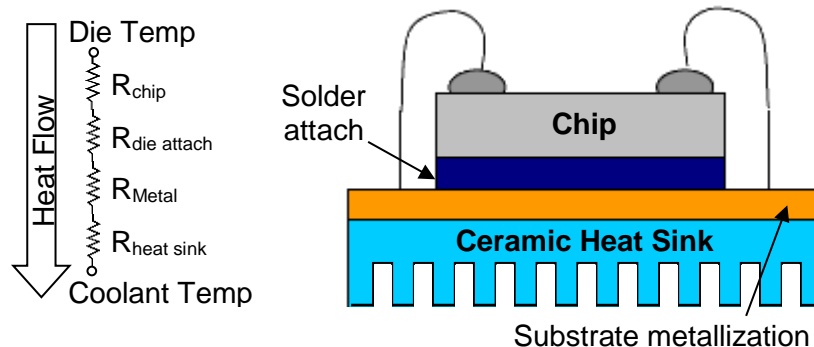


Figure 4.5 – Modified packaging and thermal stack with a number of layers and interfaces eliminated by moving the fluidic cooling into the ceramic substrate.

4.4.1. Ceramic substrate integrated cooling – fabrication approaches

Aluminum nitride ceramics have numerous qualities that make them advantageous as semiconductor substrates. In addition to the aforementioned voltage hold-off, the material’s coefficient of thermal expansion is closely matched to silicon and silicon carbide devices, and it has a high thermal conductivity [194]. These properties are summarized in Table 4.2.

Table 4.2 – Properties of Silicon, Silicon Carbide, and Aluminum Nitride [194]

Material	Thermal Expansion Coefficient [ppm/K]	Thermal Conductivity [W/mK]
Silicon	2.5	135
Silicon Carbide	4.6	280
AlN (ceramics)	4.2	170 - 200

Unfortunately along with the useful properties of AlN, it is also a brittle material that is very chemically inert. This restricts the use of standard micromachining operations for defining deep microchannels. A standard packaging substrate is ~25 mils (625 μm) thick. A few cases are presented in the literature where deep plasma etching has been successful in AlN, the most notable of which is found in [195], where the researchers were able to etch 50 μm deep using a chlorine-based plasma and a thick nickel etch mask. Unfortunately, limitations to depth currently make etching unsuitable for large scale power

electronic substrates. Two alternative techniques are evaluated in the following sections: diamond saw-cut microchannels, and stereolithographically fabricated substrates.

4.4.2. Diamond saw-cut ceramic microchannels

A relatively straightforward, high speed fabrication technique was used to fabricate a series of aluminum nitride microchannel substrates. A Disco DAD320 diamond bladed wafer dicing saw was used to make partial depth cuts in a 1" x 1" AlN substrate. The tool has a precision stage (accuracy: 3 μm lateral/1 μm vertical) with semi-automatic multiple cut capabilities, allowing the specification of cut position, number of cuts, and pitch with micron-level accuracy. Both 150 μm and 250 μm blades were used successfully to cut straight channels up to 300 μm deep into the 625 μm thick ceramic substrate. Thinner blades were found to “walk” and overlap each other when attempting to use a small cut pitch. An example of the saw-cut AlN microchannel substrates is shown in Figure 4.6.

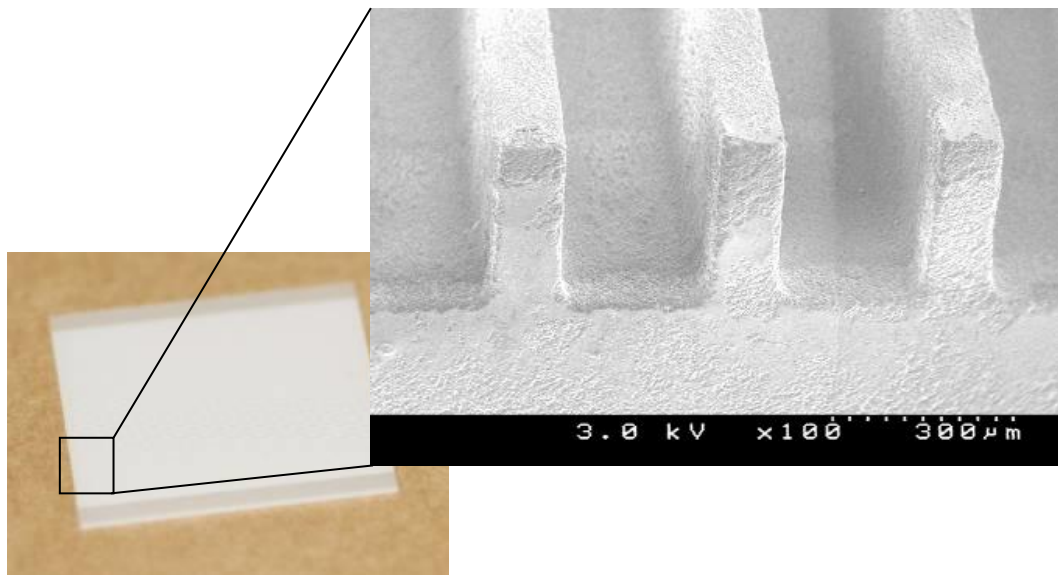


Figure 4.6 – Saw-cut aluminum nitride ceramic substrate. The channels shown were cut 300 μm deep with a 250 μm blade and a 375 μm pitch. (SEM image courtesy of Brian C. Morgan, Army Research Laboratory, Adelphi, MD.)

One concern when fabricating saw-cut channels was the dimensional accuracy that could be achieved. Cutting procedure involved zeroing the blade on the AlN top surface, then offsetting by the desired cut depth, typically 300 μm or $\sim 1/2$ the substrate thickness. The zeroing process was the most limiting aspect, as the AlN substrates were not sufficiently planar to take advantage of the saw's z-stage accuracy. As such, a series of test cuts were performed to examine cutting repeatability. Using a WYKO NT1100 Optical Profilometer, it was found that the target depth could be achieved to within $\pm 10\mu\text{m}$ across a 1 inch (~ 25.4 mm) piece. Also, cut width depended solely on the blade width, and appeared insensitive to blade translation or rotation speed. While there was some chipping on the top surface, using a relatively new blade produced near-vertical sidewalls with squared channel bottoms, as the Figure 4.6 SEM inset shows.

A primary drawback to the saw-cut microchannels is that the channels must go all the way across the substrate. Thus, it is only amenable for straight microchannels, open to the edge of the substrate, and not the more complicated channel structures mentioned earlier such as branching or manifolded structures.

Test substrates fabricated in this way were metalized prior to channel cutting. A 3-metal layer stack (50 nm Ti, 50 nm Pt, 1 μm Au) was deposited by a CHA electron-beam evaporator system. Next, the microchannels were cut into the backside of the substrate, channels centered under the die attach location. Finally, a second, flat piece of AlN ceramic was attached to cap the channels, and the two pieces were sealed together with Kapton tape and Loctite E-20HP epoxy.

Heat sources for thermal testing consisted of a 4mm 'mechanical grade' SiC Cree pin diode. The diode and copper tabs were soldered to the metalized substrate, and the top

of the die was connected using a pair of 10 mil (250 μm) aluminum wire bonds. A photograph of a packaged AlN microchannel substrate is shown in Figure 4.7.

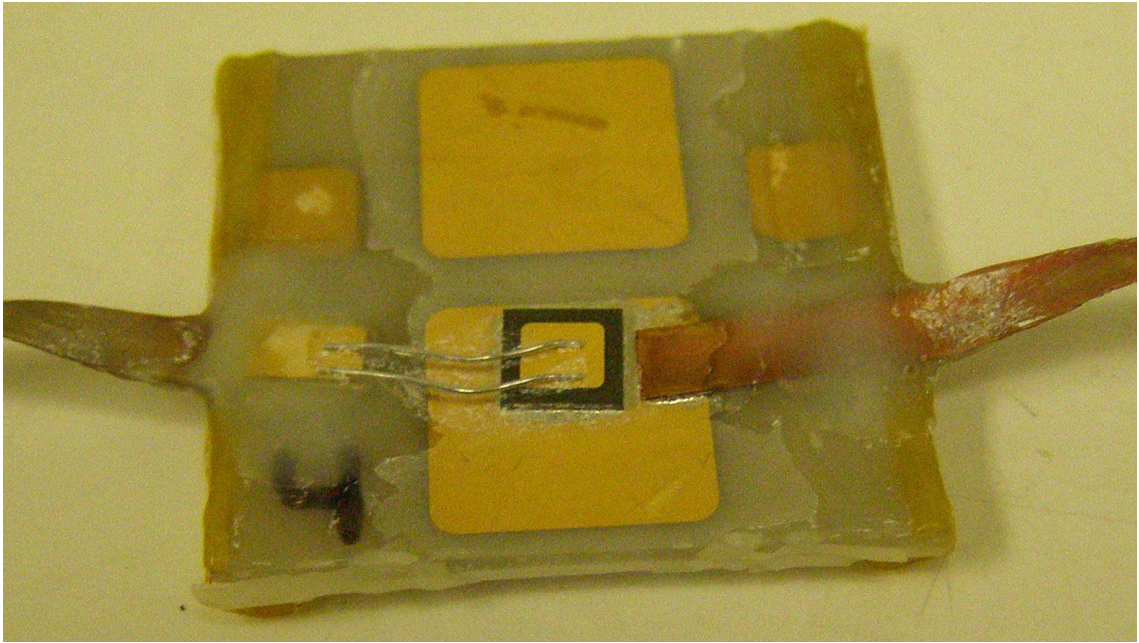


Figure 4.7 – Representative packaged and sealed AlN substrate with SiC diode heat source.

4.4.3. Stereolithographically defined ceramic microchannels

The previously described methods of fabricating AlN structures all suffer from the extra complications of enclosing channels, sealing edges, and making fluid connections. Developing a single-piece AlN microcooler with simplified fluidic connections and arbitrary geometries would overcome these difficulties. 3D printing has recently seen a surge in popularity since it was pioneered in the late 1980's by 3D Systems, Inc. Since that time there have been a number of new 3D printing techniques and materials, but most of the focus has been on plastics and metals. More recently, work has been progressing on stereolithography, one of the original 3D printing techniques, with ceramic materials. It is used to create the 'green' (unfired) ceramic part, which can then be processed into the final ceramic piece.

Technology Assessment and Transfer, Inc., (TA&T, Millersville, MD, USA) developed a ceramic stereolithography process capable of producing parts from aluminum nitride (in addition to other ceramics). With some limitations, the flexibility of stereolithographic fabrication enables creation of monolithic structures with complex features having dimensions down to about 150 μm . As mentioned before, the process involves the definition of the ceramic 'green' part in a standard 3D Systems stereolithography machine using a proprietary photosensitive ceramic resin. The system takes information from a 3D CAD file, translates the part information into machine code, and then builds the part layer-by-layer, successively laser curing the resin. The AlN material is built at a layer thickness of about 25 μm . Uncured resin is drawn from the part, and then it is fired in a high temperature furnace to achieve binder burn-off, ceramic sintering, and densification. The process is able to produce stereolithographic parts with thermal conductivity on the same order as commercial AlN substrates, typically 160-190 W/mK.

Due to limitations in part yield when producing complex microchannels (both resin removal and the firing process would cause splitting and warping on overly complex green parts), the substrates produced for this study were designed to be straight microchannels only. Fluid entrance and exit ports were able to be placed on the substrate face to ease fluid coupling relative to the edge-coupled saw-cut substrates described in the previous section. A representative sketch of a single-die substrate is shown in Figure 4.8. Following substrate fabrication, the devices were metalized and instrumented as described in Section 4.4.2, and a fully assembled substrate is shown in Figure 4.9.

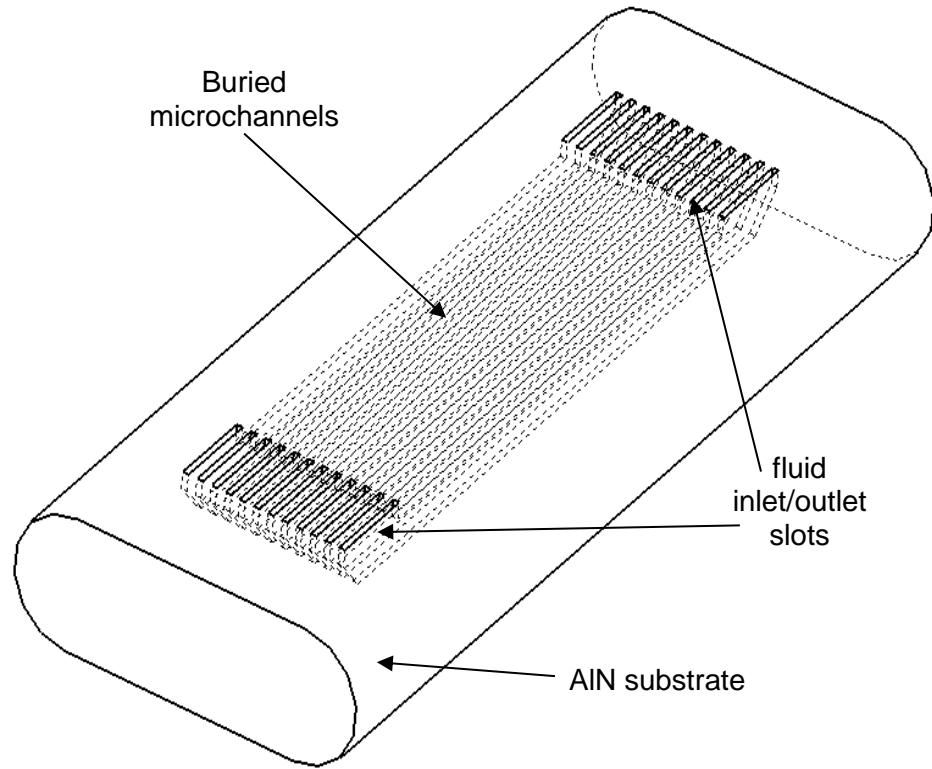


Figure 4.8 – 3D sketch of microchannel substrate used as the fabrication input file.

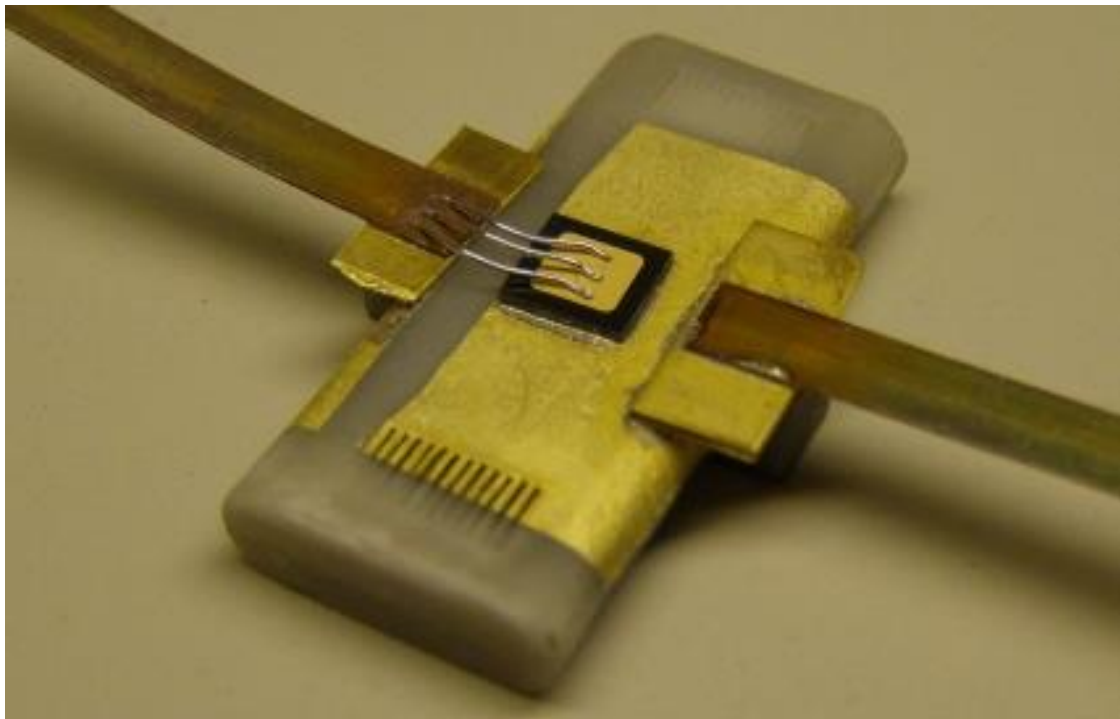


Figure 4.9 – Fully assembled stereolithographically fabricated AlN microchannel substrate.

4.4.4. Experimental Evaluation

This study measured the thermal performance of the two types of microchannel substrates described in the previous two sections to ascertain the technology's viability as a power device packaging option. The test procedure used active devices as heat sources while measuring power and temperature for a range of flow conditions, with particular focus up to the 35 kPa (5 psi) range of interest for vehicle electronics cooling.

4.4.4.1. Experimental Setup

Figure 4.10 shows the configuration of the test set used to evaluate the substrates. The system measures electrical energy into the SiC diode, heat removed by the fluid, fluid inlet and outlet temperatures, and device temperature. In addition, the setup has closed-loop fluidic control and electrical control of the power input for heat generation.

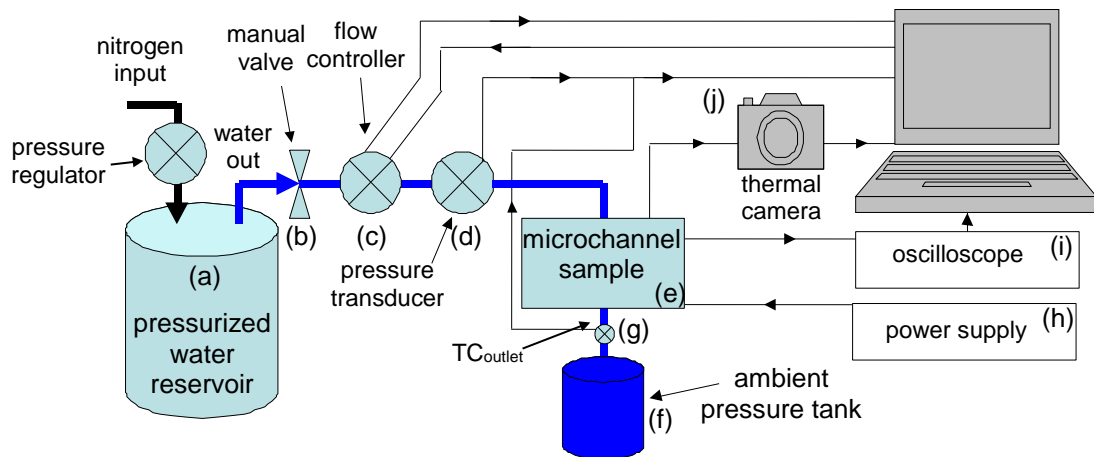


Figure 4.10 – Diagram of experimental setup for characterization of microchannel substrates.

The fluid control system consists of a pressurized tank (a) filled with room temperature (20-25°C) demineralized water that has been pressurized from 210-350 kPa (30-50 psig) by the house nitrogen line. The water flow is controlled by an Alicat Scientific LC Series flow controller (c) with a range of 0-200 mL/min ($\pm 2\%$), which also reads inlet

fluid temperature and upstream line pressure. A manual needle valve (b) before the flow controller allows coarse adjustment of the line pressure drop to facilitate stable flow control. Fluid pressure at the microcooler entrance is read by an Omega PX181b pressure transducer (d), with a full scale range of 15 psia (+/-1%FS). The flow passes through the microchannel substrate (e) and exits immediately to an ambient pressure reservoir (f). A type-K thermocouple, calibrated between 0-100°C to 0.2°C, embedded in the exit tube measures the exit temperature of the cooling water (g).

It should be noted that the system was initially designed for low flowrate measurements, and only has closed loop flow control up to 200 mL/min. Beyond this range, “open loop” flow control was performed using the needle valve (b). Prior to thermal testing, flow through each substrate was measured using a timer and graduated cylinder, and the associated pressure (as read from the PX181b transducer (d)) was recorded for that particular flow rate. Several measurements were made to average out measurement variations and estimate measurement error, and this data was used to predict the flow rate during thermal testing from the recorded pressure reading.

An American Reliance 1.2 kW power supply (h) (60 V, 20 A limits) in current controlled mode applies a forward bias to the diode bonded to the device. Delivered power is measured by a Tektronix TDS5104 Digital Oscilloscope (i). Diode average surface temperature is measured by a FLIR Systems Thermacam SC500 infrared (IR) camera (j). It should also be noted that the SIC diodes used in the experiment were ‘mechanical quality’ diodes, not fit for use as reliable components in a switching circuit. They were, however, readily available and served as excellent heat sources for the experiment as they mimic an actual die stack and have a high voltage drop (making for easier power supply

matching). However, it was noticed that some device nonuniformity gave rise to hot spots that were observed to sometimes exceed the average device temperature by more than 10-20°C. All measurements except the IR camera readings were directly captured by a Labview program on a local computer. Logs of IR camera measurements of die temperature were subsequently merged with the acquired sensor and control data for analysis.

4.4.4.2. Test sample preparation

Several substrates of each type were fabricated using the techniques described in Sections 4.4.2 and 4.4.3. For the saw-cut channels, there were significant yield issues due to the thin, brittle substrates being weakened by the diamond saw and splitting during demounting and subsequent assembly. As such, only two substrates were fully testable. The dimensions of these substrates (ALN2 and ALN4) are shown in Table 4.3. For the stereolithographic (STL) substrates, a number of dimensional variations were designed for fabrication by TA&T with channel depths ranging from 1-3 mm and channel widths from 100 to 400 μm. However, yield problems again limited the testable units to a set of four substrates, dimensions shown in Table 4.4. Primary yield issues included the ability to remove uncured resin, structural integrity of high aspect ratio features, and part splitting during firing. Surviving parts were primarily those with deeper channels and thicker channel walls.

Table 4.3 – AlN saw-cut microchannel cooler dimensions

Sample #	Channel Count	Blade Width [μm]	Pitch [μm]	Depth [μm]	Length [cm]
ALN2	10	250	470	300	2.54
ALN4	14	150	335	300	2.54

Table 4.4 – AlN stereolithographic microchannel cooler dimensions

parameter	units	TAT1	TAT2	TAT3	TAT4
Substrate Length	[mm]	27.3	27.3	27.3	27.3
Substrate Width	[mm]	11.5	11.8	11.7	12.0
Channel length ¹	[mm]	18.1	17.7	17.9	17.6
Channel width ²	[μm]	200	200	200	200
Channel pitch ²	[μm]	500	500	500	500
Channel depth ²	[mm]	2	2	2	3
Number of channels		12	13	13	13

¹ Measured between inside edges of inlet and outlet openings

² Design dimensions, not measured

For the saw-cut channels, fluid coupling was achieved using a sleeve gasket and mounting block as shown in Figure 4.11. Earlier attempts to use edge sealing or epoxy block encapsulation led to part breakage or leaking after several thermal cycles. The fixture shown uses a tapered silicone sleeve gasket (Cotronics Duraseal 1553) which makes a snug fit in the mounting block cavity. Inserting the test piece in the gasket slot and then attaching the lid compresses the gasket against the block making a water-tight seal (tested up to 200 kPa or ~30 psi). The block and lid were fabricated from ABS plastic on a Stratasys FDM Titan rapid prototyping system, and sealed with a thin layer of Loctite E-20HP epoxy.

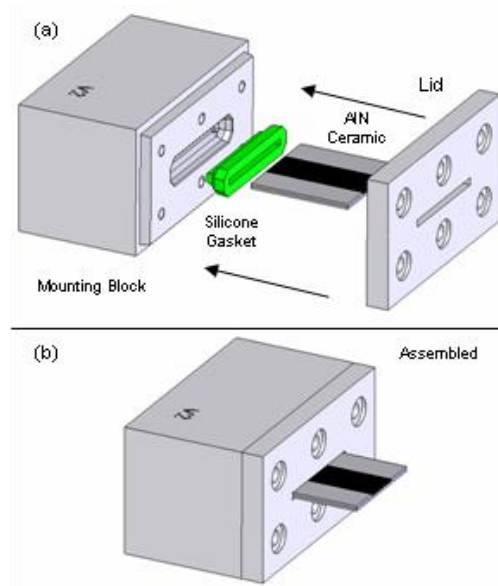


Figure 4.11 – Mounting block for AlN saw-cut microchannel coolers (a) pre- and (b) post-assembly.

Mounting the STL substrates was less cumbersome due to the face coupling entrance and exit holes. A flat butyl rubber gasket was clamped between the fluid inlet/outlet (the exposed channels seen in Figure 4.9) and the aluminum fluid header, providing leak-free sealing in excess of 210 kPa (~30 psi).

Prior to evaluation, all test pieces were coated with a thin layer of boron nitride spray (Rescor 112 by Cotronics Corporation) to increase uniformity of surface emissivity for infrared thermography. As discussed in [196], the boron nitride spray served a function similar to a matte black spray paint, providing an uniform emissivity of about 0.95, while remaining easy to remove with acetone or alcohol based solvents.

4.4.4.3. Test procedures

After ensuring leak-free mounting of the test pieces, either a flowrate was set by the Alicat controller (for flow rates below 200 mL/min), or the needle valve was adjusted to achieve a steady pressure drop across the device under test. After flow rate stabilization, a forward current was passed through the diode and gradually increased in approximately 1 A increments. At each current level the diode top surface average temperature was allowed to stabilize and data were recorded with the IR camera. Testing was terminated when die temperature approached 100°C to avoid the possibility the coolant being driven to boiling. Flowrate or pressure was then increased and the test was repeated for all flow setting and devices. Tests were generally ended at a total pressure drop of 70 kPa (or 10 psi). Following data collection, the sample's temperature, power, and flow characteristics were analyzed to quantify thermal resistance according to:

$$R_{th} = \Delta T_{d,avg} / q_{fluid} \quad (11)$$

where $\Delta T_{d,avg}$ is the increase in average diode temperature due to the applied power, and q_{fluid} is the amount of heat absorbed by the fluid, calculated via calorimetry using:

$$q_{fluid} = Q \left[(\rho c_p T)_{in} - (\rho c_p T)_{out} \right] \quad (12)$$

where Q is the volumetric flow rate, $T_{in,out}$ is the fluid temperature at the inlet and outlet of the test piece, and ρc_p are the density and specific heat of water evaluated at the temperature $T_{in,out}$ using the values found in [197]. This method of evaluating heat flow was chosen over simply using device power in order to get a more accurate value of the cooling performance of the device thermal stack. Heat loss to the environment would create an over prediction of cooling performance if device power was used, and it is expected that this non-ideal factor would not be negligible. Expected heat loss paths include conduction to the mounting fixture and fluidic connections and free convection of all heated surfaces to the surrounding air. In addition, while likely only a small contribution, a silicon carbide diode will emit light in proportion to the power applied, and that photon generation represents another method of energy loss. Thus, since the heat moving through the thermal stack was simply that absorbed by the fluid, using that and the endpoint temperatures as described by (11) permitted calculation of thermal stack resistance.

4.4.4.4. *Experimental results – microchannel fluidic behavior*

As mentioned in Section 4.4.4.2, a total of six AlN microchannel substrates were able to be tested. Only flow behavior of all six were evaluated, however, due to diode delamination at the die attach base metal between tests, and TAT3 could not be tested for thermal performance. As shown in Figure 4.12, the devices all show the expected 2nd-order polynomial dependence between pressure and flowrate, with linear dependence at low

flowrates due to channel flow, and quadratic dependence appearing for larger flowrates as other so-called ‘minor losses’ begin to dominate. (Although not shown in the figure to preserve clarity, each pressure-flowrate dataset had a 2nd-order, zero-intercept polynomial least squares fit between 99.2-99.95%.)

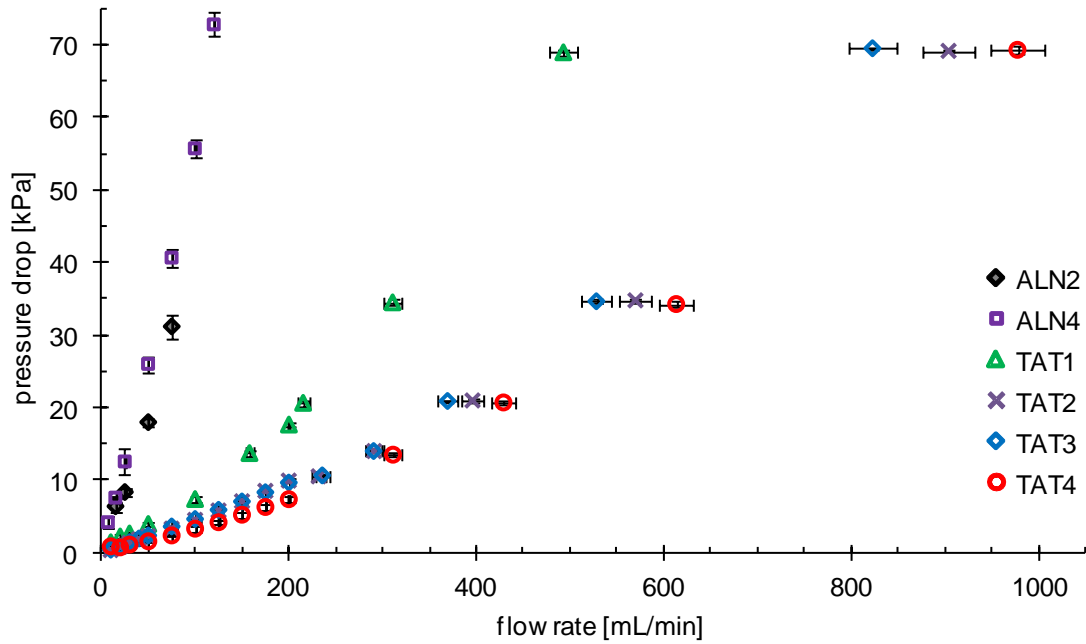


Figure 4.12 – Flowrate comparisons of the tested saw-cut and STL microchannel substrates. Note the different horizontal scales used for the two microchannel types, as they have significant differences in cross-sectional area. Horizontal and vertical error bars are included indicating +/- 3-sigma measurement variation, but are only significantly visible for high flowrate data points with manual flow measurement.

The saw-cut channels have a much smaller cross-sectional flow area than the STL channels, presenting a much higher flow restriction as evidenced by the quick pressure rise for ALN2 and ALN4 in Figure 4.12. In fact, they did not require flow testing outside the Alicat flow controller limit. Alternatively, the much deeper (several millimeters versus ~300 μ m) STL channels showed a much lower flow resistance, exceeding the Alicat flow

limit and requiring the use of manual flow measurement, as evidenced by the much wider error bars beyond 200 mL/min.

Additionally, we can look at the flow characteristics of the channels and compare them to expected, ideal channel flow. According to elementary laminar channel flow theory, the proportionality constant between pressure drop across a channel and flow through it is called the friction factor, f . (In this document we refer only to the Darcy friction factor, not the Fanning friction factor, the latter differing only by being 4x smaller than the former.) f is not a constant, as it decreases with increasing flowrate, and is defined as:

$$f = C/Re \quad (13)$$

where C is the Poiseuille Number, a constant in fully developed flow. C has a value of 64 for pipes with circular cross section, and the number varies with cross-sectional aspect ratio for rectangular channels, with a value of 96 for the limiting condition of infinite parallel plates ($AR = W/L \rightarrow 0$). C for rectangular channels can be reasonably approximated using the polynomial fit in (14) from Shah and London [198], and Table 4.5 lists the Poiseuille Numbers for the channels tested in this study.

$$C = 96(1 - 1.3553AR + 1.9467AR^2 - 1.7012AR^3 + 0.9564AR^4 - 0.2537AR^5) \quad (14)$$

Table 4.5 – Substrate idealized Poiseuille Numbers

#	AR	$C = f \cdot Re$
ALN2	0.833	57.3
ALN4	0.500	62.2
TAT1	0.075	87.2
TAT2	0.075	87.2
TAT3	0.075	87.2
TAT4	0.050	89.9

Channel behavior can be compared with these ideal values by calculating the Reynolds number and the apparent friction factor from measured flow conditions using the following formulas:

$$Re = QD_H / \nu A_c \quad (15)$$

$$D_H = 4A_c / P \quad (16)$$

$$f = \frac{2D_H}{\rho L} \frac{\Delta p}{(Q/A_c)^2} \quad (17)$$

Q is the channel volumetric flowrate, Δp is the pressure drop, ν and ρ are the fluid kinematic viscosity and density, D_H , A_c , and P are the channel hydraulic diameter, cross-sectional area, and perimeter, and L is the channel length. The measured $f \cdot Re$ product using (15)-(17) is shown in Figure 4.13 along with the calculated values from Table 4.5. In addition, the normalized Poiseuille Number, C^* , which is the measured $f \cdot Re$ normalized by the calculated values, is shown in Figure 4.14

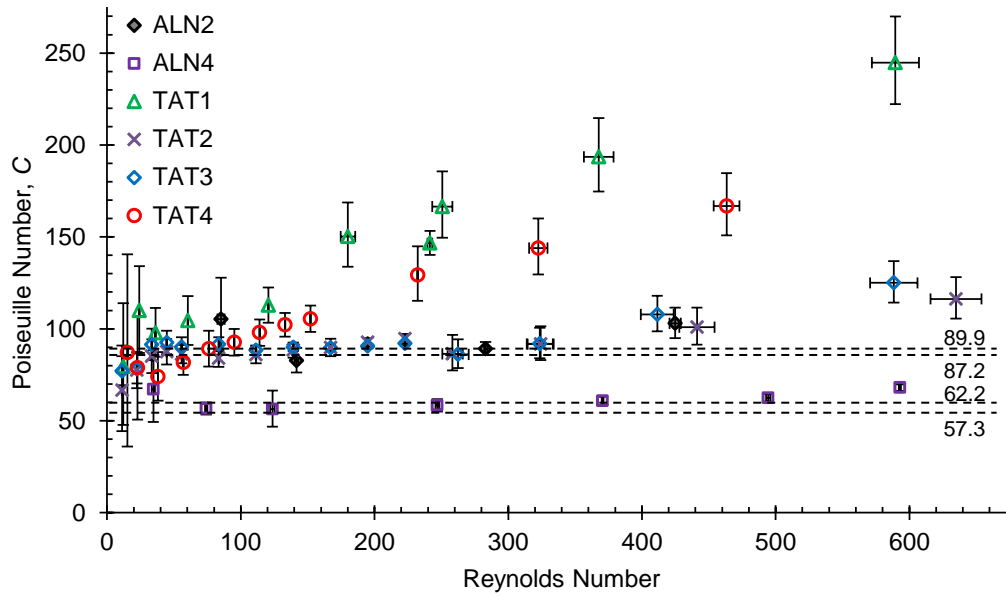


Figure 4.13 – Measured Poiseuille number (C) for the tested flow conditions. If fully developed channel flow dominated the pressure drop characteristics, C would be constant over the full laminar flow regime. Constant value lines from Table 4.5 are shown for the different channels.

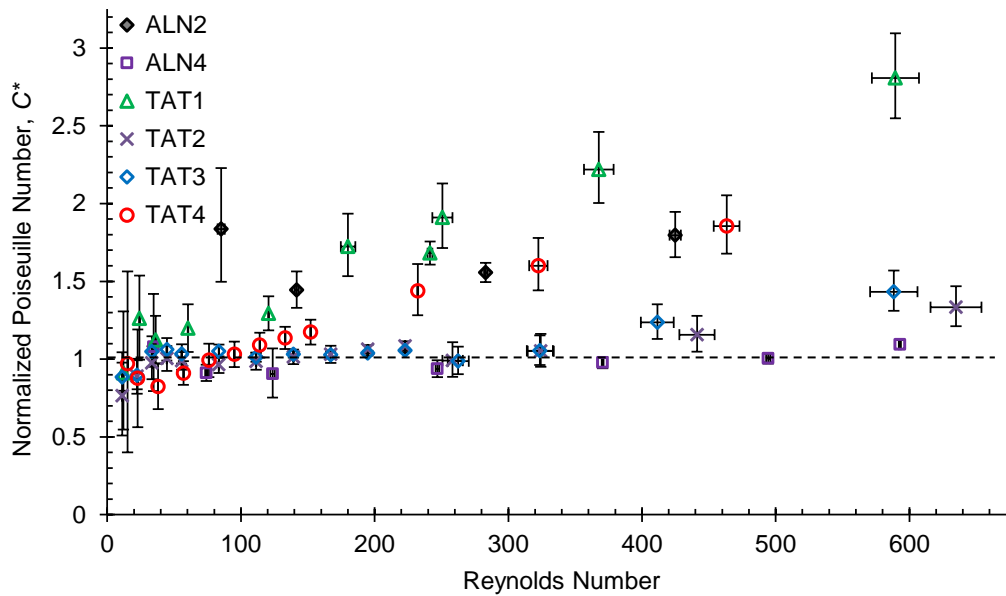


Figure 4.14 – Normalized Poiseuille number, C^* , or measured $f \cdot \text{Re}$ product divided by calculated $f \cdot \text{Re}$ for fully developed flow. Horizontal line for ideal case where $C^* = 1$ is shown.

Readily apparent from those two Figures is the fact that significant deviation from the fully developed, calculated value of C is evident for TAT1 and TAT4, which start around the right level but show increasing significantly increasing friction factors, and ALN2, which has a relatively constant Poiseuille number but at a value about 50% higher than it should be. It was recently shown that in much of the literature, a common cause of deviation from the expected value for C likely comes from the influence of entrance effects dominating microchannel flows, and significant fractions of the microchannel being in the developing flow condition [199]. In fact, several recent studies have suggested the use of an *apparent friction factor* term that accounts for the additional pressure drop due to hydrodynamically developing flow to improve predictions of microchannel flow behavior [199,200]. Developing flow length can be estimated for laminar pipe flow as:

$$x^+ = \text{Re} \cdot D_H / 20 \quad (18)$$

Along this entrance region, additional pressure drop is occurring due to increased shear stress at the channel entry point. These losses accumulate until the flow has become fully developed. Figure 4.15 shows the relative developing flow length (x^+/L) in each channel. It can be seen that testing the TAT microchannel substrates out to much higher flowrates saw developing flow lengths in excess of 50% of the total channel length. This could explain the significant deviation from the laminar fully developed flow models for most of the tested structures.

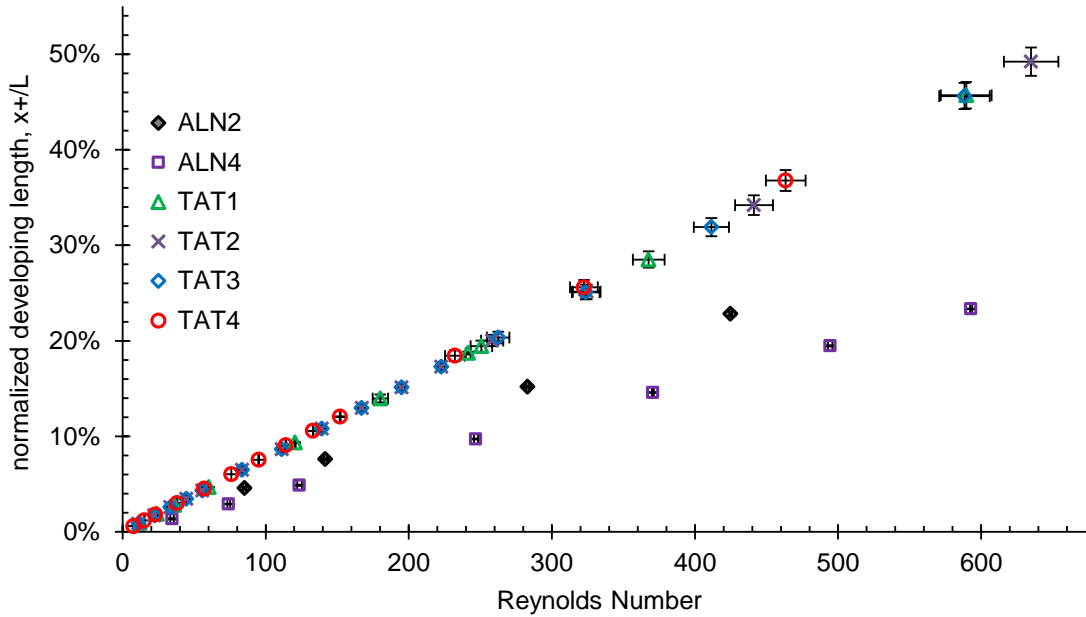


Figure 4.15 – Relative developing flow length in each of the tested microchannel substrates. The ALN substrates were only tested to flowrates that drove the developing flow lengths to about 25% of the channel length, the TAT devices were tested to much higher flowrates, driving the developing flow lengths in excess of 50% of the channel length.

The additional losses in the developing flow region can be accounted for with a modified Darcy–Weisbach equation that uses K-factors for *minor losses* in pipe systems:

$$\Delta p = \left(f \frac{L}{D_H} + K_\infty \right) \frac{\rho}{2} \left(\frac{Q}{A_c} \right)^2 \quad (19)$$

where K_∞ is the total loss term associated with hydrodynamically developing flow. Miller and Han [201] calculated the values of K_∞ , which like C are primarily dependent on channel aspect ratio. The following equation predicts their results to within 1%:

$$K_\infty = 0.658 + 1.37763AR + 0.76601AR^2 - 2.67294AR^3 + 1.30587AR^4 \quad (20)$$

Rearranging the friction terms in the above equations, we can define an *apparent friction factor*, f_{app} , that accounts for both the friction factor, developing losses, and head

loss at both the entrance and exit. (All tested microchannels experience a significant contraction/expansion heading in/out of the channels.) Also, an associated apparent Poiseuille number, C_{app} , can be defined:

$$f_{app} = f + \frac{D_H}{L} \sum K \quad (21)$$

$$\sum K = K_{in} + K_{out} + K_{\infty}, \quad (K_{in} \approx 1/2, K_{out} \approx 1) \quad (22)$$

$$C_{app} = f_{app} Re = C + Re \frac{D_H}{L} \sum K \quad (23)$$

With these definitions, we can reexamine the channel data to see if taking into account the hydrodynamically developing flow is sufficient to better predict the measured microchannel flow behavior. Figure 4.16 shows the C_{app}^* , which is the measured Poiseuille Number divided by the calculated value for C_{app} as given in (23).

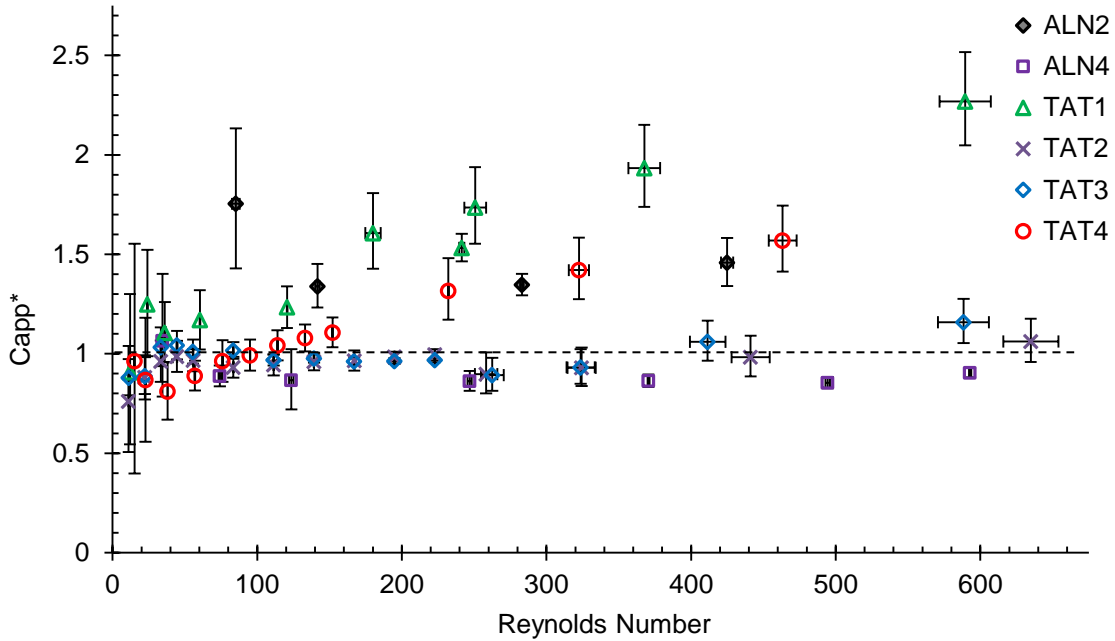


Figure 4.16 – Relative apparent Poiseuille Number which adds in the effects of entrance, exit, and developing flow losses. Significant deviation is still noticeable for some channels.

From the figure, it is apparent that ALN2, TAT1 and TAT4 have flow behavior that is still poorly predicted by the simple flow models used here. While their relative Poiseuille Numbers get closer to one by taking the additional losses into account, especially at the higher Reynolds Numbers, it is clear that there must be additional losses present in the real structures. Both TAT1 and 4 are fairly well predicted at low flow rates, indicating that the problem may be with additional second-order losses, such as channel point defects. ALN2, however, showed continued high pressure drop for all flowrates. In fact, it could be noted that applying the additional losses to the model actually decreased the predictive accuracy for ALN4, which had been right on the $C^*=1$ line, but C_{app}^* was now pushed 10-20% below one at higher flowrates.

4.4.4.5. Experimental results – thermal behavior

Prior to examining the substrates' cooling performance an energy balance was performed in an attempt to quantify the amount of heat loss to the ambient, as described in Section 4.4.4.3. The energy balance was calculated by comparing the applied electrical power, using (6), to the heat absorbed by the cooling fluid, using (12), and is shown in Figure 4.17.

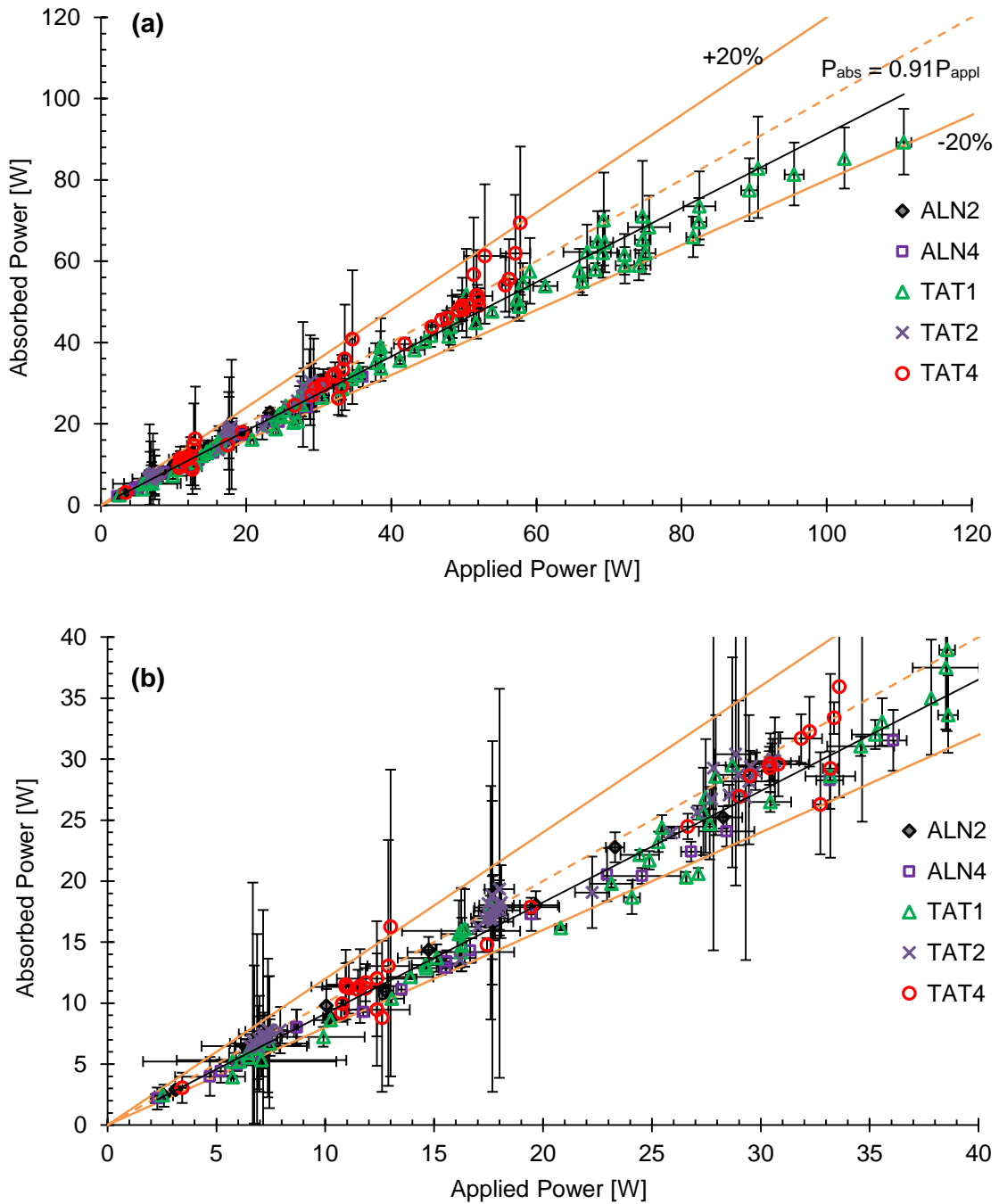


Figure 4.17 – Energy balance comparing the applied electrical power to the measured increase in fluid heat over (a) 120W range and (b) a close-up of 40W power range. Dashed and solid lines show the ideal 100% absorption values and +/- 20% deviations. The black trend line shows the average absorption over all the data to be about 91%. Error bars shown are 3-sigma deviations.

Absorbed heat is plotted against applied electrical power, and an ideal system would have all data points on a line with unit slope, shown with a dashed line in the Figure. The majority of the data falls below this line, but within a 20% error band about the ideal case. Some data actually falls above the 100% absorption line, which is a physical impossibility unless the system had an additional heat source. All of those cases, however, have much larger error bars that cross back over the 100% line. For the most part, data with such large experimental error occurred for cases of high flow rate and low power, such that the temperature rise due to absorption is not much higher than the thermocouple measurement noise. The average system loss, which is actually a combination of experimental error and system heat loss, is around 9%, as shown by the solid black line on the energy balance.

Finally, the primary metric being evaluated for these microchannel coolers is the thermal resistance at various flowrates, shown in Figure 4.18. The secondary axis is the thermal resistivity, normalized to the heat source cross-sectional area of 16mm^2 . The tested substrates show the expected power law dependence on flowrate as the thermal resistance drops quickly before about 200 mL/min, and then levels off to near steady values. At this point the fluid resistance has reached a minimum and the remaining thermal resistance is primarily due to the substrate's solid conduction resistance.

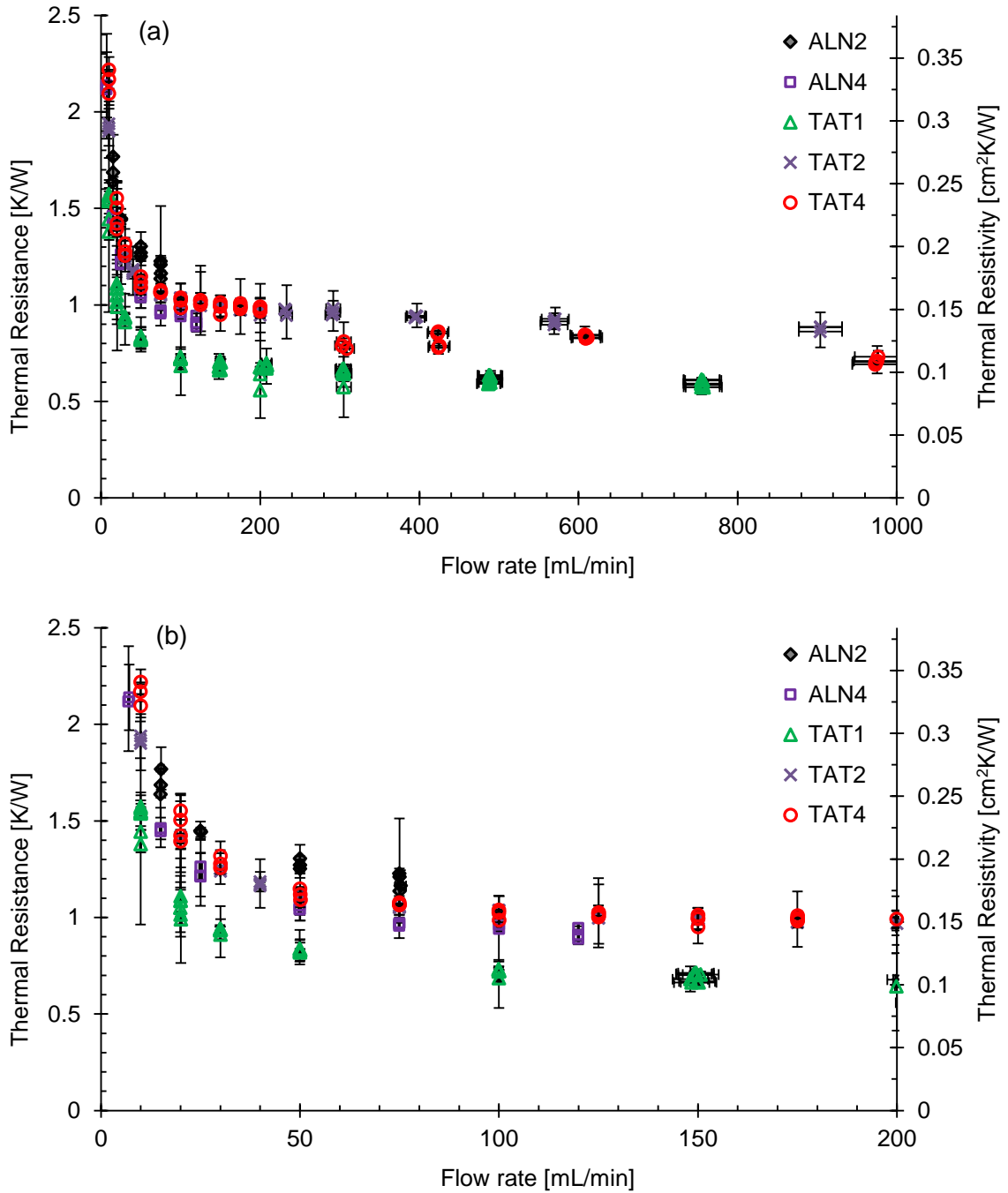


Figure 4.18 – Thermal resistance and resistivity of the tested substrate integrated microchannel coolers. (a) Full flow rate range up to about 1000 mL/min, and (b) a closer view up to 200 mL/min. Resistivity is normalized to heat source cross sectional area. Error bars shown are 3-sigma deviations.

The lowest thermal resistance over the tested range was shown by TAT1, which also had the highest flow restriction among the Stereolithographic substrates. This makes sense when compared based on total flowrate, as TAT1 has one less channel than the other two TAT test pieces. Thus for a given flowrate the channel velocity would actually be about ~8% higher than in TAT2. The ALN microchannel substrates showed similar thermal behavior to the TAT microchannels, but the higher pressure drops prevented them from achieving the same flowrates. As expected, the much taller microchannels in the TAT substrates enabled significantly improved thermal performance without the high pressure-drop penalty, although all tested devices were able to reach thermal resistivity values below $0.2 \text{ cm}^2\text{K/W}$

4.5. Summary substrate integrated cooling

The goal of this substrate microcooler evaluation was to validate the ability to demonstrate low package thermal resistance to improve the steady-state cooling of power electronic devices. Both substrate approaches, the saw-cut channels fabricated from finished AlN substrates and the Stereolithographic channels defined prior to ceramic fabrication, required only relatively standard electronic packaging approaches for die attach and assembly. The potential improvements from using these or similar substrates are significant when one considers the fact that the thermal resistivity values achieved here are typical for advanced module thermal stacks *without* the heat sink. Additionally, the microchannel dimensions used in these substrates are not exceedingly small (the TAT substrate dimensions would be considered milli-channels by some), showing that ultra-fine microchannels are not absolutely necessary to achieve net reductions in thermal resistance. These substrates encompass the total thermal path, heat sink included, and demonstrate the

immense advantages and packaging simplifications to be gained from bypassing a significant portion of the power electronics thermal stack and bringing the cooling fluid closer to the heat source in an integrated package. Improvements in the AlN microchannel substrate manufacturing methods, and scaling to larger substrates for multi-chip modules should improve viability of the approach by reducing cost, part count, and integration complexity.

Chapter 5 – Transient heat transfer in power electronics

The previous chapter described approaches and efforts to improve the thermal performance of power electronic packages by reducing the net thermal resistance of the multiple layers and convective cooling scheme. This is often adequate for systems with steady or slowly-changing heat profiles. In practice, and especially in cases of interest for Thermal Buffering or Thermal Energy Storage, a steady-state approach to thermal design is inadequate to capture the system's cooling requirements. In this chapter, we examine transient heat flow applied to multi-layer electronic packages, and evaluate the effectiveness of the aforementioned steady-state improvement approaches on non-steady state heat transfer. Specifically, we develop transient thermal circuit models to identify the limits of steady-state package improvement on transient thermal response, and lay the groundwork later chapters addressing package improvements using phase change materials to better manage transient loads.

5.1. High rate transient heat transfer – impact on power electronics

The types of packaging improvements described previously have led to the development of advanced cooling structures and packaging schemes for power electronics modules. Such improvements have involved enhancing convective performance [140], using high thermal conductivity materials [202], and reducing the number of layers in the package thermal stack [144,146]. These improvements significantly decrease thermal resistance between the cooling medium and the semiconductor devices allowing for system operation at increased power and functional density. However, as we focused on in Chapter 1 and Chapter 3, vehicle electronics are not static thermal systems. They experience thermal transients that span from milliseconds to hours. At the same time,

numerous manufacturing and technology research communities have been increasingly investigating the use of pulsed power electronic systems for a variety of performance and capability improvements [203,204]. The U.S. Army has also been investing in pulsed power electronics for a number of offensive and defensive applications [205,206]. Thus, there exists a need to understand how electronic packages perform under transient conditions to optimize their development for these applications.

As with vehicle transients, the specific definition of *pulsed* varies greatly from one application to the next. They generally feature repeated, large, fast power draws at low duty cycles. A hypothetical pulsed power profile is shown in Figure 5.1. There are two distinct phases to the thermal conditions resulting from the pulsed operation. First, the peak temperature rise is a function of the driving pulse and the package thermal impedance. Second, the generally slower heat rejection phase during the ‘off’ portion of the duty cycle is entirely driven by the cooling mechanism, and in this period a ‘thermal reset’ must occur in time to prepare the system for the next pulse.

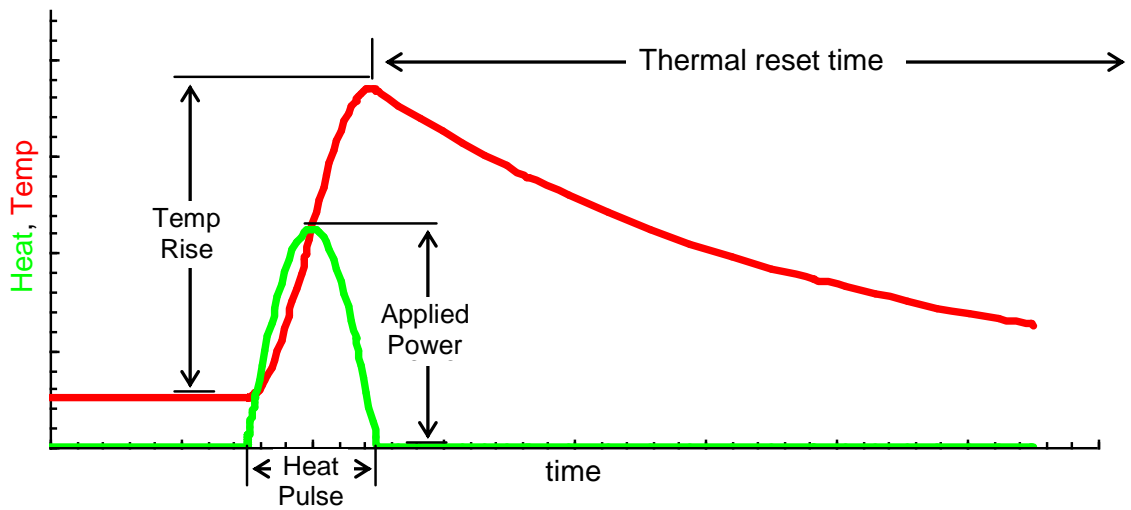


Figure 5.1 – Hypothetical low duty cycle pulsed thermal profile with a rapid temperature rise due to a sudden heat load, followed by a gradual cool down during the ‘reset’ period between pulses.

These pulsed systems create an extreme version of the same thermal overdesign problem previously described for other transient systems. The high stress, low duty cycle thermal profile imposes the challenge of rejecting the large, near instantaneous heat loads while at the same time meeting cooling system size and weight goals. The low duty cycle implies that the average power draw for these pulsed systems is much lower than the peak, and peak cooling system design will necessarily involve excessive overdesign from an energy perspective.

Electronic packages have typically been developed and improved only considering steady applications. In addition to the overdesign issue, however, there is a more critical concern that the packages could actually have degraded performance for systems with fast transients. As described in a study by Meysenc [148], most of the previously described package thermal improvement efforts have decreased local thermal capacitance (C_{th}) along with the desired reduction in thermal resistance (R_{th}). The effect of this can be estimated by looking at R_{th} , C_{th} and the thermal time constant, τ , using the following one-dimensional lumped element relationships:

$$R_{th} = l/k_{th}A_c, \quad C_{th} = \rho c_p V = \rho c_p A_c l \quad (24)$$

$$\tau = R_{th}C_{th} = l^2 \rho c_p / k_{th} = l^2 / \alpha \quad (25)$$

As can be seen from (25), while reducing the thermal stack via layer thinning or elimination reduces R_{th} linearly, it also decreases C_{th} linearly and therefore τ quadratically. Meysenc's analysis showed that because a device's thermal capacity slows the related junction temperature rise, reducing material (and capacitance) can make the devices more sensitive to a wider range of transient conditions. Whereas a package with a higher time constant would damp out the thermal response above a certain frequency or pulse rate,

packages with smaller time constants would exhibit increased temperature swings from higher frequencies such as those employed in pulsed systems. This is shown graphically in Figure 5.2.

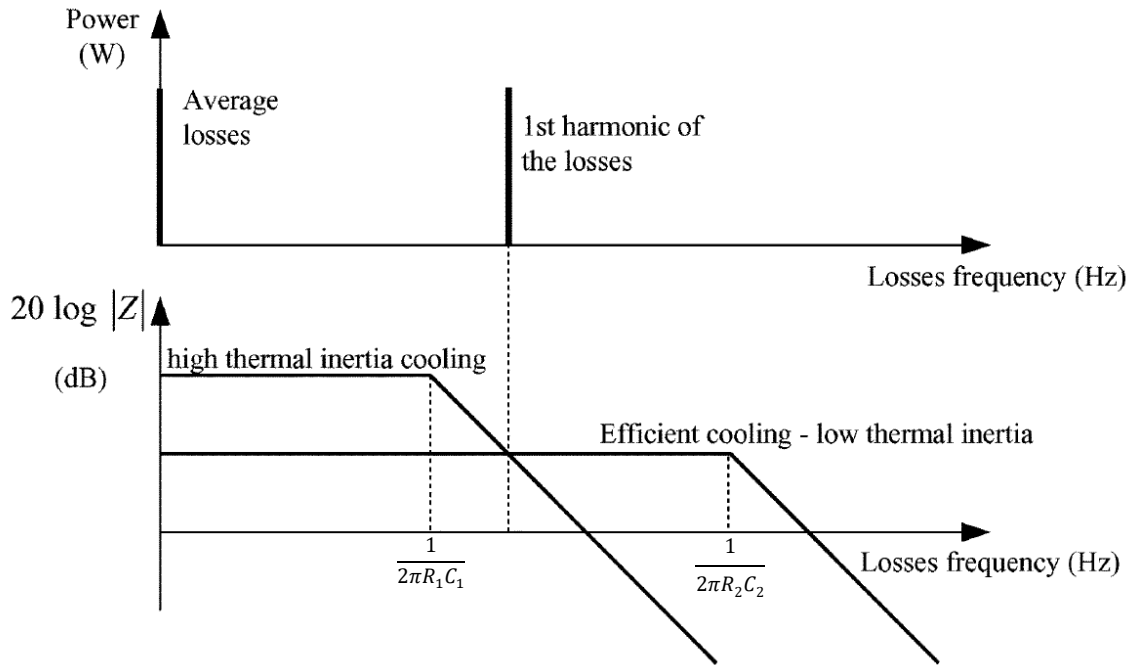


Figure 5.2 – Frequency domain losses profile for high and low thermal inertia electronics. The high thermal inertia cooling shows a response roll off at lower frequencies due to a larger RC time constant, while the low thermal inertia component shows a full response out to much higher frequencies. The crossover point between the two response curves shows the frequency above which the ‘efficient’ package will counterintuitively have a larger thermal response than the ‘inefficient’ package, adapted from [148] with permission, © 2005 IEEE.

While a review of power electronics literature has not shown many extensive transient thermal package comparisons, there have been a few studies that have shown a thermal performance inversion as Meysenc suggested. Several studies focused on the impact of the baseplate or heat spreader in a power electronics package. Lim and Pulko showed that despite a pure copper baseplate having higher thermal conductivity and

therefore lower steady state thermal resistance, a copper-molybdenum substrate had a higher density and specific heat resulting in lower temperature rise for pulses up to about 18 ms long [207]. Similarly, Asimakopoulos and Thiringer showed that in standard power modules with baseplate thicknesses ranging from 0.5-5 mm, the thickest baseplates resulted in the lowest temperature rise for pulses up to 7 sec long due to the higher heat capacity near the heat source [208]. In separate studies by Wang, et al.[209], and Cao, et al.[210], standard modules with and without separate heat spreaders were compared. In both cases, the modules with heat spreaders (and thus somewhat higher thermal resistance) had lower temperature rise for the first 0.5-1 second of transient heating. Finally, in a study of automotive inverter designs Buttay, et al., compared modules built for one- and two-sided cooling. The two-sided design had much lower steady state thermal resistance, however for up to about the first 0.1 second of transient heating the single-sided module showed slightly less heating, likely due to additional static thermal mass present on the uncooled side [211].

Thus, we can see that there exists a need to optimize both package thermal resistance and capacitance. In fact Cao and Krusius analyzed several heat absorption techniques for pulsed devices looking for conditions that maximize the supportable repetition rate (or maximizes the duty cycle) [212]. They demonstrated that an optimized transient thermal solution must address both the need to absorb heat to reduce peak temperatures (C_{th}) and the need for maximum heat removal (R_{th}) to minimize the time to return to a steady-state condition. Meeting this requirement would also achieve minimum package overhead while meeting device thermal requirements.

5.2. Transient heat transfer – thermal circuit approximations

Referring back to Section 4.2, and in particular (7), transient heat conduction in semiconductor devices is a (generally) linear potential energy flow problem. Unlike the case described in that section, however, we cannot eliminate the transient terms and simplify the thermal problem into a simple resistor stack. Heat capacity must be taken into account, and a separate analytical solution must be derived from (7) for each unique power package and heating scheme. While a number of these analytical solutions do exist, and some can be applied to arbitrary package and thermal conditions [213], implementation quickly gets excessively laborious.

An alternative to exactly solving the heat transfer equation is to develop approximate solutions by taking advantage of the thermal circuit analogy also introduced in Section 4.2. Some work is required before those equivalents can be directly applied to a power package model, however. The thermal resistance and capacitance equivalents presented in Table 4.1 are only simple nodal equations, valid for isolated homogenous, steady heat flow in the case of resistance, or steady heat flow into a fixed, isolated, and homogenous thermal reservoir in the case of thermal capacitance. Implementation for distributed systems either requires developing more complex expressions, or more preferably taking advantage of one of the various methods of discretizing spatial domains. This shifts some of the solution complexity to the interconnection between domains.

Two of the more popular discretization methods for potential flow equations are the Finite Difference Method (FDM) and the Finite Element Method (FEM). Both methods involve dividing the problem into smaller subdomains in which approximate (usually linearized) local solutions to the relevant partial differential equations can be found.

Spatially recombining these local solutions can provide reasonably accurate approximations to the total solution while avoiding the typical analytical intractability of complex systems.

5.2.1. Thermal circuit analysis – enabling electrothermal codesign

It is worth commenting on another advantage of choosing the thermal circuit approach to model electronics heat transfer. The impressive increase in computing performance over the past few decades coupled with the steady push toward smaller form-factor systems has led to challenging thermal problems for electronic product designers. Even with smart power management strategies, both mobile and high performance processors produce enough heat to make chip temperature a significant operation and reliability concern [214]. Solving these challenges has pushed standard design approaches, where electrical and thermal components are independently implemented, to their practical limit. Thus, for some years there has been a drive toward electro-thermal codesign, where the separate domains are considered in parallel during the design process. This co-design improves the ability to make thermally-informed circuit design choices, rather than discovering thermal problems late in the design cycle [215]. Making the thermal challenge part of the initial circuit design constraints could lead to improvements in component design just as ‘power aware computing’ has led to significant improvements in low power, high performance computing [216,217].

While there are numerous simulation options available for thermal designers, there is a limited degree to which many of them can integrate with electronics design tools. The thermal equivalent circuit approach, however, naturally lends itself to electro-thermal co-design because it recasts the thermal problem into the electrical domain enabling use of the

same tools. Circuit modeling software (e.g., SPICE) is already integral to electrical design and is made to solve steady and transient problems of widely varying complexity. Circuit simulation permits electrical and thermal co-simulation, as shown schematically in Figure 5.3, rather than using separate programs or decoupled iteration. Finally, moving the thermal problem into the electrical designer’s toolset will help reduce any reluctance toward the eventual adoption of electro-thermal co-design as standard practice [218].

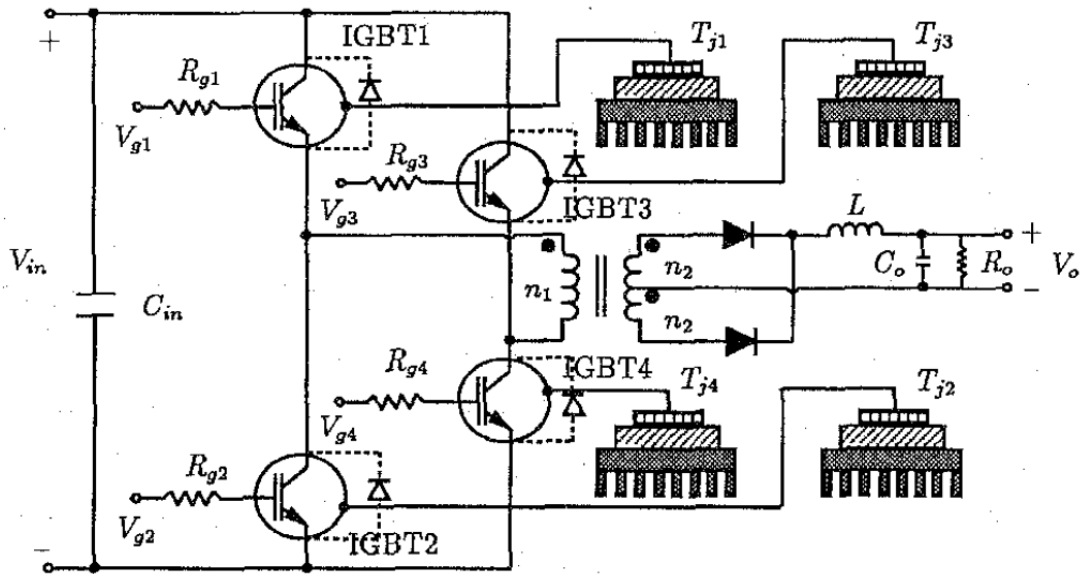


Figure 5.3 – Circuit schematic of a representative electrothermal codesign problem , where a four device full-bridge converter connects the electrical and thermal IGBT models through virtual temperature nodes, from [219] with permission, © 1996 IEEE.

5.2.2. Finite element thermal circuits

The two numerical methods previously described, FDM and FEM, can be differentiated by their approach to obtaining the approximate equations applied over the discretized problem domain. FDM is the more straightforward of the two. In the relevant heat transfer partial differential equation (PDE), algebraic difference approximations are

substituted for derivative terms. Thus, ignoring the heat generation terms for now, (7) becomes:

$$\rho c \frac{\Delta T_i}{\Delta t} = \frac{k}{h^2} [T_{i+1}(t) + T_i(t) + T_{i-1}(t)] \quad (26)$$

where h is the chosen spatial discretization, and i represents a particular node within the discretized domain. Boundary conditions are applied to the discretized model by substituting either fixed temperature values or fixed flux terms at boundary nodes. It is worth noting that because such flux terms need to be specified across two nodes in the model, there is an inherent transient error in the boundary node temperature built into the model that is directly proportional to h and the applied power. Thus, this error is exacerbated when high magnitude, short pulses are modeled [220].

Alternatively, FEM uses a variational approximation of the full heat equation to develop a discretized model [221]. Although not described here in complete detail, this technique incorporates the natural boundary conditions completely in the variational equation. This avoids the error described above with FDM and enables improved boundary accuracy with similar discretization levels for large, fast thermal transients [220]. As such high rate transients are expected to occur in power electronic systems of interest, the FEM representation is the primary approach utilized in this study.

Assembly of the discretized elementary circuit elements from Table 4.1 create a network that represents the total thermal structure. In one dimension with a heat input on one end and a fixed temperature on the other, FDM results in a Cauer network with thermal resistors between nodes and a thermal capacitor connecting each node to thermal ground, as shown in Figure 5.4(a). Hsu and Vu-Quoc have translated the finite element method to the equivalent circuit domain [222] where the primary difference in one dimension can be

seen in Figure 5.4(b). There, the FEM distributes element mass over both element nodes and incorporates a mutual capacitance term using an additional capacitor parallel to the resistor. It turns out that determination of the appropriate value for this mutual capacitor term is non-trivial, and can have a significant effect on transient solution accuracy and stability, and it will be examined in detail in the following sections.

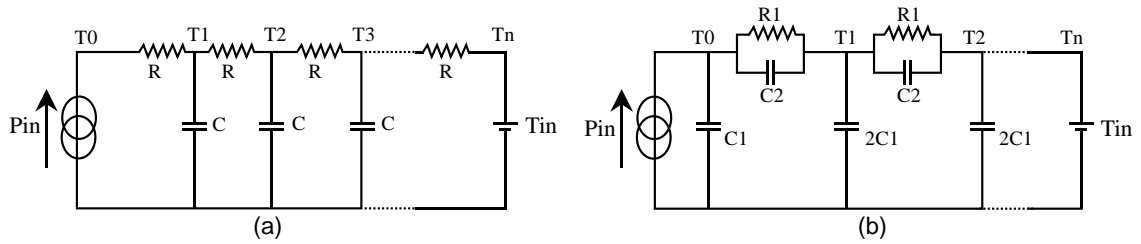


Figure 5.4 – Discretized one dimensional thermal networks using (a) the finite difference method and (b) the finite element method with temperature and heat flux boundary conditions adapted from [220] with permission, © 1999 IEEE.

5.2.3. FEM thermal circuit derivation and mass matrix considerations

Using the finite element method for transient/dynamic simulations involves choosing a mass approximation that can significantly impact the solution accuracy. Relevant to this chapter’s discussion of electro-thermal co-design, this choice would likely be hidden from, or at least non-obvious to, the circuit designer/simulator, running the risk that impacts of those design choices would be obscured or misunderstood. Apart from the thermal circuit framework, numerous studies have shown that non-physical oscillations and instabilities can appear in simulations that are poorly discretized relative to the time stepping scheme being used [223]. Depending on the devices under investigation, this effect could unacceptably complicate coupled-domain simulations.

The complete derivation of the finite element thermal circuit can be found in [219], and will only be summarized here. In brief, the finite element method relates heat flow and temperature through a semi-discrete version of the heat equation:

$$\mathbf{M}\dot{T} + \mathbf{K}T = F \quad (27)$$

where T is the nodal temperature vector and \dot{T} its time rate of change, \mathbf{K} is the thermal conductivity matrix, \mathbf{M} is the thermal mass matrix, and F is the heat input vector (the thermal forcing function). For a 1-dimensional, 2-node, linear thermal finite element, \mathbf{K}^e and \mathbf{M}^e are:

$$\mathbf{K}^e = \begin{bmatrix} k_{11}^e & k_{12}^e \\ k_{21}^e & k_{22}^e \end{bmatrix}, \quad \mathbf{M}^e = \begin{bmatrix} m_{11}^e & m_{12}^e \\ m_{21}^e & m_{22}^e \end{bmatrix} \quad (28)$$

where the individual matrix elements k_{ij} and m_{ij} are the coupling factors derived from the chosen approximation method and nodal basis functions. The standard Galerkin projection and linear, 1-dimensional finite element basis functions produce the following conductivity and mass matrices:

$$\mathbf{K}^e = \frac{\kappa A^e}{l^e} \begin{bmatrix} 1 & -1 \\ -1 & 1 \end{bmatrix} = \frac{1}{R_{th}} \begin{bmatrix} 1 & -1 \\ -1 & 1 \end{bmatrix} \quad (29)$$

$$\mathbf{M}_C^e = \rho c V^e \begin{bmatrix} 1/3 & 1/6 \\ 1/6 & 1/3 \end{bmatrix} = \frac{C_{th}}{6} \begin{bmatrix} 2 & 1 \\ 1 & 2 \end{bmatrix} \quad (30)$$

where κ , ρ , and c_p are the element's thermal conductivity, density and specific heat capacity, and l^e , A^e and $V^e (= A^e l^e)$ are the element's length, cross-sectional area, and volume. R_{th} and C_{th} represent the element's total thermal resistance and thermal capacitance, respectively. These individual element matrices are then assembled into a global matrix based on how the elements are connect and the nodal degrees of freedom are solved numerically.

The mass matrix given in (30) is often referred to as the *consistent mass* matrix (denoted with the subscript C), referring to the fact that its derivation is *consistent* with, or derived through, the same process used for the stiffness matrix. Despite the name's connotation, consistent does not necessarily imply any meaning of correctness relative to other mass matrix formulations.

A commonly used alternative approximation involves *mass lumping*, where all thermal mass is assumed to be concentrated at element nodes. This mimics the simple spring-mass system in the finite element description of the equations of motion, where there actually is no mass distributed between the nodes. In this case, the 2-node linear *lumped mass* matrix becomes:

$$\mathbf{M}_1^e = C_{th} \begin{bmatrix} 1/2 & 0 \\ 0 & 1/2 \end{bmatrix} = \frac{C_{th}}{2} \begin{bmatrix} 1 & 0 \\ 0 & 1 \end{bmatrix} = \frac{C_{th}}{2} \mathbf{I}_2 \quad (31)$$

With the primary element matrices identified, the FEM formulation can be used to turn a thermal model into a circuit model. Figure 5.5 shows the equivalent 2-node element thermal circuit as derived by Hsu and Vu-Quoc that is equivalent to \mathbf{K}^e and \mathbf{M}^e . It is composed of two shunt capacitors (C_s) and a parallel capacitor (C_p) and resistor (R_p) pair.

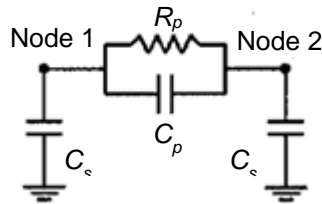


Figure 5.5 – Finite element equivalent thermal circuit, adapted from [222] with permission, © 1996 IEEE.

The values of these components as derived from the conductance and consistent mass matrices are:

$$\begin{aligned}
 C_s &= m_{11} + m_{12} = \frac{1}{2} C_{th}, \\
 C_p &= -m_{12} = -\frac{1}{6} C_{th}, \\
 R_p &= -\frac{1}{k_{12}} = R_{th}
 \end{aligned}
 \tag{32}$$

By inspection it can be seen that $C_p = 0$ for the lumped mass approximation. (Thereby eliminating the parallel capacitor altogether.) These elements can be combined into a network of 1D finite elements to represent a thermal stack, as was shown in Figure 5.4(b). In that figure a power generation boundary condition is represented by a current source, a fixed temperature boundary condition is represented by the voltage source, and where two elements are connected their thermal masses have been summed at connecting node.

5.2.4. Impacts of mass matrix selection

Both lumped and consistent mass matrix forms are mass conservative, as the sum across any row or column in (30) or (31) equals $\frac{1}{2}$ and both nodal contributions sum to 1. The primary differences between the two are the off-diagonal terms. Just as the off-diagonal terms in a conductivity (or stiffness) matrix represent elastic coupling between nodes, the off-diagonal terms in the thermal mass matrix effect an inertial coupling that occurs independent from the elastic terms. With zero inertial coupling the lumped mass matrix becomes diagonal and scalar, significantly reducing the computational cost of matrix inversion and other operations [224].

Discussions of the appropriateness of mass lumping choice for different modeling cases dates back decades, and was an especially important consideration when computational resources were much more limited. A diagonal, lumped mass matrix significantly reduces storage and memory requirements, and matrix operations like inversion become almost trivial. However, the accuracy impact of mass lumping relies upon many other factors including the type of analysis being performed. The steady-state solution is unaffected, and with sufficient mesh refinement both lumped and consistent approaches will converge toward the same solution. That said, an analysis by Harari concluded that the consistent mass approach retains 2nd order accuracy in local truncation error, while the lumped mass approach can degrade to 1st order accuracy [225]. In modal analysis it was shown that the consistent mass will tend to overpredict resonant frequencies (acting as an upper bound for the approximation) while the lumped approach underpredicts them, again with both converging at sufficient mesh refinement. This made consistent mass preferable for designers looking to maintain an upper bound on primary resonant modes [226].

Those factors may suggest consistent mass matrix superiority, however, an unfortunate side effect of the consistent mass matrix for transient simulations are oscillations or ripples in the solution, especially for undermeshed structures. In a review of numerical hydrocodes, Benson describes the lumped mass approximation being used exclusively, not just because of the computational simplification, but because of “better answers” for impulsive loads. Impulses generate stronger oscillations when the nodes are inertially coupled, and nodes downstream of the travelling shockwave are spuriously driven in the direction opposite that which is physically observed [227]. It should be noted

that “better” is limited to the distinction of the downstream nodes staying within the system permissible bounds, rather than commenting on the accuracy of the driven node.

These ripples or oscillations can be obviously erroneous and nonphysical. They often violate the *Discrete Maximum Principle* (DMP) where nodal values are driven outside the physically possible minimums and maximums. The specific numerical reasons for the DMP violations appearing in consistent mass matrices is described by Rank, but can be summarized as above by being related to inertial coupling between nodes [228].

Because of the obvious physical error of DMP violating results, much effort has gone into characterizing and avoiding these oscillations. In fact, it has become standard practice to set both upper and lower time-step bounds when mass lumping is not used to reduce spurious oscillations in the solution, or at least prevent their appearance [229]. While effective, several analyses have disparaged that approach as artificially disturbing the solution, with the critical possibility of smoothing out real disturbances or losing important model information. In fact, a paper by Gresho specifically focuses on the importance of “not suppressing the wiggles,” as they provide useful information about where the model is undermeshed and needs refinement, and artificially suppressing them can lead to ‘smooth’ yet erroneous results [223]. Essentially, “hiding” the errors does not necessarily increase accuracy. Despite this risk, however, because the lumped mass matrix eliminates any trace of these oscillations, it tends to be more popular for transient simulations.

Alternative forms of the mass matrix have been suggested, most commonly being a linear combination of the consistent and lumped forms:

$$\mathbf{M}_\lambda^e = \lambda \mathbf{M}_c^e + (1 - \lambda) \mathbf{M}_l^e \quad (33)$$

resulting in a general form of the mass matrix:

$$\mathbf{M}_\lambda^e = \frac{C_{th}}{6} \begin{bmatrix} 3 - \lambda & \lambda \\ \lambda & 3 - \lambda \end{bmatrix} \quad (34)$$

Using this notation, for $\lambda = 0$ or 1 the coupled mass matrix reverts to the lumped or consistent matrices, respectively. A common approximation uses $\lambda = 1/2$, obtaining an averaged mass matrix that “minimizes lower order dispersion” [224]. This value was also independently derived by Madoliat [230] using an inverse method to find the FE formulation with minimum discretization error. Others have suggested $3/5$ [231] and $3/4$ [232], concluding that the consistent mass matrix should get more weight to achieve higher accuracy at lower frequencies in modal analysis.

The general form of the mass matrix only modifies the FE thermal circuit by modifying C_p :

$$C_p(\lambda) = -\frac{\lambda}{6} C_{th} \quad (35)$$

Again, this shows that $\lambda = 0$ corresponds to the the lumped mass approximation with no parallel capacitor, and $\lambda = 1$ corresponds to the consistent mass matrix. Thus, any mass-conservative choice of λ that is less than 1 will diminish the role of the parallel capacitor, reducing inertial feedback in the element circuit.

An important point to note with the FEM thermal circuit is that except for the degenerate lumped element case, the coupling capacitor will always have a negative value. Ammous had reflected that while FEM provided superior transient response over FDM, it was “inconvenient” that the negative capacitance “corresponds to no physical meaning” [220]. The shunt capacitors to thermal ground can be physically explained as representing the material’s thermal mass, storing energy as the circuit warms from its initial

ground state. A positive valued parallel capacitor would act to slow the creation of a thermal gradient between element nodes. With a negative value, however, the element actually accelerates the creation of a thermal gradient, working against the inertia of the shunt capacitors. Negative impedances have been studied extensively by the circuit community, and it is recognized that they can induce instabilities, oscillations, and other problematic circuit behavior [233].

This serves to explain why a FE thermal circuit that contains only RC elements, and hence should have a purely monotonic and dissipative free response, could show non-physical oscillation. Normally a secondary, phase-shifted energy storage element, as you would find by introducing an inductor into the circuit, is required to sustain oscillations. With a negative capacitance, the frequency domain impedance of the capacitor can be expressed as:

$$Z_C(\omega) = 1/j\omega(-C) = j/\omega C \quad (36)$$

Thus, with a positive complex component the element will behave somewhat like an inductor whose impedance diminishes instead of increases with increasing frequency. It will have the ability to induce non-monotonic temperature changes in the thermal circuit, especially for very high-rate transients where the parallel capacitor can act as a virtual short between nodes. All of this coincides well with observation that inertial coupling within the finite element mass matrix causes oscillations, “wiggles”, or other deviations deemed undesirable in most cases.

5.2.5. Finite element thermal circuit – analytical form

We can derive an analytical expression for the thermal circuit to gain further insight into its behavior. Because these elements typically appear in 1-dimensional cascades, it is

convenient to use a network two-port representation for the circuit. The two-port transmission equation approach was applied to heat transfer problems not long after it was derived for electrical transmission line applications [176]. This approach permits the use of transmission matrices for the linear arrays that will be created by the 1-dimension heat equation. This two-port representation is shown schematically in Figure 5.6, where the previously described thermal circuit is shown as a symmetric-pi network.

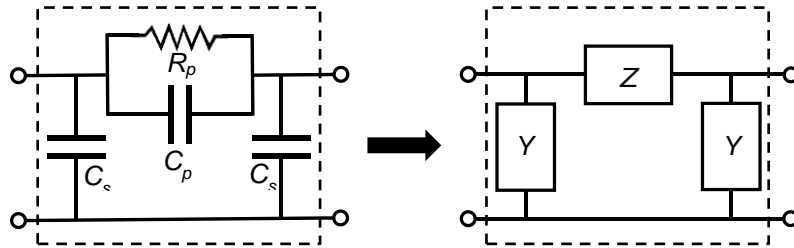


Figure 5.6 – FE equivalent thermal circuit as a symmetric-pi two-port network

In the Figure, Y is the complex admittance of the shunt elements and Z is the complex impedance of the series elements. The advantage of working with 1D network cascades is that they can be represented conveniently with transmission matrices in the s -domain, which for a pi-network has the following form as derived by Mowery [234]:

$$\mathbf{T} = \begin{bmatrix} A & B \\ C & D \end{bmatrix} = \begin{bmatrix} 1 + Y_1 Z & Z \\ Y_1 + Y_2 + Y_1 Y_2 Z & 1 + Y_2 Z \end{bmatrix} \quad (37)$$

For a symmetric network, $Y_1 = Y_2 = Y$, and this simplifies to:

$$\mathbf{T} = \begin{bmatrix} 1 + YZ & Z \\ 2Y + Y^2 Z & 1 + YZ \end{bmatrix} \quad (38)$$

For the FE thermal circuit, the shunt admittance is simply the admittance of a capacitor, or:

$$Y_1 = Y_2 = Y = sC_s = sC_{th}/2 \quad (39)$$

The series impedance is the parallel impedance of the resistor-capacitor combination. For the general coupled mass formulation this becomes:

$$Z = R_p \parallel 1/s\lambda C_p = \frac{R_p}{1 + s\lambda R_p C_p} = \frac{6R_{th}}{6 - s\lambda R_{th} C_{th}} \quad (40)$$

Combining (38), (39), and (40) yields the transmission matrix for the 1D finite element thermal circuit with the parameterized coupled mass formulation:

$$\mathbf{T} = \begin{bmatrix} A & B \\ C & D \end{bmatrix} = \begin{bmatrix} \frac{6 + (3 - \lambda)sR_{th}C_{th}}{6 - \lambda sR_{th}C_{th}} & \frac{6R_{th}}{6 - \lambda sR_{th}C_{th}} \\ \frac{sC_{th}}{2} \left(\frac{12 + (3 - 2\lambda)sR_{th}C_{th}}{6 - \lambda sR_{th}C_{th}} \right) & \frac{6 + (3 - \lambda)sR_{th}C_{th}}{6 - \lambda sR_{th}C_{th}} \end{bmatrix} \quad (41)$$

with the consistent ($\lambda = 1$) and lumped ($\lambda = 0$) forms being:

$$\mathbf{T}_C = \begin{bmatrix} \frac{6 + 2sR_{th}C_{th}}{6 - sR_{th}C_{th}} & \frac{6R_{th}}{6 - sR_{th}C_{th}} \\ \frac{sC_{th}}{2} \left(\frac{12 + sR_{th}C_{th}}{6 - sR_{th}C_{th}} \right) & \frac{6 + 2sR_{th}C_{th}}{6 - sR_{th}C_{th}} \end{bmatrix} \quad (42)$$

$$\mathbf{T}_L = \begin{bmatrix} 1 + sR_{th}C_{th}/2 & R_{th} \\ sC_{th}(1 + sR_{th}C_{th})/4 & 1 + sR_{th}C_{th}/2 \end{bmatrix} \quad (43)$$

Using this form, transient heat and temperature input/output relationships can be determined using standard techniques, and the overall transmission matrix for a cascade of elements can be found through simple matrix multiplication of the individual ABCD matrices. For the special case of a series of n identical elements (such as would exist by dividing a single domain into 1-dimensional mesh of n elements), Mowery also derived a compact form of the n -element transmission matrix as:

$$\mathbf{T}^n = (\sqrt{\Delta})^n \begin{bmatrix} T_n(x) + \frac{A - D}{2\sqrt{\Delta}} U_{n-1}(x) & \frac{B}{\sqrt{\Delta}} U_{n-1}(x) \\ \frac{C}{\sqrt{\Delta}} U_{n-1}(x) & T_n(x) + \frac{A - D}{2\sqrt{\Delta}} U_{n-1}(x) \end{bmatrix} \quad (44)$$

$$\Delta \stackrel{\text{def}}{=} |\mathbf{T}| = AD - BC, \quad x \stackrel{\text{def}}{=} (A + D)/2\sqrt{\Delta} \quad (45)$$

Where $T_n(x)$ and $U_n(x)$ are Chebyshev polynomials of the first and second kind, respectively. For a symmetric pi-network, $\Delta = 1$, $A = D$, and $x = A$. This greatly simplifies the chain transmission matrix to:

$$\mathbf{T}^n = \begin{bmatrix} T_n(A) & BU_{n-1}(A) \\ CU_{n-1}(A) & T_n(A) \end{bmatrix} \quad (46)$$

A , B , and C are the individual elements of (41), (42), or (43) as appropriate. These allow us to produce a single transmission matrix for any 1-D thermal circuit chain. We can now use these expressions to examine both the time and frequency domain behavior of these circuits and examine the impact of mass matrix selection.

5.2.6. Proof model to examine thermal circuit oscillations

To illustrate the impact of mass matrix choice, we will adopt the test case used by Madoliat and Ghasemi in examining spurious mass matrix related oscillations for finite elements [235]. By using solutions that are fully analytical in time for both the true solution and the finite element approximation, the presence of oscillations in the absence of any particular time integration strategy can be examined. Figure 5.7 shows the problem domain to be examined: a fully insulated bar with a steady heat input at the left end.

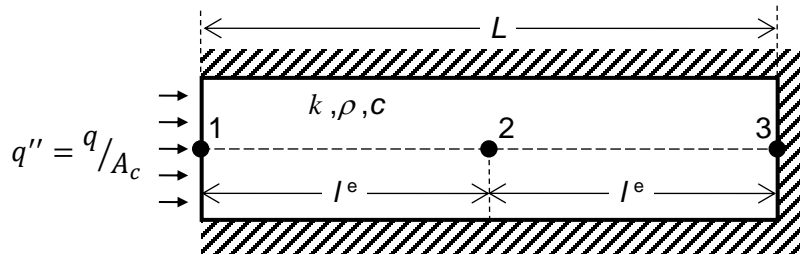


Figure 5.7 – One dimensional insulated bar with uniform heat flux and constant material properties. The heated domain has been discretized into two elements at the points shown.

A closed form expression for temperature, T , throughout the bar can be obtained by solving the transient, 1-dimensional heat equation:

$$\frac{\partial^2 T(x, t)}{\partial x^2} = \frac{1}{\alpha} \frac{\partial T(x, t)}{\partial t} \quad (47)$$

with the appropriate initial and boundary conditions as indicated in the figure.

$$T(x, 0) = 0$$

$$\frac{\partial T}{\partial x}(0, t) = -q''/k \quad (48)$$

$$\frac{\partial T}{\partial x}(L, t) = 0$$

where q'' is the uniform input heat flux, L is the total bar length, $\alpha (= k/\rho C)$ is the material thermal diffusivity, and t and x are the independent time and position parameters, with $x = 0$ corresponding to the left end of the bar with heat input.

Using a double Laplace transformation technique to derive the transient and spatial temperature profile, we can first apply the Laplace transform to the time domain ($t \rightarrow s$) leading to:

$$\bar{T}_{xx}(x, s) - \frac{1}{\alpha} [s\bar{T}(x, s) - T(x, 0)] = 0 \quad (49)$$

where for compactness the subscripts x and t are used to indicate differentiation with respect to space or time, and the overbar denotes the transformed function. The last term is eliminated by the initial condition, and the transformed boundary conditions become:

$$T_x(0, s) = -q''/ks \quad (50)$$

$$T_x(L, s) = 0$$

Taking the second Laplace Transformation in the spatial domain ($x \rightarrow p$) gives us:

$$p^2 \bar{T}(p, s) - p \bar{T}(0, s) - \bar{T}_x(0, s) - \frac{s}{\alpha} \bar{T}(p, s) = 0 \quad (51)$$

Substituting the $x = 0$ boundary condition and rearranging:

$$\bar{T}(p, s) = \frac{p \bar{T}(0, s) - q''/ks}{p^2 - s/\alpha} \quad (52)$$

Applying the inverse Laplace transform to return to the spatial domain is straightforward using transform lookup tables:

$$\bar{T}(x, s) = \bar{T}(0, s) \cosh\left(\sqrt{\frac{s}{\alpha}} x\right) - \frac{q''}{ks} \sqrt{\frac{\alpha}{s}} \sinh\left(\sqrt{\frac{s}{\alpha}} x\right) \quad (53)$$

Now, taking the spatial derivative so that we may make use of the $x = L$ boundary condition to find $\bar{T}(0, s)$:

$$\bar{T}_x(L, s) = 0 = \bar{T}(0, s) \sqrt{\frac{s}{\alpha}} \sinh\left(\sqrt{\frac{s}{\alpha}} L\right) - \frac{q''}{ks} \cosh\left(\sqrt{\frac{s}{\alpha}} L\right) \quad (54)$$

$$\bar{T}(0, s) = \frac{q''}{ks} \sqrt{\frac{\alpha}{s}} \coth\left(\sqrt{\frac{s}{\alpha}} L\right) \quad (55)$$

Substituting (55) into (53) and rearranging provides the s-domain form of the temperature profile, which can also be used to obtain the exact frequency domain response of the system:

$$\bar{T}(x, s) = \frac{q''}{ks} \sqrt{\frac{\alpha}{s}} \frac{\cosh\left((L-x)\sqrt{s/\alpha}\right)}{\sinh\left(L\sqrt{s/\alpha}\right)} \quad (56)$$

Performing the second inversion is less straightforward than the first, but is readily achievable using complex integration and Cauchy's residue theorem, as per [236]. The inverse Laplace Transform of $\bar{T}(x, s)$ can be expressed as a contour integral in the complex domain:

$$T(x, t) = \frac{q''\sqrt{\alpha}}{k} \oint_C \frac{\cosh\left((L-x)\sqrt{z/\alpha}\right)}{z\sqrt{z} \sinh\left(L\sqrt{z/\alpha}\right)} e^{tz} dz \quad (57)$$

where C is a closed contour of infinite extent surrounding all poles of the function being integrated. This permits use of the residue theorem, where the value of the integrated function is equal to the sum of the residues evaluated at the poles of the function. (Note that we have left out the multiplying factor, $2\pi i$, which simply cancels between the contour integral and the residue function.)

The complex function has a second order, single valued pole at $z=0$ from the full denominator term, and an infinite number of simple poles from the \sinh term where $iL\sqrt{z/\alpha} = n\pi$, or $z_n = -\alpha(n\pi/L)^2$. First calculating the residues associated with the second order pole, and making use of the simplifications $u = (L-x)/\sqrt{\alpha}$ and $C = L/\sqrt{\alpha}$:

$$\text{Res}_{z=0} = \lim_{z \rightarrow 0} \frac{d}{dz} \left[(z-0)^2 \frac{\cosh(u\sqrt{z})}{z\sqrt{z} \sinh(C\sqrt{z})} e^{tz} \right] \quad (58)$$

$$= \lim_{z \rightarrow 0} \frac{d}{dz} \left[\frac{\sqrt{z} \left(1 + \frac{u^2 z}{2!} + \frac{u^4 z^2}{4!} + \dots \right)}{\left(C\sqrt{z} + \frac{C^3 z^{3/2}}{3!} + \frac{C^5 z^{5/2}}{5!} + \dots \right)} \left(1 + tz + \frac{t^2 z^2}{2!} + \dots \right) \right] \quad (59)$$

$$= \lim_{z \rightarrow 0} \frac{d}{dz} \left[\frac{1}{C} \left(1 + \frac{u^2 z}{2!} + \frac{u^4 z^2}{4!} + \dots \right) \left(1 + tz + \frac{t^2 z^2}{2!} + \dots \right) \left(1 - \frac{C^2 z}{3!} + \frac{7C^4 z^2}{360} - \dots \right) \right] \quad (60)$$

$$= \lim_{z \rightarrow 0} \frac{d}{dz} \left[\frac{1}{C} \left(1 - \left(\frac{C^2}{6} - \frac{u^2}{2} - t \right) z + O(z^2) + \dots \right) \right] \quad (61)$$

Noting that only the linear- z terms will remain after differentiation and applying the limit:

$$\text{Res}_{z=0} = \frac{1}{C} \left(t + \frac{u^2}{2} - \frac{C^2}{6} \right) \quad (62)$$

Similarly, for the simple poles at $z = z_n$:

$$Res_{z=z_n} = \lim_{z \rightarrow z_n} \left[(z - z_n) \frac{\cosh(u\sqrt{z})}{z\sqrt{z} \sinh(C\sqrt{z})} e^{tz} \right] \quad (63)$$

$$= \lim_{z \rightarrow z_n} \left[\frac{\cosh(u\sqrt{z})}{z\sqrt{z}} e^{tz} \times \frac{(z - z_n)}{\sinh(C\sqrt{z})} \right] \quad (64)$$

Applying L'Hopital's rule to the indeterminate portion:

$$Res_{z=z_n} = \lim_{z \rightarrow z_n} \left[\frac{\cosh(u\sqrt{z})}{z\sqrt{z}} e^{tz} \times \frac{2\sqrt{z}}{C \cdot \cosh(C\sqrt{z})} \right] = \frac{2\cosh(u\sqrt{z_n})}{C z_n \cosh(C\sqrt{z_n})} e^{tz_n} \quad (65)$$

Substituting for z_n , factoring out the complex elements, and noting that $\cos(n\pi) = (-1)^n$:

$$Res_{z=z_n} = -\frac{2\cosh(u\sqrt{-(n\pi/C)^2})}{C(n\pi/C)^2 \cosh(C\sqrt{-(n\pi/C)^2})} e^{-(n\pi/C)^2 t} \quad (66)$$

$$= -\frac{2C(-1)^n}{\pi^2 n^2} \cos(n\pi u/C) e^{-(n\pi/C)^2 t} \quad (67)$$

Finally, summing over all residuals gives the transient temperature profile:

$$T(x, t) = \frac{q''\sqrt{\alpha}}{k} \left\{ \frac{1}{C} \left(t + \frac{u^2}{2} - \frac{C^2}{6} \right) - \frac{2C}{\pi^2} \sum_{n=1}^{\infty} \frac{(-1)^n}{n^2} \cos(n\pi u/C) e^{-(n\pi/C)^2 t} \right\} \quad (68)$$

Back-substituting for u and C , and after simplifying and collecting terms, we obtain the final form of the temperature profile:

$$T(x, t) = \frac{q''L}{k} \left\{ \frac{\alpha t}{L^2} + \left(\frac{x^2}{2L^2} - \frac{x}{L} + \frac{1}{3} \right) - \frac{2}{\pi^2} \sum_{n=1}^{\infty} \frac{\cos(n\pi x/L)}{n^2} e^{-\alpha(n\pi/L)^2 t} \right\} \quad (69)$$

We can non-dimensionalize the temperature profile by normalizing $T(x, t)$ by $q''L/k$ and making the substitutions $\delta = x/L$ and $Fo = \alpha t/L^2$, resulting in:

$$\theta(\delta, Fo) = Fo + \left(\frac{\delta^2}{2} - \delta + \frac{1}{3} \right) - \frac{2}{\pi^2} \sum_{n=1}^{\infty} \frac{\cos(n\pi\delta)}{n^2} e^{-Fo(n\pi)^2} \quad (70)$$

Note that this form differs from what Madoliat [230,235] obtained using separation of variables and Fourier series methods to solve the heat equation, although the two forms

are equivalent. We can obtain the alternate form by noting that the polynomial term in (69) is the closed form of the Fourier cosine series:

$$\left(\frac{x^2}{2L^2} - \frac{x}{L} + \frac{1}{3}\right) = \frac{2}{\pi^2} \sum_{n=1}^{\infty} \frac{\cos(n\pi x/L)}{n^2} \quad (71)$$

Substituting this into (69) and combining the summations provides the form from [235]:

$$T(x, t) = \frac{q''L}{k} \left\{ \frac{\alpha t}{L^2} + \frac{2}{\pi^2} \sum_{n=1}^{\infty} \cos(n\pi x/L) (1 - e^{-\alpha(n\pi/L)^2 t}) / n^2 \right\} \quad (72)$$

which can be non-dimensionalized as:

$$\theta(\delta, Fo) = Fo + \frac{2}{\pi^2} \sum_{n=1}^{\infty} \cos(n\pi\delta) (1 - e^{-Fo(n\pi)^2}) / n^2 \quad (73)$$

While (72) and (73) may appear more compact, we have chosen to use the expressions in (69) for this work. Keeping the spatial polynomial out of the summation has a considerable impact on the series convergence rate. (72) and (73) can require several thousand terms to converge to the same result that (69) and (70) can obtain with ten terms or less.

The finite element approximations for each node shown in Figure 5.7 can be obtained using the appropriate impedance relationships with the transmission line equations in (41) and (46) (see, for example, [237]). They can then be normalized as before, producing the following time domain expressions:

$$\begin{aligned} \theta_1(Fo) &= Fo + \frac{5}{16} - \frac{1}{4} e^{24Fo/(\lambda-3)} - \frac{1}{16} e^{48Fo/(2\lambda-3)} \\ \theta_2(Fo) &= Fo - \frac{1}{16} + \frac{1}{16} e^{48Fo/(2\lambda-3)} \\ \theta_3(Fo) &= Fo - \frac{3}{16} + \frac{1}{4} e^{24Fo/(\lambda-3)} - \frac{1}{16} e^{48Fo/(2\lambda-3)} \end{aligned} \quad (74)$$

Using (70) and (74), we can now compare the transient thermal solutions for the insulated bar. All equations are fully analytical with time, as (74) represents spatial discretization only, so any oscillations will have no dependence on time stepping scheme as has been previously asserted. Figure 5.8 shows left, midpoint, and right initial normalized temperature profiles for the bar, using three nodes (two elements) for the finite element approximations. Three values for λ , representing the lumped, averaged, and consistent mass matrices, are compared with the analytical profile.

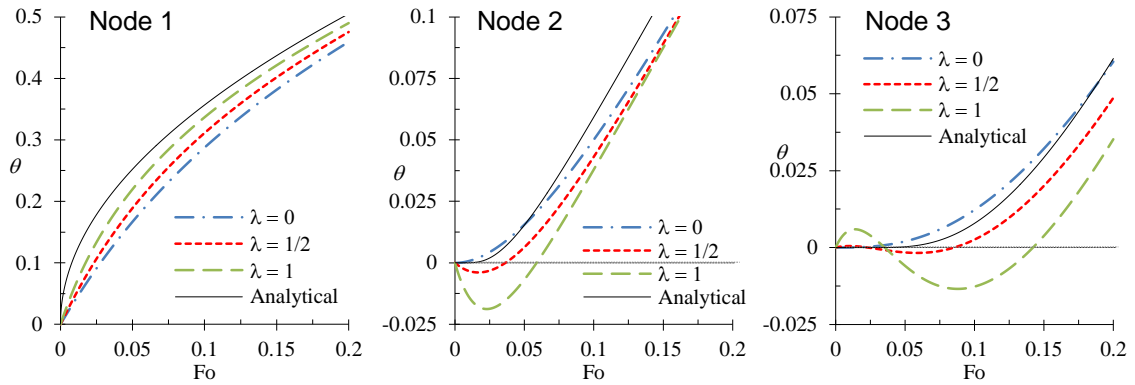


Figure 5.8 – Normalized two-element approximate temperature profiles at each node, along with the analytical temperature solution in (70). Note that while the left node is positive and monotonic for all values of λ , the other two nodes show increasing oscillatory behavior for $\lambda > 0$.

As shown in the figure, after the initial transient the solution settles into a constant, linear temperature rise proportional to time, or Fo . Most obvious from the profiles is the oscillation induced by the inertial-coupling in the $\lambda = 0.5$ and 1 approximations for nodes 2 and 3, initially driving them away from the actual solution, whereas the node 1 solutions appear to track the actual solution better than the lumped mass case for $\lambda = 0$. It turns out that the $\lambda = 1$ case actually does track the steady solution much better in all cases, when fixed discretization error is taken into account. The two-element approximations lag

behind the analytical solution by a fixed amount resulting directly from the low level of discretization. The second term in each equation from (74) should be a constant equal to the δ -polynomial expression from (70), however the difference between the ideal and approximate values has a fixed error of 1/48 for two elements.

Looking at the degree of error from the analytical solution shown in Figure 5.9, it becomes more apparent that the inertial coupling drives the solution toward the steady solution faster than the lumped case. This is at the cost of initial non-physicality of the solution, as the negative capacitor actually pulls energy from the downstream nodes pushing their values into the negative region in violation of the discrete maximum principle.

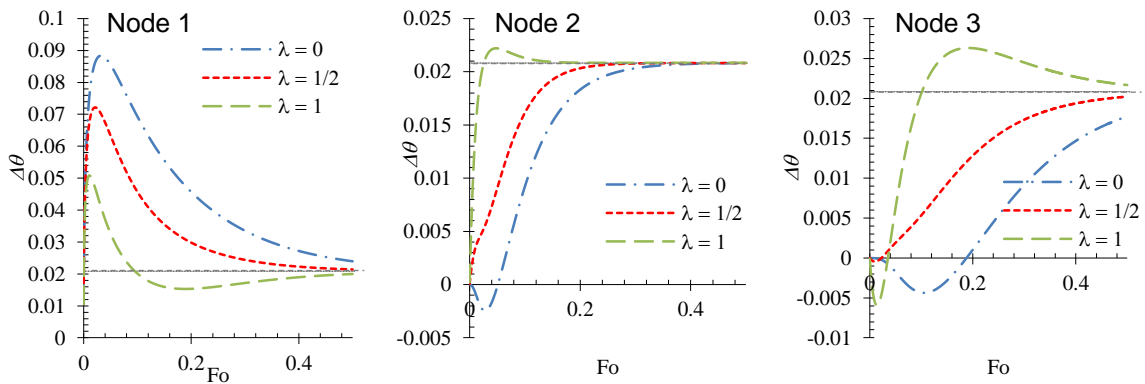


Figure 5.9 – Error in temperature prediction at each node showing that each converges to a fixed error equal to the discretization error term. Note that in all cases the $\lambda = 1$ case converges the fastest despite the DMP violation.

Thus, for a 1-dimensional element chain, it appears that using a consistent mass matrix provides a more accurate solution at the heat input boundary node for any length transient or pulse. Any solution other than lumped mass, however, will produce oscillations to some degree at layers farther down the chain, decreasing accuracy at those

points, especially for short transients. These two competing factors could be traded-off by choosing a coupled form of the mass matrix with $0 < \lambda < 1$. The impact of these errors will obviously diminish with increased mesh refinement, but will necessarily always be present to some degree so long as $\lambda > 1$.

5.2.7. Comments on FEM thermal circuit oscillations

Relative to an actual thermal circuit computation, it is worth noting that these oscillations exist independent of any particular time stepping scheme. It appears that previous efforts to define a ‘minimum time step’ below which these oscillations or instabilities would occur were simply using the averaging qualities of time integration to hide the oscillations, performing what other authors have described as arbitrary distortion and smoothing of the solution to gain the appearance of well modeled system.

This is a significant concern for electro-thermal co-design using SPICE or equivalent circuit simulation tools. Most of these tools make use of sophisticated adaptive time-stepping techniques often not completely controllable or always even known by the user. There is often a significant mismatch between relative timescales for the electrical and thermal components. In seeking a converged solution to both electrical and thermal systems, the simulation tool would often necessarily select time-steps far smaller than the ‘suggested minimum’ value for the thermal finite element chain to hide the oscillations. In addition, some device manufacturers do have existing electrothermal device models, whether implemented in actual design files or simply circuit descriptions in application notes. Because these thermal models are coded into the device description, there is the distinct possibility that the designer will be unaware of the level of thermal circuit mesh refinement used. The likely result of all of this is that the thermal model will very often be

unavoidably undermeshed relative to the simulator time step size. The inaccuracies examined in this report cannot be avoided in such cases, making it necessary for the implications of those design choices to be well understood by the simulation community. As such, it is recommended that all thermal circuits ‘hard-coded’ into device models be based on finite differences or lumped-mass finite elements, sacrificing the increased simulation accuracy to avoid DMP violation when the user is unable to make any adaptations. Alternatively, the finite element approximation could be used so long as temperature calculations are only made on ‘source nodes’, as the DMP violation only occurs at ‘downstream’ nodes. This would allow simulations to take advantage of the improved transient and boundary condition fidelity of FEM models.

As mentioned previously, the hydrocode community settled on a lumped mass approximation as the default because the sudden impacts present in many of their models almost exclusively involved time constants much smaller than recommended time steps. The oscillations, however, do serve a useful purpose. At a minimum, they serve as a useful indicator for localized mesh refinement, possibly within an automated refinement framework such that things would still be transparent to the user or designer. A simple impulse response test would indicate the presence of any DMP violation, and this could feedback into an increase in local mesh density until convergence is achieved. With respect to thermal circuit simulations, there is value in the consistent mass matrix settling to the ‘true’ solution faster than the lumped solution, especially in step-response situations such as digital switching. What is left to be seen is how these DMP violating situations would affect nonlinear thermal applications, where it may be necessary to eliminate the inertial coupling altogether to enable solution convergence.

5.2.8. Comments on multi-dimensional FEM thermal circuit simulation

The previous sections deal almost exclusively with one-dimensional thermal circuits and, accordingly, structures that can be represented one-dimensionally. Obviously the finite element method is applicable to more than one dimension. Accordingly, Hsu and Vu Quoc did derive more complex thermal circuits along with the 1-D cases, including both higher order and higher dimension [222]. Both improvements increase the ability to simulate more complicated structures with higher fidelity. An example of this is a 2-D linear rectangular element shown in Figure 5.10, and additional models for 1-D cubic Hermitian, 2-D linear triangular, and 3-D linear tetrahedral and cubic elements can be found in [222].

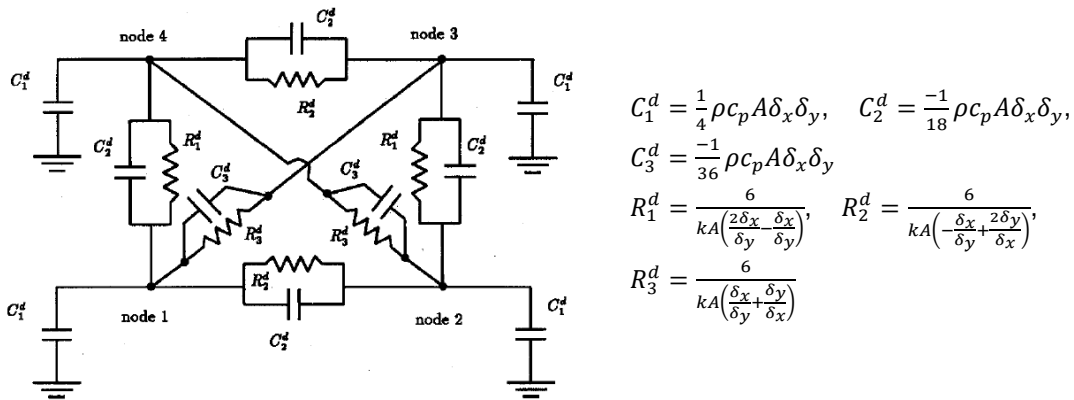


Figure 5.10 – 2-D rectangular finite element equivalent thermal circuit, adapted from [222] with permission, © 1996 IEEE.

It is worth noting that while the capability is there, there is a practicality limit to using a thermal circuit approach to simulate complex systems. The primary advantage of using a circuit simulator is that it enables the use of the same tools being used to simulate complex electrical circuits, potentially leading to coupled electrothermal design. These tools, however, are not built for high fidelity finite element simulation. Standard user-side

items for such a process involve geometry definition, methods for controlling element refinement, and tools for reporting useful simulation results. Currently, all of those things are done in a very manual process ‘shoe horning’ the technique into the circuit simulator. Even the mesh refinement technique used in the convergence study was a special, undocumented feature of the one tool used and still involved a significant amount of manual editing for every change.

In addition to this, separate from the user interface, tools designed for large, multidimensional structures with high node counts are built with specific numerical routines for efficient processing of the resulting element matrices. That specificity is lacking in any circuit simulator tool used for thermal analysis, a fact that will become more and more apparent as simulation size and complexity grows. There is no fundamental reason to think that a circuit simulator could not handle a large complex model, but at some point the question arises about whether the correct tool is being used for the task at hand.

That said, there are several approaches that could make higher complexity component simulation more amenable to the thermal circuit approach. First, almost all circuit tools have some form of circuit abstraction, whereby complex circuits can be encapsulated within a representative symbol and the user only interacts with input/output circuit elements. As the user never sees the specific internal details it would be entirely possible for more complex circuits to be defined, whether 1-, 2-, or 3-dimensional and representing complex heat spreaders, heat sinks, or packages, which could then be saved in abstracted form. Similarly, there may be cases where a combination of different dimensions might be appropriate for approximating a more complex structure, e.g., by using a 2-D or 3-D element to link multiple 1-D regions. The composite thermal circuit

would retain full simulation complexity, but when abstracted user-visible complexity would be minimized.

What is likely a more practical use of thermal circuits will be to implement compact or reduced versions of more useful structures. A manual approach to this involves attempting to extract dominant resistances and time constants from the structure or a portion thereof, and then using those values in a simpler thermal circuit. Alternatively, in a follow-up to the original FEM thermal circuit work Hsu and Vu Quoc proposed several model order reduction techniques that focused on synthesis methods to balance reduced degrees of freedom with simulation accuracy [219]. Methods investigated included superposition, mode synthesis, substructuring, and Ritz vector methods. The core idea behind these methods is that after defining important nodes for external access, a reduced internal coordinate space and the corresponding connectivity matrices are determined that sufficiently replicate external node behavior. Then that reduced model can be re-implemented as a simpler thermal circuit and simulations can be run as normal. Whatever the specific method, model order reduction appears to be the most practical approach to introducing complex structures into the thermal circuit domain and should provide a path forward for complex simulation of thermal and electronic systems.

5.3. Transient thermal circuit evaluation of power packages

As mentioned at the beginning of this chapter, power packages are being developed that improve thermal resistance and steady-state thermal performance, but these packages are being used in non-steady applications. High-rate transients and pulses produce thermal conditions that will require knowledge of the package's full thermal impedance, not just the static resistance, to fully understand. As such, we now use the thermal circuit models

examined previously to explore the transient response of a series of hypothetical power packages with varying degrees of cooling integration. The impact of improved convection mechanisms and reduced packaging material upon power device temperature will be quantified for varying pulse rates. We will attempt to validate the hypothesis that the steady-state improvements may actually degrade thermal performance for high-speed transients or pulses. (An early version of the following package analysis was first presented in [147]).

5.3.1. Modeling approach

5.3.1.1. Power packages modeled

Five power electronic package stacks are examined that include a progression of improvements typically proposed for steady-state thermal applications. The five packages, referred to hereafter as Cases 1-5, are shown in Figure 5.11.

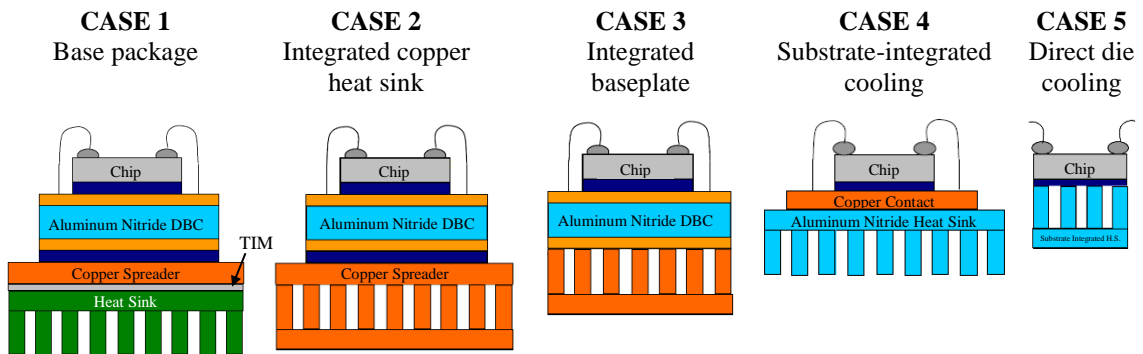


Figure 5.11 – Power package configurations used to examine transient behavior. Cases 2 through 5 represent increasing levels of cooling integration into the package thermal stack (not to scale).

Case 1 is the basic high-power electronics package consisting of a semiconductor device mounted on an AlN Direct-bond-copper (DBC) board and a copper baseplate affixed to an aluminum heat sink or cold plate using a thermal interface material (TIM). In

Case 2, the package resistance is reduced by rigidly affixing the heat sink or cold plate to the copper baseplate, eliminating the TIM and separate baseplate. In Case 3, the convective mechanism is integrated into the baseplate and directly cools the back of the DBC substrate. In Case 4, the cooling is integrated directly into the ceramic substrate (similar to that described in Chapter 4). Finally, in Case 5, the coolant is applied directly to the backside of the device, also called ‘chip level cooling’. Package material properties used for simulation are listed in Table 5.1.

Table 5.1 – Power package thermal material properties

	k_{th} [W/mK]	ρ [kg/m ³]	c_p [J/kgK]
Silicon	135	2330	704
Copper	400	8933	385
AlN ceramic	180	3330	736
Aluminum	200	2700	880
AuSn solder	57	19720	129
T.I.M. (Dow Corning TC5022)	4	3230	1100

Using (24) the resistance and capacitive thermal components of each layer can be calculated along with the associated thermal time constant for a unit device area. These thicknesses and associated thermal values are shown in Table 5.2. It should be noted that each Case uses the same device layer thicknesses except for Case 4, where it is assumed that about a half-thickness of AlN (~300 μm) remains through which heat must conduct, as was seen with the saw-cut substrates described in Section 4.4. Also, despite being part of the same material, the device junction is called out as a discrete layer (with the same silicon properties) to permit improved boundary condition fidelity and provide increased resolution near the highest heat flux region in the model. That junction’s thickness is chosen as 100 μm to represent a deep-junction high power device.

Table 5.2 – Package layer thermal characteristics

	l [mm]	R_{th}'' [cm ² K/W]	C_{th}'' [J/cm ² K]	RC [ms]
junction	0.100	0.007	0.016	0.122
die	0.400	0.030	0.066	1.94
die attach	0.050	0.009	0.013	0.112
DBC, Cu	0.300	0.008	0.103	0.774
DBC, AlN	0.625	0.035	0.153	5.32
sub. attach	0.100	0.018	0.025	0.446
Baseplate	3	0.075	1.032	77.4
T.I.M.	0.050	0.125	0.018	2.22
Al Sink	5	0.250	1.188	297

Table 5.3 gives the accumulated thermal resistivity, capacity, and layer time constant for each package, calculated using (24) and (25) for a unit cross sectional area. From that data it can be seen that while the cooling integration has the desired effect of significantly reducing thermal resistivity, they also significantly reduce package thermal capacity and thermal time constant.

Table 5.3 – Thermal Characteristics for each model Case

Case	# of layers	R_{th}'' [cm ² K/W]	C_{th}'' [J/cm ² K]	$\Sigma(R_i C_i)$ [ms]
1	10	0.563	2.717	386.1
2	9	0.188	1.511	86.9
3	6	0.096	0.454	9.1
4	5	0.070	0.271	4.2
5	2	0.037	0.082	2.1

It should be noted that the RC values given in Table 5.3 are only rough lumped-element estimates. It is only appropriate to consider the full RC values when the entire package can be assumed to heat and cool uniformly as a single mass, usually for extremely slow temperature changes. We expect in this study the majority of transient and convection conditions to operate outside that range. Still, the values are instructive for demonstrating the significant change in thermal capacity that accompanies package size reduction and thermal resistance improvement. An improved measure of package heating time will be discussed in the following section to better characterize thermal response and transient convective coupling.

5.3.1.2. Thermal Elmore delay for package transient response

While the layer time constants do provide a useful measure of how quickly individual layers will heat up, they do not themselves provide much information about how heat will move through the package. Continuing with the circuit analogy, heat moves through the package like an electrical signal through an RC network. A common metric used in circuit design for the time required for a signal to propagate between nodes is called the *Elmore delay*, T_D . The Elmore delay is sometimes also called the Elmore time constant, as it estimates the single pole response of the circuit. It should be more accurate than a simple summation of the RC products, as they do not account for any interaction between layers.

First defined in 1948 by Elmore [238], the Elmore delay is the time required for a circuit output to reach 50% of its maximum output, a point which coincides to the peak of the impulse response of the circuit. Mathematically, he defined T_D as the dominant pole, or first moment, of the transfer function between the circuit input and output nodes, making it equivalent to the mean of the output signal. In Laplace domain notation, the normalized transfer function can be expressed in rational polynomial form as:

$$\begin{aligned} h_0(s) &= \frac{H(s)}{H(0)} = \frac{a_n s^n + a_{n-1} s^{n-1} + \dots + a_1 s + 1}{b_m s^m + b_{m-1} s^{m-1} + \dots + b_1 s + 1} \\ &\approx m_0 + m_1 s + m_2 s^2 + \dots \end{aligned} \quad (75)$$

The first and second moments in (75), m_1 and m_2 , found using a Taylor expansion of the rational polynomial, were used by Elmore to approximate the delay and rise time of the circuit response. Following the procedure in [238] if $H(s)$ is known explicitly, he showed the first moment, m_1 , later defined as the Elmore delay, is equal to:

$$T_D = m_1 = b_1 - a_1 \quad (76)$$

For completeness, Elmore similarly estimated the output rise time as the square root of the second central moment of the response, expressed as:

$$T_R = \sqrt{2m_2 - m_1^2} = \sqrt{2\pi(b_1^2 - a_1^2 + 2(a_2 - b_2))} \quad (77)$$

These definitions make the assumption of a perfect Gaussian impulse response to the input, which Elmore notes becomes more valid with more stages between input and output. Gupta, et al. proved that while most output signals will have enough skew to invalidate the Gaussian assumption, the nature of RC trees make it such that the Elmore delay is *guaranteed* to be a close upper-bound on delay in those cases [239]. Numerous other delay estimates, modifications of, or improvements upon the Elmore delay have been suggested, but it still remains a very popular delay estimate for practical circuit behavior estimation due to its numerical simplicity. We apply it here to the package thermal circuit to examine transient thermal response across the package.

Beginning with Case 5, the simplest 2-layer case representing direct die cooling, we can examine the analytical Elmore delay solution. Forming the full 2-stage transfer matrix from (41):

$$T = \begin{bmatrix} A_1 & B_1 \\ C_1 & D_1 \end{bmatrix} \begin{bmatrix} A_2 & B_2 \\ C_2 & D_2 \end{bmatrix} = \begin{bmatrix} A_{eq} & B_{eq} \\ C_{eq} & D_{eq} \end{bmatrix} \quad (78)$$

The open circuit gain can be calculated as:

$$\begin{aligned} H(s) &= \frac{1}{A_{eq}} \\ &= \frac{(6 - \lambda s R_1 C_1)(6 - \lambda s R_2 C_2)}{(6 + (3 - \lambda)s R_1 C_1)(6 + (3 - \lambda)s R_2 C_2) + 3s R_1 C_2((3 - 2\lambda)s R_2 C_2 + 12)} \end{aligned} \quad (79)$$

Normalizing the transfer function and rearranging as per (75):

$$\begin{aligned}
& h_0(s) \\
&= \frac{s^2 \lambda^2 R_1 C_1 R_2 C_2 / 36 - s \lambda (R_1 C_1 + R_2 C_2) / 6 + 1}{s^2 \left((\lambda - 3)^2 - (6\lambda - 9) \frac{C_2}{C_1} \right) R_1 C_1 R_2 C_2 / 36 + s(6R_1 C_2 - (\lambda - 3)(R_1 C_1 + R_2 C_2)) / 6 + 1} \quad (80)
\end{aligned}$$

From which it can be seen that

$$\begin{aligned}
T_{D,2} \approx m_1 = b_1 - a_1 &= \frac{(6R_1 C_2 - (\lambda - 3)(R_1 C_1 + R_2 C_2))}{6} + \frac{\lambda(R_1 C_1 + R_2 C_2)}{6} \\
&= R_1 C_1 / 2 + \left(R_1 + R_2 / 2 \right) C_2 \quad (81)
\end{aligned}$$

This procedure can be repeated with Cases 1-4, but just looking at the Case 4 5-layer result:

$$\begin{aligned}
T_{D,5} \approx & R_1 C_1 / 2 + \left(R_1 + R_2 / 2 \right) C_2 + \left(R_1 + R_2 + R_3 / 2 \right) C_3 \\
& + \left(R_1 + R_2 + R_3 + R_4 / 2 \right) C_4 \\
& + \left(R_1 + R_2 + R_3 + R_4 + R_5 / 2 \right) C_5 \quad (82)
\end{aligned}$$

it is suggestive that there is a straightforward repeating pattern to the finite element based Elmore delay that may be obtained by inspection.

It is worth noting that the T_D estimates above retain no dependence on the mass matrix coupling factor, λ . This agrees with the statements by Shi that only parallel (shunt) capacitances contribute to the Elmore delay, series capacitances do not [240]. The Elmore delay is the first mode of the circuit function and comprises the dominant, lowest frequency component of the circuit response. At low frequency a capacitor appears to be an infinite impedance component, making the mass coupling component in parallel with a finite resistance irrelevant to dominant pole characteristics. Thus, the Elmore delay is insensitive to the choice of mass matrix used in the finite element thermal circuit model.

The high order polynomial complexity of deriving analytical forms for larger circuits has led to the development of algorithmic approaches that are now commonly used in circuit development. Rubinstein, et al. [241] showed that a when the circuit consists of simple RC tree networks, as shown for our one-dimensional thermal circuit analogy in Figure 5.4(a), an approximation for T_D can be constructed from repeated summation over the circuit elements. The Elmore delay between the input node and any node i in an RC tree simplifies to:

$$T_{D,i} = \sum_{k=1}^N R_{ki} C_k \quad (83)$$

where N is the total number of RC circuit stages and R_{ki} is the sum of the resistors between the input node and node k in common with the path between the input and node i . In our linear circuit with no branching paths, R_{ki} can be defined as:

$$R_{ki} = \sum_{l=1}^{\min(i,k)} R_l \quad (84)$$

For this analysis, we are always looking at the delay between the junction and coolant nodes in the thermal circuit, making the node of interest, i , always equal to the number of package layers, n , so that in all cases $k \leq n$. This simplifies (83) and (84) into:

$$T_{D,n} = \sum_{k=1}^n \sum_{l=1}^k R_l C_k \quad (85)$$

This form produces a delay estimate that can be computed using the values of layer R and C from Table 5.3. However, this estimate differs from that obtained using (75) and (76) as shown by this T_D estimate for the two and five layer cases:

$$T_{D,2} \approx R_1 C_1 + (R_1 + R_2) C_2 \quad (86)$$

$$T_{D,5} \approx R_1 C_1 + (R_1 + R_2) C_2 + (R_1 + R_2 + R_3) C_3 \\ + (R_1 + R_2 + R_3 + R_4) C_4 + (R_1 + R_2 + R_3 + R_4 + R_5) C_5$$

Trial and error shows that increasing the number of circuit elements used for each layer (i.e., applying mesh refinement) gradually converges the numerical results to that obtained from (76). The results from (76) itself, on the other hand, are independent of any additional mesh refinement. It is worth noting that this is likely due to the two forms being based on different circuit topologies. The transfer function form is based on the full finite element description of the heat transfer problem, while the Rubinstein form is based on a simple first order finite difference approximation that lumps each layer in an unrealistic fashion, with resistances arbitrarily assigned to the node preceded by the full layer capacitance as in Figure 5.12:

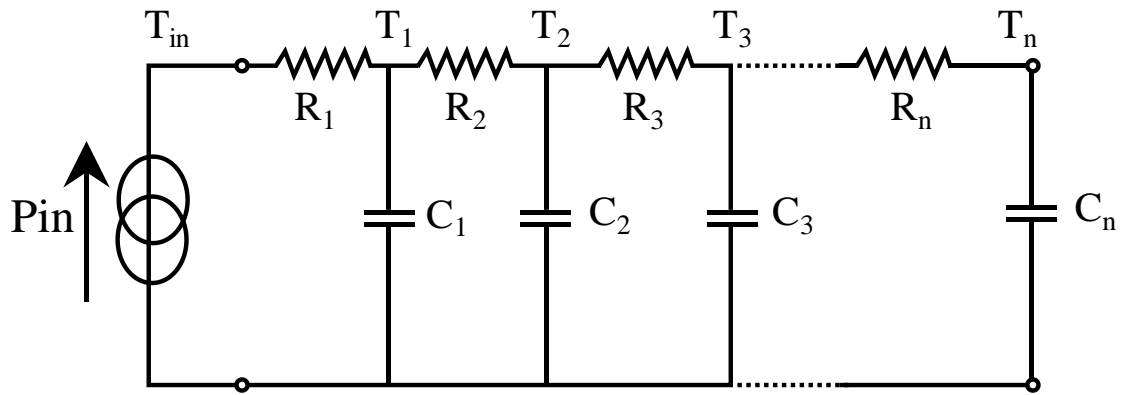


Figure 5.12 – Cauer-type finite difference thermal circuit used in the Rubenstein Elmore delay approximation where layer masses and resistances are lumped at and before a single node.

We can find a closed form expression for this convergence by refining each RC pair (or package ‘layer’) into h refined elements per layer. The refined elements have values R_k/h , C_k/h as shown in Figure 5.13.

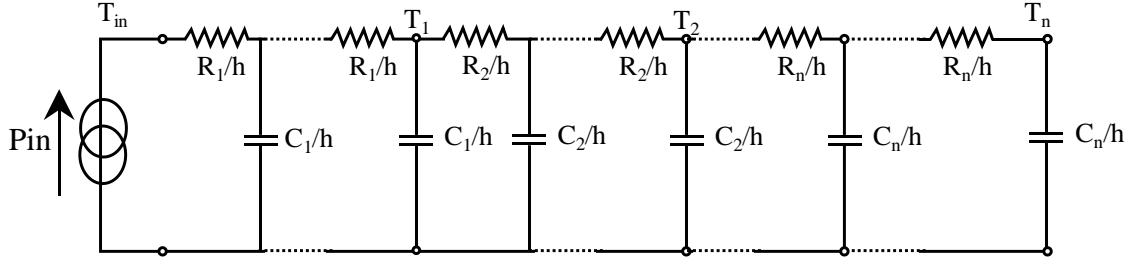


Figure 5.13 – Finite difference thermal circuit refinement for converged Elmore delay approximation.

This expands the circuit to a total of nh elements, and (85) can be expressed as:

$$T_{D,nh} = \sum_{q=1}^{nh} \sum_{p=1}^q \frac{R_{[p/h]}}{h} \frac{C_{[q/h]}}{h} \quad (87)$$

where the R and C indices use the Iverson notation for the ceiling function. A slightly simpler form of this equation can be found by expanding the layer refinement term, h , and noting that $\sum R_{[p/h]}/h$ and $\sum C_{[q/h]}/h$ terms within each layer are equal to R_l and C_k . With some algebraic manipulation this simplifies to the original summation bases producing:

$$T_{D,n,h} = \sum_{k=1}^n \sum_{l=1}^k R_l C_k - \frac{h-1}{2h} \sum_{k=1}^n R_k C_k \quad (88)$$

From (88) we see that the first term in the converging Elmore delay is simply the $h=1$ undiscretized delay from (85), $T_{D,n,1}$, reduced by a fraction of the sum of the individual layer time constants presented in Table 5.3. As $h \rightarrow \infty$, (88) reduces to:

$$T_{D,n} = \lim_{h \rightarrow \infty} T_{D,n,h} = \sum_{k=1}^n \sum_{l=1}^k R_l C_k - \frac{1}{2} \sum_{k=1}^n R_k C_k \quad (89)$$

$$T_{D,n} = T_{D,n,1} - \frac{1}{2} \sum \tau_k \quad (90)$$

The converged form in (89) produces results identical to that obtained with (76).

The difference between circuit models turns out to be the endpoint mass and resistance

distributions. At first glance, the finite element approach applies some thermal capacity to the input node, and no resistance follows the output node. As Elmore delay is based on step voltage response, neither input capacitance nor output resistance can have any impact on the result and are ignored. It is not until h approaches infinity that these endpoint differences become insignificant and the first order response of both circuits becomes identical.

It is possible to use alternative forms of the finite difference topology or the finite element circuit topology in conjunction with (83) to produce an Elmore delay estimate. See Figure 5.14, where (a) shows a *central finite-difference* discretization scheme and values, whereby the thermal mass is centered and layer resistance is distributed on either side, and (b) which shows the previously described lumped mass finite element discretization that centralizes the resistance and distributes the masses.

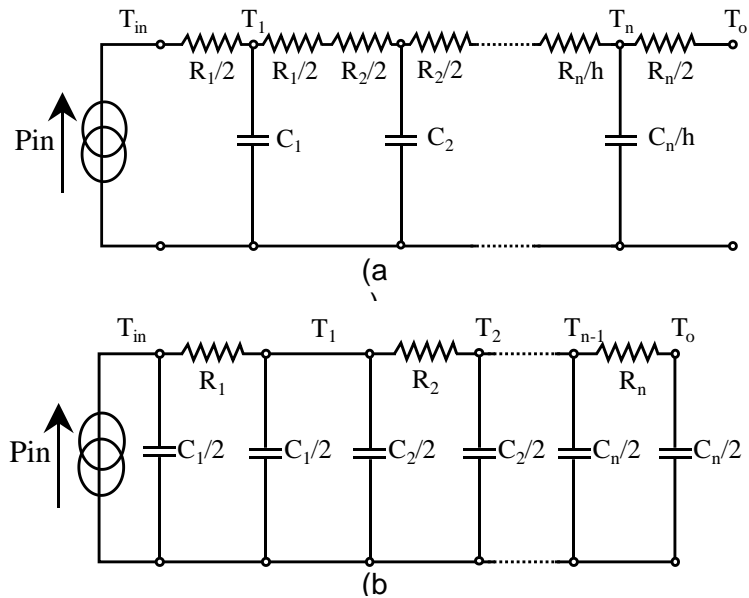


Figure 5.14 – (a) Finite difference and (b) finite element thermal circuit topologies with matched algorithmic and transfer function method Elmore delay.

Mapping the values from either Figure 5.14(a) or (b) to the Rubenstein algorithm produces the same result as (89) without the need for any additional mesh refinement. Thus, between the transfer function method and converged Rubenstein algorithms with different topologies, we have confirmed that (89) can be used with just the package layer properties to produce the best Elmore delay value with least computational effort. The Elmore delay for the five package Cases are given in Table 5.4 along with their ΣRC delay estimates for comparison.

Table 5.4 – Package delay characteristics

Case	# of package layers	$\Sigma(R_i C_i)$ [ms]	T_D [ms]
1	10	386.1	710.3
2	9	86.9	218.2
3	6	9.04	27.5
4	5	4.18	11.7
5	2	2.07	1.52

5.3.1.3. Boundary condition definition

In these models, it is assumed that the packages experience pulsed heating in the volume of the junction layer of the device, and have convective cooling at the lowest, or base, package layer. A finite element thermal circuit representation showing possible heat generation and boundary conditions is shown in Figure 5.15 [222]. A heat flux boundary condition is represented as a current source between thermal ground and the boundary node. Volumetric power generation over an element is represented by two current sources dividing the power evenly over both nodes for that element. Thus, where two heated elements connect the heat generation source has twice the magnitude, reflecting contributions from both elements. Linear convection is represented as a resistance to thermal ground, and fixed temperatures by voltage sources to ground. As shown, if the ambient temperature for a convection boundary is not zero, a voltage source is used with

the convection resistor to create this effect. However, in the following simulations we were only concerned with relative temperature changes and allowed ambient temperature to equal zero.

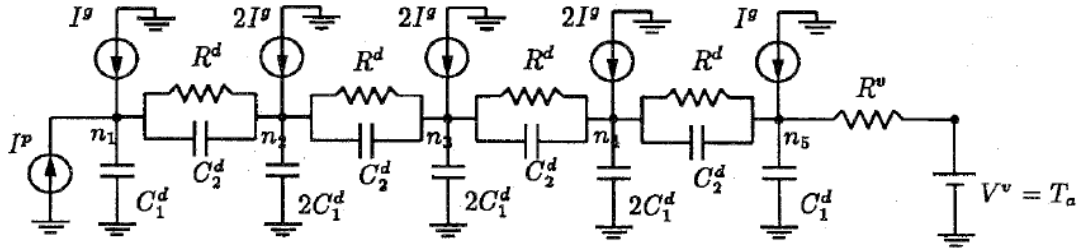


Figure 5.15 – Representative 1D thermal circuit chain showing heat generation and boundary conditions, from [222] with permission, © 1999 IEEE.

We used the same *equivalent flat plate convection* technique as described in Section 4.3 to derive values for the applied convective coefficient, h_{eff} , spanning from 100 to 500,000 W/m²K, and with a nominal ambient temperature of zero as mentioned above. The value of the convective resistor is determined from:

$$q''_{conv} = h_{eff}(T_s - T_a) \quad (91)$$

$$R''_{conv} = \Delta T/q''_{conv} = 1/h_{eff} \quad (92)$$

5.3.1.4. Simulation procedure

LTspice XVII, a SPICE simulator originally by Linear Technology Corporation (now Analog Devices) [242], was used to numerically simulate the thermal circuit models studied here. An example schematic for the Case 3 FEM thermal circuit model is shown in Figure 5.16. The other Cases are modeled similarly, with more or fewer elements according to the configurations shown in Figure 5.11. Also, note that in the representative figure only a single element is used for each layer. This particularly undermeshed case would suffer significant DMP violation, with nodes not connected to forcing sources likely

being driven substantially negative during initial pulses or step changes. Using an undocumented feature in the LTspice program for making multiple bus connections to simulate repeated circuit elements [243], we performed mesh refinement on the thermal circuit by increasing the number of elements for each layer until the DMP violation became negligible, defined as less than a 10^{-6} °C temperature swing on a step response. This convergence check is described in the following section.

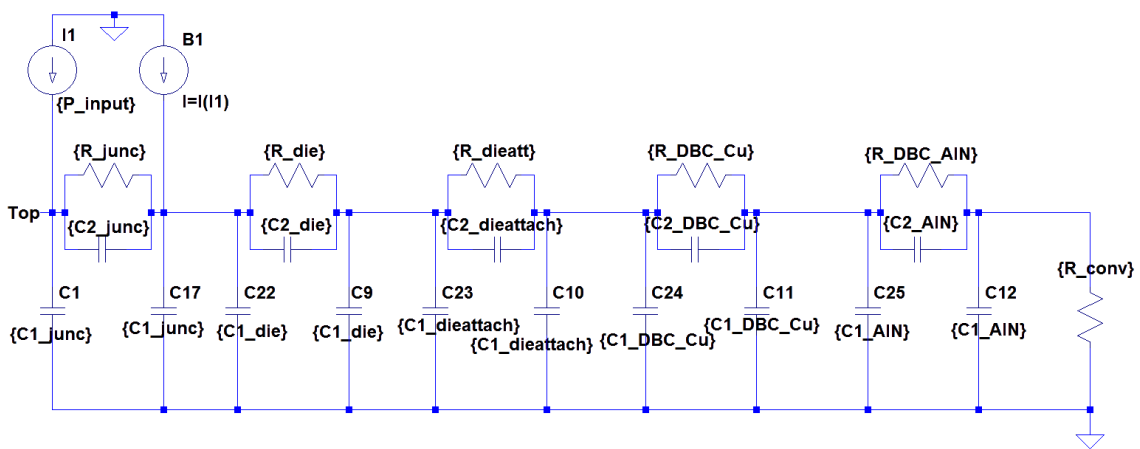


Figure 5.16 – Case 4 SPICE thermal circuit representation. Each package layer is represented here as only a single finite element for clarity. Heat generation is imposed on the nodes of the junction layer element, and a convection boundary condition to thermal ground is imposed after the base layer.

Four numerical tests were performed on the package Cases to evaluate transient thermal behavior. First, step response simulations were run while sweeping the convection coefficient over the range of 100 to 500,000 W/m²K to determine steady-state package behavior and dominate transient response characteristics. Second, a single unit square pulse was applied to each Case sweeping both convection coefficient and pulse width (from 50 μ s to 10 sec) to quantify the ability of improved convection to reduce peak junction

temperature. Third, a frequency domain small signal analysis was run for each case and convective rate to examine the applicability of claims made by Meysenc regarding package inertia. Finally, transient analyses were run with unit power step and pulse trains to examine the same behavior in the time domain. A unit heat flux was applied throughout the study since the model is linear and the resultant thermal impedance values should be representative over all power levels. All resistances and impedances are presented normalized to this unit power.

5.3.1.5. Using DMP to verify package mesh convergence

Because only using a single element for each layer would be significant under-meshing in the presence of high-speed transients (an ideal step response having zero rise time), a convergence analysis was first performed on the 5 Cases. With the model initial temperature set to zero, a unit step power input was applied to each heat input node and each interlayer nodal temperature was checked until the model reached steady state. As was shown in Section 5.2.6, the step response will induce negative temperatures downstream from the input nodes as the temperatures start to rise. The magnitude of these negative temperatures, which represent violations of the Discrete Maximum Principle due to the chosen spatial discretization, were tracked and compared as the mesh was increasingly refined. Mesh refinement was performed by increasing the number of element divisions, n , equally in each package layer.

Figure 5.17 shows the DMP magnitude for Case 1 as n is increased from 1 to 20 elements per layer. As can be seen, the order of magnitude of the error decreases very quickly in all layers, and the interlayer node with the largest amount of error was always the node closest to the heat input. For all Cases this is the node at the backside of the die.

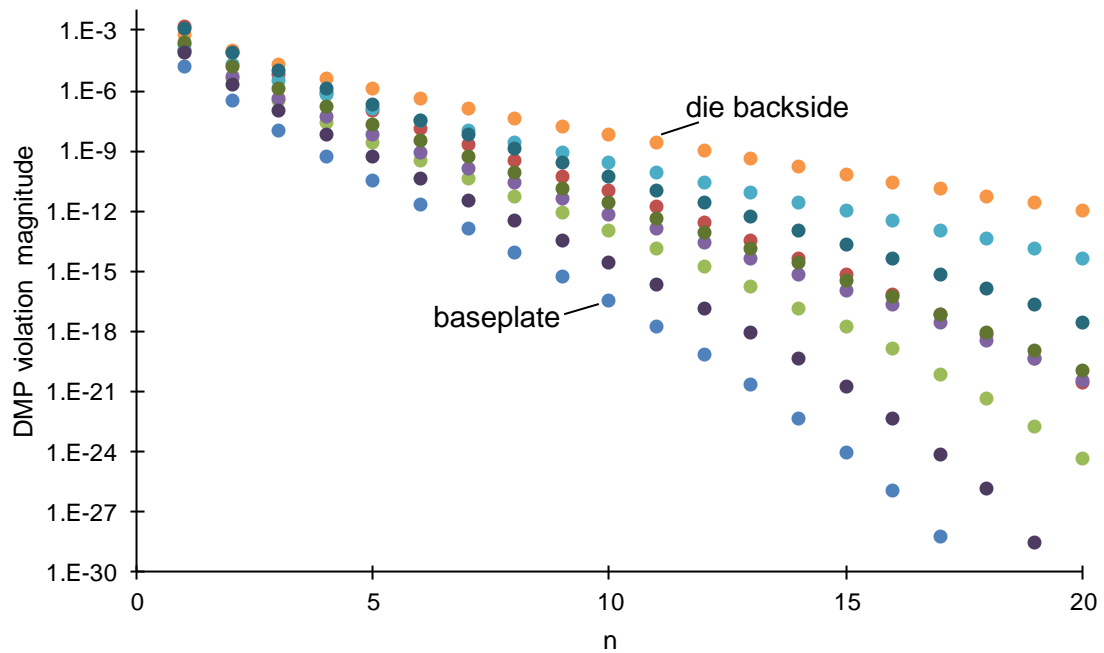


Figure 5.17 – Case 1 negative oscillation magnitude for the different layers with increasing mesh refinement. n indicates the number of elements per package layer. For clarity of the graph, only the top and bottom sets of nodes are labeled.

Figure 5.18 shows the maximum DMP violation present in each Case for each value of n . Note that the error magnitudes are nearly identical and Cases 1-4 are almost completely overlapped. This occurs because in all Cases the largest magnitude occurs in the die-backside node, and the material configuration adjacent to the junction stays largely unchanged except for the Case 5, where that node coincides with the convective surface node.

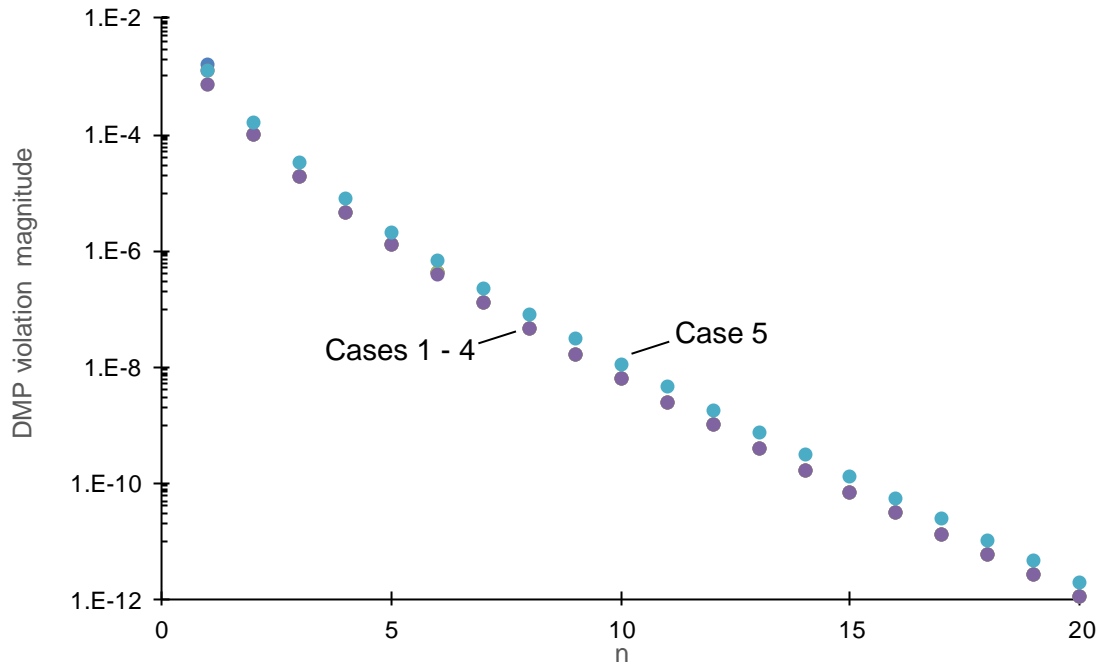


Figure 5.18 – Maximum DMP oscillation magnitude for all five Cases with increasing mesh refinement. Note that all five cases are present and largely overlap on the graph.

Because the DMP violation cannot be used to evaluate mesh convergence in driven nodes, such as the junction layer nodes in these Cases, a separate convergence examination was performed on the heat input nodes. Figure 5.19 shows the discrepancy in the maximum junction temperature for each discretization level normalized to the $n = 20$ temperature values for the early time steps (up to 0.1 seconds). Note that only the first few levels of n can be distinguished as having a significantly higher level of error than the more refined cases.

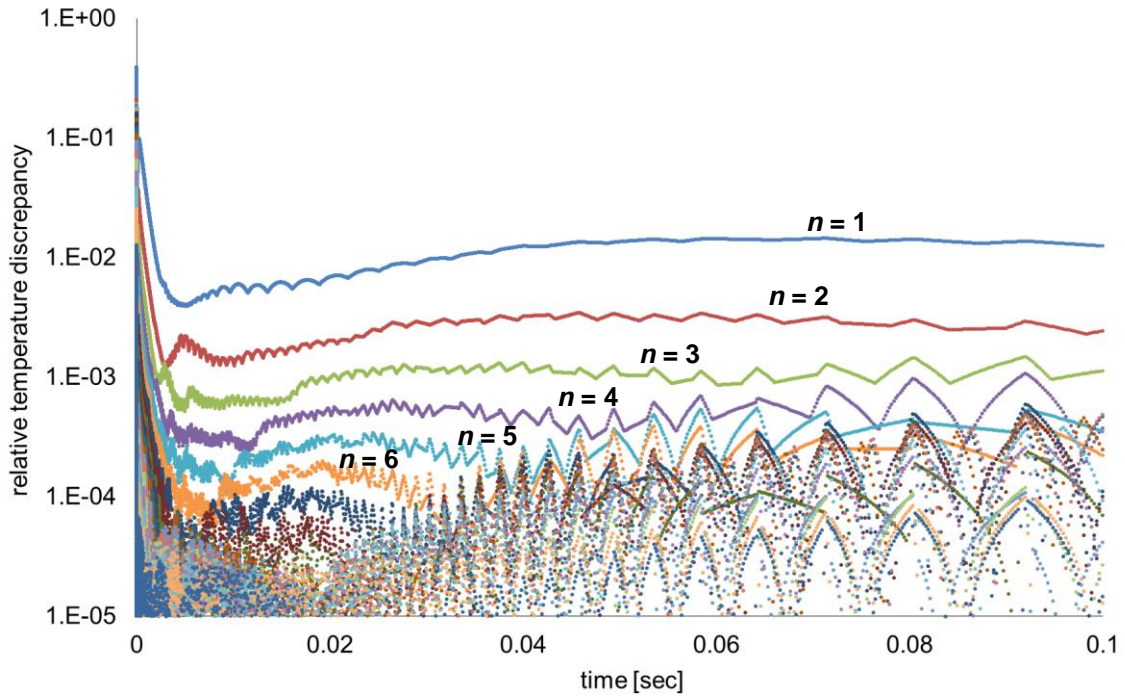


Figure 5.19 – Case 1 error accumulation (maximum device temperature relative discrepancy) with time for different values of n . Note that $n = 1$ to 20 are plotted in the graph. For clarity only the curves that can be distinguished from the bulk of the data are labeled.

From both the DMP and maximum junction temperature convergence data, it is obvious that the model performs as would be expected of a finite element model. Error decreases quickly with increasing mesh density, with gradual diminished returns at higher levels, and it does not appear that this convergence study reached the levels of overmesh that can introduce excessive numerical error. Additionally, DMP violation appears to be a useful convergence metric, showing similar levels of error reduction relative to mesh density. For the remainder of this analysis, the mesh density metric $n = 10$ will be used as it is sufficiently into the regime showing insensitivity to further meshing.

5.3.2. Transient model results

5.3.2.1. Package step response

Figure 5.20 shows the steady-state package responses as extracted from the unit step junction profiles. Flux normalized temperature rise showed strong dependence on convective rate, as expected. The R_{th} values trend toward the package values that were shown in Table 5.3 as the convection component diminishes, as expected from (9), although as amplified by the logarithmic scaling Cases 4 and 5 still appear to have significant relative convective resistance.

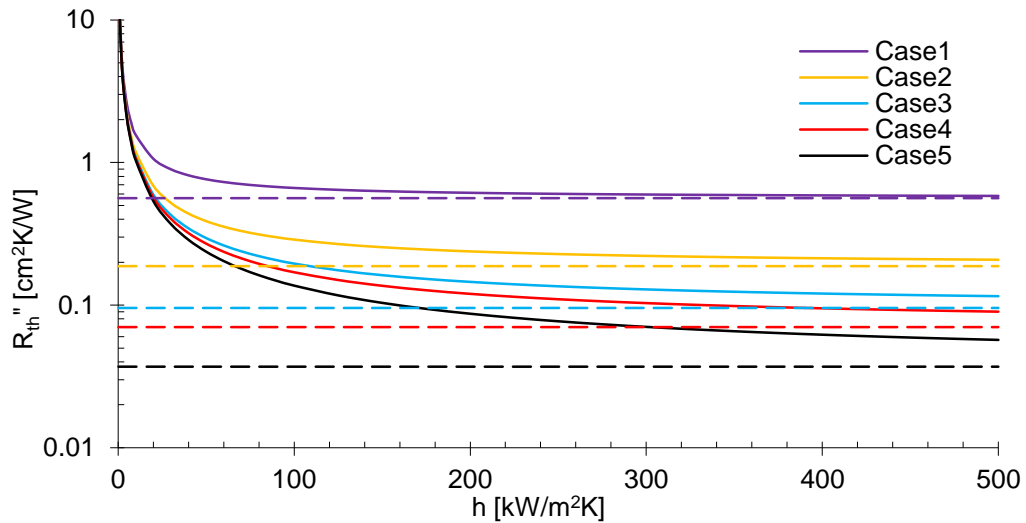


Figure 5.20 – Steady-state resistivity of the modeled packages as functions of the backside convection. The dashed lines represent the calculated values for each case from Table 5.3, towards which each approaches as the convective resistances go to zero.

In Figure 5.21, the package dominant time constant is estimated using a simple single exponential model for temperature rise:

$$T(t) = T_{ss} \left(1 - e^{-t/\tau} \right) \quad (93)$$

$$\tau = -t/\ln(1 - T(t)/T_{ss}) \quad (94)$$

For a system that is not truly lumped, this model will produce a non-constant value for τ . The values shown in the figure are the average extracted time constant values when the temperature has reached 99% of the steady-state value. For reference, the package time constant estimates from Table 5.4 are also plotted in Figure 5.21. Elmore delay as expected is an upper bound while ΣRC appears to be a lower bound to the $h_{eff} \rightarrow \infty$ effective time constant for all cases except for Case 5 which may simply not have saturated within the simulated range. Despite there being such a wide range in predicted time constants, this does support the notion that those time estimates can serve as an approximation to the package time constant for large convection rates and long heating times.

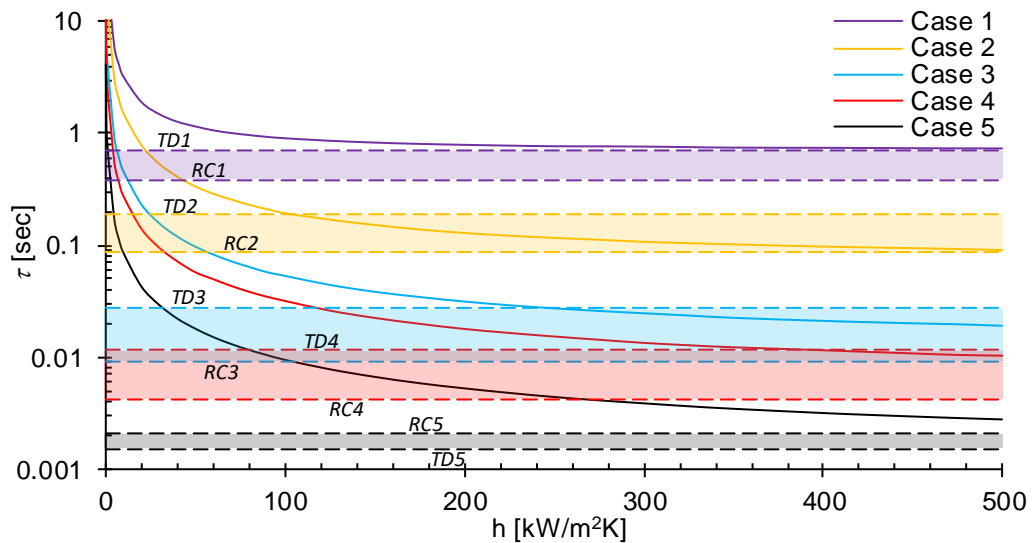


Figure 5.21 – Extracted dominant time constant of the modeled packages as functions of the backside convection. The dashed lines and shaded regions represent time constant estimates bounded by the Elmore delay ($T_D\#$) and the sum of RC constants ($RC\#$) for each package Case.

Finally, comparing the converged thermal circuit delay estimates for each package, an *open circuit* (convection coefficient = 0) unit step response was simulated for each case.

The ‘50% output circuit delay’, T_{50} , is calculated as the time for the unloaded output to reach 50% of T_{max} in response to a step input. These values are shown in Table 5.5. Again, as expected from Gupta, et al., T_D provides a guaranteed overestimate of the actual rise time [239], in this case by a consistent 30-36%.

Table 5.5 –Simulated package delay comparison

Case	# of layers	$\Sigma(R_i C_i)$ [ms]	T_D [ms]	$T_{50\%}$ [ms]	$\Sigma RC/T_{50}$	T_D/T_{50}
1	10	386.1	710.3	546.8	0.71	1.30
2	9	86.9	185.5	137.0	0.64	1.36
3	6	9.04	27.5	20.5	0.44	1.34
4	5	4.18	11.7	8.58	0.49	1.36
5	2	2.07	1.52	1.17	1.79	1.31

5.3.2.2. Convection influence on pulsed temperature rise

The Case 1 results from simulating a unit pulse applied to the package with varying convection and pulse width are shown in Figure 5.22. As expected, for long pulse-times the peak temperature rise is highly dependent on the convective resistance. However, as the pulse time decreases the device junction becomes thermally decoupled from the heat sink. As shown in the Figure 5.22 inset, despite a greater than three orders-of-magnitude change in convection rate the variation in junction temperature rise starts to become negligible for pulses smaller than the Elmore delay, T_D . The inset shows T_D , the lumped package RC constant, and the actual simulated package delay time, T_{50} . Similar graphs focusing on the shorter pulse region are shown for the remaining cases in Figure 5.23, showing similar lack of variation with effective convection rate for short pulse times.

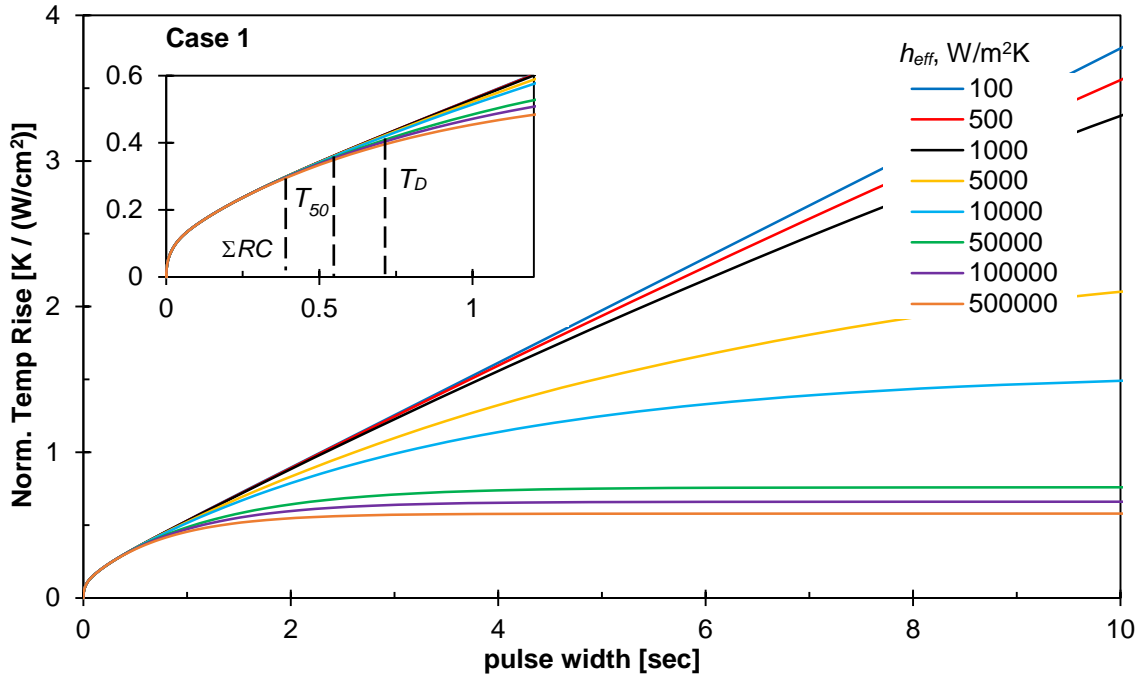


Figure 5.22 – Peak junction temperature rise under single pulse excitation for Case 1 with varying convection rates and pulse widths. The inset magnifies the range up to 1.25 seconds showing a lack of differentiation between junction heating at small pulse widths, with package time constant (ΣRC), Elmore delay (T_D), and simulated pulse delay (T_{50}) noted.

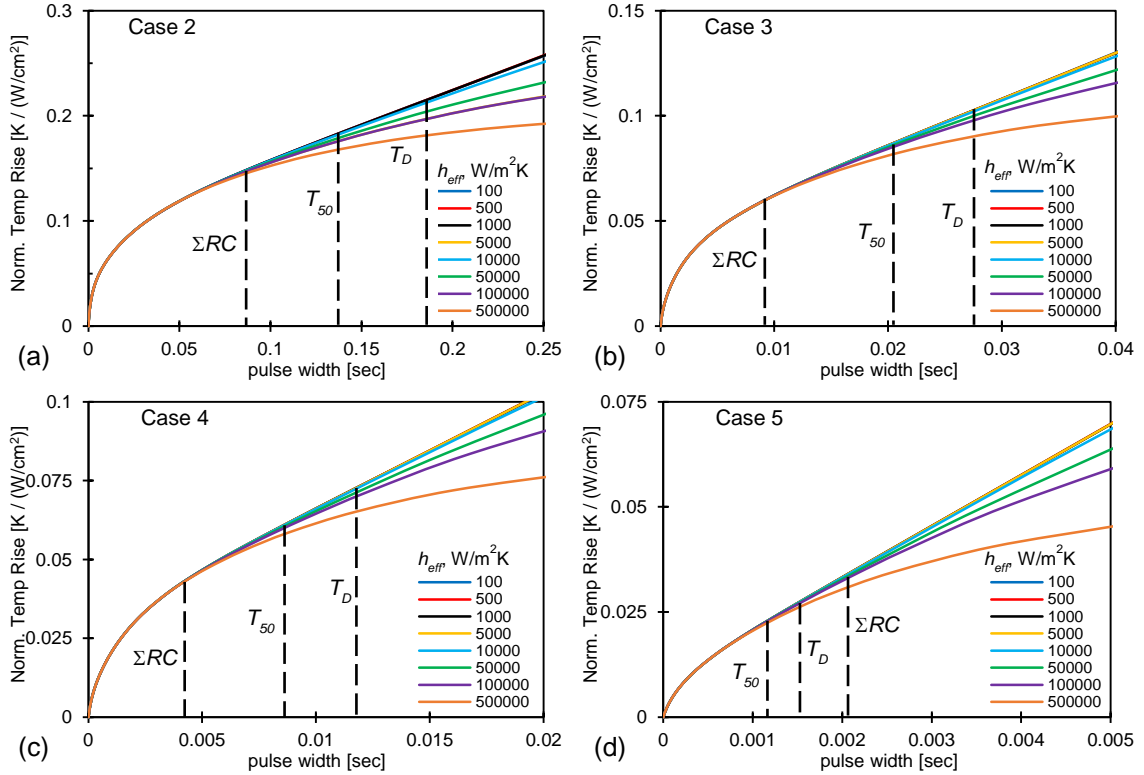


Figure 5.23 – Peak junction temperature rise under single pulse excitation for package Cases 2-5 with varying convection rate and pulse widths with package time constant (ΣRC), Elmore delay (T_D), and simulated pulse delay (T_{50}) noted.

When considering heat propagation through the package the insensitivity to convection rate is unsurprising for short pulses. There is a finite amount of time required for heat to reach the cooled backside surface and create a thermal gradient across the convective thermal resistance. Prior to this time convection can have no influence on the temperature profile upstream, regardless of magnitude. Looking at Figure 5.22 and Figure 5.23, it appears that both the lumped RC and T_D values provide some estimate of the time it takes for the package to exhibit thermal sensitivity to backside convection, and both are similar in magnitude to the simulated delay time, T_{50} .

From a physical standpoint, it make sense that Elmore delay would correlate with convective insensitivity as it is specifically designed to approximate the time for heat to reach the output of the thermal circuit, or for heat to get from the junction to the convection surface. However, because Elmore delay is an estimate of time for an ideal step response to reach 50% of the target value, a not-insignificant gradient will have developed between the onset of significant output rise and T_D causing some measurable convective impact. From the figures we can see that this is consistently the case. Comparing ΣRC and T_D as delay estimates, T_D is more consistent in its relative location to T_{50} and the convective divergence. RC generally lies farther into the insensitive region for Cases 1-4, but is actually larger than T_D and T_{50} for Case 5.

We can gain another view of this relationship by normalizing pulse time by the Elmore delay and then examining the relative temperature difference between the maximum and minimum convection rate temperature curves. Figure 5.24 shows this relative temperature difference for all five Cases and Table 5.6 provides specific values of the relative temperature change at fractional t_p/T_D values from 1/4 to 1.

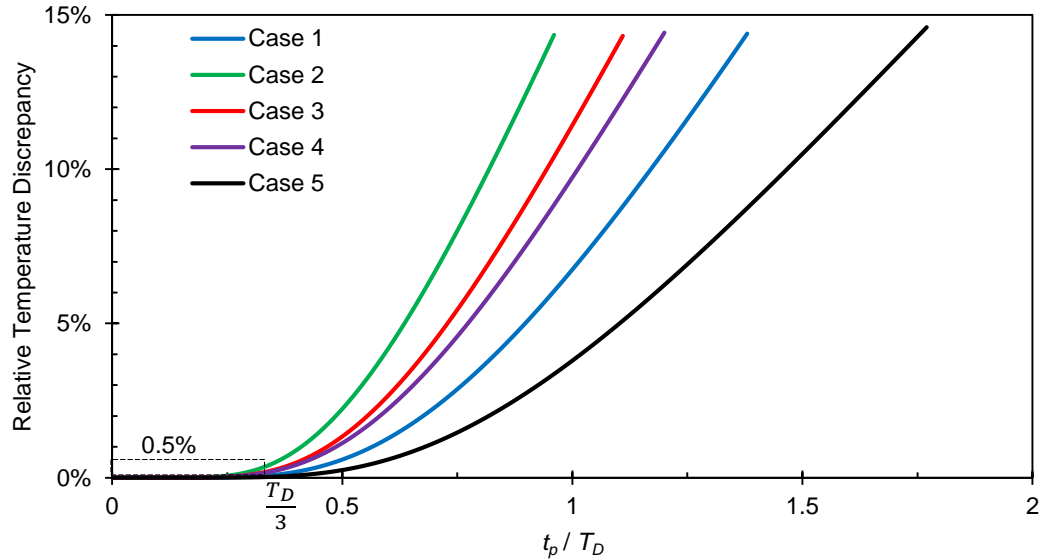


Figure 5.24 – Relative difference in temperature rise seen by package cases over simulated convection range (from 100 W/m²K to 500,000 W/m²K) as a function of the Elmore delay normalized pulse time.

Table 5.6 – Relative temperature change from a 5000x h_{eff} increase

Case	$T_D/4$	$T_D/3$	$T_D/2$	T_D
1	0.008%	0.064%	0.59%	6.8%
2	0.064%	0.36%	2.23%	15.6%
3	0.029%	0.19%	1.33%	11.4%
4	0.027%	0.16%	1.12%	9.7%
5	0.002%	0.020%	0.25%	3.8%

Figure 5.24 confirms that the temperature differences from large convective improvement are all very low for values below T_D , showing less than 20% for all package Cases. In particular below $T_D/3$ a temperature reduction of less than 0.5% is seen across all cases despite a 5000x increase in applied convection coefficient, and the discrepancy grows significantly above this point. This characteristic has significant implications for pulsed package designers, indicating that for all of the package Cases analyzed, none of the designs will be able to use improved convection to reduce temperature rise for sub-

millisecond transients. We can conclude, however, that T_D can always serve as a consistent overestimate of the convective insensitivity time, making it a useful pulsed package analysis metric that can be determined simply from layer geometry and material properties.

5.3.2.3. *Frequency domain junction response*

Recalling the suggestions by Meysenc, et al. that a low thermal inertia package will respond to sudden transients with increased temperature swing, we now examine the frequency domain response of these thermal circuits. Based on the behavior that was shown in Figure 5.2, we would expect to see a difference in switching frequency for which the packages begin to show reduced relative temperature response, and this difference may cause significant thermal performance discrepancy. As Meysenc's example was based only on the lumped semiconductor die response, it will be useful here to examine the impact of the entire package. As the roll off behavior is closely related to the resistive dissipation and capacitive storage within the package, we expect convection rate to significantly alter the roll off behavior for lower frequencies, but based on the previous section should have diminished impact at higher frequencies (equivalent to shorter pulse times).

Each of the package Cases was simulated with a unit magnitude small signal AC power input and varying convection rate. The thermal input impedance (junction temperature rise normalized to input power) for the Cases are shown in Figure 5.25, with each subfigure showing a different convection rate. From these graphs it can be seen that the behavior described by Meysenc indeed does occur for integrated power electronic packages.

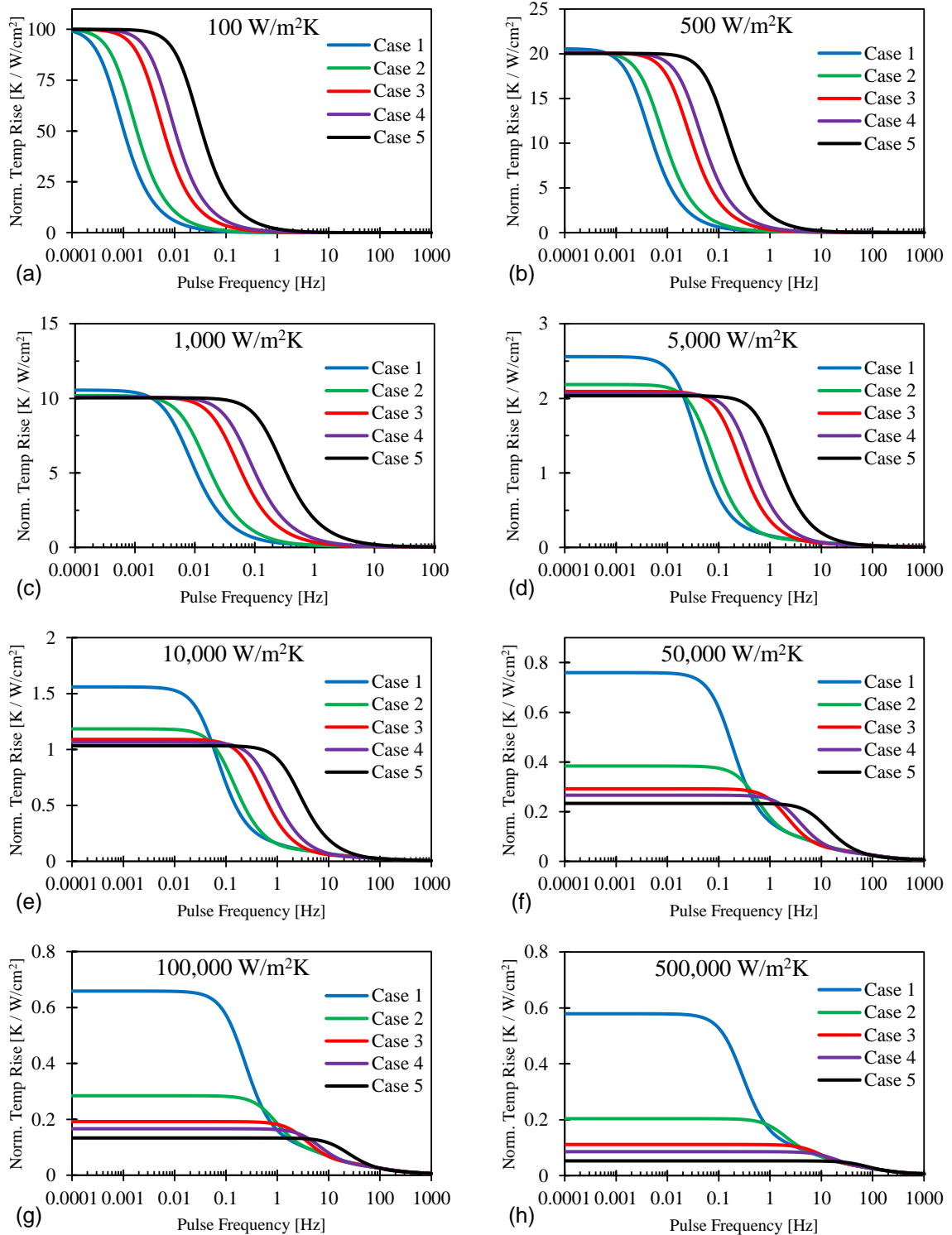


Figure 5.25 – Frequency dependent small signal thermal resistance for each Case over varied convection rates. Packages with smaller thermal time constants see thermal response roll off at higher frequencies, creating regions where lower thermal resistance packages heat up more.

Each plot in Figure 5.25 shows the expected temperature roll off that occurs as the fixed-power cycles increase in frequency and the thermal circuits act as multi-pole low-pass filters. Just as Meysenc described, the frequency after which the dominant pole, or RC constant, pulls the temperature response down occurs sooner in higher thermal inertia packages. This is seen most notably for low convection rates. For $h_{eff} < 1000 \text{ W/m}^2\text{K}$, there appears to be little transient benefit to using the advanced integrated packages. As h_{eff} increases, the steady-state temperature rise begins to decrease, and the packages' thermal resistance introduces separation between the Cases. A switching frequency range exists for all convection rates where improved packages have worse thermal performance than even the base Case 1 package. Increased convection does shift that frequency range higher as well as begin to diminish the magnitude of this effect, and at high enough frequencies this separation approaches zero. So short enough pulses diminish both benefit of convective improvement and package improvement as well.

Note that the SPICE standard AC analysis uses a constant amplitude assumption. Under a constant pulse energy assumption, the frequency dependent profiles would look much different. This may of interest in future analyses, but would require a custom algorithm.

5.3.2.4. Time domain junction response

While the frequency domain data is suggestive of the package impedance inversion, the change in thermal performance can be more clearly seen in time domain simulations. Looking again at the step response (equivalent to single pulse peak temperature rise) plots in Section 5.3.2.2, but this time superimposing the different Cases for specific convection rates, a time-domain equivalent of Figure 5.25 is constructed and shown in Figure 5.26.

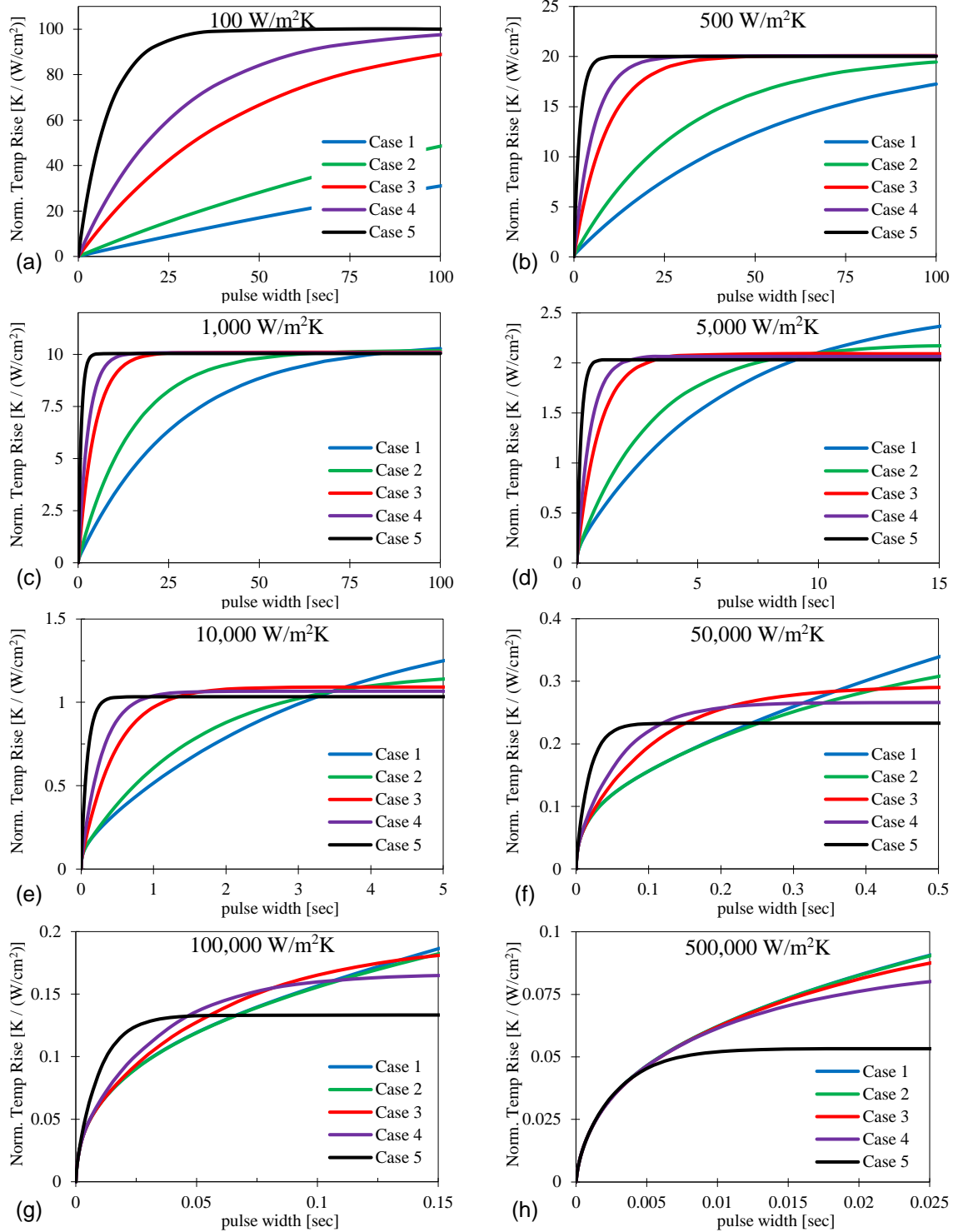


Figure 5.26 – Time domain step response temperature rise for each Case over varied convection rates. Packages with smaller thermal time constants heat up faster, resulting in higher temperatures at short pulses times, with the crossover point being temperature dependent.

It is fairly clear from these results that the low thermal inertia in highly integrated packages causes high early transient temperatures in all but the highest convection conditions. For low convection rates ($h_{eff} < 1000 \text{ W/m}^2\text{K}$) the slow temperature rise keeps the high- R_{th} packages at much lower temperatures than the low- R_{th} Cases. As h_{eff} increases and reduces the thermal resistance contribution to the thermal time constant, visible in the figure for $h_{eff} > 1000 \text{ W/m}^2\text{K}$, crossover points can be seen that shift to shorter pulse times with higher h_{eff} . Thus, as in the frequency domain, the time domain plots suggest that highly integrated packages will heat up more than less-integrated packages for pulse times significantly longer than the package time constants or Elmore delays until the convective contribution to thermal time constant has sufficiently diminished.

As step response does not convey cool down, or thermal reset, time, we also examine a pulse train to show the overlap in the information provided by the AC and time domain step responses. While there are an infinite number of pulse configurations that can be examined, we can look at the graphs in Figure 5.25 and Figure 5.26 for useful examples. In particular, between 10,000 and 100,000 $\text{W/m}^2\text{K}$, the simulations show clear cases of inversion in thermal performance between 0.1 and 10 Hz. Figure 5.27, Figure 5.28, and Figure 5.29 show 1 W/cm^2 unit pulse trains with a 1 second period and 10% duty cycle (100 ms on-time), shown for both the initial pulses and after warmup transients have saturated (around 30 sec).

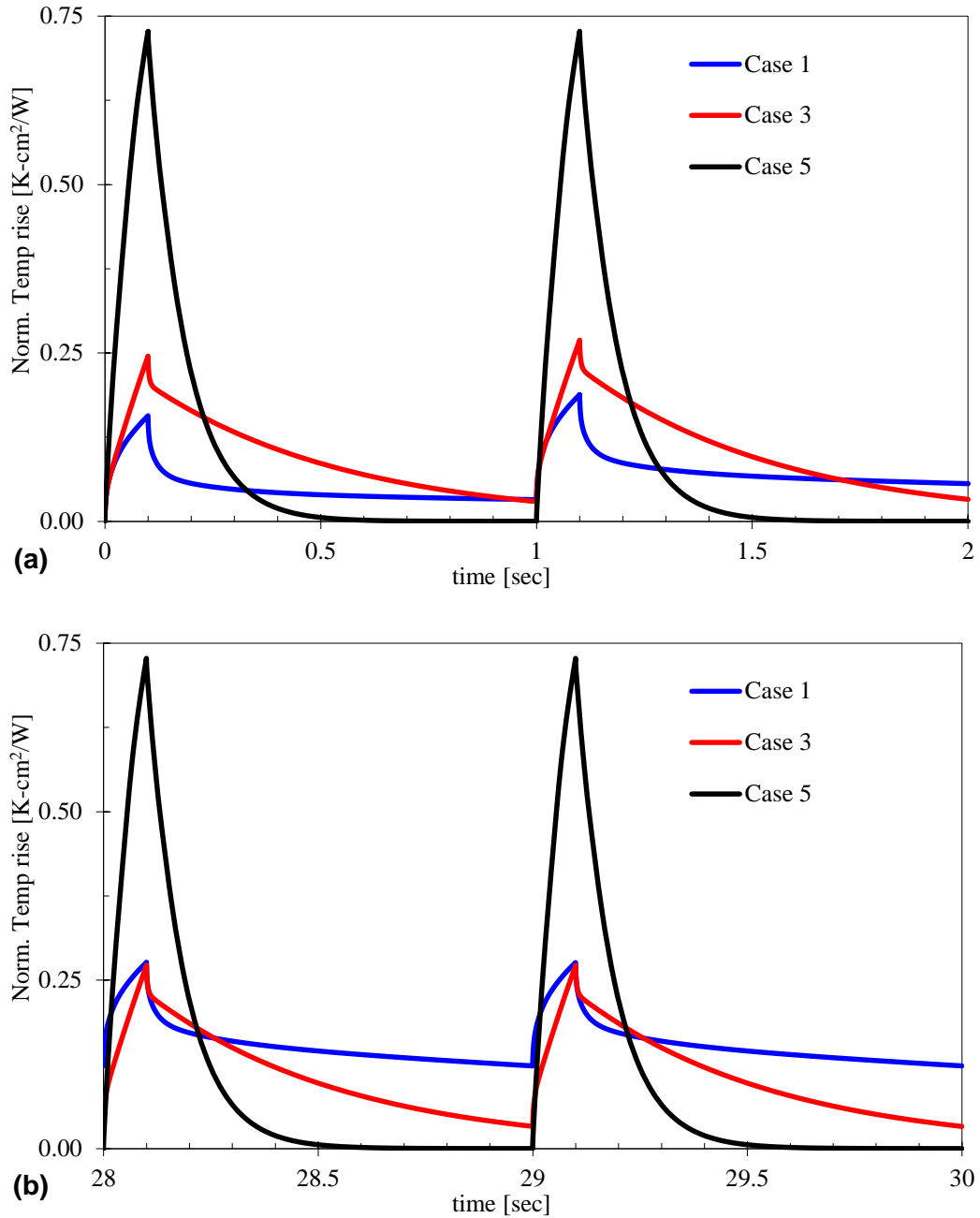


Figure 5.27 – Time domain pulsed temperature profiles for Cases 1, 3, and 5 with $h_{eff} = 10 \text{ kW/m}^2\text{K}$ subjected to a unit heat pulse train of 100 ms pulse-width and 1 second period. (a) shows the initial pulses where Case 1 and Case 3 are both warming slightly. (b) shows the temperatures for pulses after the warmup has saturated (30 sec).

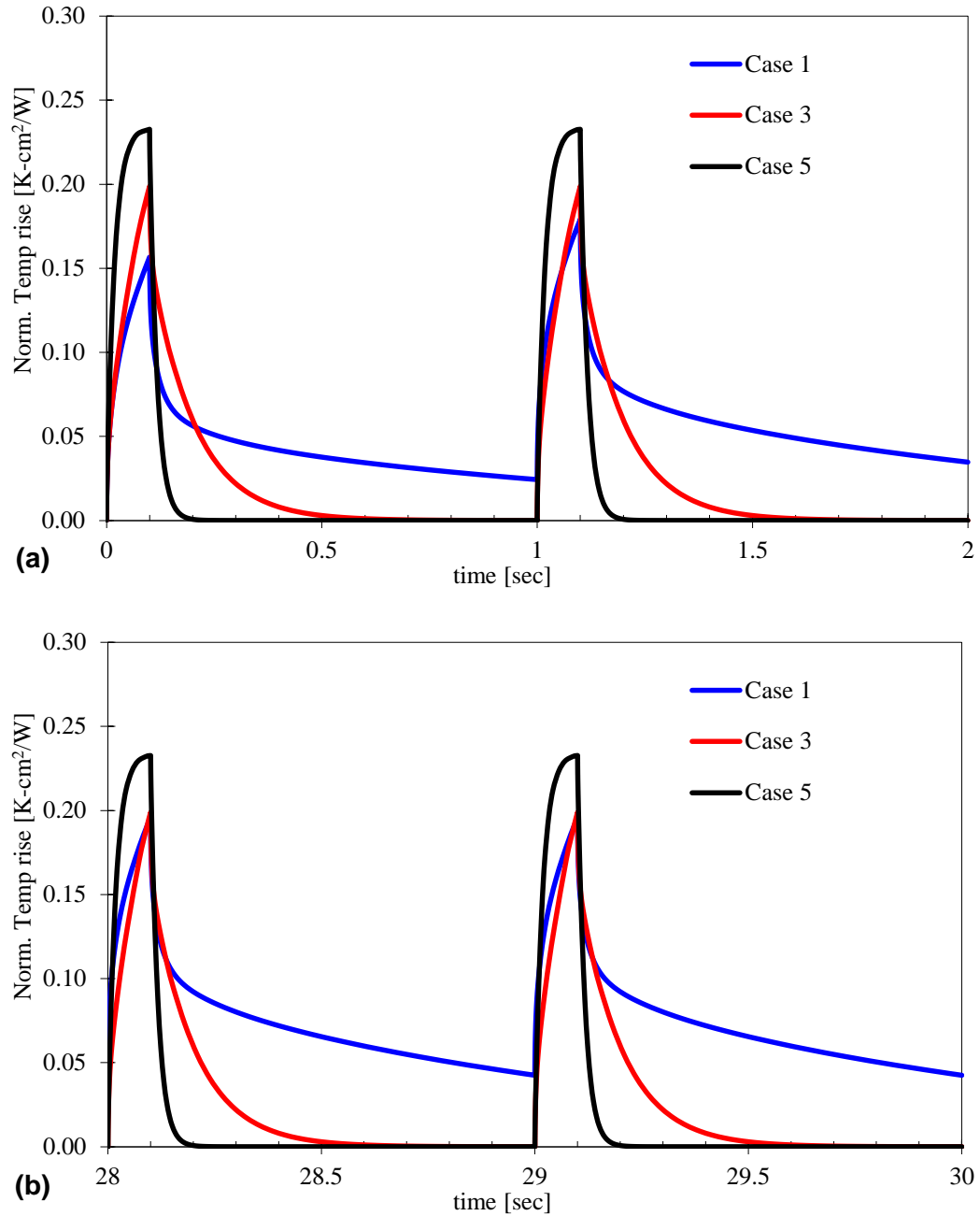


Figure 5.28 – Time domain pulsed temperature profiles for Cases 1, 3, and 5 with $h_{eff} = 50 \text{ kW/m}^2\text{K}$ subjected to a unit heat pulse train of 100 ms pulse-width and 1 second period. (a) shows the initial pulses where Case 1 and Case 3 are both warming slightly. (b) shows the temperatures for pulses after the warmup has saturated (30 sec)

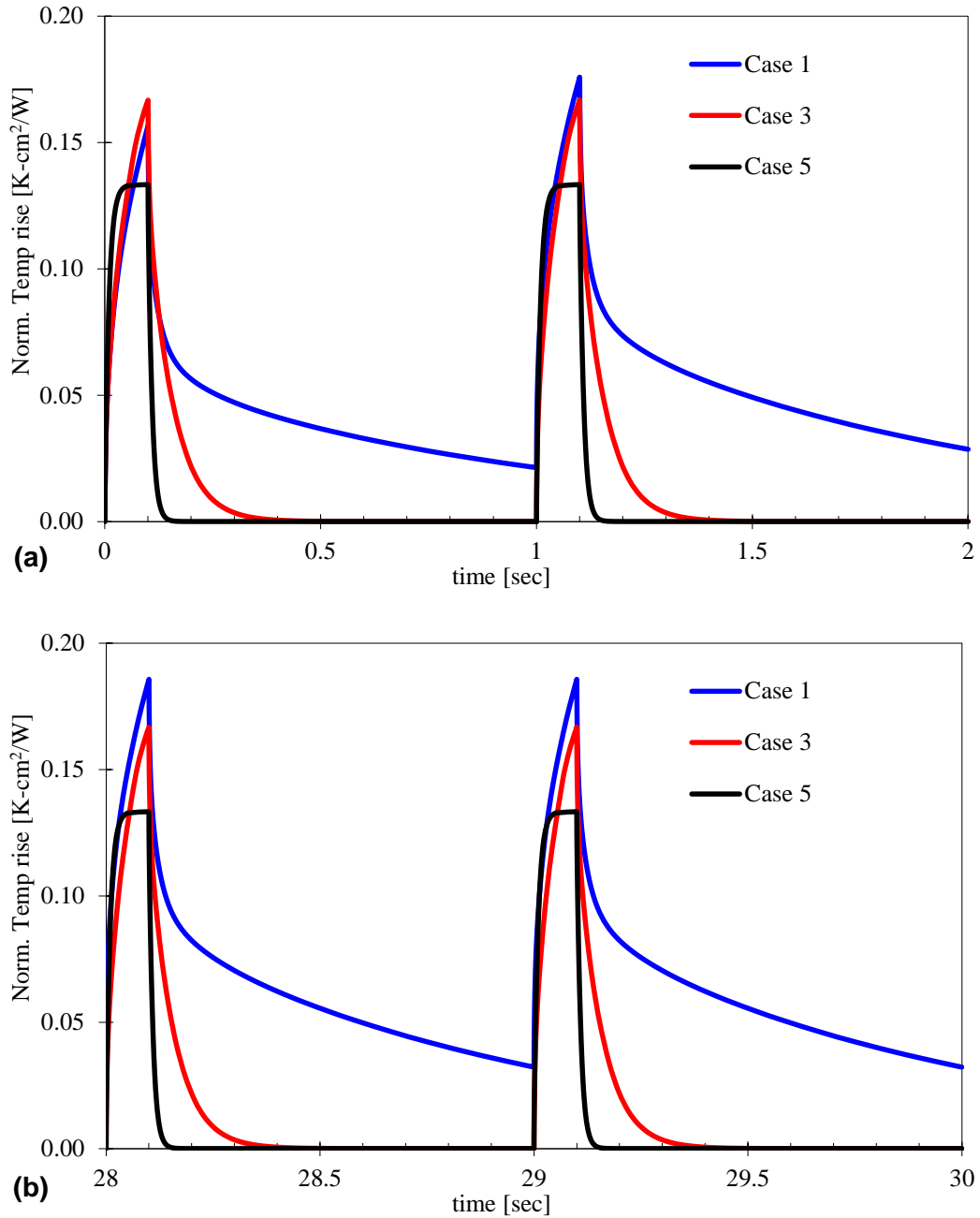


Figure 5.29 – Time domain pulsed temperature profiles for Cases 1, 3, and 5 with $h_{eff} = 100 \text{ kW/m}^2\text{K}$ subjected to a unit heat pulse train of 100 ms pulse-width and 1 second period. (a) shows the initial pulses where Case 1 and Case 3 are both warming slightly. (b) shows the temperatures for pulses after the warmup has saturated (30 sec)

The three figures above demonstrate the transient package thermal responses under varying loading conditions, as well as divergence from expected steady-state response. The lowest value of h_{eff} (10 kW/m²) highlights the inverted thermal performance due to thermal inertia quite clearly. The larger time constants in Cases 1 and 3 cause them to heat up more slowly than Case 5, which responds very quickly to the heat load. None of the packages reach steady-state temperature (T_{ss}) within the 100 ms pulse duration, but Case 5 reaches about 70% of T_{ss} due to its fast response, while Case 1 only reaches 10% of its much higher T_{ss} (see Figure 5.20). Note that Case 5 also cools off much faster, whereas the others do not return to the initial state between the early pulses. Thus, in addition to higher peak temperatures, Case 5 has a much larger temperature swing as well. This discrepancy decreases but still persists after warmup, as shown in Figure 5.27(b) where the Case 1 has warmed up to about the same level as Case 3, but both remain far below the Case 5 peak. As temperature cycling is responsible for a large number of thermal failure modes [244], this could introduce significant package reliability concerns even if the maximum temperature is within component survival limits.

Tables 5.7-5.9 list the absolute and relative peak temperature responses for the initial and warmed-up pulses for all five packages and three tested values of h_{eff} . The data shown quantifies the convection-dependent thermal performance inversion between packages. For $h_{eff} = 10\text{kW/m}^2\text{K}$, Case 5 heating up 4.6x more than Case 1 in the initial pulse. Even after allowing for pulse train warm-up, Case 5 still sees a 2.6x higher T_{max} and a 4.75x wider ΔT than Case 1. As h_{eff} is increased, this effect diminishes and eventually reverses. For $h_{eff} = 50\text{kW/m}^2\text{K}$ the Case 5 peak is only 20-50% above Case 1, and then at 100 kW/m²K it reverses to where Case 5 is 15% less than Case 1. Cases 2-4 generally

bridge the Case 1 to Case 5 span until the higher- h_{eff} condition pushes the worst performance up to higher thermal inertia packages (Case 3 having the largest response).

Table 5.7 – Normalized temperature rise from unit pulse train at $h_{eff} = 10 \text{ kW/m}^2\text{K}$

Case #	Steady-state	Pulse 1			Pulse 30 (steady-state)				
	T_{SS} [°C]	$T_{MAX} = \Delta T$ [°C]	$\frac{T_{MAX}}{T_{SS}}$	$\frac{T_{MAX}}{T_{MAX,C1}}$	T_{MAX} [°C]	ΔT [°C]	$\frac{T_{MAX}}{T_{SS}}$	$\frac{T_{MAX}}{T_{MAX,C1}}$	$\frac{\Delta T}{\Delta T_{C1}}$
1	1.563	0.157	0.10	1	0.276	0.153	0.18	1	1
2	1.188	0.158	0.13	1.01	0.233	0.153	0.20	0.85	1.00
3	1.096	0.245	0.22	1.57	0.272	0.239	0.25	0.99	1.56
4	1.070	0.344	0.32	2.20	0.353	0.341	0.33	1.28	2.23
5	1.037	0.727	0.70	4.64	0.727	0.727	0.70	2.64	4.75

Table 5.8 – Normalized temperature rise from unit pulse train at $h_{eff} = 50 \text{ kW/m}^2\text{K}$

Case #	Steady-state	Pulse 1			Pulse 30 (steady-state)				
	T_{SS} [°C]	$T_{MAX} = \Delta T$ [°C]	$\frac{T_{MAX}}{T_{SS}}$	$\frac{T_{MAX}}{T_{MAX,C1}}$	T_{MAX} [°C]	ΔT [°C]	$\frac{T_{MAX}}{T_{SS}}$	$\frac{T_{MAX}}{T_{MAX,C1}}$	$\frac{\Delta T}{\Delta T_{C1}}$
1	0.763	0.157	0.21	1	0.196	0.153	0.26	1	1
2	0.388	0.157	0.40	1.00	0.162	0.155	0.42	0.83	1.01
3	0.296	0.199	0.67	1.27	0.199	0.199	0.67	1.02	1.30
4	0.270	0.223	0.83	1.42	0.223	0.223	0.83	1.14	1.46
5	0.237	0.233	0.98	1.49	0.233	0.233	0.98	1.19	1.52

Table 5.9 – Normalized temperature rise from unit pulse train at $h_{eff} = 100 \text{ kW/m}^2\text{K}$

Case #	Steady-state	Pulse 1			Pulse 30 (steady-state)				
	T_{SS} [°C]	$T_{MAX} = \Delta T$ [°C]	$\frac{T_{MAX}}{T_{SS}}$	$\frac{T_{MAX}}{T_{MAX,C1}}$	T_{MAX} [°C]	ΔT [°C]	$\frac{T_{MAX}}{T_{SS}}$	$\frac{T_{MAX}}{T_{MAX,C1}}$	$\frac{\Delta T}{\Delta T_{C1}}$
1	0.663	0.157	0.24	1	0.186	0.153	0.28	1	1
2	0.288	0.156	0.54	1.00	0.157	0.156	0.54	0.84	1.01
3	0.196	0.167	0.85	1.06	0.167	0.167	0.85	0.90	1.09
4	0.170	0.160	0.94	1.02	0.160	0.160	0.94	0.86	1.05
5	0.137	0.133	0.97	0.85	0.133	0.133	0.97	0.72	0.87

It is obvious that these examples were selected to emphasize the primary point: both the frequency domain and time domain analyses suggest that these thermal conditions (both pulse rate and convection) would produce a response corresponding to the inverted thermal response regions in Figure 5.25(e-g). That varies significantly with both convection and pulse width/rate. To emphasize this, for the same packages and external conditions Figure 5.30 shows the response to a 1 ms pulse where the response shifts out to the far right of the

frequency response curves. There the peak responses look identical both with each other and with changing convection rate, which recalls the earlier convective insensitivity discussion.

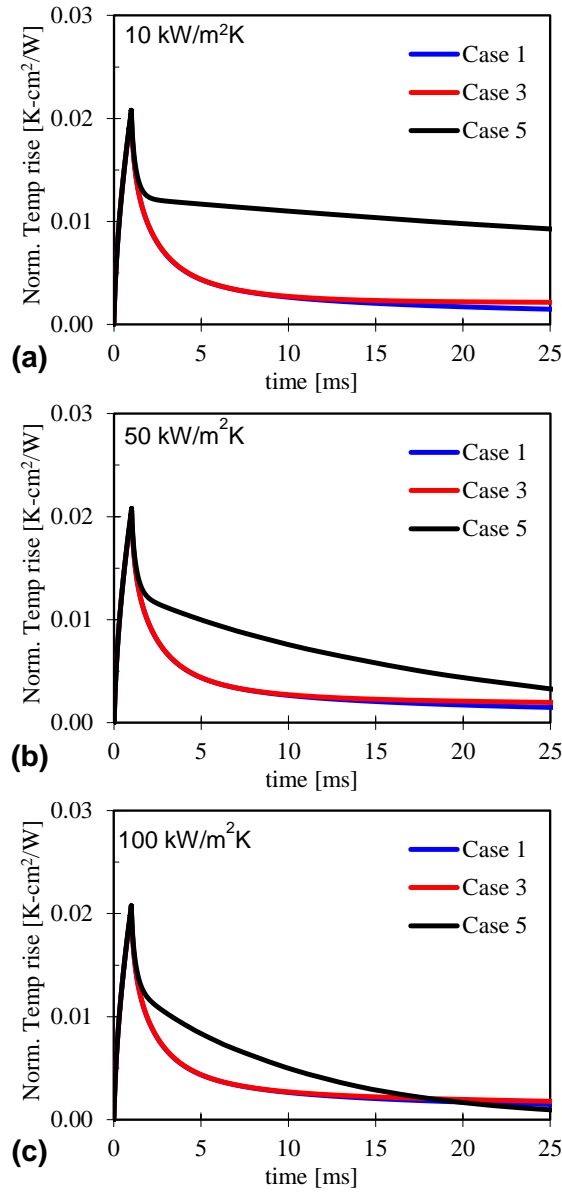


Figure 5.30 – Time domain 1 ms pulsed temperature profiles for Cases 1, 3, and 5 at multiple convection rates, showing identical fast pulse package peak response and convective insensitivity.

5.3.3. Transient model conclusions

When first asked whether the thermal improvements made for steady or slow-changing thermal systems could also benefit transient electronic systems, the answer was simply that we did not know. Anecdotally, discussion that pulsed-power engineers were still seeing device thermal failure after buying better packages, heat sinks, and cooling systems inspired the hypothesis that transient heat propagation must be sufficiently different to negate the expected performance improvement.

The overall takeaway from this transient thermal circuit modeling effort of power electronics packaging is the following:

- (1) There are transient pulse conditions that will show little to no improvement from better convection. A fast enough pulse, relative to the time it takes heat to move through the package, will be completely insensitive to any amount of improved cooling. A lower thermal inertia package will increase this upper limit on pulse speed, but enough energy in the high frequency components of the pulse could still be insensitive to cooling.
- (2) For any pulsed system, simply buying a lower thermal resistance package may not provide measurable thermal improvement. In fact, it is entirely possible that the thermal performance will worsen due to the corresponding decrease in thermal inertia.
- (3) For very low duty cycle pulsing where the package always appears to be in the ‘initial warm-up’ stage, under low convection rates it might never be thermally beneficial to choose a highly integrated package. Thermal capacity will far dominate the thermal resistance impact on thermal performance.

What these three points indicate is that exact transient thermal conditions must be known in order to design a successful transient thermal solution. As mentioned before regarding understanding how to successfully apply phase change materials to vehicle components, designing a steady-state thermal solution for a transient system will, in the best case, lead to a thermally overdesigned solution with corresponding size, weight and power (SWaP) penalty. At the worst case, however, it may not be a solution at all, resulting in a system reaching higher temperatures and seeing larger temperature swings. In addition to understanding this need, the finite element based thermal circuit models applied here-in, the transient modeling approach, and the package delay estimates all produced using standard electrical circuit modeling tools demonstrate that the capability exists for electrical circuit and package designers to incorporate transient thermal behavior into their designs.

Despite all of these transient design concerns, a low thermal resistance is still necessary in many cases, especially for systems that are not designed with clearly known transients, or for systems that are used in generally steady-conditions but requires surge or pulse survivability. Since this transient analysis has shown that the lack of thermal inertia near the junction of the device appears to be the primary problem affecting thermal response, the new question is how to increase package thermal capacity without excessive thermal resistance penalty. For this, in the next chapter we examine one potential solution that involves integrating phase change materials into the electronics package, thereby adding in an engineered nonlinear thermal capacity that can try to satisfy both demands.

Chapter 6 – Electronics integrated phase change materials

Previous chapters have addressed traditional approaches to electronics package improvement, the effect that transient thermal loading can have on those improved packages, and the availability of phase change materials for reducing transient excursions through nonlinear thermal absorption. This chapter focuses on the challenges of integrating PCMs with high performance electronics packaging to regain thermal capacity while maintaining low thermal resistance, and in particular design compatible modeling techniques for accomplishing this integration.

When describing approaches for vehicle power electronics thermal protection in Section 3.1.2.2, it was recognized that there have been a number of attempts to incorporate PCMs into electronics packages in order to engineer additional thermal capacity back into the low thermal resistance structure. Heat spreading structures of some sort are generally required to overcome the high thermal charging resistance of most low thermal conductivity PCMs. These have typically involved either partially or fully filling a heat sink or similar structure with PCM and then connecting the structure to the electronics package in a standard fashion. Some of these methods have included encapsulation of PCM in a honeycomb cell [245], loading a finned heat sink [246], or filling the interior volume of a foam [247]. Finally, it is worth noting that despite these studies focusing on smaller electronic systems, they mainly dealt with relatively slow transients and long time constants (minutes to hours) for the thermal cycle. There have been a few cases with the PCM placed close to the semiconductor junction has been shown to be able to reduce peak temperature at short time scales, in particular modeling efforts by Garrum and Evans [150,248], and more recently experimental efforts by Green, et al. on silicon CPU test

chips [249], and very recently other experimental work at ARL evaluating the use of metallic phase change materials as electronics encapsulation material [250,251].

As in the previous chapter, we recognize that successfully incorporating PCMs into electronics, and specifically close enough to the electronics to provide fast transient suppression, will require addressing the multi-domain design challenge. Thus this chapter focuses on extending the transient modeling to include a latent heat effect. The complexity of phase change requires some simplifying approaches in order to enable a general modeling capability to be incorporated into multi-domain electrothermal modeling. We begin with a description of the phase change modeling challenge and analytical and numerical approaches to modeling melting and solidification. We then propose and evaluate a particular form of phase change smoothing model to facilitate incorporation into finite element and coupled domain solvers. Finally, we examine a few case studies using this model by showing the potential impact of phase change thermal buffering within the electronics package. (Much of the smoothing model and finite element substrate simulation work was first presented in [151,252]).

6.1. Heat transfer - solid-liquid phase change models

While numerical solution of the transient heat diffusion equation is relatively straight forward, the introduction of phase change makes the problem inherently non-linear due to the latent absorption and release of energy at the typically non-stationary phase front. Additionally, while thermal modeling involves a generally uncomplicated single degree of freedom modeling domain, phase change introduces the need to track the material's state or state fraction. This extra degree of freedom can make it difficult to apply concepts similar to the previously described thermal circuit analogues, and detailed phase change

models can quickly render design problems intractable. In a one-dimensional system with only two phases, and a single interface between phases, this mathematical model is called the *Classical Stefan Problem*. It is one of the simpler models in the class of “moving boundary problems” of partial differential equations, in that there are analytically tractable solutions for simple cases [253].

6.1.1. The classical Stefan problem

The Classical Stefan Problem (summarized for one dimension below in Figure 6.1) consists of the heat diffusion equation applied separately to the solid and liquid phase regions of a single material of length l with a special interface condition, known as the *Stefan Condition*, imposing an energy balance at the solid-liquid interface. That interface is assumed to be isothermal at the material’s melting temperature and has zero width. A fixed temperature (Dirichlet type) boundary condition is imposed on one side of the domain ($x = 0$), and an insulated boundary condition (Neumann type, natural) is imposed on the other side ($x = l$). Initially the material is all a single phase either at (for a single-phase Stefan problem) or below (for a two-phase Stefan problem) the melting temperature. This figure shows an example of melting where the phase front position, $X(t)$, changes with time as the liquid region grows in thickness from the heated side. Note that $\alpha_{s,l}$ are the thermal diffusivities of the medium in the solid and liquid regions, and H_f is the latent heat of fusion of the material.

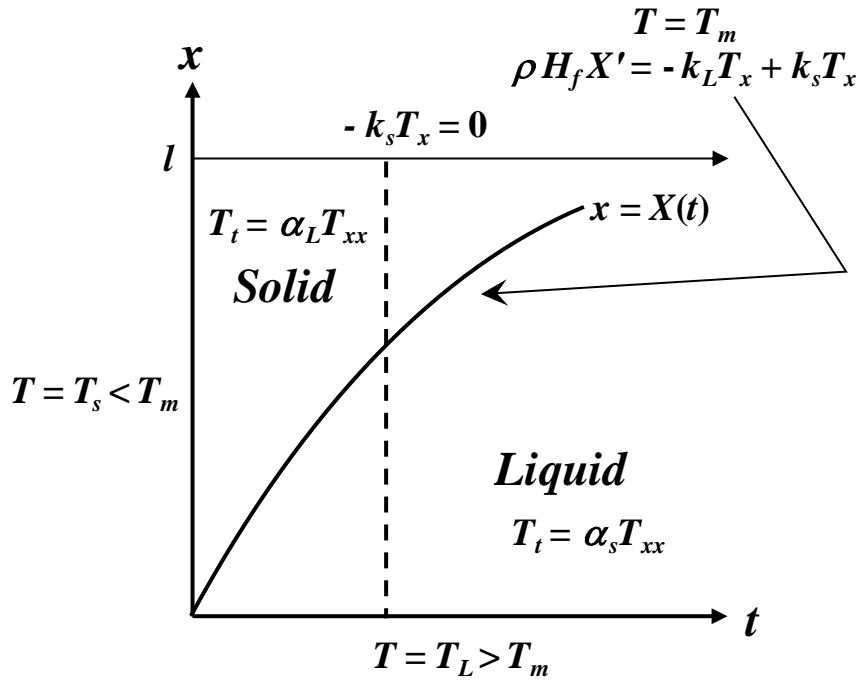


Figure 6.1 – Schematic illustration of the one-dimensional Stefan problem, where $X(t)$ represents the position of the phase interface with time. Adapted from [253].

While the actual transient phase change behavior will be heavily dependent on initial conditions and material parameters, the trend shown in the figure above is typical for a single phase front system. Similar analyses can be performed for other boundary conditions, such as periodic heating and cooling, but analytical complexity quickly increases. As an example, Figure 6.2 shows the multiple phase fronts that could develop from such a periodic heating condition. Each phase front requires the creation and imposition of a separate energy balance condition and solution function. Trying to accommodate any other physical realities, including material thermal property change, density change, finite width interfaces, supercooling, multiple dimensions, etc., quickly becomes analytically intractable, requiring the use of approximation and numerical solution techniques for useful solutions.

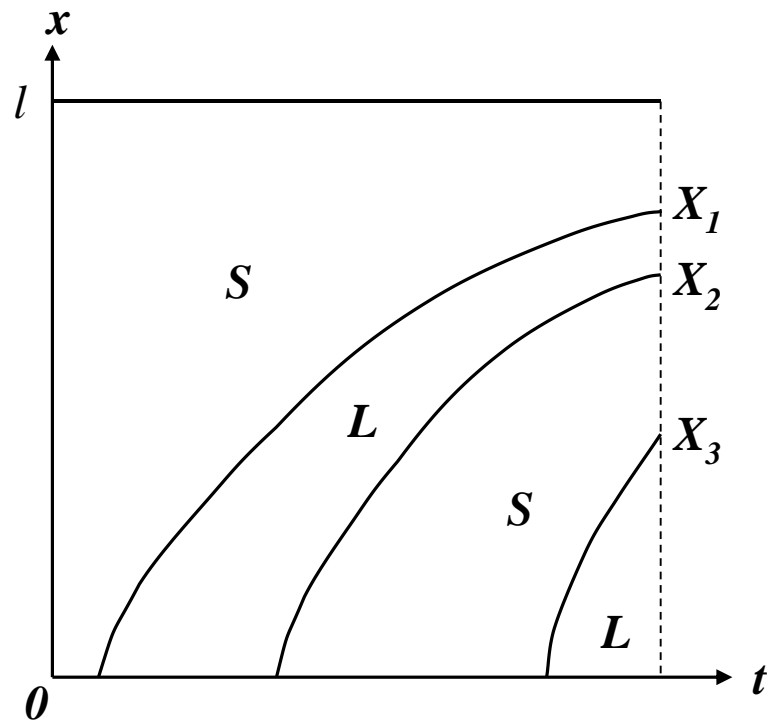


Figure 6.2 – Multiple phase front propagation in a one dimensional medium undergoing periodic heating and cooling cycles. Adapted from [253].

6.1.2. Numerical phase change modeling

There has been much work over the past several decades developing analytical approximations and numerical techniques for the accurate prediction of thermal behavior and phase change in arbitrary domains, covered in a comprehensive review by Hu and Argyropoulos [254]. As always with numerical solutions, however, there exists a trade-off between solution accuracy and complexity of approach.

Being a spatially defined problem requiring discretization for numerical solution, numerical phase change models can be categorized based on how the discretization handles the moving boundary condition. *Moving grid* or *adaptive grid* methods attempt to maintain a set of grid points along the phase change boundary. As the boundary progresses through

the medium the grid is adjusted to keep a node on the phase front. Usually thermal diffusion within the separate domains is solved independently and a Stefan or similar condition is applied to the boundary to both maintain energy balance and determine a local boundary velocity. Whether using a finite difference, finite element, or other solution scheme, sufficient grid movement might require creation or destruction of nodes or periodic remeshing of the entire domain at each time step. In addition, the explicit tracking of the boundary (similar to the tracking used in the analytical techniques) means that only simple phase front situations are practical. Initial conditions for the front may need to be arbitrarily set and tracking multiple fronts, having fronts merge or disappear, or creating new fronts all become extremely cumbersome tasks [255]. Also, multidimensional grid manipulations can be non-trivial and may require a priori knowledge of front behavior. A benefit of these methods is their ability to very precisely track the propagation and shape of a phase front, and they are often used to model dendrite and other microstructure evolution in solidification [256].

Alternatively, the fixed grid phase change modeling methods make no attempt to directly track the location of the moving phase boundary within the nodal solution set. Instead, the entire phase change domain is solved using a single form of the heat diffusion equation. Depending on the particular fixed grid method chosen, the phase change is either incorporated as a temperature dependent heat capacity or as a moving heat source (or sink) within the model. The actual location of the phase front is usually inferred from the temperature solution, which limits location precision to an interpolation over the chosen grid spacing. Sometimes additional phase tracking methods are used to determine a refined phase front position, and this knowledge may or may not be used to adjust the temperature

solution between iterations. A distinct advantage of these methods is that, because the front-tracking is not handled explicitly, difficulties with multiple dimensions and phase fronts are significantly reduced [257-259].

The most prevalent of the fixed grid methods capture the material's latent heat effect as a nonlinear temperature-dependent enthalpy jump equal to the latent heat of fusion, H_f , at the melting temperature. By defining this explicit and invertible enthalpy-temperature relationship, one of two approaches can be taken to solving the system as a single domain.

First, the *enthalpy method* solution approach directly uses this material enthalpy jump and recasts the heat diffusion equation with enthalpy as the primary variable. Alternatively, the *apparent heat capacity (AHC) method* solves the standard thermal problem by differentiating the material enthalpy model with respect to temperature and producing what appears as a temperature dependent heat capacity. Numerical solution with non-constant material properties is a well-defined process, making this method more compatible with standard heat diffusion equation solvers and easier to implement in many existing solver codes. Solutions using this method were first reported in reports by Hashemi and Sliepcevich [260] and Bonacina, et al. [261] for fixed grid finite difference and finite element methods, and a detailed review of the various fixed grid methods can be found in [262]. Figure 6.3 shows representative material enthalpy and apparent heat capacity profiles for a phase change material with an abrupt phase transition.

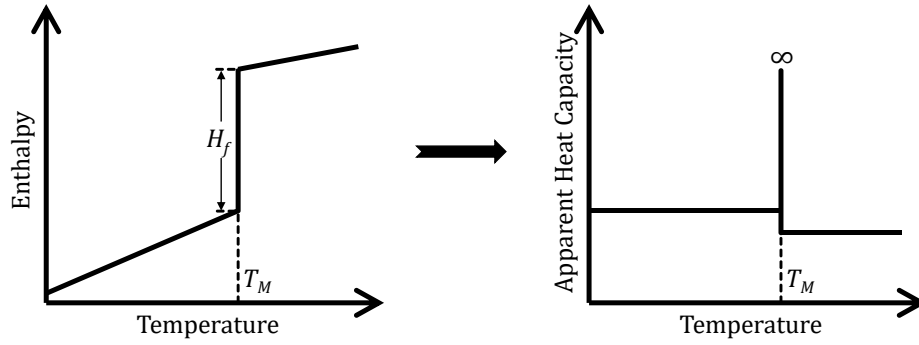


Figure 6.3 – Enthalpy and apparent heat capacity profiles for an abrupt phase transition.

As shown in the figure, the enthalpy method approximation for the material's latent heat is incorporated as a step discontinuity in the enthalpy profile at the melt temperature. The apparent heat capacity is the slope of the enthalpy curve, and the isothermal phase change temperature makes this a delta function having zero width and infinite height. This is a numerically incompatible singularity at the phase transition given by:

$$C_{app}(T) = \begin{cases} \rho_s c_s = C_s, & \text{for } T < T_M \\ C_f(T) \approx H_f \delta(T - T_f), & \text{for } T = T_M \\ \rho_l c_l = C_l, & \text{for } T > T_M \end{cases} \quad (95)$$

To correct for this singularity, the ACM approximates the jump by spreading the transition over a small *mushy zone*. Various profiles can be chosen for this transition, including a linear enthalpy resulting in the stepped, or *top-hat*, profile shown in Figure 6.4.

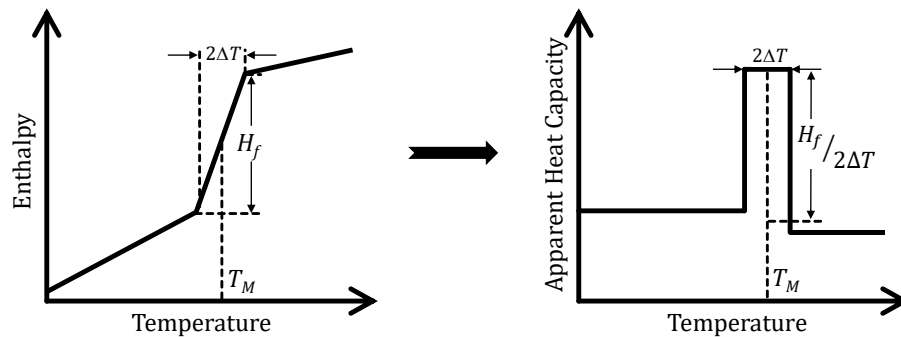


Figure 6.4 – Enthalpy and apparent heat capacity profiles for a top-hat phase change approximation.

This heat capacity profile can be implemented algebraically even though there are discontinuities around the mushy zone:

$$C_{app}(T) = \begin{cases} C_s, & \text{for } T < T_M \\ C_{MZ}(T) \approx \frac{C_s + C_l}{2} + \frac{H_f}{2\Delta T}, & \text{for } T_M - \Delta T < T < T_M + \Delta T \\ C_l, & \text{for } T > T_M \end{cases} \quad (96)$$

This linear enthalpy approximation removes the singularity but the discontinuities in the stepped heat capacity can still result in convergence difficulties. Alternative approximations have been developed that provide a smoother transition, and Civan and Sliepcevich showed that using some form of smoothing function can reduce the error in AHC compared to the linear function [263].

While this approximation does reduce the numerical instability and ease implementation, the AHC method itself does introduce certain other errors. The most egregious of these errors is the obvious spreading of the phase change over the mushy zone. While some metals and other multi-constituent materials do exhibit a sizable phase change temperature range, most other materials have an actual isothermal melting temperature, and implementation of an arbitrary width mushy zone is a physical discrepancy. Also, the apparent capacity method is generally considered less robust than the enthalpy method despite being easier to implement in existing codes. In models with large temperature gradients around the phase front, too narrow of a “phase change width” or too large of a time step can allow the local nodal temperature to jump over the arbitrarily defined phase change region. This would allow the model to essentially ‘skip’ phase change at that location. Finally, more complex but smooth forms of the heat capacity curve avoid sharp or step discontinuities, but they may introduce other non-physical artifacts to the heating profile, some of which are discussed below.

6.1.3. Mushy zone smoothing functions

Mentioned in the previous section, numerical implementation of both the AHC and enthalpy methods benefit from some sort of smoothing approximation applied to the sharp, or stepped, phase change profiles. The linear profile described by (96) improves the enthalpy method, but leaves step discontinuities in the AHC method. Other smoothing functions for $C_{MZ}(T)$ have been attempted that remove these discontinuities, with mixed success. Figure 6.5 shows examples of two forms of smoothing functions that have been used, including normal and homographic functions, each of which will be discussed in detail below.

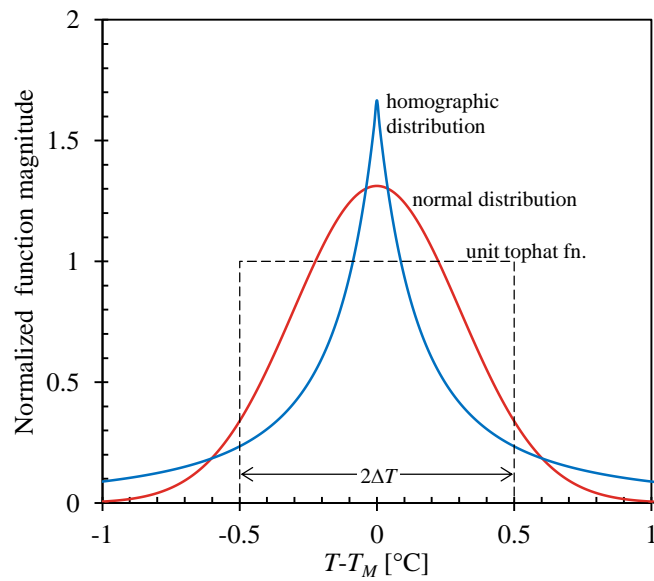


Figure 6.5 – Comparisons of smoothing functions applied to the phase change mushy zone approximation, including the unit normal distribution and the homographic distribution.

The smoothing function used by Civan and separately by Muhieddine, et al. [264] was a unit normal distribution of the form:

$$f(T) = (\epsilon/\sqrt{\pi})e^{-\epsilon^2(T-T_M)^2} \quad (97)$$

where ϵ is an arbitrary tuning parameter prescribing the normal distribution width according to:

$$\epsilon = 1/\sqrt{2}\sigma \quad (98)$$

where σ is the standard deviation of the normal distribution. Thus, setting a value for ϵ affects both the sharpness and spread of the smoothing function. One problem with using a normal distribution is that this function only reaches zero value at positive and negative infinity, meaning that any finite integration or temperature step will lose some fraction of the latent heat. Implementation must involve either distributing some of this phase change energy outside of the mushy zone, or truncating it. This can result in ‘energy leakage’ in the model, leading to either simulation non-convergence or non-physical results.

Civan proposed using a secondary equation to make an alternate tuning parameter directly tied to this non-ideal effect:

$$\text{erf}(\epsilon\Delta T) = 1 - \lambda \quad (99)$$

Because the error function, $\text{erf}(x)$, is the area under the normal distribution in the interval $[-x,x]$, λ becomes an alternative tuning parameter equal to the relative enthalpy error (i.e., the fraction of latent energy outside the mushy zone boundary). Minimizing λ to reduce error still has the side-effect of increasing the height and ‘sharpness’ of the profile thereby working against the original intent of using a smoothing function, and it also compresses the distribution function to a range narrower than the prescribed *mushy zone width* (MZW) of $2\Delta T$.

A common measure of function width for normal distributions is the Full Width at Half Maximum (FWHM) which gives a measure of the sharpness of the distribution, directly proportional to the distribution’s standard deviation:

$$\text{FWHM} = 2\sqrt{2\ln(2)} \cdot \sigma = 2\sqrt{\ln(2)}/\epsilon \quad (100)$$

Or, in terms of the tuning parameter, λ ,

$$\text{FWHM} = \sqrt{\ln 2} \cdot 2\Delta T / \text{erf}^{-1}(1 - \lambda) = \sqrt{\ln 2} \cdot 2\Delta T / \text{erfc}^{-1}(\lambda) \quad (101)$$

Thus we can see that using Civan's tuning parameter definition the smoothing function's FWHM will be directly proportional to the MZW, and inversely related to the desired relative enthalpy error. Muhieddine chose a similar approach but decided to fix ϵ to a value of $1/(\sqrt{2}\Delta T)$, which is equivalent to setting $\lambda = 1 - \text{erf}(1/\sqrt{2}) = \text{erfc}(1/\sqrt{2})$, or approximately 0.317, independent of MZW, and fixes the FWHM to $2\Delta T\sqrt{\ln 2}$, or about 0.832. Thus, between the large value for λ and the large FWHM, much of the latent energy that should be captured by the smoothing function is lost by the Muhieddine's model. Finally, while Civan limited his analysis to equal solid-liquid properties, Muhieddine superimposed this smoothing function on a linear approximation to the sensible heating producing the following mushy zone capacity function:

$$C_{MZ}(T) = \frac{C_s + C_l}{2} + \frac{C_l - C_s}{2\Delta T}(T - T_M) + (H_f/2\Delta T\sqrt{\pi})e^{-(T-T_M)^2/4\Delta T^2} \quad (102)$$

Figure 6.6(a) shows the normal distribution approximation for several values of λ , including the 0.317 value used by Muhieddine, compared to the standard unit top-hat profile. The function's compression with decreasing λ is readily apparent in the figure, as is the overly broad profile used by Muhieddine, where the amount of latent energy distributed within the mushy zone is only $\text{erf}(1/\sqrt{2})$, or 68.3% of the total. This energy error is quantified in Figure 6.6(b), which shows the percentage of latent energy that actually stays within the prescribed mushy zone for different choices in MZW, along with the corresponding increase in function compression as measured by the Full Width at Half

Max (FWHM) value for the distribution. Because these factors are inherently coupled, choosing a normal distribution smoothing function must necessarily either increase the degree of nonlinearity (function compression) or model energy error.

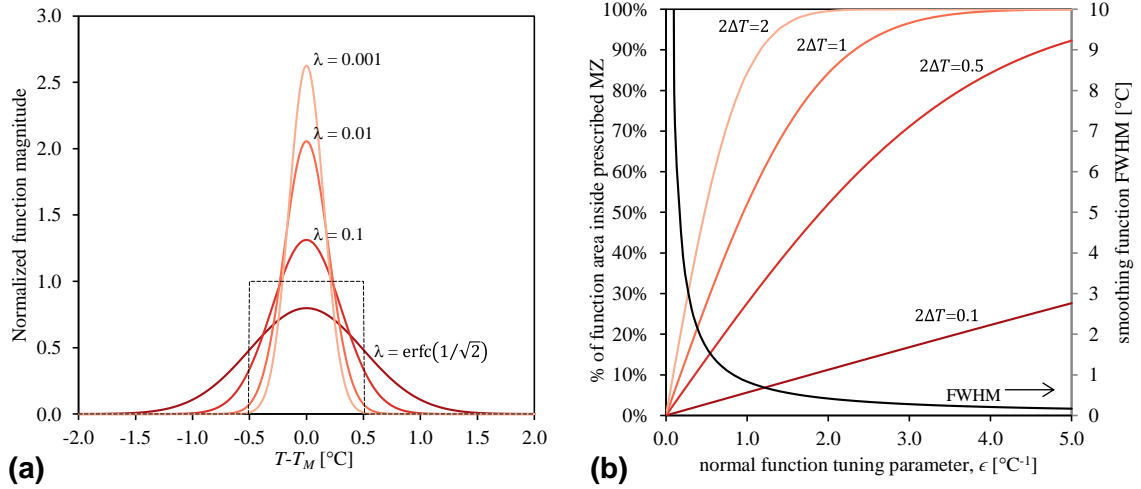


Figure 6.6 – Normalized smoothing functions based on a normal distribution as used in [263] and [264]. (a) demonstrates the amount of error permitted at the mushy zone boundary as dependent on λ , shown for a mushy zone width of 1°C, and (b) quantifies the amount of the function inside the prescribed mushy zone, showing the inverse relationship between the included fraction and the sharpness of the distribution as represented by its FWHM.

An alternative smoothing formulation was proposed by Yao and Chait [265], who represented the entire apparent capacity function with a homographic function:

$$C_{app}(T) = C_{S=l} + \frac{H_f}{2\eta} \frac{1}{(1+|T-T_M|/\eta)^2}, \text{ for } -\infty < T < \infty \quad (103)$$

In assuming constant density and specific heat for solid and liquid phases, the homographic form provides a continuous single heat capacity function for all temperatures. It avoids using an explicitly defined MZW, instead using the unitless tuning parameter η to control the function shape. As with the normal distribution, this function spreads the latent heat over an infinite width and η must also be tuned to control function compression.

Additionally, applying this function to a model with unequal solid-liquid properties may involve defining a step or mushy zone, in which case as with the normal distribution some of the energy would fall outside the desired zone and create errors in total model energy. As before, this function is shown in Figure 6.7(a) for various values of η and is compared with unit top-hat profile. The sharpness of this profile is evident in the figure, and increases quickly with decreasing η , where the peak value is equal to $1/2\eta$, and $FWHM = 2\eta(\sqrt{2} - 1)$, as shown in Figure 6.7(b).

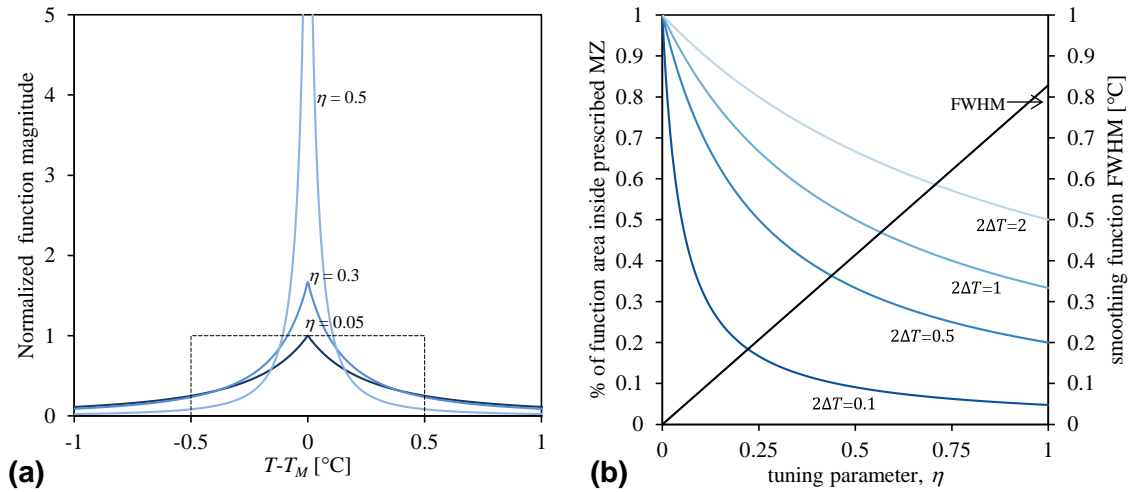


Figure 6.7 – Homographic smoothing functions used by Yao and Chait, compared to the unit step profile.

6.2. Proposed polynomial smoothing functions

The previously discussed smoothing functions require arbitrary tuning parameters to approximately match the MZ boundary conditions and avoid accumulated model energy errors, and the resulting profiles show increased constriction and decoupling from the desired smoothing width. Here we propose a polynomial smoothing function that will exactly match the desired mushy zone boundary conditions without any additional tuning

parameters. In addition, the fully defined polynomial function will have a clearly prescribed relationship between the desired mushy zone width, the peak magnitude, effective width of the apparent capacity profile, and physical/material properties.

We define $f(\theta)$ to be the polynomial representation of the enthalpy jump spread over the mushy zone using the local temperature coordinate, $\theta = T - T_M$. Thus $C_{MZ}(\theta) = f'(\theta)$ represents the apparent capacity function in the mushy zone. Table 6.1 lists the desired boundary conditions for $f(\theta)$ at the limits of the mushy zone. Both f and f' are specified such that the value and slope of the enthalpy curve at the solid and liquid state boundaries match the appropriate non-phase change values. In addition, $f''(\theta)$, the slope of the apparent capacity function, is specified to match any change with temperature at the solid and liquid zones boundaries. For constant solid and liquid state properties (as are used in this study), $f''(\pm\Delta T)$ is set to zero as shown in Table 6.1.

Table 6.1 – $f(\theta)$ boundary conditions, constant single phase properties

T	$T_M - \Delta T$	$T_M + \Delta T$
θ	$-\Delta T$	$+\Delta T$
$f(\theta)$	$C_s(T_M - \Delta T)$	$H_f + C_s T_M + C_l \Delta T$
$f'(\theta)$	C_s	C_l
$f''(\theta)$	$dC_s/dT (= 0)$	$dC_l/dT (= 0)$

A polynomial of order $P(i)$ will accommodate $i+1$ boundary conditions. As such, 1st, 3rd and 5th polynomial order enthalpy models will be examined to identify the impact of maintaining continuity and differentiability in the enthalpy and apparent capacity profiles. The P(1) model will only use of the first pair of boundary conditions and produce a continuous enthalpy profile but a discontinuous top-hat style heat capacity profile. The P(3) model will incorporate the slope boundary condition, making the enthalpy profile smoothly differentiable and the heat capacity profile continuous at $\pm\Delta T$. Finally, the P(5) model will satisfy all conditions specified in Table 6.1 and produces an apparent capacity

curve that is both continuous and smoothly differentiable at the mushy zone transition. Solving for the coefficients of 1st, 3rd, and 5th order mushy zone polynomials, defined as:

$$f(\theta) = \sum_{i=0}^n p_{ni} \theta^i, \text{ where } \theta = T - T_M \quad (104)$$

The resulting enthalpy function coefficients are shown in Table 6.2:

	1 st order	3 rd order	5 th order
p_{n0}	$\frac{H_f}{2} + \frac{C_l - C_s}{2} \Delta T + C_s T_M$	$\frac{H_f}{2} + \frac{C_l - C_s}{4} \Delta T + C_s T_m$	$\frac{H_f}{2} + \frac{3}{16} (C_l - C_s) \Delta T + C_s T_m$
p_{n1}	$\frac{H_f}{2 \Delta T} + \frac{C_s + C_l}{2}$	$\frac{3 H_f}{4 \Delta T} + \frac{C_s + C_l}{2}$	$\frac{15 H_f}{16 \Delta T} + \frac{C_s + C_l}{2}$
p_{n2}	--	$\frac{C_l - C_s}{4 \Delta T}$	$\frac{3 (C_l - C_s)}{8 \Delta T}$
p_{n3}	--	$-\frac{H_f}{4 \Delta T^3}$	$-\frac{5 H_f}{8 \Delta T^3}$
p_{n4}	--	--	$\frac{C_s - C_l}{16 \Delta T^3}$
p_{n5}	--	--	$\frac{3 H_f}{16 \Delta T^5}$

For completeness, the polynomial coefficients of an equivalent apparent heat capacity smoothing function are listed in Table 6.3, given by:

$$a_{ni} = (i + 1) p_{n(i+1)} \quad (105)$$

Table 6.3 – Apparent capacity function polynomial coefficient solution

	1 st order	3 rd order	5 th order
a_{n0}	$\frac{H_f}{2\Delta T} + \frac{C_s + C_l}{2}$	$\frac{3H_f}{4\Delta T} + \frac{C_s + C_l}{2}$	$\frac{15H_f}{16\Delta T} + \frac{C_s + C_l}{2}$
a_{n1}	--	$\frac{C_l - C_s}{2\Delta T}$	$\frac{3(C_l - C_s)}{4\Delta T}$
a_{n2}	--	$-\frac{3H_f}{4\Delta T^3}$	$-\frac{15H_f}{8\Delta T^3}$
a_{n3}	--	--	$\frac{C_s - C_l}{4\Delta T^3}$
a_{n4}	--	--	$\frac{15H_f}{16\Delta T^5}$

6.2.1. Comments on polynomial model profiles

Profiles of the polynomial smoothing functions normalized for $H_f = 1$, $C_s = C_l = 0$, and $2\Delta T = 1$ are shown in Figure 6.8(a). As expected, the P(3) and P(5) profiles exactly satisfy continuity at the MZ boundaries, while the P(1) model shows the expected top-hat jump discontinuities. The inset graphic shows the slope-matching of the P(5) model. The result of the slope-matching is an increased profile constriction, but to a far lesser degree than was shown in most of the normal or homographic profiles. Also, as shown in Figure 6.8(b), the profile shapes are directly coupled to the prescribed value of MZW, which is the only arbitrary parameter in this approximation. Previous studies have shown that too steep of an enthalpy slope (corresponding to too large of an apparent capacity peak value) in the mushy zone increases the severity of the nonlinearity and likelihood of solution oscillation [254,266]. The maximum values of the polynomial functions occurring at the melting temperature ($\theta = 0$) are shown in Table 6.4 along with the approximate relative magnitude compared to the P(1) case. In the limit of the material's average specific heat being much less than the quantity $H_f/\Delta T$ (an acceptable assumption for most solid-liquid

phase change materials and ΔT choices), the P(3) model has a peak 50% higher than P(1), and the P(5) peak 87.5% higher. Also shown in Figure 6.8(b) is the simple linear relationship between effective profile width (FWHM) and the prescribed MZW.

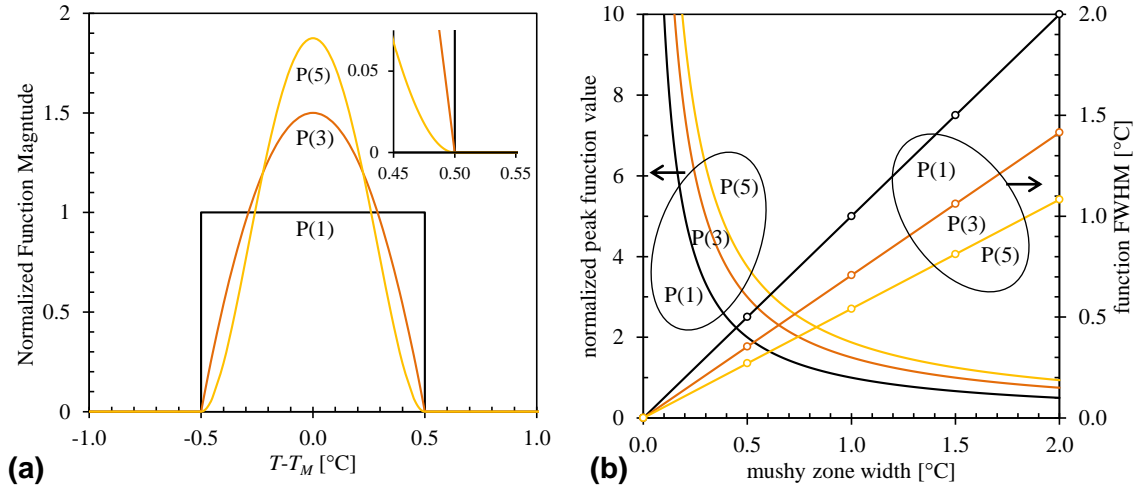


Figure 6.8 – 3rd and 5th order normalized polynomial smoothing functions compared to the standard top-hat profile. (a) shows that the profile remains perfectly constrained to the prescribed mushy zone with the inset highlighting the 5th order function slope continuity at the mushy zone edge. (b) shows the magnitude of the function peak an FWHM relative to prescribed MZW.

Table 6.4 – Peak values and function widths of polynomial solutions

$P(i)$	$C_{Mz}(0)$	Relative magnitude	FWHM	FWHM/MZW
P(1)	$\frac{1}{2} \frac{Hf}{\Delta T} + \frac{C_s + C_l}{2}$	1	$2\Delta T$	1
P(3)	$\frac{3}{4} \frac{Hf}{\Delta T} + \frac{C_s + C_l}{2}$	$\sim 3/2$	$\sqrt{2}\Delta T$	$\frac{1}{\sqrt{2}} \approx 70.7\%$
P(5)	$\frac{15}{16} \frac{Hf}{\Delta T} + \frac{C_s + C_l}{2}$	$\sim 15/8$	$\sqrt{4 - 2\sqrt{2}}\Delta T$	$\frac{\sqrt{2 - \sqrt{2}}}{\sqrt{2}} \approx 54.1\%$

The polynomial smoothing functions provide several potential benefits to the modeler that facilitate inclusion in existing modeling tools. These include the simple, closed form implementation, avoidance of any complicated mathematical functions that might not be available in a given toolset, and reduction to a single arbitrary parameter. The

form confines the full width of the latent heat profile to the integrated domain, eliminating any concern of ‘energy leakage’ in the model. There is no indication use of this format will introduce other errors or complications unique to the smoothing profile, but the next section validates the smoothing functions against a closed form phase change solution.

6.2.2. Model Validation

In order to evaluate these phase change approximations, the polynomial models are compared with the analytical solution to the one-dimensional Neumann melting model. As described in detail by Hu and Argyropoulos [254] the one-dimensional melting of a semi-infinite slab was first solved analytically by Stefan and later extended to a more general case by Neumann. In the Neumann model an initially solid volume at arbitrary cold temperature $T_C < T_M$ is placed in contact with a fixed hot temperature reservoir at $T_H > T_M$ that will drive the model into melting. The model then tracks both the location of the melt front, $X(t)$, and the temperature throughout the volume, $T(x,t)$ with time. This model is depicted in Figure 6.9.

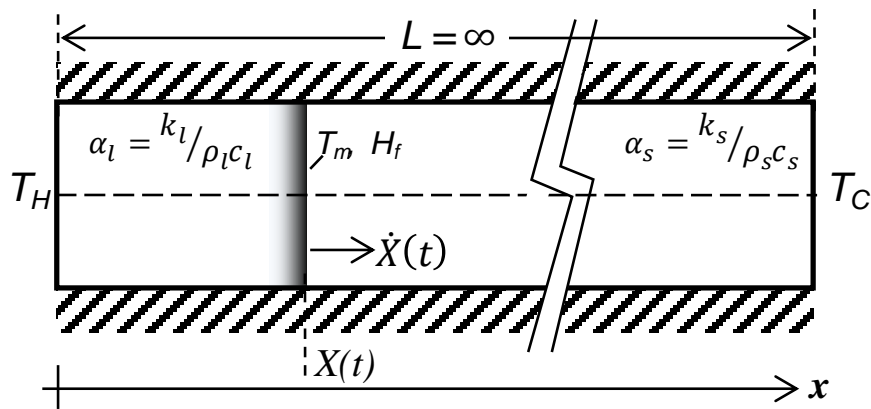


Figure 6.9 – One dimensional Neumann melting model where an infinitely long slab initially solid at uniform temperature T_C is brought into contact with a hot reservoir at $T_H > T_m$.

The solution to the Neumann model is given by:

$$X(t) = 2\lambda\sqrt{\alpha_l t} \quad (106)$$

$$T(x, t) = \begin{cases} T_H - (T_H - T_M) \frac{\operatorname{erf}\left(\frac{x}{2\sqrt{\alpha_l t}}\right)}{\operatorname{erf} \lambda}, & x < X(t) \\ T_M, & x = X(t) \\ T_C + (T_M - T_C) \frac{\operatorname{erfc}(x/2\sqrt{\alpha_s t})}{\operatorname{erfc}(\lambda\sqrt{\alpha_l/\alpha_s})}, & x > X(t) \end{cases} \quad (107)$$

where $\alpha_{s,l}$ is the material thermal diffusivity equal to $(k/\rho c)_{s,l}$ and the parameter λ is obtained by solving the transcendental equation:

$$\frac{c_l(T_H - T_M)}{\exp(\lambda^2) \operatorname{erf}(\lambda)} - \frac{c_s(T_M - T_C)\sqrt{\alpha_s}}{\sqrt{\alpha_l} \exp(\alpha_l \lambda^2/\alpha_s) \operatorname{erfc}(\lambda\sqrt{\alpha_l/\alpha_s})} = \lambda H_f \sqrt{\pi} \quad (108)$$

A representative solution for the Neumann problem is shown in Figure 6.10 using a normalized temperature variable given by:

$$T^* = (T - T_C)/(T_H - T_C) \quad (109)$$

This solution uses the materials properties of erythritol (see Table 2.4, also summarized below in Table 6.5) assuming T_M to be exactly 118°C, and sets the boundary conditions to +/- 10°C such that T_C and T_H are 108°C and 128°C, respectively. Figure 6.10(a) shows the location of the moving phase front, $X(t)$, and (b) shows the normalized temperature distribution throughout the solid as it slowly heats.

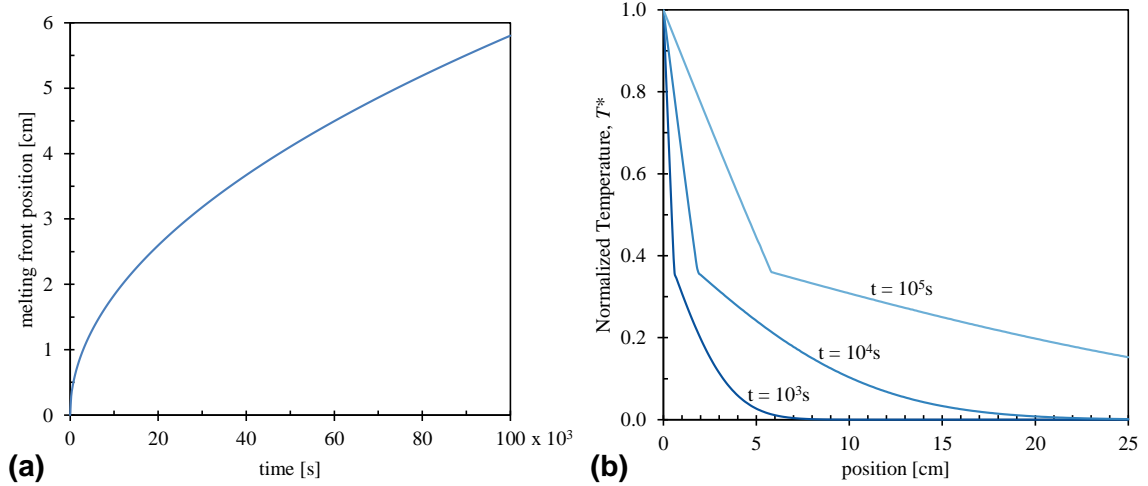


Figure 6.10 – Representative analytical solution to the Neumann problem showing (a) the location of the melting front with time, measured from the liquid edge, and (b) the domain temperature spatial profile for several time steps,.

Table 6.5 – Erythritol material properties summary

<i>property</i>	<i>Unit</i>	solid	liquid
k_{th}	W/mK	0.733	0.326
c_p	kJ/kgK	1.383	2.765
ρ	kg/m ³	1480	1300
T_M	°C		118
H_f	kJ/kg		339.8

As per [263], for easier analysis the x and t dependent solution can first be recast in terms of a single independent Boltzmann variable, y , and then mapped from an infinite to a unit spatial domain, z , according to:

$$y = x/\sqrt{t}, \quad z = 1 - \exp(-y/b) \quad (110)$$

where b is an artificial scaling constant, here set to $\sqrt{2\alpha_s}$. With that domain and scaling constant, the location of the melting front becomes a fixed point in z equal to:

$$Z_{mf} = 1 - \exp\left(-\lambda\sqrt{2\alpha_l/\alpha_s}\right) \quad (111)$$

A representative normalized temperature profile from the solution to the ideal Neumann problem solution on the unit domain is shown in Figure 6.11.

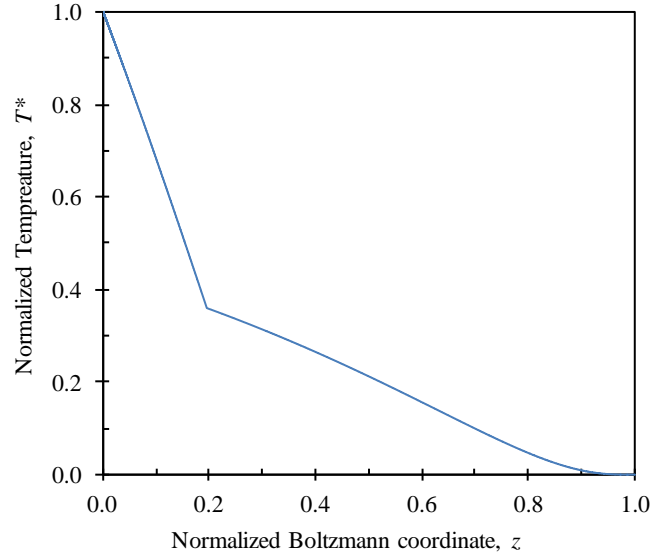


Figure 6.11 – Representative normalized solution to the Neumann melting problem.

6.2.3. Numerical comparison with the Neumann model

The polynomial smoothing function approximations are compared to results from the analytical Neumann solution by incorporating them into the material definition of a finite element model. For the purposes of this study, all numerical simulation was performed using the Heat Equation solver in the open-source finite element *Elmer* [267], which models phase change using the Apparent Capacity Method (ACM) described previously. *Elmer* implements ACM by calculating the local heat capacity in transient simulations from a prescribed material enthalpy profile using:

$$c_p(T, t) = \frac{\partial H / \partial t}{\partial T / \partial t} \quad (112)$$

The Heat Equation solver accepts temperature dependent material properties defined using either analytical functions or tabular data. As before, the base material properties used are those of erythritol as per Table 6.5

The finite element domain is constructed using one-dimensional thermal elements with boundary conditions matching the Neumann model definition, i.e., the domain is initially solid at a temperature $T_L < T_m$, and at $t = 0$ one end is raised to a temperature $T_H > T_m$. Because we cannot numerically model an infinite region, the domain is instead set to a length of 1 m. This is a much longer distance than any significant heat will reach within the simulation time in this exercise. For the range of parameters tested in these simulations, shown in Table 6.6, the analytical Neumann solution only produced a maximum melt front progression of about 5.8 cm over a 100,000 sec simulation time.

Table 6.6 – Neumann problem simulation parameters

<i>property</i>	<i>unit</i>	<i>Range</i>
T_H, T_L	°C	100, 150
MZW ($2\Delta T$)	°C	0.5, 1.0, 1.5, 2.0
Element count, h	--	100, 1000, 5000
Time step size, δt	sec	500
Total time steps, N_t	--	200

Although several of the previously mentioned modeling reviews have shown that some of the weakness of the apparent heat capacity scheme can be overcome using adaptive time stepping or mesh refinement options, we will be using both fixed grid and time steps to simplify the comparison. The fixed grid is not completely uniform, however. The half of the domain in contact with the heated boundary set has a mesh density 100x higher than the far-side half, focusing the mesh refinement where it will have the most effect and

reducing computational overhead. Finally Figure 6.12 shows an adjusted version of Figure 6.8(a) with the actual numerical values used in the simulation.

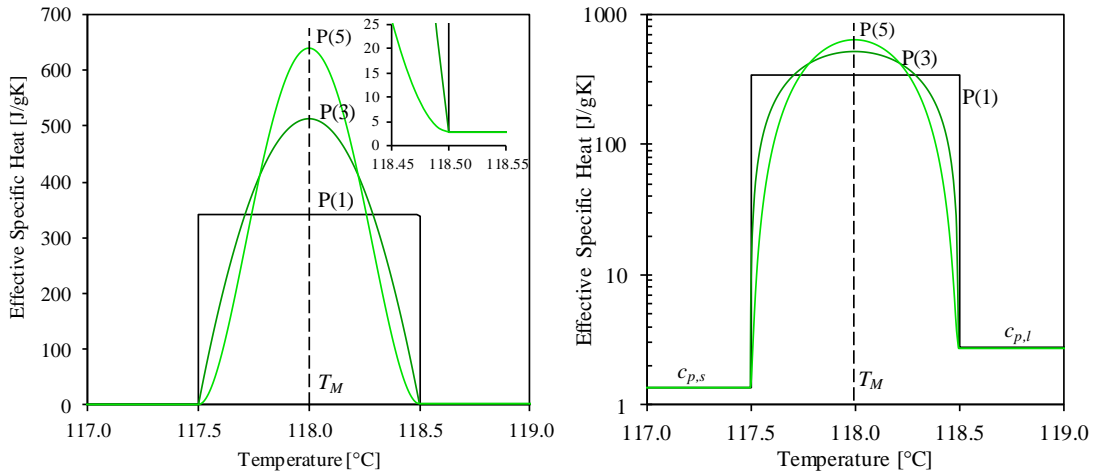


Figure 6.12 – Polynomial fit effective capacity profile for erythritol with MZW = 1°C. (b) presents the same information on a logarithmic scale to emphasize solid and liquid specific heats and highlight the two order of magnitude difference between sensible and latent portions of the profile. Inset on (a) shows the slope-matching achieved by the 5th order smoothing function.

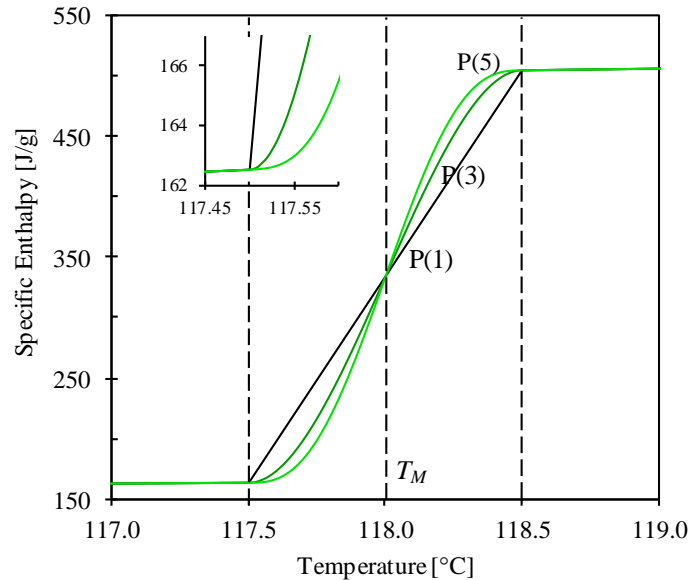


Figure 6.13 – Polynomial fit enthalpy profiles for erythritol with MZW = 1°C. Inset emphasizes the slope and curvature matching achieved by the 3rd and 5th order functions, respectively.

6.2.4. General Model Results

Representative results for the polynomial models are shown in Figure 6.14(a-f), which displays the time dependent melting front location as a function of mesh density (a-c) and mushy-zone width (d-f). The melt front profiles show similar behavior for all three polynomial orders. As expected in any numerical model, the accuracy shows a high degree of dependence on the mesh density, but even with $h = 5000$ there is still some degree of steady-state error that increases with time, more noticeably so in the P(1) model. Also, the nature of the Neumann problem introduces increased error in most solutions at $t = 0$ because of the fixed temperature boundary condition. This condition produces a nearly infinite initial melt front propagation velocity, but this initial error diminishes with time in all models. No special effort was taken to compensate for this error in these tests.

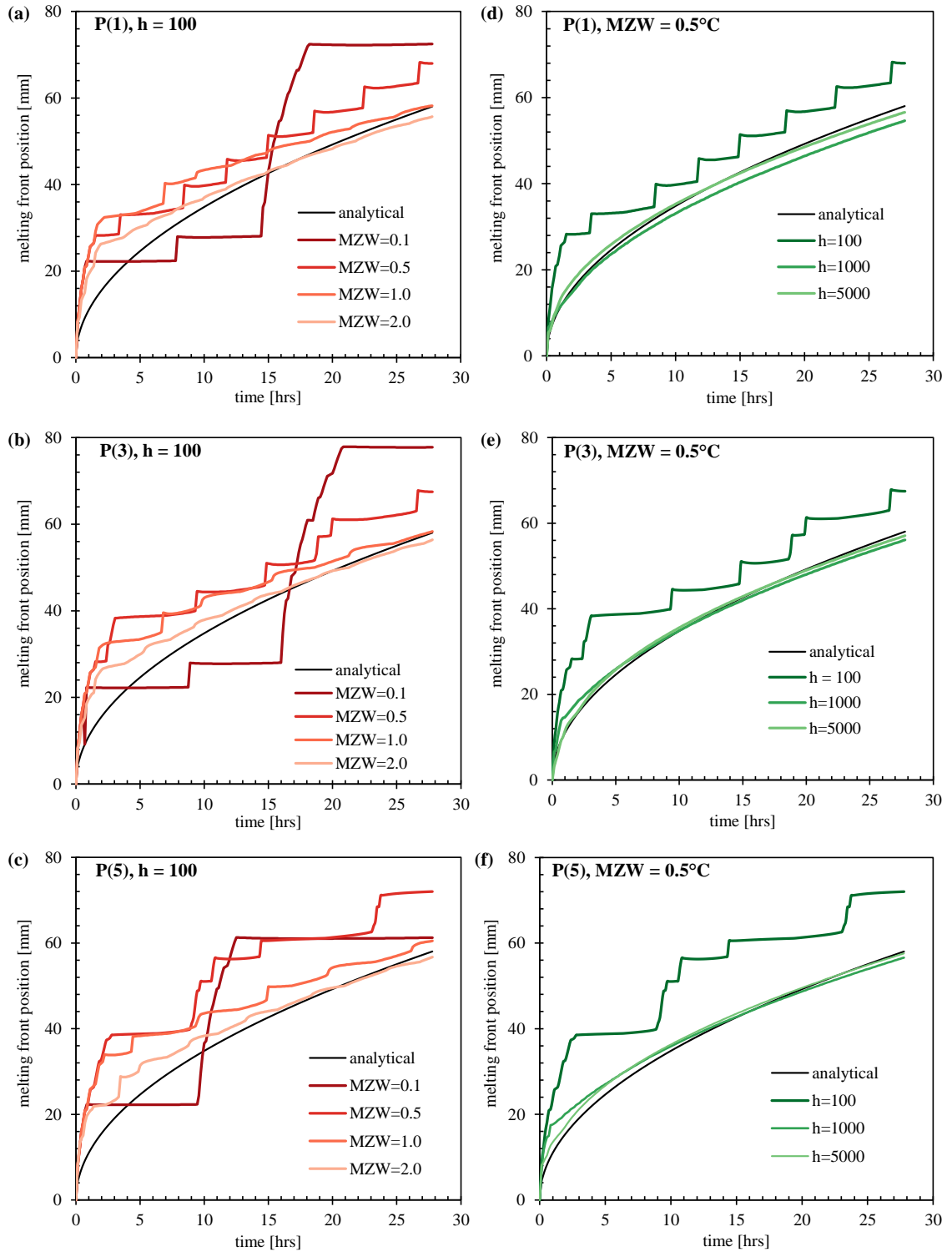


Figure 6.14 – Numerical approximations of melting front position compared to analytical profile. (a,b,c) show position as a function of mushy zone width (MZW) with fixed element count of 100, and (d,e,f) show position as a function of element count (h) with fixed MZW = 0.5°C.

For the undermeshed case ($h = 100$) an oscillating or staircase melting front profile is clearly evident, the severity of which decreases with increasing mushy zone width. This follows the explanation of Gong and Mujumdar where the oscillating melting front propagation is related to the height of the mushy zone function and the corresponding degree of nonlinearity in the apparent capacity profile [268]. Figure 6.15 shows the entire normalized numerical thermal profile for several early time steps, again for the linear model this time with sufficient mesh density to avoid oscillation ($h = 1000$). Even with error in temperature prediction around the melting front, within a short amount of time the majority of the model has settled close to the analytical solution. This suggests that when measuring total error in the thermal profile at each time step, the dominant factor will be the error about the melt front. Additionally, the fact that the solutions do eventually converge to the analytical profile confirms that the polynomial approximation does not introduce any fundamental errors into to the solution.

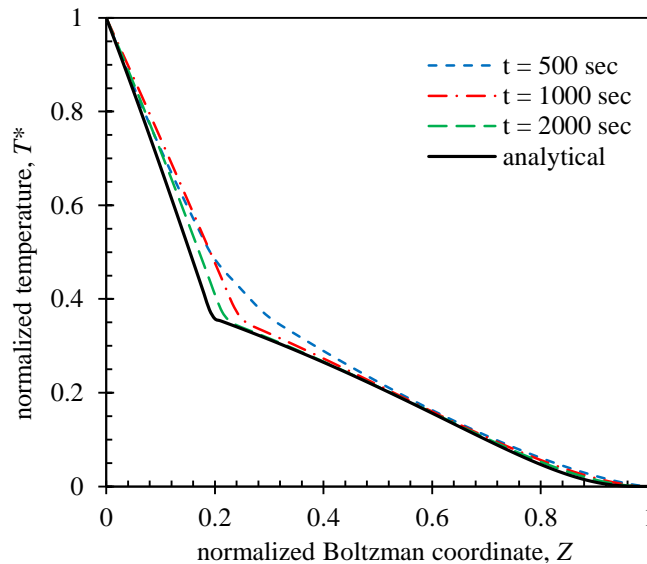


Figure 6.15 – Normalized P(3) model temperature plotted against normalized Boltzmann coordinate at different time steps with medium mesh refinement ($h = 1000$) and MZW=2°C. The initial melting front error gradually approaches the analytical solution with increasing time

6.2.5. Polynomial order error comparisons

The relative accuracies of the different polynomial models were compared by examining both melt front profile error and thermal profile error for parameters of polynomial order, mesh density and mushy zone width. Melting front error was determined by calculating the Root Mean Square Error (RMSE) according to:

$$RMSE_M = \sqrt{N_t^{-1} \sum_{i=1}^{N_t} |X_i^{err}|^2} \quad (113)$$

where X_i^{err} is the difference between calculated front location at time step i and the analytical Neumann solution $X(t_i)$, and N_t is the total number of time steps. Similarly, thermal profile error at each time step i is calculated as:

$$RMSE_{T,i} = \sqrt{N^{-1} \sum_{j=1}^N |T_{ij}^{err}|^2} \quad (114)$$

Where T_{ij}^{err} is the difference between calculated temperature at each node j and the analytical Neumann solution for $T(x_j, t_i)$ at time step i , and N is the total number of nodes in that model. Finally, total temperature profile error for a particular model is determined according to:

$$RMSE_{Tot} = \sqrt{(N_t N)^{-1} \sum_{i=1}^{N_t} \sum_{j=1}^N |T_{ij}^{err}|^2} \quad (115)$$

The total error for both melting front and temperature profiles are shown in Figure 6.16 and Figure 6.17 respectively. For both measures, the level of mesh density can be seen as having the primary impact on solution accuracy, much as was discussed with Figure 6.14. The importance of mushy zone width is evident primarily at the minimum simulated value

of 0.1°C , where almost an order of magnitude increase in solution error occurs for the medium and high mesh density cases. This small MZW increases both the degree of approximation nonlinearity as well as the likelihood of elements skipping over the melting transition during the earlier time steps with high melt front velocity.

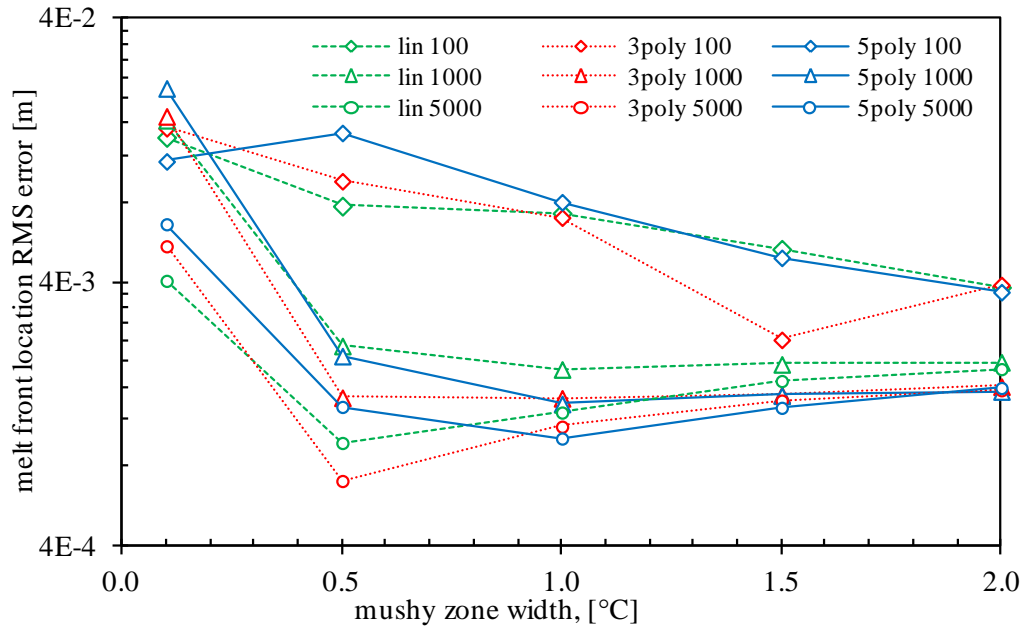


Figure 6.16 – Melting front location prediction RMSE at $t = 500\text{s}$. P(3) and P(5) show generally reduced RMSE for most values of MZW. The sole exception is that for P(5) where the error increases for values below 1°C , likely due to the increased profile ‘sharpness’.

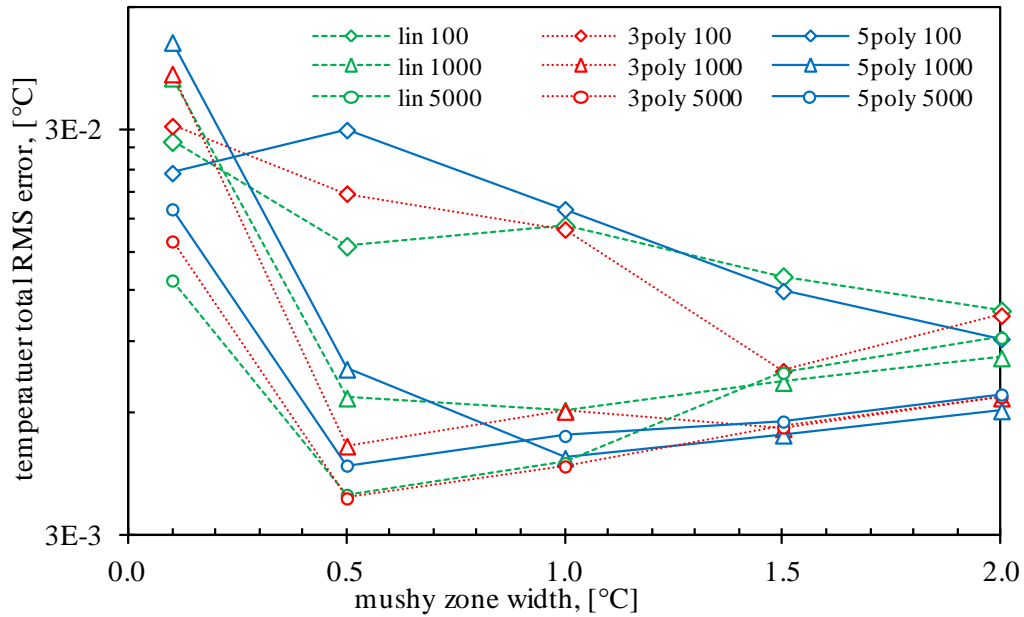


Figure 6.17 – Thermal profile RMSE at $t = 500s$. The third order functions appear to result in the lowest consistent error across the MZW span, excepting the minimum MZW again.

From the figures, it also appears that the polynomial order does have a slight impact on solution accuracy. For the melting front error in Figure 11, the P(3) model shows the lowest total error for each level of mesh density at $MZW = 0.5^{\circ}C$. P(5) exhibits similar or lower error than P(3) for most larger MZW values, but shows increasing error below $MZW = 1^{\circ}C$. It is assumed that this increase is due to the slightly high profile constriction in P(5) versus P(3). Both models show lower error than the linear model P(1), excepting the high error cases noted previously. Similar results can be seen for the total temperature error in Figure 12, except for the fact that the highly meshed P(5) case has notably more error than P(1) and P(3), and is even worse than the moderately meshed P(5) for higher MZW values. It is possible that this is a case of the model actually being overmeshed for the problem and time step used.

6.2.6. Model Conclusions

We have examined several methods of approximating the phase change process using the apparent heat capacity method. While previous studies suggested the importance of a smoothing function to reduce sharp discontinuities in the common linear or top-hat profile, previously proposed approximations suffer from several deficiencies. First, the functions used spread the total latent energy over an infinitely wide region, mandating the use of arbitrary tuning parameters to reduce truncation error at the mushy zone boundary. Second, the functions were actually decoupled from the desired mushy zone width inherent in the approximation, instead being strongly dependent on the tuning parameters. Reducing the truncation error would both decrease function width and increase peak height of the function, increasing the degree of nonlinearity imposed by the model.

The proposed polynomial models prove to be superior smoothing functions by avoiding the previously mentioned shortcomings. By definition the closed form models exactly match the desired conditions at the mushy zone boundaries, with no truncation error that could develop into accumulated energy loss. Also, this is accomplished without artificially compressing or sharpening the smoothing profile. The polynomial functions have fixed relationships between the profile peak value, function width and the prescribed mushy zone width, and the function widths can be much closer to the mushy zone width because there is no need to be concerned with truncation error.

In comparing both the melting front and temperature profile results of simulations using the 1st, 3rd and 5th order polynomials to reproduce the one-dimensional Neumann solution, it was found that both of the higher order polynomials did produce slightly lower error results than the linear model for most cases. In fact, the 3rd order model was found

to be more accurate than the 5th order model, suggesting that the smoothness of the capacity profile at the mushy zone boundary is less of a concern than the continuity of the profile. It is suspected that the slightly sharper function profile of the higher order profile may have increased the total modeling error. Otherwise, the models produced results as expected for the apparent capacity method, showing melt front oscillation for undermeshed conditions and small accumulated error developing over long simulation times. Future developments on this topic may expand the error investigation to include other solution methods including finite difference and finite volume schemes, as well as two- and three-dimensional domains. While any smoothing function profile may be applied to those cases, it is possible that they may vary in the degree of sensitivity to choice in mushy zone profile.

6.3. Substrate integrated phase change cooling

The electronics PCM integration approaches mentioned at the start of this chapter were generally non-integrated heatsinks resulting in slow transient performance. As a first case study using the phase change smoothing functions we now examine an integrated PCM package design that leverages both previous work sponsored by the U.S. Department of Energy (briefly mentioned in Section 3.1.2) and our previous substrate integrated cooling work described in Chapter 4. This DOE design incorporates a parallel (also called hybrid) PCM/coolant configuration that is hoped to reduce the degree to which the PCM impedes heat removal [27,28,79].

6.3.1. DOE / University of Tennessee Thermal Buffer Heat Sink Concept

The DOE design was initially presented in 2007 as part of the FreedomCar (later U.S. DRIVE) program, where the U.S. Department of Energy in conjunction with the

University of Tennessee reported on options for improving the power electronics heat sink in a commercial hybrid electric vehicle [41,269]. The study investigated feasibility, performance, and cost of using a PCM heat sink to design the cooling system for average instead of peak thermal load conditions. The phase change heat sink would act as a transient buffer for the coolant system, leading to the appropriately termed *Thermal Buffer Heat Sink* (TBHS). The study identified several likely candidate PCMs as well as two optimal configurations for compact and efficient TBHS implementation, shown in Figure 6.18. The two designs shown put the PCM in a parallel configuration with the coolant, with Figure 6.18(a) relying on fin conduction to bypass the PCM, and (b) placing the PCM and coolant at equal distance from the heat source. Figure 6.18(b) was described as the preferred design from a compactness and thermal performance standpoint, but (a) was selected as a more practical design based on perceived difficulties in fabrication and sealing of the separate components.

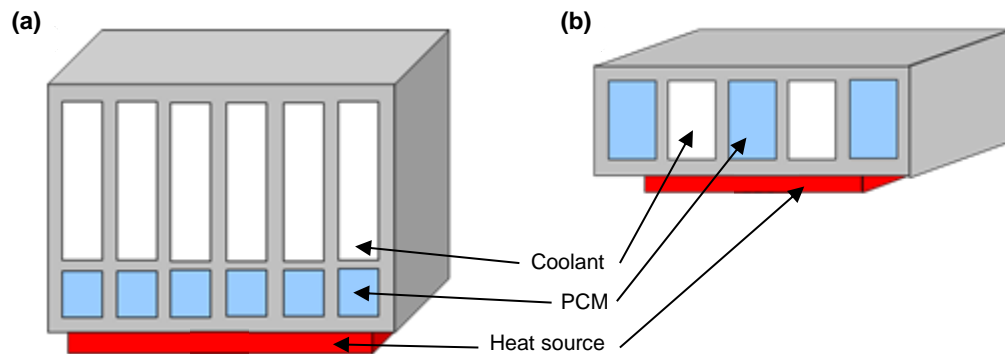


Figure 6.18 – Department of Energy developed TBHS concepts exploring compact integration of cooling and thermal energy storage. PCM and coolant regions in series (a) and in parallel (b) arrangements, adapted from [41].

Comparing the two designs, it should be noted that Figure 6.18(a) allows for a potentially larger amount of both cooling and PCM due to the double layer configuration.

Figure 6.18(b), on the other hand, creates a direct spatial tradeoff between cooling and PCM within a single layer. Additionally, allowing for the potential sealing difficulties between channels, this compact, single-layer design moves the coolant closer to the heat source and removes the PCM from the primary coolant heat removal path. As mentioned in Section 2.3.1, PCM configurations at both small and large scale can benefit from a configuration where the PCM provides additional thermal capacity outside the primary heat removal path to avoid degrading overall component thermal resistance. Both before and after phase change the typically high thermal resistance PCM provides little useful system benefit, although some PCMs may increase sensible thermal capacity relative to the regular package. A caveat to using this parallel arrangement, however, is that it increases the complexity in making effective use of the thermal storage, as there is no boundary condition maintained thermal gradient driving heat into the PCM. Instead thermal charging is driven by a transient gradient that decreases with time, and additional engineering will be required to make full use of the material. This arrangement can add to challenges with heat spreading and nonuniformity as the one-dimensional simplicity is lost.

Despite these drawbacks, this parallel arrangement will be explored as a method of an electronics integrated PCM arrangement by combining substrate integrated cooling with a phase change material thermal buffer. The following sections explore design of and material selection for these TBHS structure and then follow that with numerical thermal simulation to predict TBHS performance under transient loads. We will then use these results to assess the degree to which a TBHS structure can mitigate some of the transient packaging issues identified in Chapter 5 to suppress transient temperature rise.

6.3.2. Substrate Integrated Thermal Buffer Heat Sink

The substrate integrated cooling approaches from Chapter 4 were successful in demonstrating the feasibility of bringing coolant to the package layer immediately adjacent to the power device. Several methods of ceramic microfabrication were used to make large microchannels, attempting to show that a net improvement in thermal resistance could be achieved without the need to use exceedingly small, highly restrictive channels. In order to affect thermal transients within the electronics package, we will explore the ability to similarly incorporate both cooling channels and phase change materials in the same electronics substrate. This will produce a substrate integrated form of the TBHS. It is hypothesized that this integrated structure will provide acceptable package thermal resistance while allowing the designer to trade-off cooling and thermal absorption capacity for improved transient survivability. Here we will explore material selection and design of these TBHS structures. Later sections will use numerical simulation to predict thermal performance under transient loads.

The substrate integrated cooling work that placed microchannels in the underside of power electronics package substrates leads to a straightforward substrate integrated TBHS design. Figure 6.19 shows one design concept. The power device is attached to the package substrate using a metallized solder or die attach. The substrate has a set of partial depth channels in the backside. This substrate is then capped with another package layer, either another substrate or a conventionally machined part, which contains a fluid manifold. Interleaved openings in the manifold allow fluid to be routed to the cooling channels while isolating the PCM channels. Individual PCM and cooling channel dimensions can then be adjusted as necessary for the design.

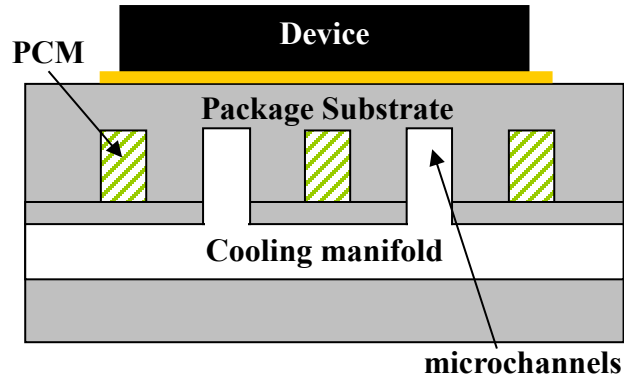


Figure 6.19 – Schematic of a substrate integrated thermal buffer heat sink with single layer PCM-coolant arrangement over a fluid delivery manifold.

This design allows a particular amount of design freedom. As Section 4.3 described, much work has occurred in improving microchannel cooling to leverage the high convection rates of narrow channels while minimizing resultant pressure drop penalties. The popular solution to this problem is to make use of a manifolded microchannel structure that uses larger, low-restriction channels to deliver fluid to short, narrow microchannels at reduced penalty. The cost of this approach is design and fabrication complexity. This TBHS design can use that same approach to maintain high convective rates. It also shares the benefit that the material used for the manifolding layer can be chosen independent of the design’s thermal requirements, as the manifold material is not required to conduct heat. It can be a low cost, conventionally machined material, and the only requirements are adequate sealing to the substrate.

6.3.3. TBHS model configuration and computational domain

A side view and unit cell of the substrate-integrated TBHS is shown in Figure 6.20 with relevant geometric and model parameters labeled. Because the structure is primarily two-dimensional with a repeating microchannel sub-unit structure, the computational

domain can be limited to a 2D region with symmetry boundary conditions on either side, as shown.

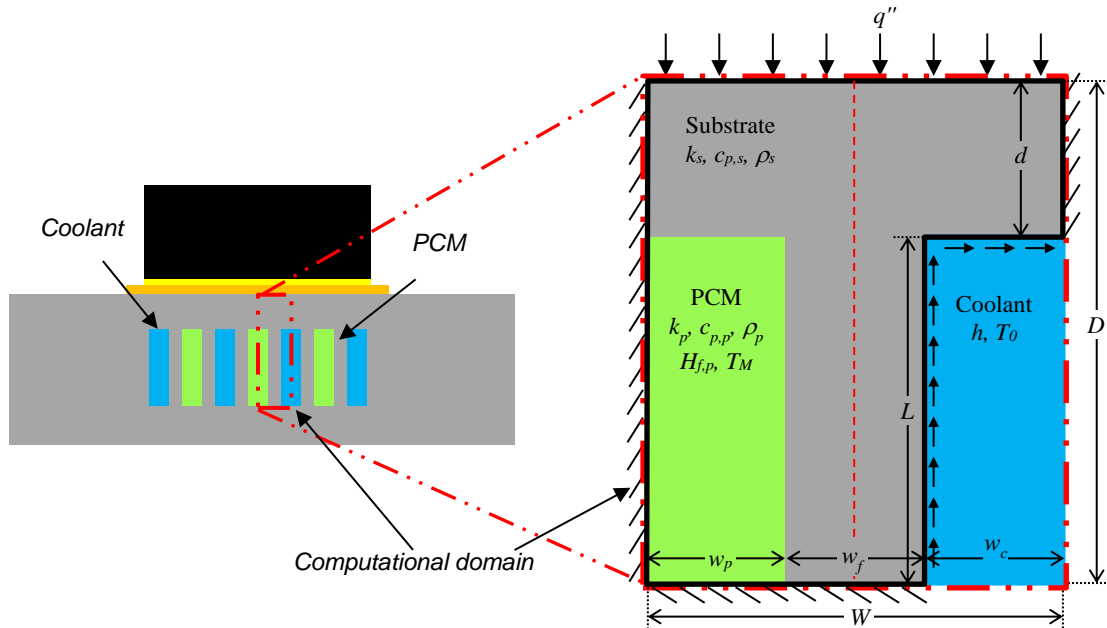


Figure 6.20 – Substrate integrated TBHS computational domain with unit cell expanded and labeled showing critical regions, boundaries, and relevant geometrical and material parameters.

The full set of modeling assumptions implied by this domain are as follows:

- Channel length is much greater than the lateral unit cell dimensions justifying a 2D model.
- Heat from the attached die is sufficiently uniform that the die can be approximated by a fixed, constant, external thermal resistance and the load can be modeled by a constant heat flux applied to the top surface of the TBHS unit cell.
- The bottom surface of PCM and fin is insulated, based on the manifold assembly and material options described previously.

- PCM volume change with temperature and phase change can be ignored in the 2D model plane, and change in thermal absorption will be accommodated in the model by volumetric property change, and there is no voiding.
- PCM volume is sufficiently small to ignore liquid phase convection.
- Coolant contribution can be approximated by uniform convection boundary condition over the wetted surface.

Following from the previous smoothing function development, this computational domain is modeled as a single two-dimensional thermal region subject to heat diffusion with non-linear, temperature dependent material properties. As before, finite element simulation was performed using the heat equation solver in *Elmer*. A constant convection boundary condition on the wetted surfaces emulates the effect of the coolant and avoids need for a liquid domain thermofluid or CFD solver. Phase change was modeled with a P(3) smoothing function and appropriate PCM material properties. (Preliminary models showed significant convergence differences in the P(1) functions, but little difference between P(3) and P(5), so P(3) was selected.) An automatic 2D mesh refinement algorithm based on the RGB subdivision scheme [270] was employed through *Elmer* to obtain mesh independent simulation results. Example initial and final meshes for a transient simulation with partial PCM melting near the fin surface are shown in Figure 6.21. It is clear that the largest thermal gradient occurs near the PCM phase front that slowly moves from the substrate and fin boundary into the PCM volume.

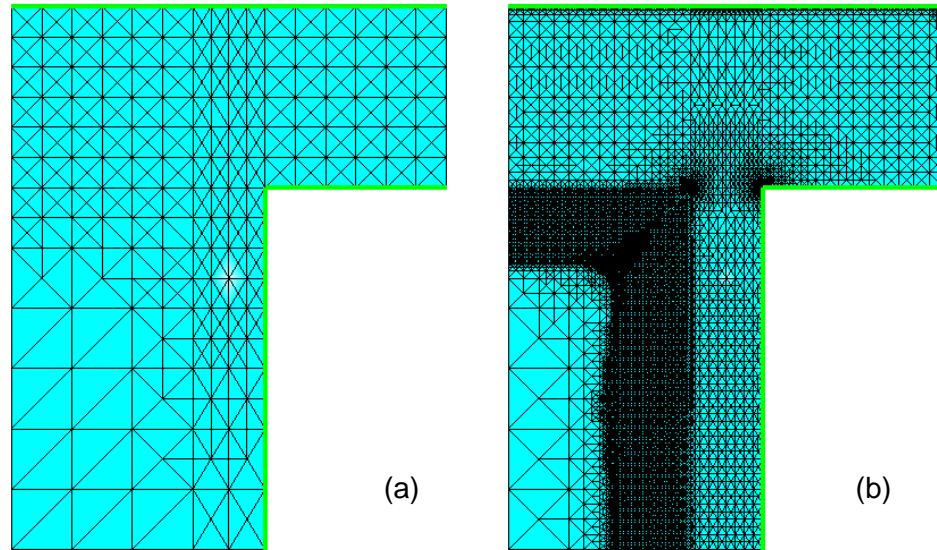


Figure 6.21 – Representative finite element meshes used in the TBHS model showing (a) the initial mesh and (b) the mesh after automatic refinement according to the local thermal gradient.

6.3.4. Model Analysis

Analysis of thermal results includes estimation of thermal performance of each simulated TBHS configuration over the examined parameter space, estimated using the steady-state and transient parameters defined in the following sections.

6.3.4.1. Steady-state analysis metrics

The main function of the TBHS is to remove heat, making thermal performance during normal operation under non-melting conditions of prime importance. Putting a low thermal resistance material into the heat sink will invariably increase overall thermal resistance. A non-uniform temperature profile is expected on the top heated surface from the uneven coolant distribution over the 2D unit cell. For the purpose of this study thermal resistivity is defined as the temperature rise per unit heat flux using the maximum surface temperature as:

$$R_{th}'' = \frac{T_{max} - T_0}{q''} \quad (116)$$

where T_0 is the coolant temperature (also always equal to the initial model temperature for transient simulations). T_{max} is expected to be located on the heated surface farthest from the coolant. However, due to nonlinear PCM heat absorption it is possible that this point may not stay at the same location throughout a transient simulation. R_{th} , however, always uses the maximum temperature even if its location changes.

The thermal resistance of the TBHS will be a combination of conductive resistance in the solid and convective resistance in the applied coolant. Recognizing that the convective resistance may dominate for low convection rate cases, a solid thermal resistivity is estimated (ignoring fin effectiveness) by subtracting out the normalized resistive contribution of the convective term:

$$R_{th,s}'' = R_{th}'' - R_{th,conv}'' = R_{th}'' - \frac{W}{h(w_c + L)} \quad (117)$$

As the unit cell design in Figure 6.20 is essentially a single one-side wetted fin, fin efficiency can be calculated as the ratio of the amount of heat removed to the amount that would be removed from a fin uniformly heated to the base temperature (i.e., an infinitely conductive fin). We can estimate fin efficiency, η_f , using the nodal temperature values from the FEM numerical results in the equation:

$$\eta_f = \frac{\int_0^L h(T(x) - T_0)dx}{hL(T_b - T_0)} \approx \frac{\sum_i (T_i - T_0)\Delta l_i}{(T_b - T_0)L} \quad (118)$$

where L is the fin length as indicated in Figure 6.20, Δl_i is the length between nodes i and $i+1$, T_i is the nodal temperature, T_b is the temperature at the base of the fin, and h is the fluid convection rate (assumed constant over the entire wetted perimeter). Note that in heat

sink design a large temperature gradient along the fin results in a low fin efficiency, typically indicating a longer fin than is necessary. Alternatively, a very high fin efficiency suggests that lengthening the fins would significantly improve heat removal.

6.3.4.2. Transient analysis metrics

Dominant thermal time constant, τ_{th} , and effective thermal capacitance of each TBHS configuration can be extracted from linear (no phase change) step response simulations by applying a least squares best fit to a single pole heating profile using the transient maximum surface temperature and steady-state thermal resistivity:

$$T(t) - T_0 = q'' R_{th}'' \left[1 - e^{-t/\tau_{th}} \right] \quad (119)$$

Noticing again that the simple RC time constant model lumps convective and conductive resistances together, and that convection can dominate calculation of τ_{th} , we can again calculate a ‘solid contribution’ thermal time constant for better component comparison. As there is no capacitive component to the convection, solid thermal time constant is simply:

$$\tau_{th} = R_{th}'' C_{th}'' = (R_{th,s}'' + R_{th,conv}'') C_{th}'' = \tau_{th,s} + R_{th,conv}'' C_{th}'' \quad (120)$$

$$\tau_{th,s} = \tau_{th} R_{th,s}'' / R_{th}'' \quad (121)$$

After extracting τ_{th} , effective thermal capacity of the substrate can again be calculated assuming a single dominant thermal time constant:

$$C_{th}'' = \tau_{th} / R_{th}'' \quad (122)$$

noting that the same capacitance value is obtained whether using total or solid contribution values for the resistance and time constant.

For melting models, because $T_0 < T_M$ there will be a finite time until melting begins that is a function of the applied heat flux and the thermal time constant of the TBHS. The minimum heat flux to initiate melting is estimated as:

$$q_m'' = (T_M - T_0) / R_{th}'' \quad (123)$$

Using this melting threshold heat flux value and the dominant single pole time constant model, non-dimensional time to melting for any configuration at a given heat flux can be estimated using:

$$t_m / \tau_{th} = \ln \left[\frac{q''}{q_m''} \right] = \ln \left[\frac{q'' / q_m''}{q'' / q_m'' - 1} \right] \quad (124)$$

Comparing this model to extracted data from the simulations can provide a quantitative evaluation of the fitness of the single time constant model for the substrates.

6.3.5. Silicon-erythritol TBHS simulation

Two independent material evaluations were performed in expectation of planned prototyping efforts. First, in anticipation of a complex manifold microchannel geometry for medium temperature power electronics as per the original DOE TBHS study, a combination of silicon substrate and erythritol PCM was simulated with parameterized geometry and thermal boundary conditions. That simulation study was initially described in [151,252] and focused on high temperature vehicle cooling loop surge capacity, where $T_0 = 100^\circ\text{C}$ and h was varied between 1, 10, and 50 kW/m²K to represent a range of single or two-phase microchannel flows.

Material and geometric parameters for the domain are specified in Table 6.7 and Table 6.8 respectively, and cover the range of a prototypical single-wafer, silicon TBHS

implementation. Thermal boundary conditions for the melting simulation were determined later after step response models estimated melting onset parameters.

Table 6.7 – Silicon TBHS simulation material properties

property	unit	silicon	erythritol
k	W/mK	135	0.733 (<i>s</i>), 0.326 (<i>l</i>)
c_p	kJ/kgK	0.704	1.383 (<i>s</i>), 2.765 (<i>l</i>)
ρ	kg/m ³	2330	1480 (<i>s</i>), 1300 (<i>l</i>)
H_f	kJ/kg	--	339.8
T_M	°C	--	118

Table 6.8 – Silicon TBHS simulation dimensions and parameter ranges

parameter	value/range [μm]
D	400
d	100
L	300
w_p	125, 250, 500
w_f	62.5, 125, 250
w_c	62.5, 125, 250
W	Σw_i

6.3.5.1. Steady-state thermal results

Figure 6.22 shows a representative steady-state TBHS heating profile below the melting temperature indicating a thermal resistivity of about 0.180 cm²K/W. The peak temperature is located in the top left corner of the unit cell, farthest from the coolant and partially ‘shielded’ from the conductive fin by the low thermal conductivity PCM.

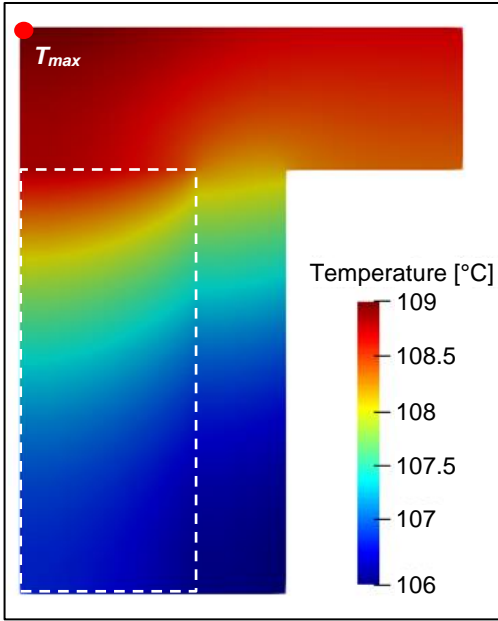


Figure 6.22 – Representative steady-state, non-melting heating profile in a silicon TBHS subject to a 50 W/cm^2 heat load with $50 \text{ kW/m}^2\text{K}$ cooling at $T_0 = 100^\circ\text{C}$. Location of hottest spot indicated.

Using the geometric and material configurations from Table 6.7 and Table 6.8, substrate thermal resistivity was calculated by applying a unit uniform heat flux (1 W/cm^2) to the top surface. The thermal resistivities of the different geometries and convection rates are shown in Figure 6.23. These values are compared with the thermal resistivities of non-PCM microchannel substrates with the same range of cooling channel geometries (w_c, w_f). It should be noted that the microchannel unit cells have half the fin width of an equivalent TBHS, as their symmetry line is the center vertical line in Figure 6.20.

Across the board we see the expected result of substituting erythritol into the substrate. The convection rate is the primary determinant of substrate resistivity for both PCM and non-PCM substrates. However, compared to the lowest resistance coolant-only microchannel substrate, thermal resistivity is increased by a factor of about 2.4 to 8.6x, and the degree of impact is positively correlated to added PCM volume. When not melting,

the addition of a PCM has not only cut the total cooling surface roughly in half, it is akin to inserting an insulating material into every other microchannel cavity in a standard microchannel heat sink. This would also look like a microchannel heat sink with extremely wide and poorly conducting fins, and the significant thermal resistivity increase is unsurprising.

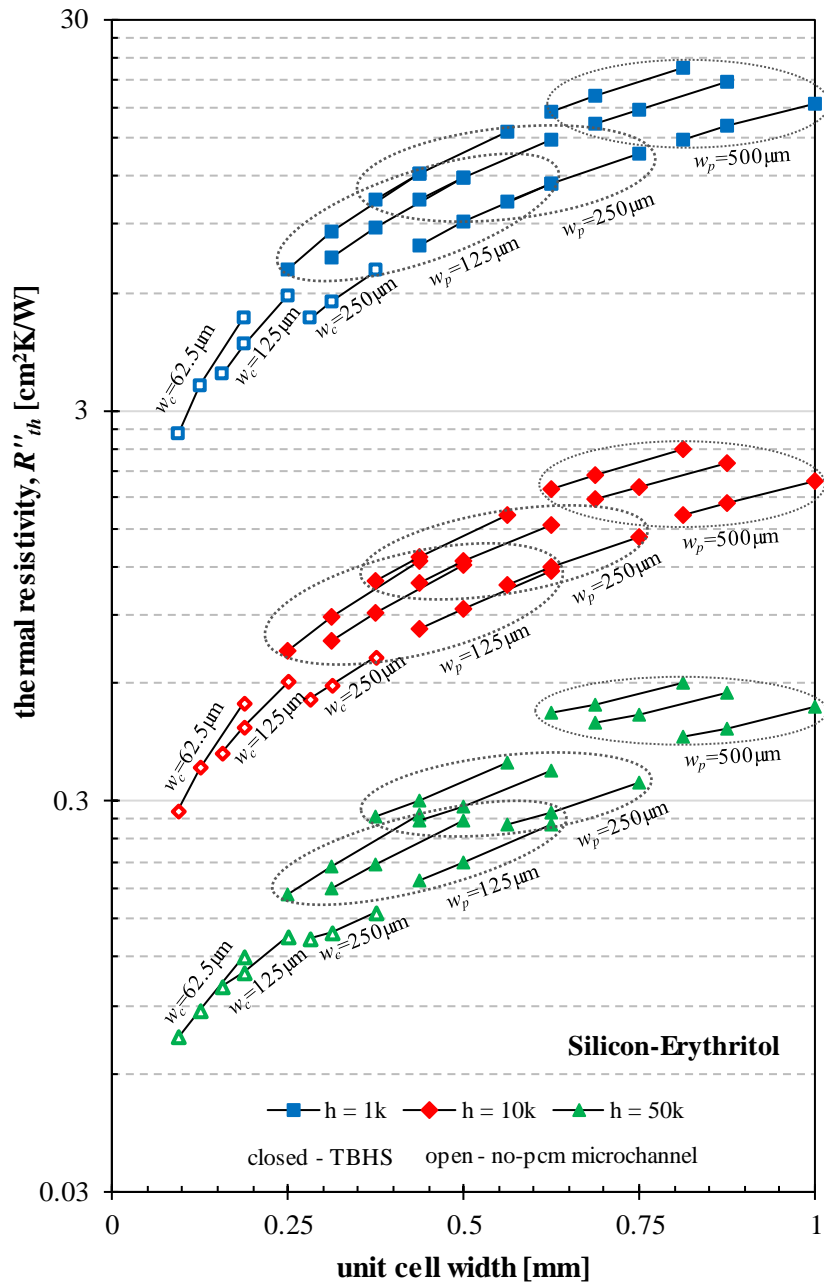


Figure 6.23 – Steady-state thermal resistivity results for silicon TBHS and equivalent microchannel heat sinks for varying geometries and convective rates.

The PCM impact on thermal resistivity can be seen more clearly by normalizing the data Figure 6.23 and subtracting out the convective resistance component as per (117). The results of this are shown in Figure 6.24, where all of the solid thermal resistivity data

has collapsed down to a single band. It is worth noting that the solid-resistivity estimate does not correct for heat spreading variation between different configurations. It assumes a one dimensional thermal resistance distributed over the wetted area having uniform influence on the location of maximum temperature rise. In actuality the low thermal conductivity PCM insulates the hot spot from the majority of the wetted fin, causing an overestimation of the amount of thermal resistance to subtract from R_{th}'' . This could explain how the lowest amount of PCM appears to have no, or even a slight negative resistance impact in Figure 6.24 for some configurations. Regardless of this anomaly, however, this view of the thermal resistance profile does show the significant thermal penalty paid by the addition of PCM to the structure.

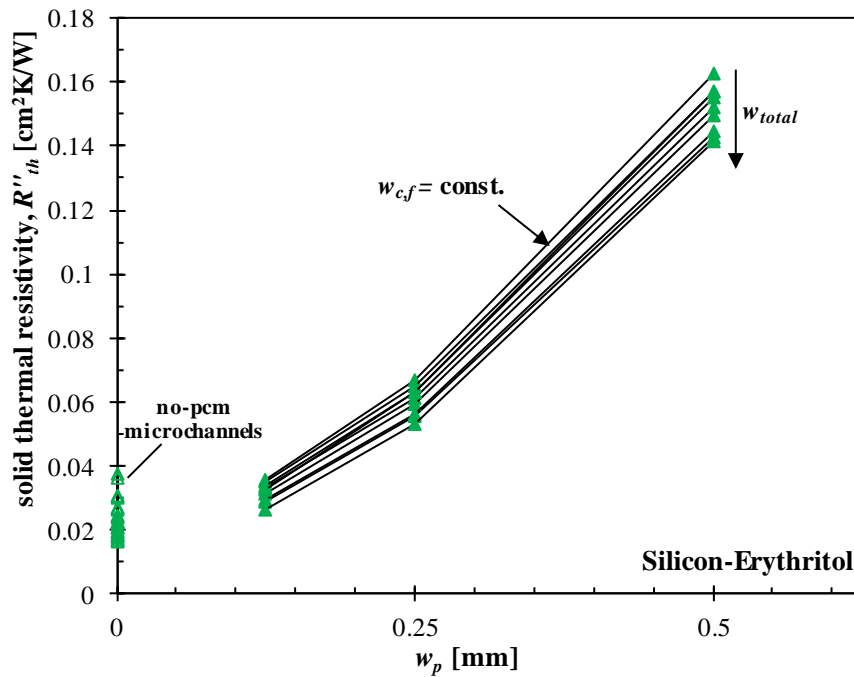


Figure 6.24 – Silicon TBHS normalized thermal resistivity showing PCM volume the primary impact on degrading steady-state thermal performance.

The microchannel cooler fin effects can be examined in more detail to gain some insight in to thermal efficiency of the design. The equivalent fin efficiency of the different designs as calculated using (118) is shown in Figure 6.25, again compared with the equivalent no-PCM microchannels. It is generally considered good practice to maintain a fin efficiency above 90%, as lower values indicate that the fins are longer than necessary as additional length provides diminishing incremental heat removal [271]. Values too high indicate that the fins might be too short and heat removal is being impaired. The figure shows all fin, PCM, and cooling channel widths, but the fin efficiency is almost completely governed by fin width (used then as the primary display variable). Thus, except for the thinnest fins with the highest convection rates, the fins are rather ‘short’ for the conditions used in the analysis, and overall performance would improve with longer/thinner fins.

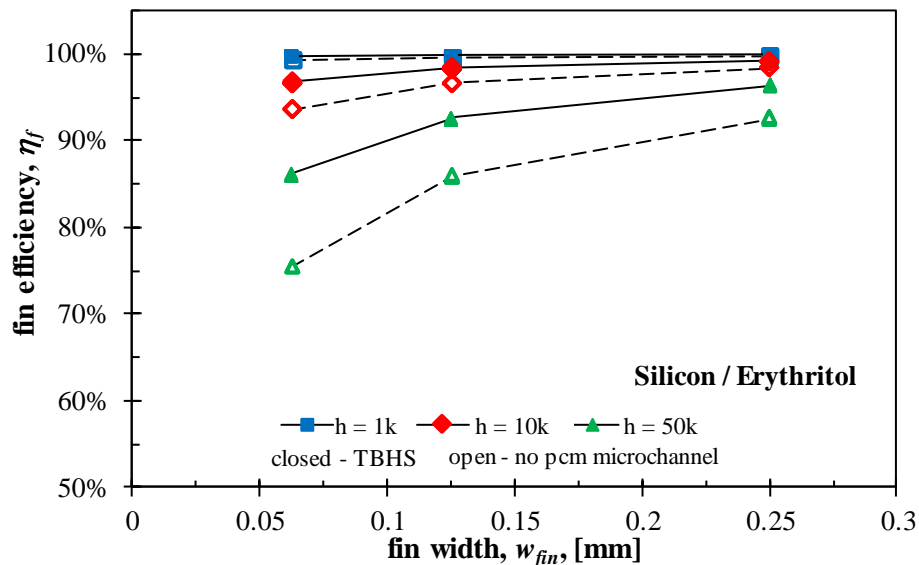


Figure 6.25 – Fin efficiency estimates for all silicon TBHS and standard microchannel (non-PCM) heat sink configurations showing that the short, substrate-thickness channels are shorter than ideal for all but the highest convective rates.

Additionally, there is clearly an increase in fin efficiency for the PCM-loaded channels, again related to the previous observation that the PCM-loaded channels effectively create doubly wide fins with an insulating core. The reduced area for heat removal per fin increases the fin temperature and the resulting fin efficiency. While not overly surprising, the fin efficiency results do agree with the substrate integrated cooling results discussed in Section 4.4. The wafer-thickness severely limits the fin length, and the amount of heat removal, for all but the highest convection rates.

6.3.5.2. *Step-response – linear transient models*

Again a unit heat input was applied to the substrates to examine the linear step response below the melting temperature. Fitting the resulting step response curves to (119), a dominant time constant, τ_{th} , was extracted for all configurations as shown in Figure 6.26. Similar to the thermal resistivity graph, it is immediately clear that the addition of the PCM creates a much higher thermal time constant relative to the equivalent no-PCM microchannel substrates. Even without phase change, the PCM substrates respond from 1-8.6x slower, almost in direct proportion to the PCM fraction. Recalling that the average thermal time constant can be estimated as $\tau_{th} = R_{th}C_{th}$, the increased R_{th} shown in Figure 6.23 leaves a factor of only about 1-2x effective increase in C_{th} . This is in line with the increased $c_{p,pcm}$ being about double $c_{p,Si}$.

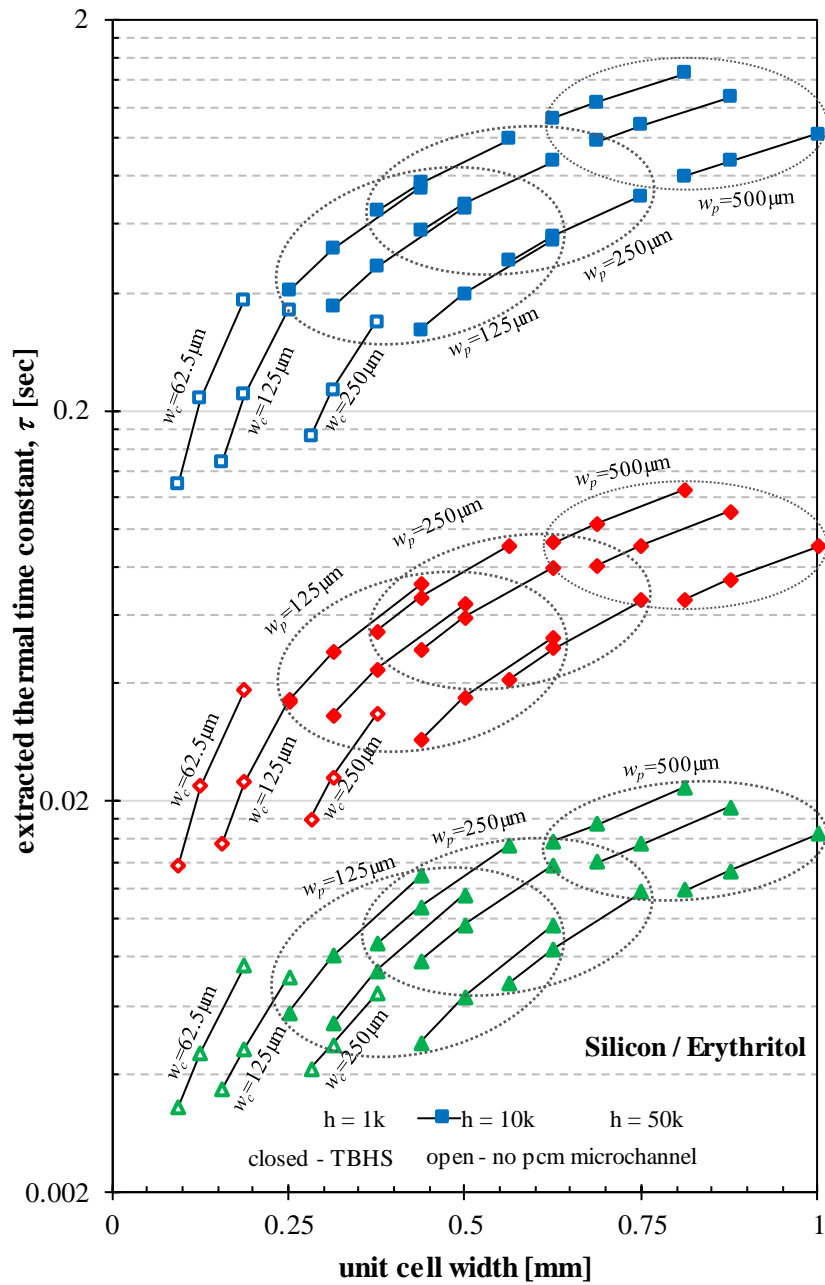


Figure 6.26 – Extracted thermal time constants for each silicon TBHS configuration at varying convective rates comparing the PCM substrates to no-PCM microchannel substrates. PCM substrate groupings by w_p are indicated by the dashed ovals.

As the thermal time constants again appear dominated by the convective thermal resistance, we can again look at the solid contribution of the thermal time constants

according to (121). While not collapsing the data to a single band as it did with thermal resistance, Figure 6.27 does emphasize how the addition of PCM to the substrates generally increases the thermal time constant in proportion to PCM volume, although there is significant variation of that impact at different convection rates. This even includes a few configurations showing lower solid thermal time constants than the microchannel cases for the highest convection rate. As this variation was not seen in the thermal resistance data we can assume that it is related to variation in the effective thermal capacity of each configuration. As such we see that the PCM addition increases $\tau_{th,s}$ by a factor of 0.9-8.5x for $h = 1 \text{ kW/m}^2\text{K}$, but by only about 0.6-4.6x for $h = 50 \text{ kW/m}^2\text{K}$.

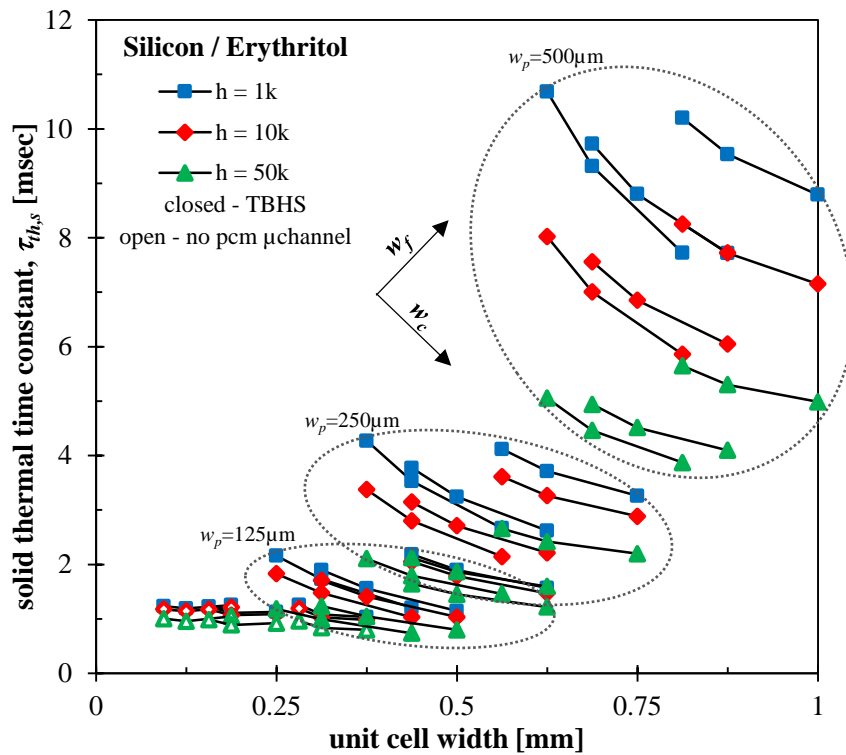


Figure 6.27 – Estimated solid contribution to silicon TBHS thermal time constant for each configuration at varying convective rates and comparing the PCM substrates to no-PCM microchannel substrates. PCM substrate groupings by w_p are indicated by the dashed ovals.

Calculated values of effective thermal capacity are shown in Figure 6.28, and they elucidate some of the aforementioned anomalous time constant values. Figure 6.28(a) shows the extracted thermal capacitance for all configurations and convection rates including the no-PCM microchannel substrates. It is evident from this figure that the addition of a PCM to the substrate provides little to no increase, and in some cases actually a decrease, in effective thermal capacity. (Case to case comparisons range from a 0.5-1.6x change, but relative to the microchannel substrate with highest C_{th} the TBHS capacitances are only 0.3-0.9x.) These counterintuitive values can be explained by a combination of two-dimensional heat spreading and disparate material properties. The thermal conductivities of the substrate and PCM differ by two orders of magnitude, limiting the ability of heat to spread into the PCM and utilize the full capacitive volume. While the specific heat capacity of solid erythritol is almost twice that of silicon, the volumetric heat capacities ($\rho \times c_p$) only differ by 25%. Replacing substrate volume by PCM volume (per unit heated surface area) has less of a linear heat capacity impact than might otherwise be expected. As emphasized by Figure 6.28(b), which shows only the high convection case, increased fin material (w_f) and decreased convection volume (w_c) have significantly more impact on C_{th} than additional PCM volume, as they both increase substrate material per unit area. (While this is highlighted in (b) for the high h case, the same groupings/trends exist in the low and medium case).

More interesting, however, we see in Figure 6.28(a), and highlighted specifically by the same data with group overlays in Figure 6.29, is that there is actually a convection rate inversion on the effect of additional PCM volume on effective capacitance. Whereas the low convection case still shows that increasing PCM volume slightly increases effective

capacitance per unit area, doing so with the medium and high convection rates actually decreases net capacity as the PCM insulates more of the solid fin material from the heat path. This shows how the effective thermal capacity is more affected by relative thermal impedance paths in the structure than by material addition.

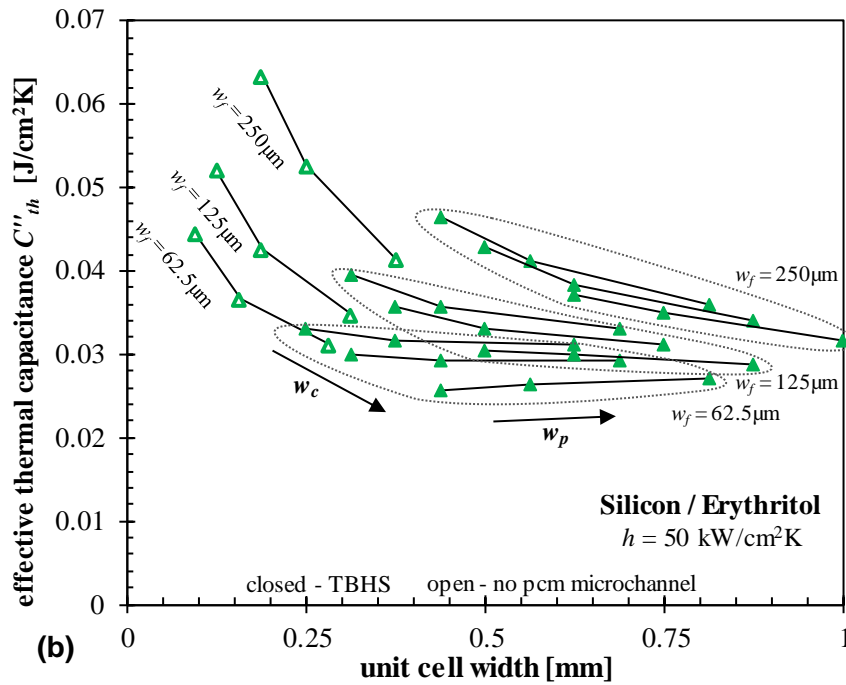
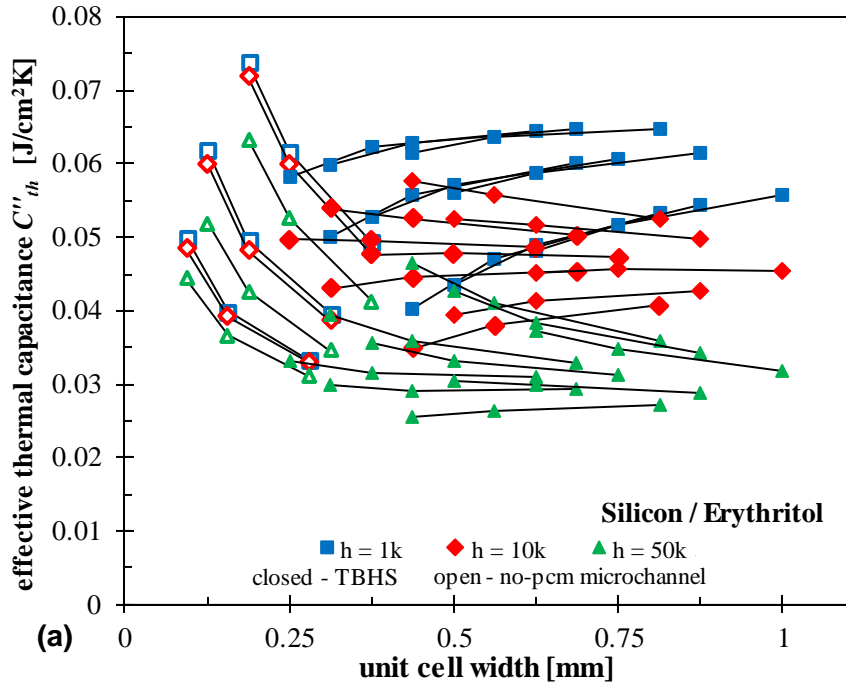


Figure 6.28 – Estimated effective thermal capacitance for each configuration at (a) all convective rates and (b) just 50kW/m²K compared to no-PCM microchannel substrates. PCM substrate groupings by w_f are indicated by the dashed ovals, and the lines represent constant values of w_c .

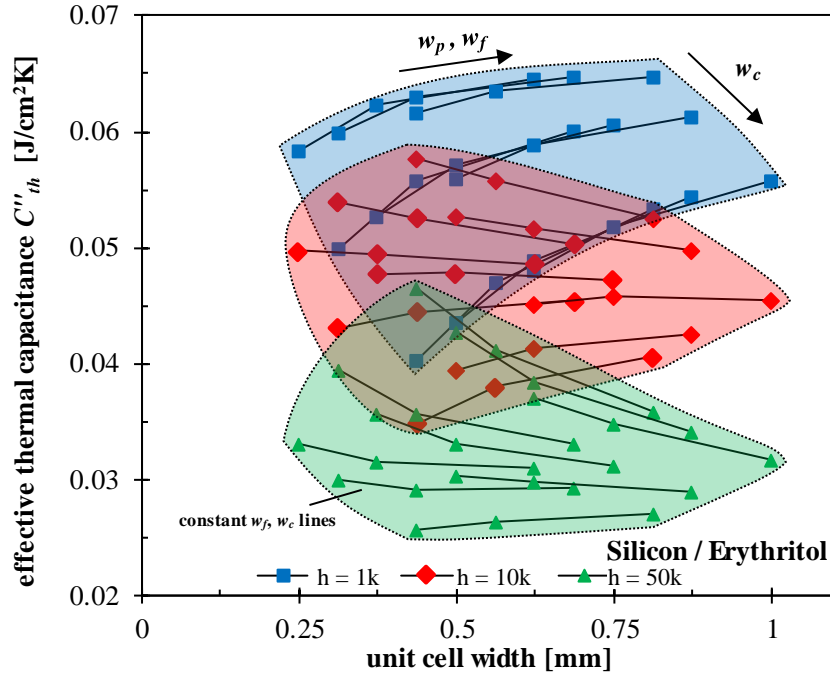


Figure 6.29 –Effective thermal capacitance emphasizing convective dependence of PCM impact for each configuration.

Even without phase change heat absorption, a higher thermal time constant can slow temperature response resulting in PCM substrates having less temperature rise for short transient conditions despite higher steady temperatures. Figure 6.30 provides an aggregate comparison of these thermal substrate figures of merit for all configurations. (a) emphasizes what was mentioned above, namely that there is little net thermal capacity benefit from additional PCM, while thermal resistivity can increase by a factor of up to 8.6x. This resistance increase is then the driving component of the increased thermal time constant, as shown in (b), which is up to 8.5x higher than no-PCM cases. Not surprisingly, the highest C_{th} and τ_{th} cases for both microchannels and TBHS occur as indicated when w_f is maximum and w_c is minimum, producing the configuration with maximum substrate material per unit area.

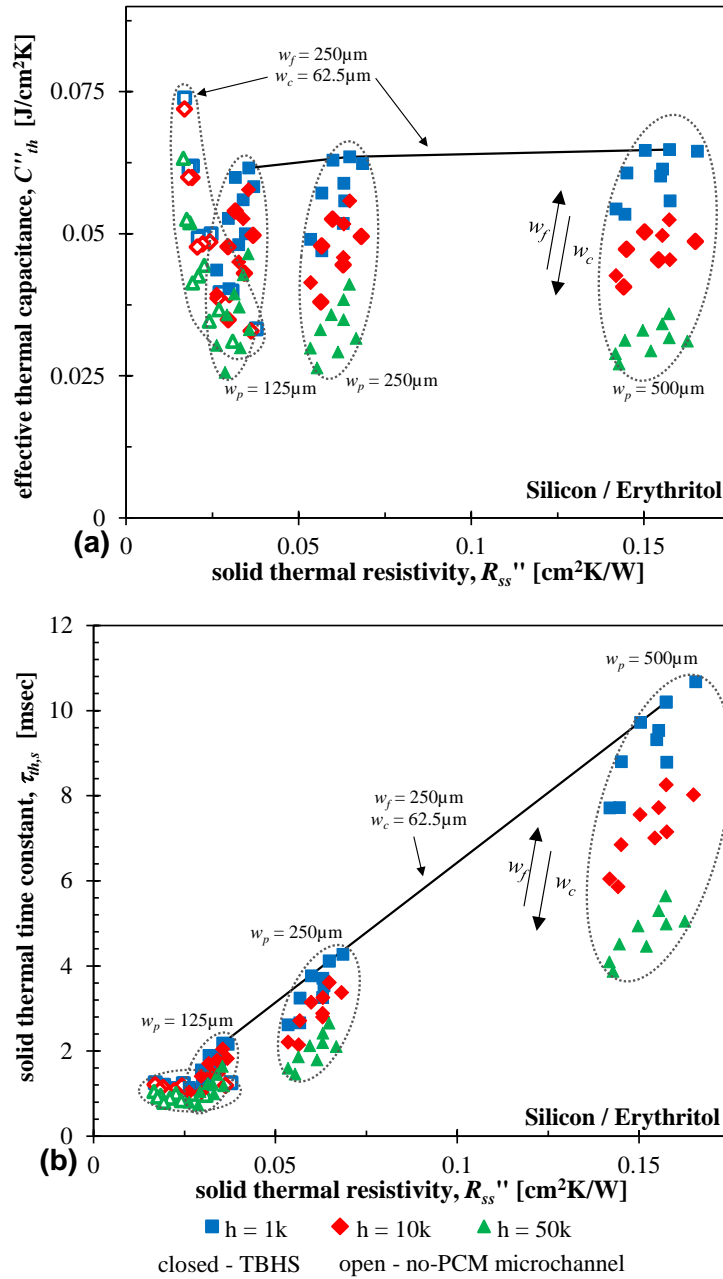


Figure 6.30 – Linear silicon TBHS figure of merit comparisons evaluating the impact on thermal resistance, time constant, and effective capacitance for each configuration. Highlighted is the case with maximum capacitance and time constant, where fin width (w_f) is maximum and convective area (w_c) is minimized for all PCM widths (w_p).

Table 6.9 provides a view of the linear thermal behavior changes created by the substrate integrated PCM. Recalling the initial problem identified in the electronic packages: decreased thermal resistance, while itself desired, resulted in decreased thermal capacity and time constants. Thus addition of a PCM would ideally increase thermal time constant through increased capacity by trading off some, but not too much, thermal resistance. The table shows that without phase change, this was generally not the case. Additional thermal resistance was substantial, no less than about 1.55x for solid resistance or 2.35x for total resistance. This did produce a general thermal time constant increase, but by replacing substrate material with low conductivity PCM, effective thermal capacitance was actually diminished. In a few cases, it actually diminished sufficiently to decrease thermal time constant, as seen by the minimum values in the Table. However, in no case did PCM addition create a net increase in unit cell capacitance over the best microchannel substrate. Absent any phase change benefit the resistance-driven thermal time constant increase runs counter to the original design intent.

Table 6.9 – Silicon TBHS linear thermal performance ratios

h [kW/m ² K]	$R_{th} / R_{th,mc,min}$				$\tau_{th} / \tau_{th,mc,max}$				$C_{th} / C_{th,mc,max}$	
	total (R_{th})		solid ($R_{th,s}$)		total (τ_{th})		solid ($\tau_{th,s}$)		<i>min</i>	<i>max</i>
	<i>min</i>	<i>max</i>	<i>min</i>	<i>max</i>	<i>min</i>	<i>max</i>	<i>min</i>	<i>max</i>		
1	2.66	8.64	1.55	9.76	0.84	3.82	0.91	8.51	0.55	0.88
10	2.57	8.48	1.56	9.77	0.75	3.27	0.85	6.79	0.48	0.80
50	2.34	8.15	1.59	9.82	0.63	2.86	0.70	5.39	0.40	0.73

6.3.5.3. Phase change thermal suppression results

Melting simulations were performed for each configuration and convection rate at different heat flux levels. These levels were determined by calculating the minimum melting heat flux for each configuration from the steady-state thermal resistivity values

using (123). The resulting values of q''_m are shown in Figure 6.31, which like thermal resistance are primarily influenced by convection rate and PCM content. These heat flux values represent the minimum heat flux for the substrate to reach T_M , and even at that heat flux there will be a lengthy time delay before melting. That delay may impact the shortest transient time that can be buffered by the heat sink since nonlinear heat absorption cannot occur any earlier, making it an important design factor for a functional TBHS. Low, medium, and high heat flux values for the melting simulations were selected such that they exceeded the calculated q''_m values for each convection rate by about 3-4x, as shown in Table 6.10. That resulted in a 5 parameter, three level simulation space (geometry, convection rate, and power) involving 243 configurations. Transient step response curves were generated for these configurations as well as for the equivalent microchannel models, involving an additional 81 configurations for simulation. Finally, each simulation was run for a total of 60 time steps, and the length of each time step (also shown in Table 6.10) was chosen such that the total simulation time would allow all linear response comparison models to reach steady-state.

Table 6.10 – TBHS melting model heat fluxes and time steps

h [kW/m ² K]	max q''_m [W/cm ²]	q'' [W/cm ²]	Δt [ms]	t_{tot} [ms]
1	2.6	10, 20, 30	7.5	450
10	25.0	100, 200, 300	1.875	112.5
50	106.1	300, 600, 900	0.625	37.5

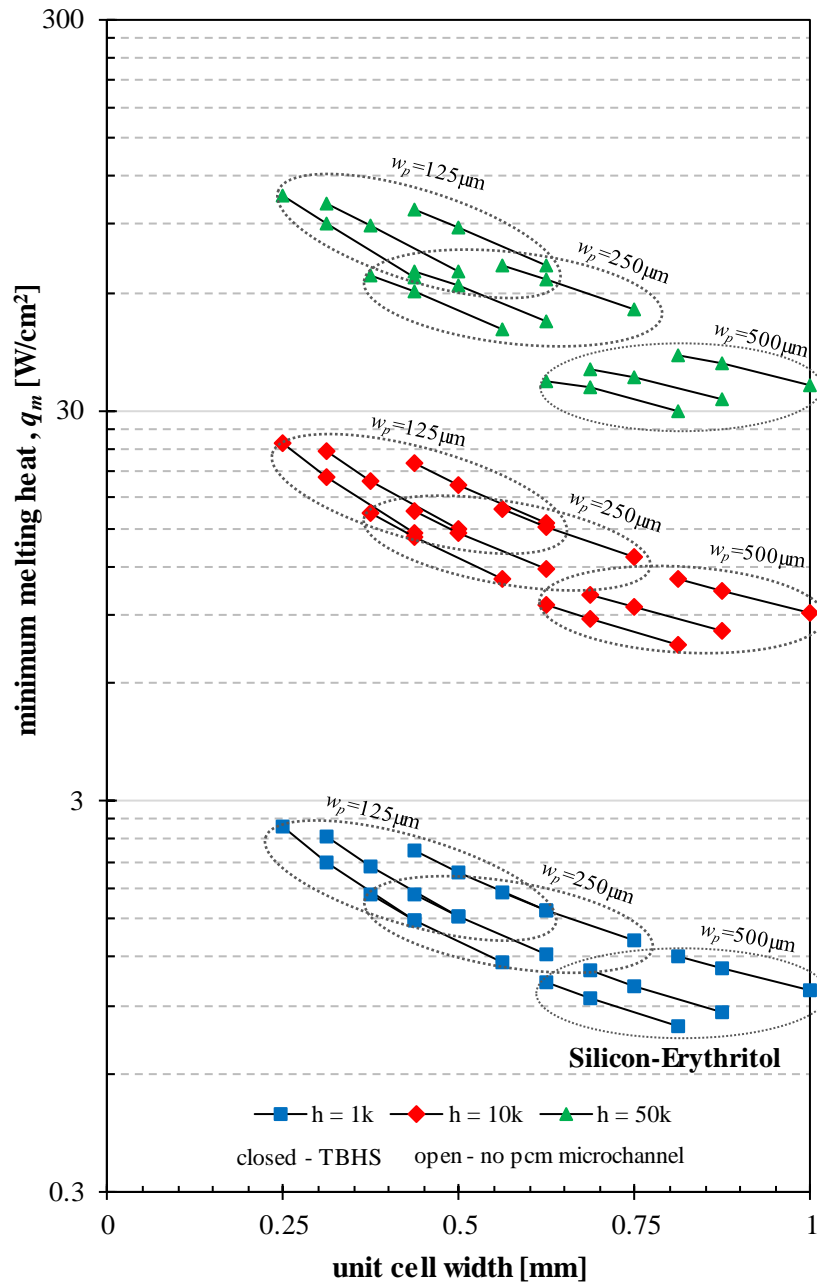


Figure 6.31 – Extracted threshold melting heat flux values for each silicon TBHS configuration at varying convective rates.

Step response melting simulations were run for each configuration, with simulation numerical convergence primarily handled through the automatic adaptive mesh refinement where each time step was required to achieve a relative local element flux error of less than

0.01%. This data, along with the dominant single time constant model and melting threshold heat flux values, lets us examine the degree of fitness of this single time constant melting estimate. Melting delay and applied heat flux, normalized by thermal time constant and minimum melting heat, respectively, are shown for all simulations in Figure 6.32 along with the simple exponential analytical model. Despite increasing scatter at higher heat fluxes, the data does show the predictive design utility of a dominant time constant model. The scatter is most likely attributable to the discrete time stepping in the model missing the exact onset of melting, especially in the high heat flux cases with rapidly changing thermal gradients. Earlier melting onset could also result from the limitation of a single time constant model for a multi-component substrate, especially with the same change in heat spreading with convection rate described for time constant and thermal capacitance.

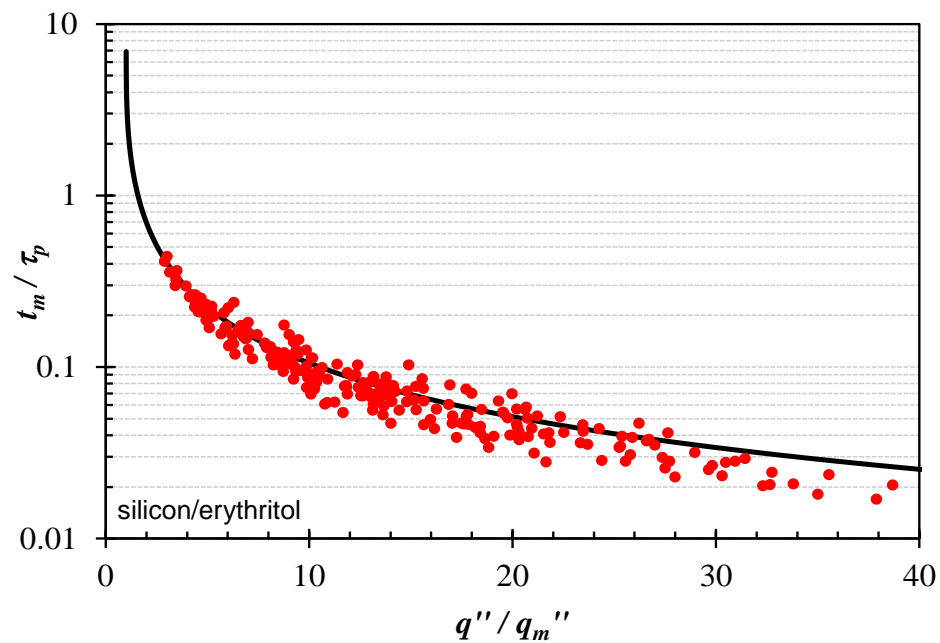


Figure 6.32 – Silicon TBHS simulated melting delay compared to the single-pole melting delay model (solid line)

Figure 6.33 shows a temperature map of a representative silicon TBHS two thirds of the way through the melting simulation ($w_p = 125 \mu\text{m}$, $w_f = 62.5 \mu\text{m}$, $w_c = 125 \mu\text{m}$, $h = 1 \text{ kW/m}^2\text{K}$, $q'' = 30 \text{ W/cm}^2$, $t = 300 \text{ ms}$). In Figure 6.33(a) the full temperature profile is shown, and the large thermal gradient across the melted portion of the PCM can be clearly seen. In (b) the temperature range is restricted to the mushy zone temperature span ($118 \pm 0.5^\circ\text{C}$) to highlight the approximate location of the melt front. The PCM's low thermal conductivity significantly degrades thermal heat absorption as time progresses and the thermal gradient between substrate and melt front grows.

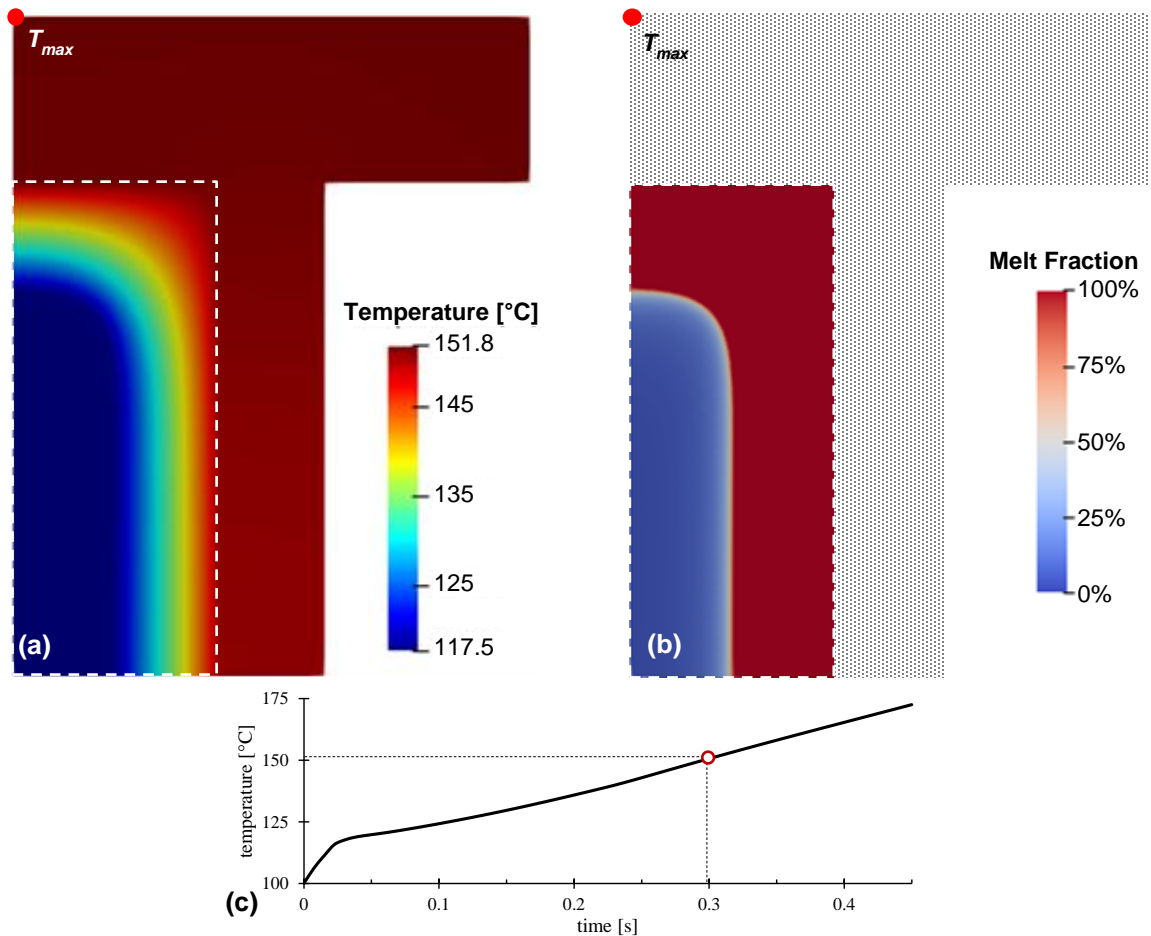


Figure 6.33 – Transient melting temperature map in a representative silicon TBHS subject to a 30 W/cm^2 heat load with a $1 \text{ kW/m}^2\text{K}$ cooling at $T_0 = 100^\circ\text{C}$, with PCM region indicated by the dashed line. (a) shows the temperature profile throughout the TBHS, (b) shows melt fraction and ‘mushy zone’ around phase front spanning $118 \pm 0.5^\circ\text{C}$, (c) shows the maximum temperature profile.

Transient melting profiles showed the widely varying degree of temperature suppression provided by the many different PCM-substrate configurations. Figure 6.34 shows step response melting curves for two representative design cases: the ‘best performing’ design providing the largest degree of temperature suppression, and the maximum substrate material configuration identified as the best linear response in Section 6.3.5.2. Each plot in Figure 6.34 shows transient temperature rise for low, medium,

and high power levels for three comparison cases: the TBHS melting model (solid lines), TBHS without melting (dotted lines), and the ‘best’ no-PCM microchannel substrate (dashed lines), which also turned out to be the minimum geometry (small w_f and w_c) configuration. The no-phase-change profiles allow us to clearly separate the impact of sensible thermal capacity change from the PCM latent heat absorption, as deviation between the dotted and solid lines would be due only to phase change and any subsequent liquid state differences, while the no-PCM microchannel substrate comparison allows us to determine how much of a transient benefit the TBHS is actually providing relative to the type of microcooler it would be replacing.

Figure 6.34(a-c) shows transient temperature profiles for the best performing configuration, which also turned out to be the minimum geometry configuration ($w_p = 125 \mu\text{m}$, $w_f = 62.5 \mu\text{m}$, $w_c = 62.5 \mu\text{m}$) just as with the microchannel case. (d-f) shows the maximum substrate material configuration ($w_p = 125 \mu\text{m}$, $w_f = 250 \mu\text{m}$, $w_c = 62.5 \mu\text{m}$), which was expected to provide the best non-phase changing performance in the linear analysis.

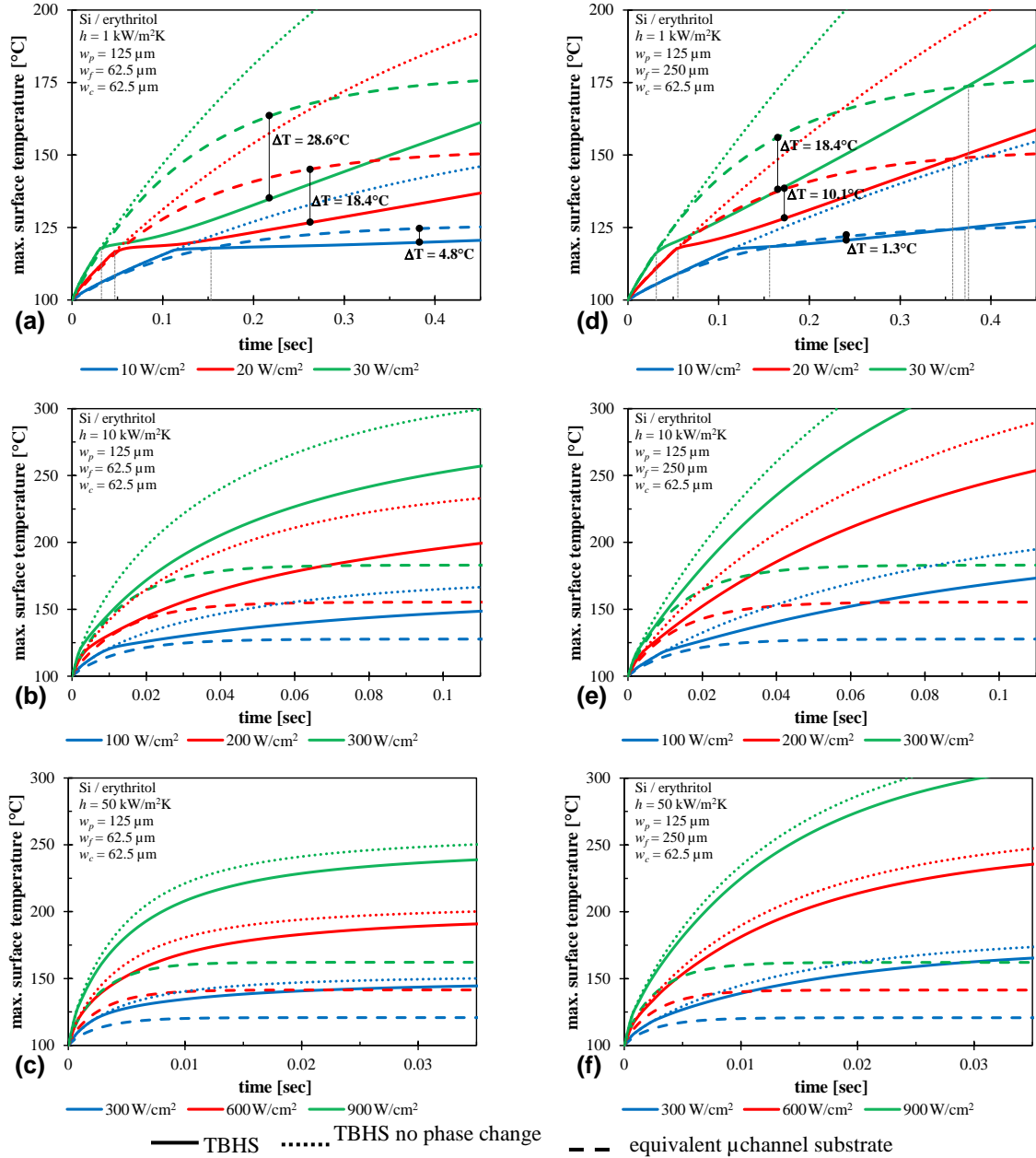


Figure 6.34 – Representative silicon TBHS melting temperature profiles for the two best performing thermal suppression configurations. (a-c) is the minimum geometry parameter case while (d-f) is the best linear response case. Each is shown for the three convection rates and power levels, with comparisons between the melting, non-melting, and microchannel substrate models.

All six plots in Figure 6.34 show that latent heat absorption provides some temperature suppression at all conditions relative to sensible heating alone (solid lines vs

dotted lines), but this effect disappears with increased convection rate. Just as with the linear thermal capacitance, in a parallel configuration the relative impedance of the convective heat path reduces the net benefit provided by the PCM, and the fixed total energy absorption of the PCM becomes less significant relative to the energy moving through the device at higher heat fluxes.

More importantly, the impact of the PCM addition relative to equivalent microchannel cooling is shown to be significant only for low convection rates. Both configurations show some degree of temperature suppression ($T_{sup} = T_{TBHS,max} - T_{mc,max}$) for a finite period of time at $h = 1\text{W/m}^2\text{K}$. The minimum geometry case shows the largest T_{sup} of all the configurations in Figure 6.34(a), and these values are summarized in Table 6.11 below. The contrasting configuration in (b), with maximum solid substrate material (max w_f), also provides notable temperature reduction, but much less so and for a shorter amount of time. (b) shows a much higher transient temperature rise than (a) during phase change due to the steeper temperature-time slope during melting. Despite the two configurations having the same PCM volume, the hotspot in configuration (b) is much farther removed from the coolant, resulting in a larger thermal gradient over time as the initial melting phase front moves farther away from the heat source. For a similar reason, it is no surprise that the two best configurations had minimum PCM volume, as the low thermal conductivity material quickly limits heat flux through the melted layer into the rest of the material, and additional PCM would provide little benefit at a significant thermal resistance cost.

Table 6.11 – Silicon TBHS best performance temperature suppression values

q'' [W/cm ²]	steady state		phase change					
	$\Delta T_{ss,mc}$ [°C]	$\Delta T_{ss,TBHS}$ [°C]	$t_{\Delta T_{sup,onset}}$ [ms]	$t_{\Delta T_{sup,max}}$ [ms]	ΔT_{mc} [°C]	ΔT_{TBHS} [°C]	$\frac{\Delta T_{max.sup}}{T_{mc}}$	$\frac{\Delta T_{max.sup}}{\Delta T_{mc}}$
10	126.1	169.3	150.9	382.5	24.7	19.9	3.8%	19.4%
20	152.2	238.7	51.6	262.5	45.1	19.6	12.7%	40.8%
30	178.3	308.0	33.6	217.5	63.4	20.0	28.6%	45.2%

Table 6.11 shows that the best silicon TBHS configuration was able to provide about 45% temperature suppression relative to the best performing microchannel substrate subjected to the same parameter constraints (28% of absolute temperature), and that this suppression occurs starting around 30 ms, with maximum suppression around 217 ms (lower powers exhibiting longer delays). That time provides an approximate optimal pulse width for this particular design, as both shorter and longer thermal pulses would see less benefit. The duration of thermal suppression did exceed the simulation time for that configuration, though, so for low convection rates it appears that even a low k_{th} PCM can make a worthwhile difference in device temperature rise for several hundred milliseconds. At elevated convection rates, however, it appears the thermal resistance penalty is enough to eliminate any thermal benefit of using this design. This underlines the need to match any thermal buffer solution to application specific conditions and thermal time constants.

Looking at the aggregate temperature suppression of all silicon TBHS configurations reinforces the concern that this design lacks general utility. Figure 6.35 summarizes the aggregate absolute and relative temperature suppression over the best case non-PCM microchannel substrate. The lack of any measurable thermal suppression for the medium and high convection rates, and the diminishing performance with increased PCM volume reaffirms the notion that low thermal conductivity PCM addition to the substrate

cannot on its own provide a general tool for pulsed electronics thermal buffering. At least for this material combination, the PCM is simply too low thermal conductivity to promote good utilization of the entire material volume without significant thermal resistance separating the phase front from the heat source. Note that there should be a smaller PCM volume where the thermal suppression begins to reduce due to full melting and the design approaches the zero w_p limit of the microchannel substrates. It may be that some value in that range would optimize both thermal resistance and phase change absorption for this material combination.

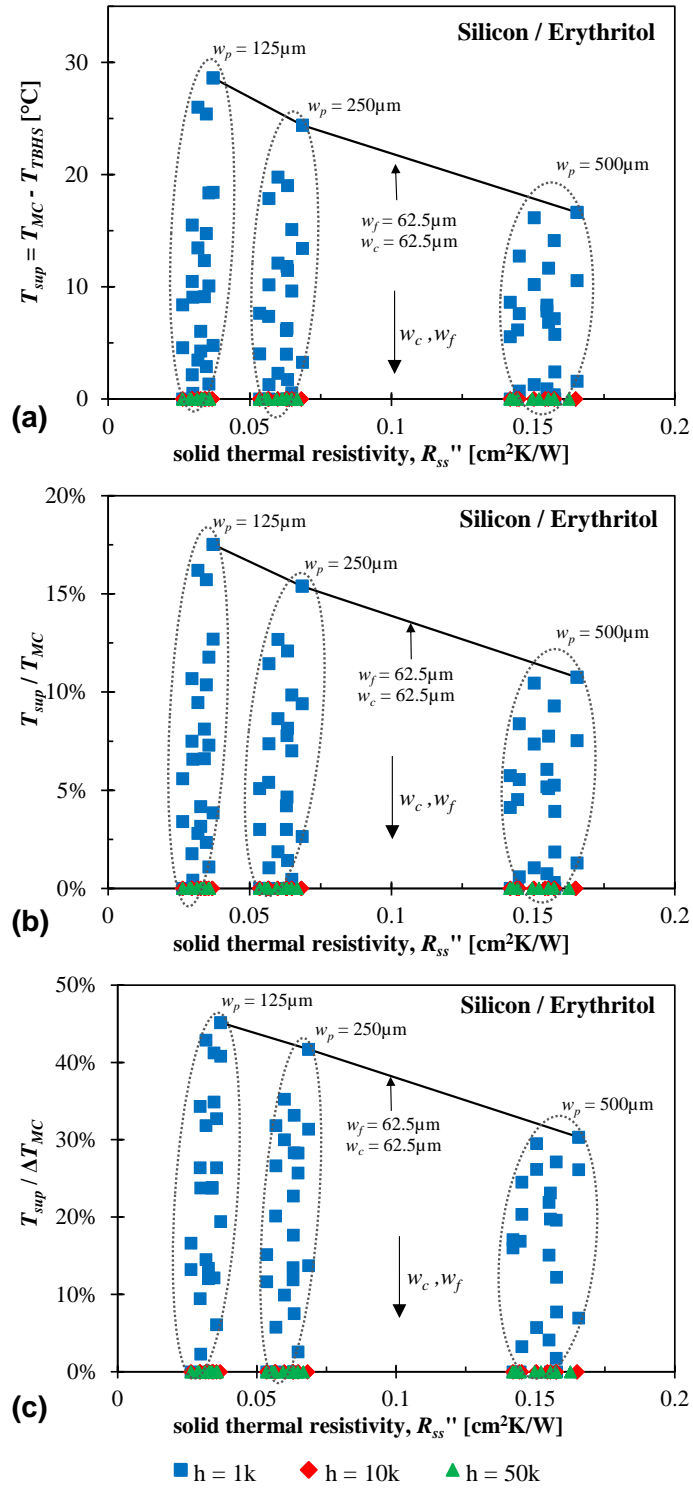


Figure 6.35 – Aggregate (a) absolute and (b,c) microchannel relative silicon-erythritol TBHS temperature suppression relative to the best performing microchannel substrates under equivalent conditions.

6.3.6. TBHS alternative materials study

As mentioned in the previous section, the silicon-erythritol substrate integrated TBHS provided less than ideal thermal performance. The additional thermal resistance was significant with minimal linear capacitive benefit, and the latent benefit was significant, but only for low convection rates. Separately, the silicon substrate material was also found to be non-ideal, showing significant brittle mechanical failure as a PCM package in preliminary prototyping, detailed in Appendix C. As such, this section looks at the benefit of using the same AlN ceramic substrates used for microchannel cooling in Chapter 4 while also expanding the PCM choices to several other material classes. The PCMs compared here are again erythritol, and also gallium and lithium nitrate trihydrate (LNT), both lower temperature metallic and salt hydrate materials. While these materials do have a much lower melting temperature, they were each identified as likely candidate power electronics thermal buffer materials with high volumetric heats of fusion within 10% of that of erythritol. (It is understood that pure gallium has reaction and compatibility concerns with many materials including aluminum, however that material is still included here due to its material data and properties lending to useful comparison with LNT). AlN also has a higher thermal conductivity than silicon, with a higher density and similar specific heat, which may reduce thermal charging resistance and provide more structural capacity. Material properties for this second simulation study are given in Table 6.19.

Table 6.12 – Thermal properties used in AlN TBHS model

property	unit	aluminum nitride	erythritol	lithium nitrate trihydrate	gallium
<i>type</i>	--	ceramic	sugar alcohol	salt hydrate	pure metal
k_{th}	W/mK	180	0.733 (<i>s</i>), 0.326 (<i>l</i>)	0.770 (<i>s</i>), 0.575 (<i>l</i>)	33.7 (<i>s</i>), 29.4 (<i>l</i>)
c_p	kJ/kgK	0.736	1.383 (<i>s</i>), 2.765 (<i>l</i>)	1.8 (<i>s</i>), 2.8 (<i>l</i>)	0.340 (<i>s</i>), 0.384 (<i>l</i>)
ρ	kg/m ³	3330	1480 (<i>s</i>), 1300 (<i>l</i>)	1567.5 (<i>s</i>), 1401 (<i>l</i>)	5905 (<i>s</i>), 6093 (<i>l</i>)
H_f	kJ/kg	--	339.8	291.5	80.2
$H_{f,v}$	MJ/m ³	--	502.9	456.9	473.6
T_M	°C	--	118	30	30

Layout, boundary conditions, and loading conditions of the AlN TBHS are the same as for the silicon study. Geometric parameters are also the same except for the solid portion of the substrate thickness. The previous AlN substrate coolers had 300 μm of uncut material to maintain structural integrity during the diamond saw channel fabrication. Assuming that this restriction would still be present in addition to the need for sufficient material to withstand the PCM expansion pressures, the designs were evaluated at both $d = 100$ and 300 μm using a fixed fin length, L , of 300 μm . The computational domain unit cell geometry is repeated in Figure 6.36, and the complete geometric parameter set for this material study is given in Table 6.13.

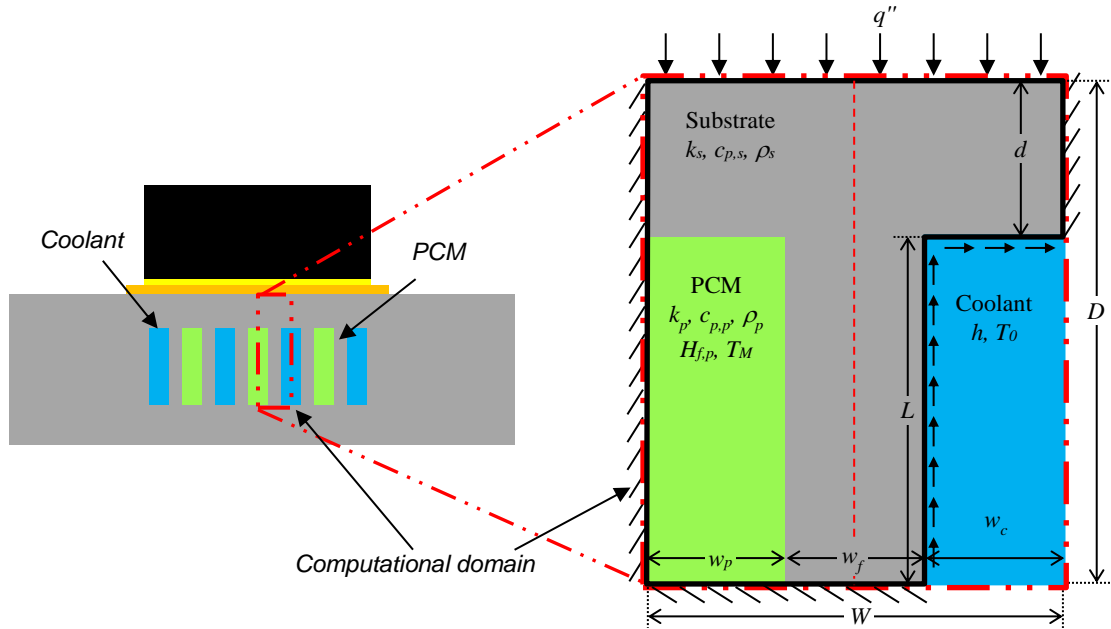


Figure 6.36 – Substrate integrated TBHS computational domain (repeated).

Table 6.13 – AlN TBHS simulation dimensions and parameter ranges

D	400, 600 μm	W	Σw_i
d	100, 300 μm	w_p	125, 250, 500 μm
L	300 μm	w_f	62.5, 125, 250 μm
		w_c	62.5, 125, 250 μm

The same simulations and evaluations performed for the silicon substrate integrated TBHS were repeated for the materials, geometries, and conditions above. Steady-state, transient linear, and transient melting performance characteristics were evaluated and compared against equivalent microchannel coolers.

6.3.6.1. Steady-state results

Unit input heat flux simulations produced the steady-state unit cell thermal resistivity values shown in Figure 6.37. Just as with the silicon substrates, the resistivity is primarily dictated by the convection rate with PCM volume being the largest secondary

factor. The thermal conductivity of both erythritol and LNT are low enough that the resistivities of both are nearly identical, with the differences being indistinguishable on the scale used in Figure 6.37(a), even at the higher convection rates. Additionally, the thicker substrate creates no noticeable difference in total thermal resistance until the convection rate gets up to $50\text{kW/m}^2\text{K}$ (shown by dashed lines). There a difference can also be seen between the erythritol and LNT resistances in (a) and the gallium substrate resistances in (b), where the higher thermal conductivity metallic PCM appears to slightly decrease total resistance as well as reduce the difference between the two substrate thicknesses.

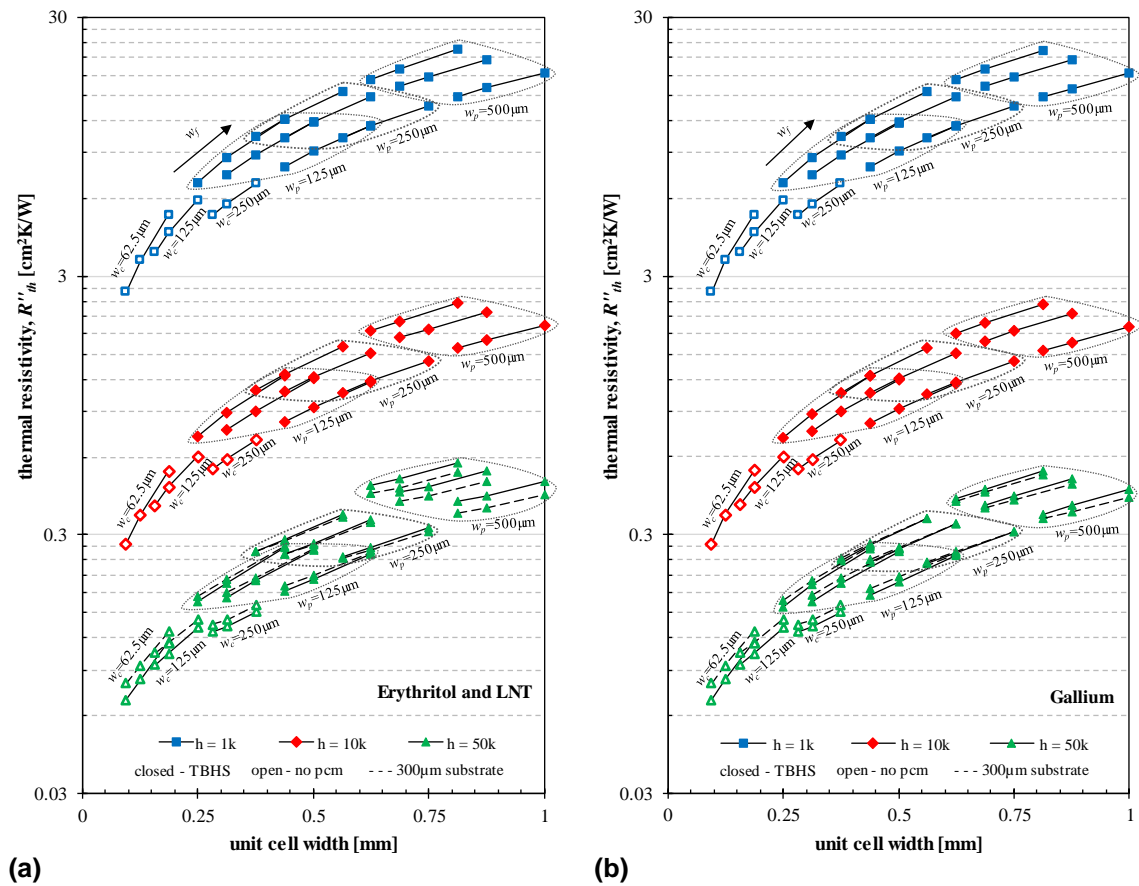


Figure 6.37 – Steady-state thermal resistivity results for the AlN TBHS with (a) erythritol and LNT, and (b) gallium compared to equivalent microchannel heat sinks.

Noting as with the silicon substrates that the solid resistivity contribution can be compared by subtracting out the convective resistance component, Figure 6.38 shows the resistivities collapsed down to single bands. As before, these plots emphasize the fact that the PCM volume (w_p) is the primary contributing parameter to solid thermal resistivity. The impact of the metallic PCM is more clearly evident here, though, as the increase in resistance is almost halved for gallium relative to the low conductivity materials. Of additional interest is the effect of the thicker substrate for all materials. At low values of w_p , the thicker substrate results in higher thermal resistivity as expected. However with increasing w_p comes a crossover where the thinner substrate produces a higher thermal resistivity. This is much more significant for erythritol and LNT than gallium, indicating that the heat spreading resistance in the substrate above the PCM is a primary thermal bottleneck. Thicker substrate material allows that heat to flow with less constriction to the convection region, and the low conductivity PCMs having k_{th} values $\sim 240x$ lower than the substrate make them act effectively as thermal insulators under the hotspots. With the metallic PCM, the thermal conductivity is only a factor of ~ 6 less than the AlN, so the penalty is less and the PCM can contribute to the heat spreading.

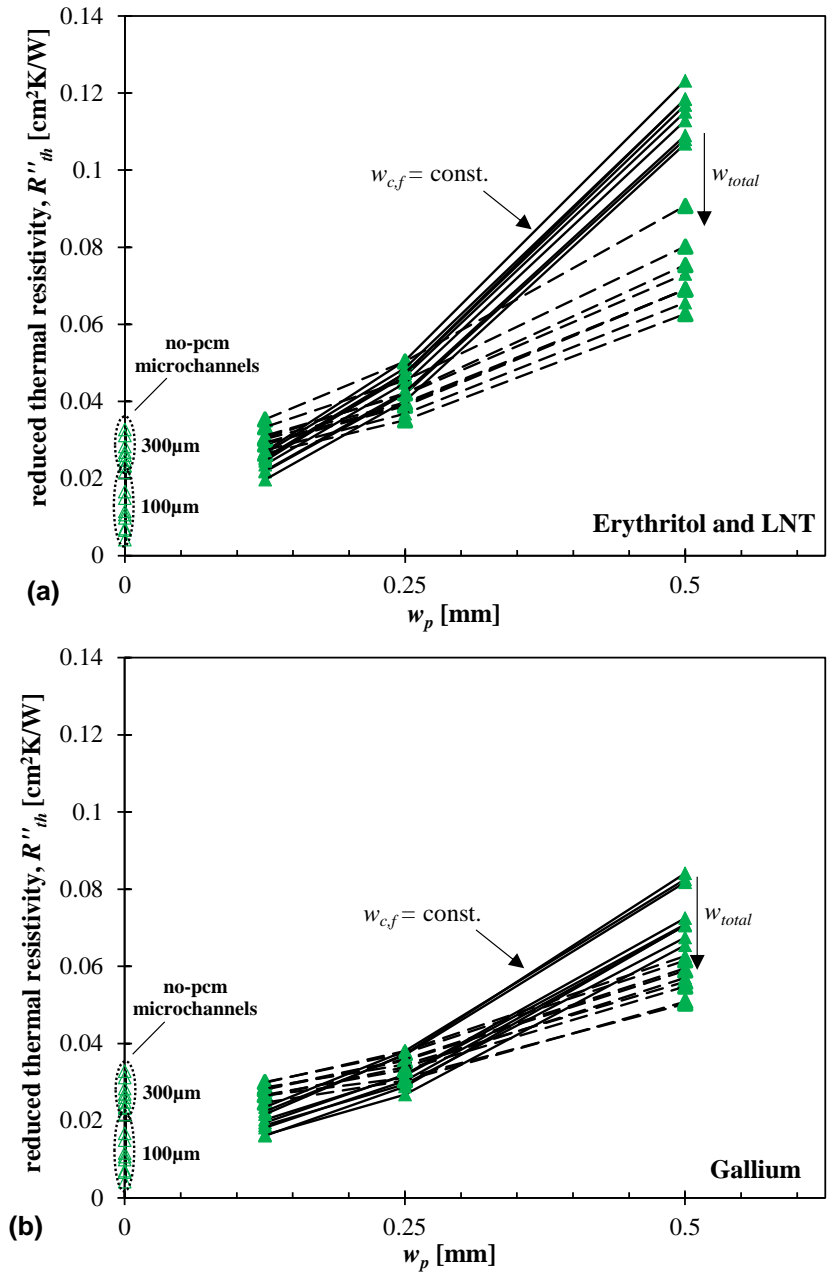


Figure 6.38 – AIN TBHS normalized thermal resistivity values for (a) erythritol and LNT and (b) gallium PCM, for both thin and thick substrates.

Another point emphasizing the heat spreading factor provided by the gallium PCM can be seen in the fin efficiency plots shown in Figure 6.39. Again, the erythritol and LNT characteristics are indistinguishable, this time for all configurations with only fin width

(w_f) affecting the efficiency for any particular geometry and convection rate. Contrasted with this is the fin efficiency in the gallium substrates, where the additional heat spreading makes PCM volume (w_p) a significant secondary factor, especially for the higher convection rate. Comparing the values for those high h cases, gallium PCM results in higher fin efficiencies than the other two materials, indicating that heat is being better conducted to the end of the fin.

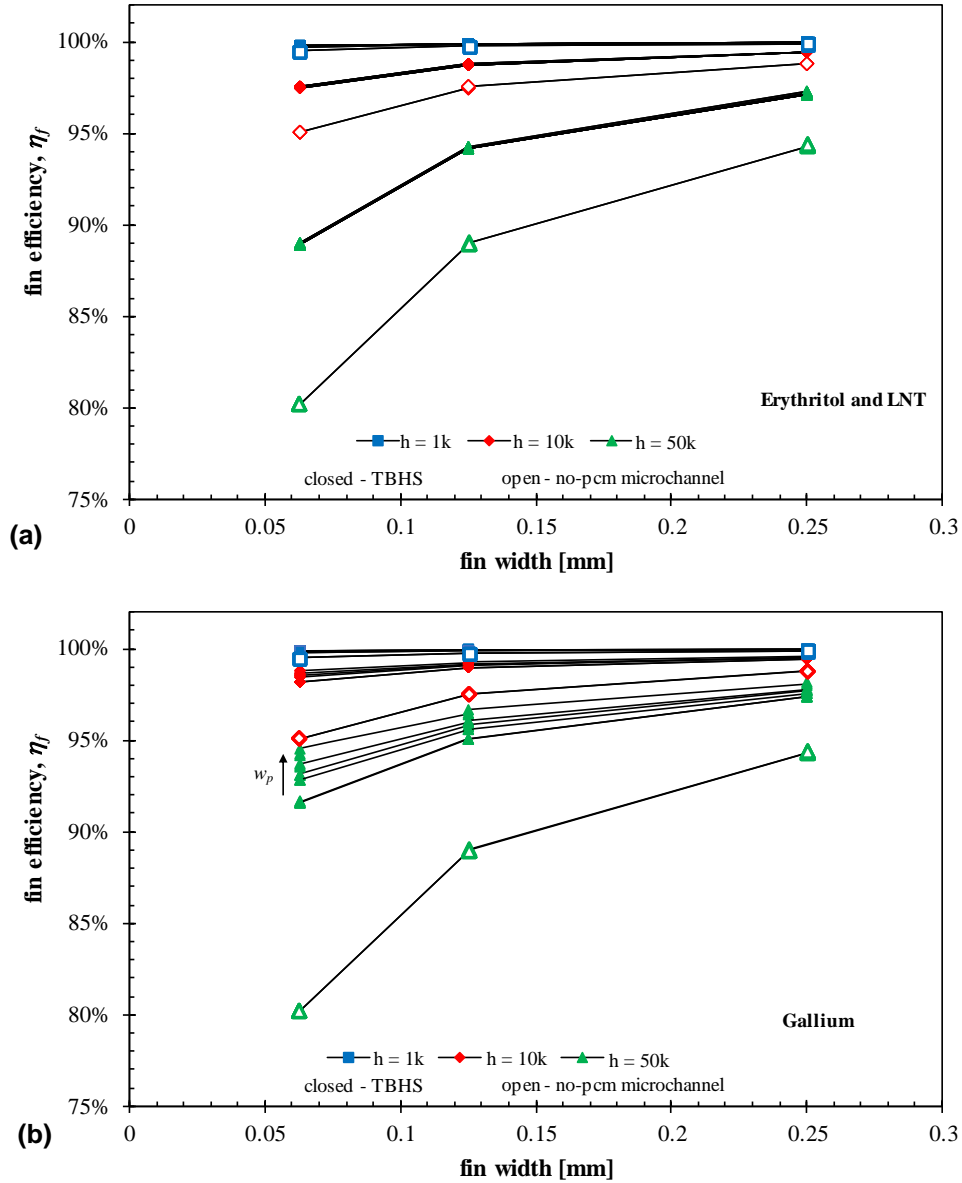


Figure 6.39 – Fin efficiency for AlN TBHS substrates for (a) erythritol and LNT and (b) gallium PCM, for both thin and thick substrates compared to equivalent microchannels.

6.3.6.2. Step-response – linear transient models

Dominant thermal time constants were again extracted from the substrate models, shown in Figure 6.40. The erythritol and LNT again overlap sufficiently to be represented by a single plot in (a), while the gallium containing substrates are shown in (b) to have a

slightly higher thermal time constant that becomes more noticeable for higher convection coefficients and larger PCM volumes (w_p). Additionally, while substrate thickness showed a thermal resistance inversion with increasing PCM volume, the thermal time constant of thicker substrates is always higher, suggesting that the thermal capacity must be compensating for that effect.

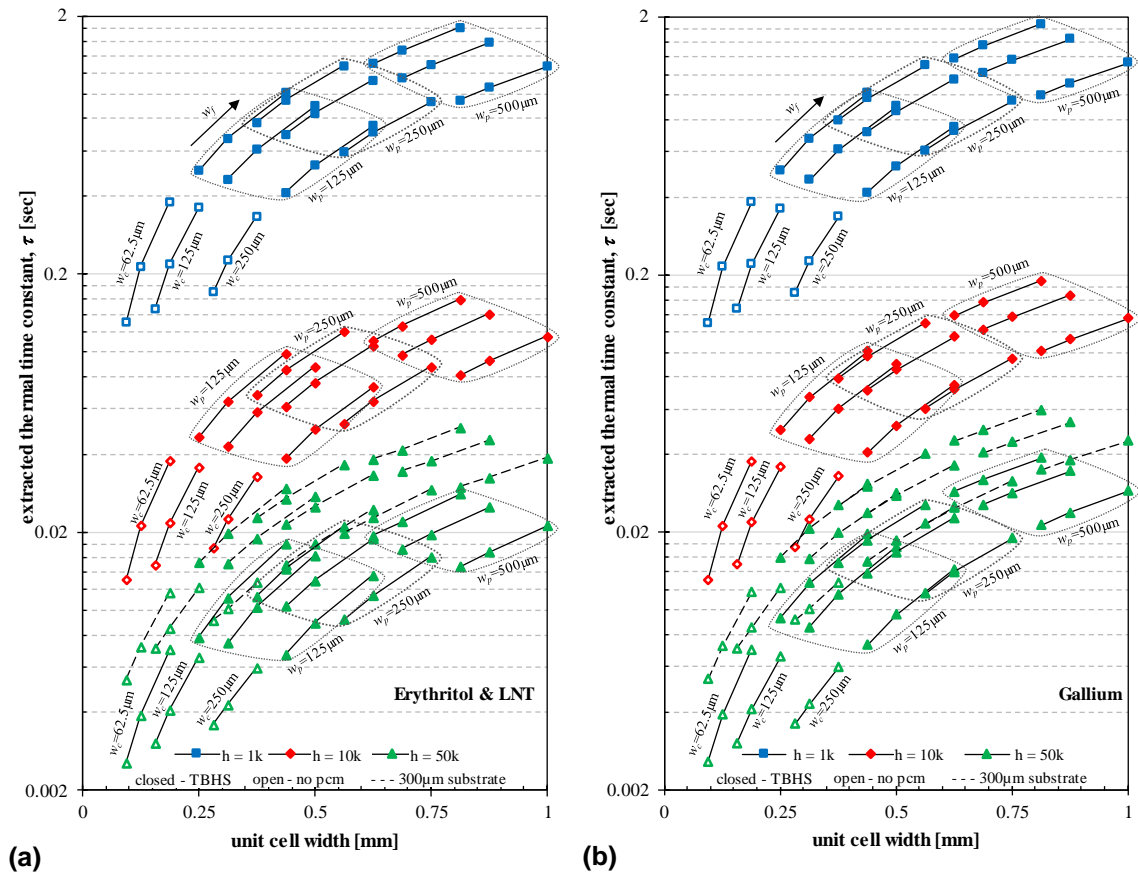


Figure 6.40 – Extracted thermal time constants for each AlN TBHS configuration at varying convective rates for (a) erythritol and LNT and (b) gallium, comparing the PCM substrates to no-PCM microchannel substrates. Substrate PCM widths (w_p) are indicated by dashed groupings.

Normalizing these thermal time constants by removing the convective component, we obtain the solid thermal time constant profiles shown in Figure 6.41, with (a-c) showing data for 100 μm substrates and (d-f) showing 300 μm thick substrates.

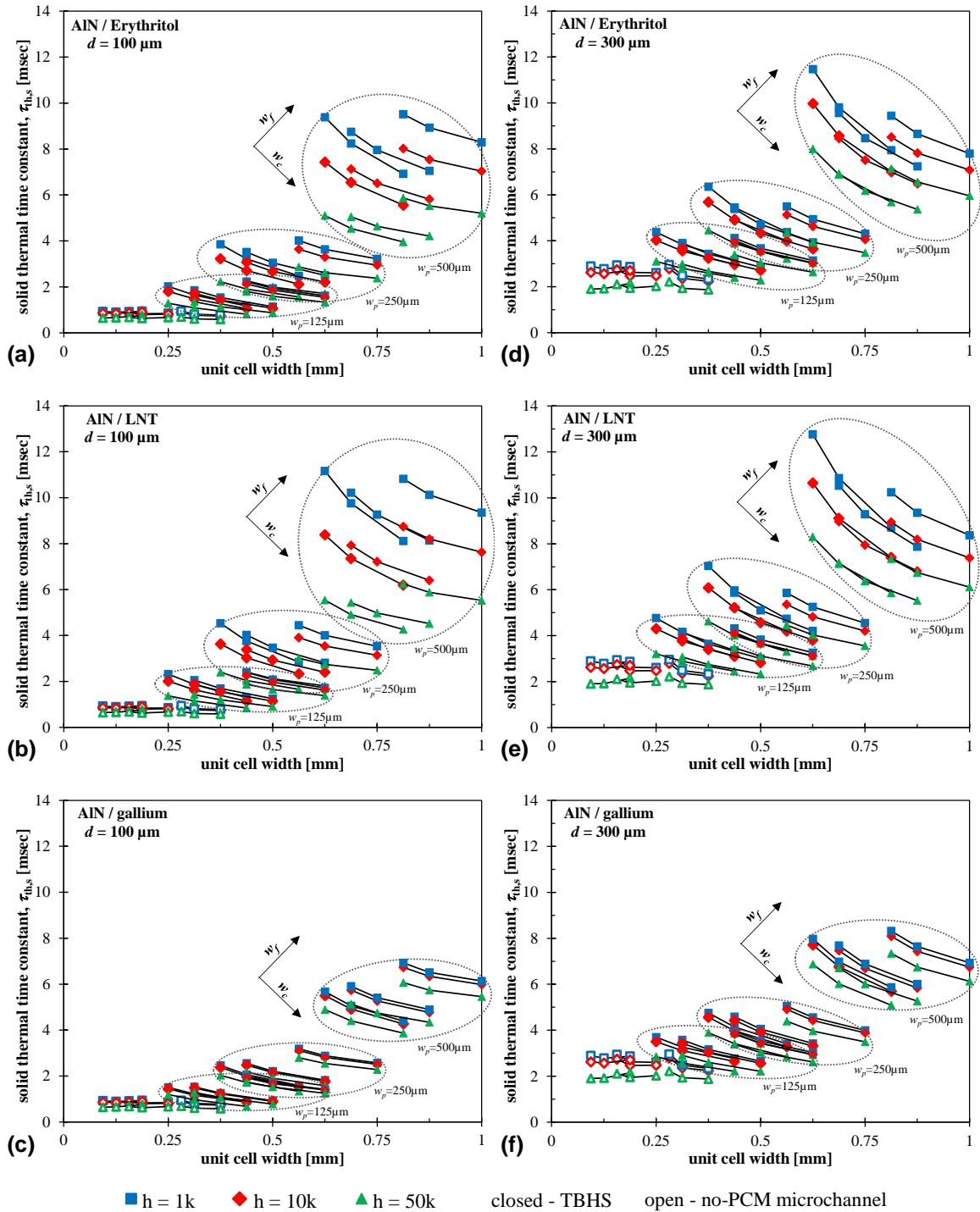


Figure 6.41 – Estimated solid contributions to AIN TBHS thermal time constant for each configuration and material at varying convective rates, with no-PCM microchannel substrate comparisons. (a-c) and (d-f) plots show the materials at $d = 100 \mu\text{m}$ and $300 \mu\text{m}$, respectively.

These profiles again show that the addition of PCM has the largest compositional impact on the substrate's thermal time constant. Interestingly, while the direct thermal time constants showed slightly higher τ_{th} for gallium, after subtracting out the convective component it appears that the gallium has a much lower thermal time constant than the others. This tracks better with the expectation of the thermal resistance comparison between materials. The much higher thermal conductivity of gallium resulting in lower thermal resistance should result in a lower thermal time constant absent any significant thermal capacity impacts.

Looking specifically at effective thermal capacity as determined from the thermal resistivity and time constants, Figure 6.42 again shows the sharp contrast in behavior between the low and high thermal conductivity PCMs. Just as with the silicon-erythritol substrates, all configurations show significant decrease in thermal capacitance with increasing convection rate suggesting less PCM and fin utilization due to reduced heat spreading. However, while AlN-erythritol and -LNT show the same PCM volume dependence as silicon-erythritol (where capacitance increases slightly with w_p at low h , but decreases with w_p at high h), gallium shows no such behavior. Instead, the improved heat spreading in the gallium creates a consistent increase in C_{th} with w_p for all values of h . Additionally, it is worth noting that the increase in substrate thickness makes little difference to the C_{th} parameter dependence, whereas it made a significant difference in thermal resistance due to reduced spreading resistance. The additional thickness results in a consistent upward shift in capacitance, suggesting that any spreading/utilization change is insufficient to noticeably shift overall unit cell capacitance.

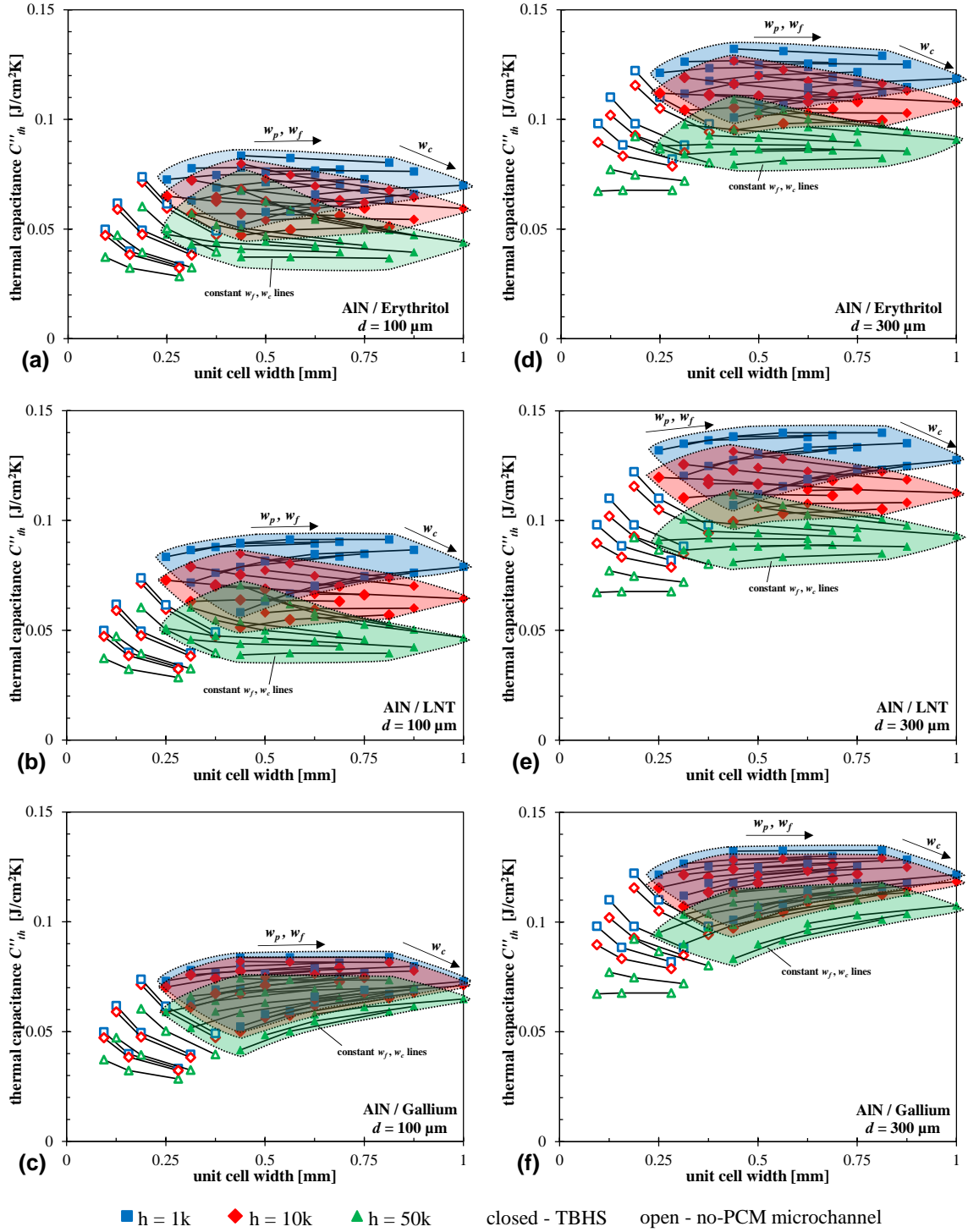


Figure 6.42 – AIN TBHS effective thermal capacitance emphasizing convective dependence of PCM impact for each configuration. The 100 μm (a-c) and 300 μm (d-f) substrates show similar but shifted capacitance behavior, while the metallic PCM shows much less convective impact.

The aggregate impact of PCM addition on AlN TBHS linear transient behavior for all configurations can be seen in Figure 6.43 and Figure 6.44, which show thermal resistivity versus thermal capacitance and thermal time constant, respectively. Just as with the silicon substrates, we see quite clearly that the substantial thermal resistance penalty from increasing PCM volume (w_p) provides no significant increase in linear thermal capacity. This is even the case for the higher thermal conductivity gallium PCM. However, there is an increase from the microchannel to the smallest (w_p) case, suggesting that there must be smaller values that would show (w_p) sensitivity. While the PCM addition does proportionally increase thermal time constant, as mentioned before this is almost entirely due to the thermal resistance component, with the resultant decrease in steady-state thermal performance.

The impact of the higher thermal conductivity gallium PCM is clearly evidenced in both Figures, where the thermal resistivity penalty, and consequently the thermal time constant, is much less than the other PCMs. Additionally, all three PCMs see a similar resistivity improvement and capacity increase with the thicker substrate as it reduces heat flow constriction. Just as with the silicon substrates, the highest thermal capacitance and time constant configuration with the lowest thermal resistance is that with the highest fraction of solid substrate material (maximum w_f , minimum w_c and w_p) as highlighted in each figure.

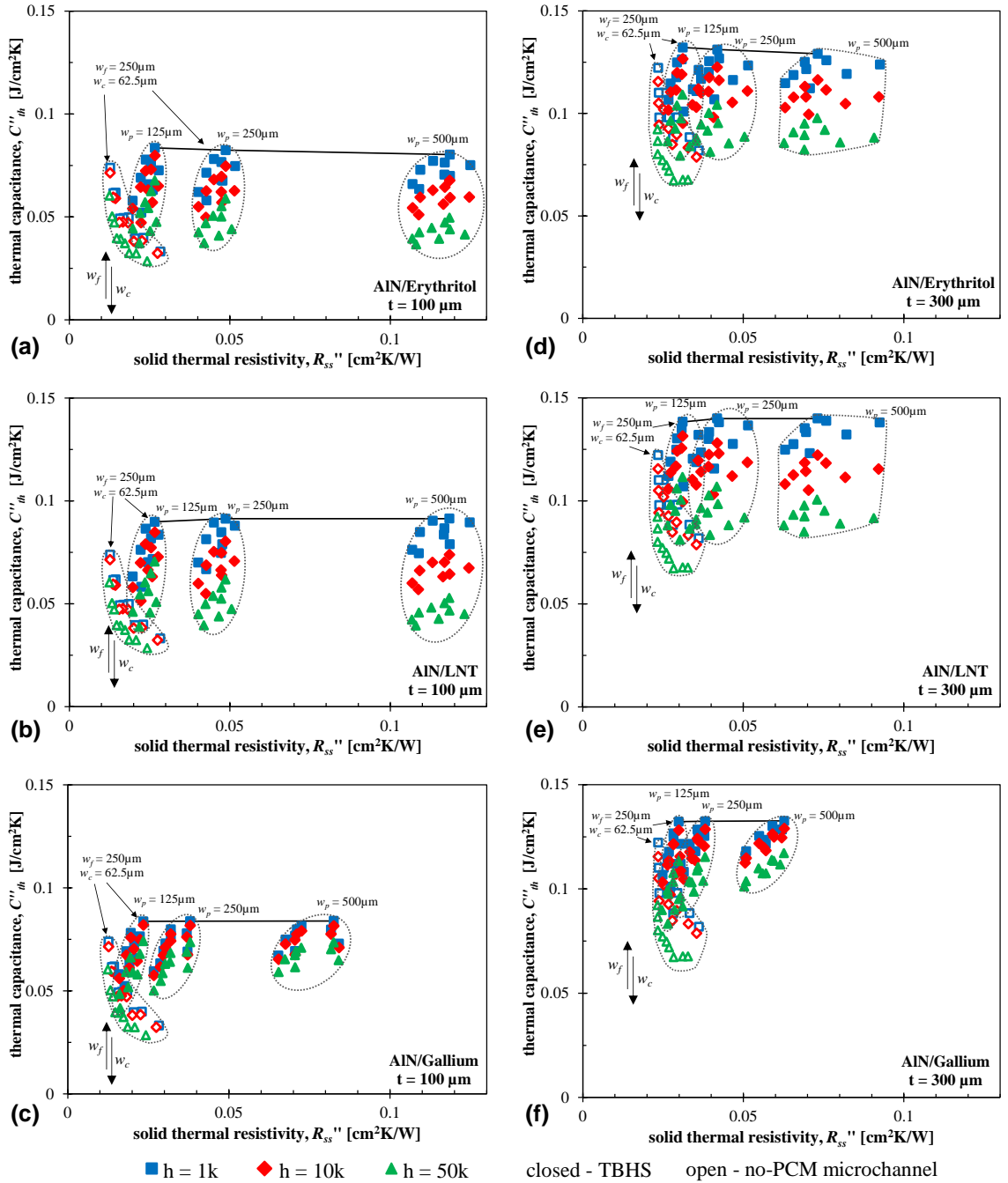


Figure 6.43 – AIN TBHS capacitance-resistance figure of merit comparisons evaluating the impact of PCM addition on the different material and substrate thickness configurations. The maximum capacitance case (maximum fin width (w_f), minimum convective area (w_c)) is highlighted.

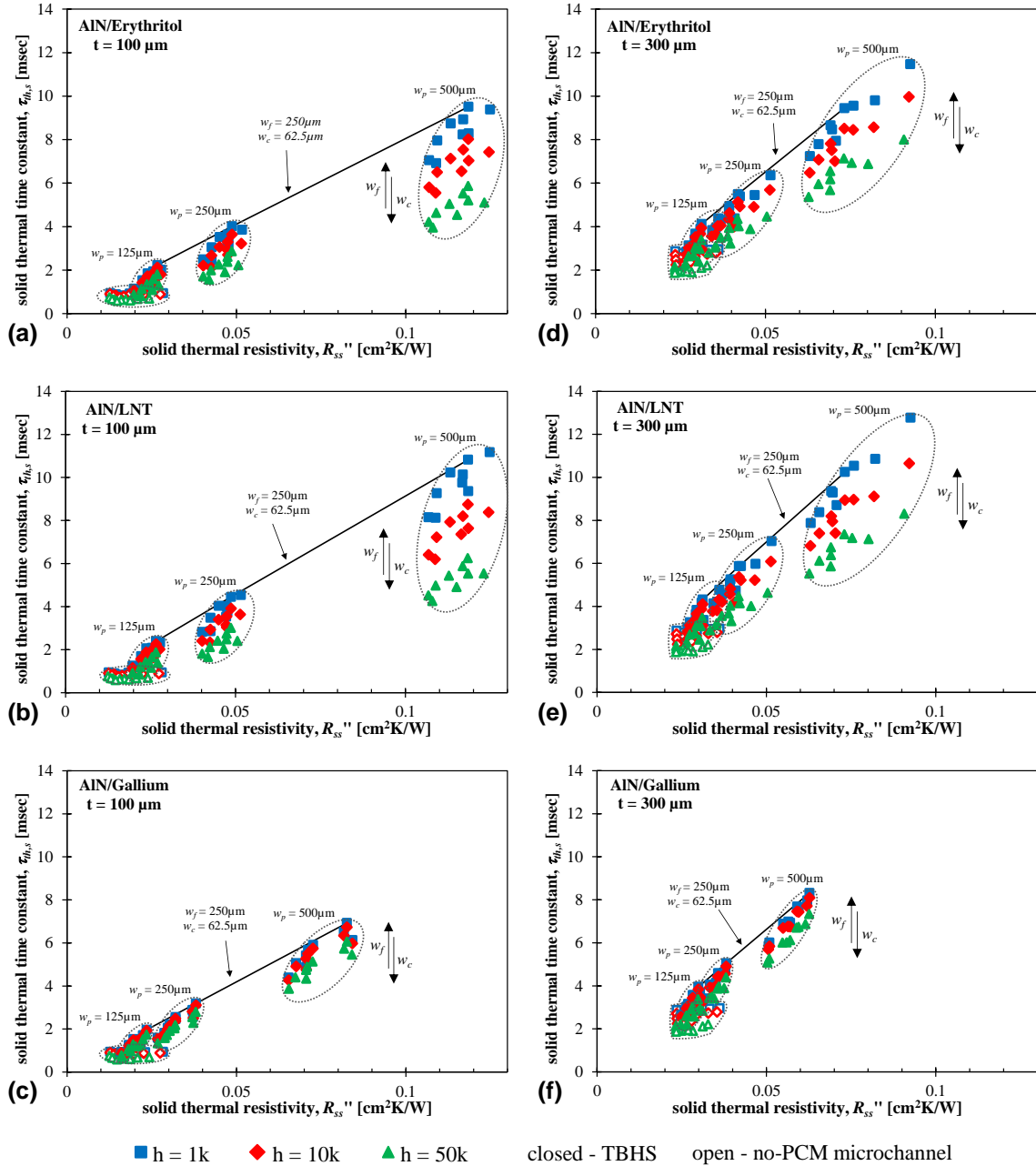


Figure 6.44 – AIN TBHS thermal time constant-resistance figure of merit comparisons evaluating the impact of PCM addition on the different material and substrate thickness configurations. The maximum time constant case (maximum fin width (w_f), minimum convective area (w_c)) is highlighted.

As with the silicon substrates, AlN TBHS linear thermal performance changes relative to AlN microchannel substrates did not show much improvement from PCM addition. A summary of this is seen in Table 6.14 which breaks out the comparison across substrate thickness and PCM, and includes the previous silicon results for comparison. There are notable differences that echo the features identified previously. The total thermal resistances show little difference when convection is dominant, but the solid contributions reflect the much higher gallium thermal conductivity and the decreased constriction of the thicker substrate. The AlN substrates also have a higher total thermal capacity, which produces an increased thermal time constant in proportion to the aforementioned thermal resistance differences.

Again, linear thermal performance of the AlN TBHS structures alone do not provide much improvement to justify the modification. The desired thermal capacity and time constant increase still comes at the cost of excessive thermal resistance penalty. Unless phase change benefit is significant may result in a worse overall transient design than just focusing on an improved microcooler.

Table 6.14 – AlN TBHS linear thermal performance ratios

<i>D</i> [μm]	PCM	<i>R_{th}</i> / <i>R_{th,mc,min}</i>				<i>τ_{th}</i> / <i>τ_{th,mc,max}</i>				<i>C_{th}</i> / <i>C_{th,mc,max}</i>	
		total (<i>R_{th}</i>)	solid (<i>R_{th,s}</i>)		total (<i>τ_{th}</i>)	solid (<i>τ_{th,s}</i>)		<i>C_{th}</i>	<i>C_{th,mc,max}</i>		
		<i>Min</i>	<i>max</i>	<i>min</i>	<i>Max</i>	<i>min</i>	<i>max</i>	<i>min</i>	<i>max</i>	<i>min</i>	<i>max</i>
100	<i>silicon / erythritol</i>	2.34	8.64	1.55	9.82	0.63	3.82	0.70	8.51	0.40	0.88
	erythritol	2.39	8.65	1.55	9.86	0.96	4.73	1.07	10.11	0.61	1.13
100	LNT	2.39	8.65	1.55	9.85	1.00	5.38	1.12	11.87	0.64	1.24
	gallium	2.29	8.64	1.26	6.73	1.04	5.57	0.90	8.04	0.69	1.23
	erythritol	2.17	8.60	1.14	3.94	1.17	4.33	0.96	3.87	0.82	1.18
300	LNT	2.17	8.60	1.14	3.94	1.20	4.70	1.01	4.31	0.86	1.21
	gallium	2.10	8.59	1.06	2.69	1.18	4.49	0.89	3.18	0.82	1.22

6.3.6.3. Phase change thermal suppression results

Transient melting simulations were repeated for all AIN configurations as with the silicon substrates using the same heat flux and time step conditions from Table 6.10. Note that as a high temperature PCM, erythritol simulations were run both for $T_0 = 100^\circ\text{C}$ (like the silicon models) and $T_0 = 25^\circ\text{C}$ to match the other material models. As before, we can look at the aggregate melting delay behavior of these substrates. The normalized results of mapping this heat flux dependent melting delay are shown superimposed on a single time constant melting delay model in Figure 6.45. The data from all AIN models again show fairly good agreement with the ideal curve, with most scatter growing for high heat flux and short time-to-melt simulations where q'' was 20x or more larger than q_m'' . High thermal conductivity material data points also comprised a significant portion of the above-the-line error, indicating that the model was less accurate at capturing that multi-material structure's heat propagation. Despite this, a single pole model still appears adequate for estimation of melting delay using extracted linear transient behavior.

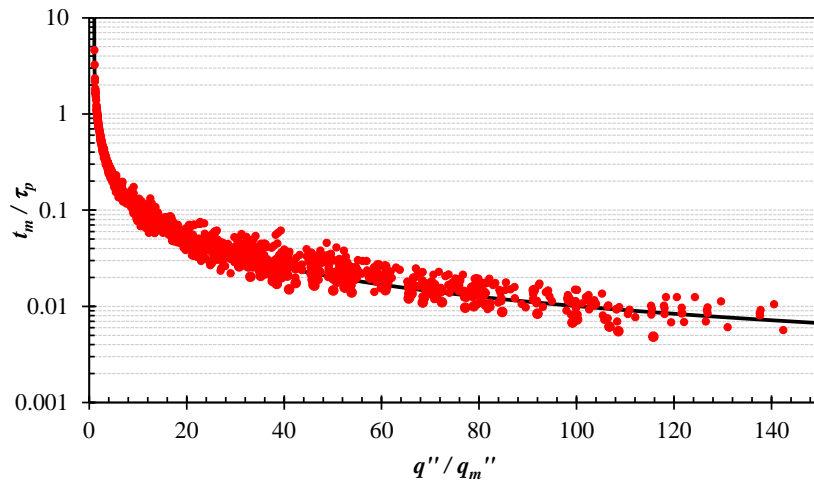


Figure 6.45 – Aggregate AIN TBHS simulated melting delay compared to the single time constant melting delay model (solid line).

Comparative temperature maps of one representative configuration with two different PCMs, LNT and gallium, are shown in Figure 6.46. The profiles for LNT (a-b) look very similar to the silicon phase change temperature distribution in Figure 6.33, with a very tight phase change mushy zone and a large liquid-side temperature gradient between the melt front and the substrate material. The gallium profile (b-c) looks much different, with a very broad mushy zone as the high thermal conductivity allows heat to penetrate farther into the PCM. There is also a much smaller thermal gradient to the solid and a consequently lower maximum temperature at the surface. Finally, it is worth noting that the location of T_{max} is different for the gallium materials. Whereas with silicon-erythritol and the AlN-LNT substrates the hotspot was the farthest point from the coolant, in the gallium substrate it is instead directly over the coolant. Both before and after phase change, the temperature reverts to the expected location over the gallium. This indicates that for gallium, the combination of PCM absorption and low ‘charging’ resistance is providing a stronger transient thermal sink than the coolant itself. Note also that the width of the gallium mushy zone could indicate that the prescribed 1°C mushy zone width might be too wide for this combination of material, temperature range, and heating profile to produce highly accurate tracks of melting behavior, but preliminary sensitivity analyses did not show particular impact on substrate maximum temperature results.

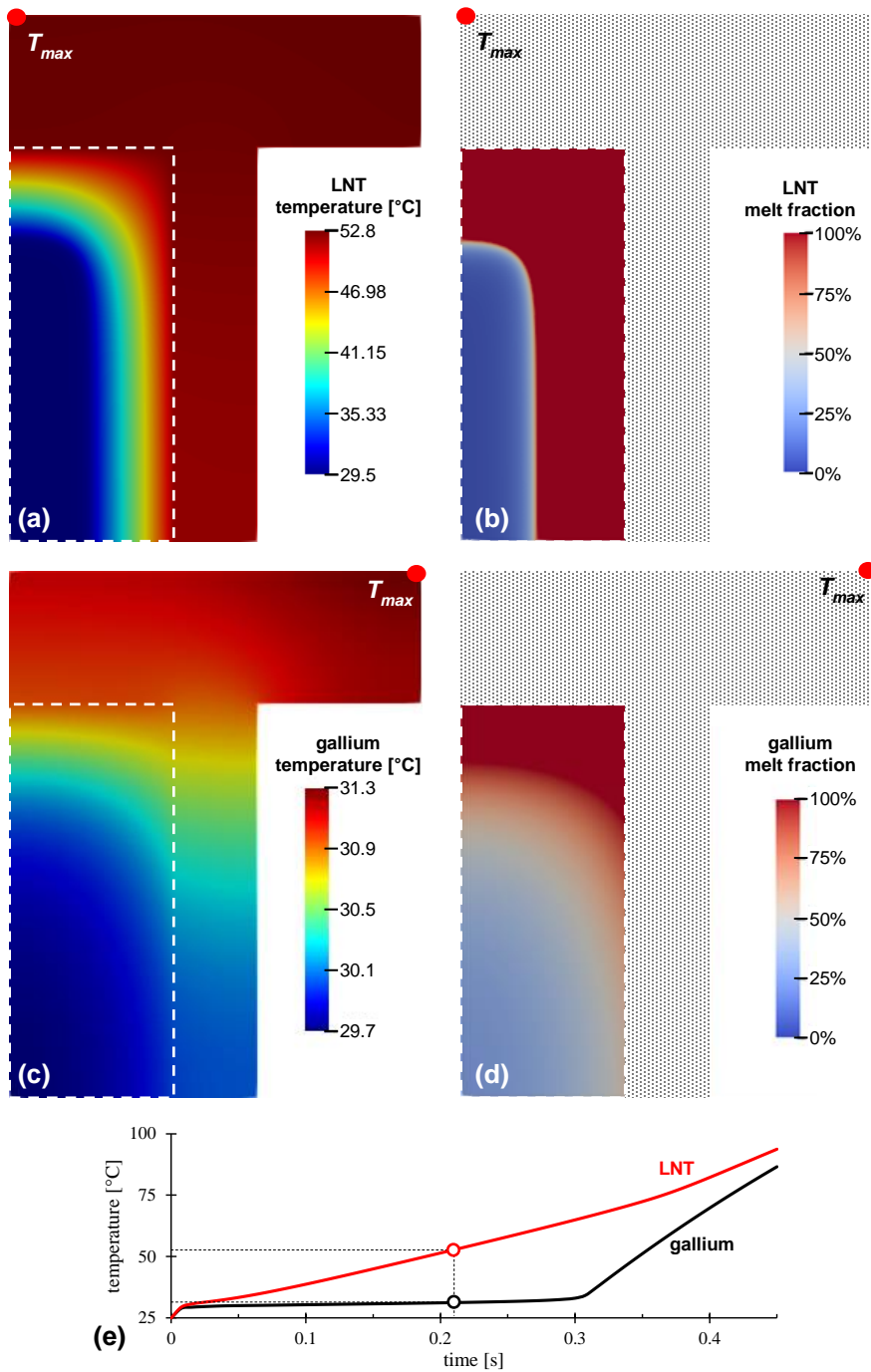


Figure 6.46 – Comparative transient melting temperature maps in LNT and gallium AIN TBHS subject to a 30 W/cm^2 heat load, $1 \text{ kW/m}^2\text{K}$ cooling at $T_0 = 25^\circ\text{C}$, with PCM regions indicated by the dashed line. (a, c) show the full temperature profiles throughout the TBHS. (b, d) show melt fraction and ‘mushy zone’ around phase front spanning $30 \pm 0.5^\circ\text{C}$. (e) shows the maximum temperature profiles.

The aggregate absolute and relative thermal suppression results from all AlN simulations for 100 μm and 300 μm substrate thicknesses are shown in Figure 6.47 and Figure 6.48, respectively. The results again have much similarity to the silicon results. The best TBHS and microchannel comparison cases are the minimum material condition configurations ($w_f = w_c = 62.5 \mu\text{m}$), with that case highlighted for all three w_p values in the Figures. Apart from the $T_0 = 25^\circ\text{C}$ erythritol case, all three PCM substrates show substantial thermal suppression at the low convection rate, but only gallium shows any significant thermal suppression at higher values of h . The amount of temperature suppression shows little dependence on amount of PCM. Erythritol and LNT generally show better thermal suppression at the minimum PCM value while gallium shows both much larger thermal suppression values as well as a slight increase from the minimum to medium values of PCM thickness. These two factors suggest that the increased heat spreading through the gallium enables better material utilization for heat absorption and corresponding slight benefit from additional material. The results for the 300 μm substrates are similar to that of the 100 μm substrates, with the previously mentioned less-severe PCM thermal resistance penalty but also significantly reduced thermal suppression due to the larger thermal gradient between substrate and PCM.

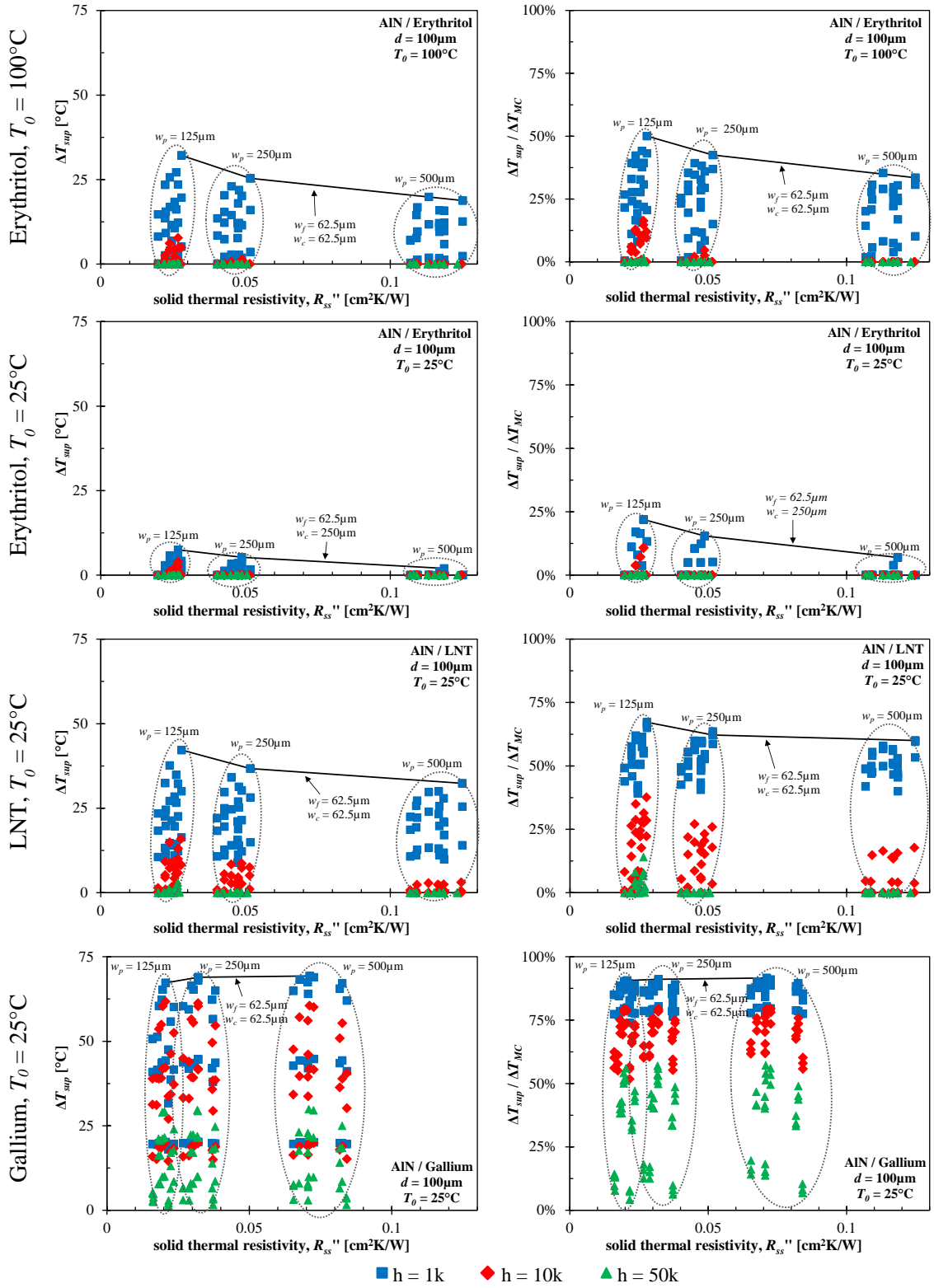


Figure 6.47 – Aggregate AIN TBHS thermal suppression results for 100 um substrates.

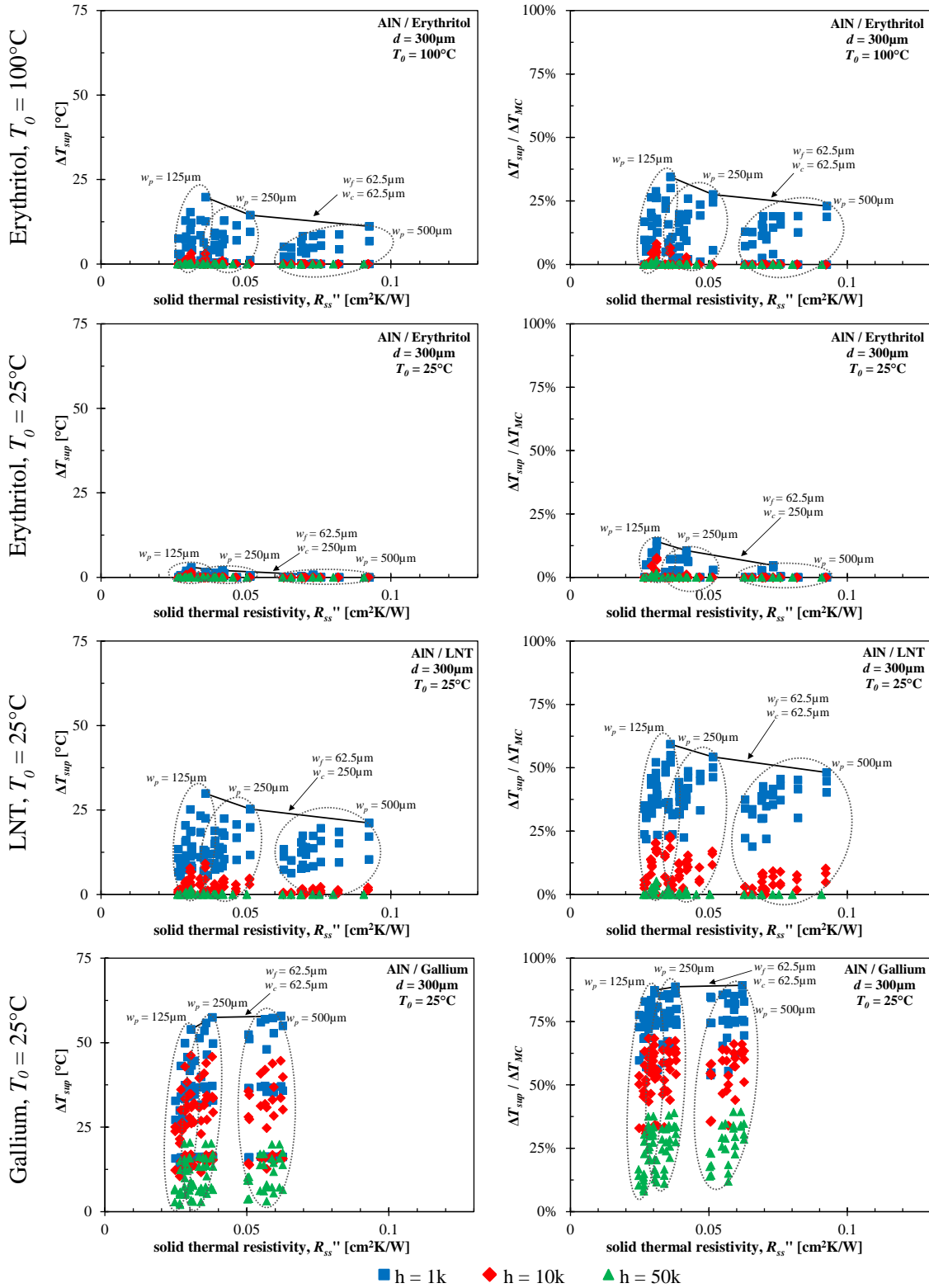


Figure 6.48 – Aggregate AIN TBHS thermal suppression results for 300 um substrates.

Finally, transient melting profiles for the two best performing AlN configurations are shown for all PCMs at all heat fluxes and select convection rates in Figures 6.49-6.52. The same configurations are chosen as for the silicon simulations: minimum feature size (minimum w_p , w_f , and w_c) and maximum substrate material (minimum w_p , w_c , maximum w_f). As before, minimum feature size reduces thermal resistance resulting in much lower temperature rise during melting and higher thermal suppression. Just as with the silicon tests, almost no temperature suppression is seen at higher convection rates with the low k_{th} PCMs due to the much lower microchannel thermal resistance.

Figure 6.49 shows the two configurations at $h = 1 \text{ kW/m}^2\text{K}$ for the thin substrate ($d = 100 \text{ }\mu\text{m}$). Apart from the low temperature erythritol case (where only the highest power case reaches T_M and by that time has far exceeded the equivalent microchannel temperature), all three PCMs provide some degree of phase change temperature suppression. It is quickly apparent that the gallium thermal benefit far surpasses that of the low conductivity materials, with peak suppression values about double that of LNT or erythritol. The impact of improved heat spreading in the metallic material is evidenced by the flat temperature profile during phase change, whereas the other materials see a steep temperature rise from the developing thermal gradient as the phase front moves away from the substrate. The heat must be driven through the liquid layer to provide additional absorption, as was described for Figure 6.46. The same set of plots are shown for the $d = 300 \text{ }\mu\text{m}$ case in Figure 6.50. The general behavior is similar, except that the substrates have overall both a lower and slower temperature rise. This is mainly due to a combination of the aforementioned lower thermal resistance from the improved heat spreading above the PCM and the higher unit cell thermal capacity.

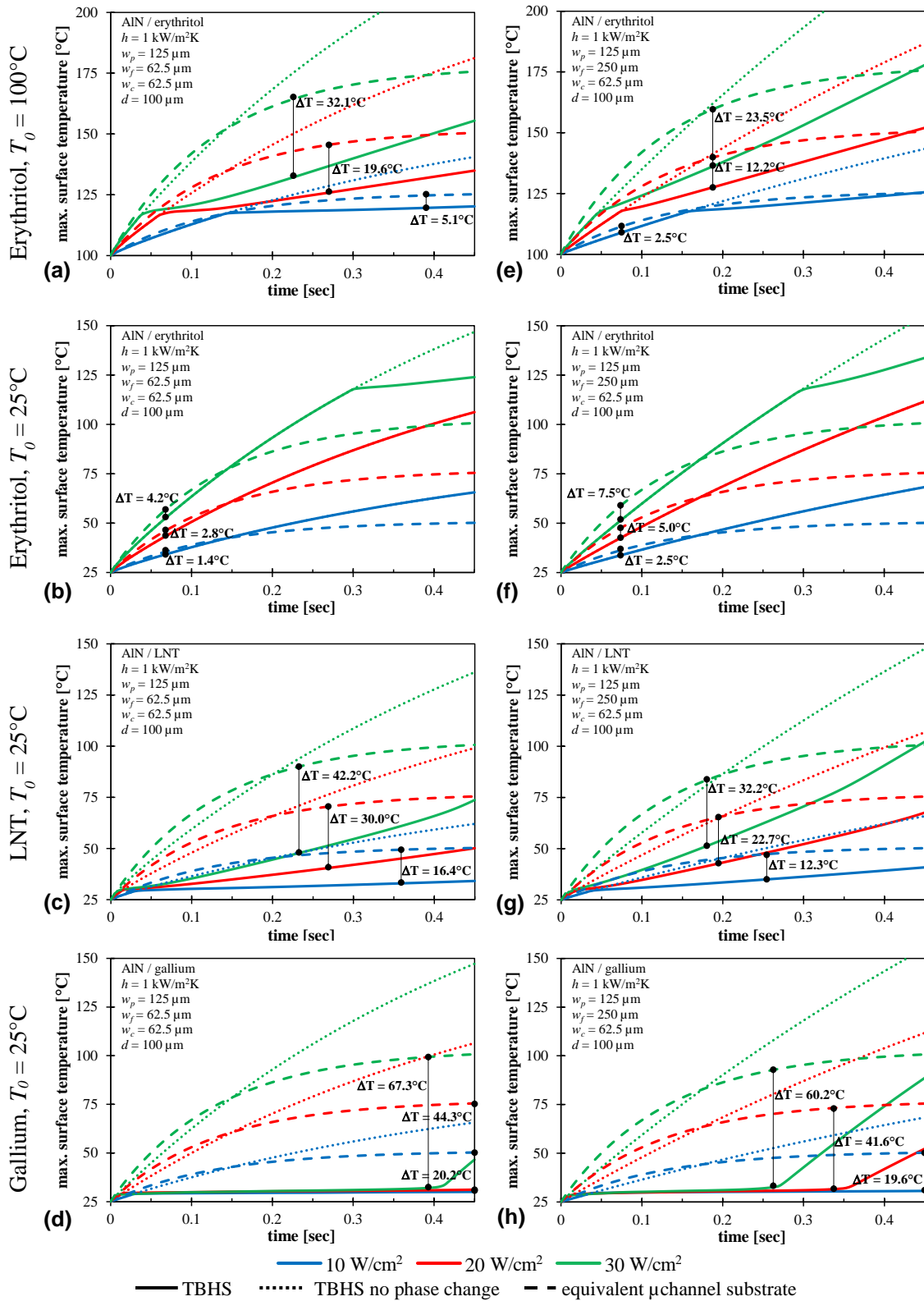


Figure 6.49 – Select AlN TBHS melting temperature profiles for $d = 100 \mu\text{m}$ and $h = 1 \text{ kW/m}^2\text{K}$ for the two best performing thermal suppression configurations and all PCMs and heat fluxes.

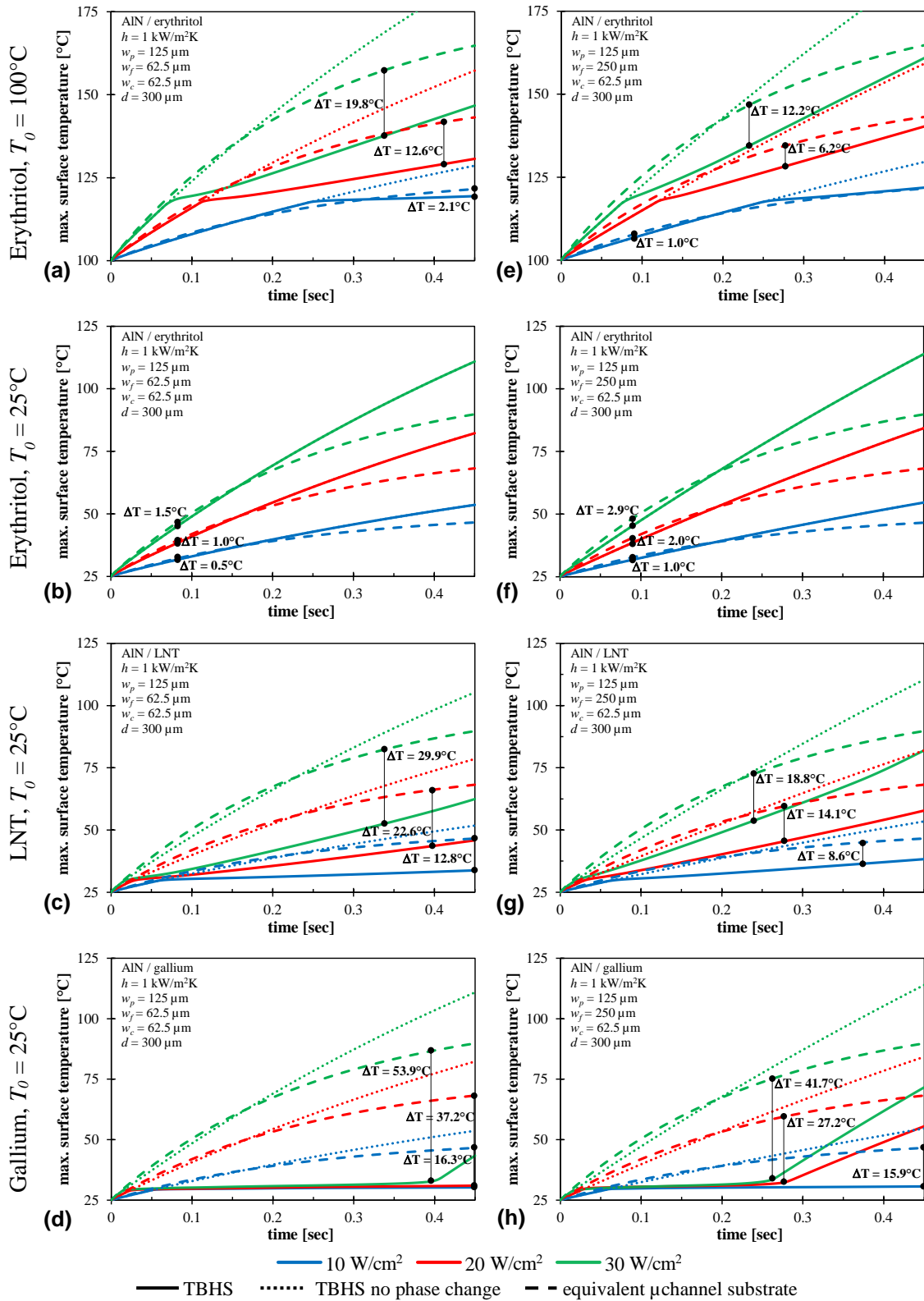


Figure 6.50 – Select AlN TBHS melting temperature profiles for $d = 300 \mu\text{m}$ and $h = 1 \text{ kW/m}^2\text{K}$ for the two best performing thermal suppression configurations and all PCMs and heat fluxes.

Key values from these plots summarizing the thermal suppression performance for the best performing AlN TBHS (minimum geometry parameter) are shown in Table 6.15. The table only shows the low convection and high power case, as thermal suppression was only seen in the low thermal conductivity PCMs under those conditions. As mentioned previously, with the increased thermal mass relative to the microchannel cooler, all of these cases showed immediate slight thermal suppression that then became much larger following the onset of melting. The table shows that under this high power condition all of the PCMs provide 10's of degrees of thermal suppression, representing from 15-90% reduced temperature rise relative to a microchannel cooler. At the longer time constants that come with the lower convection rate, this significant suppression lasts for several hundred milliseconds, and melting begins as soon as 10-75 milliseconds after the pulse begins. Again, gallium's thermal suppression is almost 50% larger than the low thermal conductivity cases while being the fastest and longest lasting as well.

Table 6.15 – AlN TBHS best temperature suppression values for $h = 1 \text{ kW/m}^2\text{K}$, $q'' = 30 \text{ W/cm}^2$

d [μm]	PCM *	steady state		phase change					
		$\Delta T_{ss,mc}$ [$^{\circ}\text{C}$]	$\Delta T_{ss,TBHS}^{**}$ [$^{\circ}\text{C}$]	t_{melt} [ms]	$t_{\Delta T_{sup,max}}$ [ms]	ΔT_{mc} [$^{\circ}\text{C}$]	$\Delta T_{max.sup}$ [$^{\circ}\text{C}$]	$\frac{\Delta T_{max.sup}}{T_{mc}}$	$\frac{\Delta T_{max.sup}}{\Delta T_{mc}}$
100	Erythritol	178.1	307.7	45	225	64.2	32.1	19.6%	50.0%
	LNT	103.1	232.7	15	232.5	65.0	42.2	46.9%	64.9%
	gallium	103.1	232.5	11.25	390	74.2	67.3	67.8%	90.6%
300	erythritol	178.5	308.0	75	337.5	132.3	19.8	12.6%	14.9%
	LNT	103.5	233.0	22.5	337.5	57.3	29.9	36.3%	52.1%
	gallium	103.5	232.5	22.5	397.5	61.7	53.9	62.2%	87.4%

* PCM base temperatures: erythritol - 100 $^{\circ}\text{C}$, LNT & gallium - 25 $^{\circ}\text{C}$

** solid heating estimate without phase change

As the gallium substrates are the only ones to show improvement at higher convection rates, gallium plots are shown for the selected configurations at all three

convection coefficients and at substrate thicknesses of 100 μm and 300 μm in Figure 6.51 and Figure 6.52, respectively. Again, the minimum feature size case shows better performance for all conditions primarily due to its minimum thermal resistance. At all convection rates, some thermal profiles show full phase change and return to sensible heating emphasizing the fact that thermal improvement only exists for a fixed duration, after which the aforementioned thermal resistance penalties will result in significant warming beyond that of the microchannel cooler. Still, the thermal suppression is significant, with some cases showing the microchannel case almost 70°C warmer while the TBHS has barely heated above the 30°C phase change temperature. Additionally, all of the gallium cases show thermal suppression begin very quickly, with phase change creating thermal suppression in just under 10 ms at the lowest convection coefficients, and well under 0.5 ms for the highest power and convection cases.

The 300 μm substrate has the effect of creating a slightly higher thermal gradient, and thus higher temperature, during phase change. After phase change completes then the reduced thermal constriction results in a somewhat shallower warming rate for the duration of the simulation. Additionally, the larger thermal time constant slows down the initial temperature rise and increases time to reach phase change and thermal suppression by a factor of about two relative to the 100 μm cases.

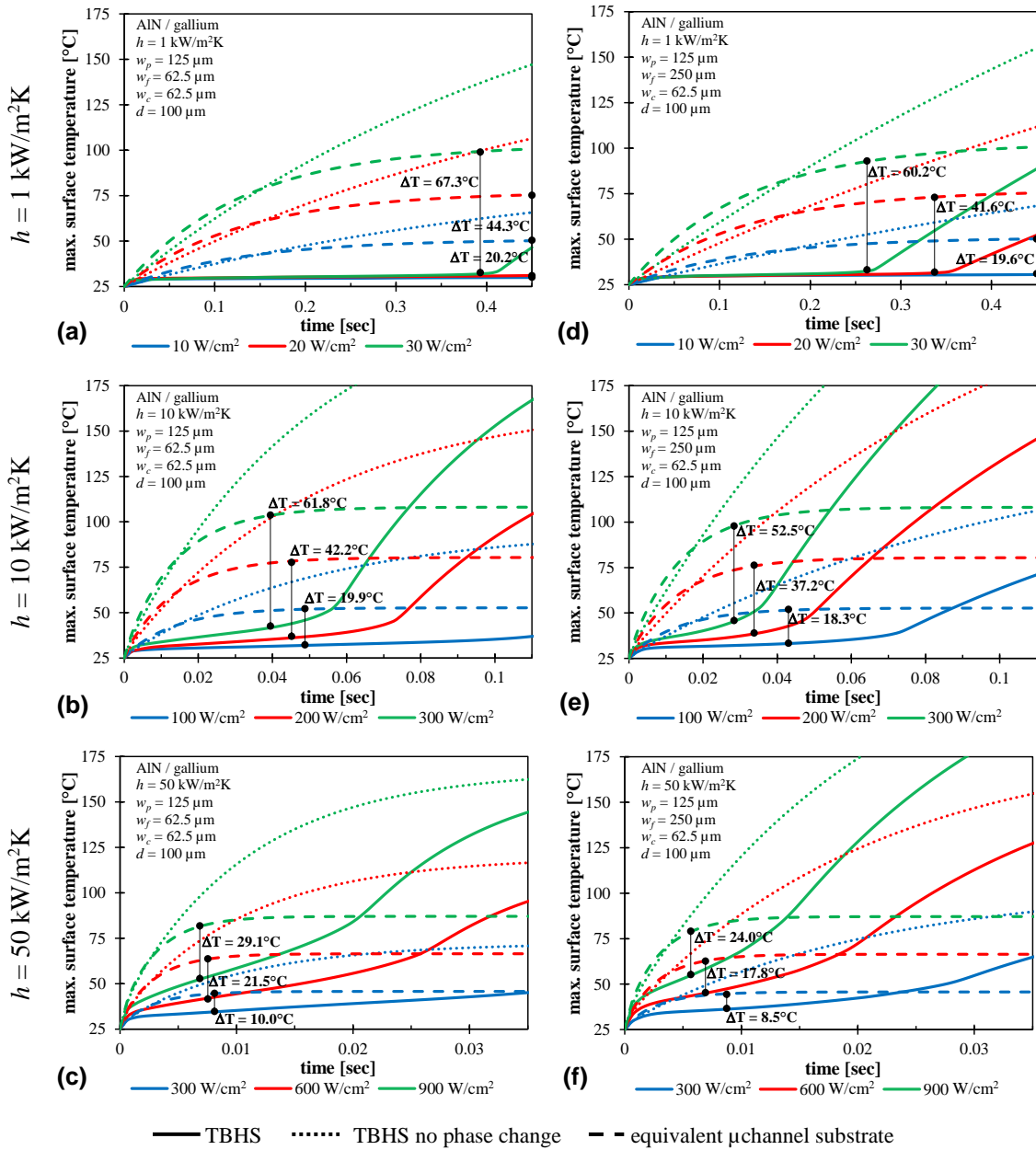


Figure 6.51 – Select AlN-gallium TBHS transient melting profiles for $d = 100 \mu\text{m}$ for the two best performing thermal suppression configurations and all heat fluxes, and convection coefficients.

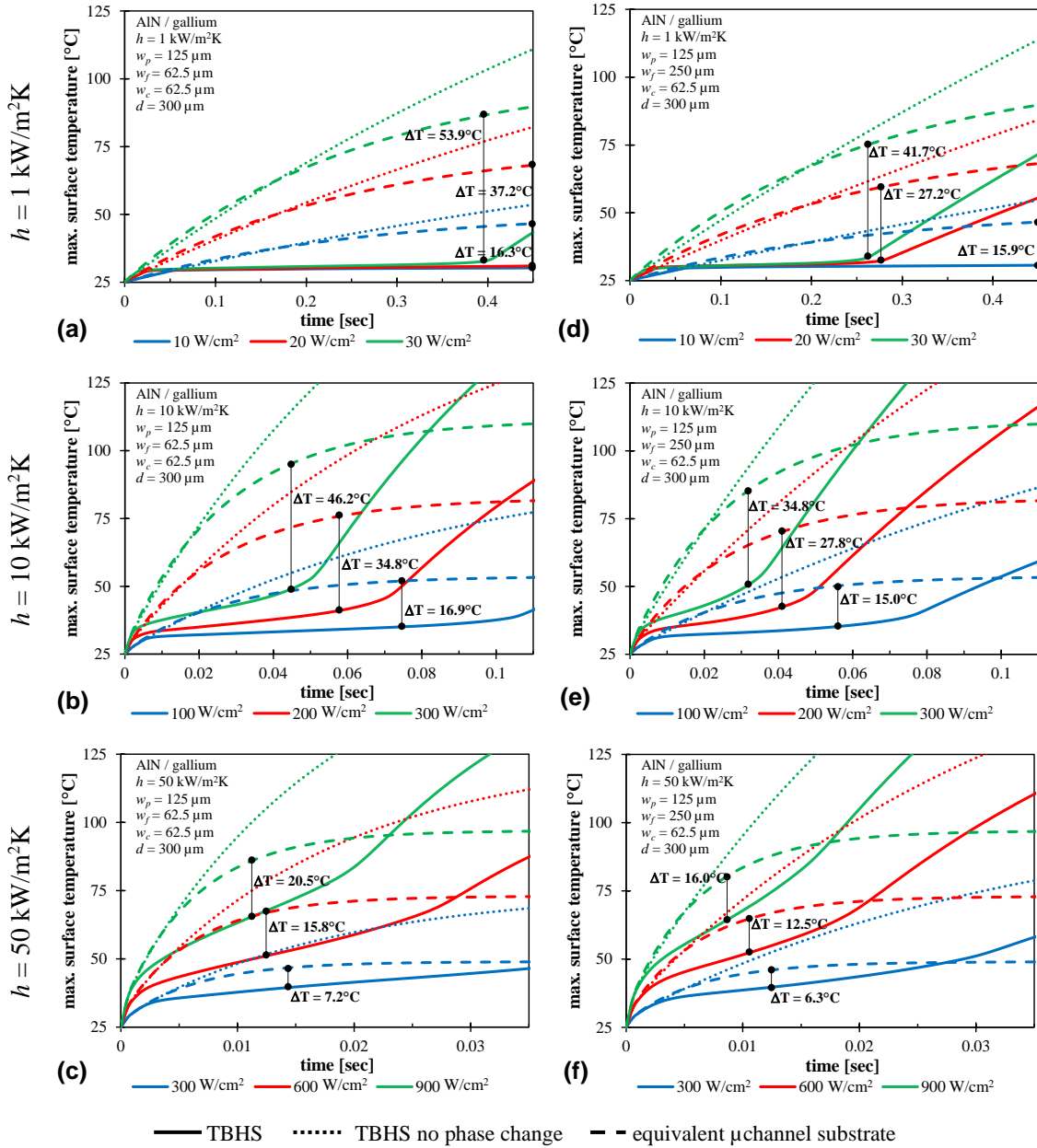


Figure 6.52 – Select AlN-gallium TBHS transient melting profiles for $d = 300 \mu\text{m}$ for the two best performing thermal suppression configurations and all heat fluxes, and convection coefficients.

Tables 6.16 and 6.17 summarize the linear and phase change thermal suppression data, respectively, for the best performing TBHS configurations. Unsurprisingly these are gallium PCM substrates in the maximum substrate material and minimum geometry parameter configurations, where the former provided the best linear thermal response and

the latter the best phase change thermal response. Table 6.16 highlights the fact that both configurations actually have fairly low thermal time constant and capacity relative to the full configuration parameter space as shown back in Table 6.14. The low thermal resistances minimized the thermal gradient penalties and promoted heat spreading, which turned out to impact transient performance far more than the small amount of thermal capacity that could be added.

Table 6.16 – AlN TBHS linear thermal performance ratios

config.	d [μm]	h [$\text{W}/\text{m}^2\text{k}$]	Thermal Resistance [$\text{cm}^2\text{K}/\text{W}$]				Thermal Time Constant [ms]				Therm. Capacitance. [$\text{mJ}/\text{cm}^2\text{K}$]	
			R	R/R_{mc}	R_s	$R_s/R_{s,mc}$	τ	τ/τ_{mc}	τ_s	$\tau_s/\tau_{s,mc}$	C_{th}	C_{th}/C_{mc}
minimum geometry	100	1k	6.92	2.66	20.6	1.62	505.4	1.32	1.51	1.60	73.1	0.99
		10k	0.71	2.56	20.6	1.62	49.9	1.32	1.44	1.59	70.3	0.98
		50k	0.16	2.29	20.3	1.62	9.3	1.33	1.19	1.58	58.9	0.98
	300	1k	6.93	2.65	30.4	1.29	837.6	1.25	3.67	1.24	120.9	0.99
		10k	0.72	2.50	30.3	1.29	82.0	1.23	3.45	1.24	113.9	0.99
		50k	0.17	2.10	30.0	1.29	15.6	1.22	2.78	1.25	92.8	1.01
maximum substrate volume	100	1k	12.09	4.64	23.5	1.85	1012.1	2.64	1.97	2.09	83.7	1.13
		10k	1.23	4.44	23.5	1.85	100.8	2.66	1.93	2.13	81.9	1.15
		50k	0.26	3.84	23.5	1.88	19.6	2.81	1.74	2.31	74.1	1.23
	300	1k	12.10	4.63	29.9	1.27	1593.2	2.38	3.94	1.33	131.7	1.08
		10k	1.24	4.30	29.9	1.27	156.3	2.35	3.78	1.35	126.3	1.09
		50k	0.27	3.39	29.8	1.28	29.8	2.32	3.27	1.48	109.7	1.19

Alternatively, as shown in the previous plots, the minimum geometry case performed best in all phase change simulations, and this carried through for both gallium and non-metallic PCMs. Better linear transient performance made little difference when it was at the expense of thermal resistance. Thermal gradients developing both before phase change and during melting dominated the response and created the greatest separation between designs. The gallium phase change thermal suppression data in Table 6.17 shows that even with a steady-state heating disadvantage the embedded metallic PCM provided fast, substantial temperature suppression in all cases. In fact, it is worth noting that the

gallium table lists t_{melt} rather than the onset time for temperature suppression because in all cases the microchannel relative temperature suppression time began at $t = 0$, unlike with silicon-erythritol. After t_{melt} , which is in the sub-millisecond range for high convection cases, the significant melting suppression period began and lasted for tens to hundreds of milliseconds. The amount of thermal benefit was inversely correlated with convection rate. Just as with the non-metallic PCMs, the most benefit occurred at low h values, but this benefit was as much as a 90% reduction in temperature rise. Finally, whereas the non-metallic PCMs showed no benefit for higher convection rates the gallium TBHS just showed a gradual reduction in suppression, still staying above 33%.

Table 6.17 – Minimum geometry AlN-gallium TBHS temperature suppression values

d [μm]	h [$\text{kW}/\text{m}^2\text{K}$]	q'' [W/cm^2]	steady state		phase change					
			$\Delta T_{ss,mc}$ [$^{\circ}\text{C}$]	$\Delta T_{ss,TBHS}^*$ [$^{\circ}\text{C}$]	t_{melt} [ms]	$t_{\Delta T_{sup,max}}$ [ms]	ΔT_{mc} [$^{\circ}\text{C}$]	ΔT_{TBHS} [$^{\circ}\text{C}$]	$\frac{\Delta T_{max,sup}}{T_{mc}}$	$\frac{\Delta T_{max,sup}}{\Delta T_{mc}}$
100	1	10	51.0	94.2	33.75	450	25.2	5.0	40.2%	80.0%
		20	77.1	163.3	18.75	450	50.4	6.1	58.7%	87.8%
		30	103.1	232.5	11.25	390	74.2	7.0	67.8%	90.6%
	10	100	52.7	96.0	3.75	48.75	26.9	7.0	38.3%	73.8%
		200	80.4	167.0	1.88	45	53.4	11.2	53.9%	79.1%
		300	108.1	238.1	0.94	39.375	78.5	16.7	59.7%	78.7%
	50	300	45.7	72.5	0.94	8.125	19.5	9.5	22.4%	51.2%
		600	66.4	119.9	0.63	7.5	38.4	16.9	33.9%	56.0%
		900	87.1	167.4	0.31	6.875	56.6	27.4	35.8%	51.6%
300	1	10	51.2	94.3	60.0	450	21.6	5.3	35.1%	75.6%
		20	77.3	163.5	30.0	450	43.2	6.0	54.6%	86.1%
		30	103.5	232.8	18.75	397.5	61.7	7.8	62.2%	87.4%
	10	100	53.8	97.0	6.56	75	27.0	10.1	32.5%	62.6%
		200	82.6	169.0	3.75	58.125	51.0	16.2	45.8%	68.3%
		300	111.4	241.0	2.81	45	70.3	24.1	48.5%	65.7%
	50	300	49.0	75.4	2.19	14.375	21.8	14.5	15.5%	33.3%
		600	73.0	125.7	1.25	12.5	42.0	26.2	23.6%	37.7%
		900	97.0	176.1	0.94	11.25	61.0	40.5	23.8%	33.6%

* solid heating estimate without phase change

6.3.7. Substrate integrated TBHS conclusions

Standard electronics packaging was shown in Chapter 5 to have problems with insufficient thermal capacity and excessive convection delay thereby limiting transient performance. The primary goal of this analysis was evaluate the Thermal Buffer Heat Sink design as a transient, substrate integrated cooler to mitigate those problems by creating a spatial design trade between thermal resistance and both linear and nonlinear thermal capacity. A successful design would lower the temperature rise seen during fast, high power transients while minimizing any steady-state thermal performance penalty. The TBHS simulation results showed great success at the former goal of pulsed temperature rise for some materials and configuration, but the steady-state tradeoff penalty was significant and generally unfavorable.

The hoped for compact design trade between thermal resistance and linear thermal capacity was virtually non-existent. Across all configurations, the cooling area reduction and introduction of a lower k_{th} material increased steady-state resistance from 2-9x relative to a tightly integrated microchannel cooler, yet the unit cell sensible thermal capacity was in most cases actually reduced. The resulting TBHS-to-microchannel capacitance ratio ranged from 0.4-1.3. While the RC combination did produce a higher thermal time constant to slow down temperature rise, that gain occurring solely from a resistance penalty is a problem for any components that must operate outside of a phase change condition. While the magnitude of that resistance penalty was heavily dependent on the choice of phase change material, and the use of a metallic PCM reduced the solid portion of the thermal resistance by about a third, it was still significant enough to prevent many of the

configurations from showing any thermal suppression due to the excessive thermal gradients.

The simulation did show that all substrate phase change material combinations provided some degree of heat absorption and net thermal benefit with the lower thermal resistance designs. The low thermal conductivity PCMs were able to utilize phase change absorption to suppress temperature rise for a duration, but only when the parallel cooling resistance was high (low convection), and only until the developing resistive thermal gradient offset the transient phase change gradient. At higher values of h , the phase change usually occurred at substrate temperatures higher than the microchannel substrate's steady-state temperature, eliminating any benefit.

Alternatively, the gallium containing substrates provided temperature suppression in every configuration, and this extended to all powers and convection rates. There was some slight benefit in having more than the minimal amount of gallium, indicating that the improved thermal spreading aided in material utilization. In fact, phase change was often still ongoing at the end of the simulation time, making it difficult to assess an optimal gallium PCM volume. The higher volumes still created significant resistive increase, however, so it appears that the likely maximal case for this study is still the minimum geometric parameter substrate. Note, however, that this is in conflict with the best linear transient configuration, creating another highly application dependent design tradeoff.

It is worth repeating the difficulty in evaluating substrate benefit absent an actual transient use case. Depending on the magnitude of the transient temperature swing and amount of sensible versus latent heat absorption (i.e., the Stephan number for the application), the linear behavior may or may not be a concern. Any electronic design not

operating in a primarily pulsed mode may find the steady-state thermal resistance penalty too much of a system cooling power cost to tolerate. However, in an appropriately selected system a substrate integrated TBHS could reduce temperature rise sufficiently without a corresponding increase in steady cooling power, producing an improved, passively buffered system improved component.

Additionally, the microchannel substrate comparison cases were not necessarily fair comparisons. While the lowest thermal resistance configuration was chosen for comparison with the TBHS designs, some microchannel substrate configurations have slightly lower steady-state resistance while others have somewhat larger thermal time constants. This means that even among the microchannels the ‘best’ case will depend on total pulse length. The microchannel substrates also have roughly twice the coolant flow area as the TBHS substrates (the PCM volume substituting for half of the cooling volume) but the comparison simulations were made using the same wetted-surface convection coefficient. Assuming the same fluid source, achieving the same h value would require the same flowrate per channel, which would require $\sim 2x$ the total flowrate for the substrate. Using the same h in effect applies a “constant pressure” flow boundary condition, when in practice a “constant pumping power” boundary condition may have been more realistic. In that case increasing the number of flow passages would have decreased the per channel flowrate from the same source, resulting in a lower h . Thus a more ‘fair’ flowrate comparison would have decreased microchannel substrate performance, and increased the relative merit of the THBS configurations. Despite both of these potential issues, it is still estimated that the net result applied consistently provided a fair comparison of TBHS designs and materials.

Finally, returning to the initial DOE study that prompted this investigation, it may be that their preference for a multilayer, rather than single layer TBHS arrangement could hold true for more than just manufacturability reasons. The multilayer design restores the full cooling area, but puts additional thermal distance and constriction between it and the heat source. Noting the significant thermal performance penalty seen here due to the PCM and decreased cooling area, perhaps independent multiple layers would be enough to create a minimum resistance design and open up the design space for other materials. Also, as the original DOE study had much larger heat sink components and did not consider high thermal conductivity PCMs (their considered PCMs all in effect being thermal insulators), it is possible that a high thermal conductivity PCM would eliminate the constriction problem, and may make for a thermally optimum case. Recalling that one of the manifold microchannel cooler design benefits is the decoupling and independent design flexibility of the different flow layers, future investigations may identify a multilayer, manifolded PCM microcooler structure that minimizes the conductive path to the coolant and provides the nonlinear thermal capacity sought to solve the package thermal response problem.

6.4. Phase change integrated SPICE models

As stated in Chapter 5, transient electrical circuit modeling is extremely well established, and coupled electro-thermal models of electrical components become more available every year. There is a need to integrate thermal and electrical design to prevent unexpected thermally driven device degradation from becoming a critical failure. Electrical circuit modeling tools like SPICE have enabled rapid prototyping of complex devices. This is far less prevalent in the thermal modeling world, as running a full finite element thermal analysis for each design iteration (as was done in the Section 6.3 TBHS

evaluation) would slow the design process to a crawl. Rapid phase change modeling and thermal prediction is needed to understand the impact that a phase change material can have on electrical device behavior. With that goal, this section explores the integration of thermal phase change into the same SPICE framework used for linear thermal circuits, and concludes with a re-examination of the packaging study using PCMs to improve thermal performance.

6.4.1. SPICE and non-linear thermal capacitance

One difficulty with doing thermal design in a circuit framework is that certain, normally straightforward, modeling tasks such as mesh refinement are manual and cumbersome. Despite this, SPICE still allows us to approximate thermal phase change as a non-linear, temperature-dependent material property, as most SPICE modeling tools have constructs for deriving voltage-dependent component parameters. Voltage dependent capacitances in particular can emulate temperature dependent thermal capacity to implement the apparent heat capacity method (and as shown later in some cases even the enthalpy method). Specific nomenclature for variable material properties will vary across SPICE applications. Discussed below is the implementation used in *ngspice*, a free open-source successor to the original Berkeley spice [272], and in *LTspice XVII*, the free but proprietary SPICE implementation used for the simulation in the Chapter 5 thermal circuit modeling.

In *ngspice*, a nonlinear capacitor can be specified simply by using a capacitance expression in terms of defined capacitors and node voltages. This only permits use of the apparent capacity model, but can be done using a simple if-else operator to define the

profile as per (96) and the polynomial constants from Table 6.3. As an example, the code for a shunt nonlinear capacitor with positive and negative nodes P and N is:

```
C_shnt P N c=' ((V(P)-V(N))<{T_low}) ? ({C_s}/2) :
                ((V(P)-V(N))>{T_high}) ? ({C_l}/2) :
                (0.5*(a32*((V(P)-V(N))-Tm)**2+
                 a31*((V(P)-V(N))-Tm)+a30))
```

using a nested if-else notation: “logical test ? output-if-true : output-if-false” to specify thermal capacity in solid (C_s) or liquid (C_l) states if outside the mushy zone (the temperature between T_{low} and T_{high}), and a quadratic smoothing function incorporating the latent heat if inside the mushy zone. The a-terms refer to polynomial coefficients defined in Table 6.3.

While the finite element segment can be captured as a single subcircuit and added repeatedly, *Ngspice* has no built in mechanism for automatic component repetition usable for mesh refinement. In addition to this limitation, there is no option for implementing an enthalpy function into *ngspice*, which would be the equivalent of specifying charge storage on the capacitor. LTspice, on the other hand, permits the definition of a charge state (Q) as a function of voltage difference. Thus, in addition to the ability to define capacity as done above for *ngspice*, the following code example shows the definition of an enthalpy function using state of charge notation:

```
C_shnt P N Q = if( x < T1, {Cths} * x,
                 if( x > T2, Cths*TM + Ef + Cthl*(x-TM),
                   p33*(x-TM)**3 + p32*(x-TM)**2+
                   p31*(x-TM) + p30))
```

The p terms above refer to the polynomial coefficients defined in Table 6.2, x is LTspice’s notation for the voltage difference equivalent to $V(P)-V(N)$. E_f is the latent heat capacity in Joules, or in this one dimensional model, E_f'' is the latent heat capacity per area in J/m^2 , defined as:

$$E_f'' = \rho_s l_{el} H_f \quad (125)$$

Using both the aforementioned LTspice undocumented bus connection feature for circuit element repetition and the charge element definition feature, the remainder of this section demonstrates the use of phase change finite element thermal circuits.

6.4.2. PCM thermal circuit validation

We can verify the successful implementation of the enthalpy approximation of phase change by returning to the 1D phase change proof model from Section 6.2.2. As a closed form solution is available, we can construct a thermal circuit domain of the same problem and compare the results.

As with the finite element approximation to the problem, the domain could not be infinite length, and is set to a 1-meter long erythritol bar. The bar is initially at $T_L = 100^\circ\text{C}$, the right boundary is insulated, and at $t = 0$ the left boundary is instantaneously set to $T_H = 150^\circ\text{C}$. Material properties are as per Table 6.5, and the temperatures and MZW are as per Table 6.6. Mesh refinement and time-stepping were handled differently than in the previous FEA model, working within what was permitted by the SPICE framework. In particular, only a fixed, equal mesh spacing was created using LTspice's circuit repetition feature. Time stepping used the built-in adaptive SPICE routine with a modified trapezoidal integration method. Each simulation was only run for 1000 seconds.

Figure 6.53 shows a simple 1-dimensional thermal circuit in LTspice that can be used to emulate phase change by setting the component values as functions of temperature. Note that the thermal circuits do not use a coupling capacitor parallel to the resistor, which is equivalent to using a lumped mass approximation with mass coupling factor $\mu = 0$. Built in SPICE components with variable property capabilities use the nodal voltage difference

as the primary variable. This works for the shunt thermal capacitor elements that reference nodal temperature to thermal ground, but not parallel elements. For similar reasons the model does not support variable thermal conductivity, which would require a variable resistor referenced to ground. Implementing these components will require custom variable components and is left as a future task.

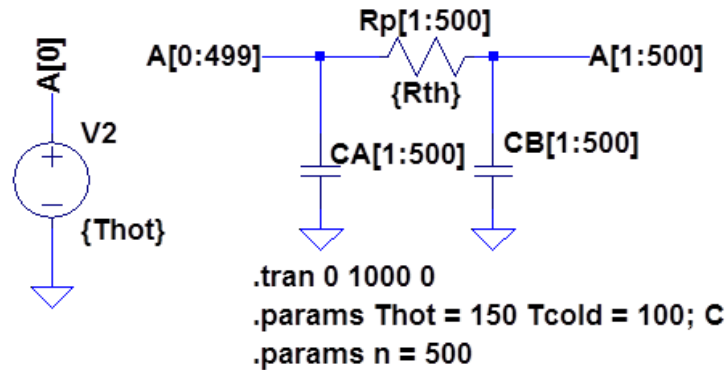


Figure 6.53 – Simple 1D FEM thermal circuit used for phase change model evaluation. This model uses a lumped mass approximation (no parallel coupling capacitor) as the nonlinear elements reference properties to the nodal voltage difference while temperatures need to be referenced to ground. The resistor and nonlinear capacitors are repeated n times in the circuit ($n = 500$ as shown) to create the element mesh.

As before, the two primary factors can be examined are the location of the melting front, $X(t)$, and the temperature profile with time, $T(x,t)$. Figure 6.54(a-d) shows an estimate of the melt front position with time for mesh densities of 100, 500, 1000, and 5000 elements, and for MZW varying from 0.1-2.0°C. The numerical solution shows the position of elements that are undergoing melting at any particular time. Each plot also includes the Neumann model analytical solution, which shows that after 1000 seconds the melt front has only progressed about 9.45 mm. The finite mushy zone width and the

idiosyncrasies of the enthalpy method allow heat to move through the melt front and warm the following elements, which is why there are numerous regions with multiple elements undergoing phase change.

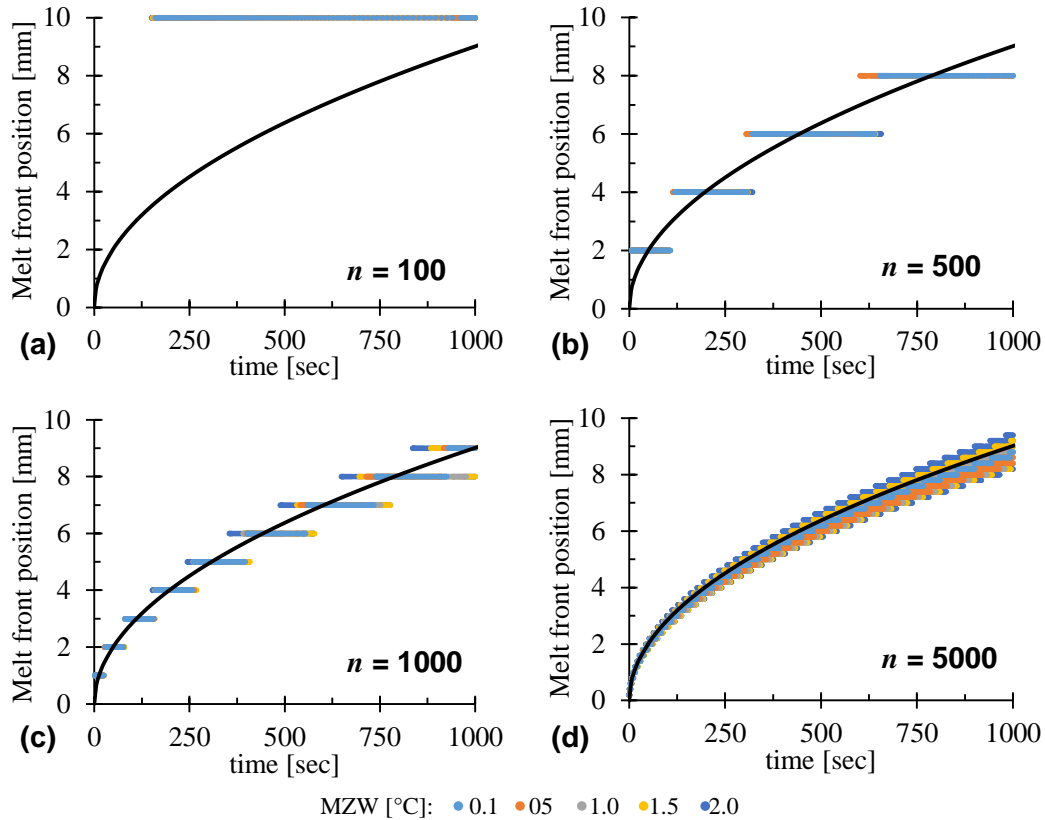


Figure 6.54 – PCM thermal circuit melting front estimates for different mushy zone widths and levels of mesh refinement. Data indicates location of elements undergoing melting. The analytical solution is shown as a solid black line for comparison.

The melt front progresses steadily with time following the Neumann data trend, and again the spatial width of the mushy zone is represented by the overlap in melting elements. As the 100 element mesh spacing is itself only 10 mm, that case is unable to capture the melt front with any resolution. After about 160 ms, the first element begins melting and gradually changes phase over the remainder of the simulation, as shown in Figure 6.54(a). The other cases (b-d) show a more refined estimate of the melting behavior. For $n = 500$,

1000, and 5000, the simulation moves the melting front across 4, 9, and 47 elements, respectively. The melting front is typically two elements wide in the 500 and 1000 element cases, and about four elements wide in the 5000 element case. This spatially broad melting front is a slight function of the temperature magnitude of the mushy zone width. In most cases the wider MZW broadened the melting time for each element, as it inherently increased the ΔT defined as melting. That said, the MZW choice made little difference in the ability of the melt center to follow the analytical trend.

A more refined melt front estimate can be made simply by interpolating between the nodal temperatures. While this does add an additional level of computation, linear interpolation is an integral part of finite element formulation and should not impose significant computational overhead. Figure 6.55(a-d) shows the melting front estimate in the same manner as Figure 6.54, but this time the solution nodal temperatures have been used with a simple linear interpolation to estimate the location of the melting front as being the point at $T = T_M$.

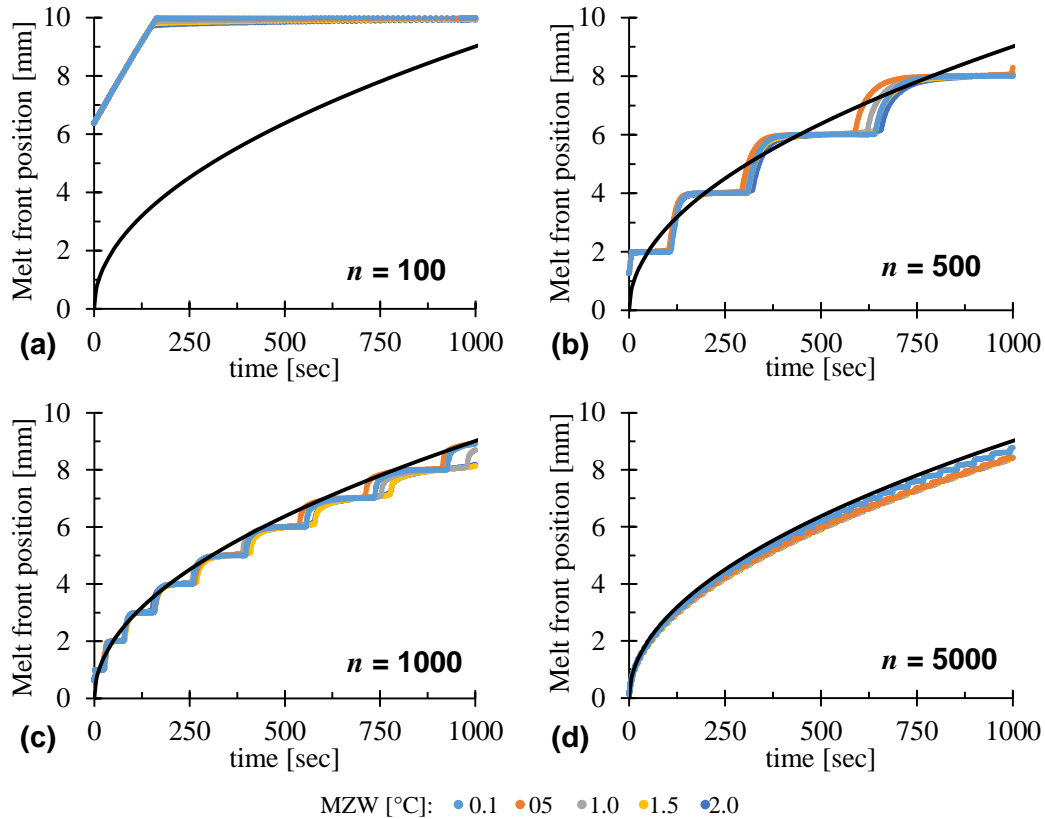


Figure 6.55 – PCM thermal circuit interpolated melting front estimates for different mushy zone widths and levels of mesh refinement. Data indicates estimated location of the melting front using linear interpolation of the element nodal temperatures. The analytical solution is shown as a solid black line for comparison.

The data in Figure 6.55 exhibit the same staircase behavior as the previous uninterpolated results, but the nodal temperature averaging is able to provide better location estimates, especially for times when the melting zone spans multiple elements. As mesh refinement increases and the prediction curve starts to track the expected profile, the results begin to universally underpredict the analytical solution.

Using the same Boltzmann normalization process that was used in Section 6.2.2, we can also examine the developing temperature profiles along the entire PCM slab. Figure 6.57 and Figure 6.57 show the normalized temperature profiles for different mesh densities

and mushy zone widths at a logarithmic progression of simulation times. The first observation from this data is that there is no significant variation in temperature profile data with mushy zone width for any of the mesh refinement values. This is likely due to the large model temperature span relative to the maximum MZW, and the slowness of the overall melt front propagation. Thus, further discussion in this simulation can ignore MZW considerations.

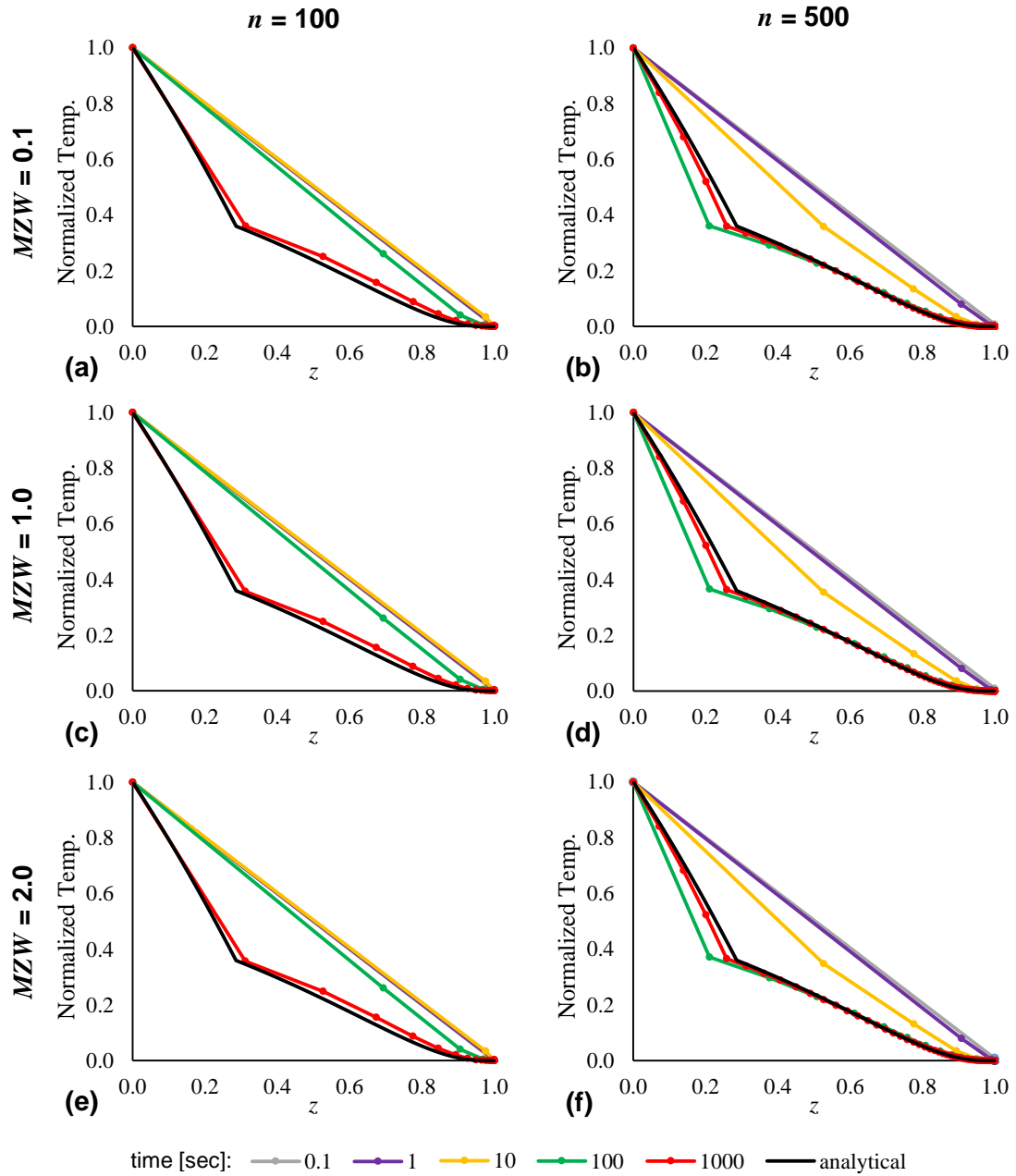


Figure 6.56 – PCM thermal circuit temperature profile estimates for $n = 100$ & 500 , different mushy zone widths, and a logarithmic progression of simulation times. Data indicates location of elements undergoing melting. The analytical solution is shown as a solid black line for comparison.

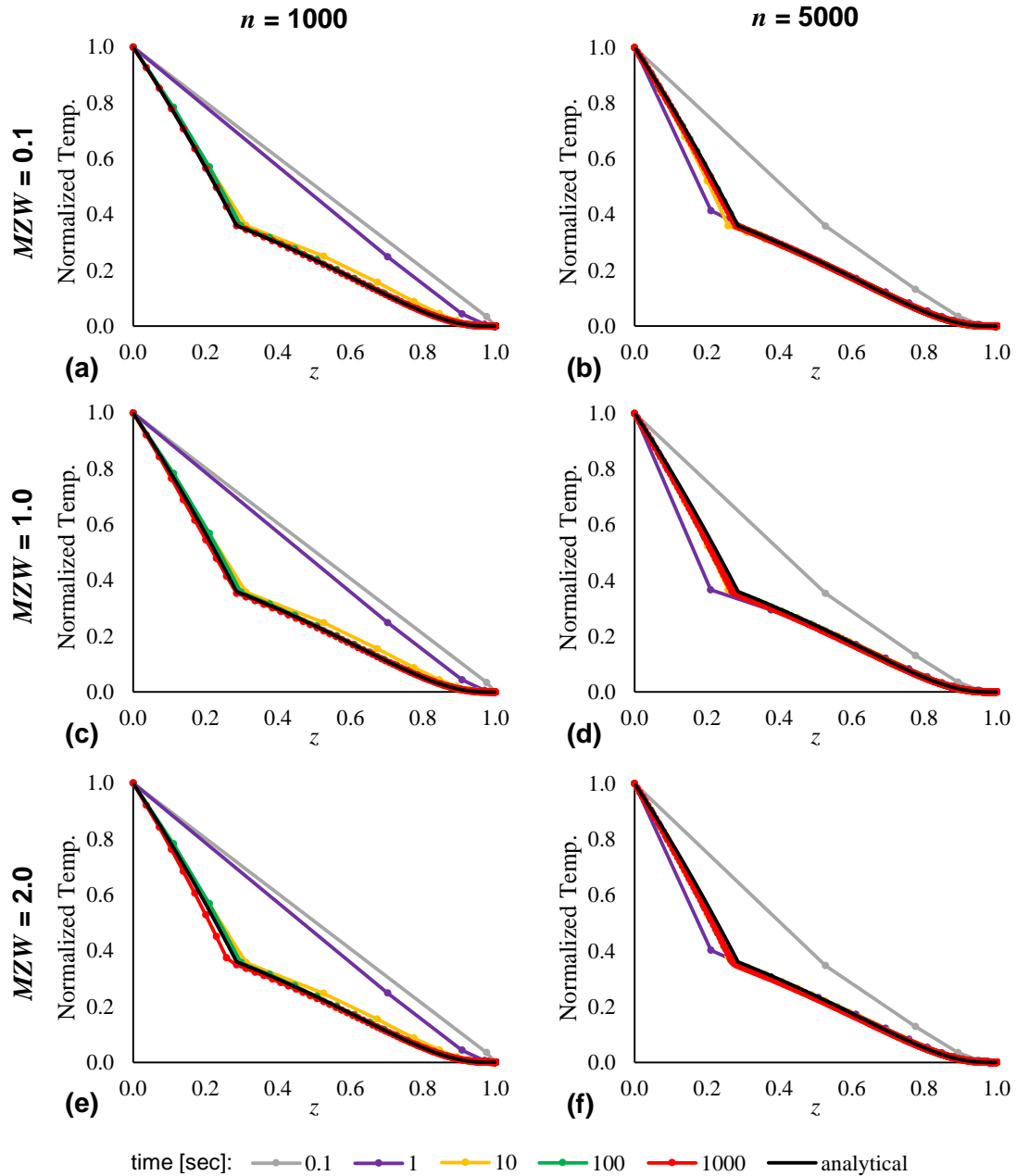


Figure 6.57 – PCM thermal circuit temperature profile estimates for $n = 1000$ & 5000 , different mushy zone widths, and a logarithmic progression of simulation times. Data indicates location of elements undergoing melting. The analytical solution is shown as a solid black line for comparison.

While the thermal circuit melting front prediction appeared to track fairly well, the limited mesh density appear to introduce significant profile prediction error in the early

time steps for all mesh densities. Increasing mesh density does correspond directly to increased accuracy at earlier times, however. This is expected simply because increased density allows better resolution of the high initial thermal gradient and the gradient around the melt front. Looking at temperature profiles, the number of temperature nodes in the region of interest can be seen as markers on each plot. For short time steps even the highest mesh refinement only has a few markers in the normalized region of interest. Because of the slow melting progression of erythritol, there are no nodal points in the melt region at 0.1 seconds in any of the models, leading to those temperature profiles “missing” the characteristic bend in the curve at the melt front location.

Although this is a simplified model, the presence of a closed form solution may permit us to extract a relationship between time step and mesh spacing to prevent the situations above where under-meshing restricts melt front tracking at early time steps. Referring back to (106), in the Neumann model the Boltzmann representation of the melt front is fixed in position by material parameters and the driving thermal conditions (through λ):

$$y_{mf} = x_{mf} / \sqrt{t_{mf}} = 2\lambda\sqrt{\alpha_l} \quad (126)$$

Thus for a simple one dimensional model we can estimate the melting front progression and determine the mesh spacing required to provide sufficient refinement for a given time step. For the given problem, to put at least one node at the middle of the melted zone (at $x_{mf}/2$) at each time of interest in the simulations above, the first nodal location would be as given in Table 6.18:

Table 6.18 – Melt front locations and melt region midpoints

<i>time</i> [sec]	<i>x_{mf}</i> [mm]	<i>x_{mf}/2</i> [mm]
0.1	0.090	0.045
1	0.285	0.143
10	0.901	0.451
100	2.85	1.43
1000	9.01	4.51

The smallest mesh spacing used in the simulations above was 0.2 mm ($n = 5000$), making it fairly clear why even that mesh was unable to capture the $t = 0.1$ sec melting front and the overall temperature distribution was distorted as a result. Using a fixed spacing refinement would have required $n > 22,000$ to have resolved it. This is briefly examined in Figure 6.58 and Figure 6.59. Here the same models were re-run with $MZW = 1.0$ (chosen as an intermediate value since these models were shown to be insensitive to that parameter), but this time two nodes were added at $x = 0.045\text{mm}$ and 0.090mm .

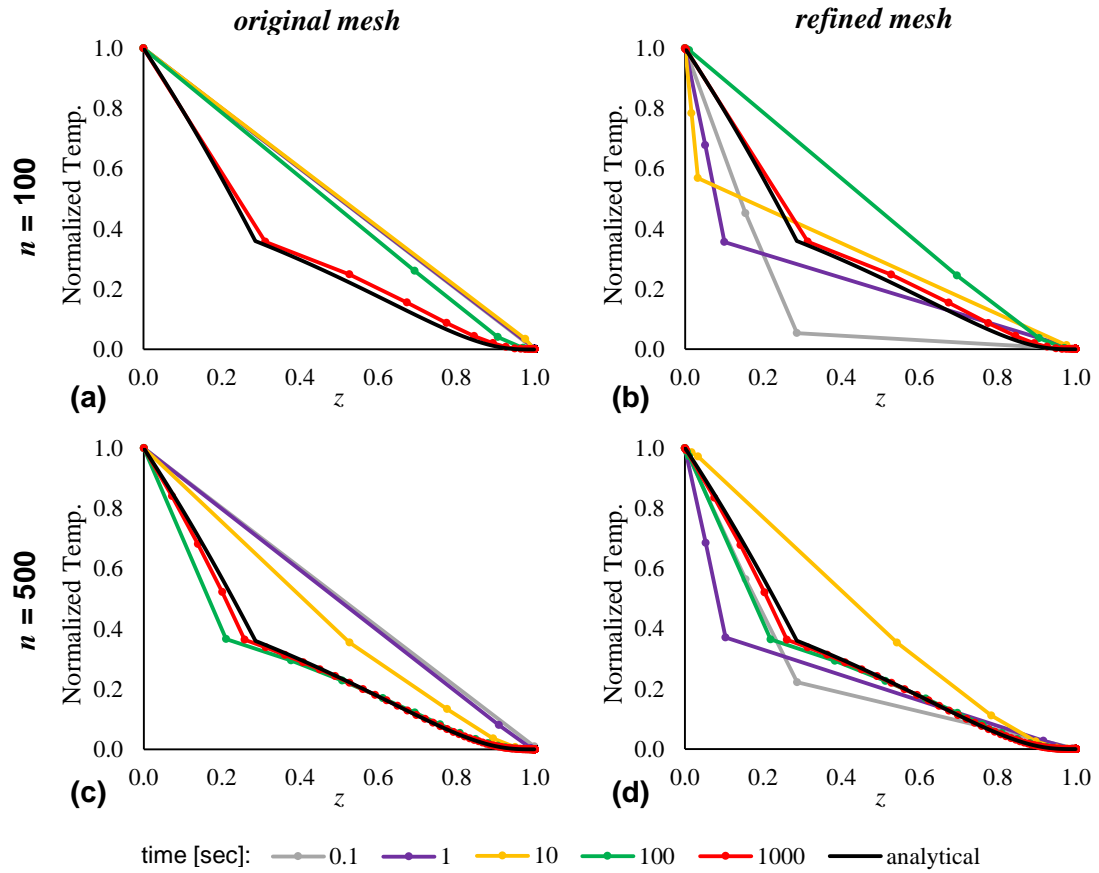


Figure 6.58 – PCM thermal circuit temperature profile comparison with refined melt front node spacing for $n = 100$ & 500 , $MZW = 1.0$, and a logarithmic progression of simulation times. Data indicates location of elements undergoing melting. The analytical solution is shown as a solid black line for comparison.

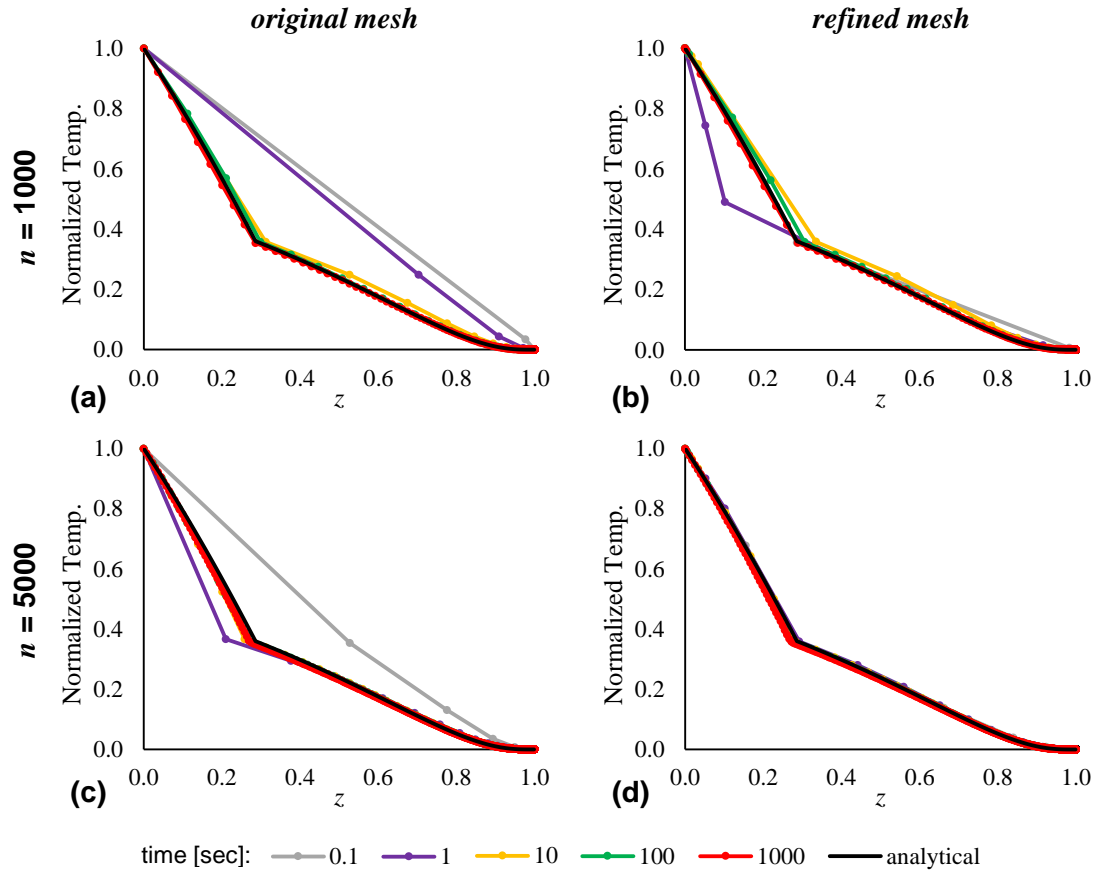


Figure 6.59 – PCM thermal circuit temperature profile comparison with refined melt front node spacing for $n = 1000$ & 5000 , $MZW = 1.0$, and a logarithmic progression of simulation times. Data indicates location of elements undergoing melting. The analytical solution is shown as a solid black line for comparison.

The increase in short time accuracy from the additional two nodes is quickly apparent, although merely adding those nodes does not provide complete temperature profile resolution. Almost all models resolve a melt front at the first node as soon as $t = 0.1$ sec, as evidenced by a noticeable knee in the curve for many of the iterations that appeared as linear thermal profiles with the original mesh. The significant melt front location error in the low-mesh-density models is simply evidence that one pair of extra nodes at the front cannot correct for the forced linear temperature profile over too coarse

of a mesh elsewhere. The $n = 5000$ model is able to fully predict x_{mf} for all time steps, and all models are able to indicate the presence of a melt front at $t = 0.1$ sec in areas where they had not previously. What is interesting is that the $n = 100$ and 500 models each have a later time at which they are unable resolve any melting location despite having resolved it earlier (100 sec and 10 sec respectively). Looking at the actual nodal locations, we can see that in these cases the melt front has simply moved past the high resolution nodes and the next regular-spacing node remains too distant to force the solution from the linear average over the element. Thus, resolving temperature profiles at a distribution of simulation times requires a properly distributed set of nodal spacings.

We can briefly examine the applicability of this thermal circuit phase change model to general (non-electronics) phase change systems. Zivkovic and Fujii performed a numerical and experimental PCM melting analysis of a flat panel PCM volume such as might be present in the unit cell of a plate-fin heat exchanger in a solar heating system [273]. Using the PCM melting model we can approximate their numerical and experimental results using our 1-D thermal circuit model. The domain in question is a 20 mm thick rectangular slab of calcium chloride hexahydrate (see Table D.14 for material properties) initially at 15°C , insulated on the edges, and subjected on both faces to a uniform hot convection of $h_\infty = 16 \text{ W/m}^2\text{K}$ at $T_\infty = 60^\circ\text{C}$. Using $n = 200$ phase change thermal elements, the simulation produces the phase change profile shown in Figure 6.60. As can be seen, the 1-D thermal circuit model closely follows the Zivkovic and Fujii numerical model, and both models adequately predict the experimental profile. Discrepancy for both models is largely attributed to liquid PCM thermal behavior not being adequately matched by either model. In any case, it is apparent that the thermal circuit

model can capably predict phase change heat transfer models as long as conditions are such that a static enthalpy model adequately represents the physics at hand.

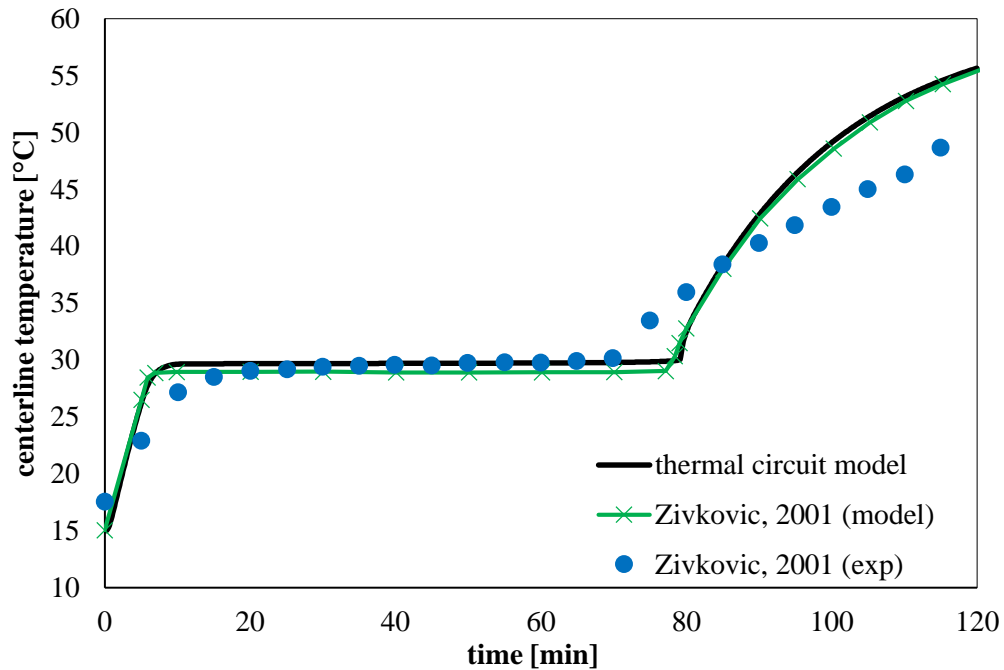


Figure 6.60 – Thermal circuit prediction of Zivkovic and Fujii phase change center line temperature profile. Comparison model and experimental data extracted from [273].

We can conclude then that, while the methods described in this chapter are sufficient to reproduce general behavior for phase change models, more accurate numerical modeling is, as expected, dependent on judicious placement of fixed refinement regions near phase change zones, or proper implementation of computationally efficient auto-refinement methods. For fixed refinement approaches, the one-dimensional Neumann problem can provide a useful estimator of front progression rate and required mesh spacing near the region of melting onset using the Boltzmann normalization in (126). The SPICE implementation used here is useful for thermal analysis, but it is far from a perfect thermal simulation tool. As a discrete component solver, most SPICE implementations lack a convenient method of implementing mesh refinement, either manual or automatic. We

took advantage of an undocumented bus feature in LTspice to brute-force a refinement effect, but more elegant methods would be needed to make this a practical feature. Given that allowance, the technique appears quite capable of approximating the solution to phase change problems related to heat exchange, energy storage, and as will be shown in the next section, electronics cooling.

6.4.3. Transient thermal circuits with PCM buffering

In this section we use the new phase change thermal circuit models to examine how well incorporating PCMs directly into the device package can mitigate the transient heating problems identified in Section 5.3. Again, those two primary problems were related to (1) package thermal resistance improvements actually worsening transient performance, and (2) convective improvement being unable to impact device heating for short pulses relative to package thermal transport times. We will step through a simple set of re-evaluations of the one-dimensional Chapter 5 package models, this time incorporating a PCM on top of the device using the one-dimensional phase change model from the previous section. Additionally, we will conclude with an examination of the significance of PCM-to-package thermal interface resistance and the impact on thermal buffer performance.

6.4.3.1. PCM capped package models

Cases 1-5 are re-implemented in LTspice for this study, this time with a block of non-linear PCM circuit elements connected to the top side of the device. Based loosely on the experimental work performed by Gonzalez-Nino, et al., [250,251], elements representing a 2 mm thick block of a phase change material were connected to the surface node of the Case model thermal circuit. An example of this for Case 5 is shown in Figure

6.61. There a 200 element PCM block is connected to the top node of the package model through an interface resistor (set to zero resistance in this model). The topside node of the PCM has no thermal connection, emulating a perfect insulation boundary condition. Note this is a boundary condition change from the Gonzales-Nino experiment, which was open to air, but was chosen in this study to match the previous modeling and reduce potential variables. It is expected that this difference will only be a factor for longer pulses.

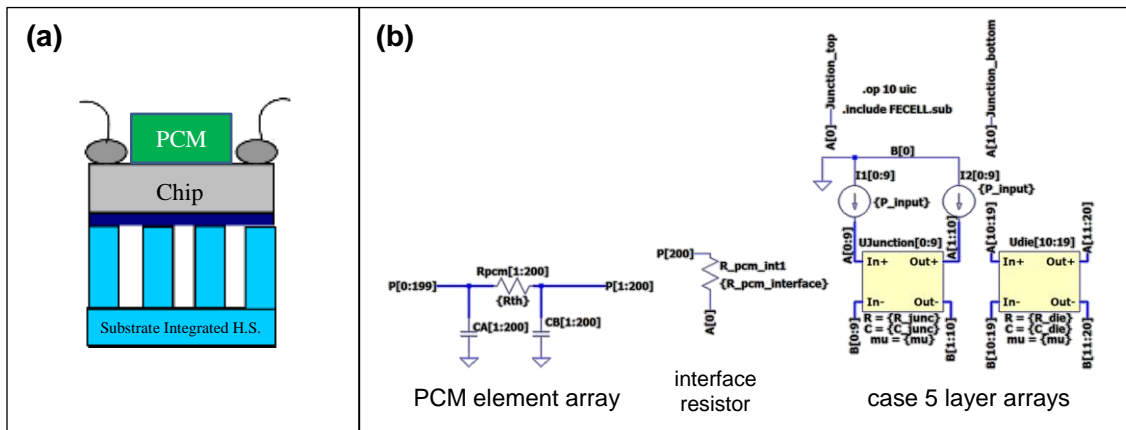


Figure 6.61 – Case 5 thermal circuit model with topside PCM block shown (a) graphically and (b) as a package thermal circuit. Package circuit has the $n = 10$ layer discretization used previously, while the PCM block has a uniform $n_{pcm} = 200$ discretization. The model also has a parameterized interface resistance between the PCM and package surface, R_{pcm_int1} , here set to zero.

The same PCMs are chosen for this simulation as for the substrate integrated PCM investigation in Section 6.3: erythritol, gallium, and lithium nitrate trihydrate. Step and pulsed response models will be examined for each material and compared with the thermal profiles from the previous linear thermal circuit models. Material properties are summarized in Table 6.19 using midpoint values of the properties from Chapter 2.

Table 6.19 – PCM properties used in the SPICE package model

property	unit	gallium	lithium nitrate trihydrate	erythritol
<i>type</i>	--	pure metal	salt hydrate	sugar alcohol
k_{th}	W/mK	33.7 (s), 29.4 (l)	0.770 (s), 0.575 (l)	0.733 (s), 0.326 (l)
c_p	J/kgK	340 (s), 384 (l)	1800 (s), 2800 (l)	1383 (s), 2765 (l)
ρ	kg/m ³	5905 (s), 6093 (l)	1567.5 (s), 1401 (l)	1480 (s), 1300 (l)
H_f	kJ/kg	80.2	291.5	339.8
$H_{f,v}$	MJ/m ³	473.6	456.9	502.9
T_M	°C	30	30	118
E_{max}	J/cm ²	94.7	91.4	100.6

Convection dependent linear step response models were run first to examine any changes in thermal behavior due to the additional sensible thermal mass at the junction to establish a “loaded” baseline for each Case. Following this, pulse train models examine the degree to which the PCM integration can suppress temperature rise, and whether it corrects the package thermal inversion caused by low thermal capacity. All Cases are compared to the linear, non-PCM models from Chapter 5. Note that whereas the previous linear package models could all be normalized to a unit input power, non-linear models exhibiting phase change must be run at absolute power levels and temperatures which adds some complexity to comparison efforts.

6.4.3.2. Linear step response models

Package linear response is summarized in Figures 6.62-6.66, generally showing similar behavior to non-PCM loaded packages with some slower thermal response due to additional linear thermal capacity. It is worth noting that the earlier models completely ignored any thermal impedance from package encapsulation. This is equivalent to a vacuum sealed package with no thermal contact outside the primary removal path, or approximately equivalent to an extremely low thermal capacity, low thermal conductivity

encapsulating material, such as an aerogel. Most practical package encapsulants would be a silicone gel or other plastic or organic material providing some nominal thermal impedance. As such, the linear step responses of the organic materials (erythritol and LNT) may serve more useful baseline heating cases than the no-PCM cases. As will be shown, the gallium loaded package shows the most significant deviation in transient behavior in large part due to its much lower thermal impedance.

Figure 6.62 is a representative example showing the junction temperature rise for the Case 5 package for each PCM. There are two features of note in these plots: First, PCM loading made little noticeable difference to the convective insensitivity at short pulse rates. Second, the addition of gallium to the package did noticeably reduce temperature as the lower thermal impedance provided a significant temporary heat flow path at short pulse times. This behavior is consistent for all package Cases, which can be seen in Appendix A, Figure A.1 and Figure A.2.

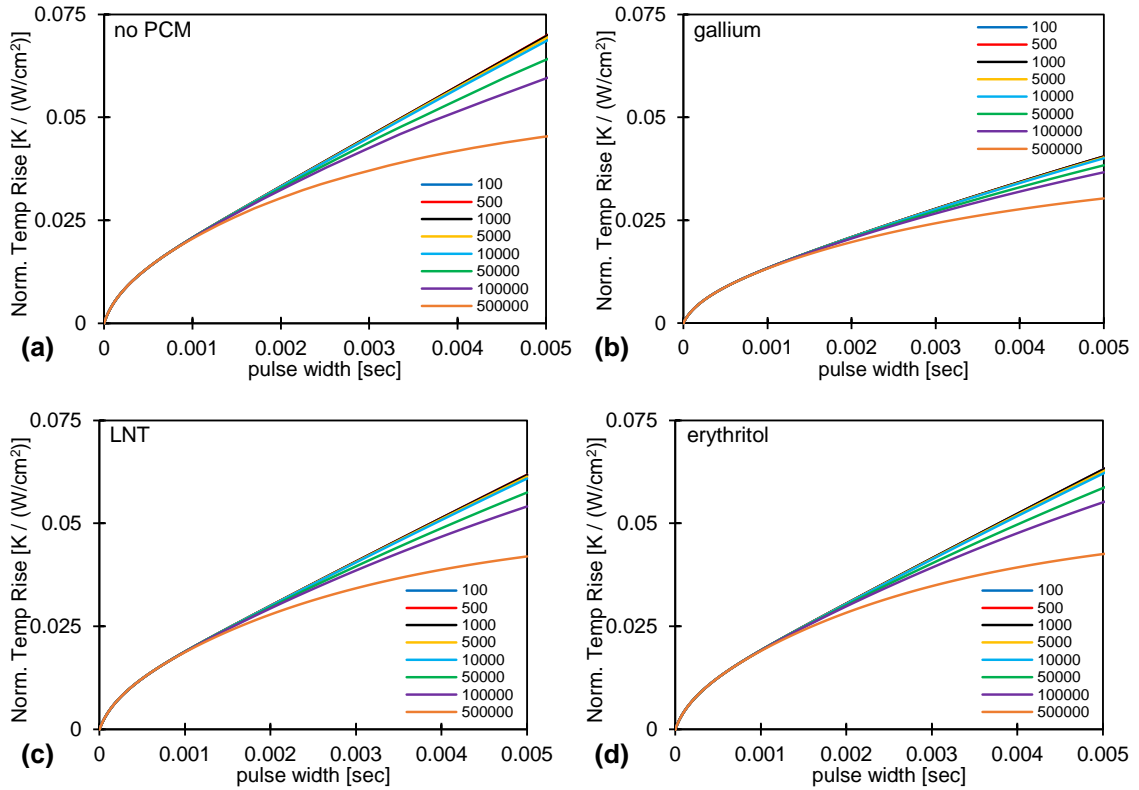


Figure 6.62 – Comparison of convection dependent peak junction temperature for Case 5 with topside PCM loading for varying convection rates and pulse widths. While the low thermal impedance of gallium results in lower absolute temperature rise, the convective deviation is generally unchanged by the addition of PCM.

Figure 6.63 shows that PCM loading makes little difference to package convective insensitivity. As before a convection rate spanning 100 to 500,000 $\text{W}/\text{m}^2\text{K}$ (a 5,000x increase in applied cooling) reduces temperature rise less than 1% for the highest thermal inertia package, and far less than that for the others. Table 6.20 provides the magnitude of convective improvement. Note that gallium shows about 1/3 less thermal discrepancy than other materials except for Case 5, likely due to gallium’s parallel thermal path reducing the amount of heat reaching the convective surface at short timescales.

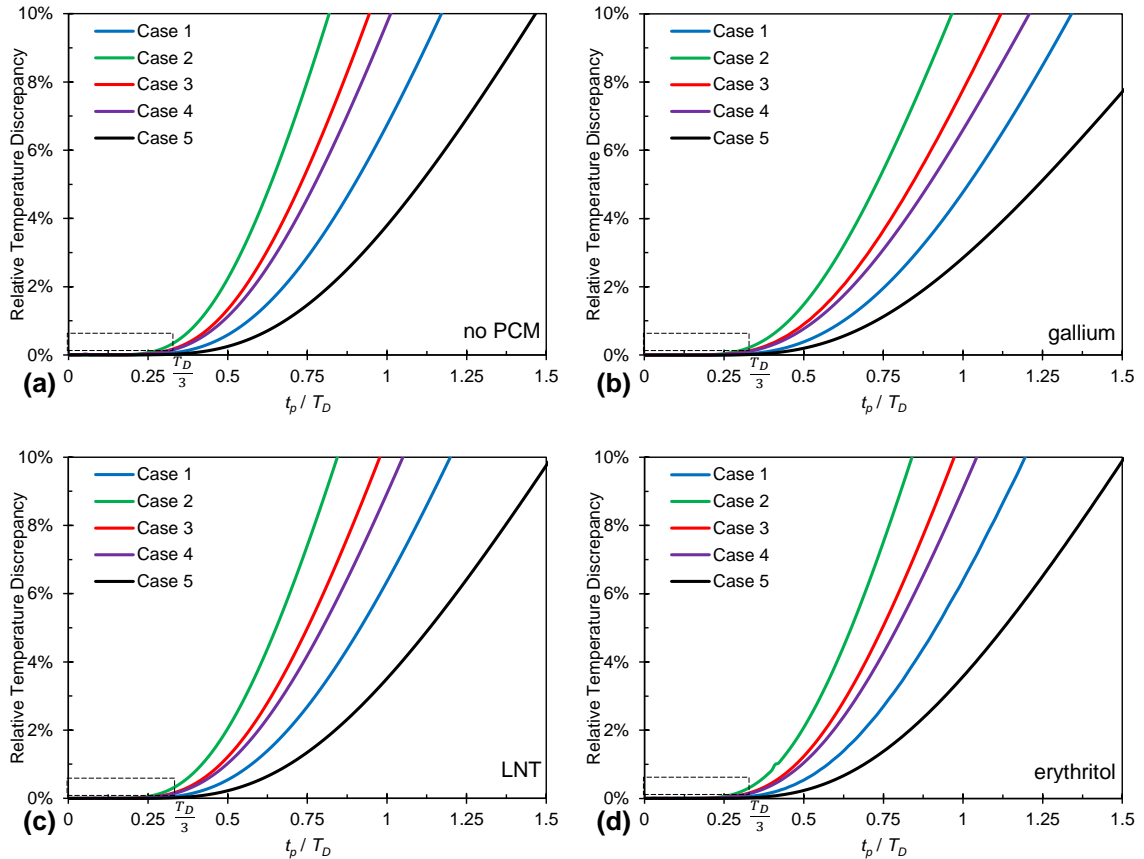


Figure 6.63 – Thermal impedance impact on convective sensitivity in PCM loaded packages showing little difference between no-PCM and PCM loaded packages. The 0.5% - $T_D/3$ box on each plot shows that T_D still serves as a useful measure of convective insensitivity despite the additional capacitive loading.

Table 6.20 – $T_D/3$ convective sensitivity change with PCM loading

Case	No-PCM	Gallium	LNT	Erythritol
1	0.06%	0.04%	0.06%	0.06%
2	0.36%	0.24%	0.33%	0.34%
3	0.19%	0.13%	0.17%	0.17%
4	0.16%	0.11%	0.15%	0.15%
5	0.02%	0.02%	0.02%	0.02%

It is worth noting that Figure 6.63 refers to the same Elmore delay calculated for the non-PCM loaded packages. Although the presence of a PCM obviously adds thermal capacity to the source node of the thermal circuit, and this additional source capacity should

slow down temperature rise and heat propagation to the convective surface, either mode of Elmore delay calculation ignores source node capacitance. When calculating T_D as the lowest order mode of the circuit transfer function, that transfer function is an input-output voltage ratio. Imposing a voltage step or impulse function on the source node ignores input node impedance (the forced step implies sufficient energy is added to drive the local impedance) and source node capacitance completely drops out of the T_D formula. Alternatively, using the discrete circuit traversal algorithm, an arbitrary amount of PCM is lumped into a source node capacitor according to the level of PCM discretization used. As this capacitance is multiplied by zero source thermal resistance, it again drops out of the equation. All other PCM capacitance nodes are ignored because they do not lie on the primary path to the thermal sink. Thus, while the values calculated above show Elmore delay is still effective in estimating convective insensitivity with PCM loaded packages, a higher-order delay calculation method would be needed to accurately calculate the effect of source loading on package delay.

Finally, Figures 6.64-6.66 show the step response at fixed convection coefficients to demonstrate that the packages continue to exhibit the thermal inversion described in Chapter 5. These figures show that the PCM has little effect on that inversion, although the increased thermal capacity does make a significant difference in the rate of package temperature rise. In particular, we can note that presence of the PCM drastically reduces temperature rise in the low thermal inertia packages at low and moderate convection rates due to the source capacitive loading. All three PCMs significantly drop the Case 3-5 temperature rise at a low h_{eff} of 100 W/m²K, while gallium has a more pronounced impact at 10 kW/m²K. At 500 kW/m²K the effect is on the profile is negligible except for

gallium's overall lower temperature rise. The low, medium and high convective rates exhibit the same inverse progression of thermal inversion as packages without PCM. The full set of graphs for each convective rate showing similar behavior for all simulated values of h_{eff} can be found in Appendix A, Figures A.3-A.10.

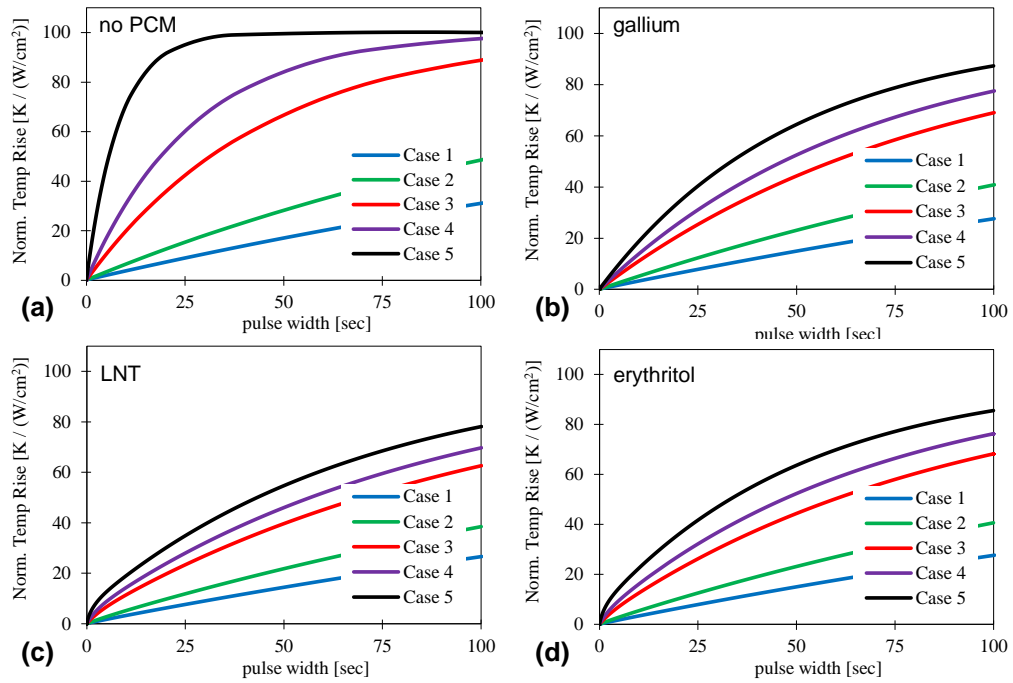


Figure 6.64 – PCM loaded package temperature step response comparison for $h_{eff} = 100 \text{ W/m}^2\text{K}$ showing continued package thermal inversion for low convection rates.

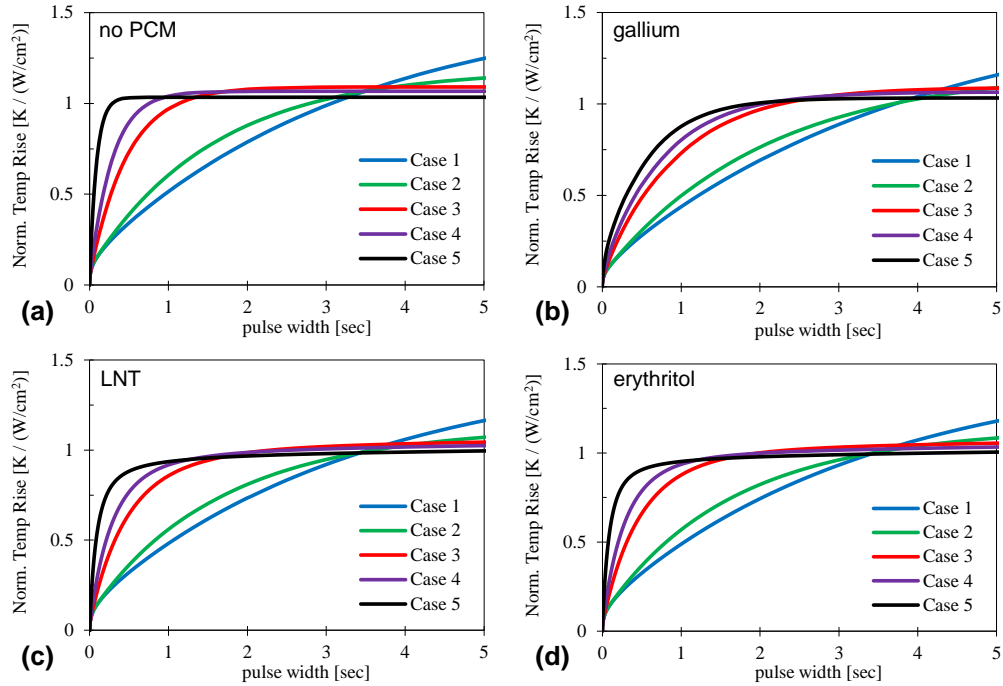


Figure 6.65 – PCM loaded package temperature step response comparison for $h_{eff} = 10,000 \text{ W/m}^2\text{K}$ showing package thermal inversion crossover occurring between 1 and 4 seconds.

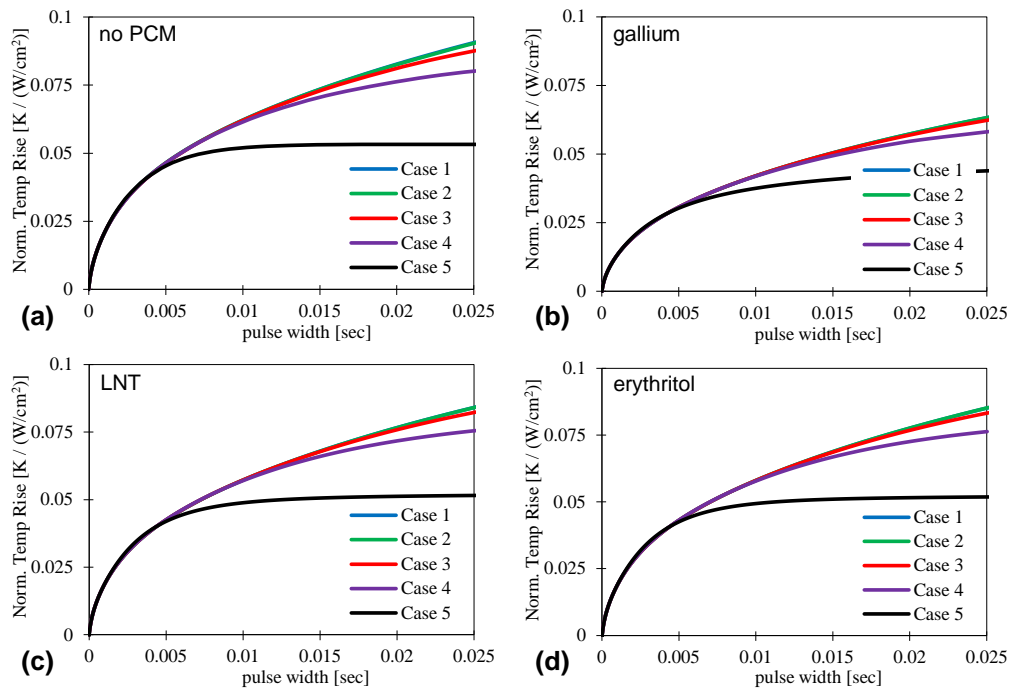


Figure 6.66 – PCM loaded package temperature step response comparison for $h_{eff} = 500,000 \text{ W/m}^2\text{K}$ showing no package thermal inversion at high convection rates.

6.4.3.3. *Nonlinear phase change step-response models*

The previous section demonstrated that, predictably, the presence of a source connected thermal capacitance is sufficient to reduce temperature rise relative to the original package models. Thus, in this section we will examine the degree to which phase change provides additional temperature suppression. We will examine both step and pulsed package responses when driven past phase change, looking at low (150 W/cm^2) and high (750 W/cm^2) power cases for the different materials. (Low and high power levels chosen to ensure melting is reached by all packages under both low the lowest and highest convection conditions). These responses will be compared against both the no-PCM cases previously simulated, as well as cases with PCM present but no phase change occurring so that estimates of sensible and latent thermal suppression can be separately quantified. This is accomplished by simply turning off the latent heat component in the PCM element model, and assuming that the material stays solid for the duration of the transient. It is recognized that this ignores the eventual transition to liquid state properties, however this impact should be minor next to the significant impact of suppressing phase change in those models.

Figure 6.67 and Figure 6.68 show representative sets of high power (750 W/cm^2) step responses for the different PCMs at long and short timescales for Cases 1 and 5, respectively. Each is shown for the same three values of h_{eff} used in the linear model pulse testing (10, 50, and $100 \text{ kW/m}^2\text{K}$). The figures show the fairly extreme difference in thermal suppression provided by the metallic phase change material. Unlike many other PCM investigations, including most configurations from which FOMs are derived, the material is not in the primary heat removal path, instead being a parallel thermal

impedance. Because of this there is a time dependent division of heat flow between the parallel paths, and the metallic PCM's much lower thermal impedance improves overall PCM utilization with a smaller melt front-to-thermal junction temperature gradient. It can be seen in both sets of figures that the gallium's phase change thermal suppression is seen for about 0.5 sec, whereas the two low- k_{th} materials show very little effect at short or long timescales. The full set of melting profiles for all Cases at low and high power levels can be found in Appendix A, Figures A.11-A.16.

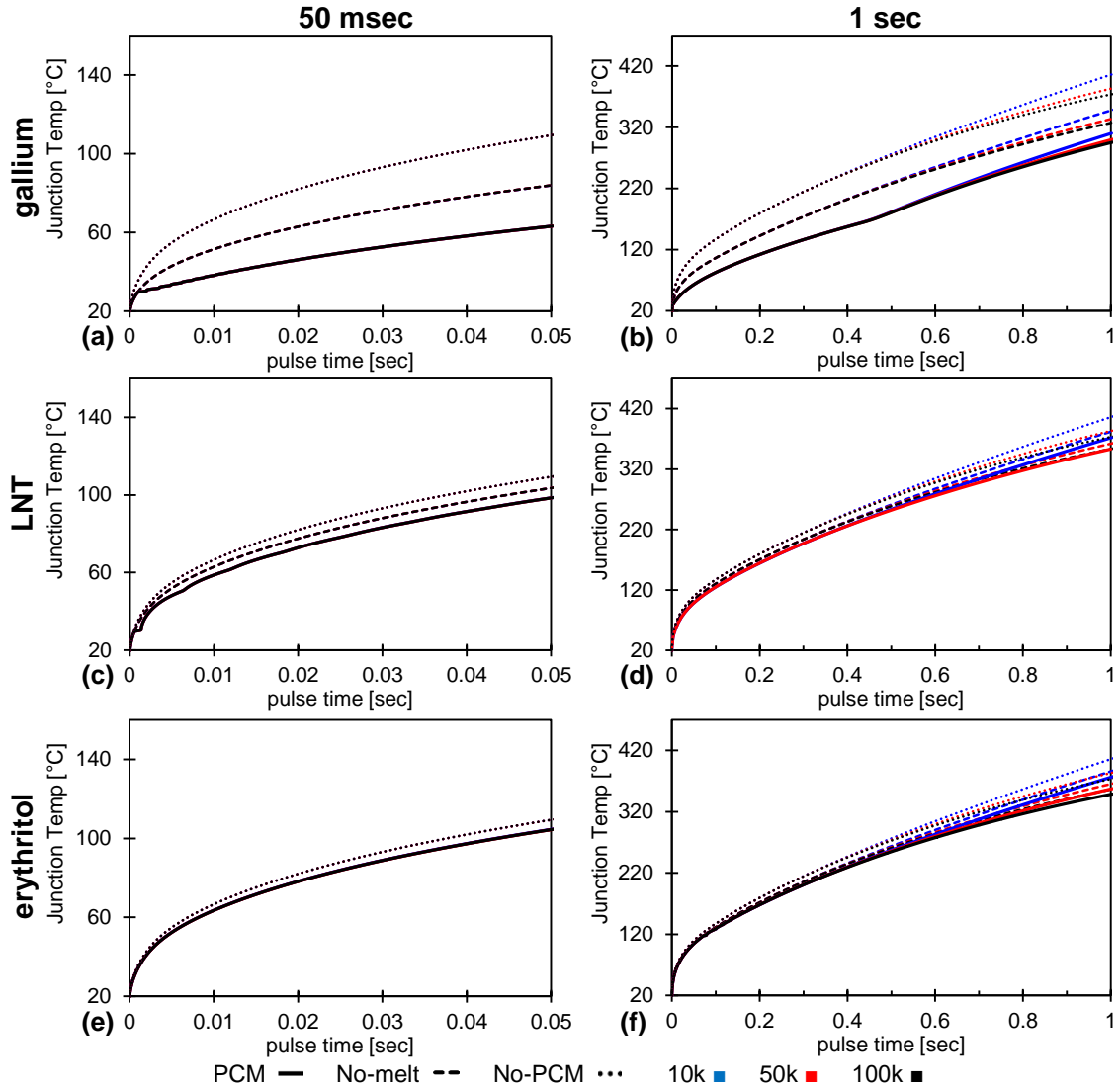


Figure 6.67 – Package phase change step responses for Case 1 at 750 W/cm^2 , $h_{eff} = 10, 50$, and $100 \text{ kW/m}^2\text{K}$, $T_0 = 20^\circ\text{C}$. Short (a, c, e) and long (b, d, f) time response compared against cases without PCM (dotted lines) and with PCM but without phase change (dashed lines).

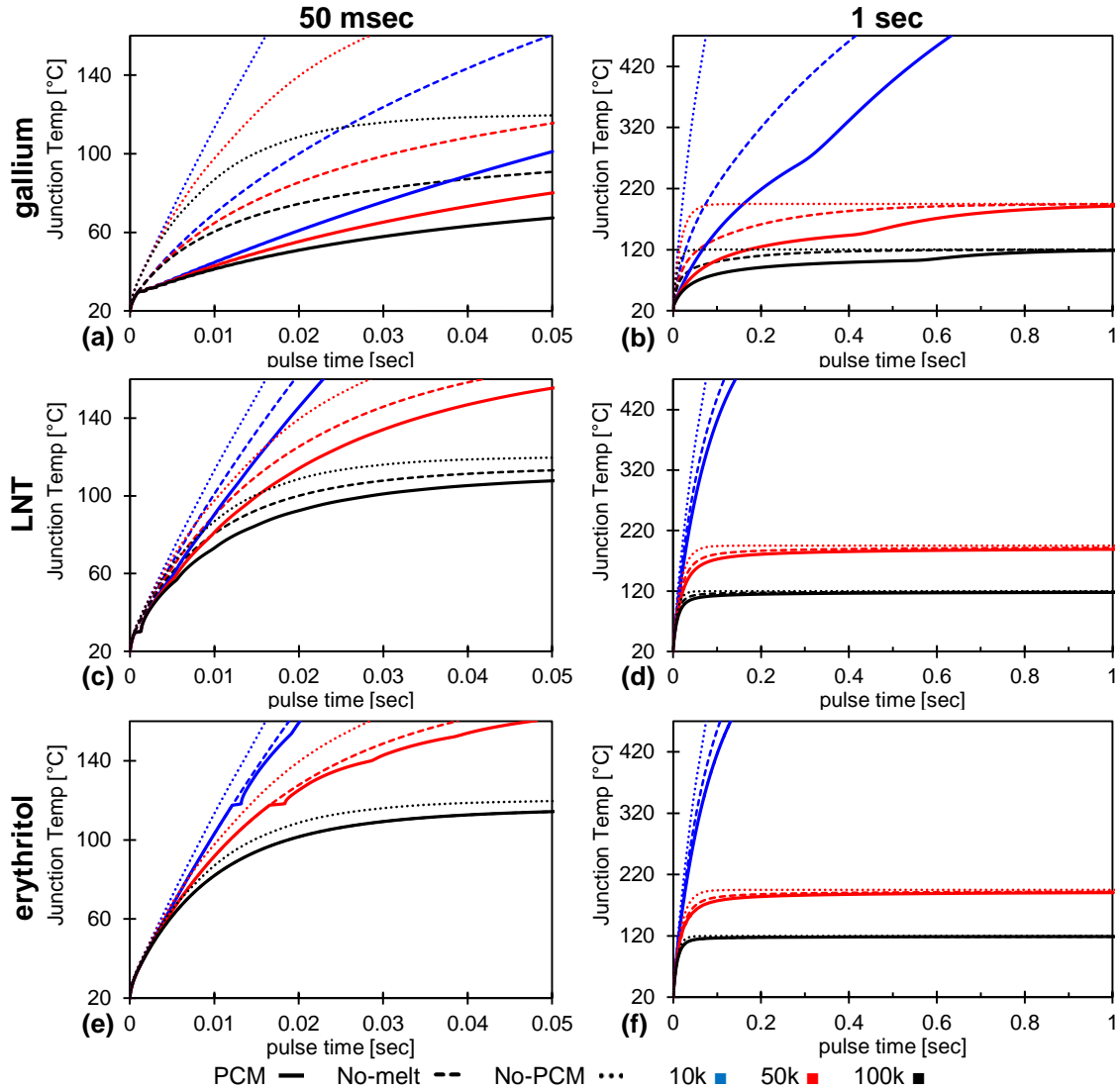


Figure 6.68 – Package phase change step responses for Case 5 at 750 W/cm^2 , $h_{\text{eff}} = 10, 50$, and $100 \text{ kW/m}^2\text{K}$, $T_0 = 20^\circ\text{C}$. Long (a, c, e) and short (b, d, f) time response compared against response without PCM (dotted lines) and with PCM but without phase change (dashed lines).

Matching what was shown with the linear response models, about half of the thermal suppression is caused simply by the sensible thermal capacity of the added material. The impact of this and the latent capacity of the materials is rather slight in the high thermal inertia Case 1 package, but for the Case 5 package where thermal capacity had previously been minimized, the additional material produced significantly slower

temperature rise. Even the low- k_{th} materials show tens of degrees of thermal suppression below 50 ms from the sensible heat absorption, but gallium's thermal suppression overshadows this by almost an order of magnitude. More thermal capacity is available for absorption in the gallium case simply due to the high thermal conductivity creating a low impedance thermal path, shown clearly by the difference between no-PCM and no-phase-change curves in Figures 6.67(b) and 6.68(b).

The latent effect follows similar behavior, where the phase change is noticeable but not overly significant for LNT and erythritol, whereas gallium's phase change produces additional thermal suppression on the same order as that of the sensible absorption (approximately 20°C for Case 1 and from 20-60°C for Case 5 at 50 ms). At longer timescales, the phase change effect from gallium lasts out to about 0.5 seconds in Case 1 and from 0.3 to 0.7 seconds for Case 5. This is in stark contrast to the non-metallic PCMs that showed little phase change suppression to begin with, approximately 10-20°C at maximum, and whose effect was nearly unnoticeable after 0.1 to 0.2 seconds.

It is worth noting that there was no real change in the package convective insensitivity discussed in earlier chapters. The temperature profiles all converge at similar times for each Case, as expected from the package delay metric, T_D . In this way, we see that for pulse times below the convective insensitivity limit, adding thermal capacity provides far more benefit than increasing convection. As an example, looking at gallium in Figure 6.67(a), after 10 ms at high power the ΔT in Case 1 is reduced from 40°C with no PCM to about 10°C with phase change, whereas the order of magnitude convective improvement (from 10-100 kW/m²K) makes no noticeable temperature difference (the profiles are indistinguishable out to greater than 0.5 seconds). Similarly with the integrated

Case 5 package in Figure 6.67(e), at 5 ms, the same 10x convective improvement has about 5°C of impact while adding gallium reduces the ΔT from 50°C to about 15°C. Figure 6.69 shows a magnification of the first 10 ms of temperature rise for both LNT and gallium, emphasizing the degree of fast thermal suppression capable by using metallic PCM under ideal conditions.

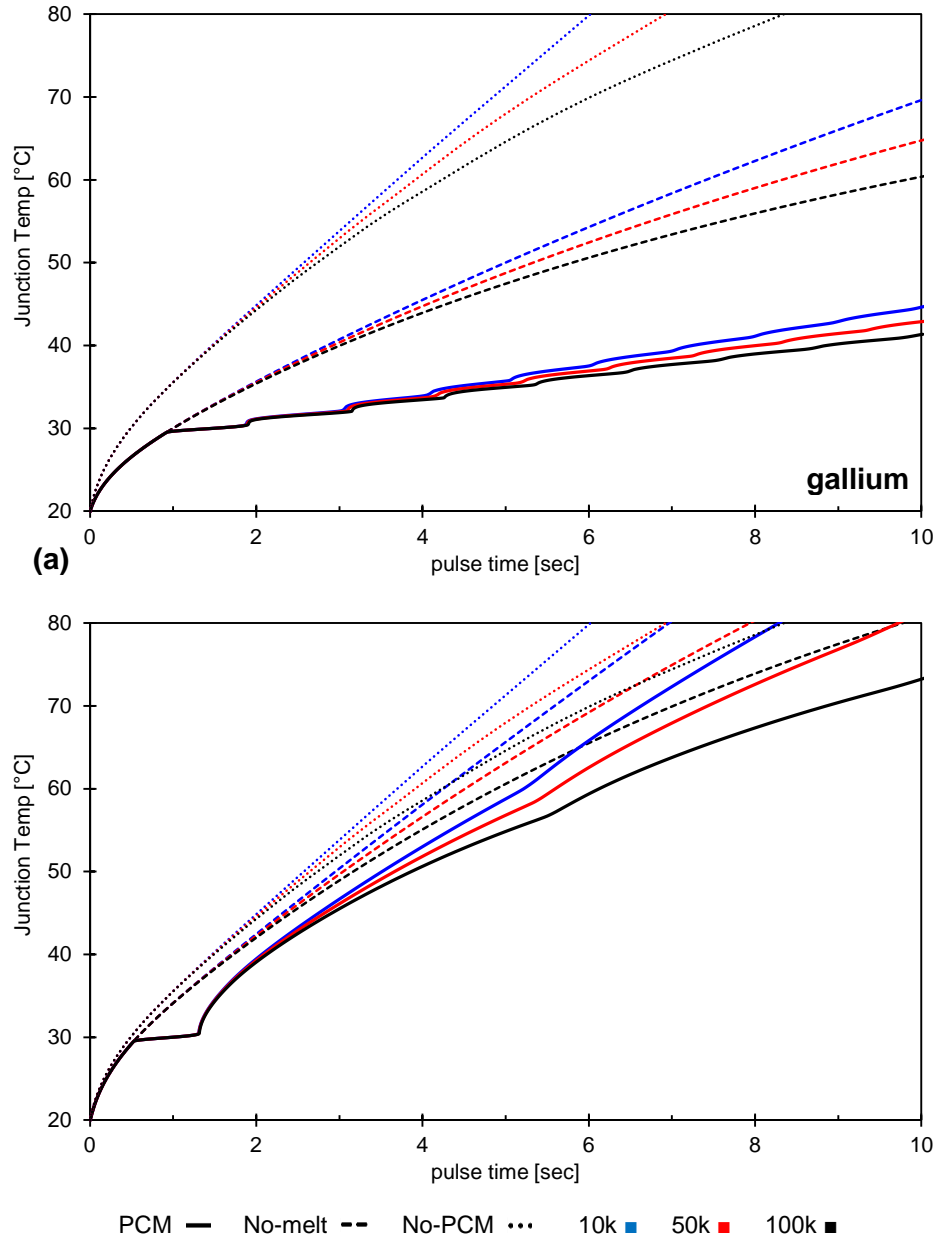


Figure 6.69 – Close up of melting onset for (a) gallium and (b) LNT during Case 5 phase change step responses at 750 W/cm^2 , $h_{eff}=10, 50, \text{ and } 100 \text{ kW/m}^2\text{K}$, $T_0 = 20^\circ\text{C}$, compared against response without PCM (dotted lines) and with PCM but without phase change (dashed lines).

Comparing the initial temperature rise for the two packages in Figure 6.69, both cases show that there is no visible convective sensitivity until 2-3 ms. Before this, as the junction with the less conductive LNT heats faster, it reaches the 30°C melt temperature in

about 0.5 ms, versus about 1 ms for gallium. Note that at the sub-ms time scale, the presence of the LNT and the associated thermal capacity provides very little thermal suppression relative to the base package, whereas at 1 ms the gallium package's low thermal impedance has already provided about 6°C (out of 16°C, or 37.5%) of temperature reduction. Beyond this point phase change causes significant nonlinear temperature response for both packages, and the limits of insufficient (non-converged) discretization becomes apparent. The first temperature plateau for both materials is due to the thermal capacitor connected directly to the junction, as there is no material thermal resistance to slow the absorption. Staircasing is visible in subsequent absorption, but the stark difference between gallium and LNT for the second step shows the impact of having a high thermal conductivity and high latent heat material. LNT's 'charging resistance' causes a steep temperature rise and the thermal slope closely follows that of the no-phase-change case, and the presence of subsequent phase change provides little additional benefit. Conversely, gallium's low thermal impedance provides continued thermal suppression, and the much faster staircasing indicates better utilization of the material away from junction. While the staircasing in Figure 6.69 is indicative of under-meshing at this timescale, the sudden change in thermal slope in LNT after the first thermal capacitor saturates is significantly more non-physical than for gallium. Improved meshing would likely smooth or average out this behavior after onset of phase change. The gallium profile would still generally follow a similar trend after this smoothing, but for LNT the entire initial temperature suppression would likely be diminished as the averaging pulled the early response upward. Thus, while the mesh is too coarse for extensive use of the temperature suppression values

for LNT, the general thermal charging behavior is still instructive for seeing the impact of the high thermal impedance.

Reinforcing this last point, Figure 6.70 shows the melt fraction for LNT and gallium over the first second of heating under the same conditions as Figure 6.69. Gallium’s low thermal impedance enables much faster utilization of the full 2-mm thickness of PCM in under 0.5 seconds, unlike LNT which has not even reached 50% melt fraction in twice that time. Without the low thermal conductivity acting as a high thermal charging resistance, the LNT is simply unable to provide enough absorption to prevent a significantly higher junction temperature rise over that time span.

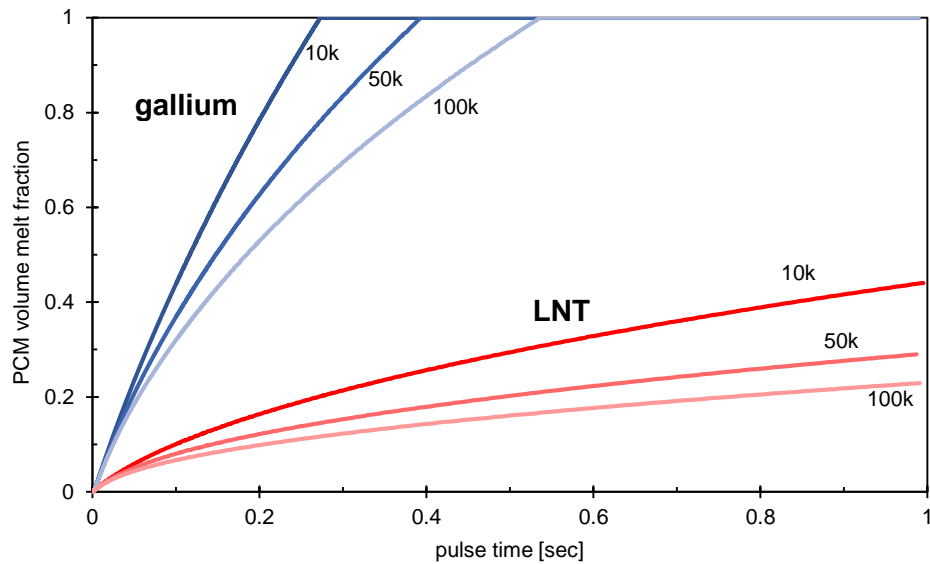


Figure 6.70 – Case 5 PCM melt fraction for gallium (blue) and LNT (red) during step response simulations. Convection coefficients indicated as labeled from $h_{eff} = 10\text{-}100 \text{ kW/m}^2\text{K}$.

6.4.3.4. Phase change pulsed response models

For a final comparison and to examine whether there was any impact on package performance inversion, we now examine a selection of pulsed power models. While package heating profiles will follow the exact same trends as the step response curves, we

will more directly compare the individual package Cases as well as the effect of the cool-down portion of the duty cycle. (This is a distinct advantage of the simulation speed provided by the compact SPICE models, as the simulation time precluded full pulse analysis in the previous section's FEA TBHS modeling study.)

Using the same power and boundary conditions as for the step response curves, Figure 6.71 shows a series of high power pulse response curves for each PCM under the same conditions as the step response curves in Figure 6.67. Just as with the previous step response curves, each case is superimposed on the linear pulsed temperature response described in Section 5.3.2.4 (light dotted lines) as well as the temperature response with the PCM but without the effect of phase change (dashed line) in order to separate the effects of the material's linear thermal capacity from its latent absorption effect. Additionally, the Figure shows both the initial and 'final' pulse, arbitrarily chosen as pulse number 30, by which point all simulations showing gradual warming had saturated. First pulse peak temperature data is summarized in Table 6.21.

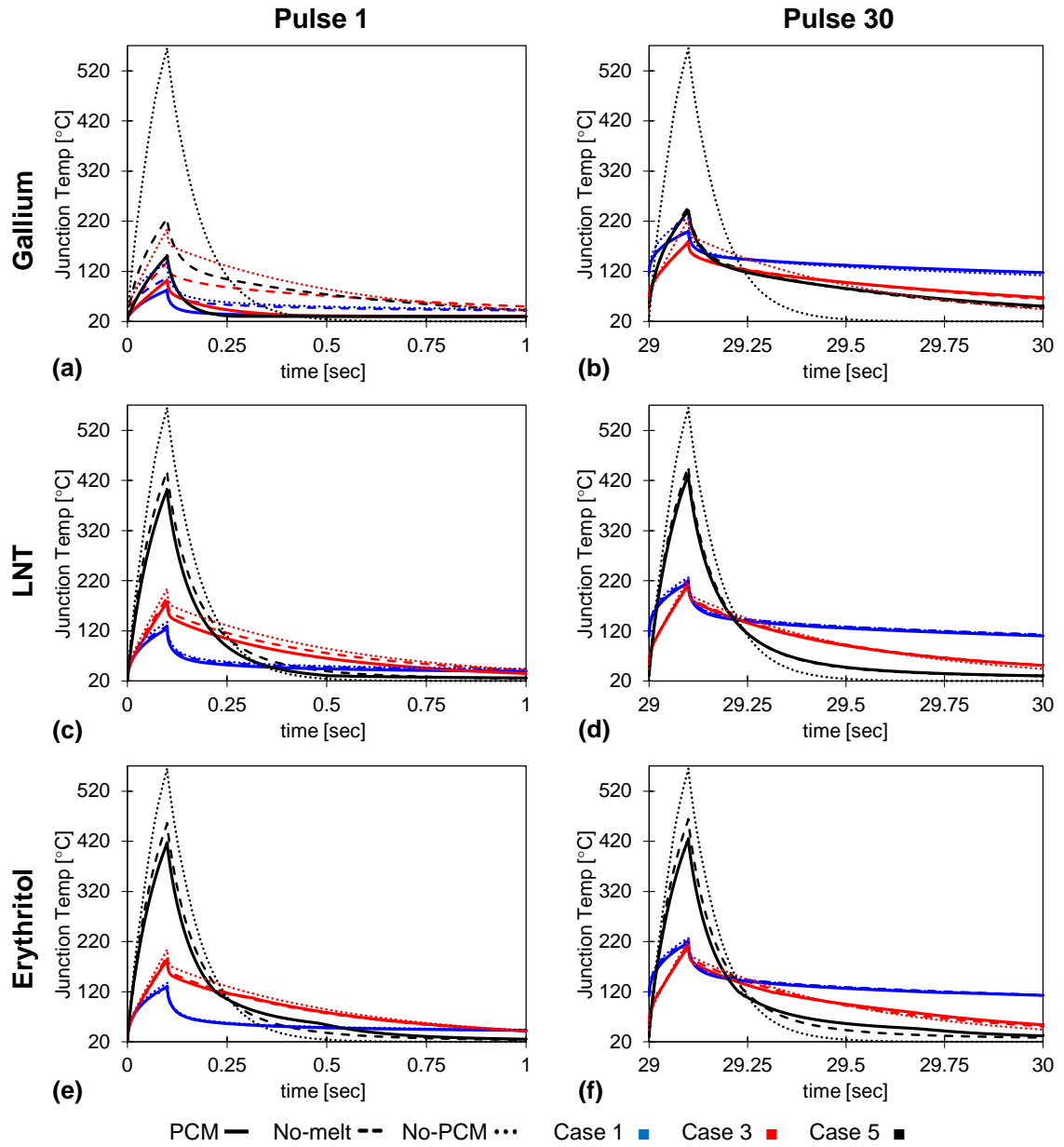


Figure 6.71 – 100 ms, 750 W/cm² pulsed responses of PCM loaded packages at $h_{eff} = 10 \text{ kW/m}^2\text{K}$, and $T_0 = 20^\circ\text{C}$, compared against no-PCM response (dotted lines) and with PCM but without phase change (dashed lines).

Table 6.21 – PCM loaded package thermal suppression comparison for $h_{eff}=10\text{kW/m}^2\text{K}$

PCM	Package Case #	PCM		vs. no phase change				vs. no PCM			
		T_{max}	ΔT	T_{max}	ΔT	T_{sup}	$T_{sup}/\Delta T$	T_{max}	ΔT	T_{sup}	$T_{sup}/\Delta T$
gallium	1	82.8	82.8	106.7	106.7	23.9	22%	137.5	137.5	54.7	40%
	3	102.0	102.0	138.6	138.6	36.6	26%	204.0	204.0	102.0	50%
	5	150.6	150.6	225.6	225.6	74.9	33%	565.4	565.4	414.8	73%
LNT	1	124.9	124.9	130.3	130.3	5.3	4%	137.5	137.5	12.6	9%
	3	177.3	177.3	187.2	187.2	10.0	5%	204.0	204.0	26.8	13%
	5	401.5	401.5	438.6	438.6	37.0	8%	565.4	565.4	163.9	29%
erythritol	1	128.6	128.6	131.4	131.4	2.8	2%	137.5	137.5	8.9	6%
	3	183.9	183.9	189.9	189.9	5.9	3%	204.0	204.0	20.1	10%
	5	417.2	417.2	455.6	455.6	38.5	8%	565.4	565.4	148.3	26%

All temperatures are in °C

The behavior shown in Figure 6.71 generally matches that described for the step response profiles. Significant thermal benefit comes simply from capacitive loading for all three materials, and minimal thermal suppression occurs from latent heat absorption for the non-metallic materials (Less than 10% according to Table 6.21.) However, in the case shown gallium’s phase change reduces the peak temperature from a 100 ms pulse by an additional 75°C to about 150°C, while peak temperatures under LNT and erythritol exceed 400°C. As the material volumetric latent heat and thermal capacities are similar, this suggests that gallium’s thermal conductivity enables much better utilization of its sensible and latent heat absorption.

In the lower convection coefficient case shown, all three materials show significant warming over the course of the full pulse train. For all materials but erythritol, the package heats sufficiently that by pulse 30 the PCM junction temperature stays above T_M . Thus, the package reverts to linear heating and absorption, and as can be seen in the Figure 6.71(b,d,f) the solid phase change curves rise to merge with the dashed no-phase-change curves. This reinforces one of the concerns with using a PCM: Following the exhaustion of available latent absorption, how does the system respond. In this case, the phase change

material lies outside the path to heat removal, rather than being a series impedance. The behavior reverts to the case where no phase change is available, rather than heating more than if the PCM had not been used at all. (This degraded condition was seen in the TBHS study when phase change was exhausted and the packages performed worse.) This is the opposite of how most PCMs have been evaluated for use and how their FOMs were derived, where they exist directly in the heat removal path. In either case, the use of a low thermal impedance material appears to be of critical benefit both before, during, and after phase change for this reason. Thus, the remainder of this section will focus on the performance of packages with gallium. For completeness, pulsed profiles for erythritol and LNT can be found in Appendix A, Figures A.17 and A.18.

Figure 6.72 shows the same pulse conditions for the gallium package at three different convection rates. Just as with the linear package models, increasing convection rate diminishes and then eliminates the package performance inversion. There is somewhat more sensitivity to the convection rate as it relates to the phase change recovery, in particular after the package has warmed. The high thermal mass of the Case 1 package prevents thermal reset at pulse 30 regardless of h_{eff} . The high values of h_{eff} primarily drive the fast reset time, such that they would support much higher duty cycles without seeing thermal reset problems.

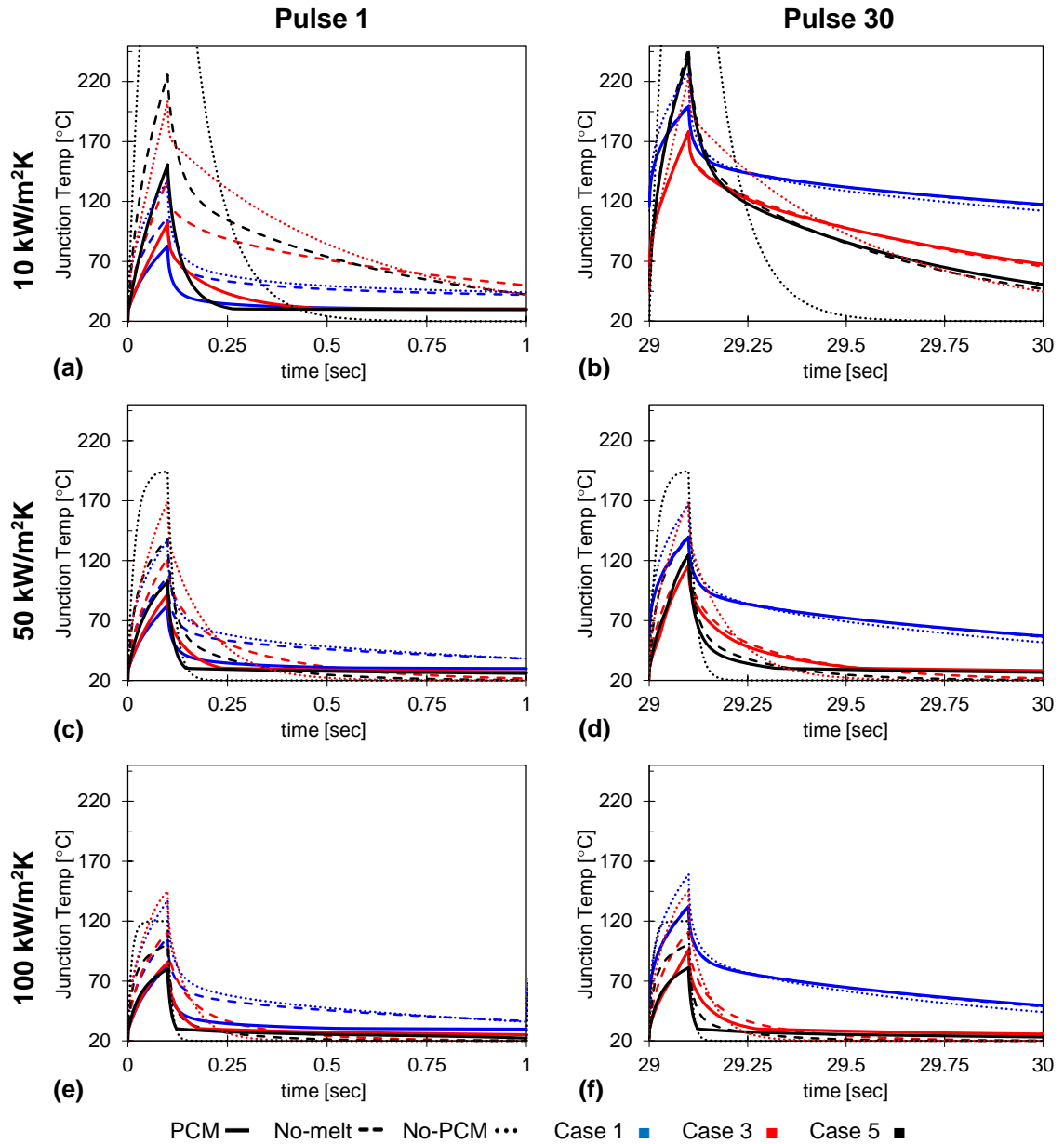


Figure 6.72 – 100 ms, 750 W/cm^2 pulsed responses of gallium loaded packages at varied convection rates, and $T_0 = 20^\circ\text{C}$, compared against no-PCM response (dotted lines) and with PCM but without phase change (dashed lines).

Figure 6.73 shows the same gallium comparison, but this time for a lower power (150 W/cm^2) pulse train. The primary difference in these cases are that in all but (b) the phase change thermal suppression lasts for the duration of the heating pulse. In (b), the

low convection case warms to the phase change temperature and phase change suppression stops playing a significant role. In the other cases, the well matched phase change volume minimizes temperature rise across the board, and as shown in (d,f) even after warm-up phase change continues to provide significant temperature suppression. Case 3 and 5 have similar maximum temperatures at both 50 and 100 kW/m²K, with only a slight difference in reset speed.

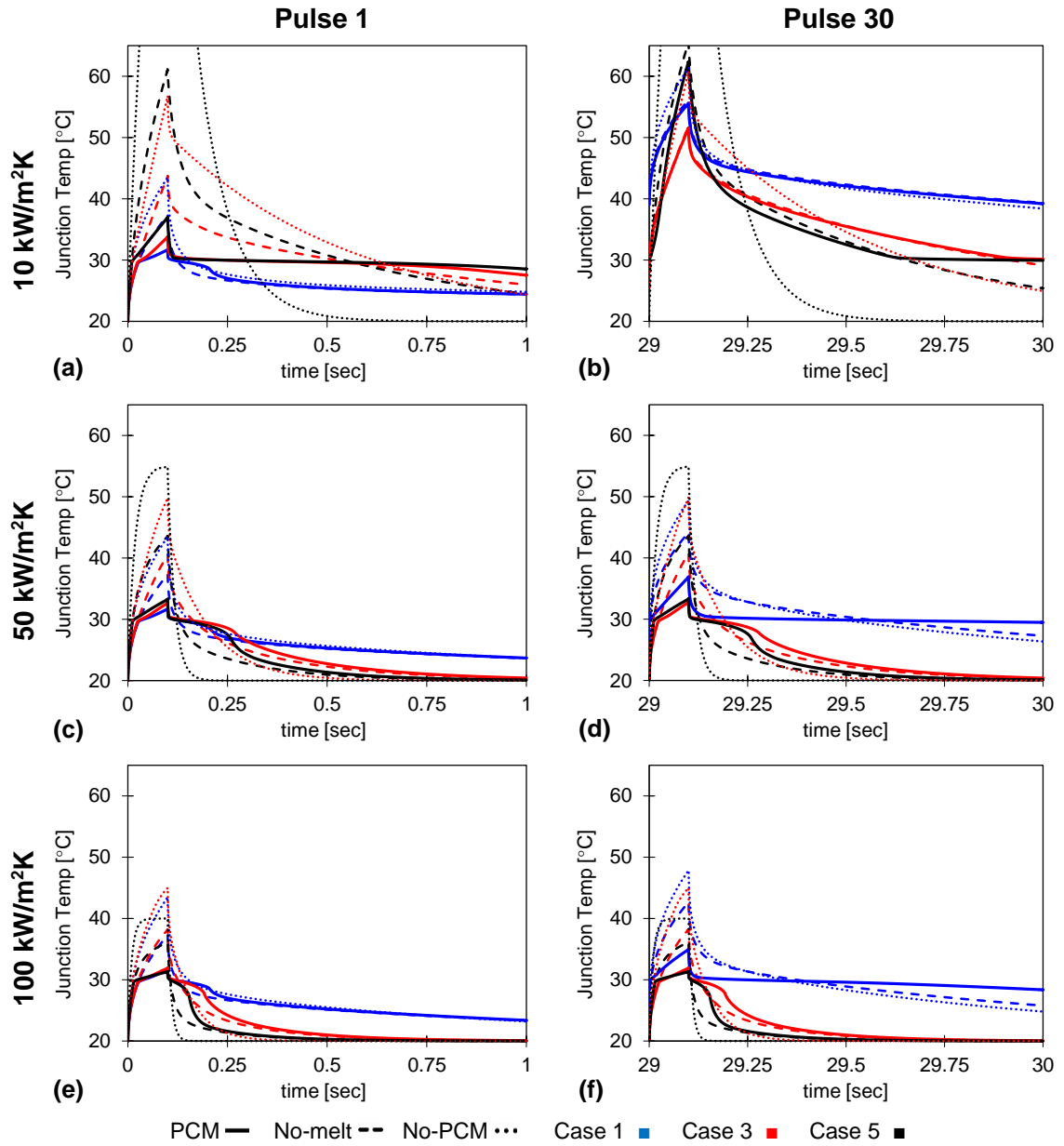


Figure 6.73 – 100 ms, 150 W/cm² pulsed responses of Gallium loaded packages at varied convection rates, and $T_0 = 20^\circ\text{C}$, compared against no-PCM response (dotted lines) and with PCM but without phase change (dashed lines).

Table 6.22 – Gallium loaded package thermal suppression summary

q'' [W/cm ²]	h_{eff} [kW/m ² K]	Package Case #	PCM		vs. no phase change				vs. no PCM			
			T_{max}	ΔT	T_{max}	ΔT	T_{sup}	$T_{sup}/\Delta T$	T_{max}	ΔT	T_{sup}	$T_{sup}/\Delta T$
150	10	1	31.7	11.7	37.3	17.3	5.6	32%	43.5	23.5	11.8	50%
		3	33.8	13.8	43.7	23.7	9.9	42%	56.8	36.8	23.0	62%
		5	37.0	17.0	61.1	41.1	24.1	59%	129.1	109.1	92.1	84%
	50	1	31.7	11.7	37.3	17.3	5.6	32%	43.5	23.5	11.8	50%
		3	32.7	12.7	40.5	20.5	7.8	38%	49.8	29.8	17.1	57%
		5	33.3	13.3	43.6	23.6	10.3	44%	54.9	34.9	21.6	62%
	100	1	31.7	11.7	37.3	17.3	5.6	32%	43.5	23.5	11.8	50%
		3	31.9	11.9	38.2	18.2	6.2	34%	45.0	25.0	13.1	52%
		5	31.3	11.3	36.1	16.1	4.8	30%	40.0	20.0	8.7	43%
750	10	1	82.8	62.8	106.7	86.7	23.9	28%	137.5	117.5	54.7	47%
		3	102.0	82.0	138.6	118.6	36.6	31%	204.0	184.0	102.0	55%
		5	150.6	130.6	225.6	205.6	74.9	36%	565.4	545.4	414.8	76%
	50	1	82.8	62.8	106.7	86.7	23.9	28%	137.5	117.5	54.7	47%
		3	92.4	72.4	122.5	102.5	30.1	29%	169.1	149.1	76.7	51%
		5	102.5	82.5	137.9	117.9	35.4	30%	194.5	174.5	92.1	53%
	100	1	82.8	62.8	106.7	86.7	23.9	28%	137.5	117.5	54.7	47%
		3	85.3	65.3	110.8	90.8	25.5	28%	145.1	125.1	59.7	48%
		5	79.9	59.9	100.6	80.6	20.7	26%	120.0	100.0	40.1	40%

All temperatures are in °C.

Finally, just as with the linear models we can examine the effect of short, high power pulses on the PCM loaded package. Figure 6.74 compares the responses of gallium loaded Case 1, 3 and 5 packages subjected to 1 millisecond pulses at heat fluxes of 1 and 10 kW/cm². Remembering from Figure 5.30 that the packages are well into the convective insensitivity range at that timescale only the $h_{eff} = 100$ kW/m²K case is shown, but the 50 and 100 kW/m²K cases show identical behavior.

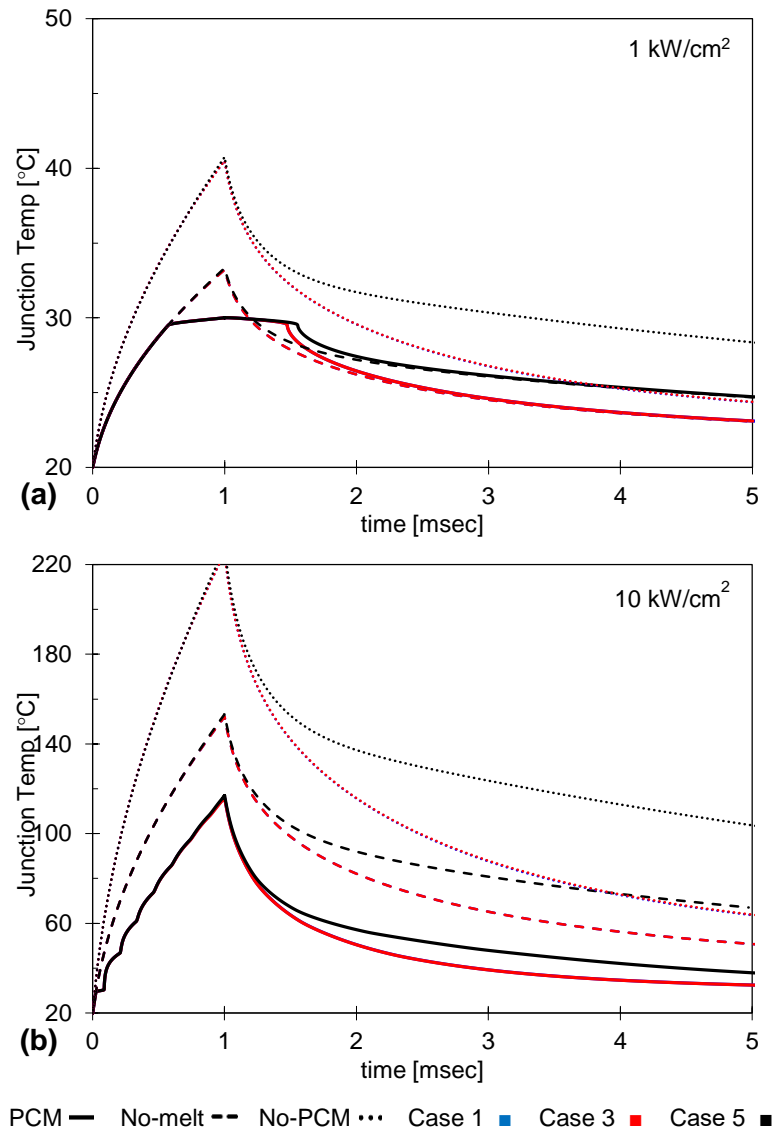


Figure 6.74 – High power 1 ms pulsed responses of Gallium loaded packages at $h_{eff} = 100 \text{ kW/m}^2\text{K}$ and $T_0 = 20^\circ\text{C}$, compared against no-PCM response (dotted lines) and with PCM but without phase change (dashed lines). Case 1 and 3 responses are present but indistinguishable.

Both figures show the different packages to have to be indistinguishable pulsed responses except for their cool down rates, as the additional thermal mass in the Case 1 and 3 packages provides a temporarily larger local thermal sink than the convective surface. During the heating pulse, however, it is clearly evident that phase change absorption plays

a significant role in shaving the peak off of the temperature spike. The 1 kW/cm² pulse drives the PCM into melting, but does not saturate the absorption before the end of the pulse resulting in a temperature plateau that is 3.3°C (25% of ΔT) lower than the spike without phase change, or 10.7°C (52%) lower than the no-PCM case. The higher power 10 kW/cm² pulse creates enough of a temperature gradient during melting that the heating profile is still a spike, but the absorption lowers the peak temperature by 36.4°C (31%), or by 133.3°C (53%) relative to the no-PCM case. The telltale temperature rise scalloping or staircasing can be seen in Figure 6.74(b), indicating that mesh refinement could be improved for slightly more local accuracy to smooth out that model, but the overall profile should not be expected to change significantly. Table 6.23 summarizes the high power fast pulse results.

Table 6.23 – Fast pulse gallium loaded package thermal suppression

q'' [kW/cm ²]	PCM		vs. no phase change				vs. no PCM			
	T_{max}	ΔT	T_{max}	ΔT	T_{sup}	$T_{sup}/\Delta T$	T_{max}	ΔT	T_{sup}	$T_{sup}/\Delta T$
1	30.0	10.0	33.3	13.3	3.3	25%	40.8	20.8	10.7	52%
10	116.8	96.8	153.3	133.3	36.4	31%	227.5	207.5	110.7	53%

- Specific data shown for Case 5 package with $h_{eff} = 100 \text{ W/m}^2\text{K}$. All other cases within 1%.
 - All temperatures are in °C

The key takeaways from this pulsed study are that not only does the presence of a direct contact PCM provide significant temperature suppression, but the addition of high thermal conductivity PCM can reduce temperature rise even in packages unaffected by improved or integrated cooling or package layer thinning. Thermal suppression is seen in Figure 6.74 far into the sub-millisecond range, which bodes well for targeted, optimized designs being able to provide thermal protection for fast, high power electronics that cannot be improved with standard packaging techniques. The large thermal gradient in the 10 kW/cm² case, however, shows that even the higher thermal conductivity gallium may

not be high enough for integrated systems with extremely high heat fluxes. Research into fast, high thermal conductivity phase change materials and the methods to integrate them into electronic packages or even the devices themselves is needed to address these concerns.

6.4.3.5. Impact of PCM thermal interface resistance

The thermal circuit in Figure 6.61 included a thermal resistor between the device and PCM package sections. While the previous models showed that a metallic PCM can have a large thermal buffering effect, this is primarily because its low thermal resistance helps heat spread throughout the material. The presence of an additional thermal resistance at the ‘thermal charging’ interface will necessarily degrade this spreading ability. It is well documented that interface quality in solders and other metals can vary greatly based on material compatibility, fabrication conditions, and thermal cycling [274], and in a phase change package the deliberately repeated melting and resolidification could produce poor wetting with resulting poor thermal contact. This may occur even if the initial assembly and fill started with a pristine solid interface. Added to this is the practical issue that electronics typically include some type of electrical isolation, such as a dielectric material coating on the top of the device to prevent shorting, that would act as an additional interface between the PCM and device junction. Finally, it is recognized that as package volumes decrease and PCMs become more integrated into the package and even the device, surface-to-volume ratios will increase with corresponding increases in relative importance of surface resistances relative to the bulk. Taken as a whole it is clear that proper design of these direct contact PCM thermal buffers, and really any high heat flux PCM, must take into account the impact of any thermal interfaces.

With that in mind, the last part of this thermal circuit package analysis provides a quick look into the potential impact of thermal interface resistance degrading package performance. As there has been little-to-no study of solid-liquid phase change material thermal interfaces to date, here we use a simple single parameter, R_{int} , to model the magnitude of the interface resistivity. This resistance represents only the actual contact line resistance between PCM and device. It has effectively zero thickness and does not incorporate any of the solid conduction in the PCM. This differs from some definitions of thermal interface resistance in the packaging literature that refer to the total thermal resistance of an interstitial material between two nominally flat surfaces, and includes the two contact surfaces plus the solid material in between. Based on a brief review of literature measurements of metal-semiconductor contact and interface resistances, it was found that liquid metals and high pressure metal-metal interfaces would have resistivity values on the order of 5-50 m²K/MW, while other solid, foil, and solder contacts could range up as high as many hundreds of m²K/MW [275-277].

Additionally, common die coating layers used on semiconductors can include deposited passivating films like silicon dioxide or silicon nitride. These films are typically only up to about 1 μm thick, with both materials having thermal conductivities ranging from 1.1-1.4 W/mK. These films would only be protecting the semiconductor layers, as top level metal layers are left open for making wire bonds and other electrical connections. When the entire upper surface is passivated after making electrical connections thicker coatings of a material able to conformally coat the top device surface are usual used. A common material choice for this is parylene, a vapor deposited highly conformal polymer. This material is able to be deposited reliably with void free coatings at thicknesses ranging

from about 6-25 μm , and the low thermal conductivity material varies from 0.082-0.120 W/mK [278]. All of these potential barrier layers are shown in Table 6.24 with their approximate contributions to R_{int} .

Table 6.24 –Thermal interface resistances from various electronic materials

Type	material or interface	k_{th} [W/mK]	thickness [μm]	R_{int} range [$\text{m}^2\text{K}/\text{MW}$]	Ref.
deposited device isolation layers	Silicon dioxide	1.1-1.4	< 1	< 0.7 - 0.9	
	Silicon nitride	1.2	< 1	< 0.8	
package insulating layers	Paralyne-N	0.12	6 - 25	53 – 212	[278]
	Paralyne-C	0.082	6 - 25	77 – 310	[278]
	Insulating sheet ¹	--	--	138-368	[276]
liquid/paste interfaces	Ga-oxide paste	--	--	2.6 – 9.1	[277]
	Ga-In-Sn eutectic ²	--	--	7.1 - 7.3	[275]
	Thermal grease ¹	--	--	48-171	[276]
metallic interface layers	Indium foil ¹	--	--	15 – 100	[276]
	Au foil ²	--	--	50-135	[275]
	Indium foil ²	--	--	300-760	[275]
bare contact	Copper-Copper ¹	--	--	105-217	[276]

¹ R_{int} variation due to 40 - 90 K temperature variation at fixed 7 MPa pressure

² R_{int} variation due to 100 – 1100 kPa pressure variation at fixed temperature

From the table it is apparent that a wide range in potential thermal interface resistances are possible between the PCM and the top surface of the die, all dependent on whether contact is made with metal or semiconductor, whether there is a dielectric insulation layer, whether the PCM is solid or liquid, and even on what temperature and pressure the contact is taking place. Thus for the purpose of this simulation, order of magnitude steps in R_{int} from 1-1000 $\text{m}^2\text{K}/\text{MW}$ were used to adequately span the range from “perfect interface” to “infinite resistance”, recognizing that the most likely values when good contact is present will lie between 1-100 $\text{m}^2\text{K}/\text{MW}$. Using this parameter range, step

and pulse models of the Case 5 package with gallium were evaluated for fixed power and convection levels of $150\text{W}/\text{cm}^2$ and $10\text{ kW}/\text{m}^2\text{K}$ respectively.

Figure 6.75 shows the step and pulsed response temperature profiles for the Case 5 package. As expected, increasing the thermal interface resistance reduces the phase change thermal suppression shown in the previous section. In Figure 6.75(a) we can see that the onset of phase change suppression is delayed by the additional thermal gradient across the interface, resulting in a much higher junction temperature during absorption. In (b) we see that the presence of the interface causes the thermal profile to gradually increase, surpassing the ‘non-phase changing PCM’ case used as a sensible capacity baseline, and eventually reverting to that of the original no-PCM Case 5 model. Thus, even the presence of ‘good’ thermal interface resistances appear to significantly degrade thermal storage, and resistances worse than that can completely eliminate any benefit of incorporating a PCM into the package.

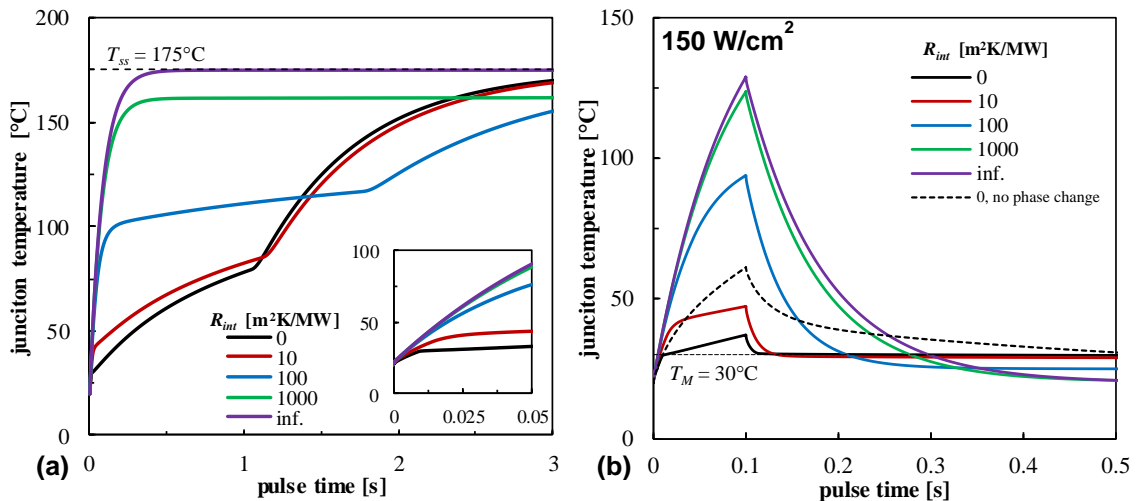


Figure 6.75 – Decrease in PCM thermal buffering due to interface thermal resistance shown for Case 5 with gallium at $150\text{ W}/\text{cm}^2$ and $h_{eff} = 10\text{ kW}/\text{m}^2\text{K}$. (a) shows phase change step response and (b) 100 ms pulse response for a range of thermal interface resistivity (R_{int}) values.

Looking at Figure 6.76, the melt fraction profiles for the step and pulse responses help validate the notion that the interface resistance reduces utilization of the PCM thermal storage. This PCM loaded package is a parallel heat path arrangement, and increasing PCM thermal impedance relative to the primary heat removal path reduces the total amount of heat driven into the PCM. Similar in effect to a low thermal conductivity PCM resulting in lower utilization of thermal storage in Figure 6.70, a thermal interface resistance reduces thermal absorption and eventually eliminates heat flow into the PCM.

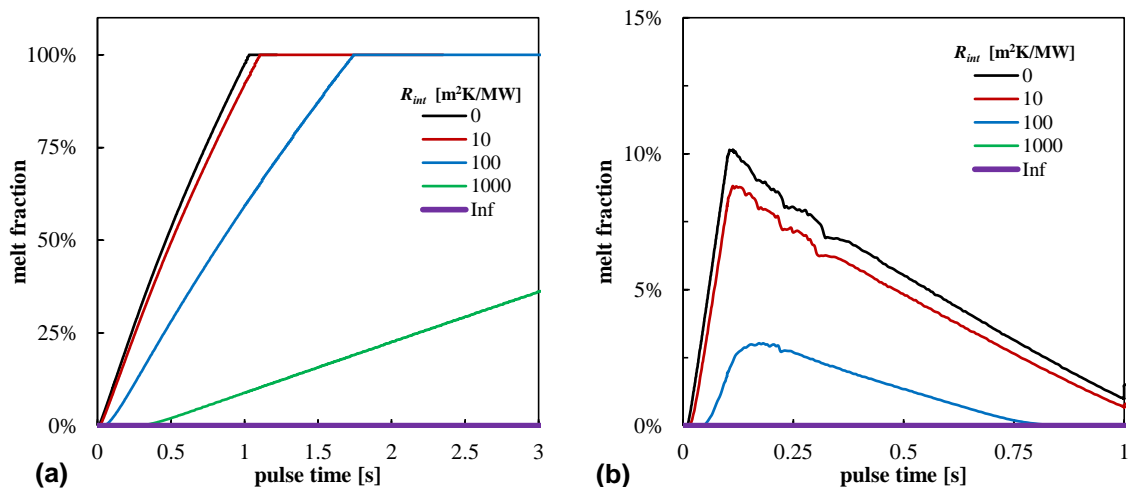


Figure 6.76 –PCM melt fraction impact of varying interface thermal resistance shown for Case 5 with gallium at 150 W/cm² and $h_{eff} = 10$ kW/m²K. The melt fraction is shown for (a) steady heating step response, and (b) 100 ms pulsed response for a range of thermal interface resistivity values.

Finally, we can look at the impact of thermal interface resistance on the fast, high power pulses examined at the end of the previous section. Figure 6.77 shows the Case 5 direct cooling package subjected to 1 ms pulses at 1 and 10 kW/cm² heat flux. Note that in this case, the impact of the high heat flux is such that the lowest values of R_{int} cause severe loss of temperature suppression. At $q'' = 1$ kW/cm², even $R_{int} = 1$ m²K/MW causes all gains from of the phase change material to be lost. It appears that the incomplete phase

change coupled with interface-degraded latent absorption causes the problem to be quite sensitive to R_{int} . For $q'' = 10 \text{ kW/cm}^2$, being driven to complete phase change provides some additional benefit, and the crossover is somewhere between 1-10 $\text{m}^2\text{K/MW}$.

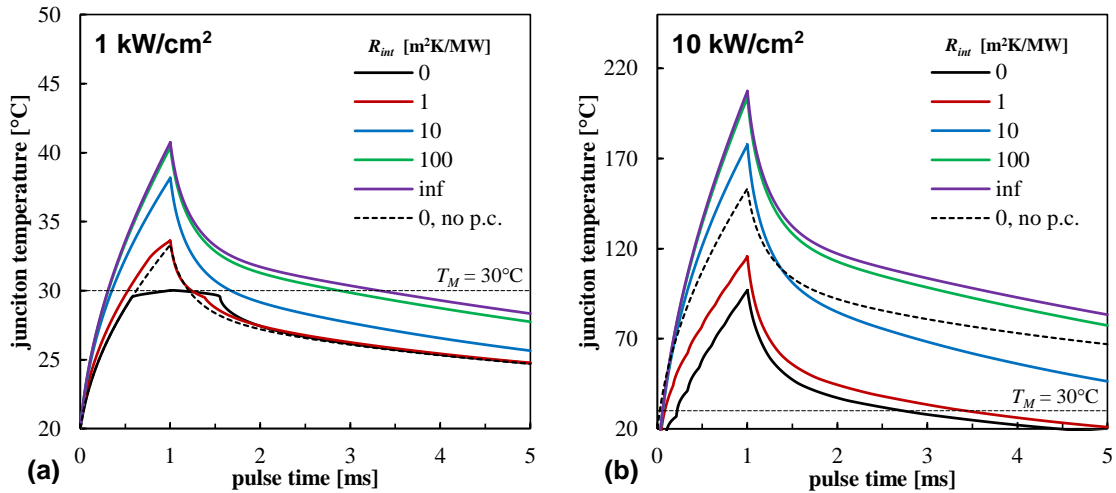


Figure 6.77 –PCM interface thermal resistance impact on 1 ms high power pulses shown for Case 5 with gallium at $h_{eff} = 100 \text{ kW/m}^2\text{K}$ and $T_0 = 20^\circ\text{C}$. Temperature profiles shown for a range of thermal interface resistivity (R_{int}) values and compared against the no-phase change temperature (sensible heat absorption but no phase change).

It appears that as we move to higher thermal conductivity PCMs for high rate thermal buffering, we will need to begin addressing the thermal resistance presented by the PCM-device interface. At very high speed and heat flux, even high quality interfaces may impose enough thermal resistance to severely degrade any useful thermal buffering. It is anticipated that the magnitude of the interface thermal resistance could change significantly throughout the melting-resolidification cycle, and conceivable that a poor interface could develop over time in a system that will see repeated solidification and re-wetting. Both of these situations have the potential to significantly degrade or even eliminate the benefit of incorporating a PCM into the package, and could even introduce a transient component

into the interface resistance value. Measurement and prediction of this thermal behavior will be a necessary part of using any PCM in a high power package. Fortunately, there is an extensive history of electronics packaging work focusing on wettability of solders that should serve as a solid starting point for future work in this area.

6.4.4. PCM enhanced thermal circuit package models - summary

In this section we successfully reevaluated the pulsed electronic packages with the addition of a PCM thermal buffer layer to add nonlinear thermal capacity right at the device. The use of the polynomial enthalpy and apparent capacity functions enabled the incorporation of closed form, energy conservative melting models in the thermal circuit framework. This permitted fast parameter space evaluation in a co-design compatible circuit design tool to test the hypothesis that non-linear thermal capacity could alleviate the two primary transient package concerns, performance inversion and convective insensitivity, as well as provide thermal improvement for fast pulses insensitive to standard improvements.

The first observation of note is that, just as in the substrate integrated PCM study, this exercise reinforced the notion that metallic phase change materials can provide high speed thermal protection for pulsed circuits. Low k_{th} materials showed minimal benefit as a phase change thermal buffer lying outside the primary thermal path. This is an important observation, as many PCM selection metrics are based on models where the PCM directly impedes heat removal, which forces thermal storage utilization but imposes a significant resistance cost. When the PCM is completely outside the primary heat path, not only is the charging resistance increased, but lacking a primary thermal gradient to drive heat flux their selection is unwise. A second point of note is that in most cases the largest thermal

benefit came from the addition of significant linear thermal capacity to the package topside, as the original models had a perfectly insulated boundary condition, equivalent to a zero conductance and zero capacity insulation such as a vacuum package or extremely low thermal mass aerogel. Such packaging is apparently a poor choice for a pulsed or transient package, at least from a thermal perspective. In practice, most packages are filled with a low thermal conductivity gel encapsulant or potting compound. These will provide some thermal capacity and change the transient and frequency domain package behaviors.

The combination of linear and phase change thermal absorption did make a significant difference in the pulsed temperature rise profiles of all packages. Apart from the linear capacitive contribution, under certain conditions the addition of a properly chosen PCM as able to sufficiently suppress temperature rise to make transient behavior irrelevant to package choice. Those cases required the power level and pulse duration to be such that the charging thermal gradient was not too high and the PCM was never exhausted. There was no real change to the linear behavior, package performance inversion, or convective insensitivity, but during phase change those details were irrelevant. This indicates that with careful design, because the PCM after exhaustion does not create a thermal impediment, transient and steady-state design can be at least partially decoupled. Adding a carefully selected amount of PCM to a low resistance package can result in both low transient and steady-state temperature rise, even for transients normally too fast to be addressed by other means.

Finally, it is worth noting that these model cases did show the difficulty that can be encountered in selecting a type and amount of PCM for a package. Depending on the package, heat load, pulse rate, and convection condition, achieving maximum thermal

performance depends on a design that ensures temperatures cross T_M between each pulse, and that there is sufficient material to absorb the full heat load. It appears that one thermal design still cannot translate well across all thermal conditions. Operating bounds will need to be identified for any phase change thermal package, and this will require both sufficient knowledge of the system thermal transient, and sufficiently robust design models for material and package evaluation. In addition, it was shown that other practical concerns, such as interface quality, could not only degrade the phase change benefit, but could completely eliminate all of the previously described benefits if not carefully controlled.

6.5. Discussion on PCM integrated package design and modeling

This chapter looked at the challenge of integrating phase change materials into an electronic package after previous analysis identified the competing constraints of steady-state and transient thermal requirements. Recognizing that one particular challenge is the ability to perform responsive and reliable component design with inherently complex, nonlinear physical phenomena, we set about developing a widely applicable smoothing function for the apparent heat capacity and enthalpy phase change models. This function is simply defined, energy consistent, and compatible with a wide array of thermal modeling tools. After confirming utility, two simulation case studies put this model to use in examining electronic packages. First, a straightforward implementation in a thermal finite element analysis tool examined the Thermal Buffer Heat Sink design as a PCM integrated substrate. Second, we extended the thermal circuit framework to include phase change using nonlinear elements and evaluate the impact of a direct contact PCM layer in improving the packages modeled in Chapter 5. Both of these simulation studies were

successful in demonstrating the ability to improve package pulsed response, but also in demonstrating the utility of the modeling techniques.

Without repeating the detailed results of the modeling studies, a few key points were revealed that are worth emphasizing. First, both studies highlighted the key performance to be had by implementing high volumetric latent heat *metallic* phase change materials. In all cases, the low thermal impedance of the metallic PCM caused the material to far outperform the other non-metallic materials. As mentioned in Chapter 2, for decades PCM research has focused on complicated schemes to overcome the low thermal conductivity problem with conventional PCMs. That problem is almost completely eliminated with the use of a metal, and the result is the removal of the large thermal charging resistance that grows with melt fraction and severely degrades PCM performance. It is not unreasonable to hypothesize that the lack of successful adoption of PCM technology is at least partly due to this narrow focus on trying to fix low thermal conductivity materials. Electronic packaging and similar compact components do not suffer from the weight penalties of larger, high-volume energy systems, eliminating the primary reason to avoid a metal PCM. The elimination of complex, potentially expensive conductivity boosting or heat spreading structures simply adds to both the energy density and potential cost-effectiveness of a metallic PCM system.

Second, both simulation efforts demonstrated that, with proper design and high thermal conductivity phase change materials, pulsed thermal systems can see temperature suppression down in to the millisecond and even sub-millisecond regime. Historically, again, almost all phase change material work has been ‘slow’. Timescales are generally measured in hours or minutes, sometimes as small as seconds. True ‘pulsed’ power

systems have transients much faster. It is not uncommon to have pulsed power devices switching in the microsecond timescale. Addressing these transients will require minimizing the linear thermal impedance that imposes warming delays and creates thermal gradients to the PCM, and then implementing a PCM that can respond quickly, absorb the energy, and spread it throughout the package. Almost all high power electronic device failures are thermal in nature. Pushing the envelope on high-rate pulsed package design will require electrothermal co-design strategies that account for transient thermal behavior using transient design solutions.

Finally, the two simulation studies looked at two very different aspects of the package using two very different simulation techniques. The TBHS substrate model used multi-dimensional FEA for higher-fidelity parameter space evaluation, while the package model used much faster, lower accuracy one-dimensional SPICE simulation. It is expected that the latter is the type of simulation that will eventually be compatible with co-design and system level simulation tools. Complex systems simply cannot afford the overhead of a high fidelity simulator in the design loop. The two different tools are complementary, however. More complex designs could be handled in SPICE. Implementing multi-dimensional FEA equivalent models can be done, and the same simulation domain could be constructed as was done in *Elmer* for the TBHS, but that is not what a compact model simulator is useful for. More likely, it will become necessary to develop a framework for parameter extraction from a high fidelity FEA simulation, to be fed into a compact model tool like Spice. A geometric abstract or primitive for a particular component could allow sufficient fidelity to examine, as an example, substituting a TBHS for the DBC substrate

in any of the examined package Cases. Determining the important aspects of this parameterization will be a significant but necessary challenge moving forward.

Chapter 7 – Conclusions

This work has addressed a number of topics with a central theme: vehicle and power electronics heat transfer systems are inherently transient in nature, and thermal improvement can only be achieved by using transient thermal solutions. The past several decades have seen hybrid and electric vehicles transition from a niche market to a sizable fraction of the vehicle fleet. This is putting more electronics under the hood subjected to highly variable drive and thermal conditions, and the U.S. military has followed that technology trend. As the U.S. Army develops future systems like the Next Generation Combat Vehicle, Unmanned Ground and Aerial Vehicles, and other autonomous systems, it is a safe assumption that they will adopt electrical architectures making increased use of high power electrical components for drive, hotel, and payload functions.

At the same time we are beginning to see diminishing returns from conventional cooling approaches applied to systems needing higher levels of integration. For some time we have been able to get away with applying steady-state cooling solutions to challenging thermal problems, but cannot expect to continue keeping pace with the demand for high performance, high power, and high functional density systems. There is inertia that must be overcome before transient solutions will move into mainstream usage. This will require simple, validated design approaches along with the tools to understand and predict design impact and provide feedback into non-thermal problem domains.

A large focus of this work was on identifying and investigating approaches to transient thermal management in high power electronics such as those used in vehicles and military systems. We posed a number of research questions related to the applicability of traditional thermal improvement techniques to transient problems, explored whether phase

change materials and thermal energy storage can improve vehicle and high power pulsed electronics, and developed design tool compatible modeling approaches to demonstrate electronics package thermal improvement. The remainder of this section provides a brief review of the outcomes of this work, summarizing the key research contributions made and providing an overview of potential directions for future improvement.

7.1. Research Summary

A substantial review of the research literature revealed that the primary mode being investigated for passive transient thermal management is the use of Thermal Energy Storage, and in particular Phase Change Materials, to absorb excess energy that would otherwise result in undesired temperature rise. Chapters 1-3 provide a comprehensive review of phase change materials and their potential vehicle applications. This review matches materials to applications, but more importantly it identifies gaps in material and system research. The primary gaps included: (1) incomplete material data for comprehensive modeling and design for most materials, (2) lack of comprehensive test standards for phase change materials leaving significant variability in reported data, (3) poor material metrics creating selection bias in past research, practically ignoring metallic and solid-state materials until very recently, (4) a lack of robust transient problem descriptions for most vehicle and electronic systems reducing the ability to design effective thermal solutions. Of these, the material selection bias is probably the most impactful gap in the set. For years the primary thermal characteristic used to 'rank' phase change materials was specific heat of fusion, or latent heat. While this makes sense for the large, slow thermal systems that have received primary attention in the past, it has resulted in low thermal conductivity organic materials with moderate energy density getting almost all of

the research attention. Correspondingly, almost every investigation has been plagued by problems of insufficient thermal charging and discharging rates, and material development efforts shifted to thermal conductivity enhancements of widely varying effectiveness to ‘fix’ this material problem. Revisiting the primary driving thermal equations of phase change and resulting Figures of Merit, the density-latent heat product, or volumetric latent heat, is the primary driving factor with thermal conductivity of equal importance. A higher volumetric latent heat decreases the thermal path-length heat must travel to reach the phase front, and that combined with thermal conductivity reduces the thermal charging resistance. This new focus has driven recent interest into metallic, high volumetric latent heat, and other high thermal conductivity materials necessary to thermally buffer fast transients.

Investigating the different options available for using phase change materials to thermally buffer vehicle thermal systems, it was apparent that power electronics still present significantly challenging transient cooling problems. Improved electronics cooling often focuses on tighter cooling integration with the packaging stack. Chapter 4 describes two approaches taken at ARL to put microchannel cooling directly into ceramic substrates, one using 3D printing and the other diamond saw cutting. These substrates were characterized on a thermofluid test loop where it was determined that low thermal resistances can be achieved without going to high-constriction microchannels by putting the cooling closer to the devices. Completing this steady-state substrate integrated cooling study, it was then necessary to examine how similar approaches would impact transient electronics cooling.

Chapter 5 examined power electronics transient heat transfer from the perspective of modeling and design tools. Acknowledging the utility of the thermal circuit analogy for

steady-state analysis, we looked at how to apply it in transient analyses. Focusing on thermal circuit solutions provides the opportunity to improve coupled domain co-design tools that are needed for improved electrical component design. While thermal effects are being included in more and more electrical circuit design tools, thermal design within electronic component development is still not generally done. Transient thermal simulations add an extra level of complexity that relegates them to being performed after electrical design is largely complete. Additionally, despite electrical component models including thermal elements, they are generally closed models (as in not open for inspection) that may or may not be appropriate for the thermal package implementation being developed by the designer. For all of these reasons, developing a robust thermal circuit approach for design-level transient package analysis provides a path toward normalizing thermally aware design within a standard electronics design framework.

Starting with the SPICE circuit modeling framework, this work leveraged Hsu and Vu Quoc's finite element circuit model for package analysis. This began by examining the utility of the seemingly non-physical negative coupling capacitor (which had often been ignored as 'cumbersome'), focusing on its connection to FEM mass matrix choice. Deriving a mass-matrix-generalized closed-form transfer function model for the FEM thermal circuit along with an analytical proof model, it was shown that while a *consistent* mass matrix produces seemingly non-physical DMP-violating results, it actually tracks transient response better than the usual alternative lumped mass approximation. Additionally it was shown that the DMP-violation can be a useful convergence check for transient mesh refinement.

This thermal circuit formulation was then used to examine traditional modes of thermal improvement for electronics devices and packages, and it was clear that steady-state improvement methods cannot fully address transient thermal protection requirements. It was demonstrated that package thinning and cooling integration can decrease thermal inertia, push package thermal response out to higher switching frequencies, and under certain conditions result in 'improved' packages exhibiting temperature swings many times larger than 'unimproved' high inertia packages. Put simply, this performance inversion means that good steady-state packages can be bad pulsed packages. Second, it was shown that all packages suffer from convective insensitivity once transients become fast enough, where even a three order-of-magnitude convection jump was shown to provide near-zero improvement. Adapting a circuit delay metric called *Elmore delay* to the thermal FEM circuit, it was shown that Elmore delay can consistently bound this convective insensitivity region and serve as a useful transient thermal package design metric. Developing closed-form delay expressions for one-dimensional multi-layer models, it was shown that pulses faster than approximately $T_D/3$ show virtually no improvement from any practical amount of improved convection. Thus, there is a need for other approaches to minimizing temperature rise in transient systems, preferably ones that maintain the low thermal resistance required for steady-state heating, while countering the decreased capacitive component of thermal impedance that comes along with these approaches.

Taking the information from the phase change material study on how to add a nonlinear thermal component to a system, Chapter 6 looks at ways to integrate PCMs into electronic packages. The initial question focused on whether we could work within the framework of current electronics packaging and integrated cooling schemes to incorporate

a PCM and increase thermal impedance with minimal resistive penalty. This required first examining methods to incorporate phase change into thermal conduction models. Energy methods that recast the nonlinear domain problem into an approximated nonlinear material property are appealing as they enable the use of traditional, unmodified heat equation solvers. These model options are fairly mature, but the nonlinear latent heat effect creates convergence difficulties in many simulation tools. A surprisingly simple yet effective latent heat approximation smoothing function was developed based on a closed-form polynomial model. This model avoids some numerical challenges of other smoothing functions including incomplete energy coverage and arbitrary tuning parameters. The simple algebraic polynomial function can also be incorporated into most thermal tools that allow for a functionally defined, temperature-dependent material property, even those with limited mathematical function capabilities. The smoothing function was validated against an analytical melting model using an open-source finite element analysis tool that allowed functionalized material property definition.

The remainder of Chapter 6 focused on demonstrating this polynomial smoothing function using two PCM simulation studies that built on work from previous chapters. The first combined the Chapter 4 substrate integrated cooling concept with a novel parallel PCM-heat sink design, the Thermal Buffer Heat Sink first proposed by the University of Tennessee and U.S. Department of Energy. The simulation study investigated the substrate integrated TBHS material and geometry parameter space, including different PCMs, substrate materials, and geometric parameters. The simulation was effective in evaluating the parameter space and showed that properly chosen substrate-integrated PCMs could be highly effective in suppressing transient temperature rise relative to the microchannel

substrates investigated in Chapter 4. In addition, the aforementioned benefits of metallic PCMs were highlighted as the only material able of providing fast (sub-millisecond) thermal suppression. The thermal resistance penalty for all TBHS designs was shown to be substantial, however, and could be unacceptable for designs expected to operate past the exhaustion of phase change capacity. Additionally, the TBHS parallel thermal path configuration was shown to be a detriment to thermal charging of the PCM, and rendered low-thermal conductivity PCMs completely ineffective at high convection rates.

The second case study was an attempt to merge the thermal circuit work from Chapter 5 with phase change melting and freezing models. The end goal of incorporating PCMs into coupled-domain circuit design would be to allow a greater degree of electro-thermal co-design for transient power applications. A nonlinear thermal capacitor enthalpy model was used to implement the new PCM smoothing function in the FEM thermal circuit framework, which was then validated against the same analytical melting model used earlier in the chapter. The new model was shown to be robust, fast, and sufficiently accurate to perform rapid simulation and design evaluation.

This validated PCM thermal circuit was then used to reevaluate the package simulations from Chapter 5, this time adding different PCMs to the topside of the power device. The PCM thermal circuits successfully and quickly simulated melting and freezing behavior, and the simulation demonstrated significant evidence of thermal package improvement under pulsed loads. Of the materials examined, again only the metallic PCM was able to provide any significant temperature reduction at either long or short timescales. The low thermal conductivity PCMs simply could not get heat into the material to take advantage of the latent heat, especially in the tested parallel thermal buffer configuration

lacking any external thermal gradient to drive heat into the thermal storage elements. The package performance behaviors seen in Chapter 5 (performance inversion and convective insensitivity) were generally unchanged, but a metallic PCM sized appropriately for the heat load was shown to be able to keep temperature pinned regardless of the package being used. Furthermore, it was demonstrated that metallic PCMs could even provide significant temperature suppression at higher powers and speeds than could be addressed through either improved convection or package integration. This suggests that a properly selected PCM in direct contact with the device and outside the thermal path could almost eliminate the transient problem seen Chapter 4 enabling a thermal solution good for both steady-state and transient applications. A final aspect of this study used the thermal circuit tool to perform a quick evaluation of a package with an interface thermal resistance between the device and PCM, and unfortunately showed that there is potential to reduce or even eliminate any phase change benefit if such factors are not addressed in the future.

Taken as a whole, this work explored the current state of the art and challenges in performing transient thermal mitigation in modern vehicle and electronics devices. Preliminary questions regarding the limits and challenges of transient electronic package design were answered. Tools have been developed that can enable power electronics designers to incorporate linear and nonlinear transient behavior into the component development process. And the stage has been set for phase change thermal buffering to be part of the future thermal solution set. We must stop treating thermal management as an afterthought or something to be done after the functional design work is complete. Meeting system demands requires that we stop overdesigning power systems and begin solving transient problems with transient solutions.

7.2. Future Directions

Thermal energy storage using phase change materials is a field that has gone through several cycles of increased research interest. The energy crises of the last century inspired much early research and many of the review studies cited herein, looking mostly at building and vehicle climate control and energy systems. More recent phase change material interest has been driven by the development of electric vehicles, the push for more *green* energy technology, and even concerns over environment and climate change, while the defense sector focus has primarily been on high-energy pulsed offensive and defensive systems and energy system efficiency for increased mission capability. We expect larger, higher power, and most notably faster thermal systems to drive energy storage and PCM research in the years to come. As such, several areas for continued research have been identified over the course of completing the work described here. Some of these research areas have already been initiated, as will be noted below.

7.2.1. Phase change materials:

1. The material review listed several recommendations, but foremost among these is more organized collection of PCM material data. This includes both experimental measurement and cataloging and dissemination. Just during the duration of this project certain material information sources have ‘disappeared’ from the non-archival public literature. It is worth noting that standardization of material data has been an ongoing effort of the IEA ECES activity, primarily in Europe, but the wide range of materials available for study should warrant an organized data collection effort, possibly sponsored

by a government science or research body or an industry or academic consortium.

2. Specific to material recommendations made here, metallic materials need to be better characterized for electronics applications. Non-metallics have little hope of addressing transients in the millisecond or faster timescale. This effort has been initiated on multiple fronts by colleagues at the DEVCOM Army Research Laboratory. Work by Gonzalez-Nino, et al., have performed simulation and experimental work on power electronic packages using low temperature solder alloys and have shown significant millisecond scale thermal improvement [250,251]. Additionally, recent material development efforts led by Sharar, et al., have identified metallics with solid-state phase transitions (primarily in the nickel-titanium shape memory alloy system) with composition tunable phase change temperature and very high PCM Figures of Merit [279]. These have the additional potential to completely change the way PCMs are designed by removing both the ‘different materials for each temperature’ and liquid containment problems, and have inspired exploration into a whole new area of uninvestigated solid-solid PCMs.
3. Non-ideal aspects of PCM behavior need to be solved to facilitate system design. In particular, methods for mitigating PCM hysteresis, or supercooling, must be developed before many of the high latent heat materials can be used. Appendix B describes a preliminary experiment into electrically stimulating nucleation in erythritol. Continued electrochemical

work in this direction met significant challenges in control and repeatability that need to be revisited and solved. More recent work is ongoing elsewhere looking at mechanical and electrical modes of nucleation enhancement, in addition to the more traditional attempts at seeding and compositional adjustment. It is also unclear if there are corresponding hysteresis controls that could be imposed on solid-state transitions with known, significant hysteresis. This is a problem that must be solved for any thermal protection system to use these materials and not suffer significant performance penalties.

7.2.2. Thermal circuit modeling

1. The transfer function models provide closed form analytical expressions for circuit behavior, but they are high complexity rational functions. It is difficult to extract useful component information from them. Looking at the frequency domain response of the package models, it appears that there are two or three primary thermal response ‘zones’ that could be identified and derived from material/layer properties. This may provide pseudo-analytical transfer function forms that can be used to directly calculate features like crossover points in the power package ‘performance inversion’, or provide a more precise relationship between convective improvement and Elmore delay.
2. Phase change thermal circuits currently cannot use the inertial coupling capacitor to improve transient response due to the way SPICE nonlinear capacitors reference voltage as ΔV across the capacitor terminals, and

nonlinear effects must reference an absolute temperature. The use of custom behavioral elements should be able to accommodate this change, and then the benefit of different mass matrices on phase change model performance could be examined.

3. Modeling hysteresis (supercooling) in PCM packages may be useful for estimating its performance impact. However, this requires phase state tracking to differentiate between an element being in a solid or supercooled state. In full FEM this is done through an additional nodal variables using level set methods or other tracking techniques. In a PCM thermal circuit this would have to be accomplished through some additional voltage state, perhaps a binary switch or other digital logic. Additionally, triggered heterogeneous nucleation requires knowledge of neighbor phase state which implies additional connections between adjacent elements. Finally, as discussed in recent work by Davin, et al., there must be some ruleset to determine how quickly nucleation propagates between elements since the energy state could propagate information ‘infinitely fast’ through the circuit network [280]. All of this considered, the ability to model supercooling is a current area of research in the literature and would be a useful addition to a PCM thermal circuit design tool.
4. The PCM package model includes an interface thermal resistor, set near zero for most of the models reported here. In one single case the parameter was swept and it was shown how interface resistances over the range measured for metal-semiconductor interfaces can severely degrade PCM

thermal suppression. The full impact of PCM interface thermal resistance needs to be examined, both numerically and confirmed experimentally, across the phase transition and with PCM cycling. Interfacial thermal resistance is a thermal charging barrier, and as PCM volumes diminish with higher integration the surface-to-volume ratio will increase accordingly, making that resistance more and more important to design. As it stands, there has been very little work on PCM thermal interfaces. It is surmised that the quality of the PCM-substrate thermal contact may correlate with surface energy or the wetting angle between the two materials. This may permit thermal modeling to predict the performance degradation of an interfacial resistance component, and then material characterization to estimate the interfacial coupling between PCM and container materials, and finally for experimental work to validate the prediction and develop a surface energy correlation.

7.2.3. Electronic phase change thermal buffering

1. The models implemented in this work were useful in showing that PCMs can solve fast, high power thermal problems. However, as the thermal interface study showed, practical implementation concerns could render such benefits moot. Experimental validation with linear and phase change thermal components will be necessary to identify inherent shortcomings in the idealized models. In particular, experimental verification will help determine the proper mass matrix selection for transient prediction, the importance of mushy zone width for accurate tracking of melt front

behavior, and the limitations of 1-D and 2-D models in simulating real world components.

2. Compact electronics packaging creates significant challenges for PCM integration. In addition to the nonlinear thermal problem, by their very nature phase change can induce large mechanical stresses leading to system failure. As exhibited in Appendix C, even open-to-air PCM expansion can cause brittle packaging components to shatter despite providing void space. This is a problem because in addition to increasing non-functional package volume, such a solution becomes orientation and even rate dependent. Sufficiently strong solid PCMs may not even expand sufficiently for a void to be of much use. As a critical failure mode, characterizing material expansion on phase change is a *necessary* component of any PCM development. Efforts to develop low expansion PCMs, or even volume-compensating PCMs through tailored alloys or blends would be of significant benefit to the field.
3. While direct die integration has shown promise in addressing millisecond scale thermal transients, how to address high speed, sub-ms pulses is still an open question. There is simply a fundamental limit to how quickly heat can be generated within a high power device and propagated to the surface for the PCM to begin absorption. At some point it may become necessary to look at transient aspects of heat propagation within the electronic device, and determine how additional thermal capacity can be engineered into it without disturbing electrical function. Whether through some sort of device

integrated phase change material, or other embedded high capacity material, near-junction transient thermal engineering is going to be necessary to prevent failures in future high speed power devices.

4. Aforementioned work with metallic materials has already begun looking at the packaging benefit of direct die-contact PCMs. However, it is recognized that the multiple size- and time-scales present in a large, transient thermal system may require thermal storage at multiple levels to minimize cooling system burden. It is likely the driving requirements for these levels could dictate the need for significantly different materials. Fast transients at the device may require direct contact metals, but a large air cooled heat exchanger rejecting long pulse heat to ambient air may require a large volume of material at much lower heat fluxes. For cost, size, and weight reasons an organic or salt-hydrate material with heat spreaders could be an optimum material choice *for that component*. Time constant matching the thermal components to the local loads and right-sizing the thermal system will require both improved component design and system level nonlinear optimization. Effort is needed to develop component requirements for phase change thermal systems that take into account transient interaction between the cooling loop and connected components, nonlinear effects within components, and predictive control strategies to maintain peak function.

7.3. Contributions Summary

The overall objective of this study was to examine the current approaches and barriers to effective transient thermal electronics design, and to develop knowledge and techniques to improve such design moving forward. The focus of the transient design became the use of phase change materials as thermal buffers. Despite many decades of investigation, these materials and devices still mainly exist as laboratory experiments and prototypes, with few examples of real world transition. This work has made progress in moving the state of the technology to where we may start seeing electronics and other power systems make practical use of phase change materials in the not-too-distant future. Specific contributions from this investigation can be identified in the following areas:

Materials and Applications Analysis

- Compiled a comprehensive phase change material database from disparate academic and materials literature that is currently being used for future electronic system materials selection and component design.
- Applied the material set to the vehicle thermal system as a whole, providing the first comprehensive analysis of vehicle transient systems and potential PCM thermal enhancements for those systems.
- Corrected the general practice in the PCM field of determining material potential by specific instead of volumetric latent heat, emphasizing the equal weighting of volumetric latent heat and thermal conductivity.
- Used this metric to emphasize the importance of certain under-investigated material sets including metallic and solid-state PCMs,

which has directly led to recent expanded work focusing on both of those material categories.

Transient package modeling and design

- Elucidated the mass matrix behavior of the inertial coupling capacitor in Hsu and Vu-Quoc's FEM thermal circuit, as many previous studies ignored the element as non-physical and recommended eliminating it. Showed its relevance in FEM circuits' improved transient response.
- Demonstrated the ability to use DMP violations in a consistent mass matrix as a convergence criterion for thermal circuits.
- Developed a closed analytical transfer function form of the FEM thermal circuit usable for thermal simulation.
- Proved Elmore delay to be a usable bound for convective insensitivity limits in an electronics package and developed a closed form expression for multi-layer Elmore delay derivable from base material properties and geometry.
- Demonstrated that improved steady-state package designs show inverted performance in transient conditions, dependent on pulse rate and boundary conditions, due to reduced thermal inertia.

Phase change material modeling

- Developed and validated a closed form polynomial smoothing function for the apparent heat capacity and enthalpy methods of modeling phase change that conserves energy and eliminated arbitrary fitting parameters.

- Demonstrated the utility of the Thermal Buffer Heat Sink design in reducing pulsed temperature rise for fast transients when using metallic PCMs, while determining that the DOE identified design and material set are not ideal for faster transients due to significant thermal resistance penalties.
- Developed and validated the first PCM integrated FEM thermal circuit model using the polynomial smoothing function.
- Demonstrated the utility of metallic PCMs in providing significant temperature reduction even for fast transients unable to be mitigate through standard packaging methods.
- First analysis of PCM thermal interface resistance having the potential to become a significant obstacle to thermal component performance.

Experimental contributions:

- Established substrate integrated ceramic microchannel cooling as capable of providing significant cooling benefit at low pumping power without the need to change device level packaging methods.
- Demonstrated the first case of supercooling control and reduction in erythritol using a direct electrical current (Appendix B).
- Developed fabrication schemes and preliminary assemblies for substrate integrated thermal buffer heat sinks (Appendix C).

Appendix A – PCM thermal circuit package study - complete results

Following are the full sets of simulation results from the SPICE integrated PCM analysis of power electronic packages described in Section 6.4.3.

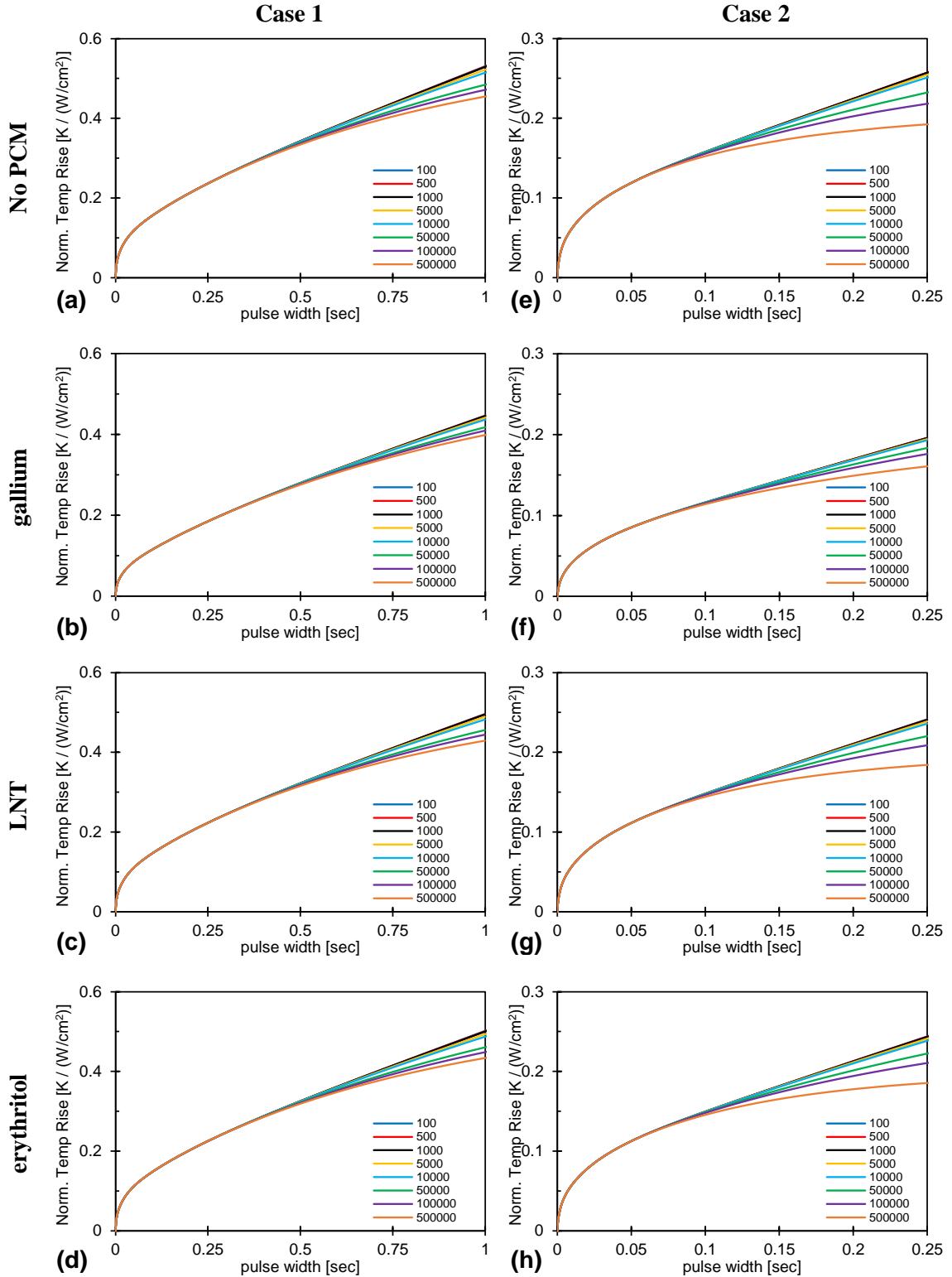


Figure A.1 – Single pulse peak junction temperature comparison for Cases 1 and 2 with topside PCM loading for varying convection rates and pulse widths. (See Figure 6.62.)

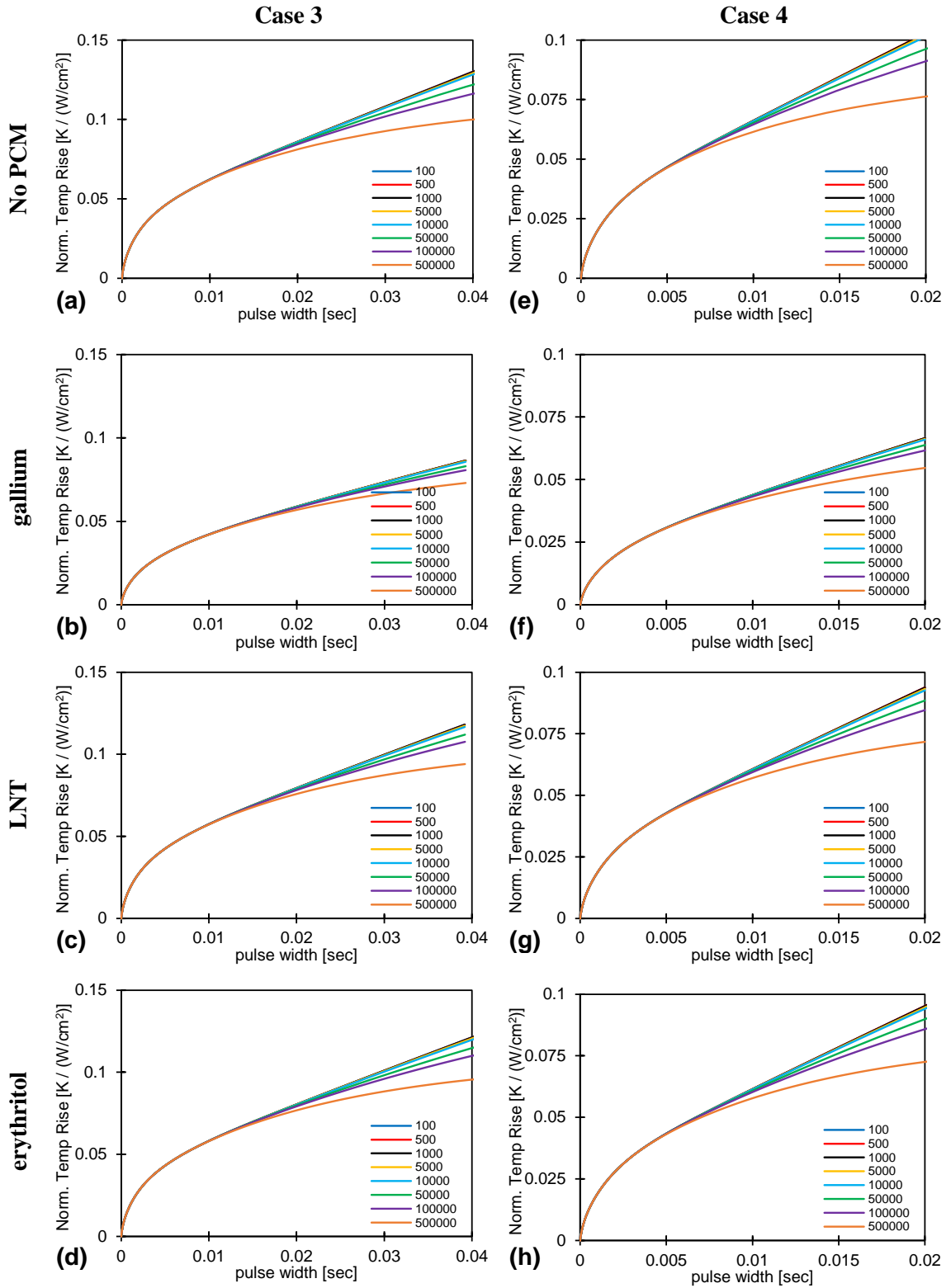


Figure A.2 – Single pulse peak junction temperature comparison for Cases 3 and 4 with topline PCM loading for varying convection rates and pulse widths. (See Figure 6.62.)

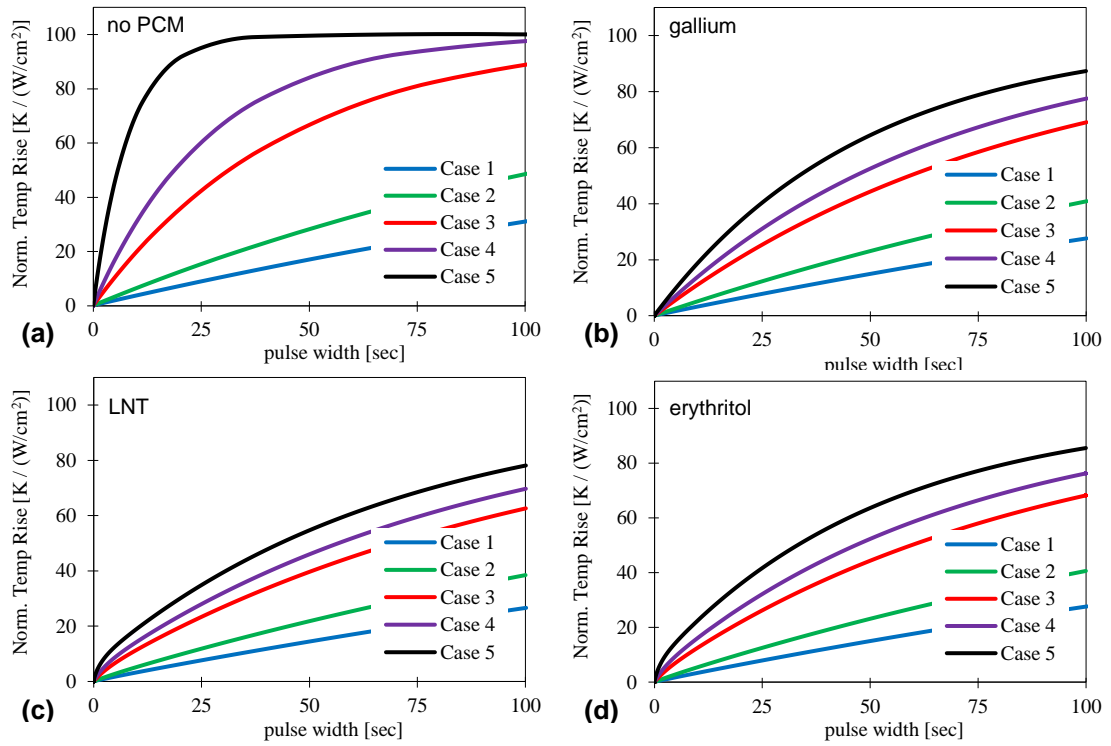


Figure A.3 – PCM loaded package temperature step response comparison for $h_{eff} = 100 \text{ W/m}^2\text{K}$

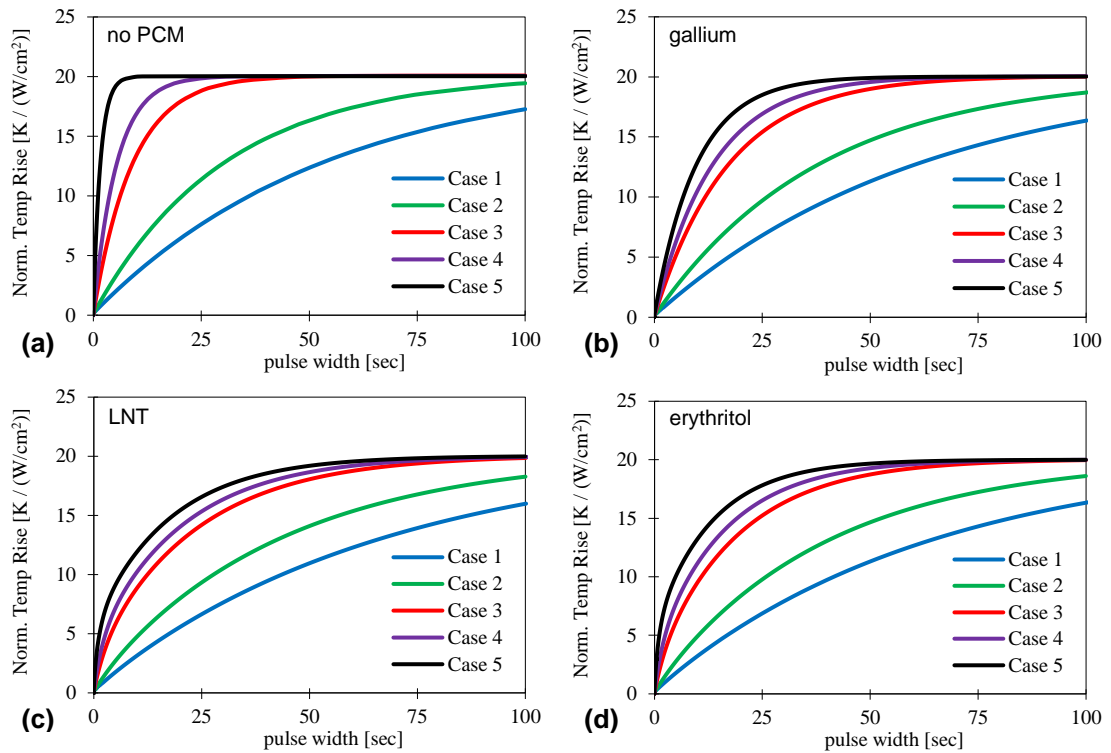


Figure A.4 – PCM loaded package temperature step response comparison for $h_{eff} = 500 \text{ W/m}^2\text{K}$

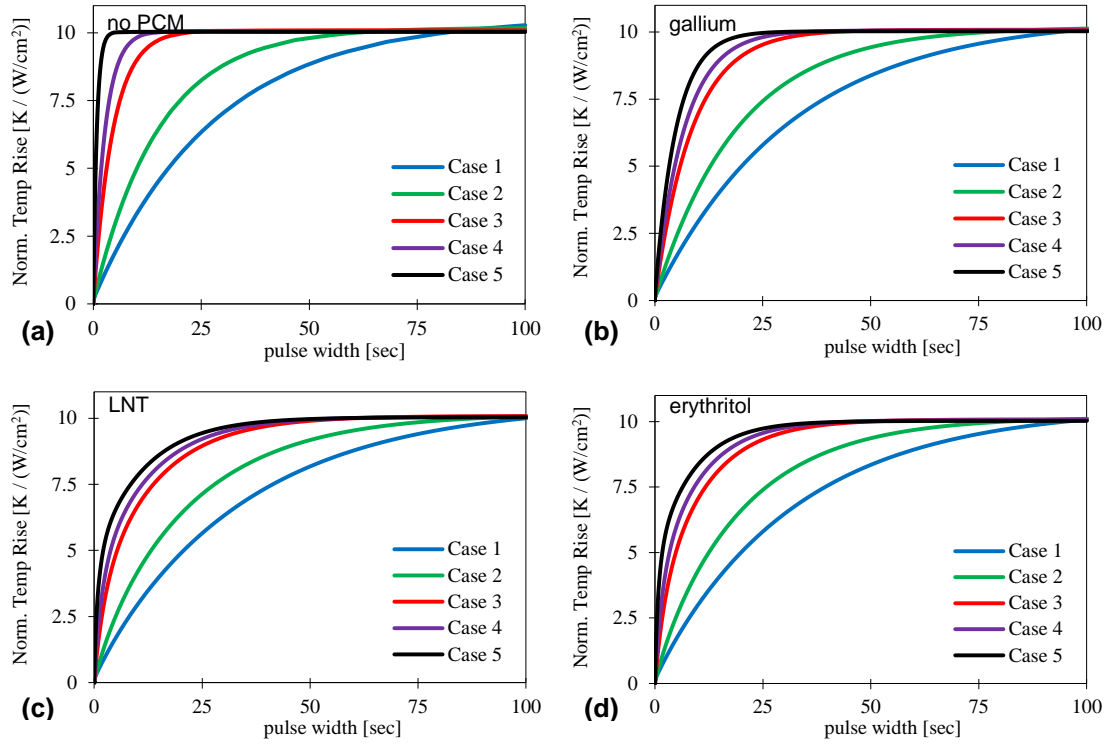


Figure A.5 – PCM loaded package temperature step response comparison for $h_{eff} = 1 \text{ kW/m}^2\text{K}$

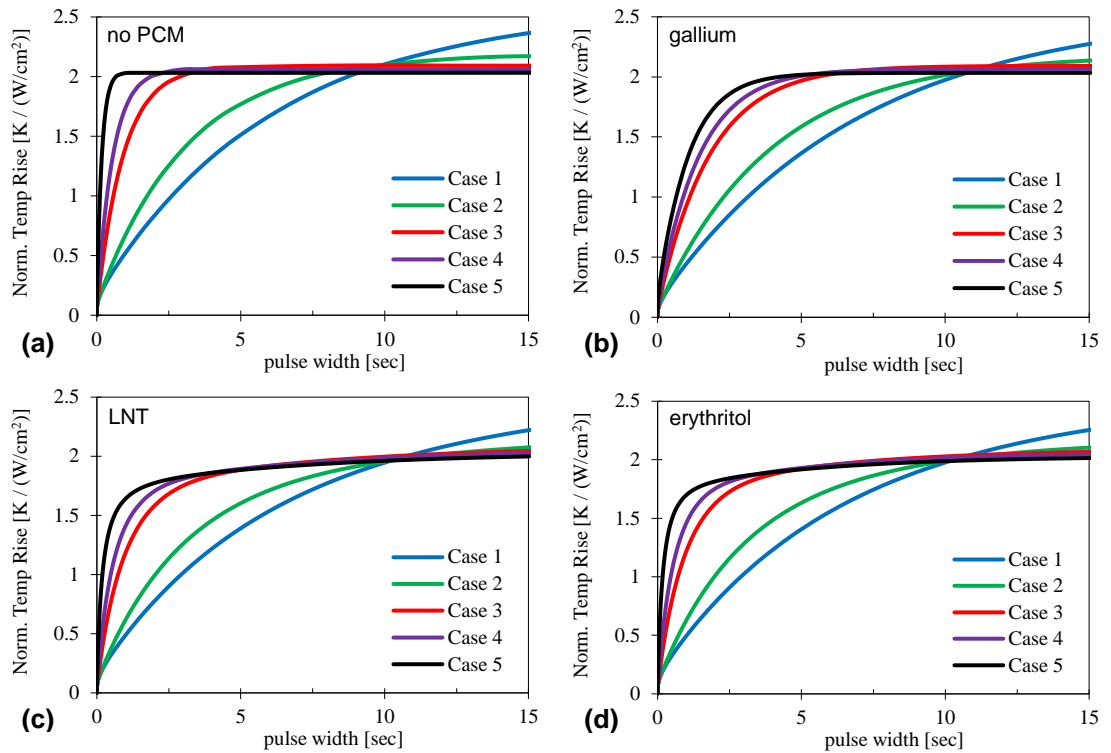


Figure A.6 – PCM loaded package temperature step response comparison for $h_{eff} = 5 \text{ kW/m}^2\text{K}$

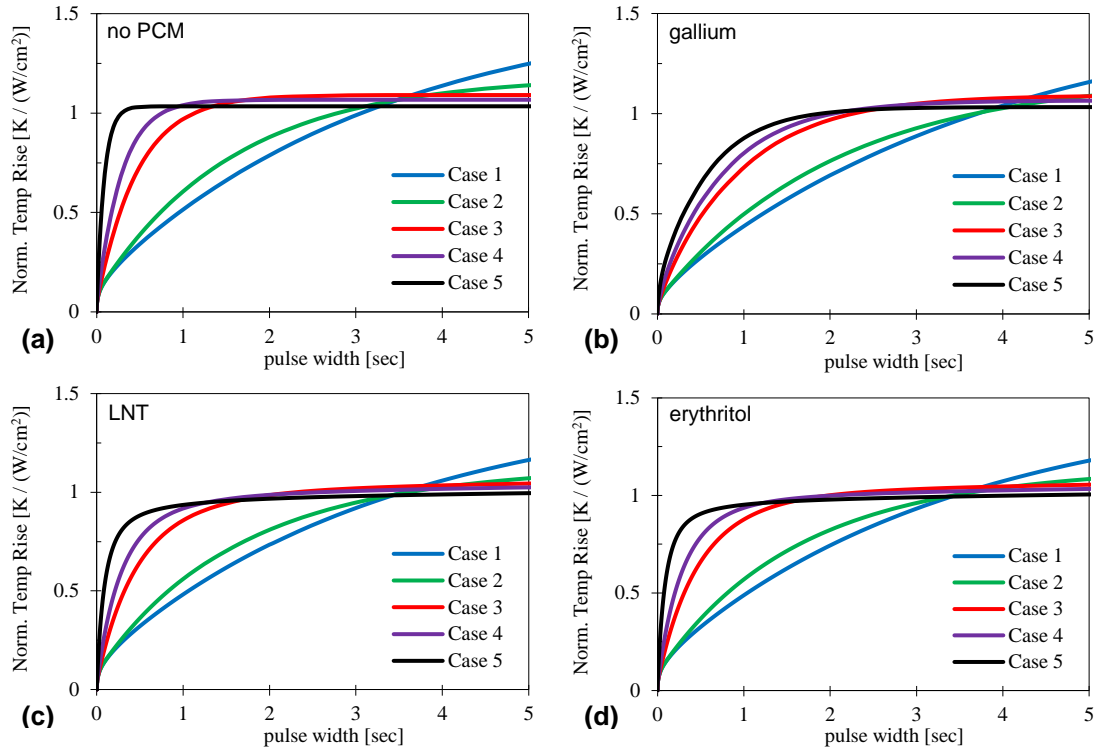


Figure A.7 – PCM loaded package temperature step response comparison for $h_{eff} = 10 \text{ kW/m}^2\text{K}$

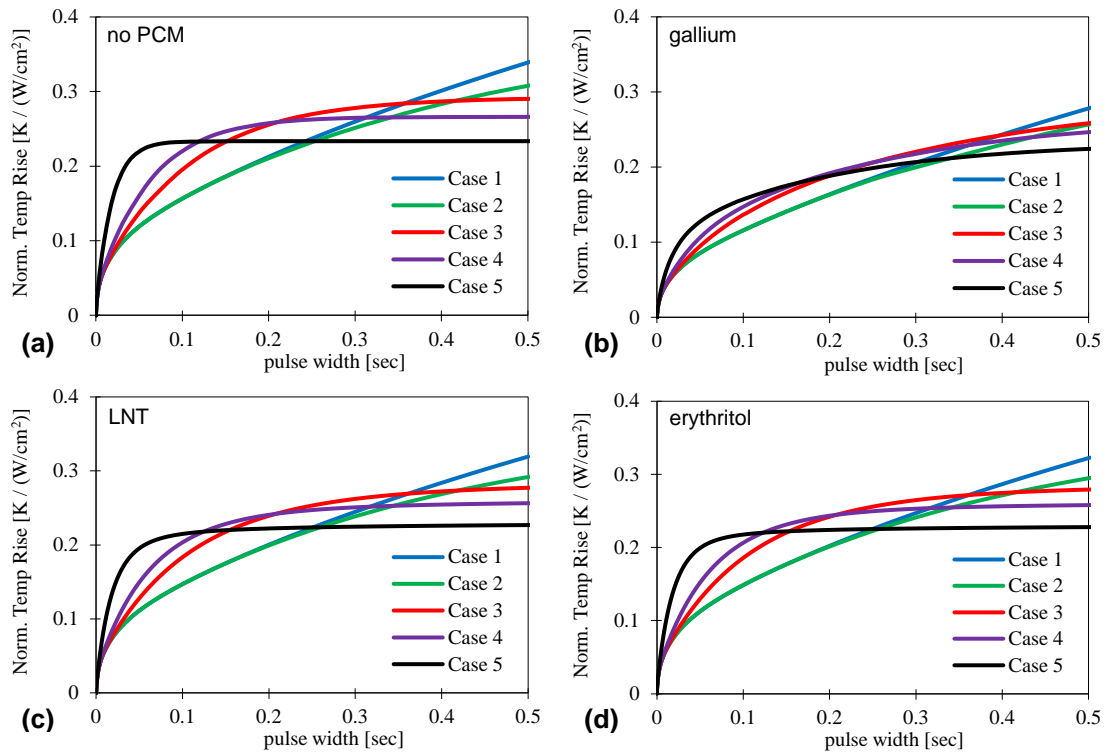


Figure A.8 – PCM loaded package temperature step response comparison for $h_{eff} = 50 \text{ kW/m}^2\text{K}$

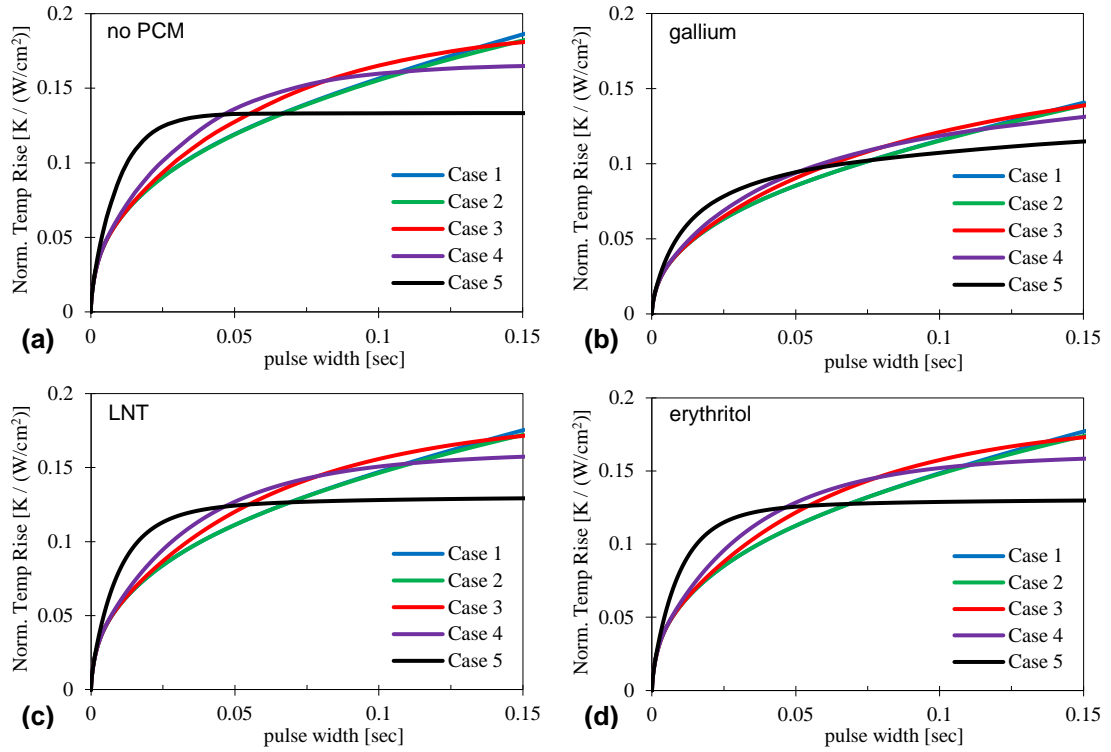


Figure A.9 – PCM loaded package temperature step response comparison for $h_{eff} = 100 \text{ kW/m}^2\text{K}$

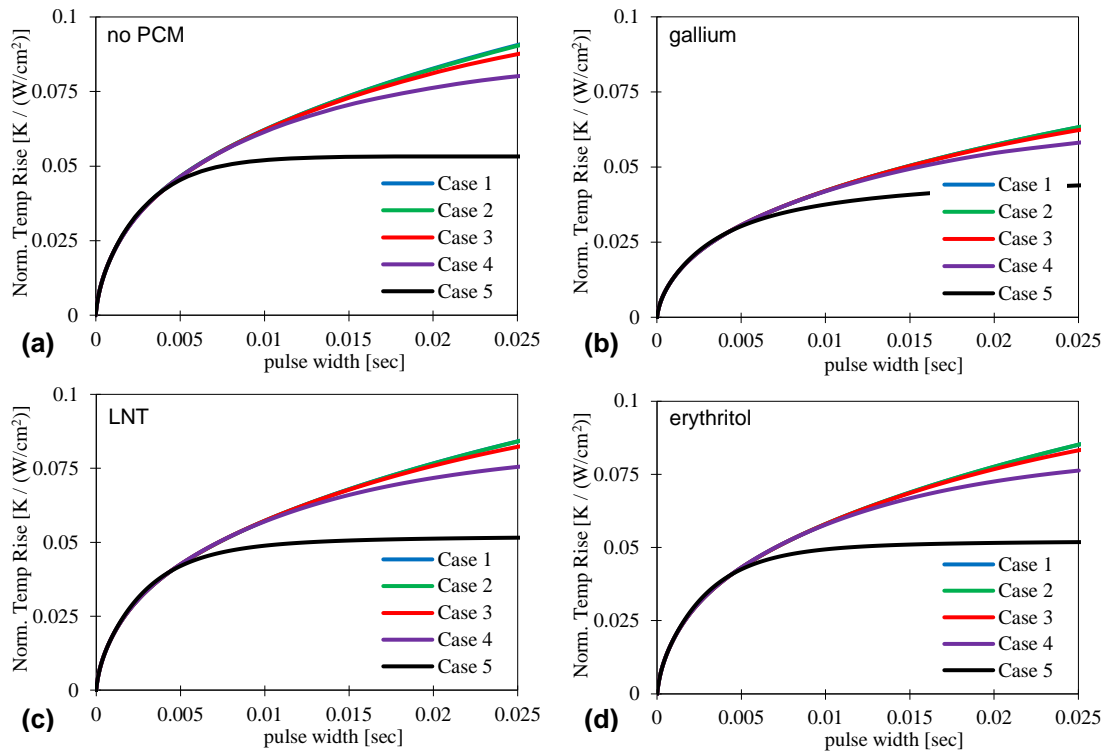


Figure A.10 – PCM loaded package temperature step response comparison for $h_{eff} = 500 \text{ kW/m}^2\text{K}$

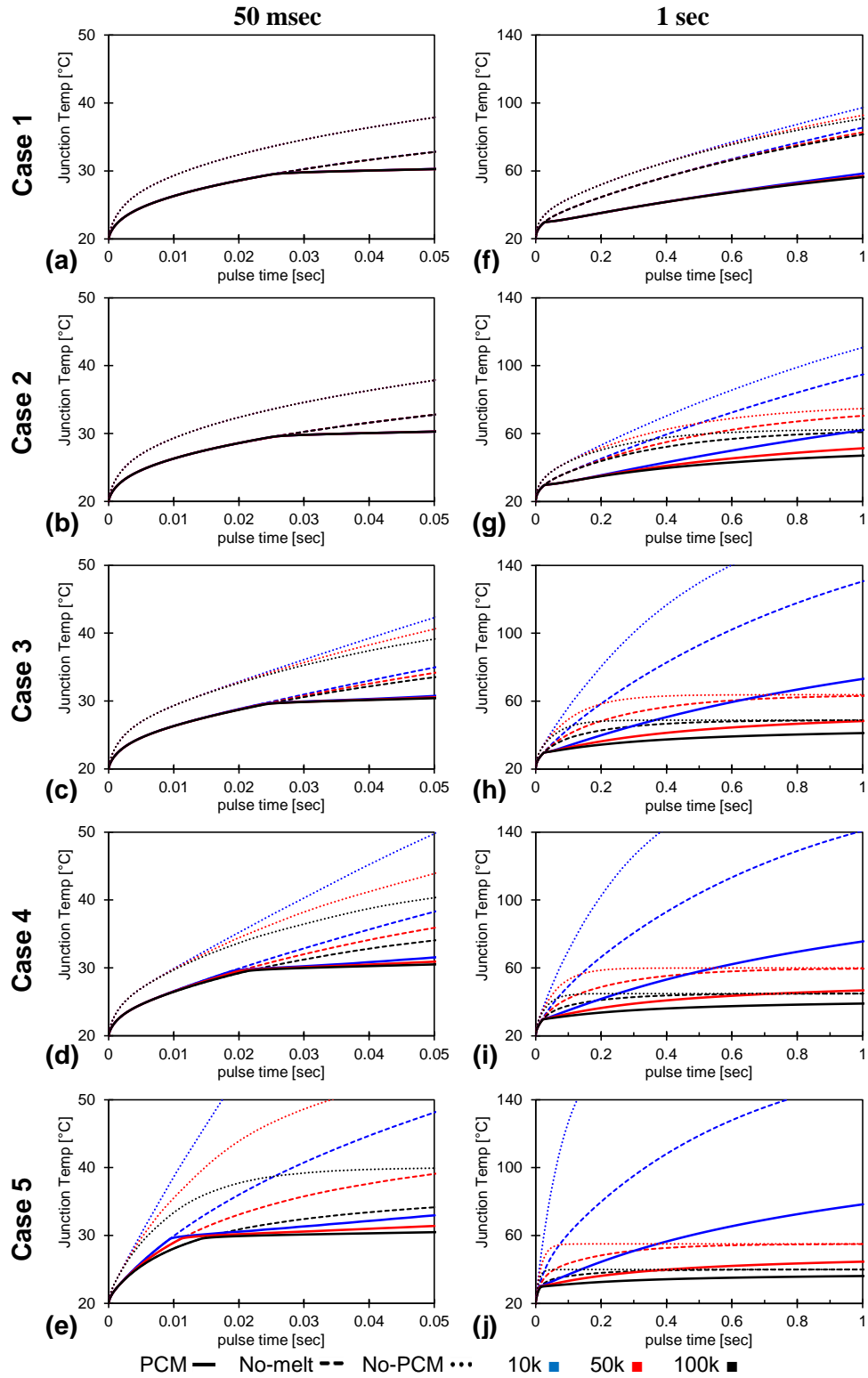


Figure A.11 – Low power package phase change step response with gallium at 150 W/cm^2 , $T_0 = 20^\circ\text{C}$. Short (a-e) and long (f-j) response compared against cases without PCM or phase change.

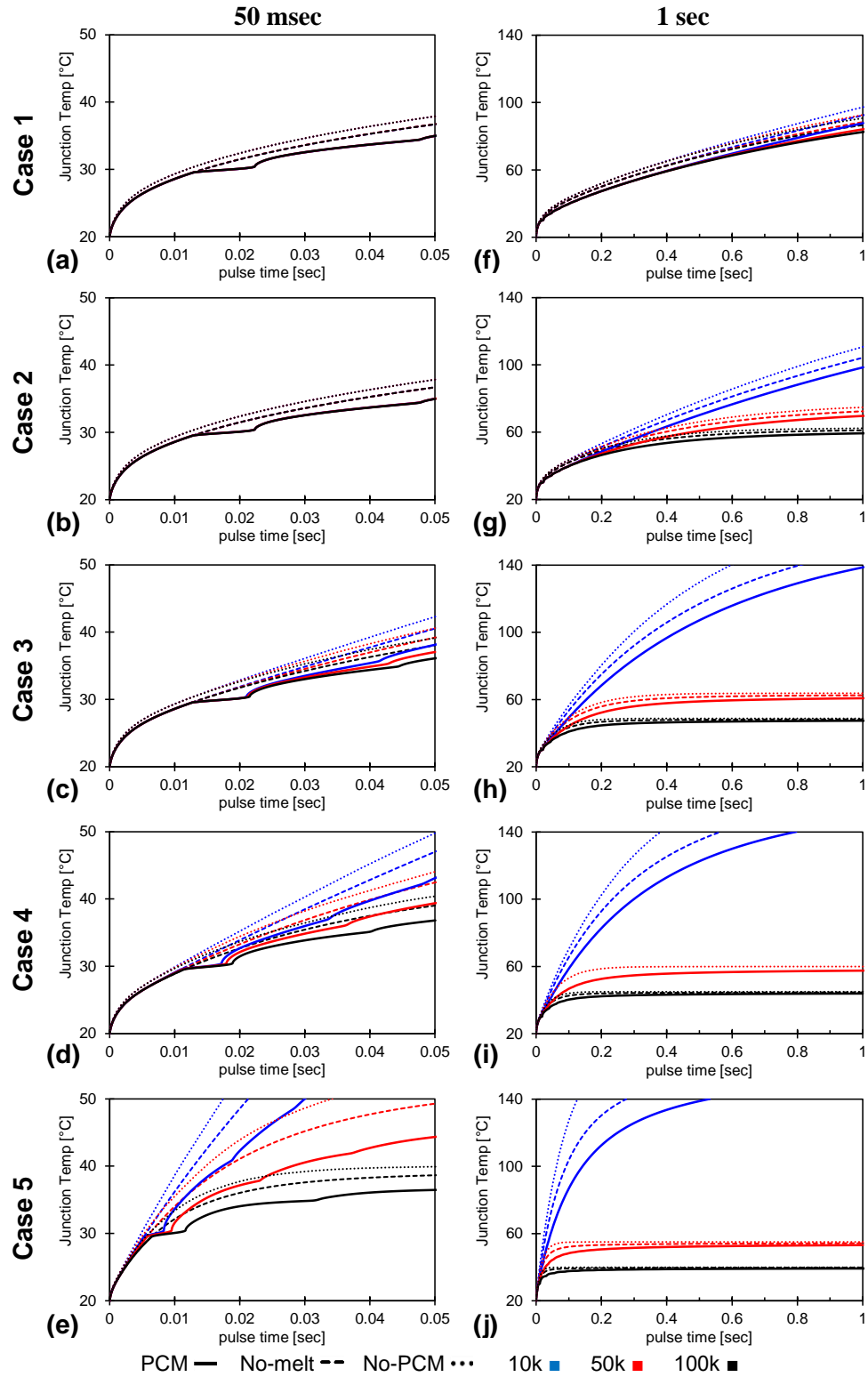


Figure A.12 – Low power package phase change step response with LNT at 150 W/cm^2 , $T_0 = 20^\circ\text{C}$.

Short (a-e) and long (f-j) response compared against cases without PCM or phase change.

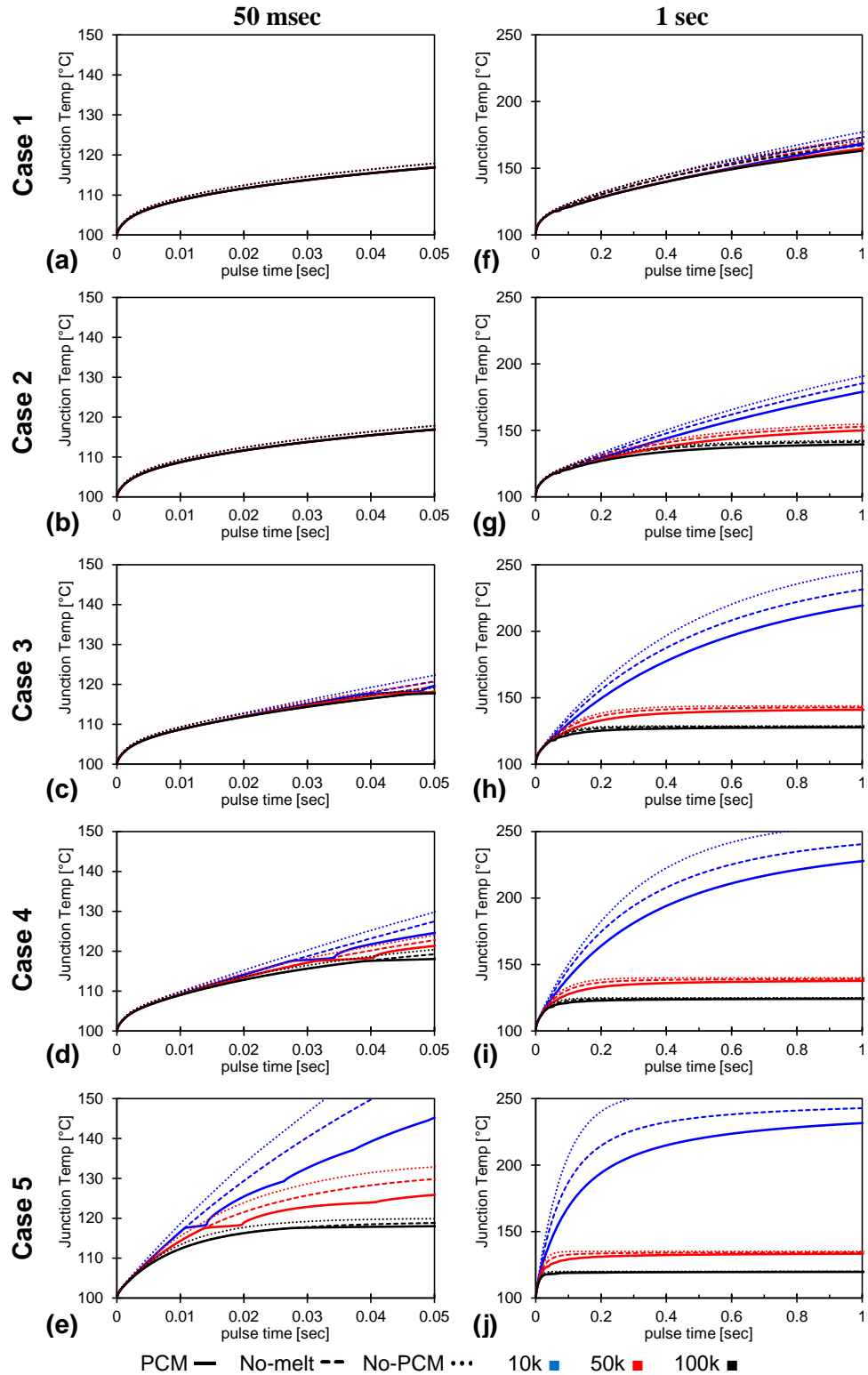


Figure A.13 – Low power package phase change step response with erythritol at 150 W/cm^2 , $T_0 = 100^\circ\text{C}$. Short (a-e) and long (f-j) response compared against cases without PCM or phase change.

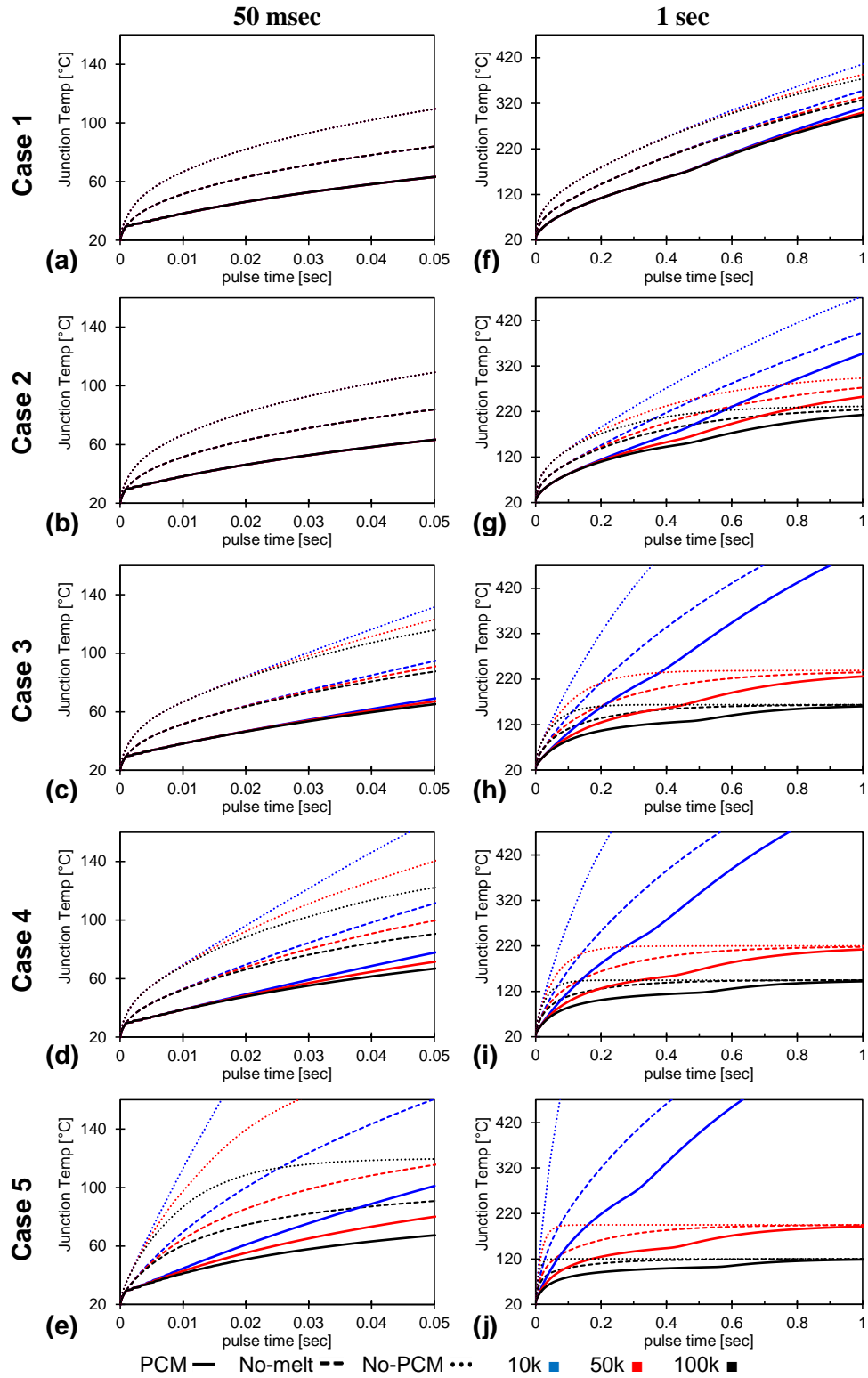


Figure A.14 – High power package phase change step response with gallium at 750 W/cm^2 , $T_0 = 20^\circ\text{C}$. Short (a-e) and long (f-j) response compared against cases without PCM or phase change.

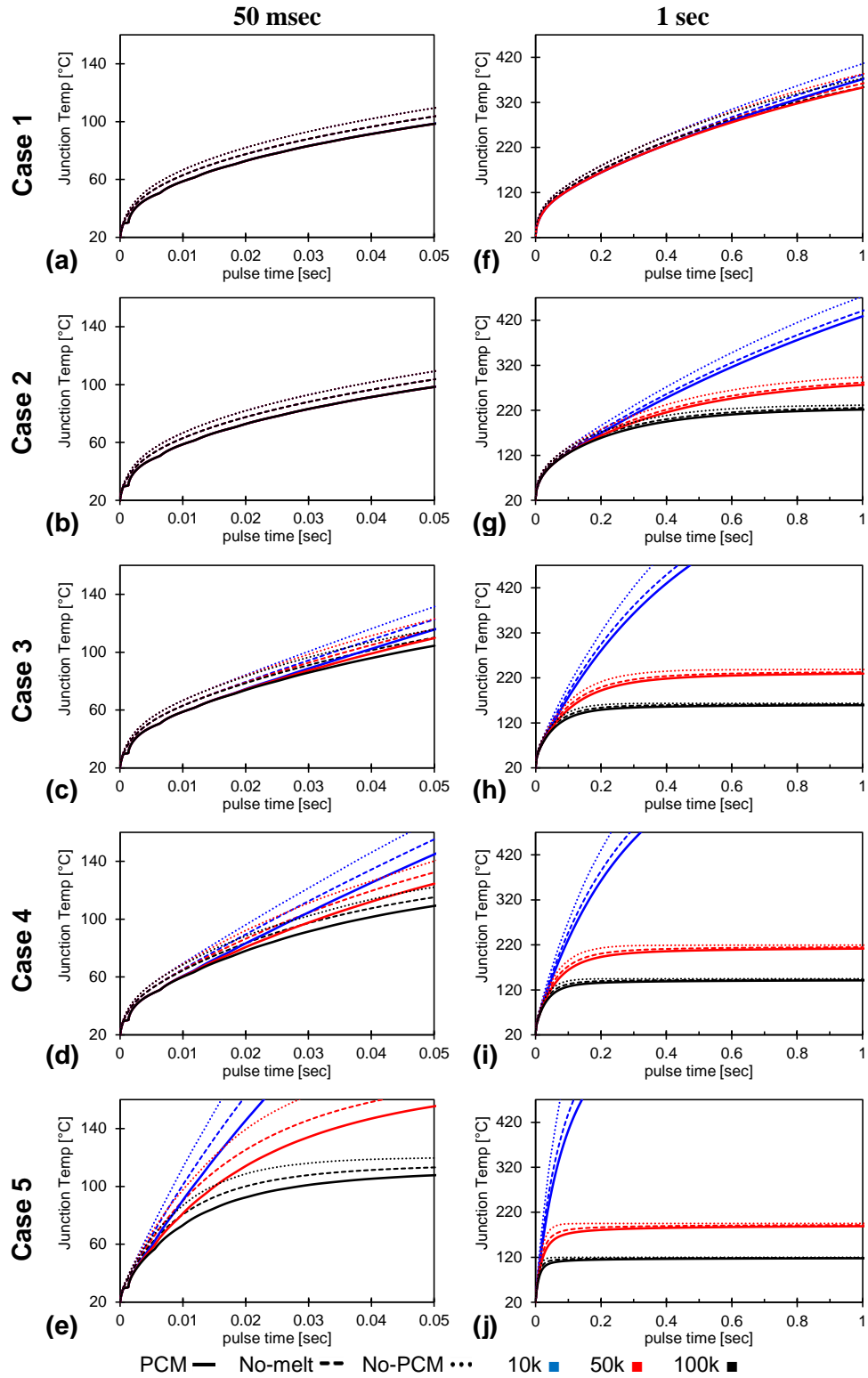


Figure A.15 – High power package phase change step response with LNT at 750 W/cm^2 , $T_0 = 20^\circ\text{C}$.

Short (a-e) and long (f-j) response compared against cases without PCM or phase change.

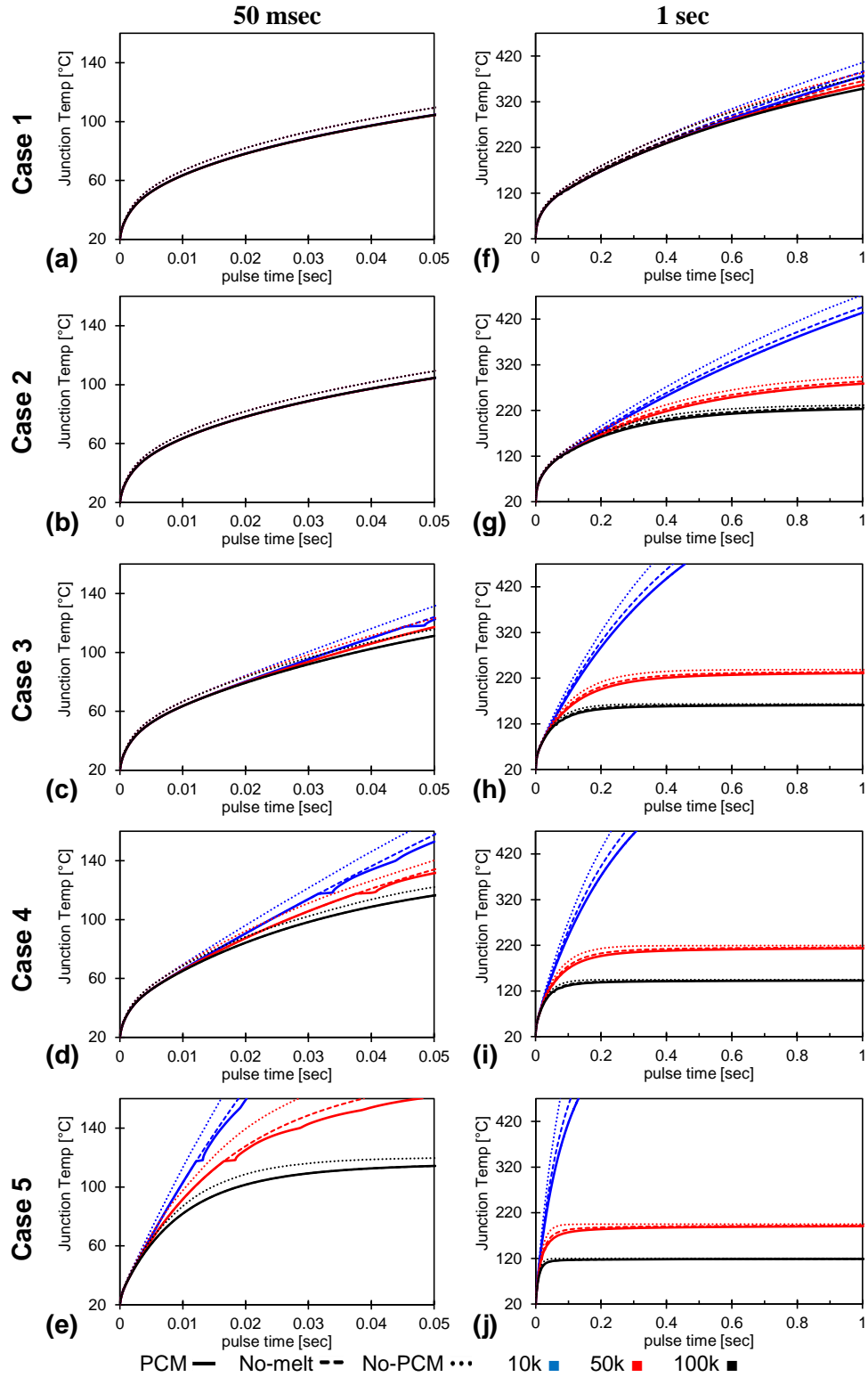


Figure A.16 – High power package phase change step response with erythritol at 750 W/cm^2 , $T_0 = 20^\circ\text{C}$. Short (a-e) and long (f-j) response compared against cases without PCM or phase change.

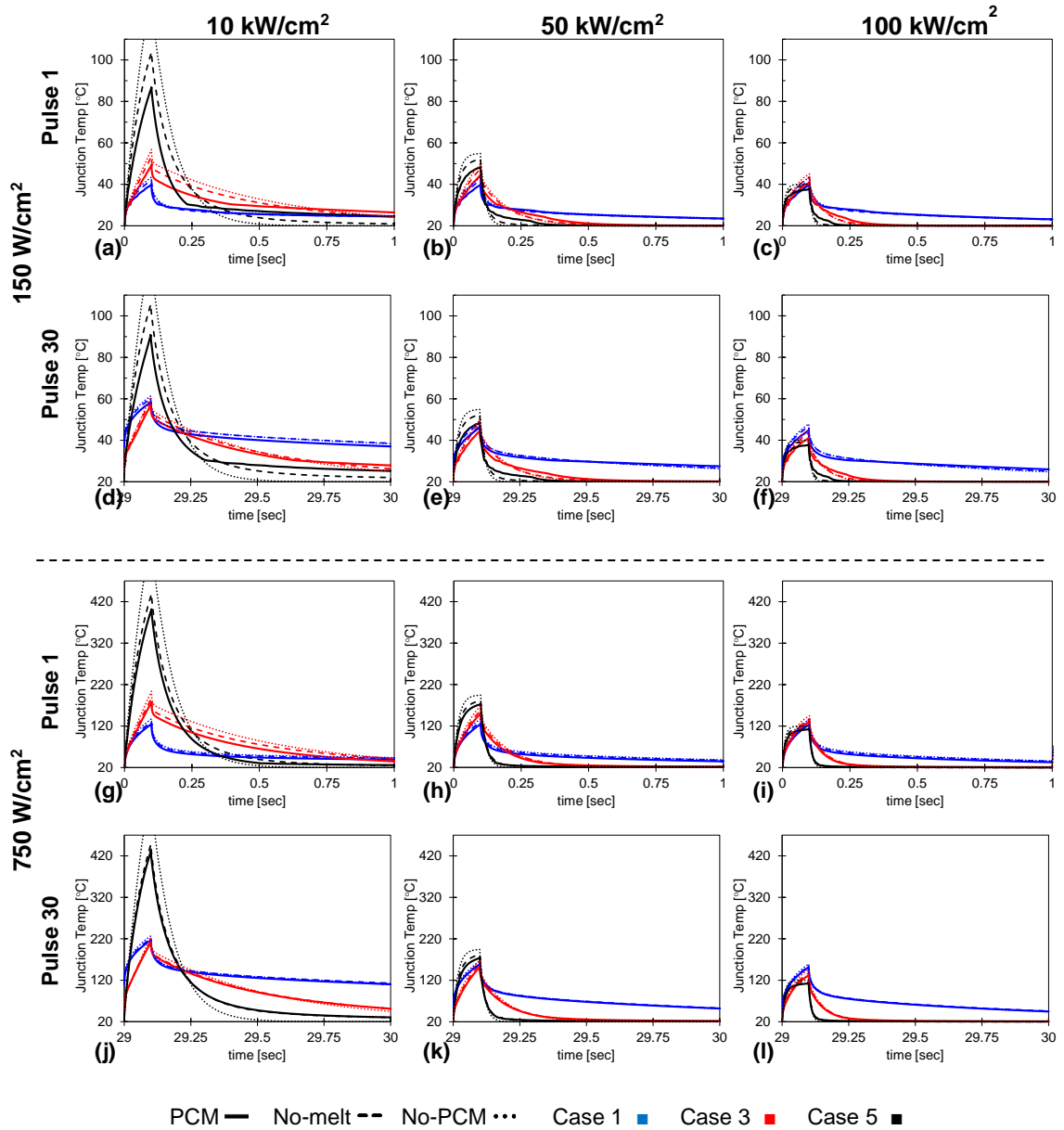


Figure A.17 – 100 ms pulsed phase change response of LNT loaded packages at all convection rates and heat fluxes compared against no-PCM response (dotted lines) and with PCM but without phase change (dashed lines).

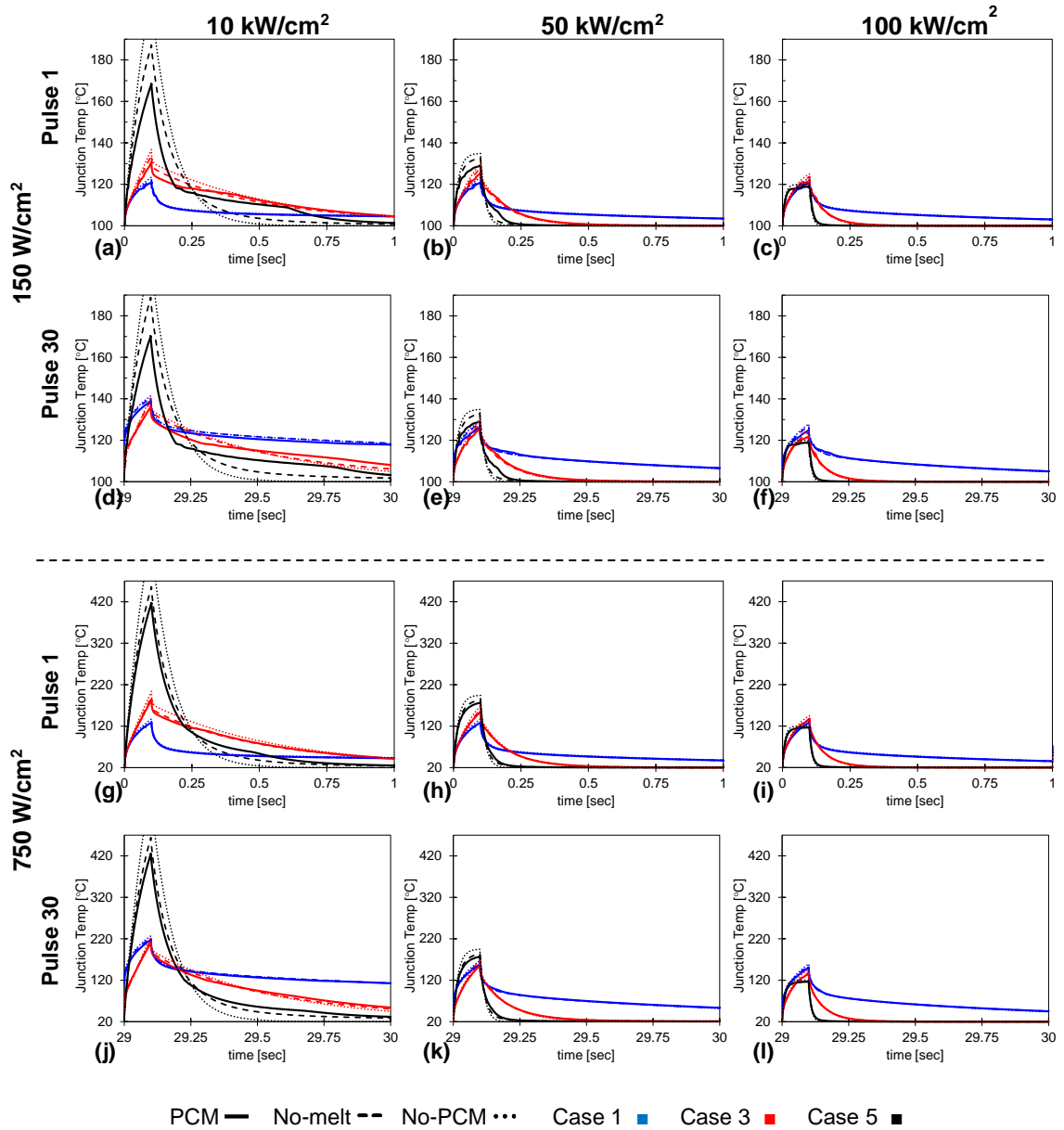


Figure A.18 – 100 ms pulsed phase change response of erythritol loaded packages at all convection rates and heat fluxes compared against no-PCM response (dotted lines) and with PCM but without phase change (dashed lines).

Appendix B– Preliminary investigation of electrical supercooling mitigation in erythritol

As described in Section 2.2 and shown in Figure 2.1, non-ideal phase change behavior includes such characteristics as non-isothermal phase change, non-constant heat absorption properties with temperature, soft instead of sharp transitions between solid and liquid heating zones, and hysteresis between heating and cooling profiles for the material. This last characteristic can make it particularly difficult to design cyclical thermal protection systems that must operate consistently and reliably over multiple thermal cycles. In the case of solid-to-liquid phase change the most often exhibited cause of hysteresis is called either sub- or supercooling, and refers to the need to drive the temperature some magnitude below the melting point before nucleation will occur allowing for resolidification and latent heat release.

The problem with supercooling in a thermal protection system is illustrated in Figure B.1, which depicts the temperature of a hypothetical phase change system subjected to periodic pulsed thermal loads and various degrees of supercooling. In (a) the system undergoes a normal transition where temperature rise is mitigated by the latent heat absorption of the PCM, which resolidifies and cools to the ‘thermal reset’ condition before the second pulse arrives. In (b), the PCM exhibits a small amount of supercooling that is manageable within the available temperature margins. The PCM nucleates at a temperature below the melt temperature, but still resolidifies and cools to an acceptable temperature before the next pulse, again reaching ‘thermal reset’. Finally, (c) shows a system that exhibits a much larger degree of supercooling. The melted PCM can only be brought down to the coolant temperature, which is not low enough to induce solidification. Thus, at the

next thermal pulse all heat absorption occurs sensibly within the still-liquid PCM and the increased system temperature could cause catastrophic device failure.

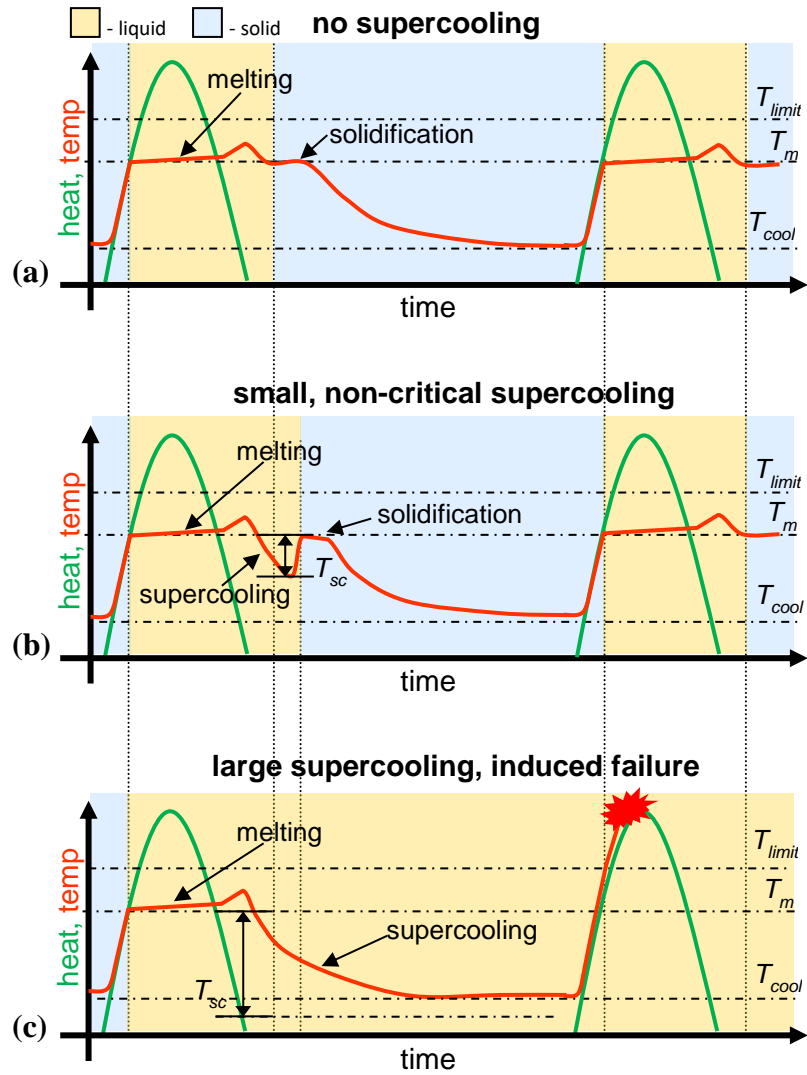


Figure B.1 – Potential effects of supercooling on a thermal protection system. (a) Normal behavior, no supercooling, thermal reset condition reached. (b) Supercooling present, but nucleation occurs within temperature limits, thermal reset condition reached. (c) Supercooling present where nucleation does not occur due to cooling limits, resulting in device sensible heating to failure.

A phase change thermal protection system must guarantee thermal reset between events. This chapter reviews attempts to mitigate supercooling and/or control nucleation

in phase change materials. In addition, preliminary attempts to demonstrate an electronics compatible technique of electrically reducing supercooling in erythritol will be described. The material in this Appendix was initially presented in [44].

B.1. Delayed Nucleation Onset and Supercooling

The supercooling phenomenon has been studied for well over a century, with much attention being given to the nucleation and freezing of water including seminal experimental work by Bigg and Hallett [281,282]. Using Turnbull's description from a review of the supercooling of liquids (sometimes called undercooling or subcooling), unlike the melting point, which can be correctly described as a point, the freezing point of a liquid is the maximum temperature at which solidification *can* begin, and is a misnomer more properly termed the *equilibrium crystallization temperature* [283]. Kauzmann describes supercooling as a metastable condition where the system must overcome a local free energy barrier that is preventing stable formation and/or growth of a crystal nucleus [284]. Alexiades mathematically specified a critical nucleate size as that at which "the Gibbs free energy of formation of solid from supercooled liquid has a local maximum, so that smaller nuclei tend to dissolve and larger ones tend to grow" [285]. In other words, the barrier to nucleation is the energy needed for a large enough seed crystal to spontaneously form so that its growth is energetically favorable. The characteristics of this nucleation energy barrier and what influences its magnitude are the primary factors in the existence of a supercooled state.

Studies by Bigg and Turnbull provided general characterizations of the supercooling effect: (a) supercooled nucleation is a stochastic event with probability of occurrence being strongly tied to the supercooling magnitude, (b) the cooling rate has a

mild but noticeable effect on the supercooling magnitude, with higher cooling rates permitting greater supercooling, and (c) small fluid volumes will tend to supercool to a greater degree than large fluid volumes, as more molecules in the volume increase the chance of a random nucleation event occurring [281,283].

In addition to this, a NASA review of solid-liquid PCMs for thermal control by Bentilla, Sterrett, and Karre [11] states that nucleation occurs in a supercooled liquid by one of four general methods:

1. homogeneous nucleation, where random fluctuations in molecular configuration eventually produce a stable nucleus
2. heterogeneous nucleation, where random fluctuations in molecular configuration around a foreign surface or particle create a stable crystal nucleus
3. nucleation by cavitation, where small cavities are dynamically created and collapse resulting in large local pressures spikes and shifts in the equilibrium crystallization temperature
4. growth of new crystals from existing crystal surfaces

Efforts to maximize supercooling have focused on minimizing surface sites or surrounding droplets with inert fluids, thus attempting to leave homogeneous nucleation as both the only possible solidification mechanism and the least likely to occur [283]. This supports the generalization that heterogeneous nucleation has a lower energy barrier than homogeneous nucleation, with growth from an existing solid state of the same material (whether a phase front or a seed crystal) being the lowest.

B.1.1. Crystal growth from existing material

Attempts have been made to quantify the height of the similar material nucleation energy barrier for various cases. From classical nucleation theory [286], the activation energy for generating a stable crystal nucleus on a solid surface, ΔF^* , can be expressed as:

$$\Delta F^* = \frac{16\pi\sigma^3}{3\Delta F^2} \quad (127)$$

where ΔF is the Gibbs free energy difference between the liquid and crystal states for a volume of infinite extent, and σ is the surface stress between the solid and liquid states. Starting with the balance of relative free energy of the new surface formed by a nucleation event to the free energy without nucleation, the effect of an existing surface on nucleation is expressed in the Gibbs-Thompson relation:

$$\Delta T_{SC} = T_m - T_{fr} = \Gamma\kappa \quad (128)$$

where the degree of supercooling ΔT_{SC} , defined as the amount the local freezing temperature, T_{fr} , is reduced from the equilibrium crystallization (or melting) temperature, T_m , is proportional to surface tension at a phase interface with curvature κ , where Γ is a scaled ratio of surface tension to latent heat [253]. Equation (128) describes the (simplified) condition under which nucleation and crystal growth continues from an existing phase front or crystal nucleus (the fourth NASA described mechanism). Thus, if the PCM is not completely melted or a seed crystal is introduced to the melt, crystallization will propagate in the directions around the crystal where the local freezing temperature is above the actual temperature. As the crystals grow, local curvature of the phase front will change, and local freezing temperature at different locations may drift above or below the actual temperature. This can create intricate freezing patterns depending on material

crystal properties, one of the most well know examples of this being *dendritic* crystal growth in ice, including snowflakes and frost patterns on glass.

B.1.2. Nucleation within a volume (spontaneous homogeneous nucleation)

For cases of homogeneous nucleation, where a phase front does not initially exist, Alexiades, et al., derived a modified Gibbs-Thompson relation for the degree of supercooling at which a spontaneous spherical nucleus would be thermodynamically stable [285]. This modification incorporated surface area terms and identified a critical radius, and is given by:

$$\Delta T = \frac{4}{3} \frac{\gamma_0 T_m}{\rho_s H_f R_{cr}} \quad (129)$$

where γ_0 is the surface free energy per unit area, ρ_s is the density of the solid, H_f is the specific enthalpy of fusion, and R_{cr} is the critical radius of the nucleus. Note that both (128) and (129) assume equal solid and liquid material properties.

Thus, for a given level of supercooling a spontaneously formed (spherical) nucleus with radius smaller than R_{cr} will be unstable, and will return to its liquid state. Greater degrees of supercooling reduce this required critical size, making stable nucleation more likely to occur. Increased supercooling reduces the height of the local free energy barrier maintaining the metastable supercooled state and decreases the energy required to overcome the barrier. Also, it should be noted that in (129) most other parameters in the equation (latent heat, surface energy, density, and melt temperature) are direct properties of the material at the given conditions.

B.1.3. Heterogeneous Nucleation (Crystal growth from dissimilar materials)

The second nucleation mechanism described in the NASA report involves crystal growth on a dissimilar material, whether a small particle or a large surface. An excellent review of heterogeneous nucleation effects is given in the study by Turnbull and Vonnegut on nucleation catalysis [286]. The primary difference between the crystal breeding case and heterogeneous nucleation is the crystalline lattice mismatch that exists between the solid surface and the preferred solid structure of the supercooled melt. How well matched the solid structures are directly affects the amount of energy required to initiate crystal growth. If the minimum work required to create a new nucleus in the supercooled liquid (i.e., overcoming the metastable energy barrier in the crystal breeding case) is ΔF^* as given in (127), then the introduction of a dissimilar solid surface multiplies that work value by a *catalytic potency factor*, $f(\theta)$, given as:

$$\Delta F_c^* = f(\theta) \cdot \Delta F^* \quad (130)$$

$$f(\theta) = \frac{1}{4}(2 + \cos \theta)(1 - \cos \theta)^2 \quad (131)$$

where θ is the liquid-solid contact angle (in air) which ranges from 0 to 180°, causing $f(\theta)$ to vary from 0 to 1 as shown in Figure B.2.

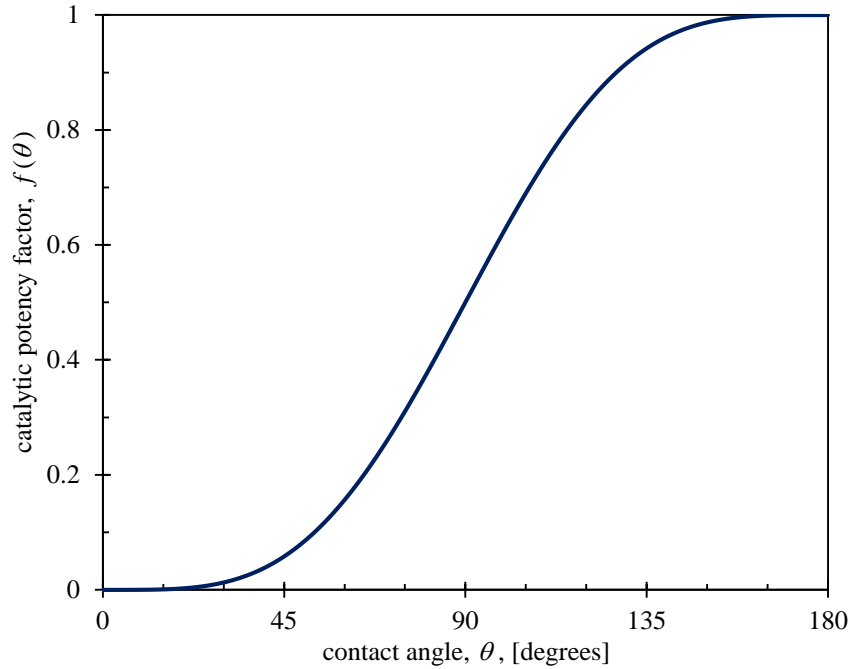


Figure B.2 – Variation of the catalytic potency factor, $f(\theta)$, with surface wetting angle.

Thus, in all practical cases the presence of a solid surface will decrease the nucleation energy barrier, with some materials giving more of a catalytic benefit than others. Although usually empirically measured, the contact angle can be calculated from the surface stress between materials from:

$$m = \cos \theta = (\sigma_{CL} - \sigma_{CS}) / \sigma_{LS} \quad (132)$$

where σ is the surface stress and the subscripts C , L , and S , denote the crystal (or catalyst), liquid, and solid states, respectively.

As surface wetting angle and surface tension are macroscopic manifestations of crystal behavior, the microscale crystalline qualities of the material can also be examined directly to determine their effect on nucleation potential. Numerous researchers have reported that the heterogeneous nucleation of ice in the presence of silver iodide is due to the close lattice match on low index planes between the two materials [286-288]. In fact,

the two materials share the same tetrahedral crystal structure, and one can identify a nondimensional parameter called the *disregistry*, δ , between the materials, defined as:

$$\delta = \Delta a/a_0 = (a_c - a_0)/a_0 \quad (133)$$

where a_0 is the low index lattice spacing of the solidifying crystal, and a_c is the corresponding catalyst or solid surface lattice spacing. For ice ($a_0 = 4.535$ Å) and AgI ($a_c = 4.585$ Å), the disregistry, δ , is only 0.011, or 1.1%. In addition, the c dimension for ice and AgI are also only mismatched by ~1%, making an extremely good match between the two materials and explaining the high amount of interest AgI received in early ice nucleation studies. Turnbull and Vonnegut summarize a number of other material sets that demonstrate effective nucleation characteristics with water and also have close crystal lattice spacings [286]. These materials are also summarized in Table B.1.

Table B.1 – Effective heterogeneous nucleation materials, from [286]

Crystalline material	Nucleating surface or additive	Low order disregistry (δ)
Ice	Silver Iodide (AgI)	1.1%
Glauber's Salt	Borax ($\text{Na}_2\text{B}_4\text{O}_7 \cdot 10\text{H}_2\text{O}$)	1.5%
Aluminum	Vanadium Carbide (VC)	1.4%
...	Tungsten Carbide (W_2C)	3.5%
...	Aluminum Boride (AlB_2)	3.8%
...	Titanium Boride (TiB_2)	4.8%
...	Titanium Carbide (TiC)	6.0%
Mercury	Unknown Mercury compound (“HgX”)	~5-10%
...	Mercury Sulfide (HgS)	19%

In the same study, Turnbull and Vonnegut estimated that the solid-crystal portion of the surface energy (σ_{SC}) must be proportional to the dislocation density that would be created between the two surfaces with mismatched lattice spacing. Reducing this portion of the surface energy term would modify the $\cos\theta$ term (m) in (132), although the exact effect of this term on heterogeneous nucleation energy would depend strongly on the relative values of the various stress terms. In short, they do make the following claims and

simplifying assumptions on the relation of the heterogeneous nucleation energy barrier to the crystal structure disregistry:

1. With ‘compatible’ crystal structure (similar low index planes), a material’s catalytic potency will be proportional to $1/\delta$. (I.e., a lower disregistry catalyst should have a lower nucleation energy barrier).
2. Small enough values of δ will promote ‘coherent’ nucleation on top of the solid surface, with the small lattice strain creating a small nucleation energy barrier, where $|\Delta F|=c\delta^2$.
3. For larger δ , the crystal will form incoherently on the surface without straining the crystal lattice, but with an increased energy barrier that will increase linearly with δ .

B.2. Methods of promoting or inducing nucleation

In addition to the electronics thermal protection, other engineering applications including TES for cogeneration [37], solar heating [24], and environmental control, as well as flash freezing and freeze drying for food processing and medical industries [289] depend on the predictable and repeatable control of liquid-to-solid phase change. In some cases there is a desire to maximize the degree of supercooling, such as Hirano, et al. proposing to use supercooled liquid for energy storage and transport with low heat loss [290]. Other researchers attempting to maximize liquid supercooling have done so by using ultrapure liquids in smooth, passivated containers, or droplets suspended in another insoluble liquid [281,291]. Even in this application, however, there is a need to induce nucleation at a particular time for controlled heat release. Thus, there have been numerous efforts to

affect the natural tendency of a material to exhibit supercooling and the stochastic nature of nucleation onset.

B.2.1. Surface modification

Most passive nucleation promoting methods take advantage of the lower energy barrier of heterogeneous nucleation. This makes it natural to examine the effect of the PCM container on the degree of supercooling. Much work has been published by Saito and Okawa on this effect for the supercooling of water [292-296]. They demonstrated that roughened metallic surfaces can show a statistically significant change in the degree of supercooling of water by as much as 50%, with non-insignificant dependence on cooling rate [292]. These results were later confirmed by Faucheux, et al. [297]. Surface oxidation of a copper surface, despite significant increase in roughness, was shown to inhibit nucleation likely due to chemical passivation [293]. Finally, in a computational molecular dynamics simulation of the nucleation of water on an arbitrary solid surface, they demonstrated that variation of solid lattice constant had significant effects on nucleation potential. Maintaining a lattice match between ice and the solid of a few percent would facilitate nucleation, with greater effect when the solid lattice was smaller than the ice lattice. Okawa and Saito suggested that these findings could be of great importance as guidelines for the selection of nucleating materials in future efforts [296].

B.2.2. Nucleation promoting additives

Because often the design freedom may not be present to change the container of a PCM to promote nucleation, a more commonly used passive method of supercooling mitigation has been the addition of nucleation promoting additives to the material. This

was briefly described in the Section B.1.3 on heterogeneous nucleation along with some examples from Turnbull. Much work on promoting water nucleation dates back to some of the initial efforts to understand supercooled water droplets in clouds and ways to induce precipitation. Many weather focused experiments were performed at the General Electric Research Laboratory in the mid-20th century by Schaefer, Vonnegut, and Turnbull where droplets or clouds were seeded with various materials, including dry ice, silver iodide, mercury-compounds, metal-carbides, volcanic ash, and others [286,287,298]. Silver iodide was one of the materials commonly found to be effective in significantly affecting supercooling, theorized by Turnbull and Vonnegut as being due to the close lattice matching between the catalyst and the crystalline solid. Ice and silver iodide have unit cell lattice parameters within 1%, and later testing by Okawa confirms this dependency, adding that the effect of supercooling mitigation is directly proportional to the total surface area of added catalyst [299]. Adding nucleating additives is a passive system change that should modify nucleation behavior but can run into difficulties maintaining consistency over multiple phase change cycles [25].

B.2.3. Cavitation induced nucleation

Mechanical agitation has been used to successfully increase nucleation likelihood, but simply shaking, mixing, or stirring show mixed success at best and are highly unreliable [300,301]. Kurz and Fisher described the unlikelihood that the time and spatial scales of most mechanical disturbances could affect molecular level configurations to induce nucleation [302]. Ultrasonic agitation, however, has been shown by several research groups to successfully control or even eliminate supercooling in several materials [303,304]. Several reports by Inada, et al., detailed the use of ultrasonic vibration to control

the nucleation temperature of supercooled water [303,305]. The researchers demonstrated that both purified and conventional tap water could be induced to nucleate by proper tuning of ultrasonic intensity. Depending on the temperature at initial application and the amount of energy, the entire volume could be induced to nucleate with as little as 1.5°C of supercooling, compared to the nominal 10-13°C of supercooling typically seen.

Recalling that cavitation was the third of Bentilla's nucleation mechanisms mentioned in Section B.1, ultrasonic agitation is effective in nucleating a supercooled liquid because of the minute cavitation bubbles induced in the melt. Careful studies by Hunt and Jackson identified the mechanism from three competing hypotheses on why cavitation bubble formation and collapse induces nucleation [306]:

1. Sudden evaporation in the void space cools the surface sufficiently to cause nucleation.
2. The cavity collapse induces a pressure shock-wave with sudden, large positive then negative local pressures that can shift the local freezing temperature.
3. The large negative pressure spike induces cooling of the liquid sufficient to cause nucleation.

Their experiment decoupled and individually validated these mechanisms. They determined that only the pressure wave induced change in freezing temperature was able to demonstrate consistent impact on nucleation (theory 2). Estimates for this change in local solidification temperature, ΔT_m , due to pressure changes, ΔP , can be given by the Clapeyron equation:

$$\Delta T_m / \Delta P = T \cdot \Delta V / \Delta H_f \quad (134)$$

where T is the nominal temperature, ΔV and ΔH are the change in volume and enthalpy on phase change. The sign of ΔV is material dependent, but because ΔP goes both positive and negative during cavity collapse, the absolute value need only be considered.

Referring back to both (128) and (129), it is clear that the supercooling magnitude, and hence the depth of the metastable potential well keeping the melt in a supercooled liquid state, is directly proportional to the local equilibrium melting temperature. Sudden fluctuations in pressure local to the cavitation event (estimated at 10^4 - 10^5 atm during bubble collapse [306]) and corresponding increase in nominal melting temperature with minimal change in actual local temperature causes the liquid around the bubble to experience extreme levels of supercooling during the pressure wave. This will effectively overcome the nucleation energy barrier, permitting stable formation of crystals that would have normally fallen below the critical nucleus size as described in (129).

Experiments by Ona, et al., verified that ultrasonic cavitation could induce nucleation, and showed that the effect can be related to both the homogeneous and heterogeneous nucleation potentials [304]. At lower levels of ultrasonic energy nucleation was only induced on solid surfaces in the test chamber, suggesting that the lower ultrasonic energy was sufficient to overcome the heterogeneous nucleation energy barrier, but not the higher homogeneous nucleation barrier. Higher energy levels caused numerous fine crystals to spontaneously form uniformly throughout the supercooled melt, indicating the additional energy was sufficient to push it over the higher homogeneous energy barrier.

B.2.4. Electric field induced nucleation

There has been much debate about the mechanism by which liquid nucleation might be induced by the application of electrical energy, including decades of mixed reports on the effectiveness this approach. Abbas and Pruppacher provide separate discussions of the back-and-forth arguments in the literature about the actual mechanisms by which electric fields could affect nucleation [307, 308].

The earliest work Abbas reports is by Rau in 1951 who induced nucleation in water droplets by sparking them from a nearby electrode. In addition, he proposed that application of a strong static electric field (without sparking) would reorient water molecules and induce nucleation [309]. This was later performed by R. W. Salt, who applied a 15 kV_{AC} signal to droplets and claimed similar causality [310]. According to Abbas, there was contention of impurities in the study and possible electrode contamination. In 1963, H. R. Pruppacher performed a series of experiments in an attempt to confirm or disprove Salt's findings [311]. He performed several experiments with strong electric fields without exposing the fluid to any metallic electrodes or known nucleation-promoting materials. He demonstrated that nucleation could be induced, but eliminated dielectric molecular reorientation as a cause, and theorized that the presence of a moving triple-interface was necessary to transfer charge and induce nucleation. Abbas instead agreed with theories proposed by L. B. Loeb [312] that nucleation was induced by mechanical disturbances in droplet shape, rather than direct electrical influence, pointing to cases where the triple-interface moved but failed to nucleate.

Several years later Pruppacher criticized this notion with an experimental review of his own [308], pointing out that further studies on molecular orientation indicate that

bulk mechanical deformation would have little effect on repeatable molecular behavior. His experiments supported a theorem by L. F. Evans [313], who stated that a solid surface must first adsorb a liquid layer which can then serve as a seed layer for subsequent crystal formation. Pruppacher extended this theory to electrofreezing, stating that strong electric fields make certain local charged surface sites very active adsorbers, enhancing the formation of the seed liquid layer, followed by ice. This idea that enhancement requires liquid contact with a material capable of developing a surface charge with local asperities was somewhat supported by Doolittle and Vali in 1974 [314]. They performed experiments with water droplets seeded with silver iodide or organic contaminants, but varnished over the electrodes to prevent any direct contact. Electric fields up to 6 kV/cm were applied without any effect on nucleation temperature.

More recent efforts have still attempted to demonstrate whether utilizing an electric field (without conduction) can induce nucleation. A detailed molecular dynamics (MD) numerical model was developed by Svishchev and Kusalik to examine the effect of strong fields on water's dielectric response, and any increased tendency to nucleate [315]. The simulations indicated that with very strong electric fields (on the order of 50 MV/cm) supercooled water molecules would undergo rearrangement that could reduce the energy barrier to formation of ice-like structures. This indicates that molecular rearrangement would be a mechanism by which electric fields could promote nucleation.

Experimentally, Petersen, et al., have used pulsed electric fields to induce controlled nucleation in a freeze drying application [289]. Using insulated electrodes, 4 kV 2.5 ms long pulses were applied every 3 seconds after reaching the desired nucleation temperature. Although performance varied significantly with composition of the liquid,

pure water could be nucleated reliably within about 1.1°C of the desired nucleation temperature. Other aqueous solutions including glucose, sucrose, mannitol, and glycine were able to be nucleated within about 4°C of the desired nucleation temperature. Finally, an effort in 2008 by Wei, et al., attempted to verify the predictions by Svishchev on strong field induced nucleation [316]. By applying electric field pulses on the order of 1 kV/cm, an increase of about 1.6°C was seen in freezing temperature. Both Petersen and Wei used electric fields many orders of magnitude below those modeled by Svishchev and Kusalik. This does suggest that the nucleation mechanism in those cases may not have been purely homogeneous nucleation via dielectric rearrangement, similar to the cases reviewed by Abbas and Pruppacher.

B.2.5. Electric current induced nucleation

Despite the confusion on mechanisms with electric field induced nucleation, there is far less disagreement over whether or not passing an electric current through a supercooled melt can induce nucleation. Many of the earlier studies described in the previous section were criticized for possibly permitting corona discharges or leakage currents to induce nucleation of the water droplets. Studies where discharge was the intent produced nucleation events with very high probability despite the lack of conclusive mechanism. Some suggestions were that corona discharges produce ions and free radicals as nucleation sites, or that sudden discharges create mechanical shock waves or cavitation within the liquid [310,317]. Spark discharges being a high intensity, difficult to control event, others have examined application of lower voltage currents through dielectric melts for effect on nucleation as well. Rather than liquid droplets, most of these studies have looked at systems of electrodes submerged in a melted volume. The majority of this work

has been experimental in nature, and theory on driving mechanisms behind the effects seen has not been rigorously studied.

More recently than most of the other electrofreezing studies, two groups from Japan investigated the freezing of a body of supercooled water with submerged electrodes, and the two sets of experiments showed similar results. First, Shichiri, et al., from Osaka City University in 1980 [318], and second, Hozumi, et al., from the Tokyo Institute of Technology in 2003 [294], investigated the effect of direct current on supercooled water with different electrode materials. They showed that the material's effect on nucleation could be related to its *ionization tendency* (also expressed by the material's *standard electrode potential*, E^0). Both groups demonstrated that the electrode on which nucleation occurred relates directly to E^0 , where negative values (or large ionization tendency) induced nucleation on the anode and positive values (or small ionization tendency) induced nucleation on the cathode. This effect was verified by reversing polarity with a particular set of electrodes, and the nucleation electrode switched accordingly.

While their results were in general agreement, the proposed explanations of the exhibited behavior given with each experimental description were not. In their first experiment the Shichiri group identified the polarity-ionization tendency and theorized that cation formation is primarily responsible for inducing nucleation. In the case of small ionization tendency materials (Ag, Pt, and Au), ions in the water are attracted to both electrodes, and the cations attracted to the cathode must significantly affect heterogeneous nucleation tendency (based on the fact that nucleation only occurred on the cathode). In the case of large ionization tendency materials (Mg, Al, Ti, and Zr), metal dissolution readily forms metallic ions at the anode. These metallic cations form faster than the rate

of cation accumulation on the cathode, resulting in a higher concentration on the anode. Those cations that do reach the cathode are “plated out rapidly on the electrode” reducing total concentration there. Finally, in addition to the metallic cation formation on the anode, they theorized that coordination compounds with water may form providing a further enhanced heterogeneous nucleation surface.

In a follow-on experiment Shichiri, et al. looked at the effect of different types of electrical signal on supercooled water [319] and only worked with Pt and Ti electrodes. A DC signal promoted nucleation as before, while an AC signal had only a very slight effect on nucleation. Applying a static field with passivated electrodes had no effect on the fluid. In addition, hydrolysis was noticed at the electrode tips, and nucleation always occurred at the point of bubble contact when it detached from the electrode. They theorized that the moving three-phase contact enabled enough change in local surface states to allow small seed crystals to form which then acts as a breeder crystal upon bubble detachment. They assumed that hydrolysis is constant throughout the process, despite the fact that bubbles may be too small to detect visually.

In the Hozumi group’s first study, they related the electrode voltage required to reduce the amount of supercooling for nucleation, and showed that large ionization tendency materials (negative E^0) have a greater effect in nucleating water at lower voltages. This consideration includes the effect of an oxidizing surface being produced on the electrode by the water, and the resulting order of tested materials was “Al=Cu>Ag>Au>Pt>C” [294]. They also noted the same polarity dependence of nucleation on the material ionization tendency, with high ionization tendency materials nucleating on the anode, and low ionization tendency on the cathode. Their group focused

on the assumption that nucleation was dictated not by bubbles, but by the coordination compounds formed at the anode surface with the ionized metal. They claim that the discrepancy between the coordination compound and the crystal most strongly affects nucleation potential. As Aluminum was the most active metal used, they show that a particular Aluminum/ice coordination compound has an O-O bond length of 2.8Å, compared to pure ice with an O-O bond length of 2.76Å, or a discrepancy of only 1.4%. The relative ranking of discrepancy closely matches the ranking of nucleation effectiveness mentioned above.

Finally, the second experiment in 2005 by Hozumi, et al., investigated the effect of electrode shape on freezing [295]. They used aluminum electrodes, which had previously exhibited the greatest material effect, and tried multiple combinations of sharp and flat end surfaces to isolate the impact of field strength on nucleation. Against intuition, the flat electrodes with supposedly weaker imposed electric field had the greatest potential for reducing supercooling. The researchers theorized that either the surface roughness created a larger amount of asperities at closer distances to the opposing potential on the flat electrode than on the pointed one (which actually had a finite radius), or the increased electric field from the pointed electrodes reduced buildup of metal coordination compounds on the anode, driving diffusion toward the cathode. The group also noticed hydrolysis and bubble formation for larger voltages, and theorized that the increased bubble formation on the sharp end electrodes could also play a factor in disturbing nucleation on the anode.

Despite the lack of consensus on mechanism between the two groups, it is worth noting that all experiments with voltage applied to the electrodes showed a change in nucleation behavior. Spontaneous nucleation only occurred at the cooler container walls

and induced nucleation always occurred on the electrodes. This induced nucleation also always occurred at a higher temperature than for the cases with no current applied. That said, Shichiri's group used higher voltages (1000 V, or about 5.5 kV/cm with 1.75-2 mm separated electrodes) while Hozumi's group used lower voltages (50-120 V), with closer electrodes (~300 μm), and lower resultant field strengths (~1.7-4 kV/cm). Both groups produced noticeable bubble formation in their latter experiments but under different conditions, and while Shichiri's first experiment used a pulsed current (applied for < 1 second for every 0.5°C decrease in melt temperature), Hozumi's experiments all used a constant applied voltage for 30-90 sec. The varied factors between these experiments leave many questions unanswered regarding mechanism and potential for general use in controlling supercooling and nucleation.

B.3. Reducing the Supercooling of Erythritol

Chapters 2 and 3 described the need for a moderate temperature, high energy density thermal storage material for vehicle and power electronics thermal protection, and that the sugar alcohol erythritol had been identified by several groups as being a prime candidate. Its 118°C melting temperature and relatively high specific and volumetric latent heat (344 kJ/kg and 502.9 J/cm³, respectively) are only offset by its low thermal conductivity (~0.7 W/mK, admittedly 2-4x higher than most other organic materials). While these properties make erythritol a leading material candidate, it unfortunately has been shown to exhibit a high degree of supercooling that has the potential to render it unusable for vehicle-based applications.

Ona, et al. showed that erythritol was able to stay in a supercooled state as much as 70°C below the nominal melting temperature with an average supercooling magnitude in

the range of 42 +/- 26°C [43,320]. This behavior was quite variable between different samples and tests. Kakiuchi, et al., found erythritol to typically recrystallize between 54 and 100°C [37,42], while Shukla, et al., saw no more than 15°C of supercooling in repeated cycling experiments with large volumes of material [40,321]. From the example at the beginning of this chapter on potential supercooling induced failure and the lower temperature bounds on vehicle cooling loops described in Section 3.1.2, it is clear that erythritol's high potential for supercooling could easily exceed available cooling capacity. Controlling erythritol's supercooling is thus a necessary element for using it in a thermal protection system, but there have only been a few studies looking at how to accomplish this. These studies will be reviewed in the following sections, followed by a preliminary experiment exploring a potential supercooling mitigation approach.

B.3.1. Previous attempts at reducing supercooling in erythritol

B.3.1.1. Passive techniques

The only reported passive supercooling mitigation method for erythritol is the use of material additives for nucleation enhancement. A comprehensive discussion on this comes from a Mitsubishi Chemical Corporation U. S. Patent (by Hiroyuki Kakiuchi, et al) on the effect of different additives to erythritol for long term PCM temperature stabilization [42]. The patent description details numerous experiments performed on the effect of different combinations and concentrations of sparingly-soluble salts on recrystallization temperature and high-temperature stability of erythritol. Most combinations caused some reduction in melting temperature, but materials that had a positive effect in reducing supercooling are shown in Table B.2.

Table B.2 – Materials showing erythritol supercooling mitigation, from [42]

Additive	Wt%	Average recrystallization temp (°C)	Additive	Wt%	Average recrystallization temp (°C)
Calcium Tertiary Phosphate	5.0	110.6	Silver phosphate	0.5	109.3
Calcium Sulfate	5.0	112.0	Silver bromide	0.5	110.7
Calcium pyrophosphate	5.0	107.5	Silver chloride	0.5	109.0
Aluminum phosphate	5.0	110.9	Calcium stearate	5.0	109.0
Silver iodide	0.5	107.5	None	n/a	53.4

The information in Table B.2 shows that supercooling was reduced from about 65°C to 10°C, but it is difficult to judge the validity of that measurement. The patent mentions that a large melted volume was analyzed using a single thermocouple in the center of the melt, which would be the warmest part of the melt during cooling. It does not mention where nucleation occurred, but it is likely that it occurred at an edge of the volume, which should be the point of minimum melt temperature. While there appears to be a significant effect on nucleation, the actual amount of supercooling was 10°C *at a minimum*, and could have been much larger.

A patent application for Nikken Chemicals Company (by Hiroyuki Khono, et al) contained information about additives to sugar alcohol based PCMs (including erythritol) in order to maintain phase change temperature stability over repeated cycling [45]. The application states that “it is known” that erythritol degrades if it is repeatedly cycled at temperatures exceeding 140°C, especially in the presence of oxygen. Materials including zeolite, zinc hydroxide, and magnesium hydroxide were demonstrated as preventing significant material degradation over 700+ phase change cycles, even when temperatures exceeded 140°C. The application mentioned that these materials also reduced the supercooling effect in erythritol, but no quantitative data was given in that regard.

Other studies attempting to modify or improve erythritol have looked at blending it with other PCMs with similar melt temperatures. Most of these efforts had the goal of reducing the effective melting temperature to below 100°C, in order to have direct use in generating domestic hot water without the risk of inducing boiling. Materials tested included MCHH [55] and a number of other polyalcohols [322] all over a range of concentrations. In all cases the mixture experienced some degree of melt-temperature suppression or broadening, and latent heat was reduced from that of pure erythritol. Supercooling seemed to be present to some degree in almost all mixtures as well, and was largely unaffected in the MCHH mixture. Also, while the polyalcohol blends showed repeated phase change stability, the MCHH blend exhibited noticeable phase segregation after repeated cycles, as would be expected from a typical salt-hydrate.

B.3.1.2. Active techniques

Only one group at Nagoya University has extensively studied ways of relaxing erythritol's supercooling. Ona, et al., issued several reports detailing mechanically induced nucleation in melted erythritol. In one study [43], they took about 40 samples of erythritol and demonstrated the severe levels of supercooling that the material typically exhibits ranging from 15.7 to 68.4°C, with an average of about 52°C (or a median spread of about 42+/-26°C). In the same study, the group explored the mitigating effect of various mechanical agitations, including ultrasonic irradiation, bubbling gas through the melt, and stirring with and without crystal seeding. Only stirring without seeding was shown to have no noticeable effect on supercooling. With seeding, stirring could only reduce supercooling to about 10°C (about the same as that shown in the passive studies with additives). Bubbling with nitrogen was effective, but only when the gas was at room

temperature, indicating that the large temperature difference could have been more of a cause than the bubbling agitation. Finally, when ultrasonic agitation was used, it was found that the amount of supercooling could be changed or even eliminated by modifying the initial application temperature, amount of energy, and duty cycle. Thus, elimination of supercooling in erythritol was demonstrated as possible using properly tuned ultrasound energy. It was noted that the fluid temperature did rise as it initially absorbed the ultrasound energy, so optimization would be required to minimize time to nucleation.

A follow-on study focused on measuring the effect of ultrasound on the temperature distribution throughout the melt [304,320]. The group showed that by sonicating the fluid, the temperature throughout the fluid is relatively uniform at the time of nucleation, and that nucleating crystals appear to be spread evenly throughout the melt. Most TES studies on erythritol after this point cite these reports as demonstrating *the de facto* solution for mitigating supercooling in erythritol, despite the limited number of other mechanisms to have ever been studied.

It is noted that no studies were identified where electrical nucleation of erythritol was attempted.

B.3.2. Initial experiment on electrical supercooling mitigation with erythritol

Previous successful attempts to reduce supercooling of erythritol either required material additives that reduced material energy density or long term cycling reliability, or required a complicated mechanical apparatus to generate ultrasonic agitation. Neither of these approaches are particularly applicable to use in the power electronic heat sinks described in Chapter 4. On the other hand, the current-based electrical techniques described in Section B.2.5 as being used successfully for water should (assuming material

compatibility) be easily integrated into a standard or substrate-integrated heat sink. The remainder of this chapter describes an experimental demonstration of electrical supercooling mitigation in erythritol (originally published in [44]). The overall goal of this experiment was to test the hypothesis that applying an electrical current to supercooled erythritol would shift the material's nucleating behavior in the same way that was demonstrated for water. The test procedure involves the repeated melting of a fixed quantity of erythritol with selective application of electrical current during the trials. Temperature of the melt and the time and location of nucleation events were recorded in each trial. The collection of data for nucleation events with and without electrical current were then examined to identify any impact on erythritol nucleation behavior.

B.3.2.1. Experimental Setup

A 30 mL glass vial was filled with 5 grams of granular, food grade erythritol. (A single sample of erythritol was used throughout the experiment.) A hot oil bath was used to melt the erythritol, maintained at about 140°C in a 500 mL beaker over a hot plate with a stirrer bar magnet. The electrode assembly consisted of two 375 μm (0.015 in.) diameter silver wires soldered to a ceramic package. The wires had been trimmed with standard wire cutters creating triangular, pointed tips, and were positioned such that the tips were separated by a gap of about 350 μm. A type-K bare wire thermocouple (designated TC1) was attached to the package with the junction about 1 mm away from the electrode gap. A photograph of the electrode package and wires can be seen in Figure B.3(a). The electrode assembly was suspended in the vial such that the electrode package was submerged in the melt. The package was fixed to the vial to maintain a separation distance of about 2 mm between the electrodes and the glass base of the vial, as seen in Figure B.3(b). A second

thermocouple (TC2) was placed inside the vial in contact with the glass at approximately the same height as the electrode set. After assembly the granulated erythritol was melted then the sample was permitted to cool and solidify around the electrodes.

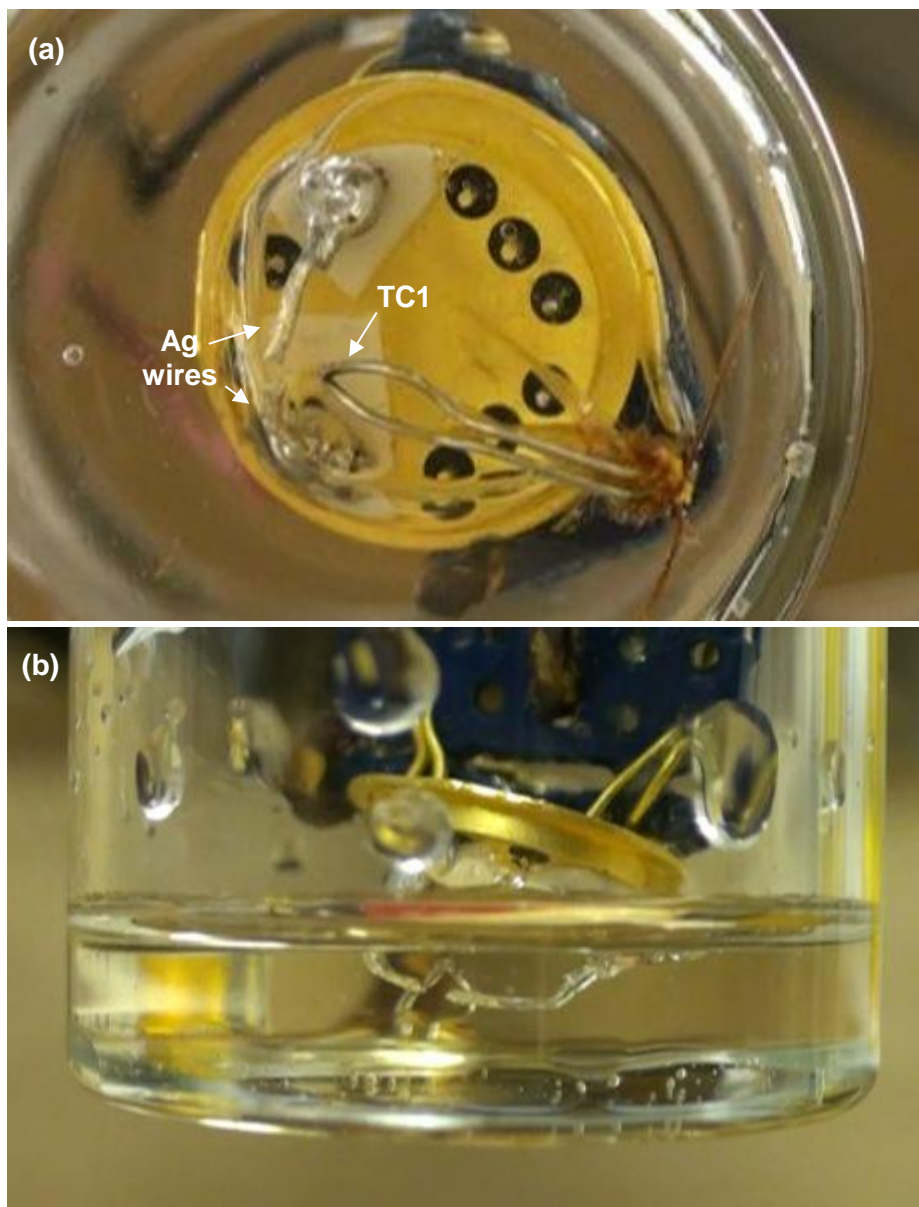


Figure B.3 – Electrical supercooling reduction electrode set shown from (a) the bottom and (b) the side of the glass vial.

Thermocouple measurements were recorded using a National Instruments SCXI-1303 Thermocouple terminal block with a Labview interface. For electrical input, a 1 kV_{DC} power supply was connected to the sample electrodes with a manual contact switch between the high voltage terminal and the sample. For reasons discussed in the next section, the switch was configured such that the positive electrode was electrically ‘floating’ when the contact was released. Applied voltage was measured with a BK Precision digital multimeter. The experiments were visually recorded on a high-definition digital camcorder (standard video frame rate) to identify the time and location of nucleation events during cooling. A photograph of the experimental setup is shown in Figure B.4.

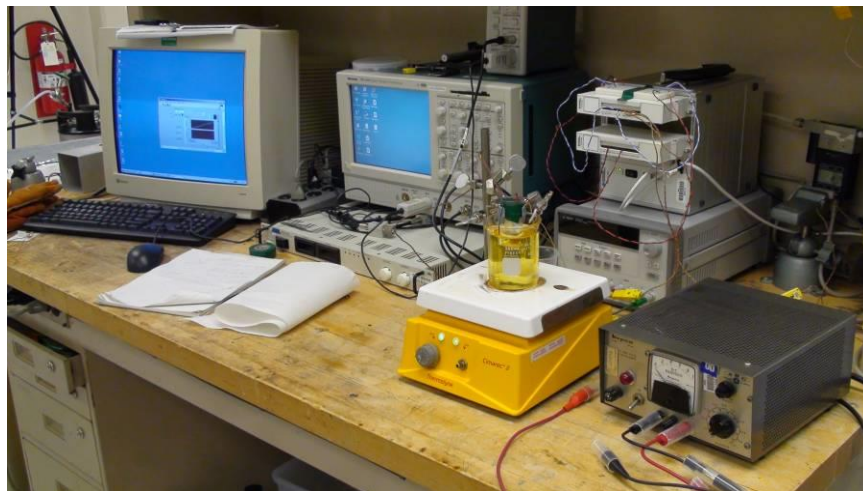


Figure B.4 – Experimental setup for electrically induced nucleation tests

B.3.2.2. Preliminary observations

Prior to performing the planned experiment, a number of preliminary trials were run to identify an effective testing range and procedure. The first point is that the supercooling mitigation effect was only exhibited with silver electrodes. Preliminary tests with copper and aluminum wires showed no change in nucleation behavior on the electrodes using voltages up to 300V. Filing wire ends to remove native oxidation failed

to make any difference, but the literature on water mentioned that too strong a voltage could inhibit the effect. That could have been the case here, but was not explored in depth.

A second preliminary test involved verifying what voltage level would produce the desired nucleating effect with the silver electrodes. Initially, the contacting switch was configured such that both electrodes were grounded when the switch was released. In this configuration, no electrode induced nucleation was observed at any voltage up to 300V. It was not until the positive electrode was allowed to 'float' when the contact was released that any electrode induced nucleation finally occurred. A likely theory for this behavior coincides with Shichiri's second water study that showed [319] an AC voltage was ineffective at nucleating supercooled water. If reducing the nucleation energy barrier is dependent on an ion accumulation at the electrode surface, then grounding the electrode (or reversing polarity in the case of AC) would subsequently remove the net charge accumulation and interrupt the ionization build up. Additionally, precise current values were not captured during this experiment but it was determined that electrical currents would be in the sub-mA range.

Third, at higher voltages around 300V, a dark cloud was observed forming between the electrodes. Nucleation failed to occur on the electrodes when this happened, and the discoloration persisted with subsequent melting and cooling of the sample even without further applied voltage. Lowering the voltage by 50V increments, it was noticed that at 200V no noticeable discoloration of the erythritol occurred over multiple trials, and nucleation was induced on the electrodes.

Finally any nucleation to occur on the electrodes always occurred on the positive electrode. This was verified by reversing polarity of the electrodes, after which the location

switch to the new positive electrode. This also coincides with the experiments by Shichiri and Hozumi that indicated the nucleation behavior in water was strongly related to ionization at the electrode surface, and possibly the formation of coordination compounds or a preferential surface on the favorable electrode. Because no bubble formation was observed in any erythritol trials, the theory that hydrolysis might have been a dominant factor in their earlier experiments seems less likely in this case.

B.3.2.3. Experimental Procedure

The trials began by slowly heating the sample in the oil bath until the sample had visually melted and TC1 indicated a central melt temperature of about 130°C (~12°C above the nominal melting temperature). The sample was then removed from the bath and held to freely cool in air by natural convection ($T_{air} \sim 23^{\circ}\text{C}$) while nucleation events and temperatures were recorded. No agitation was used during the heating or cooling cycles.

In trials where an electrical input was to be applied, when the TC1 reading indicated the temperature of the melt had cooled to 115°C, 200V_{DC} was applied to the electrodes using the manual switch for a period of about three seconds (manually counted). Time and location of nucleation in the sample was recorded, and thermocouple temperatures were recorded for the duration of the trial for later reference. In the cases where nucleation was electrically induced around the electrodes, time and location of any spontaneous nucleation events elsewhere in the melt was also recorded.

A representative heating and cooling cycle temperature profile is shown in Figure B.5. The vial was heated until TC1 reached 130°C (TC2 at the vial edge about 138°C). Removed from the bath, the vial edge cools much faster as shown by the quickly dropping TC2 temperature. In this example nucleation occurred first on the outside of the

vial away from TC2 and recrystallization reached TC1 first when it was around 100°C. The latent heat release raised the local temperature up toward the melting temperature. Shortly thereafter a similar temperature rise is seen when the recrystallization front reaches TC2 when it was around 70°C, followed by a similar latent heat release and associated temperature rise.

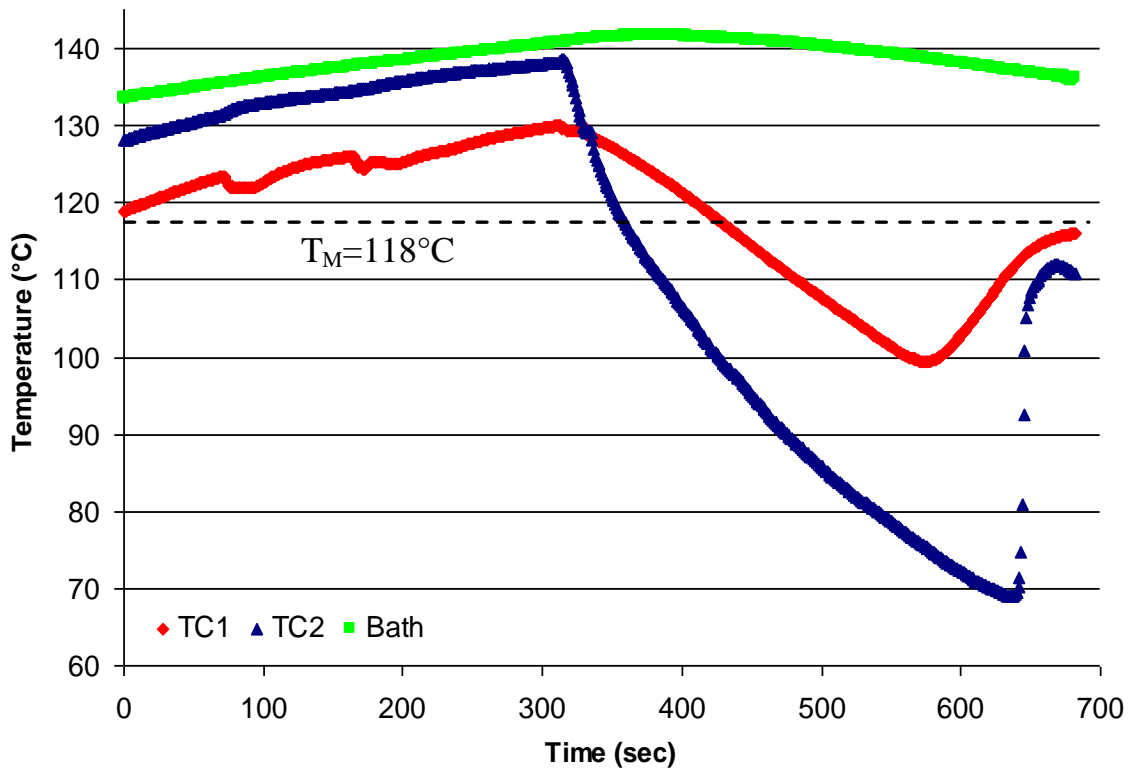


Figure B.5 – Representative supercooling experiment heating and cooling profile showing the sample heating in the oil bath followed by free cooling in air until nucleation occurs.

The experiment was first performed five times without voltage applied to the sample to establish a baseline (Trial designation PRE##). Following this, ten trials were run with voltage applied as described previously (Trial designation V##). Finally, another ten trials were run without electricity applied to verify that behavior of the erythritol had not been significantly affected by the electrical trials (Trial designation POST##).

Note that there was a slight delay between removing the vial from the hot oil bath and positioning/focusing the camera to visually record nucleation events. In two trials (one with and one without voltage applied) nucleation had occurred on the vial edge prior to recording. As such, no useful nucleation time/temperature data could be obtained for those trials and the data were excluded from the results that follow.

B.3.2.4. Experimental Results

The results of the experiment are summarized in Tables B.3-B.6. Each table shows the initial nucleation location, any secondary nucleation location, and the local time and temperature. Note that local temperature is assumed to be TC1 if nucleation occurred on the electrode and TC2 if it occurred on the vial edge. Secondary nucleation events were only seen in the voltage-applied trials where nucleation occurred separately on both the electrodes and vial edge.

Table B.3 – Pre-test results, no voltage applied

trial #	1 st nucleation location	T_N [°C]	T_{SC} [°C]
PRE01	vial edge	88.4	29.6
PRE02	vial edge	101.2	16.8
PRE03	vial edge	76.4	41.6
PRE04	vial edge	78.9	39.1
PRE05	vial edge	85.7	32.3
range		24.8	24.8
average		86.1	31.9
std dev		9.7	9.7

Table B.4 – Test results, voltage applied

trial #	1 st nucleation event			2 nd nucleation event		
	Location	T_N [°C]	T_{Sc} [°C]	location	T_N [°C]	T_{Sc} [°C]
V01	vial edge	88.4	29.6	pos. electrode	109.0	9.0
V02	--	--	--	--	--	--
V03	vial edge	108.5	9.5	pos. electrode	110.1	7.9
V04	pos. electrode	108.1	9.9	vial edge	85.3	32.7
V05	pos. electrode	109.7	8.3	none	n/a	n/a
V06	vial edge	95.7	22.3	pos. electrode	111.6	6.4
V07	pos. electrode	109.6	8.4	vial edge	84.8	33.2
V08	vial edge	107.4	10.6	pos. electrode	108.4	9.6
V09	vial edge	92.6	25.4	pos. electrode	108.5	9.5
V10	vial edge	96.6	21.4	pos. electrode	109.2	8.8

Table B.5 – Voltage applied, Location summarized results

	Vial edge nucleation		Electrode nucleation	
	T_N [°C]	T_{Sc} [°C]	T_N [°C]	T_{Sc} [°C]
min	84.8	9.5	108.1	6.4
max	108.5	33.2	111.6	9.9
range	23.7	23.7	3.5	3.5
average	94.9	23.1	109.4	8.6
std dev.	9.2	9.2	1.1	1.1

Table B.6 – Post-test results, no voltage applied

trial #	1 st nucleation location	T_N [°C]	T_{SC} [°C]
POST01	vial edge	67.8	50.2
POST02	vial edge	67.3	50.7
POST03	vial edge	66.6	51.4
POST04	vial edge	99.8	18.2
POST05	vial edge	108.9	9.1
POST06	vial edge	102.7	15.3
POST07	vial edge	90.1	27.9
POST08	vial edge	85.0	33
POST09	vial edge	92.3	25.7
POST10	--	--	--
range		42.3	42.3
average		86.7	31.3
std dev		16.2	16.2

Qualitatively, it can be seen that nucleation in the PRE and POST data sets always occurred on the vial edge, which is consistent with the theory that nucleation will have the highest probability at the location with lowest temperature and maximum degree of supercooling. Absent any solid erythritol, it can be assumed that the glass surface provides the lowest energy barrier heterogeneous nucleation surface. Second, in all cases where voltage was applied, nucleation was seen to occur on the positive electrode. In eight out of the nine trials, because the edge of the vial would be anywhere from 10 to 30 degrees cooler than the electrode location, spontaneous nucleation occurred on the vial edge in addition to the induced nucleation on the electrodes. Because the solidification front progressed slowly through the melt, no edge nucleation influence on electrode temperature (TC1) was seen prior to electrode nucleation.

Examining the nucleation data, which is also depicted in Figure B.6, we see that as expected spontaneous nucleation in the PRE and POST trials showed a significant variance in the amount of supercooling before nucleation. This conforms to the previous data showing large and stochastic degree of supercooling with erythritol. Similar behavior before and after the electrical tests also suggests that the electric current did not permanently change the material's nucleation behavior. During the electrical tests, we see that the nucleation that occurred on the edge of the vial was similar to that seen in the PRE and POST tests. There was somewhat less supercooling but the number of samples was not large enough to discount normal variability, and in at least one case the electrode nucleation spread throughout the entire melt before any secondary, stimulated nucleation event was seen.

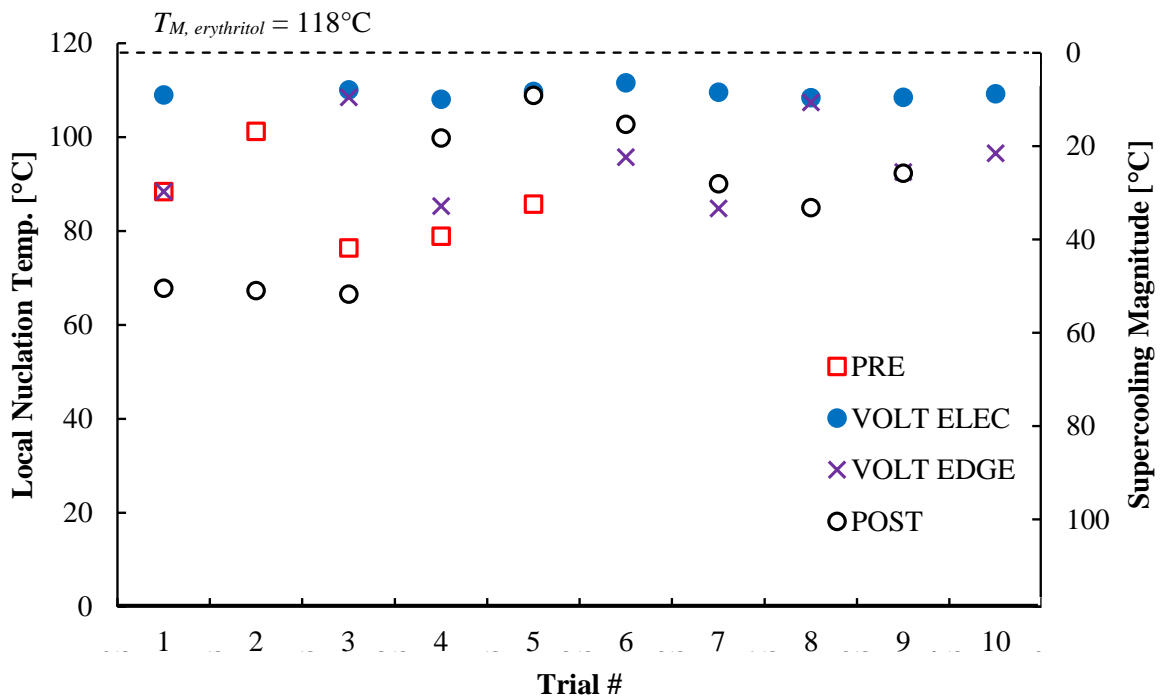


Figure B.6 – Nucleation temperatures seen during the erythritol supercooling experiment. Nominal erythritol melting temperature is indicated by the 118°C dashed line. The PRE and POST series temperatures show significant supercooling and wide variability both before and after the electrical tests. During the test the VOLT series of data is separated into nucleation events occurring on the electrodes (VOLT ELEC) and on the vial edge (VOLT EDGE). The edge data shows similar variability as the PRE and POST data. The electrode data shows much less supercooling and much less variability.

Examining the nucleation data that occurred on the electrodes, which again only occurred in the cases where a voltage was applied, we see a very different nucleation behavior. The voltage was applied when supercooling reached about 3°C (at 115°C), and nucleation on the electrodes occurred at less than 10°C of supercooling. The nucleation also occurred over a much narrower temperature span (about 5-10x reduction in T_N range,

and about an order of magnitude reduction in standard deviation). This significant deviation from the control events appears to confirm that the applied voltage does induce a stimulated nucleation, whereas all of the vial-edge nucleations appear to be spontaneous heterogeneous nucleation events.

Table B.7 and Figure B.7 summarize the stimulated and aggregate spontaneous nucleation events, under the reasonable assumption that the electrode nucleation only occurred due to electrical stimulation. As shown in the figure, there is a noticeable difference in nucleation behavior between events occurring on the electrodes and those occurring on the vial edge. First, it again becomes apparent that the electrode nucleation (in the warmer part of the melt) only occurs during trials with voltage applied. Relative to all other nucleation events, the totality of those electrode nucleations occurred in a tight temperature band. All other nucleation events occurred on the colder vial edge over a much wider spread of temperatures. From the table we see again that the average nucleation temperature was almost 20°C higher on the electrodes than on the vial edge, with over a factor of ten reduction in standard deviation.

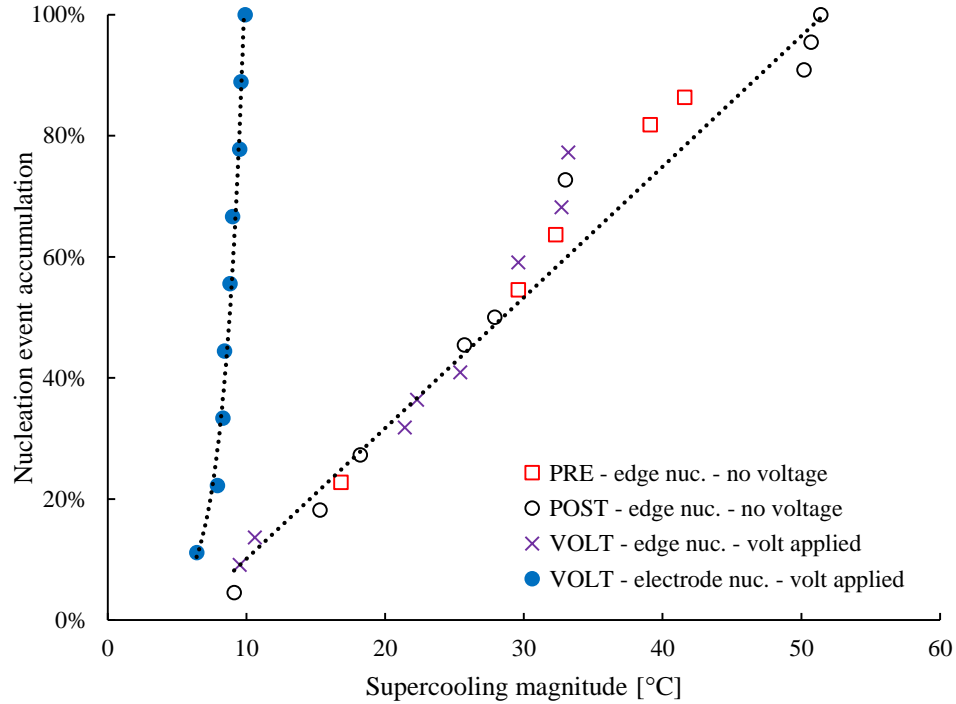


Figure B.7 – Location dependent nucleation accumulation curves for the electrical supercooling mitigation experiment. Accumulation curves are separated by nucleation location, whether occurring on the vial edge (edge nuc.) or the electrodes (electrode nuc). The nucleation events on the vial edges occurred over a wide range of temperatures for the three experiments. Electrode nucleation only occurred when a voltage was applied, and occurred at much lower and tightly bounded supercooling temperatures. Note that the lines on each grouping are provided only for visual aid.

Table B.7 – Summary of spontaneous and electrically stimulated nucleation

	Spontaneous edge nucleation		Stimulated electrode nucleation	
	T_N [°C]	T_{SC} [°C]	T_N [°C]	T_{SC} [°C]
min	66.6	9.1	108.1	6.4
max	108.9	51.4	111.6	9.9
range	42.3	42.3	3.5	3.5
average	89.6	28.4	109.4	8.6
std dev.	12.8	12.8	1.1	1.1

This work was far from a comprehensive investigating of the electrical supercooling mitigation mechanism. However, it does provide support to the idea that supercooling can be actively avoided as a critical failure mode in phase change thermal protection systems. Additionally, the fact that nucleation always occurred on the positive electrode, even when switching polarity, suggests the possibility of an electrochemical cause of stimulated nucleation. The fact that a change of the erythritol was seen at high voltages raises concern that even at the lower voltages this process could be modifying the material in non-recoverable ways, and this would need to be investigated in any attempted use of the technique.

Appendix C – Preliminary substrate integrated TBHS fabrication

In parallel with the TBHS simulations described in Section 6.3, we began preliminary efforts to explore methods of fabricating substrate integrated TBHS devices in several materials. For reference the general configuration of a substrate integrated TBHS that was shown in Figure 6.19 is repeated in Figure C.1, showing the three primary components to the TBHS design: (1) PCM & Cooling layer, (2) sealing/interface layer, (3) cooling manifold layer.

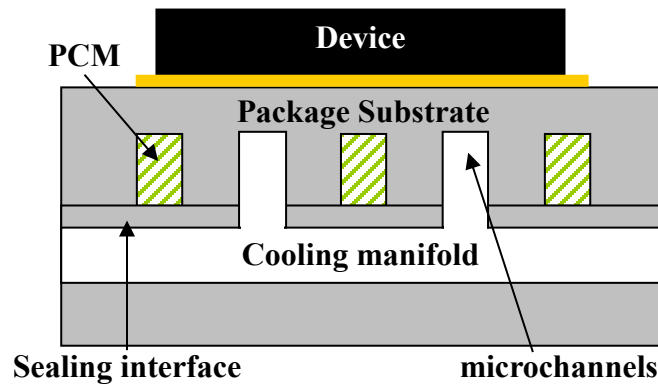


Figure C.1 – Substrate integrated thermal buffer heat sink schematic with single layer PCM-coolant arrangement over a fluid delivery manifold. (repeated)

The initial fabrication concept is described in [151] and focused on a silicon manifold microchannel design with erythritol as the PCM due to prior microfabrication experience and material availability from the supercooling mitigation experiment described in Appendix B. Following this, a more robust aluminum nitride ceramic packaging was devised to overcome the material strength limits of silicon. For reasons shown in the simulations related to low erythritol performance and compatibility limits of gallium PCMs with aluminum based substrates, evaluation was halted after initial fabrication.

C.1. Silicon TBHS substrate fabrication

Similar to the substrate integrated cooling experiment, the target application here is power semiconductor device cooling for vehicle electronics. As described in Chapter 3, vehicle power electronics cooling can impose tight temperature margins on the PCM selection problem. The lower transition temperature limit is set by the available coolant temperature, which can range from 60-105°C. The upper is set by the device temperature limits, nominally 125°C for silicon devices. For a thermal protection application a melting temperature closer to the upper limit provides maximum margin for PCM supercooling and resolidification in the case of coolant temperature excursions. The PCM material database in Chapter 2 provides a number of likely candidates for this application, but the sugar alcohol erythritol was selected as the best choice based on having the highest latent heat in the range of 110 – 120°C. It is recognized that it will have a low thermal conductivity and has exhibited an extremely large degree of supercooling [44]. However, it was also selected by DOE in the TBHS design review as a prime candidate material to enable the use of silicon electronics on a 105°C cooling loop, while permitting 30 - 50% reduction in electronics heat sink size and weight relative to a non-PCM baseline. Also, making use of a PCM with high $H_{f,v}$ will help minimize the negative impact of the capacitance-resistance tradeoff by reducing the material required for a particular amount of energy absorption and freeing up more space for cooling. Finally, erythritol is relatively inexpensive, water soluble, and safe to handle.

C.1.1. Silicon PCM substrates

While standard power packaging generally makes use of high thermal conductivity, dielectric ceramic materials for substrates, the ability to use precision micromachining with

silicon makes it an attractive prototyping material. In fact, separate work by the author with colleagues at the U.S. Army Research Laboratory used micromachined silicon to bring coolant directly to the backside of a power electronic device, achieving very high local convection with single phase coolant and a high aspect ratio manifolding structure [191]. For this process and implementation neither extremely small microchannels nor complex manifolding are required. However, precision etching and alignment processes will provide tight control over structural dimensions and significant design freedom.

The process for forming the silicon PCM & Cooling layer is shown in Figure C.9. (A1) The process began with a bare silicon wafer, typically a dual-side polished wafer about 400-450 μm thick for a 100 mm diameter wafer. (A2) Next an AZ9245 photoresist was spun on the wafer to a thickness of about 10 μm . (A3) This resist was photo-patterned using UV contact lithography and developed to define both the PCM and fluid channels. (A4) A Bosch Deep Reactive Ion Etching (DRIE) process was then used to etch holes to the desired microchannel depth (typically about 300 $^{\circ}$ μm) into the wafer. (A5) Finally the photoresist was stripped off in an Axcelis downstream ashing tool leaving a microchannel etched substrate wafer. Individual test pieces were then able to be cleaved or diced from the wafer (not shown).

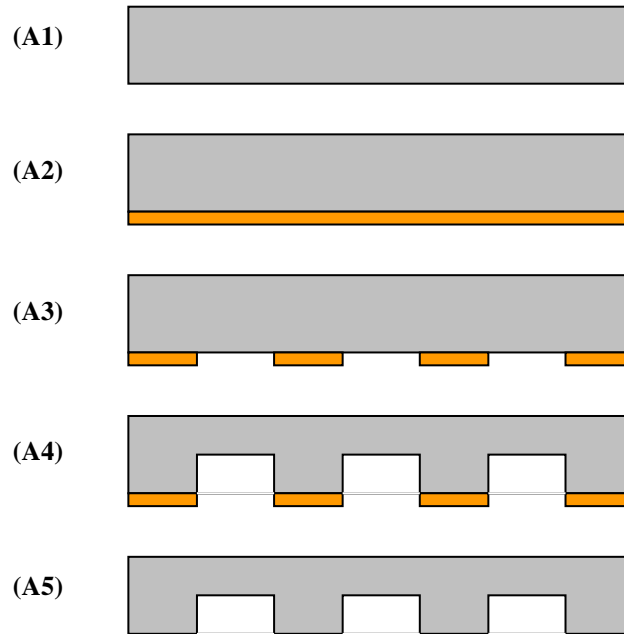


Figure C.2 – Process for forming a Layer 1 from silicon where gray layers are silicon and orange layers are photoresist.

The mask layout used for the silicon channel layer is shown in Figure C.3. The layout contains six designs of varying microchannel and PCM channel widths and spacing. The ~1-inch (25.4 mm) die are centered on 1 cm-square heat sources on the back side. The PCM and fluid channels alternate, with the PCM channels only being 1 cm long and the fluid channels extending beyond the 1 cm region to a common perpendicular manifold. The six different die are marked with small square etch pits at the die edge. The markings at the far right and left are alignment marks for lithographic patterning. The dimensions used in this set of TBHS substrates are given in Table C.1. (Unlike the definition used for the models as shown in Figure 6.20, w_{fin} , w_{pcm} , and w_{mc} dimensions in this Table are all full channel/fin widths. The unit cell dimension matches the model definition as the full w_{fin} plus half of w_{pcm} and w_{mc} .) Figure C.4 shows photographs of (a) the completed silicon test wafer and (b) a close up photograph of SiTBHS5.

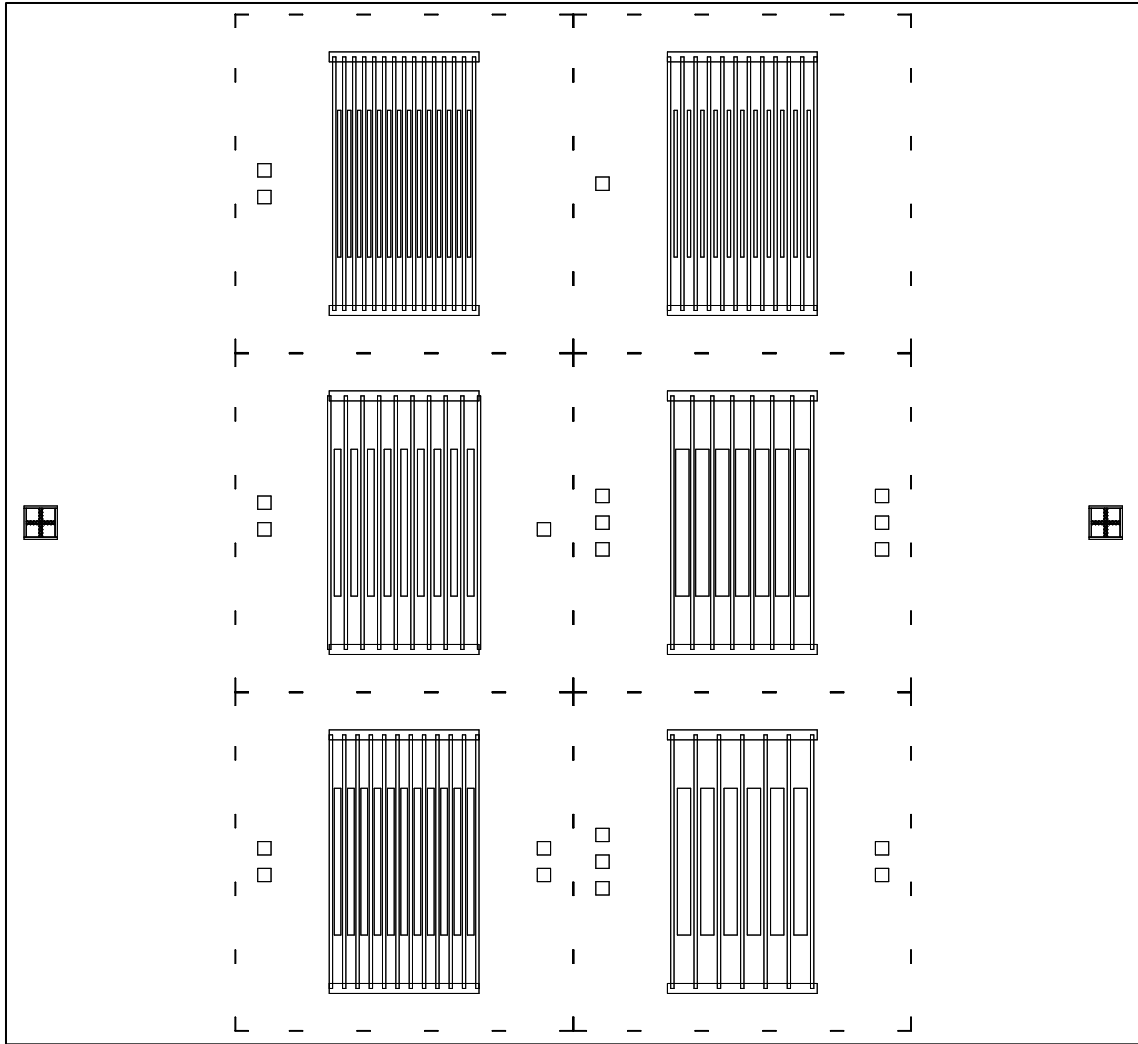


Figure C.3 – Mask layout for silicon TBHS (SiTBHS) wafer. The wafer contains six individual TBHS designs with varying microchannel and PCM channel widths. The microchannels extend past the PCM channels and are connected by a common manifold. Each configuration (1-6) is identified by a number of square etch pits at the outside of each die.

Table C.1 – SiTBHS design dimensions

Die #	w_{pcm} [μm]	w_{mc} [μm]	w_{fin} [μm]	$w_{unit-cell}$ [μm]
1	125	125	250	375
2	125	125	125	250
3	250	125	250	437.5
4	250	125	125	312.5
5	500	125	250	562.5
6	500	125	125	437.5

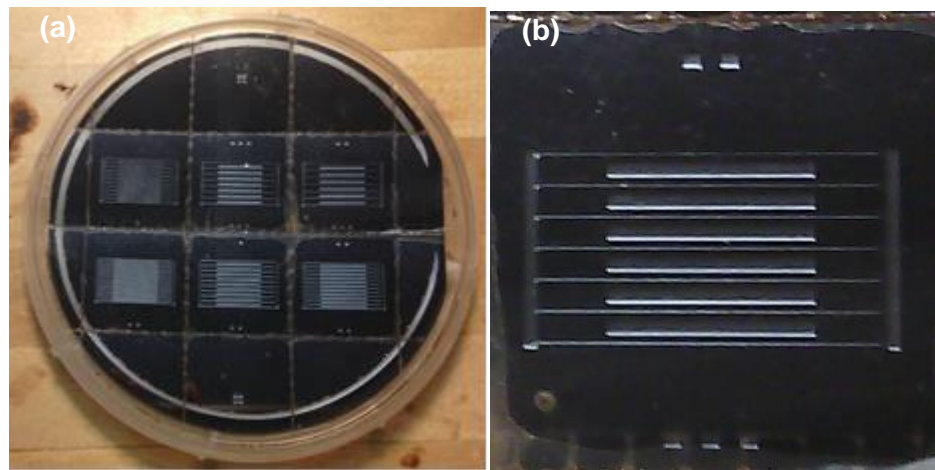


Figure C.4 – (a) Photograph of etched 100mm silicon test wafer with (b) a close up of SiTBHS5.

1 cm² copper serpentine heaters were patterned onto the backside of the silicon wafers to create surrogate heat sources for the test devices. After completing the channel-side process, a sputtering tool was used to coat the second side of the wafer with a 2 μm layer of copper. Next a 5 μm AZ5214 photoresist was spun on the wafer and photo-patterned with UV contact lithography to transfer the heater mask pattern (shown in Figure C.5) into the resist. Before developing this pattern, the resist was baked and then given a flood overexposure to reverse the image tone (from positive to negative). This resist was then developed into the heater pattern. A 1:1 Ferric Chloride – H₂O copper etching solution was used to remove exposed copper and define the heater shape. Electrical

measurement of the heaters indicated that they had a resistance of approximately 6.5-7 Ohms. The serpentine heaters consisted of 26 copper lines 1 cm long, 340 μm wide with 61.2 μm spacing, spanning a total width of 1.037 cm. A 5.7 x 6.8 mm contact pad was patterned on each corner for making the external electrical connections. A photograph of fabricated copper heaters on a diced SiTBHS wafer are shown in Figure C.6.

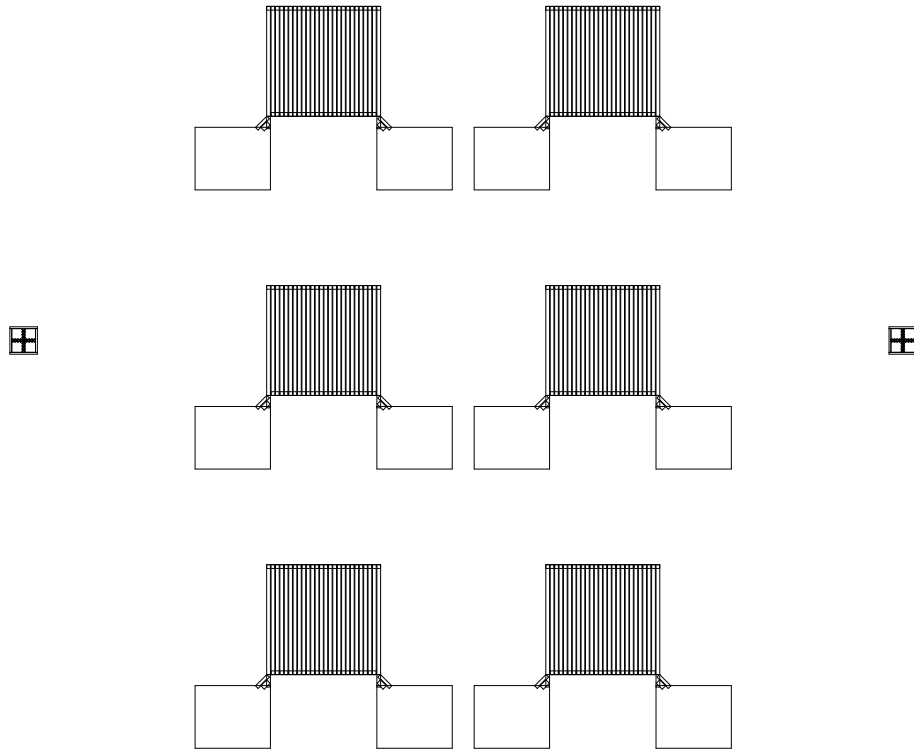


Figure C.5 – Mask layout for SiTBHS serpentine heater array. The identical heaters are positioned with the alignment marks such that the heater areas will be positioned over the center PCM channels etched into the wafer backside.

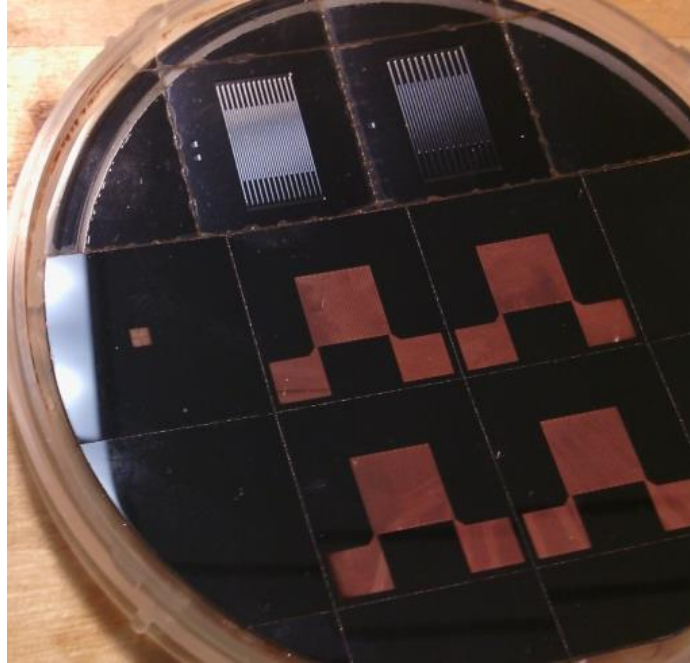


Figure C.6 – Photograph of patterned heaters on the backside of fabricated SiTBHS channels.

C.1.2. Silicon TBHS PCM Filling, Assembly, Mounting, and Structural Failure

Because the PCM channels are completely sealed they were filled prior to assembly with the coolant delivery manifold. The filling and assembly plan is shown in Figure C.7. (B1) First the TBHS die was placed on a $\sim 130^{\circ}\text{C}$ hotplate and the entire etched cavity was filled with liquid erythritol ($T_M = 118^{\circ}\text{C}$). Filling was accomplished by placing solid erythritol granules onto the heated structure until the melt over-filled the cavity. The substrate was then removed from the hotplate and the PCM was allowed to solidify. (A supercooling delay was avoided by adding a single erythritol crystal to the cooled melt to initiate nucleation.) (B2) A razorblade was then used to shave the overfilled PCM back until it was flush with the silicon surface.

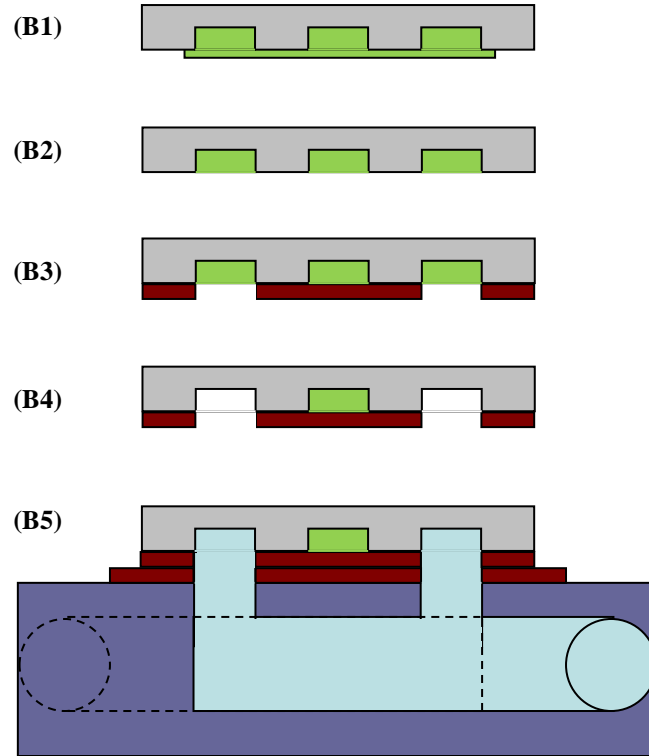


Figure C.7 – Process of filling and assembling the SiTBHS substrate and manifold.

(B3) After PCM filling, the structure was sealed by applying a thick (1/8" or ~3mm) layer of Dow Corning 732 RTV Sealant. This clear, flexible material provided a soft wall to accommodate PCM expansion on melting while permitting visual inspection of the channels. Holes were knife-cut through the epoxy over the fluid inlet and outlet manifolds. An image at this stage is shown with SiTBHS1 in Figure C.8(a). (B4) After the epoxy has cured, the substrate was placed back on the hotplate to melt the PCM. The melted erythritol was removed from the fluid channels using a combination of flushing with hot water and drawing with an absorbent cloth. This is shown with SiTBHS3 in Figure C.8(b-d). (B5) The final step involved mounting the sealed substrate onto a plastic manifold with a matching gasket seal, and sealing with either a compression fixture or adhesive.

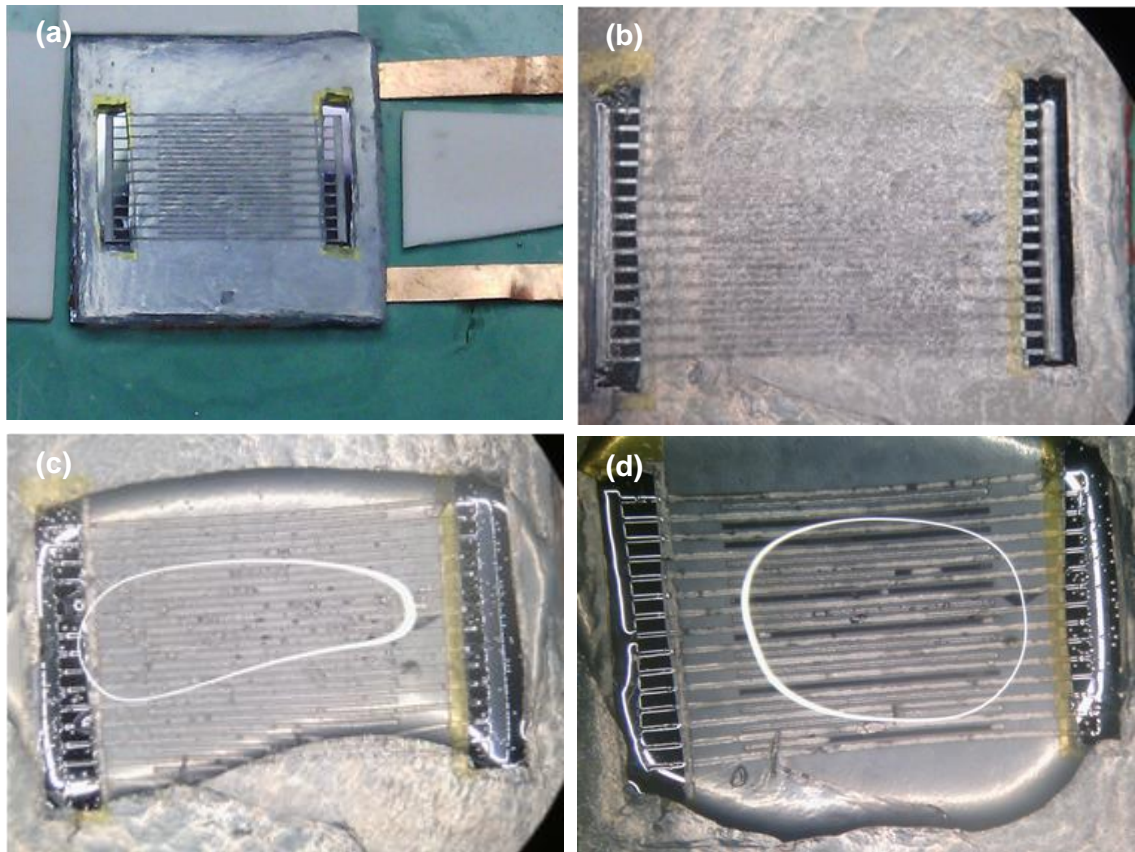


Figure C.8 – Photographs of SiTBHS1 (a) after epoxy cap, and STBHS3 (b) during heated melt, (c) water flush, and (d) resolidification. The water overflow provides an index match and clear visibility through the epoxy to the channels. In (d), the solidifying PCM can be seen as darker lines providing some indication of how well cleared out the fluid channels are.

The manifold block was constructed to permit face mounting of the sample over fluid inlet/outlet ports using a compliant Dow Corning 732 RTV seal around fluid openings. The block was connected to the flow loop via 1/8" NPT fittings fixed to the inlet/outlet ports, and two Type-K thermocouples were inserted into the fluid passages. The plastic parts made using fused deposition molding are not inherently watertight, so a thin layer of Cotronics 4460 epoxy was used to seal all wetted manifold surfaces, fix in place and seal the NPT fittings and thermocouples, and coat the thermocouple tips for

electrical isolation. The manifold design is shown in Figure C.9(a), and a photograph of the 3D printed part mounted on the test board is shown in Figure C.9(b).

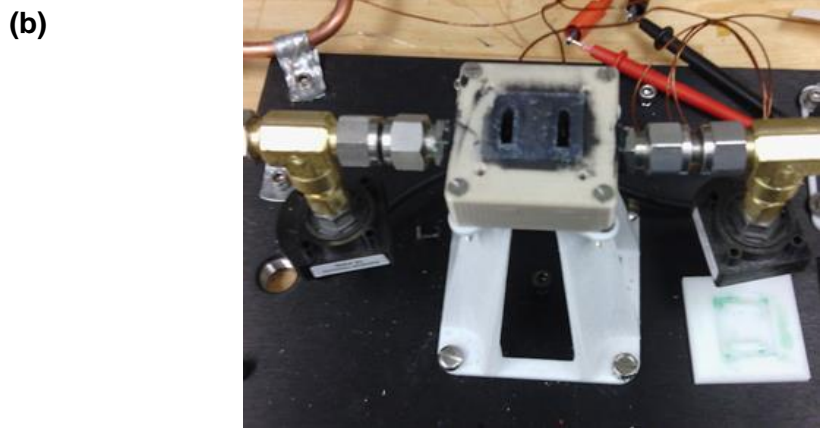
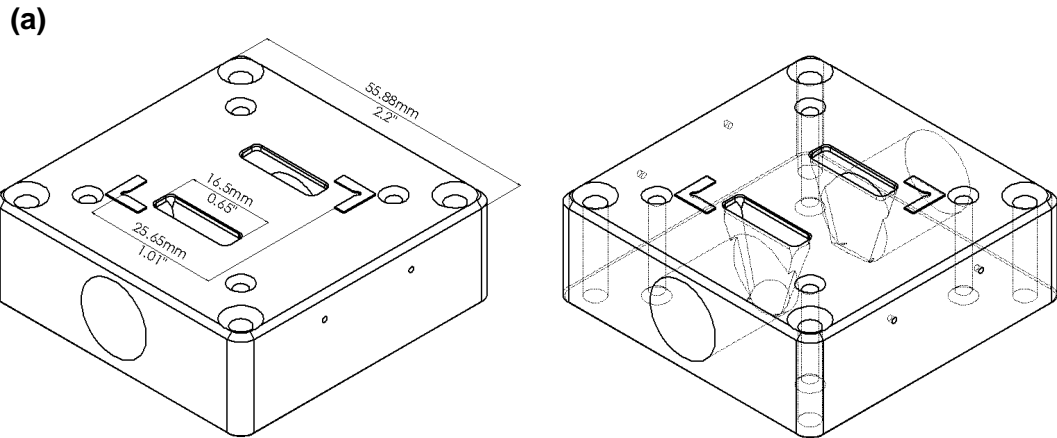


Figure C.9 – 3D sketches of the TBHS manifold block highlighting (a) notable outer dimensions and (b) revealed interior features. Indicated features are (1) fluid inlet/outlet ports, (2) sample mount location, (3) sample inlet/outlet fluid manifolds, (4) fluid inlet/outlet thermocouple ports.

At this point it is worth noting that the Silicon substrates began to fail catastrophically during the filling and flushing assembly steps. Silicon is a brittle material, and the expansion forces that developed when the erythritol melted were not sufficiently relieved. SiTBHS2-5 all cracked on the first remelt after capping with the epoxy and attempting to flush the erythritol from the coolant channels. SiTBHS6 was first seen to

have an air pocket trapped in the PCM after filling. The erythritol was remelted by placing it back on the hotplate before it was capped. Despite the top of the PCM channels being open to air, giving what should have been a minimal resistance path for expansion, the device shattered as the PCM melted and expanded outward. It had been assumed that the erythritol would expand uniformly, rather than the bottom, captive erythritol melting first and applying pressure to all surrounding solids, and also that the capping erythritol would be brittle enough to provide a stress relief path on melting if necessary. This appeared to not be the case. Finally, SiTBHS1 cracked immediately upon attempting compression mounting on the plastic test stand.

These failures served as a lesson that while silicon is an excellent mechanical material, it may not be tough enough to serve as a useful prototype PCM substrate. A number of previous PCM heat sink studies have identified the need to accommodate expansion volume by building in void space or a ‘soft wall’. Despite using the soft epoxy as an encapsulant, however, the silicon was unable to withstand the local expansion pressure presented by the initial melting front. As there is little likelihood of developing a prototype design that will avoid a situation where melting erythritol is surrounded by rigid silicon and solid erythritol, it was decided to continue prototyping with ceramic substrates. This has several advantages: (1) ceramic substrates are more likely to be used in practice in a power electronics package, (2) ceramics are generally much tougher materials and should be capable of withstanding the expansion pressures that cause silicon to fail, (3) we can take advantage of the ceramic microchannel fabrication methods described in Section 4.4. The remainder of this chapter focuses on implementing the TBHS structure in aluminum nitride ceramic substrates.

C.2. Ceramic PCM substrate fabrication

The overall structure of the ceramic PCM substrates is nearly identical to that of the silicon substrates. Because ceramic stereolithographic capabilities were not available for this prototyping effort, a diamond saw was used to pattern aluminum nitride substrates as described in Section 4.4. This did lead to a difficulty in creating the separate PCM and fluid channels. Diamond saw cuts can only practically be made to cut all the way across the wafer. However, as shown in the TBHS layout in Figure C.3, the microchannels are supposed to extend to the inlet and outlet manifolds, but the PCM channels are only supposed to extend to the edge of the 1 cm heater area. Similarly, the inlet and outlet manifolds are wide pockets in the substrate. A method of making partial length and multiple-width cuts was required to create the desired TBHS layout.

It was decided that combining a selective ordering of saw cuts and partial backfill with a high temperature epoxy should enable fabrication of the more complicated designs. Additionally, the diamond dicing saw has enough cut placement precision to use multiple, overlapping cuts to create wider channels. It should be noted that 1-inch square TBHS pieces were made from both 1" x 1" (25.4 x 25.4 mm) and 2" x 2" (50.8 x 50.8 mm), 25 mil thick (~625 μm) AlN ceramic substrates. No difference in procedure was introduced with different substrate sizes, but cuts still did go all the way across the full wafer whether it was 1 or 2 inches wide. This affected planning of cuts for multiple substrates and different dimensional configurations.

Before cutting any channels, similar heaters to those previously described were patterned on the centers of the ceramic pieces because they could not go into metal deposition tools after being epoxied. These heaters used an alternative metal fabrication

process as well due to unavailability of the previously used copper sputtering process. The heater design was first patterned onto the substrates with an AZ5214 photoresist, and then a thin Titanium-Platinum layer was evaporated over the pattern. A metal lift off process was then performed by stripping the remaining photoresist using an ultrasonically agitated PRS3000 bath. This removed the photoresist and any metal not in direct contact with the substrate, leaving the Ti-Pt heater pattern. This thin metal was too high-resistance (~60 Ohms) for the desired heaters, so a copper electroplating bath was used to deposit copper until the desired 6-7 Ohms was reached. A thick layer of photoresist was then applied over the heaters to protect them during channel fabrication on the dicing saw.

Following heater fabrication, channels were made on the back side of the substrate using the same Disco DAD320 dicing saw described previously. First, a series of parallel cuts were made for the PCM channels according to the desired channel width and spacing. Channels wider than the diamond saw blade were made by cutting multiple, slightly overlapping cuts. The gap between cuts was wide enough to accommodate another cut for the fluid channels and the desired width of solid material (the fin) between them. Before making the next series of cuts, the portions of the PCM channels outside of the 1 cm square center region were backfilled using Dow Corning 732 epoxy, drawn across the channels with a razorblade or other knife-edge. After this epoxy has cured, separate channels were cut for the fluid channels in the center of the gap between the PCM channels. Next, the wafer was rotated 90° and a series of overlapping cuts created 3 mm wide fluid manifolds at both ends of the substrate. Finally, the same procedure used to backfill the PCM channels was used to seal the three sides of the manifold headers and prevent leakage to the substrate edge.

Following fabrication of the ceramic channels, the process of PCM filling and epoxy capping the substrates followed the same procedures described in Section C.1.2 for the silicon TBHS structures. Note that none of the ceramic substrates experienced catastrophic failure due to repeated PCM melting like the silicon substrates. Photographs of AINTBHS fabrication are shown in Figure C.10. Dimensions of the initial AINTBHS prototypes are given in Table C.2.

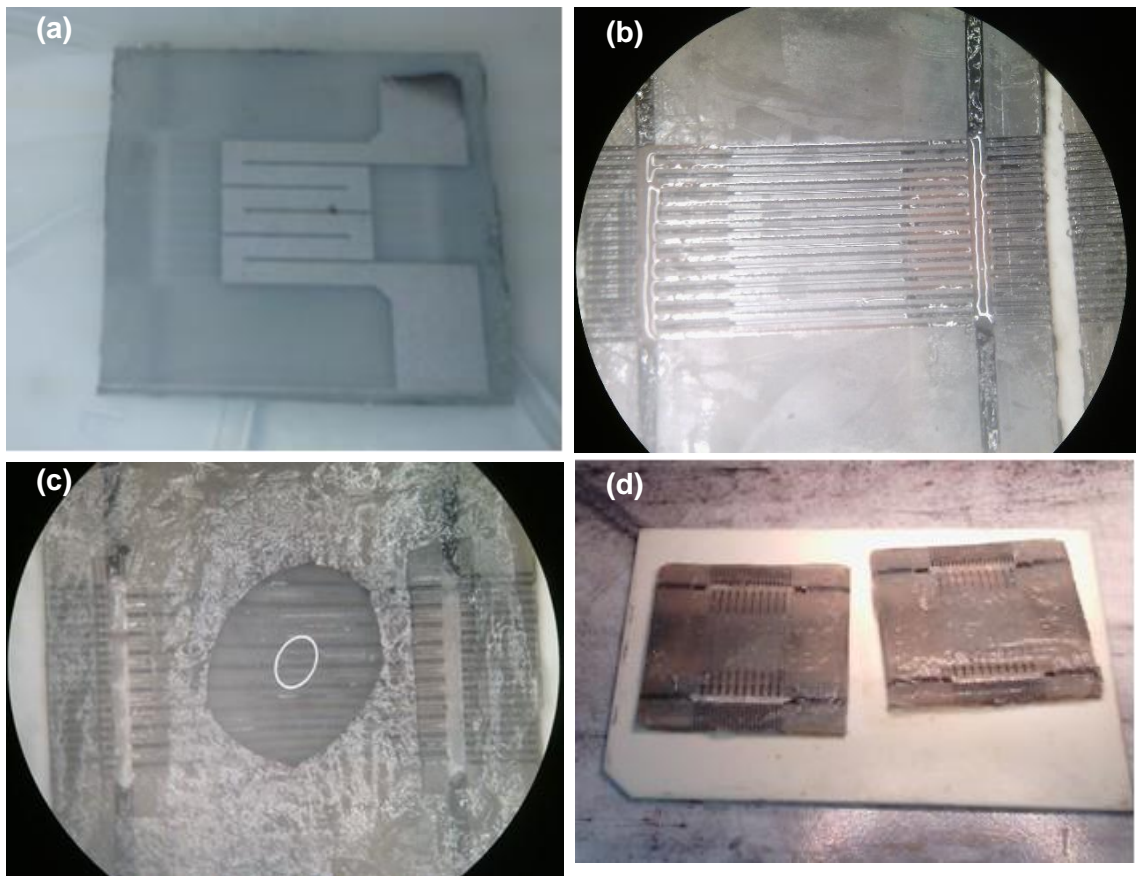


Figure C.10 – Photographs of AINTBHS_1 (a) Pt heater, (b) during heated melt, (c) water flush, and (d) after full PCM loading.

Table C.2 – AlNTBHS design dimensions

Die #	w_{pcm} [μm]	w_{mc} [μm]	w_{fin} [μm]	$w_{unit-cell}$ [μm]
1	250	250	125	375
2	500	250	125	500
3	250	250	125	375
4	500	250	125	500
5	250	250	250	500

These substrates did survive mounting and clamping on the fluid manifold. Initial step response tests were performed at low heat and temperatures. However, due to inability to discern phase change during the step response aligning with poor performance seen in room temperature erythritol TBHS models in Chapter 6, evaluation was terminated pending future planning for electronics cooling materials and design. Base on promising results of later stage modeling and redirected application interest, expected future directions will include a wider parameter space investigation of geometries and package compatible materials.

Appendix D – Complete PCM property tables

Table D.1 – Paraffins from $n = 10$ to 100

Name	N	CAS #	T_M [°C]	H_f [kJ/kg]	$H_{f,v}$ [MJ/m ³]	ρ [kg/m ³]	k_{th} [W/mK]	c_p [kJ/kgK]	Ref
Decane	10	124-18-5	-29.65	202	147	726 (l)	--	--	29
Undecane	11	1120-21-4	-25.6	177	130	737 (l)	--	--	29
Dodecane	12	112-40-3	-9.6	216	161	745 (l)	--	--	29
Tridecane	13	629-50-5	-5.4	196	148	753 (l)	--	2.21 (l)	29
Tetradecane	14	629-59-4	5.5-5.8	227-228	187-188	825 (s) 771 (l)	0.15 (s)	2.07 (s)	23,29
Pentadecane	15	629-62-9	10	205-210	157-161 (l)	765-768 (l)	--	--	11,23,29
Hexadecane	16	544-76-3	16.7-18.1	236-237	200	835 (s) 770-776 (l)	0.15 (s)	2.11 (s)	23,29
Heptadecane	17	629-78-7	21.7-22.0	213-216	166	775-778	--	--	11,23,29
Octadecane	18	593-45-3	27.5-28	243-244	198-211	814-865 (s) 774-780 (l)	0.15-0.36 (s) 0.15 (l)	1.9-2.14 (s) 2.3-2.66 (l)	13,15,23, 29,30
Nonadecane	19	629-92-5	32	222	174	782	--	--	23,29
Eicosane	20	112-95-8	36.7	247	192	785 (s) 778 (l)	0.15 (s)	2.21 (s) 2.01 (l)	23,29
Heneicosane	21	629-94-7	40-41	200-216	152-170	758-788	--	--	11,23,29
Docosane	22	629-97-0	44	246-252	188-199	763-791	--	--	11,23,29
Tricosane	23	638-67-5	47.5	232-234	177-186	764-793	--	--	23,29
Tetracosane	24	646-31-1	50.6	255	203	796	--	--	29
Pentacosane	25	629-99-2	53.5-54	238-240	190-192	798	--	--	11,29
Hexacosane	26	630-01-3	56-56.3	250-258	193-206	770-800	--	--	11,23,29
Heptacosane	27	593-49-7	58.8	235	181-189	773-802	--	1.92 (s) 2.44 (l)	23,29
Octacosane	28	630-02-4	61-61.6	252-254	196-204	779-803	--	--	11,23,29
Nonacosane	29	630-03-5	63.2	239	192	805	--	--	23,29
Triacontane	30	638-68-6	65.4	252	203	806	--	--	29
Hentriacontane	31	630-04-6	67.9	242	196	808	--	--	29
Dotriacontane	32	544-85-4	69.43	266	215	809	--	--	29
Trtriacontane	33	630-05-7	71.4	256	207	810	--	--	29
Tetraatriacontane	34	14167-59-0	73.1-75.9	268-269	217-218	811	--	--	14,29
Pentatriacontane	35	630-07-9	74.7	257	209	812	--	--	29
Hexatriacontane	36	630-06-8	76.2	269	219	814	--	--	29
Heptatriacontane	37	7194-84-5	77.7	259	211	815	--	--	29
Octatriacontane	38	7194-85-6	79	271	221	815	--	--	29
Nonatriacontane	39	7194-86-7	80.3	271	221	816	--	--	29
Tetracontane	40	4181-95-7	81.5	272	222	817	--	--	29
Dotetracontane	42	7098-20-6	84.17	273	223	817	--	--	29
Tritetracontane	43	7098-21-7	85.5	273	224	819	--	--	29
Tettratetracontane	44	7098-21-7	86.4	274	225	820	--	--	29
Hextetracontane	46	7098-24-0	88.	276	227	822	--	--	29
Octatetracontane	48	7098-22-8	90.3	276	227	823	--	--	29
Pentacontane	50	6596-40-3	92	276	228	825	--	--	29
Hexatcontane	60	7667-80-3	99	279	232	831	--	--	29
Heptacontane	70	7719-93-9	105.5	281	235	836	--	--	29
Hectane	100	6703-98-6	115.25	285	241	846	--	--	29

Table D.2 – Paraffin waxes and blends

Name	T_M [°C]	H_f [kJ/kg]	$H_{f,v}$ [MJ/m ³]	ρ_s [kg/m ³]	k_{th} [W/mK]	c_p [kJ/kgK]	Ref
Tetradecane + octadecane	-4.02-2.1	227.52	--	--	--	--	39
91.67% Tetradecane + 8.33% Hexadecane	1.70	156.20	--	--	--	--	20
Tetradecane + docosane	1.5-5.6	234.33	--	--	--	--	20
Tetradecane + heneicosane	3.54-5.56	200.28	--	--	--	--	20
Paraffin blend (n=14-16)	5-6	152	119	783	--	--	24
Pentadecane + heneicosane	6.23-7.21	128.25	--	--	--	--	20
Paraffin blend (n=15-16)	8	147-153	115-119	751.6-809.5	--	--	24
Pentadecane + docosane	7.6-8.99	214.83	--	--	--	--	20
Pentadecane + octadecane	8.5-9.0	271.93	--	--	--	--	20
Paraffin blend (n=16-18)	20-22	152	--	--	--	--	13
Octadecane + heneicosane	25.8-26	173.93	--	--	--	--	20
Octadecane + docosane	25.5-27	203.80	--	--	--	--	20
"Paraffin wax"	32-32.1	251	208	830	0.514 (s) 0.224 (l)	3.26 (s) 1.92 (l)	15
"Medicinal paraffin"	40-44	146	121	830	0.5 (s) 2.1 (l)	2.2 (s) 2.3 (l)	15
"Commercial paraffin wax"	52.1	243.5	197.1	809.5 (s) 771 (l)	0.15 (s)	2.89 (s)	15
"Paraffin wax"	54.4	146	128	880	--	--	23
Beeswax	61.8	177	168	950	--	--	23
"Paraffin wax"	64	173.6	159	916 (s) 790 (l)	0.339-0.346 (s) 0.167 (l)	--	13

Table D.3 – Fatty acid materials

Name	Formula	CAS #	T_M [°C]	H_f [kJ/kg]	$H_{f,v}$ [MJ/m ³]	ρ kg/m ³	$k_{th,l}$ [W/mK]	c_p [kJ/kgK]	Ref
Caprylic acid	CH ₃ (CH ₂) ₆ -COOH	124-07-2	16-16.7	148.18-	145.4-	981-1033(s)	0.145-0.149	2.11(s)	31
- octanoic acid				149	153.9	862-901(l)		1.95(l)	
Capric acid	CH ₃ (CH ₂) ₈ -COOH	334-48-5	31.5-32	152.7-	153.3-	1004(s)	0.149-0.153	2.10(s)	31
- decanoic acid				162.83	163.5	853-886(l)		2.09(l)	
Lauric acid	CH ₃ (CH ₂) ₁₀ -COOH	143-07-7	41-44.2	177.4-	178.6-	1007(s)	0.139-0.192	1.76-2.14(s)	13,25,
- dodecanoic acid				211.6	213.1	848-870(l)		2.15-2.27(l)	31
Elaidic acid	C ₈ H ₁₇ C ₉ H ₁₆ -COOH	112-79-8	47	218	185.5 (l)	851(l)	--	--	23
Myristic acid	CH ₃ (CH ₂) ₁₂ -COOH	544-63-8	49-58	186.6-	184.7-	990(s)	--	1.59-2.8(s)	23,25,
- tetradecanoic acid				204.5	202.5	844-861(l)		2.16-2.7(l)	31
Pentadecanoic acid	CH ₃ (CH ₂) ₁₃ -COOH	1002-84-2	52.5	178	--	--	--	--	14
Palmitic acid	CH ₃ (CH ₂) ₁₄ -COOH	57-10-3	55-64	163-	161.2-	989(s)	0.103-0.172	2.06-2.2(s)	13,23,
- hexadecanoic acid				211.8	209.5	845-850(l)		1.7-2.48(l)	31,32
Stearic acid	CH ₃ (CH ₂) ₁₆ -COOH	57-11-4	55-71	186.5-	175.5-	941-965(s)	0.097-0.172	2.07-2.83(s)	13,25,
- octadecanoic acid				210	202.7	839-848(l)		1.9-2.38(l)	31,32

Table D.4 – Fatty acid blends

Composition	T_M [°C]	H_f [kJ/kg]	Ref
65% Capric acid + 35% Lauric acid	13-18	116.76-148	13,31
73% Capric acid + 27% Lauric acid	18.2	120	323
61.5% Capric acid + 38.5% Lauric acid	19.1	132	31
45% Capric acid + 55% Lauric acid	21	143	13
73.5% Capric acid + 26.5% Myristic acid	21.4	152	31
75.2% Capric acid + 24.8% Palmitic acid	22.1	153	31
34% Myristic acid + 66% Capric Acid	24	147.7	13
86.6% Capric acid + 13.4% Stearic acid	26.8	160	31
62.6% Lauric acid + 37.4% Myristic acid	32.6	156	324
80% Lauric acid + 20% Palmitic acid	32.7	147	323
64% Lauric acid + 36% Palmitic acid	32.8	165	31
77% Lauric acid + 23% Palmitic acid	33	150.6	39
85% Lauric acid + 15% Stearic acid	34	152	323
66% Lauric acid + 34% Myristic acid	34.2	166.8	20
69% Lauric acid + 31% Palmitic acid	35.2	166.3	15
75.5% Lauric acid + 24.5% Stearic acid	37.3	171	31
91% Lauric Acid + Acetamide	39.4	183	24
51% Myristic acid + 49% Palmitic acid	39.8	174	324
58% Myristic acid + 42% Palmitic acid	42.6	169.7	39
65.7% Myristic acid + 34.3% Palmitic acid	44	181	324
89% Myristic Acid + Acetamide	48.7	199	24
64.9% Palmitic acid + 35.1% Stearic acid	50.4	179	31
72.5% Palmitic acid + 27.5% Stearic acid	51.1	159	323
64.2% Palmitic acid + 35.8% Stearic acid	52.3	181.7	39
89% Palmitic acid + Acetamide	57.2	172	24
81% Palmitic acid + Acetamide	59.1	177	24
83% Stearic acid + 11% Palmitic acid + other	60-66	206	20
95% Stearic acid + 5% Palmitic acid	65-68	209	20
83% Stearic acid + Acetamide	65.4	213	24

Table D.5 – Fatty acid derivative materials

Name	Formula	CAS #	T_M [°C]	H_f [kJ/kg]	$H_{f,v}$ [MJ/m ³]	ρ [kg/m ³]	$k_{th,s}$ [W/mK]	c_p [kJ/kgK]	Ref
1-Decanol	C ₁₀ H ₂₁ OH	112-30-1	6	206	171	830.1(s)	--	--	24
Propyl palmitate	C ₁₉ H ₃₈ O ₂	2239-78-3	10	186	--	--	--	--	31
Isopropyl palmitate	C ₁₉ H ₃₈ O ₂	142-91-6	11	95-100	--	--	--	--	13
Ethyl myristate	CH ₃ (CH ₂) ₁₂ COOC ₂ H ₅	124-06-1	11	184	--	--	--	--	23
Isopropyl stearate	C ₂₁ H ₄₂ O ₂	112-10-7	14-18	140-142	--	--	--	--	13
Butyl stearate	C ₂₂ H ₄₄ O ₂	123-95-5	18-23	123-200	--	--	0.21	--	20
1-Dodecanol	C ₁₂ H ₂₆ O	112-53-8	26	200	--	--	--	--	20
Ethyl palmitate	C ₁₈ H ₃₆ O ₂	628-97-7	23	122	--	--	--	--	20
Vinyl stearate	C ₂₀ H ₃₈ O ₂	111-63-7	27-29	122	--	--	--	--	13
Methyl palmitate	C ₁₇ H ₃₄ O ₂	112-39-0	29	205	--	--	--	--	23
Methyl stearate	C ₁₉ H ₃₈ O ₂	112-61-8	29	169	--	--	--	--	20
Cetyl caprate	C ₂₆ H ₅₂ O ₂	29710-34-7	29.38	182.5-190.2	--	--	--	2.68 (s) 2.15 (l)	33
Trimyristin	(C ₁₃ H ₂₇ COO) ₃ C ₃ H ₃	555-45-3	33	204	--	--	--	--	11
1-Tetradecanol	C ₁₄ H ₃₀ O	112-72-1	38	205	--	--	0.36	--	13
Cetyl laurate	C ₂₈ H ₅₆ O ₂	20834-06-4	38.24	192.2-198.9	--	--	--	1.65 (s) 2.17 (l)	33
Stearyl laurate	C ₃₀ H ₆₀ O ₂	3234-84-2	42.21	201.03-201.53	--	--	--	1.97 (s) 2.31 (l)	34
Methyl 12-Ahydroxystearate	C ₁₉ H ₃₈ O ₃	141-23-1	42-43	120-126	--	--	--	--	13
Methyl eicosanoate	C ₂₁ H ₄₂ O ₂	1120-28-1	45	230	--	--	--	--	23
Stearyl myristate	C ₃₂ H ₆₄ O ₂	3234-81-9	48.86	203.39-203.53	--	--	--	2.07 (s) 2.33 (l)	34
Cetyl alcohol	CH ₃ (CH ₂) ₁₅ OH	36653-82-4	49.3	141	--	--	--	--	14
Cetyl myristate	C ₃₀ H ₆₀ O ₂	2599-01-1	49.44	222.0-228.4	--	--	--	1.97 (s) 2.44 (l)	33
Cetyl palmitate	C ₃₂ H ₆₄ O ₂	540-10-3	51.21	214.6-220.3	--	--	--	2.51 (s) 2.93 (l)	33
Methyl behenate	C ₂₄ H ₄₆ O ₂	929-77-1	52	234	--	--	--	--	23
Ethyl tetracosanoate	C ₂₆ H ₅₂ O ₂	24634-95-5	54	218	--	--	--	--	23
Methyl oxalate	C ₄ H ₆ O ₄	553-90-2	54.3	178	--	--	--	--	14
Cetyl stearate	C ₃₄ H ₆₈ O ₂	1190-63-2	54.63	212.1-216.3	--	--	--	1.99 (s) 2.6 (l)	33
Tristearin	(C ₁₇ H ₃₅ COO) ₃ C ₃ H ₅	68334-00-9	56	190.8	164.4	862(l)	--	--	23
Stearyl palmitate	C ₃₄ H ₆₈ O ₂	2598-99-4	57.34	219.74-219.88	--	--	--	1.55 (s) 1.89 (l)	33
Stearyl stearate	C ₃₆ H ₇₂ O ₂	2778-96-3	59.22	214.75-214.93	--	--	--	1.86 (s) 2.15 (l)	33
Cetyl arachidate	C ₃₆ H ₇₂ O ₂	22413-05-4	59.32	224.2-228.7	--	--	--	1.98 (s) 2.31 (l)	33
Ethyl cerotate	C ₂₈ H ₅₆ O ₂	29030-81-7	60	226	--	--	--	--	23
Stearyl arachidate	C ₃₈ H ₇₆ O ₂	22432-79-7	64.96	226.12-226.23	--	--	--	1.93 (s) 2.35 (l)	33
Dimethyl fumarate	(CHCO ₂ CH ₃) ₂	624-49-7	102	242	253	1045.2(l)	--	--	23

Table D.6 – Sugar and sugar alcohol materials

Name	Formula	CAS #	T_M [°C]	H_f [kJ/kg]	$H_{f,v}$ [MJ/m ³]	ρ_s [kg/m ³]	k_{th} [W/mK]	c_p [kJ/kgK]	Ref
Glycerol	C ₃ H ₈ O ₃	56-81-5	17.9	198.7	250 (l)	1260 (l)	--	--	23
Xylitol	C ₅ H ₁₂ O ₅	87-99-0	92.7-94.5	232-263.3	353-400	1520	--	--	35,36,37
Sorbitol	C ₆ H ₁₄ O ₆	50-70-4	95-97.7	110-185	165-278	1500	--	--	35,36,37
Erythritol	C ₄ H ₁₀ O ₄	149-32-6	117-118	315-344	466-509	1480 (s) 1300 (l)	0.733 (s) 0.326 (l)	1.383 (s) 2.765 (l)	35,36,37
Glucose	C ₆ H ₁₂ O ₆	50-99-7	141	174	269	1544	--	--	23
Fructose-D	C ₆ H ₁₂ O ₆	57-48-7	144-145	145	--	--	--	--	16
Isomalt	C ₁₂ H ₂₄ O ₁₁	64519-82-0	145	170	--	--	--	--	16
Maltitol	C ₁₂ H ₂₄ O ₁₁	585-88-6	145-152	173	--	--	--	--	16
Lactitol	C ₁₂ H ₂₄ O ₁₁	585-86-4	146-152	135-149	--	--	--	--	16
Xylose-D	C ₅ H ₁₀ O ₅	58-86-6	147-151	216-280	330-428	1530	--	--	16
Xylose-L	C ₅ H ₁₀ O ₅	609-06-3	147-151	213	326	1530	--	--	16
d-Mannitol	C ₆ H ₁₄ O ₆	69-65-8	165-168	294-341	438-518	1489-1520	--	--	23,36,37
Galactitol	C ₆ H ₁₄ O ₆	608-66-2	188-189	351.8	517	1470	--	--	37

Table D.7 – Carboxylic acid based materials

Name	Formula	CAS #	T_M [°C]	H_f [kJ/kg]	$H_{f,v}$ [MJ/m ³]	ρ_s [kg/m ³]	k_{th} [W/mK]	c_p [kJ/kgK]	Ref
Formic acid	HCOOH	64-18-6	7.8	247	303	1226.7	--	--	23
Acetic acid	CH ₃ COOH	64-19-7	16.7	187	196 (l)	1050 (l)	0.18	2.04 (s) 1.96 (l)	23
d-Lactic acid	CH ₃ CHOHCOOH	10326-41-7	26	184	230	1249	--	--	23
beta-Chloroacetic acid	C ₂ H ₃ ClO ₂	79-11-8	56	147	--	--	--	--	14
Chloroacetic acid	C ₂ H ₃ ClO ₂	79-11-8	56	130	205	1580	--	--	23
Heptadecanoic acid	C ₁₇ H ₃₄ O ₂	506-12-7	60.6	189	--	--	--	--	23
alpha-Chloroacetic acid	C ₂ H ₃ ClO ₂	79-11-8	61.2	130	--	--	--	--	14
Glycolic acid	HOCH ₂ COOH	79-14-1	63	109	--	--	--	--	23
Acrylic acid	CH ₂ =CHCO ₂ H	79-10-7	68	115	--	--	--	--	14
Phenylacetic acid	C ₈ H ₈ O ₂	103-82-2	76.7	102	--	--	--	--	14
Glutaric acid	(CH ₂) ₃ (COOH) ₂	110-94-1	97.5	156	223	1429	--	--	23
Benzoic acid	C ₆ H ₅ COOH	65-85-0	121.7	143	181	1266	--	--	23
Sebacic acid	(HOOC)(CH ₂) ₈ (COOH)	111-20-6	130-134	228	290	1270	--	--	16
Maleic acid	HOOC-CH=CH-COOH	110-16-7	131-140	235	374	1590	--	--	16
Malonic acid	HOOC-(CH ₂)-COOH	141-82-2	132-136	--	--	1620	--	--	16
trans-Cinnamic acid	C ₉ H ₈ O ₂	140-10-3	133	153	191	1250	--	--	16
Chrolobenzoic acid	C ₇ H ₅ ClO ₂	118-91-2	140	164	253	1540	--	--	16
Suberic acid	(CH ₂) ₆ (COOH) ₂	505-48-6	141-144	245	250	1020	--	--	16
Adipic acid	(CH ₂) ₄ (COOH) ₂	124-04-9	151-155	260	354	1360	--	--	16
Salicylic acid	HOC ₆ H ₄ COOH	69-72-7	159	199	287	1443	--	--	23

Table D.8 – Clathrate hydrate materials

Name	Formula	CAS #	T_M [°C]	H_f [kJ/kg]	Ref
Tetrabutylammonium benzoate 32-hydrate	Bu ₄ NC ₆ H ₅ CO ₂ ·32H ₂ O	--	3.5	--	24
Tetrahydrofuran clathrate hydrate	C ₄ H ₈ O·17.2H ₂ O	18879-05-5	4.4	255	24
Tetrabutylammonium nitrate 32-hydrate	Bu ₄ NNO ₃ ·32H ₂ O	--	5.8	--	24
Trimethylamine semi clathrate hydrate	(CH ₃) ₃ N·10.25H ₂ O	15875-97-5	5.9	239	24
Sulfur dioxide clathrate hydrate	SO ₂ ·6.0H ₂ O	--	7	247	24
Ethylene oxide clathrate hydrate	C ₂ H ₄ O·6.9H ₂ O	--	11.1	--	24
Tetrabutylammonium bromide 32-hydrate	Bu ₄ NBr·32H ₂ O	--	11.7-12.5	193-205	24,46
Sulfur dioxide clathrate hydrate	SO ₂ ·6.1H ₂ O	--	12.1	--	24
Tetrabutylammonium formate 32-hydrate	Bu ₄ NCHO ₂ ·32H ₂ O	--	12.5	184	24
Tetrabutylammonium chloride 32-hydrate	Bu ₄ NCl·32H ₂ O	37451-68-6	14.7-15.7	200.7	24,46
Tetraisoamylammonium formate 40-hydrate	i-Am ₄ NCHO ₂ ·40H ₂ O	--	15-20	--	24
Tetrabutylammonium acetate 32-hydrate	Bu ₄ NCH ₃ CO ₂ ·32H ₂ O	--	15.1	209	24
Di-tetrabutylammonium oxalate 64-hydrate	(Bu ₄ N) ₂ C ₂ O ₄ ·64H ₂ O	--	16.8	--	24
Di-tetrabutylammonium hydrogen phosphate 64-hydrate	(Bu ₄ N) ₂ HPO ₄ ·64H ₂ O	--	17.2	--	24
Tetrabutylammonium bicarbonate 32-hydrate	Bu ₄ NHCO ₃ ·32H ₂ O	--	17.8	--	24
Tetrabutylammonium fluoride 32-hydrate	Bu ₄ NF·32H ₂ O	22206-57-1	24.9-28.3	223.1-240.5	24,46
Tetraisoamylammonium chloride 38-hydrate	i-Am ₄ NCl·38H ₂ O	--	29.8	--	24
Tetrabutylammonium hydroxide 32-hydrate	Bu ₄ NOH·32H ₂ O	147741-30-8	30.2	--	24
Tetraisoamylammonium hydroxide 40-hydrate	i-Am ₄ NOH·40H ₂ O	--	31	--	24
Tetraisoamylammonium fluoride 40-hydrate	i-Am ₄ NF·40H ₂ O	--	31.2	--	24

Table D.9 – Miscellaneous organic materials

Name	Formula	CAS #	T_M [°C]	H_f [kJ/kg]	$H_{f,v}$ [MJ/m ³]	ρ [kg/m ³]	k_{th} [W/mK]	c_p [kJ/kgK]	Ref
Ethylene Glycol	HOCH ₂ CH ₂ OH	107-21-1	-13	146	162 (l)	1113 (l)	--	--	23
Diethylene Glycol	(HOCH ₂ CH ₂) ₂ O	111-46-6	-10(-7)	247	296 (l)	1200 (l)	--	--	20
Triethylene glycol	C ₆ H ₁₄ O ₄	112-27-6	-7	247	296 (l)	1200 (l)	--	--	20
Tetrahydrofuran (THF)	(CH ₂) ₄ O	109-99-9	5	280	272	970 (s)	--	--	21
Polyglycol 400	H(OCH ₂ CH ₂) _n OH	25322-68-3	8	99.6	122	1228 (s)	0.185-	--	13
						1125 (l)	0.187(l)		
Dimethyl sulfoxide	(CH ₃) ₂ SO	67-68-5	16.5	85.7	86	1009 (s)	--	--	13
Polyglycol 600	H(OCH ₂ CH ₂) _n OH	25322-68-3	20-25	127.2-146	157-180	1232 (s)	0.16-	2.26(s)	13,23
						1100-	0.189(l)		
						1126(l)			
Lithium Chloride Ethanolate	LiCl·4C ₂ H ₆ O	--	21	186	--	--	--	--	11
Dimethyl sebacate	C ₁₄ H ₂₆ O ₄	110-40-7	21	120-135	--	--	--	--	13
Octadecyl 3-mercaptopropionate	C ₂₁ H ₄₂ O ₂ S	31778-15-1	21	143	--	--	--	--	20
Octadecyl thioglycolate	C ₂₀ H ₄₀ O ₂ S	10220-46-9	26	90	--	--	--	--	20
13-Methyl Pentacosane	C ₂₆ H ₅₄	22331-48-2	29	197	--	--	--	--	23
Polyglycol 900	H(OCH ₂ CH ₂) _n OH	25322-68-3	34	150.5	181	1200 (s)	0.188(s)	2.26(s)	15
						1100 (l)	0.188(l)	2.26(l)	
2-Dimethyl-n-docosane	C ₂₄ H ₅₀	--	35	198	--	--	--	--	11
Camphenilone	C ₉ H ₁₄ O	13211-15-9	39	205	--	--	--	--	23
1-Bromodocosane	C ₂₂ H ₄₄ Br	6938-66-5	40	201	--	--	--	--	23
Caprylone	(CH ₃ (CH ₂) ₆) ₂ CO	818-23-5	40	259	--	--	--	--	23
1-Cyclohexyloctadecane	C ₂₄ H ₄₈	4445-06-1	41	218	--	--	--	--	23
4-Heptadecanone	C ₁₇ H ₃₄ O	53685-77-1	41	197	--	--	--	--	23
7-Heptadecanone	C ₁₇ H ₃₄ O	6064-42-2	41	198	--	--	--	--	11
Phenol	C ₆ H ₅ OH	108-95-2	41	120	--	--	--	--	14
8-Heptadecanone	C ₁₇ H ₃₄ O	14476-38-1	42	201	--	--	--	--	23
p-Toluidine	C ₇ H ₉ N	106-49-0	43.3	167	--	--	--	--	14
Cyanamide	HNCNH	420-04-2	44	209	226	1080 (s)	--	--	23
2-Heptadecanone	C ₁₇ H ₃₄ O	2922-51-2	48	218	--	--	--	--	23
3-Heptadecanone	C ₁₇ H ₃₄ O	84534-29-2	48	218	--	--	--	--	23
Hydrocinnamic acid (3-Phenylpropionic acid)	C ₉ H ₁₀ O ₂	501-52-0	48	118	--	--	--	--	14
O-Nitroaniline	C ₆ H ₄ (NH ₂)(NO ₂)	88-74-4	50	93	--	--	--	--	14
Camphene	C ₁₀ H ₁₆	79-92-5	50	238	201 (l)	842 (l)	--	--	23
9-Heptadecanone	C ₁₇ H ₃₄ O	540-08-9	51	213	--	--	--	--	23
Thymol	C ₁₀ H ₁₄ O	89-83-8	51.5	115	--	--	--	--	14
Diphenylamine	(C ₆ H ₅) ₂ NH	122-39-4	52.9	107	--	--	--	--	14
p-Dichlorobenzene	C ₆ H ₄ Cl ₂	106-46-7	53.1	121	--	--	--	--	14
o-Xylene dichloride	C ₈ H ₈ Cl ₂	612-12-4	55	121	--	--	--	--	14
Hypophosphoric acid	H ₄ P ₂ O ₆	7803-60-3	55	213	--	--	--	--	23
Nitro naphthalene	C ₁₀ H ₇ NO ₂	86-57-7	56.7	103	--	--	--	--	14
p-Bromophenol	C ₆ H ₅ BrO	106-41-2	63.5	86	--	--	--	--	14
Polyglycol 6000	H(OCH ₂ CH ₂) _n OH	25322-68-3	66	190	230	1212 (s)	--	--	13
						1085 (l)			
Azobenzene	C ₁₂ H ₁₀ N ₂	103-33-3	67.1	121	--	--	--	--	14
p-Chloroaniline	ClC ₆ H ₄ NH ₂	106-47-8	69	156	189	1213 (s)	--	--	23
2,4-Dinitrotoluene	C ₆ H ₃ (CH ₃)(NO ₂) ₂	121-14-2	70	111	--	--	--	--	14
Biphenyl	(C ₆ H ₅) ₂	92-52-4	71	119.2	139	1166 (s)	--	--	13
						991 (l)			
Thiosinamine	C ₄ H ₈ N ₂ S	109-57-9	77	140	--	--	--	--	14
Bromocamphor	C ₁₀ H ₁₅ OBr	76-29-9	77	174	252 (l)	1449 (l)	--	--	23
Benzylamine	C ₆ H ₅ CH ₂ NH ₂	100-46-9	78	174	--	--	--	--	14
Propionamide	C ₃ H ₇ NO	79-05-0	79	168.2	--	--	--	--	13
Durene	C ₁₀ H ₁₄	95-93-2	79.3	156	131	838 (s)	--	--	23
Napthalene	C ₁₀ H ₈	91-20-3	80	147.7	169	1145 (s)	0.310	--	13
						976 (l)	-0.341(s)		
							0.132(l)		
Acetamide	CH ₃ CONH ₂	60-35-5	81	241	280	1159 (s)	--	--	23
						999 (l)			
Methyl 4-bromobenzoate	BrC ₆ H ₄ CO ₂ CH ₃	619-42-1	81	126	--	--	--	--	23
Diethyl tartrate	(COOCH ₂) ₂ CHOH	87-91-2	87	147	191	1300 (s)	--	--	23
Ethyl Lithium	LiC ₂ H ₅	811-49-4	95	389	--	--	--	--	23
1-Naphthol	C ₁₀ H ₇ OH	90-15-3	96	163	178	1095 (s)	--	--	23
p-Xylene Dichloride	C ₈ H ₈ Cl ₂	623-25-6	100	138.7	--	--	--	--	23
High Density Polyethylene		9002-88-4	100-150	200-233	--	--	--	--	13,16
Catechol	C ₆ H ₄ (OH) ₂	120-80-9	104.3	207	283	1370 (s)	--	--	23

Name	Formula	CAS #	T_M [°C]	H_f [kJ/kg]	$H_{f,v}$ [MJ/m ³]	ρ [kg/m ³]	k_{th} [W/mK]	c_p [kJ/kgK]	Ref
Quinone	C ₆ H ₄ O ₂	106-51-4	115	171	226	1318 (s)	--	--	23
Acetanilide	C ₈ H ₉ NO	103-84-4	115-119	152-222	184-269	1210 (s)	--	--	14,23
Mandelic acid	C ₆ H ₅ CH(OH)CO ₂ H	90-64-2	118-121	161	209	1300 (s)	--	--	16
Succinic anhydride	(CH ₂ CO) ₂ O	108-30-5	119	204	225	1104 (s)	--	--	23
Picric acid	C ₆ H ₃ N ₃ O ₇	88-89-1	121-122	75	--	--	--	--	16
E-Stilbene	(C ₆ H ₅ CH) ₂	103-30-0	124	167	--	970- 1164(s)	--	--	16,23
Benzamide	C ₆ H ₅ CONH ₂	55-21-0	127.2	169.4	227	1341 (s)	--	--	23
Phthalic anhydride	C ₈ H ₄ O ₃	85-44-9	131	159	243	1530 (s)	--	--	16
Trometamol (TAM)	H ₂ NC(CH ₂ OH) ₃	77-86-1	132	285	385	1350 (s)	--	--	16
Urea	CO(NH ₂) ₂	57-13-6	133-135	170-258	228-346	1340 (s)	--	--	16
Phenacetin	C ₁₀ H ₁₃ NO ₂	62-44-2	134-137	137	--	--	--	--	16,23
Dimethyl terephthalate	C ₆ H ₄ (CO ₂ CH ₃) ₂	120-61-6	142	170	219	1290 (s)	--	--	16
Trans-1,4-polybutadiene (TPB)	C ₄ H ₆	25038-44-2	145	144	--	--	--	--	13
p-Acetotoluidide	C ₉ H ₁₁ NO	103-89-9	146-151	180	--	--	--	--	16,23
Anthranilic acid	C ₆ H ₄ (NH ₂)COOH	118-92-3	147	148	209	1410 (s)	--	--	16
Benzaldehyde henyhydrazone	C ₆ H ₅ CH ₂ N ₂ HC ₆ H ₅	588-64-7	155	134.8	--	--	--	--	23
Benzanilide	C ₆ H ₅ CONHC ₆ H ₅	93-98-1	161	162	--	--	--	--	23
Hydroquinone	C ₆ H ₄ (OH) ₂	123-31-9	172.4	258	351	1358 (s)	--	--	23
p-Aminobenzoic Acid	H ₂ NC ₆ H ₄ COOH	150-13-0	187	153	--	1113 (l)	--	--	23

Table D.10 – Miscellaneous organic blends

composition	T_M [°C]	H_f [kJ/kg]	$H_{f,v}$ [MJ/m ³]	ρ [kg/m ³]	k_{th} [W/mK]	c_p [kJ/kgK]	Ref
H ₂ O+polyacrylamid	0	292	305.7 (l)	1047 (l)	0.486 (l)	--	13
Olefin blend (n=15/16)	3-4	36	29	806 (s)	--	--	24
90% Capric-lauric acid + 10% Pentadecane	13.3	142.2	--	--	--	--	13
38.5% Trimethylolethane + 31.5% Water + 30% Urea	14.4	160	187	1170 (s) 1140 (l)	0.66 (s) 0.37 (l)	4.22 (s) 3.09 (l)	39
48% butyl palmitate + 48% butyl stearate +3 %other	17	140	--	--	--	--	20
65-90% methyl palmitate+35-10%Methyl Stearate	22-25.5	120	--	--	--	--	20
34% C14H28O2+66% C10H20O2	24	147.7	--	--	--	--	14
50% CH3CONH2+50% NH2CONH2	27	163	--	--	--	--	14
50% CH3CONH2+50% NH2CONH2	27	163	--	--	--	--	20
62.5% Trimethylolethane + 37% water	29.8	218	244	1120 (s) 1090 (l)	0.65 (s) 0.21 (l)	2.75 (s) 3.58 (l)	39
40% CH3COONa· 3H2O+60% NH2CONH2	30	200.5	--	--	--	--	14
Acetamide + 91% Stearic Acid	39.4	183	--	--	--	--	24
50% Na(CH3COO)· 3H2O+50% HCONH2	40.5	255	--	--	--	--	13
53% NH2CONH2+47% NH4NO3	46	95	--	--	--	--	14
Acetamide + 89% Myristic Acid	48.7	199	--	--	--	--	24
Acetamide + 89% Palmitic Acid	57.2	172	--	--	--	--	24
Acetamide + 81% Palmitic Acid	59.1	177	--	--	--	--	24
50% CH3CONH2+50% C17H35COOH	65	218	--	--	--	--	14
Acetamide + 83% Stearic Acid	65.4	213	--	--	--	--	24
67.1% Naphthalene+32.9% benzoic acid	67	123.4	--	--	0.257-0.282 (s) 0.130-0.136 (l)	--	13
66.6% NH2CONH2+33.4% NH4Br	76	151	--	--	--	--	14

Table D.11 – Organic solid-solid transition materials

Name	CAS #	T_i [°C]	H_i [kJ/kg]	T_M [°C]	H_f [kJ/kg]	H_{total} [kJ/kg]	ρ_s [kg/m ³]	$c_{p,s}$ [kJ/kgK]	Ref
Neopentane	463-82-1	-133	35.9	-16.54	45.2	81.1	--	--	47
Neopentyl alcohol	75-84-3	-31	50.6-53.3	51-55	45.9-46.1	96.5-99.4	--	2.79	47,48
Neopentyl glycol	126-30-7	40-48	110.4-131	125-126	44.2-45.3	--	1060	--	23,47,48
Diaminopentaerythritol	36043-16-0	68	184	--	--	--	--	--	23
Ammediol	115-69-5	78-80	223.9-264	110-112	28-31.7	251.9-295.7	--	1.79	23,47,48
Nitroisobutylglycol	77-49-6	79-80	190-201	149-153	28-32	218-233	--	--	23,47
Tris(hydroxymethyl)nitromethane	126-11-4	80-82	149	--	--	--	--	--	47
Pentaglycerine	77-85-0	81-89	139-193	197-198	44.6-46	--	1160-1220	1.71	23,47,48
Monoaminopentaerythritol	36043-15-9	86	192	--	--	--	--	--	23
Tris(hydroxymethyl)acetic acid	2831-90-5	124	205	--	--	--	--	--	23
Tris(hydroxymethyl)-aminomethane	77-86-1	131-135	269.9-285.3	166-172	25-27.6	294.9-312.9	--	1.80	23,47,48,49
Form-stable HDPE	9002-88-4	133	188	--	--	--	960	--	47
Dimethylolpropionic acid	4767-03-7	152-155	287-289	194-197	26.8-27	313.8-316	--	--	23,47
Pentaerythritol	115-77-5	182-188	269-303.3	258-260	36.8-37.2	325.8-340.5	1390	--	23,47,48,49

Table D.12 – Layered perovskite solid-solid PCMs

Name	CAS #	T_i^a [°C]	H_i [kJ/kg]	ρ_s [kg/m ³]	Ref
C ₁₀ Mn	58675-50-6	32.8	70.34	--	50
C ₁₀ Cu	--	33.8-36.9	62.57	--	50
C ₁₂ Cu	71163-11-6	52.5-63.8	70.15, 147.13 ^a	1111	50,51
C ₁₂ Mn	75899-75-1	54.1-56.4	80.80	--	50
C ₁₂ Co	56104-91-7	60.7-88.0	92.89	--	50
C ₁₄ Cu	--	69.2-79.5	163.99	1186	52
C ₁₅ Cu	--	72.3-87.8	126.42	1245	52
C ₁₆ Cu	63643-59-4	72.8-96.0	79.76	--	50
C ₁₆ Mn	53290-99-6	73.1-91.0	104.48	--	50
C ₁₀ Co	56104-89-3	77.7, 82	74.28	--	50,53
C ₁₀ Zn	--	80.1-162.8	100.92	--	50
C ₁₂ Zn	57947-14-5	88.2-156.0	120.23	--	50
C ₁₆ Co	56104-95-1	93.4-164.1	153.79	--	50,53
C ₁₆ Zn	57947-17-8	99.1-160.5	137.52	--	50

a – multiple latent heat values represent discrepancy in reported heat release data between sources.

Table D.13 – Dialkyl ammonium salt solid-state PCMs – from [54]

Name	Formula	T_f [°C]	H_f [kJ/kg]
dioctylammonium iodide	DC ₈ I	-2-6 ^a	58
dioctylammonium hydrogen sulfate	DC ₈ HSO ₄	16-190 ^a	30
dioctylammonium chloride	DC ₈ Cl	21	132
dioctylammonium perchlorate	DC ₈ ClO ₄	23	108
dioctylammonium bromide	DC ₈ Br	30	78
dioctylammonium chlorate	DC ₈ ClO ₃	32	122
dioctylammonium nitrate	DC ₈ NO ₃	45	176
didecylammonium chloride	DC ₁₀ Cl	48	119
dioctylammonium dihydrogen phosphate	DC ₈ H ₂ PO ₄	50-70 ^a	--
didecylammonium chlorate	DC ₁₀ ClO ₃	55.5	154
didecylammonium bromide	DC ₁₀ Br	57	100
didecylammonium nitrate	DC ₁₀ NO ₃	60	179
didodecylammonium chlorate	DC ₁₂ ClO ₃	61.5	159
didodecylammonium perchlorate	DC ₁₂ ClO ₄	62	159
didodecylammonium iodide	DC ₁₂ I	65	80
didodecylammonium chloride	DC ₁₂ Cl	65	123
didodecylammonium nitrate	DC ₁₂ NO ₃	66	185
dioctadecylammonium hydrogen sulfate	DC ₁₈ HSO ₄	70-82 ^a	176
didodecylammonium bromide	DC ₁₂ Br	73	113
didodecylammonium hydrogen sulfate	DC ₁₂ HSO ₄	74-100 ^a	66.5
didecylammonium dihydrogen phosphate	DC ₁₀ H ₂ PO ₄	81	153
dioctadecylammonium chlorate	DC ₁₈ ClO ₃	84-91 ^a	154
dioctadecylammonium perchlorate	DC ₁₈ ClO ₄	88.1	185
didodecylammonium dihydrogen phosphate	DC ₁₂ H ₂ PO ₄	90	183
dioctadecylammonium chloride	DC ₁₈ Cl	91.2	174
dioctadecylammonium iodide	DC ₁₈ I	93	116
dioctadecylammonium nitrate	DC ₁₈ NO ₃	93.5	186
dioctadecylammonium bromide	DC ₁₈ Br	98	135

^a – range in temperatures indicates multiple phase transitions over the range. H_f is total over all transitions.

Table D.14 – Aqueous and hydrated salt material properties

Name	T_M [°C]	H_f [kJ/kg]	$H_{f,v}$ [MJ/m ³]	ρ [kg/m ³]	k_{th} [W/mK]	c_p [kJ/kgK]	Ref
Al(NO ₃) ₃ (30.5 wt%) +H ₂ O	-30.6	131	163.9	1251 (s) 1283 (l)	--	--	20
NaCl (22.4 wt%) +H ₂ O	-21.2	222	246.0	1108 (s) 1165 (l)	--	--	20
KCl (19.5 wt%) +H ₂ O	-10.7	283	312.7	1105 (s) 1126 (l)	--	--	20
H ₂ O	0	333- 335	305- 307	917 (s) 990-1000(l)	2.2-2.4(s) 0.57-0.61(l)	2.04-2.09(s) 4.18-4.21(l)	13,15, 23,25
Lithium Chlorate Trihydrate (LiClO ₃ ·3H ₂ O)	8.1	253	435.2	1720 (s)	--	--	13
Dipotassium phosphate Hexahydrate (K ₂ HPO ₄ ·6H ₂ O)	13-14	109	--	--	--	--	13,14
Potassium Fluoride Tetrahydrate (KF·4H ₂ O)	18.5	231- 246	336- 358	1439-1455(s) 1445-1447(l)	0.608-0.672(s) 0.479-0.493(l)	1.41-1.84 (s) 2.39-2.68(l)	25,60
Iron Bromide Hexahydrate (FeBr ₃ ·6H ₂ O)	21- 27	105	--	--	--	--	14
Manganese Nitrate Hexahydrate (Mn(NO ₃) ₂ ·6H ₂ O)	25.5- 25.8	125.9- 148	226- 266	1795 (s) 1728-1738(l)	--	--	13,14
Calcium Chloride Hexahydrate (CaCl ₂ ·6H ₂ O)	27.45- 30	161.15- 192	272- 346	1682.4-1802(s) 1496-1620(l)	1.088 (s) 0.53-0.56(l)	1.4 (s) 2.2 (l)	13,15, 24,32
Lithium Nitrate Trihydrate (LiNO ₃ ·3H ₂ O)	29.6- 29.9	296	460	1550 (s) 1430 (l)	0.8 (s) 0.56 (l)	1.8 (s) 2.8 (l)	23,61
Sodium Sulfate Decahydrate (Na ₂ SO ₄ ·10H ₂ O)	31- 32.4	251.1- 254	372	1485 (s) 1458-1460(l)	0.544 (s)	1.93 (s)	13,23,25
Sodium Carbonate Decahydrate (Na ₂ CO ₃ ·10H ₂ O)	32- 36	246.5- 251	355- 362	1440-1442(s)	--	--	13,23,32
Potassium Iron Sulfate Dodecahydrate (KFe(SO ₄) ₂ ·12H ₂ O)	33	173	--	--	--	--	14
Lithium Bromide Dihydrate (LiBr ₂ ·2H ₂ O)	34	124	--	--	--	--	14
Calcium Bromide Hexahydrate (CaBr ₂ ·6H ₂ O)	34	115.5- 138	253- 303	2194 (s) 1956 (l)	--	--	13,14
Disodium Hydrogen Phosphate Dodecahydrate (Na ₂ HPO ₄ ·12H ₂ O)	35- 40	265- 281	422- 427	1507.1-1522(s) 1442 (l)	0.514 (s) 0.476 (l)	1.69 (s) 1.94 (l)	13,14,23, 24,25
Zinc Nitrate Hexahydrate (Zn(NO ₃) ₂ ·6H ₂ O)	36- 36.4	134- 147	269	1937-2065(s) 1828 (l)	0.464-0.469(l)	1.34 (s) 2.26 (l)	13,24,25
Iron Chloride Hexahydrate (FeCl ₃ ·6H ₂ O)	37	226	--	--	--	--	23
Manganese Nitrate Tetrahydrate (Mn(NO ₃) ₂ ·4H ₂ O)	37.1	115	--	--	--	--	14
Cobalt Sulfate Heptahydrate (CoSO ₄ ·7H ₂ O)	40.7	170	--	--	--	--	23
Potassium Fluoride Dihydrate (KF·2H ₂ O)	41.4- 42	162	--	--	--	--	13,14
Magnesium Iodide Octahydrate (MgI ₂ ·8H ₂ O)	42	133	--	--	--	--	14
Calcium Iodide Hexahydrate (CaI ₂ ·6H ₂ O)	42	162	--	--	--	--	14
Calcium Nitrate Tetrahydrate (Ca(NO ₃) ₂ ·4H ₂ O)	42.7- 47	142- 153	259	--	--	--	13,14,24
Zinc Nitrate Tetrahydrate (Zn(NO ₃) ₂ ·4H ₂ O)	45	110	--	--	--	--	14
Dipotassium phosphate Heptahydrate (K ₂ HPO ₄ ·7H ₂ O)	45	145	--	--	--	--	14
Sodium Thiosulfate Pentahydrate (Na ₂ S ₂ O ₃ ·5H ₂ O)	45- 51.3	200- 217.2	344- 376	1720-1730(s) 1660-1690(l)	375.756 (s)	1.46 (s) 2.39 (l)	23,24, 25,32
Magnesium Nitrate Tetrahydrate (Mg(NO ₃) ₂ ·4H ₂ O)	47	142	--	--	--	--	14
Iron Nitrate Nonahydrate (Fe(NO ₃) ₃ ·9H ₂ O)	47- 47.2	155	261	1684 (s)	--	--	14,23
Dipotassium phosphate Trihydrate (K ₂ HPO ₄ ·3H ₂ O)	48	99	--	--	--	--	14
Sodium Silicate Tetrahydrate (Na ₂ SiO ₃ ·4H ₂ O)	48	168	--	--	--	--	14
Magnesium Sulfate Heptahydrate (MgSO ₄ ·7H ₂ O)	48.4	202	--	--	--	--	23
Calcium Nitrate Trihydrate (Ca(NO ₃) ₂ ·3H ₂ O)	51	104	--	--	--	--	14
Zinc Nitrate Dihydrate (Zn(NO ₃) ₂ ·2H ₂ O)	55	68	--	--	--	--	14

Name	T_M [°C]	H_f [kJ/kg]	$H_{f,v}$ [MJ/m ³]	ρ [kg/m ³]	k_{th} [W/mK]	c_p [kJ/kgK]	Ref
Iron Chloride Dihydrate (FeCl ₃ ·2H ₂ O)	56	90	--	--	--	--	14
Nickel Nitrate Hexahydrate (Ni(NO ₃) ₂ ·6H ₂ O)	57	169	--	--	--	--	14
Manganese Chloride Tetrahydrate (MnCl ₂ ·4H ₂ O)	58	151	--	--	--	--	14
Magnesium Chloride Tetrahydrate (MgCl ₂ ·4H ₂ O)	58	178	--	--	--	--	23
Sodium Acetate Trihydrate (Na(CH ₃ COO)·3H ₂ O)	58- 58.4	226- 264	--	--	--	--	13
Lithium Acetate Dihydrate (Li(CH ₃ COO)·2H ₂ O)	58- 70	150- 377	--	--	--	--	14,23
Iron Nitrate Hexahydrate (Fe(NO ₃) ₂ ·6H ₂ O)	60.5	126	--	--	--	--	14
Sodium Aluminum Sulfate Decahydrate (NaAl(SO ₄) ₂ ·10H ₂ O)	61	181	--	--	--	--	14
Sodium Hydroxide Monohydrate (NaOH·H ₂ O)	64.3	227.6- 272	385- 468	1690-1720(s)	--	--	13,23
Sodium Phosphate Dodecahydrate (Na ₃ PO ₄ ·12H ₂ O)	65- 69	190	--	--	--	--	14,20
Aluminum Nitrate Nonahydrate (Al(NO ₃) ₂ ·9H ₂ O)	70	155	241	1555 (s)	--	--	24
Sodium Pyrophosphate Decahydrate (Na ₂ P ₂ O ₇ ·10H ₂ O)	70	184	--	--	--	--	13
Barium Hydroxide Octahydrate (Ba(OH) ₂ ·8H ₂ O)	78	265.7- 301	657	2070-2180(s) 1937 (l)	1.255 (s) 0.653-0.678(l)	1.17 (s)	13,23
Magnesium Nitrate Hexahydrate (Mg(NO ₃) ₂ ·6H ₂ O)	89- 95	149.5- 162.8	245- 267	1636-1640(s) 1550 (l)	0.611-0.669(s) 0.490-0.502(l)	0.9 (s)	13,15,24
Aluminum Potassium Sulfate Dodecahydrate (AlK(SO ₄) ₂ ·12H ₂ O)	91	184	--	--	--	--	23
Ammonium Aluminum Sulfate Hexahydrate ((NH ₄)Al(SO ₄) ₂ ·6H ₂ O)	95	269	--	--	--	--	13
Magnesium Chloride Hexahydrate (MgCl ₂ ·6H ₂ O)	115- 117	165- 172	265- 269	1560-1570(s) 1442-1450(l)	0.694-0.704(s) 0.57-0.598(l)	1.72-2.25(s) 2.61-2.82(l)	13,15,23, 24,25

Table D.15 – Hydrated salt blends

Composition	T_M [°C]	H_f [kJ/kg]	$H_{f,v}$ [MJ/m ³]	ρ_s [kg/m ³]	k_{th} [W/mK]	Ref
56.9% KF·4H ₂ O+ 43.1% KF·2H ₂ O	9.1	205	310	1530	--	60
31% Na ₂ SO ₄ +13% NaCl+16% KCl+40% H ₂ O	4	234	--	--	--	21
6.16% NH ₄ Cl+6.66% NaCl+32.5% Na ₂ SO ₄ +41.4% H ₂ O	13	146	--	--	--	32
50% CaBr ₂ ·6H ₂ O+50% CaCl ₂ ·6H ₂ O	14	140	--	--	--	47
55% CaBr ₂ ·6H ₂ O+45% CaCl ₂ ·6H ₂ O	14.7	140	--	--	--	14
45-52% LiNO ₃ ·3H ₂ O+48-55% Zn(NO ₃) ₂ ·6H ₂ O	17.2	220	--	--	--	20
55-65% LiNO ₃ ·3H ₂ O+ 35-45% Ni(NO ₃) ₂ ·6H ₂ O	24.2	230	--	--	--	20
45% Ca(NO ₃) ₂ ·4H ₂ O+55% Zn(NO ₃) ₂ ·6H ₂ O	25	130	251	1931 (s)	--	24
66.6% CaCl ₂ ·6H ₂ O+33.3% MgCl ₂ ·6H ₂ O	25	127	202	1590 (s)	--	13
50% CaCl ₂ ·6H ₂ O+50% MgCl ₂ ·6H ₂ O	25	95	--	--	--	14
48% CaCl ₂ ·6H ₂ O+4.3% NaCl+0.4% KCl+47.3% H ₂ O	26.8-27	188	--	1640 (s) 1530 (l)	--	20
67% Ca(NO ₃) ₂ ·4H ₂ O+33% Mg(NO ₃) ₂ ·6H ₂ O	30	136	228	1676 (s)	--	24
18% Mg(NO ₃) ₂ ·6H ₂ O+82% Zn(NO ₃) ₂ ·6H ₂ O	32	130	249	1915 (s)	--	24
28% Al(NO ₃) ₂ ·9H ₂ O+72% Ca(NO ₃) ₂ ·4H ₂ O	35	139	240	1727 (s)	--	24
61.5% Mg(NO ₃) ₂ ·6H ₂ O+38.5% NH ₄ NO ₃	52	125.5	213	1696 (s) 1515 (l)	0.552 (s) 0.494-0.515 (l)	13
58.7% Mg(NO ₃) ₂ ·6H ₂ O+41.3% MgCl ₂ ·6H ₂ O	58-59	132-132.2	215	1630 (s) 1550 (l)	0.678 (s) 0.510-0.565 (l)	13,14
50% Mg(NO ₃) ₂ ·6H ₂ O+50% MgCl ₂ ·6H ₂ O	58-59.1	132.2-144	215-235	1630 (s)	--	14,47
80% Mg(NO ₃) ₂ ·6H ₂ O+20% MgCl ₂ ·6H ₂ O	60	150	--	--	--	20
53% Mg(NO ₃) ₂ ·6H ₂ O+47% Al(NO ₃) ₂ ·9H ₂ O	61	148	249	1682 (s)	--	24
59% Mg(NO ₃) ₂ ·6H ₂ O+41% MgBr ₂ ·6H ₂ O	66	168	--	--	--	14
86% Mg(NO ₃) ₂ ·6H ₂ O+14% LiNO ₃ ·3H ₂ O	72	180	--	1610 (s) 1590 (l)	--	13

Table D.16 – Pure salts

Name	T_M [°C]	H_f [kJ/kg]	$H_{f,v}$ [MJ/m ³]	ρ_s [kg/m ³]	k_{th} [W/mK]	c_p [kJ/kgK]	Ref
Aluminum Chloride (AlCl ₃)	192-192.4	272-280	664-683	2440	--	--	32
Lithium Nitrate (LiNO ₃)	250-254	360-373	857-888	2380	--	--	17,18, 32,62
Sodium Nitrite (NaNO ₂)	270-282	180-216	--	--	--	--	18
Zinc Chloride (ZnCl ₂)	280	75	218	2907	0.5 (s)	0.74 (l)	15
Sodium Nitrate (NaNO ₃)	306-310	172-199	388-450	2257-2261	0.5 (s)	1.1 (s),1.82 (l)	13,15,17, 18,63
Rubidium Nitrate (RbNO ₃)	312	31	--	--	--	--	17
Sodium Hydroxide (NaOH)	318	159-165	334-347	2100	0.92 (l)	2.08 (l)	15,18
Potassium Nitrate (KNO ₃)	330-336	88-266	186-561	2109-2110	0.5(s),0.5(l)	0.935(s),1.22(l)	13,63
Potassium Hydroxide (KOH)	360-380	134-150	273.4-307	2040-2044	0.5(s),0.5(l)	1.34(s),1.47(l)	13,15,17, 18,63
Sodium Peroxide (Na ₂ O ₂)	360	314	--	--	--	--	32
Cesium Nitrate (CsNO ₃)	409	71	--	--	--	--	17
Lithium Hydroxide (LiOH)	462	875	1269	1450	--	--	18,62
Lithium Chromate (Li ₂ CrO ₄)	485	168	--	--	--	--	17
Potassium Perchlorate (KClO ₄)	527	1253	3158	2520	--	--	32,62
Strontium Iodide (SrI ₂)	538	57	--	--	--	--	17
Lithium Bromide (LiBr)	550	203	--	--	--	--	17
Rubidium Iodide (RbI)	556	104	--	--	--	--	17
Calcium Nitrate (Ca(NO ₃) ₂)	560	145	--	--	--	--	17
Barium Nitrate (Ba(NO ₃) ₂)	594	209	--	--	--	--	17
Lithium Chloride (LiCl)	610	416	--	--	--	--	17
Cesium Iodide (CsI)	632	96	--	--	--	--	17
Magnesium Iodide (MgI ₂)	633	93	--	--	--	--	17
Cesium Bromide (CsBr)	638	111	--	--	--	--	17
Cesium Chloride (CsCl)	645	121	--	--	--	--	17
Strontium Nitrate (Sr(NO ₃) ₂)	645	231	--	--	--	--	17
Strontium Bromide (SrBr ₂)	657	41	--	--	--	--	17
Sodium Iodide (NaI)	661	158	--	--	--	--	17
Potassium Iodide (KI)	681	145	--	--	--	--	17
Sodium Molybdate (Na ₂ MoO ₄)	688	109	--	--	--	--	17
Rubidium Bromide (RbBr)	692	141	--	--	--	--	17
Lithium Hydride (LiH)	688-699	2678-3260	2800	859	--	--	32,64
Sodium Tungstate (Na ₂ WO ₄)	696	107	--	--	--	--	17
Cesium Fluoride (CaF ₂)	703	143	--	--	--	--	17
Lithium Molybdate (Li ₂ MoO ₄)	703	281	--	--	--	--	17
Barium Iodide (BaI ₂)	711	68	--	--	--	--	17
Magnesium Bromide (MgBr ₂)	711	214	--	--	--	--	17
Magnesium Chloride (MgCl ₂)	714	452-454	211-212	2140	--	--	13,17,18
Rubidium Chloride (RbCl)	723	197	--	--	--	--	17
Lithium Carbonate (Li ₂ CO ₃)	732	509	--	--	--	--	17
Potassium Bromide (KBr)	734	215	--	--	--	--	17
Lithium Tungstate (Li ₂ WO ₄)	740	157	--	--	--	--	17
Calcium Bromide (CaBr ₂)	742	145	--	--	--	--	17
Sodium Bromide (NaBr)	742	255	--	--	--	--	17
Potassium Chloride (KCl)	770-771	353-355	--	--	--	--	17,18
Calcium Chloride (CaCl ₂)	772	253	--	--	--	--	17
Calcium Iodide (CaI ₂)	783	142	--	--	--	--	17
Sodium Chromate (Na ₂ CrO ₄)	794	146	--	--	--	--	17
Rubidium Fluoride (RbF)	795	248	--	--	--	--	17
Sodium Chloride (NaCl)	800-802	466.7-492	1008-1063	2160	5 (s)	--	13,17,18
Lithium Fluoride (LiF)	848-868	932-1041	--	--	--	--	18,32
Sodium Carbonate (Na ₂ CO ₃)	854-858	165-275.7	2163-2173	2533	2 (s)	--	13,17
Barium Bromide (BaBr ₂)	857	108	--	--	--	--	17
Potassium Fluoride (KF)	857-858	452-507	1071-1202	2370	--	--	13,17,18
Lithium Sulphate (Li ₂ SO ₄)	858	84	--	--	--	--	17
Strontium Chloride (SrCl ₂)	875	103	--	--	--	--	17
Sodium Sulphate (Na ₂ SO ₄)	884	165	--	--	--	--	17
Potassium Carbonate (K ₂ CO ₃)	897-900	200-235.8	458-540	2290	2 (s)	--	13,17,18
Potassium Tungstate (K ₂ WO ₄)	923	86	--	--	--	--	17
Potassium Molybdate (K ₂ MoO ₄)	926	163	--	--	--	--	17
Cesium Molybdate (Cs ₂ MoO ₄)	935	75	--	--	--	--	17
Rubidium Tungstate (Rb ₂ WO ₄)	952	78	--	--	--	--	17
Cesium Tungstate (Cs ₂ WO ₄)	953	63	--	--	--	--	17
Rubidium Molybdate (Rb ₂ MoO ₄)	955	140	--	--	--	--	17

Name	T_M [°C]	H_f [kJ/kg]	$H_{f,v}$ [MJ/m ³]	ρ_s [kg/m ³]	k_{th} [W/mK]	c_p [kJ/kgK]	Ref
Barium Chloride (BaCl ₂)	961	76	--	--	--	--	17
Potassium Chromate (K ₂ CrO ₄)	973	41	--	--	--	--	17
Cesium Chromate (Cs ₂ CrO ₄)	975	94	--	--	--	--	17
Magnesium Carbonate (MgCO ₃)	990	698	--	--	--	--	17
Sodium Fluoride (NaF)	993-996	750-801	--	--	--	--	17,18,32

Table D.17 – Salts blends

Name	T_M [°C]	H_f [kJ/kg]	$H_{f,v}$ [MJ/m ³]	ρ_s [kg/m ³]	k_{th} [W/mK]	c_p [kJ/kgK]	Ref
25% LiNO ₃ +65% NH ₄ NO ₃ +10% NaNO ₃	80.5	113	--	--	--	--	14
14.9% KNO ₃ +26.4% LiNO ₃ +58.7% NH ₄ NO ₃	81.5	116	--	--	--	--	14
27% LiNO ₃ +5% NH ₄ Cl+68% NH ₄ NO ₃	81.6	108	--	--	--	--	14
49.4% KNO ₃ +29% LiNO ₃ +17% NaNO ₃ +4.6% Sr(NO ₃) ₂	105	110	--	--	--	--	17
67% KNO ₃ +33% LiNO ₃	133	170	--	--	--	--	18
68.3% KNO ₃ +31.7% LiNO ₃	135	136	--	--	--	--	17
53% KNO ₃ +40% NaNO ₂ +7% NaNO ₃	142	80	--	--	--	--	18
40.1% KCl+55.4% LiNO ₃ +4.5% NaNO ₃	160	266	--	--	--	--	17
41.9% KCl+58.1% LiNO ₃	166	272	--	--	--	--	17
50% KOH+50% NaOH	169-171	202-213	--	--	--	--	18,17
1.4% LiCl+47.9% LiNO ₃ +50.7% NaNO ₃	180	265	--	--	--	--	17
57% LiNO ₃ +43% NaNO ₃	193	248	--	--	--	--	17
49% LiNO ₃ +51% NaNO ₃	194	265	--	--	--	--	18
45% LiNO ₃ +47% NaNO ₃ +8% Sr(NO ₃) ₂	200	199	--	--	--	--	17
87% LiNO ₃ +13% NaCl	208	369	--	--	--	--	17
30% LiOH+70% NaOH	210-216	278-329	--	--	--	--	18,17
50% NaNO ₃ +50% KNO ₃	220-222	100-100.7	192-193.3	1920	0.56 (s)	2.25 (s) 1.35 (l)	15,18
46% KNO ₃ +54% NaNO ₃	222	117	--	--	--	--	17
80% NaNO ₂ +20% NaOH	230-232	206-252	--	--	--	--	18,17
68.1% KCl+31.9% ZnCl ₂	235	198	491	2480	0.8 (s)	2.25 (s)	13,15
27% NaNO ₂ +73% NaOH	237-238	249-295	--	--	--	--	18,17
3.6% NaCl+18.3% NaNO ₃ +78.1% NaOH	242	242	--	--	--	--	17
72% NaNO ₃ +28% NaOH	246-247	182-257	--	--	--	--	18,17
70% NaNO ₃ +30% NaOH	247	158	--	--	--	--	17
4.2% NaCl+40.2% NaNO ₃ +55.6% NaOH	247	213	--	--	--	--	17
97.4% LiNO ₃ +2.6% Ba(NO ₃) ₂	253	368	--	--	--	--	17
(28.5-28.9)% LiCl+(43.5-44.5)% CsCl +(13.7-14.1)% KCl+(13.3-13.5)% RbCl	253-259	375-380	--	--	--	--	17
93.6% LiNO ₃ +6.4% NaCl	255	354	--	--	--	--	17
18.5% NaNO ₃ +81.5% NaOH	256-258	251-292	--	--	--	--	18,17
36% LiCl+63% LiOH	262	485	752	1550	1.1 (s)	2.4 (s)	17
NaNO ₂ ·NaOH	265	313	--	--	--	--	18
41% NaNO ₃ +59% NaOH	266	221-278	--	--	--	--	18,17
40.85% Ca ₂ +59.15% LiCl	270	167	--	--	--	--	17
NaNO ₃ ·2NaOH	270	295	--	--	--	--	17
NaNO ₃ ·NaOH	271	265	--	--	--	--	17
34.5% LiCl+65.5% LiOH	274	339	--	--	--	--	17
5.3% NaCl+6.4% Na ₂ CO ₃ +88.3% NaOH	282	279	--	--	--	--	17
1.5KCl+36.5% LiCl+62% LiOH	282	300	--	--	--	--	17
7.8% NaCl+6.4% Na ₂ CO ₃ +85.8% NaOH	282	316	673	2130	--	2.51 (s)	17
8.4% NaCl+86.3% NaNO ₃ +5.3% Na ₂ SO ₄	287	177	--	--	--	--	17
8% NaCl+5% NaF+87% NaNO ₃	288	224	--	--	--	--	17
6.1% NaCl+6.6% Na ₂ CO ₃ +87.3% NaOH	291	283	--	--	--	--	17
16.2% NaCl+6.6% Na ₂ CO ₃ +77.2% NaOH	318	290	--	--	--	--	17
6.4% BaCl ₂ +39.4% KCl+54.2% LiCl	320	170	--	--	--	--	17
95.5% KNO ₃ +4.5% KCl	320	74	155.4	2100	0.5 (s)	1.21 (s)	63
41.5% LiCl+7% LiF+16.4% LiVO ₃ +35.1% Li ₂ CrO ₄	340	177	--	--	--	--	17
(46.8-47.0)% KCl+(3.2-3.4)% LiCO ₃ +(47.4-47.7)% LiCl+(2.1-2.4)% LiF	340-343	375-380	--	--	--	--	17
42% KCl+58% LiCl	348	170	--	--	--	--	17
28.7% KCl+45% MnCl ₂ +26.3% NaCl	350	215	--	--	--	--	17
41.3% KCl+58.7% LiCl	352.7	251.5	473	1880	--	0.95 (s) 1.33 (l)	152

Name	T_M [°C]	H_f [kJ/kg]	$H_{f,v}$ [MJ/m ³]	ρ_s [kg/m ³]	k_{th} [W/mK]	c_p [kJ/kgK]	Ref
(23.4-24.2)%LiCl+(24.8-25.3)%LiVO ₃ +(27.1-27.6)%Li ₂ MoO ₄ +(17.3-17.8)%Li ₂ SO ₄ +(6.1-6.2)%LiF	360-363	278-284	--	--	--	--	17
42%LiCl+17.4%LiF+11.6%Li ₂ MO ₄ +17.4%LiVO ₃ +11.6%Li ₂ SO ₄	363	277-291	--	--	--	--	17
20.4%KCl+60%MgCl ₂ +19.6%NaCl	380	400	720	1800	--	0.96 (s)	63
21.6%KCl+45.4%MgCl ₂ +33%NaCl	385	234	--	--	--	--	18
14%KCl+63%MgCl ₂ +22.3%NaCl	385	461	1037	2250	0.95 (l)	0.96 (s)	17
(18.5-22.5)%KCl+(57.0-53.0)%MgCl ₂ +(22.5-26.5)%NaCl	385-393	405-410	--	--	--	--	17
45.5%KCl+34.5%MnCl ₂ +20%NaCl	390	230	--	--	--	--	17
22%KCl+51%MgCl ₂ +27%NaCl	396	290	--	--	--	--	17
20%KCl+50%MgCl ₂ +30%NaCl	396	291	--	--	--	--	17
25%K ₂ NO ₃ +43.5%Li ₂ CO ₃ +31.5%Na ₂ CO ₃	397	274	--	--	--	--	18
35%K ₂ CO ₃ +32%Li ₂ CO ₃ +33%Na ₂ CO ₃	397	276	635	2300	2.02 (l)	1.67 (s) 1.63 (l)	17
37.7%KCl+37.3%MnCl ₂ +25%NaCl	400	235	--	--	--	--	17
51.5%LiCl+16.2%LiF +16.2%Li ₂ MoO ₄ +16.2%Li ₂ SO ₄	402	291	--	--	--	--	17
(40.0-40.4)%KCO ₄ +(8.6-8.7)%KCl +(33.2-33.8)%KF+(17.6-17.7)%LiF	422-426	407-412	--	--	--	--	17
20%LiF+80%LiOH	426	869	1390	1600	--	0.88 (s) 1 (l)	17
50%LiF+50%LiOH	427	512	--	--	--	--	32
25%LiF+16.5%Li ₂ MoO ₄ +14.8%Li ₂ SO ₄ +43.8%LiVO ₃	428	260	--	--	--	--	17
44%MgCl ₂ +56%NaCl	430	320	--	--	--	--	17
80%LiF+20%LiOH	430	528	--	--	--	--	17
55%MgBr ₂ +45%NaBr	431	212	740	3490	0.9 (l)	0.5 (s) 0.59 (l)	17
54%KCl+46%ZnCl ₂	432	218	525	2410	0.83 (l)	0.67 (s) 0.88 (l)	17
2KCl·MgCl ₂	435	184	--	--	--	--	18
61%KCl+39%MgCl ₂	435	351	741	2110	0.81 (l)	0.8 (s) 0.96 (l)	17
38.5%MgCl + 61.5%NaCl	435	328	708	2160	--	--	13,
1.8%BaF ₂ +41.2%KF+45.7%LiF+11.3%NaF	438	332	--	--	--	--	17
(2.8-3.0)%KCl+(41.0-43.0) %KF +(42.5-45.5)%LiF+(10.7-11.5)%NaF	440-448	682-692	--	--	--	--	17
67%KF+33%LiF	442-493	458-618	1159-1564	2530	3.98 (l)	1.34 (s) 1.63 (l)	17
58.5%LiCl+17.9%Li ₂ MoO ₄ +23.6%Li ₂ SO ₄	445	327	--	--	--	--	17
36%KCl+64%MgCl ₂	448-470	236-388	517-850	2190	0.83 (l)	0.84 (s) 0.96 (l)	17
49%LiCl+12.75%Li ₂ SO ₄ +38.25%LiVO ₃	449	450	--	--	--	--	17
55.1%KF+27.1%LiF+5.9%MgF ₂ +11.9%NaF	449	699	--	--	--	--	17
50%MgCl ₂ +50%NaCl	450	429	961	2240	0.96 (l)	0.93 (s)	17
52%MgCl ₂ +48%NaCl	450	430	959	2230	0.95 (l)	0.92 (s) 1 (l)	17
39.9%MgCl ₂ +60.1%NaCl	450	293-328	--	--	--	--	18,17
42%KF+46.5%LiF+11.5%NaF	454	400	--	--	--	--	18
59%KF+29%LiF+12%NaF	454	590	1493	2530	4.5 (l)	1.34 (s) 1.55 (l)	17
47.6%CaCl ₂ +8.1%KCl+41.3%NaCl+2.9%NaF	460	231	--	--	--	--	17
41.6%CaCl ₂ +2.2%KCl+8.8%MgCl ₂ +47.4%NaCl	460	245	--	--	--	--	17
50%CaCl ₂ +7.25%KCl+42.75%NaCl	465	245	--	--	--	--	17
42%KCl+58%MgCl ₂	470	392	--	--	--	--	18
8.7%BaCl ₂ +52.3%KCl+18.2%MgCl ₂ +20.7%NaCl	475	248	--	--	--	--	17
13.1%BaCl ₂ +16.9%CaCl ₂ +47.3%KCl+22.7%NaCl	478	208	--	--	--	--	17
9.3%BaCl ₂ +22.2%CaCl ₂ +42.7%KCl+25.8%NaCl	479	217	--	--	--	--	17
69.5%LiCl+26.5%LiF+4%MgF ₂	484	157	--	--	--	--	17
26.4%LiCl+73.6%LiF	485	403	--	--	--	--	17
27%CaCl ₂ +25%KCl+48%MgCl ₂	487	342	865	2530	0.88 (l)	0.8 (s) 0.92 (l)	17
50%KF+50%LiCl	487	344	--	--	--	--	17
38%K ₂ NO ₃ +62%Li ₂ CO ₃	488	370	--	--	--	--	18

Name	T_M [°C]	H_f [kJ/kg]	$H_{f,v}$ [MJ/m ³]	ρ_s [kg/m ³]	k_{th} [W/mK]	c_p [kJ/kgK]	Ref
53%K ₂ CO ₃ +47%Li ₂ CO ₃	488-491	321-342	706-752	2200	1.99 (l)	1.03 (s) 1.34 (l)	17
50%CaCl ₂ +1.5%CaF ₂ +48.5%NaF	490	264	--	--	--	--	17
(52.3-55)%CaCl ₂ +(45-47.2)%NaCl	490-500	233-239	--	--	--	--	17
18%LiF+29.0%Li ₂ MoO ₄ +53.0%LiVO ₃	493	297	--	--	--	--	17
44%Li ₂ CO ₃ +56%Na ₂ CO ₃	496	370	858	2320	2.09 (l)	1.8 (s) 2.09 (l)	17
53.3%Li ₂ CO ₃ +46.7%Na ₂ CO ₃	496	372	--	--	--	--	18
72%K ₂ CO ₃ +28%Li ₂ CO ₃	498	263	589	2240	1.85 (l)	1.46 (s) 1.8 (l)	17
71.5%K ₂ CO ₃ +28.5%Li ₂ CO ₃	498	316	--	--	--	--	17
52.8%CaCl ₂ +47.2%NaCl	500	239	--	--	--	--	17
67%CaCl ₂ +33%NaCl	500	281	607	2160	1.02 (l)	0.84 (s) 1 (l)	17
13%KCl+19%NaCl+68%SrCl ₂	504	223	613	2750	1.05 (l)	0.67 (s) 0.84 (l)	17
66%CaCl ₂ +5%KCl+29%NaCl	504	279	600	2150	1 (l)	1.17 (s) 1 (l)	17
65%K ₂ CO ₃ +35%Li ₂ CO ₃	505	344	777	2260	1.89 (l)	1.34 (s) 1.76 (l)	17
43%NaBr+2%NaF+55%Na ₂ MoO ₄	506	241	--	--	--	--	17
20.1%NaF+79.9%ZrF ₄	510	255	--	--	--	--	17
21%KF+62%K ₂ CO ₃ +17%NaF	520	274	652	2380	1.5 (l)	1.17 (s) 1.38 (l)	17
40%NaBr+5%NaCl+55%Na ₂ MoO ₄	524	215	--	--	--	--	17
40%KCl+23%KF+37%K ₂ CO ₃	528	283	645	2280	1.19 (l)	1 (s) 1.26 (l)	17
37%MgCl ₂ +63%SrCl ₂	535	239	664	2780	1.05 (l)	0.67 (s) 0.8 (l)	17
3.3%BaF ₂ +8.1%BaMoO ₄ +18.5%CaF ₂ +36.1%LiF+34%NaF	536	653	--	--	--	--	17
3.5%CaMoO ₄ +59.8%Li ₂ SO ₄ +36.7%Li ₂ MoO ₄	538	406	--	--	--	--	17
53%BaCl ₂ +28%KCl+19%NaCl	542	221	667	3020	0.86 (l)	0.63 (s) 0.8 (l)	17
20%K ₂ CO ₃ +20%Li ₂ CO ₃ +60%Na ₂ CO ₃	550	283	674	2380	1.83 (l)	1.59 (s) 1.88 (l)	17
62%K ₂ CO ₃ +22%Li ₂ CO ₃ +16%Na ₂ CO ₃	550-580	288	674	2340	1.95 (l)	1.8 (s) 2.09 (l)	17
47%BaCl ₂ +29%CaCl ₂ +24%KCl	551	219	642	2930	0.95 (l)	0.67 (s) 0.84 (l)	17
94.5%LiCl+5.5%MgF ₂	573	131	--	--	--	--	17
95.2%NaCl+48%NiCl ₂	573	558	--	--	--	--	17
60%KBr+40%KF	576	315	--	--	--	--	17
(27.0-27.25)%CaF ₂ +(25.67-25.76)%LiF +(10.63-10.67)%MgF ₂ +(36.45-36.57)%NaF	593-595	510-515	--	--	--	--	17
45%KCl+55%KF	605	407	--	--	--	--	17
23%NaBr+38.5%NaCl+38.5%Na ₂ MoO ₄	612	168	--	--	--	--	17
26.5%CaF ₂ +35.2%LiF+38.3%NaF	615	636	--	--	--	--	17
13%CaF ₂ +52%LiF+35%NaF	615	640	--	--	--	--	17
65%KBr+35%K ₂ MoO ₄	625	90.5	--	--	--	--	17
46%LiF+10%MgF ₂ +44%NaF ₂	632	858	1922	2240	1.2 (s)	1.4 (s)	17
73%NaBr+27%NaF	642	360	--	--	--	--	17
33.4%LiF+17.1%MgF ₂ +49.9%NaF ₂	650	860	2425	2820	1.15 (s)	1.42 (s)	17
(24.5-25.0)%CaF ₂ +(34.51-34.79)%LiF +(37.25-37.6)%MgF ₂ +(3.21-3.31)%NaF	651-657	460-470	--	--	--	--	17
60%LiF+40%NaF	652	816	--	--	--	--	17
38.5%CaCl+4%CaMoO ₄ +11%CaSO ₄	673	224	--	--	--	--	17
66.5%NaCl+33.5%NaF	675	572	--	--	--	--	17
6.56%CaMoO ₄ +11.44%CaSO ₄ +82%Li ₂ SO ₄	680	207	--	--	--	--	17
62%LiF+19%MgF ₂ +19%NaF	693	690	--	--	--	--	17
51%K ₂ CO ₃ +49%Na ₂ CO ₃	710	163	391	2400	1.73 (l)	1.67 (s) 1.56 (l)	17
47.8%K ₂ CO ₃ +52.2%Na ₂ CO ₃	710	176	--	--	--	--	17
70%LiF+30%MgF ₂	728	520	--	--	--	--	17
23%CaF ₂ +12%MgF ₂ +65%NaF	745	574	907	1580	--	1.17 (s)	17
67%LiF+33%MgF ₂	746	947	2491	2630	--	1.42 (s)	17

Name	T_M [°C]	H_f [kJ/kg]	$H_{f,v}$ [MJ/m ³]	ρ_s [kg/m ³]	k_{th} [W/mK]	c_p [kJ/kgK]	Ref
13% KF+74% LiF+13% MgF ₂	749	860	--	--	--	--	17
20% CeF ₃ +80% LiF	756	500	--	--	--	--	17
21% CaF ₂ +79% LiF	765	757	--	--	--	--	18
19.5% CaF ₂ +80.5% LiF	767-769	816-820	1950-1960	2390	3.8 (s), 1.7 (l)	1.77 (l)	15,17
15% CaF ₂ +85% KF	780	440	--	--	--	--	17
85% KF+15% MgF ₂	790	520	--	--	--	--	17
16% KF+20% MgF ₂ +64% NaF	804	650	--	--	--	--	17
15% KF+22.5% MgF ₂ +62.5% NaF	809	543	--	--	--	--	17
32% CaF ₂ +68% NaF	810	600	--	--	--	--	17
33% MgF ₂ +67% NaF	832	616	1318	2140	4.65 (l)	1.42 (s) 1.38 (l)	17
25% MgF ₂ +75% NaF	832	650	1742	2680	4.66 (l)	1.42 (s)	17
49% CaF ₂ +9.6% CaMoO ₄ +41.4% CaSO ₄	943	237	--	--	--	--	17
64% MgF ₂ +36% NaF	1000	794	--	--	--	--	18

Table D.18 – RoHS non-compliant metallic materials

Formula (Name)	T_M [°C]	H_f [kJ/kg]	$H_{f,v}$ [MJ/m ³]	ρ_s [kg/m ³]	$k_{th,s}$ [W/mK]	$c_{p,s}$ [kJ/kgK]	Ref
Mercury	-38.87	11.4	154.4 (l)	13546	8.34	0.139	65,67
74Ga/22Sn/4Cd	20.2	75.2	449.9	5983	--	--	64
93Ga/5Zn/2Cd	24.6	85.03	511.9	6020	--	--	64
44.7Bi 22.6Pb 19.1In 8.3Sn 5.3Cd	47	36.8	337	9160	15	0.163 (s) 0.197 (l)	66
Bi/Pb/Sn/In ^a	57	29.5	267	9060 (s) 8220 (l)	33.2 (s) 10.6 (l)	0.323 (s) 0.721 (l)	68
47.5Bi 25.4Pb 12.6Sn 9.5Cd 5In	57-65	36	341	9470	15	0.159 (s) 0.188 (l)	66
49Bi 21In 18Pb 12Sn (Cerrolow Eutectic)	58	28.9	260	9010	10	0.167 (s) 0.201 (l)	23,66
33Bi/16Cd/51In	61	25	201-251	8040-10040	--	--	23
50Bi 26.7Pb 13.3Sn 10Cd (Wood's metal)	70	32.6-45.8	287-439	9400-9580	18-19	0.146-0.167(s) 0.167-0.184(l)	23,64, 66
52Bi/26Pb/22In	70	29	234-293	8069-10103	--	--	23
42.5Bi 37.7Pb 11.3Sn 8.5Cd	71-88	34.3	336.483	9810	--	0.146 (s)	66
52Bi 30Pb 18Sn	96	34.7	333	9600	13	0.151 (s) 0.167 (l)	66
55.5Bi 44.5Pb	124-125	20.9	218	10440	4	0.126 (s) 0.155 (l)	23,66
85Pb 10Sb 5Sn	245-255	0.9	9	10360	--	0.15 (s)	66

a – specific formulation unknown

Table D.19 – RoHS compliant metallic materials

Formula (Name)	T_M [°C]	H_f [kJ/kg]	$H_{f,v}$ [MJ/m ³]	ρ_s [kg/m ³]	$k_{th,s}$ [W/mK]	$c_{p,s}$ [kJ/kgK]	Ref
67Ga-20.5In-12.5Zn	10.7	67.2	415	6170	--	--	64
78.55Ga-21.45In	15.7	69.7	432	6197	--	--	64
82Ga-12Sn-6Zn	18.8	86.5	516	5961	--	--	64
86.5Ga-13.5Sn	20.55	81.9	482	5885	--	--	64
96.5Ga-3.5Zn	25	88.5	526	5946	--	--	64
Cesium	28.65	16.4	29.5 (l)	1796 (l)	17.4 (l)	0.236 (l)	65,67
Gallium	29.8-30	80.3	469	5903 (s)	33.7 (s)	0.34 (s)	23,65,66,67
				6093 (l)	24 (l)	0.397 (l)	
Rubidium	38.85	25.74	37.8378	1470 (l)	29.3 (l)	0.363 (l)	65,67
Potassium	63.2	59.59	39.56776	664 (l)	54 (l)	0.78 (l)	65,67
66.3In 33.7Bi	72	25	200-203	7990-8100	--	--	23,66
Sodium	97.83	113.23	104.95289	926.9 (l)	86.9 (l)	1.38 (l)	65,67
60Sn 40Bi	138-170	44.4	361	8120	30	0.18 (s)	66
						0.213 (l)	
58Bi 42Sn	138.3	44.8	384	8560	19	0.167 (s)	66
						0.201 (l)	
Indium	156.7	28.47	208	7310	86	0.243	65,66,67
91Sn 9Zn	199	71.2	518	7270	61	0.239 (s)	66
						0.272 (l)	
46.3Mg 53.7Zn	340	185	851	4600	--	--	65,66,67
52Zn 48Mg	340	180	--	--	--	--	65,66
96Zn-4Al	381	138	915	6630	--	--	17,64
55Mg-28Cu-17Zn	400	146	330	2260	--	--	17
59Al-35Mg-6Zn	443	310	738	2380	--	1.63 (s)	17,64
						1.46 (l)	
60Mg-25Cu-15Zn	452	254	711	2800	--	--	17
52Mg-25Cu-23Ca	453	184	368	2000	--	--	17
34.65Mg-65.35Al	497	285	614	2155	--	--	17
60.8Al-33.2Cu-6.0Mg	506	365	1113	3050	--	--	17
64.6Al-5.2Si-28Cu-2.2Mg	507	374	1646	4400	--	--	17,64
54Al-22Cu-18Mg-6Zn	520	305	958	3140	--	1.51 (s)	17,64
						1.13 (l)	
68.5Al-5.0Si-26.5Cu	525	364	1069	2938	--	--	17,64
64.3-34.0Cu-1.7Sb	545	331	1324	4000	--	--	17
66.92Al-33.08Cu	548	372	1339	3600	--	--	17,64
83.14Al-11.7Si-5.16Mg	555	485	1213	2500	--	--	17,64
87.76Al-12.24Si	557	498	1265	2540	--	--	17,64
46.3Al-4.6Si-49.1Cu	571	406	2257	5560	--	--	17,64
65Al-30Cu-5Si	571	422	1152	2730	--	1.3 (s)	17,64
						1.2 (l)	
86.4Al-9.4Si-4.2Sb	575	471	1272	2700	--	--	17,64
88% Al-12% Si	576	560	1512	2700	160	1.038 (s)	17
						1.741 (l)	
80% Al-20% Si	585	460	--	--	--	--	17,64
Zn ₂ Mg	588	230	--	--	--	--	17
49Zn-45Cu-6Mg	703	176	1526	8670	--	0.42	18
91Cu-9P	715	134	750	5600	--	--	17
69Cu-17Zn-14P	720	368	2576	7000	--	--	17
74Cu-19Zn-7Si	765	125	896	7170	--	--	17
56Cu-27Si-17Mg	770	420	1743	4150	--	0.75	17
84Mg-16Ca	790	272	375	1380	--	--	17
47Mg-38Si-15Zn	800	314	--	--	--	--	17
80Cu-20Si	803	197	1300	6600	--	0.5	17
83Cu-10P-7Si	840	92	633	6880	--	--	17
Mg ₂ Cu	841	243	--	--	--	--	17
49Si-30Mg-21Ca	865	305	686	2250	--	--	17
56Si-44Mg	946	757	1438	1900	--	0.79	17
Gold	961	104.6	1098	10500	--	--	17

Table D.20 – RoHS compliant Indium Corp. alloys lacking H_f data, from [66]

Ind. #	Formula	T_M [°C]	Ind. #	Formula	T_M [°C]
46L	61Ga 25In 13Sn 1Zn	6.5-7.6	244	99.3Sn 0.7Cu	227
51	62.5Ga 21.5In 16Sn	10.7	160	97Sn 3Cu	227-300
60	75.5Ga 24.5In	15.7	172	98Sn 2As	231-330
77	95Ga 5In	15.7-25	128	100Sn	232
19	51In 32.5Bi 16.5Sn	60	131	97Sn 3Sb	232-238
174	57Bi 26In 17Sn	79	173	99Sn 1Ge	232-345
27	54.02Bi 29.68In 16.3Sn	81	209	65Sn 25Ag 10Sb	233
224	52.2In 46Sn 1.8Zn	108	129	99Sn 1Sb	235
53	67Bi 33In	109	133	95Sn 5Sb	235-240
1E	52In 48Sn	118	148	100Bi	271
1	50In 50Sn	118-125	182	80Au 20Sn	280
71	52Sn 48In	118-131	183	88Au 12Ge	356
87	58Sn 42In	118-145	199	99.4Au 0.6Sb	360-1030
203	95In 5Bi	125-150	184	96.76Au 3.24Si	363
139	95Bi 5Sn	134-251	194	98Au 2Si	370-800
282	57Bi 42Sn 1Ag	139-140	176	95Zn 5Al	382
225	90In 10Sn	143-151	186	55Ge 45Al	424
3	90In 10Ag	143-237	177	75Au 25In	451-465
290	97In 3Ag	143.3	178	82Au 18In	451-485
88	99.3In 0.7Ga	150	189	86Al 10Si 4Cu	521-585
90	99.4In 0.6Ga	152	187	45Ag 38Au 17Ge	525
91	99.6In 0.4Ga	153	188	88.3Al 11.7Si	577
92	99.5In 0.5Ga	154	190	92.5Al 7.5Si	577-610
231	86.5Sn 5.5Zn 4.5In 3.5Bi	174-186	191	95Al 5Si	577-630
227	77.2Sn 20In 2.8Ag	175-187	214	60Ag 30Cu 10Sn	600-720
226	83.6Sn 8.8In 7.6Zn	181-187	179	61Ag 24Cu 15In	603-705
254	86.9Sn 10In 3.1Ag	204-205	217	56Ag 22Cu 17Zn 5Sn	620-650
249	91.8Sn 4.8Bi 3.4Ag	211-213	211	80Cu 15Ag 5P	640-705
241	95.5Sn 3.8Ag 0.7Cu	217-220	192	Al	660
252	95.5Sn 3.9Ag 0.6Cu	217-220	208	85Cu 8Sn 7Ag	665-985
256	96.5Sn 3.0Ag 0.5Cu	217-220	221	63Ag 28.5Cu 6Sn 2.5Ni	690-800
246	95.5Sn 4Ag 0.5Cu	217-225	220	71.5Ag 28Cu 0.5Ni	775-785
251	96.2Sn 2.5Ag 0.8Cu 0.5Sb	217-225	193	72Ag 28Cu	780
121	96.5Sn 3.5Ag	221	195	80Au 20Cu	890
123	97.5Sn 2.5Ag	221-226	196	82Au 18Ni	950
132	95Sn 5Ag	221-240	198	50Au 50Ag	1000-1020
156	90Sn 10Ag	221-295	222	99Au 1Ga	1025-1030
243	99Sn 1Cu	227	--	--	--

Table D.21 – RoHS non-compliant Indium Corp. alloys lacking H_f data, from [66]

Ind.#	Formula	T_M [°C]	Ind.#	Formula	T_M [°C]
15	42.91Bi 21.7Pb 18.33In 7.97Sn 5.09Cd 4Hg	38-43	2	80In 15Pb 5Ag	149-154
16	44.7Bi 22.6Pb 16.1In 11.3Sn 5.3Cd	47-52	9	70Sn 18Pb 12In	154-167
17	49.14Bi 20.89In 17.92Pb 11.55Sn 0.5Cd	54-56	240	46Sn 46Pb 8Bi	160-173
21	49Bi 18Pb 18In 15Sn	58-69	204	70In 30Pb	165-175
147	48Bi 25.63Pb 12.77Sn 9.6Cd 4In	61-65	235	58In 39Pb 3Ag	165-195
18	61.72In 30.78Bi 7.5Cd	61.5	234	49.75Sn 41.75Pb 8Bi 0.5Ag	166-172
22	50.5Bi 27.8Pb 12.4Sn 9.3Cd	70-73	111	55.5Pb 40.5Sn 4Bi	170-197
23	50Bi 25Pb 12.5Sn 12.5Cd	70-73	205	60In 40Pb	173-181
24	50Bi 24.95Pb 12.5Sn 12.5Cd 0.05Ag	70-73	103	67.8Sn 32.2Cd	177
26	50Bi 34.5Pb 9.3Sn 6.2Cd	70-78	115	55Pb 44Sn 1Ag	177-210
43	40.5Bi 27.8Pb 22.4Sn 9.3Cd	70-102	100	62.6Sn 37Pb .4Ag	178-182
47	35.3Bi 35.1Pb 20.1Sn 9.5Cd	70-105	104	62.5Sn 36.1Pb 1.4Ag	179
65	46Pb 30.7Bi 18.2Sn 5.1Cd	70-123	137	61.5Sn 35.5Pb 3Ag	179-189
55	40Bi 33.4Pb 13.3Sn 13.3Cd	72-113	127	60Pb 37Sn 3Ag	179-232
35	50Bi 39Pb 7Cd 4Sn	73-93	210	70Pb 27Sn 3Ag	179-253
59	38.14Bi 31.67Sn 26.42Pb 2.64Cd 1.07Sb 0.06Cu	75-118	142	50Sn 47Pb 3Ag	179-260
28	50Bi 39Pb 8Cd 3Sn	77-82	154	57Pb 40Sn 3Ag	179-289
25	48.5Bi 41.5In 10Cd	77.5	213	62Sn 38Pb	182.7-183.3
31	50.31Bi 39.2Pb 7.99Cd 1.5Sn 1In	80-89	106	63Sn 37Pb	183
32	50.9Bi 31.1Pb 15Sn 2In 1Cd	80-89	107	65Sn 35Pb	183-184
29	50.31Bi 39.2Pb 8Cd 1.49In 1Sn	81-85	108	70Sn 30Pb	183-186
34	52Bi 31.67Pb 15.33Sn 1Cd	83-92	109	60Sn 40Pb	183-191
33	51.08Bi 39.8Pb 8.12Cd 1In	87-91	110	75Sn 25Pb	183-192
36	51.45Bi 31.35Pb 15.2Sn 2In	87-93	112	80Sn 20Pb	183-199
37	52Bi 31.7Pb 15.3Sn 1In	90-94	113	55Sn 45Pb	183-200
197	51.6Bi 40.2Pb 8.2Cd	92	114	85Sn 15Pb	183-205
63	56.85Bi 41.15Pb 2Cd	92-121	116	50Sn 50Pb	183-212
8	44In 42Sn 14Cd	93	118	90Sn 10Pb	183-213
40	50Bi 31Pb 19Sn	93-99	119	50Sn 49.5Pb 0.5Sb	183-216
68	38Pb 37Bi 25Sn	93-127	120	52Pb 48Sn	183-218
257	52Bi 32Pb 16Sn	95-95.5	122	95Sn 5Pb	183-222
38	52.5Bi 32Pb 15.5Sn	95-96	125	55Pb 45Sn	183-227
46	56Bi 22Pb 22Sn	95-104	130	60Pb 40Sn	183-238
57	50Bi 30Pb 20Sn	95-104	135	65Pb 35Sn	183-247
50	46Bi 34Pb 20Sn	95-108	141	70Pb 30Sn	183-257
44	50Bi 25Pb 25Sn	95-115	145	75Pb 25Sn	183-268
69	51.6Bi 37.4Sn 6In 5Pb	95-129	149	80Pb 20Sn	183-280
76	36Bi 32Pb 31Sn 1Ag	95-136	153	85Pb 15Sn	183-288
78	36.45Bi 31.75Pb 31.5Sn 0.25Cd 0.05Ag	95-136	7	50In 50Pb	184-210
80	36.5Bi 31.75Pb 31.75Sn	95-137	144	73.7Pb 25Sn 1.3Sb	184-263
42	46Bi 34Sn 20Pb	96	146	79Pb 20In 1Sb	184-270
49	45Bi 35Pb 20Sn	96-107	126	58Pb 40Sn 2Sb	185-231
72	34Pb 34Sn 32Bi	96-133	134	63.2Pb 35Sn 1.8Sb	185-243
74	38.41Bi 30.77Pb 30.77Sn 0.05Ag	96-135	138	68.4Pb 30Sn 1.6Sb	185-250
81	43Pb 28.5Bi 28.5Sn	96-137	206	60Pb 40In	197-231
83	38.4Pb 30.8Bi 30.8Sn	96-139	238	90Sn 10Au	217
85	33.33Bi 33.34Pb 33.33Sn	96-143	236	83Pb 10Sb 5Sn 2Ag	237-247
105	60Sn 25.5Bi 14.5Pb	96-180	152	92Pb 5Sn 3Sb	239-285
48	52.2Bi 37.8Pb 10Sn	98-105	10	75Pb 25In	240-260
54	51.6Bi 41.4Pb 7Sn	98-112	143	90Pb 10Sb	252-260
41	50Bi 28Pb 22Sn	100	157	95Pb 5Sb	252-295
45	54Bi 26Sn 20Cd	102-103	150	81Pb 19In	260-275
52	54.5Bi 39.5Pb 6Sn	102-108	202	82.6Cd 17.4Zn	266
58	52.98Bi 42.49Pb 4.53Sn	103-117	228	88Pb 10Sn 2Ag	267-290
217-440	48Bi 28.5Pb 14.5Sn 9Sb	103-227	159	90Pb 10Sn	275-302
56	54.4Bi 43.6Pb 1Sn 1Cd	104-113	242	89.5Pb 10.5Sn	275-302
61	53.75Bi 43.1Pb 3.15Sn	108-119	151	92.5Pb 5Sn 2.5Ag	287-296
62	55Bi 44Pb 1Sn	117-120	12	90Pb 5In 5Ag	290-310
64	55Bi 44Pb 1In	120-121	155	90Pb 5Ag 5Sn	292
89	42Pb 37Sn 21Bi	120-152	163	95.5Pb 2.5Ag 2Sn	299-304
98	50Sn 40Pb 10Bi	120-167	6	92.86Pb 4.76In 2.38Ag	300
70	40In 40Sn 20Pb	121-130	164	92.5Pb 5In 2.5Ag	300-310
79	55.1Bi 39.9Sn 5Pb	121-136	11	95Pb 5In	300-313
93	54.55Pb 45.45Bi	122-160	168	98Pb 2Sb	300-320
253	74In 26Cd	123	161	97.5Pb 2.5Ag	303
67	58Bi 42Pb	124-126	237	93Pb 3Sn 2In 2Ag	304
13	70In 15Sn 9.6Pb 5.4Cd	125	229	94.5Pb 5.5Ag	304-365

Ind.#	Formula	T_M [°C]	Ind.#	Formula	T_M [°C]
73	56.84Bi 41.16Sn 2Pb	128-133	175	95Pb 5Ag	305-364
101	50Pb 30Sn 20Bi	130-173	171	95Pb 5Sn	308-312
99	51.5Pb 27Sn 21.5Bi	131-170	165	97.5Pb 1.5Ag 1Sn	309
84	45Sn 32Pb 18Cd 5Bi	132-139	169	98.5Pb 1.5Sb	310-322
5	37.5Pb 37.5Sn 25In	134-181	239	91Pb 4Sn 4Ag 1In	313
75	57.42Bi 41.58Sn 1Pb	135	167	98Pb 1.2Sb 0.8Ga	315
230	54Sn 26Pb 20In	140-152	170	100Pb	327
95	48Sn 36Pb 16Bi	140-162	185	95Cd 5Ag	340-395
86	60Bi 40Cd	144	215	45Ag 24Cd 16Zn 15Cu	605-620
97	43Sn 43Pb 14Bi	144-163	219	35Ag 26Cu 21Zn 18Cd	605-700
181	51.2Sn 30.6Pb 18.2Cd	145	212	30Ag 27Cu 23Zn 20Cd	605-710
94	50Sn 25Cd 25Pb	145-160	216	50Ag 18Cd 16.5Zn 15.5Cu	625-635
102	47.47Pb 39.93Sn 12.6Bi	146-176	218	50Ag 16Cd 15.5Cu 15.5Zn 3Ni	630-690

Table D.22 – Commercial organic PCMs

Name	Paraffin C#	T_M [°C]	H_f [kJ/kg]	$H_{f,v}$ [MJ/m ³]	ρ [kg/m ³]	$k_{th,s}$ [W/mK]	c_p [kJ/kgK]	Ref
RT 6 ^a	--	8	140	120	860 (s) 770 (l)	0.2	1.8 (s) 2.4 (l)	39
RT 5 ^a	--	9	205	--	--	--	--	13
Dowtherm A ^b	--	12	97.9	105 (l)	1060 (l)	--	--	23
5913 ^c	13-24	22-24	189	170	900 (s) 760 (l)	0.21	2.1 (l)	25
RT 20 ^a	--	22	172	151	880 (s)	--	--	20
GR25 ^a	--	23.2-24.1	45.3	--	--	--	1.2 (s) 1.2 (l)	15
RT 26 ^a	--	25	131	115	880 (s)	--	--	20
RT25-RT30 ^a	--	26.6	232	182	785 (s) 749 (l)	0.19 (s) 0.18 (l)	1.41 (s) 1.8 (s)	15
E28 ^d	--	28	193	148	769 (s)	0.21	2.22 (s)	39
RT30 ^a	--	28	206	--	--	--	--	13
RT 27 ^a	--	28	146-179	127-156	870 (s) 750 (l)	0.2	1.8 (s) 2.4 (l)	20,39
RT 32 ^a	--	31	130	--	--	--	--	20
A32 ^d	--	32	145	123	845 (s)	0.21	2.2 (s)	39
6106 ^c	16-28	42-44	189	172	910 (s) 765 (l)	0.21	2.1 (l)	25
Suntech P116 ^e	20-32	43-56	209-266	171-218	817-818 (s) 760-786 (l)	0.14-0.24 (s) 0.24-0.277 (l)	2.89-2.95 (s) 2.5-2.89 (l)	15,19,29
RT40 ^a	--	43	181	--	--	--	--	13
RT 42 ^a	--	43	150	132	880 (s) 760 (l)	0.2	1.8 (s) 2.4 (l)	39
Paraffin 44 ⁱ	--	44	167	--	--	--	--	39
RT 41 ^a	--	45	125	110	880 (s) 760 (l)	0.2	1.8 (s) 2.4 (l)	39
5838 ^c	20-33	48-50	189	172	912 (s) 769 (l)	0.21	2.1 (l)	25
P56-58 ^f	--	48.86-58.06	250	--	--	--	1.84 (s) 2.37 (l)	15
RT 52 ^a	--	52	138	124	900 (s) 760 (l)	0.2	1.8 (s) 2.4 (l)	39
Unicere 55 Paraffin ^g	--	52.5-53.7	182-189	--	--	--	--	39
Paraffin 53 ⁱ	--	53	164	160	978 (s) 795 (l)	0.28 (s) 0.19 (l)	2.13 (s) 2.62 (l)	39
Paraffin wax 53 ⁱ	--	53	184	--	--	--	2.05 (s)	39
Paraffin 56 ^h	--	56±2	72-86	76-91	1060 (s)	0.75	--	325
RT 54 ^a	--	55	148-179	133-161	900 (s) 770 (l)	0.2	1.8 (s) 2.4 (l)	20,39
Paraffin 57 ^h	--	57±2	98	--	--	0.7	--	325
6035 ^c	22-45	58-60	189	174	920 (s) 795 (l)	0.21	2.1 (l)	25
RT 60 ^a	--	58-60	214	182	850 (s) 775 (l)	0.2	0.93 (s)	39
RT 58 ^a	--	59	154	139	900 (s) 760 (l)	0.2	1.8 (s) 2.4 (l)	39

Name	Paraffin C#	T_M [°C]	H_f [kJ/kg]	$H_{f,v}$ [MJ/m ³]	ρ [kg/m ³]	$k_{th,s}$ [W/mK]	c_p [kJ/kgK]	Ref
Paraffin 63 ^h	--	63±2	60	--	--	--	--	325
6403 ^c	23-45	62-64	189	173	915 (s) 790 (l)	0.21	2.1 (l)	25
RT 65 ^a	--	64	154-207	140-188	910 (s) 790 (l)	0.2	1.8 (s) 2.4 (l)	20,39
Paraffin 64 ^h	--	64	210	--	--	--	--	39
6499 ^c	21-50	66-68	189	176	930 (s) 830 (l)	0.21	2.1 (l)	25
Paraffin natural wax 79 ^h	--	79±2	80	--	--	0.63	--	325
RT 80 ^a	--	79-81	140-209	129-192	920 (s) 770 (l)	0.2	1.8 (s) 2.4 (l)	13,39
PK 80 A6 ^a	--	81	119	107	900 (s)	0.2	2 (s)	39
Paraffin natural wax 84 ^h	--	84±2	85	--	--	0.72	--	325
RT 90 ^a	--	90	163-197	152-183	930 (s) 770 (l)	0.2	1.8 (s) 2.4 (l)	13,39
RT100 ^a	--	99	137-168	129-158	940 (s) 770 (l)	0.2 (s) 0.2 (l)	1.8 (s) 2.4 (l)	15,39
Paraffin natural wax 106 ^h	--	106±2	80	--	--	0.65	--	325
RT110 ^a	--	112	213	--	--	--	--	13
A164 ^d	--	164	306	459	1500 (s)	--	--	39

a Rubitherm GmbH (Germany) [www.rubitherm.de].

b Dow Corning Corporation (US), [www.dow.com].

c Ter Hell Paraffin (1983), now Ter Hell & Co. GmbH (Germany) [www.terhell.com].

d Environmental Process Systems, Ltd (EPS Ltd, United Kingdom). [www.epsLtd.co.uk]. Now lists all products as sourced by PCM Products, Ltd. [www.pcmproducts.net], with different product nomenclature.

e Sun Oil Company [www.sunocoinc.com]. Sunwax product line sold to HollyFrontier Co. [hollyfrontier.com]. P-116 product discontinued.

f Merck KGaA (Germany) [merckgroup.com].

g Stochem, Inc., now Univar Canada CASE Specialties [www.univarspecialties.com].

h Russian source, specifics unknown.

i unknown source.

Table D.23 – Commercial inorganic PCMs

Name	T_M [°C]	H_f [kJ/kg]	$H_{f,v}$ [MJ/m ³]	ρ_s [kg/m ³]	$k_{th,s}$ [W/mK]	$c_{p,s}$ [kJ/kgK]	Ref
SN33 ^a	-33	245	304	1240	--	--	13
TH-31 ^b	-31	131	--	--	--	--	13
SN29 ^a	-29	233	268	1150	--	--	13
SN26 ^a	-26	268	324	1210	--	--	13
ClimSel C-21 ^c	-21	288	374	1300	0.5-0.7	3.6	326
SN21 ^a	-21	240	269	1120	--	--	13
STL-21 ^d	-21	240	269	1120	--	--	13
TH-21 ^b	-21	222	--	--	--	--	13
ClimSel C-18 ^c	-18	288	374	1300	0.6-0.7	3.6	326
SN18 ^a	-18	268	324	1210	--	--	13
TH-16 ^b	-16	289	--	--	--	--	13
SN15 ^a	-15	311	317	1020	--	--	13
SN12 ^a	-12	306	324	1060	--	--	13
SN10 ^a	-11	310	344	1110	--	--	13
STLN10 ^d	-11	271	285	1050	--	--	13
TH-10 ^b	-10	283	--	--	--	--	13
SN06 ^a	-6	284	304	1070	--	--	13
STL-6 ^d	-6	284	304	1070	--	--	13
TH-4 ^b	-4	286	--	--	--	--	13
SN03 ^a	-3	328	331	1010	--	--	13
STL-3 ^d	-3	328	331	1010	--	--	13
ClimSel C7 ^c	7	130-140.4	185-199	1420	0.5-0.7	3.6	13, 326
ClimSel C10 ^c	10.5	126	176	1400	0.5-0.7	3.6	326
ClimSel C15 ^c	15	130	--	--	--	--	13
ClimSel C21 ^c	21	125.2	173	1380	0.5-0.7	3.6	326
E21 ^e	21	150	222	1480	0.43	0.68	39
ClimSel C23 ^c	23	148	219	1480	--	--	13
E23 ^e	23	155	229	1475	0.43	0.69	39
ClimSel C24 ^c	24	108-126	149-174	1380	0.5-0.7	3.6	20, 326
TH 24 ^b	24	157.95	253	1600 (s) 1500 (l)	0.8	6.075 (s) 5.28 (l)	39
S27 ^a	27	207	304	1470	--	--	13
STL27 ^d	27	213	232	1090	--	--	13
ClimSel C28 ^c	28	162.3	230	1420	0.5-0.7	3.6	326
TH 29 ^b	29	166.3-188	284-321	1710 (s) 1560 (l)	1.09 (s) 0.54 (l)	1.41 (s) 2.28 (l)	13, 39
E30 ^e	30	201	262	1304	0.48	0.69	39
ClimSel C32 ^c	32	162-212	230-301	1420	0.5-0.7	3.6	13, 326
E32 ^e	32	186	272	1460	0.51	0.78	39
E44 ^e	44	105	166	1584	0.43	1.61	39
STL47 ^d	47	221	296	1340	--	--	13
ClimSel C48 ^c	48	216-227	294-309	1360	0.5-0.7	3.6	13, 326
E48 ^e	48	201	336	1670	0.45	0.7	39
E50 ^e	50	104	167	1601	0.43	1.59	39
STL52 ^d	52	201	261	1300	--	--	13
STL55 ^d	55	242	312	1290	--	--	13
ClimSel C58 ^c	58	259-288	352-392	1360	0.5-0.7	3.6	13, 326
E58 ^e	58	167	251	1505	0.69	2.55	39
TH58 ^b	58	200.4-226	291-328	1450 (s) 1280 (l)	--	2.78 (s) 4.58 (l)	13, 39
ClimSel C70 ^c	70	194-396	330-673	1700	0.6-0.7	2.1	13, 326
E71 ^e	71	123	208	1690	0.51	1.86	39
E72 ^e	72	140	233	1666	0.58	2.13	39
E83 ^e	83	152	243	1600	0.62	2.31	39
E89 ^e	89	163	253	1550	0.67	2.48	39
TH89 ^b	89	139.6-149	229-244	1640	0.69 (s) 0.6 (l)	1.84	39
E117 ^e	117	169	245	1450	0.7	2.61	39

a Cristopia Energy Systems (India) [www.cristopia.com].

b TEAP Energy (Australia) [formerly at teapenergy.com]. Corporate liquidation in 2008. Corporate website obtained by PCM Energy P., Ltd (India), no apparent affiliation. Does not offer TH-series products. TEAP energy possibly reincorporated as Phase Change Products Pty Ltd [pepaustralia.com.au], offering products similar to TH-series under different trade names. Most literature references still point to original teapenergy.com.

c Climator Sweden AB (Sweden) [www.climator.com].

d Mitsubishi Chemical Corporation (Japan) [www.m-kagaku.co.jp].

e Environmental Process Systems, Ltd (EPS Ltd, United Kingdom). [www.epsLtd.co.uk]. Now lists all products as sourced by PCM Products, Ltd. [www.pcmproducts.net], with different product nomenclature.

Bibliography

1. *Next Generation Combat Vehicles*, United States Army, Washington, DC, USA, 2018 Feb 22 (accessed 2018 Jun 10). [Online] Available: www.army.mil/standto/archive_2018-02-22
2. A. Feickert, "The Army's Optionally Manned Fighting Vehicle (OMFV) program: Background and issues for Congress," Washington DC, USA, CRS Report No. R45519, Jul. 20, 2020. [Online]. Available: crsreports.congress.gov/product/pdf/R/R45519/16
3. *Army Modernization Strategy 2008*, United States Army, Washington, DC, USA, July 25, 2008. Available: apps.dtic.mil/dtic/tr/fulltext/u2/a494621.pdf
4. E. W. Leathers, Jr., E. Danielson, G. Frazier, and B. Wong, "Combat hybrid power system – Evolutionizing power and energy development," *Army AL&T Magazine*, pp. 54-59, Jul. 2005. Available: asc.army.mil/docs/pubs/alt/archives/2005/Jul-Aug_2005.pdf
5. "Energy for the warfighter: Operational energy strategy," US Department of Defense, Office of Assistant Secretary of Defense for Operational Energy, Plans, and Programs, Washington, DC, USA, DTIC Accession No.: ADA544100, May 2011. Available: apps.dtic.mil/sti/citations/ADA544100
6. T. K. Kelly, J. E. Peters, E. Landree, L. R. Moore, R. Steeb, and A. Martin, "The U.S. combat and tactical wheeled vehicle fleets: Issues and suggestions for Congress," RAND National Defense Research Institute, Santa Monica, CA, USA, U.S. Office of the Secretary of Defense, Technical Report: LCCN:2011921602, Feb 2011. Available: apps.dtic.mil/sti/citations/ADA539921
7. "Electrical and electronics technical team roadmap," US Department of Energy, Office of Energy Efficiency and Renewable Energy, Washington, DC, USA, Technical Report, OSTI No.: 1220125, June 1, 2013, doi: 10.2172/1220125
8. K. T. Chau and C. C. Chan, "Emerging Energy-Efficient Technologies for Hybrid Electric Vehicles," *Proceedings of the IEEE*, vol. 95, no. 4, pp. 821–835, Apr. 2007, doi: 10.1109/JPROC.2006.890114.
9. G. Khalil, E. Barshaw, E. Danielson, and M. Chait, "Power supply and integration in future combat vehicles," in *Proceedings of the NATO RTO AVT Symposium on Functional and Mechanical Integration of Weapons and Land and Air Vehicles*, Williamsburg, VA, USA, Jun. 7-9, 2004, pp. 39-1 - 39-12, DTIC Accession No.: ADA468635. Available: www.dtic.mil/docs/citations/ADA468635
10. M. M. Freeman and M. R. Perschbacher, "Hybrid power - an enabling technology for future combat systems," in *Proceedings of the 12th IEEE International Pulsed Power Conference*, Monterey, CA, USA, Jun. 27-30, 1999, pp. 17–22, doi: 10.1109/PPC.1999.825416.
11. E. W. Bentilla, K. F. Sterrett, and L. E. Karre, "Research and development study on thermal control by use of fusible materials," Northrop Space Laboratories, Hawthorne, CA, USA, National Aeronautics and Space Administration, Contract No.: NAS 8-11163, Final Report No. N66-26691, Apr. 1996. hdl: 2060/19660017401.
12. A. Hauer, H. Mehling, P. Schossig, M. Yamaha, L. Cabeza, V. Martin, and F. Setterwall, "Final Report IEA/ECES Annex 17: Advanced thermal energy storage through Phase change materials and chemical reactions – Feasibility studies and demonstration projects," *International Energy Agency*, Energy Conservation through Energy Storage Implementing Agreement, Annex 17, Final Report, 2004.
13. B. Zalba, J. M. Marin, L. F. Cabeza, and H. Mehling, "Review on thermal energy storage with phase change: materials, heat transfer analysis and applications," *Applied Thermal Engineering*, vol. 23, no. 3, pp. 251–283, Feb. 2003, doi: 10.1016/S1359-4311(02)00192-8.

14. A. Sharma, V. V. Tyagi, C. R. Chen, and D. Buddhi, "Review on thermal energy storage with phase change materials and applications," *Renewable and Sustainable Energy Reviews*, vol. 13, no. 2, pp. 318–345, Feb. 2009, doi: 10.1016/j.rser.2007.10.005.
15. F. Agyenim, N. Hewitt, P. Eames, and M. Smyth, "A review of materials, heat transfer and phase change problem formulation for latent heat thermal energy storage systems (LHTESS)," *Renewable and Sustainable Energy Reviews*, vol. 14, no. 2, pp. 615–628, Feb. 2010, doi: 10.1016/j.rser.2009.10.015.
16. D. Haillot, T. Bauer, U. Kroner, and R. Tamme, "Thermal analysis of phase change materials in the temperature range 120-150°C," *Thermochimica Acta*, vol. 513, no. 1-2, pp. 49–59, Jan. 2011, doi: 10.1016/j.tca.2010.11.011.
17. M. M. Kenisarin, "High-temperature phase change materials for thermal energy storage," *Renewable and Sustainable Energy Reviews*, vol. 14, no. 3, pp. 955–970, Apr. 2010, doi: 10.1016/j.rser.2009.11.011.
18. T. Nomura, N. Okinaka, and T. Akiyama, "Technology of latent heat storage for high temperature application: A review," *ISIJ International*, vol. 50, no. 9, pp. 1229–1239, Sep. 2010, doi: 10.2355/isijinternational.50.1229.
19. A. Gil, M. Medrano, I. Martorell, A. Lázaro, P. Dolado, B. Zalba, and L. F. Cabeza, "State of the art on high temperature thermal energy storage for power generation. Part 1 - Concepts, materials and modellization," *Renewable and Sustainable Energy Reviews*, vol. 14, no. 1, pp. 31–55, Jan. 2010, doi: 10.1016/j.rser.2009.07.035.
20. F. Cabeza, A. Castell, C. Barreneche, A. de Gracia, and A. I. Fernández, "Materials used as PCM in thermal energy storage in buildings: A review," *Renewable and Sustainable Energy Reviews*, vol. 15, no. 3, pp. 1675–1695, Apr. 2011, doi: 10.1016/j.rser.2010.11.018.
21. E. Oró, A. de Gracia, A. Castell, M. M. Farid, and L. F. Cabeza, "Review on phase change materials (PCMs) for cold thermal energy storage applications," *Applied Energy*, vol. 99, pp. 513–533, Nov. 2012, doi: 10.1016/j.apenergy.2012.03.058.
22. N.R. Jankowski and F.P. McCluskey, "A review of phase change materials for vehicle component thermal buffering," *Applied Energy*, vol. 113, pp. 1525–1561, Jan. 2014, doi: 10.1016/j.apenergy.2013.08.026.
23. D. V. Hale, M. J. Hoover, and M. J. O'Neill, "Phase change materials handbook," National Aeronautics and Space Administration, Huntsville, AL, USA, Technical Report No.: NASA-CR-61363, Contract No.: NAS8-25183, Sep. 1971, hdl: 2060/19720012306.
24. H. G. Lorsch, K. W. Kauffman, and J. C. Denton, "Thermal energy storage for solar heating and off-peak air conditioning," *Energy Conversion*, vol. 15, no. 1-2, pp. 1–8, Jan. 1975, doi: 10.1016/0013-7480(75)90002-9.
25. A. Abhat, "Low temperature latent heat thermal energy storage: Heat storage materials," *Solar Energy*, vol. 30, no. 4, pp. 313–332, 1983, doi: 10.1016/0038-092X(83)90186-X.
26. T. J. Lu, "Thermal management of high power electronics with phase change cooling," *International Journal of Heat and Mass Transfer*, vol. 43, no. 13, pp. 2245–2256, Jul. 2000, doi: 10.1016/S0017-9310(99)00318-X.
27. S. Krishnan and S. V. Garimella, "Analysis of a phase change energy storage system for pulsed power dissipation," *IEEE Transactions on Components and Packaging Technologies*, vol. 27, no. 1, pp. 191–199, Mar. 2004, doi: 10.1109/TCAPT.2004.825758.
28. D. Pal and Y. K. Joshi, "Application of phase change materials to thermal control of electronic modules: A computational study," *Journal of Electronic Packaging*, vol. 119, no. 1, pp. 40–50, Mar. 1997, doi: 10.1115/1.2792199.

29. S. Himran, A. Suwono, and G. A. Mansoori, "Characterization of alkanes and paraffin waxes for application as phase change energy storage medium," *Energy Sources*, vol. 16, no. 1, pp. 117–128, Jan. 1994, doi: 10.1080/00908319408909065.
30. P. J. Shamberger and D. E. Forero, "Towards high energy density, high conductivity thermal energy storage composites," in *Proceedings of the Third ASME Micro/Nanoscale Heat & Mass Transfer International Conference*, Atlanta, GA, Mar. 3-6, 2012, pp. 545–555, doi: 10.1115/MNHMT2012-75039.
31. D. Rozanna, T. G. Chuah, A. Salmiah, T. S. Y. Choong, and M. Sa'ari, "Fatty acids as phase change materials (PCMs) for thermal energy storage: A review," *International Journal of Green Energy*, vol. 1, no. 4, pp. 495–513, Jan. 2005, doi: 10.1081/GE-200038722.
32. S. M. Hasnain, "Review on sustainable thermal energy storage technologies, Part I: Heat storage materials and techniques," *Energy Conversion and Management*, vol. 39, no. 11, pp. 1127–1138, Aug. 1998, doi: 10.1016/S0196-8904(98)00025-9.
33. A. A. Aydin and A. Aydin, "High-chain fatty acid esters of 1-hexadecanol for low temperature thermal energy storage with phase change materials," *Solar Energy Materials and Solar Cells*, vol. 96, pp. 93–100, Jan. 2012, doi: 10.1016/j.solmat.2011.09.013.
34. A. A. Aydin, "High-chain fatty acid esters of 1-octadecanol as novel organic phase change materials and mathematical correlations for estimating the thermal properties of higher fatty acid esters' homologous series," *Solar Energy Materials and Solar Cells*, vol. 113, pp. 44-51, Jun. 2013, doi: 10.1016/j.solmat.2013.01.024.
35. R. A. Talja and Y. H. Roos, "Phase and state transition effects on dielectric, mechanical, and thermal properties of polyols," *Thermochimica Acta*, vol. 380, no. 2, pp. 109–121, Dec. 2001, doi: 10.1016/S0040-6031(01)00664-5.
36. A. Kaizawa, N. Maruoka, A. Kawai, H. Kamano, T. Jozuka, T. Senda, N. Maruoka, N. Okinaka, and T. Akiyama, "Thermophysical and heat transfer properties of phase change material candidate for waste heat transportation system," *Heat and Mass Transfer*, vol. 44, no. 7, pp. 763–769, May 2008, doi: 10.1007/s00231-007-0311-2.
37. H. Kakiuchi, M. Yamazaki, M. Yabe, S. Chihara, Y. Terunuma, Y. Sakata, and T. Usami, "A study of erythritol as phase change material," in *Proceedings of the 2nd Workshop on PCMs and Chemical Reactions for Thermal Energy Storage*, International Energy Agency ECES Annex 10, Sofia, Bulgaria, April 11-13, 1998.
38. A. J. L. Jesus, S. C. C. Nunes, M. R. Silva, A. M. Beja, and J. S. Redinha, "Erythritol: Crystal growth from the melt," *International Journal of Pharmaceutics*, vol. 388, no. 1-2, pp. 129–135, Mar. 2010, doi: 10.1016/j.ijpharm.2009.12.043.
39. M. Kenisarin and K. Mahkamov, "Solar energy storage using phase change materials," *Renewable and Sustainable Energy Reviews*, vol. 11, no. 9, pp. 1913–1965, Dec. 2007, doi: 10.1016/j.rser.2006.05.005.
40. A. Shukla, D. Buddhi, S. D. Sharma, and K. Sagara, "Accelerated thermal cycle test of erythritol for the latent heat storage application," presented at the 4th *Workshop for the International Energy Agency, Energy Conservation through Energy Storage Implementing Agreement, Annex 17*, Indore, India, Apr. 21-24, 2003.
41. C. W. Ayers, "Thermal buffer heat sink for time-averaged operating conditions" in *FY2007 Annual Progress Report for the Advanced Power Electronics and Electric Machinery Program*, U.S. Department of Energy, Office of Energy Efficiency and Renewable Energy, Vehicle Technologies Office, Washington, DC, USA, pp. 14-21, Dec. 2007, doi: 10.2172/1216752.
42. H. Kakiuchi, S. Chihara, M. Yamazaki, and T. Isaki, "Heat storage material composition," US patent 5,785,885; Jul. 28 1998.

43. E. P. Ona, X. Zhang, K. Kyaw, F. Watanabe, H. Matsuda, H. Kakiuchi, M. Yabe and S. Chihara, "Relaxation of supercooling of erythritol for latent heat storage," *Journal of Chemical Engineering of Japan*, vol. 34, no. 3, pp. 376–382, 2001, doi: 10.1252/jcej.34.376.
44. N. R. Jankowski and F. P. McCluskey, "Electrical supercooling mitigation in erythritol," in *Proceedings of the 14th International Heat Transfer Conference*, vol. 7, Washington, DC, USA, Aug. 8-13, 2010, pp. 409-416, doi: 10.1115/IHTC14-22306.
45. H. Kohno, S. Maruyama, H. Yasaki, and T. Uraji, "Heat storage composition," European Union Patent Application EP0722997; Jan 10, 1996.
46. P. Zhang, Z. W. Ma, and R. Z. Wang, "An overview of phase change material slurries: MPCs and CHS," *Renewable and Sustainable Energy Reviews*, vol. 14, no. 2, pp. 598–614, Feb. 2010, doi: 10.1016/j.rser.2009.08.015.
47. D.K. Benson, J.D. Webb, R.W. Burrows, J.D.O. McFadden, and C. Christensen, "Materials research for passive solar systems: Solid-solid phase change materials," *U.S. Department of Energy, Solar Energy Research Institute*, Golden, CO, USA, Technical Report No.: 255-1828, Mar. 1985. doi: 10.2172/5923397.
48. D. Chandra, W.-M. Chien, V. Gandikotta, and D. W. Lindle, "Heat capacities of "plastic crystal" solid state thermal energy storage materials," *Zeitschrift für Physikalische Chemie*, vol. 216, no. 12, pp. 1433–1444, Dec. 2002, doi: 10.1524/zpch.2002.216.12.1433.
49. Q. Yan and C. Liang, "The thermal storage performance of monobasic, binary and triatomic polyalcohols systems," *Solar Energy*, vol. 82, no. 7, pp. 656–662, Jul. 2008, doi: 10.1016/j.solener.2007.12.008.
50. W. Li, D. Zhang, T. Zhang, T. Wang, D. Ruan, D. Xing, and H. Li, "Study of solid-solid phase change of $(n\text{-C}_n\text{H}_{2n+1}\text{NH}_3)_2\text{MCl}_4$ for thermal energy storage," *Thermochimica Acta*, vol. 326, no. 1-2, pp. 183–186, Feb. 1999, doi: 10.1016/S0040-6031(98)00497-3.
51. D.-H. He, Y.-Y. Di, Y. Yao, Y.-P. Liu, and W.-Y. Dan, "Crystal structure, low-temperature heat capacities, and thermodynamic properties of bis(dodecylammonium) tetrachlorocuprate $(\text{C}_{12}\text{H}_{28}\text{N})_2\text{CuCl}_4(\text{s})$," *Journal of Chemical & Engineering Data*, vol. 55, no. 12, pp. 5739-5744, Dec. 2010, doi: 10.1021/je100699g.
52. D.-H. He, Y.-Y. Di, Z.-C. Tan, F.-F. Yi, W.-Y. Dan, and Y.-P. Liu, "Crystal structures and thermochemistry on phase change materials $(n\text{-C}_n\text{H}_{2n+1}\text{NH}_3)_2\text{CuCl}_4(\text{s})$ ($n=14$ and 15)," *Solar Energy Materials and Solar Cells*, vol. 95, no. 10, pp. 2897-2906, Oct 2011, doi: 10.1016/j.solmat.2011.06.014.
53. D. Ruan, W. Li, L. He, and Q. Hu, "Phase diagrams of binary systems of alkylammonium tetrachlorometallates(II)," *Journal of Thermal Analysis*, vol. 45, no. 1, pp. 235–242, Jul. 1995, doi: 10.1007/BF02548685.
54. S. Steinert, W. Voigt, R. Glausch, and M. Neuschütz, "Thermal characteristics of solid-solid phase transitions in long-chain dialkyl ammonium salts," *Thermochimica Acta*, vol. 435, no. 1, pp. 28–33, Sep. 2005, doi: 10.1016/j.tca.2005.04.019.
55. M. Kubota, E. P. Ona, F. Watanabe, H. Matsuda, H. Hidaka, and H. Kakiuchi, "Studies on Phase Change Characteristics of Binary Mixtures of Erythritol and $\text{MgCl}\cdot 6\text{H}_2\text{O}$," *Journal of Chemical Engineering of Japan*, vol. 40, no. 1, pp. 80–84, 2007, doi: 10.1252/jcej.40.80.
56. G. A. Lane, *Solar Heat Storage: Latent Heat Materials. Volume I: Background and Scientific Principles*. Boca Raton, FL, USA: CRC Press, 1983.
57. F. C. Porisini, "Salt hydrates used for latent heat storage: Corrosion of metals and reliability of thermal performance," *Solar Energy*, vol. 41, no. 2, pp. 193–197, 1988, doi: 10.1016/0038-092X(88)90136-3.

58. E. Oró, L. Miró, C. Barreneche, I. Martorell, M. M. Farid, and L. F. Cabeza, "Corrosion of metal and polymer containers for use in PCM cold storage," *Applied Energy*, vol. 109, pp. 449–453, Sep. 2013, doi: 10.1016/j.apenergy.2012.10.049.
59. S. Guillot, A. Faik, A. Rakhmatullin, J. Lambert, E. Veron, P. Echegut, C. Bessada, N. Calvet, and X. Py, "Corrosion effects between molten salts and thermal storage material for concentrated solar power plants," *Applied Energy*, vol. 94, pp. 174–181, Jun. 2012, doi: 10.1016/j.apenergy.2011.12.057.
60. P. J. Shamberger and T. Reid, "Thermophysical properties of potassium fluoride tetrahydrate from (243 to 348) K," *Journal of Chemical & Engineering Data*, vol. 58, no. 2, pp. 294–300, Feb 2013, doi: 10.1021/jc300854w.
61. P. J. Shamberger and T. Reid, "Thermophysical properties of lithium nitrate trihydrate from (253 to 353) K," *Journal of Chemical & Engineering Data*, vol. 57, no. 5, pp. 1404–1411, May 2012, doi: 10.1021/jc3000469.
62. W. M. Haynes, Ed., *CRC Handbook of Chemistry and Physics*, 92nd ed., Boca Raton, FL, USA: CRC Press, 2011.
63. H. Michels and R. Pitz-Paal, "Cascaded latent heat storage for parabolic trough solar power plants," *Solar Energy*, vol. 81, no. 6, pp. 829–837, Jun. 2007, doi: 10.1016/j.solener.2006.09.008.
64. A. M. Gasanaliyev and B. Y. Gamataeva, "Heat-accumulating properties of melts," *Russian Chemical Reviews*, vol. 69, no. 2, pp. 179-186, Feb. 2000, doi: 10.1070/RC2000v069n02ABEH000490.
65. H. Ge, H. Li, S. Mei, and J. Liu, "Low melting point liquid metal as a new class of phase change material: An emerging frontier in energy area," *Renewable and Sustainable Energy Reviews*, vol. 21, pp. 331–346, May 2013, doi: 10.1016/j.rser.2013.01.008.
66. *Indalloy Specialty Alloys*, Indium Corporation, Clinton, NY. c2010 (accessed Jan 28, 2012) [Online]. Available: www.indium.com/products/alloysolderchart.php
67. K. Ma and J. Liu, "Liquid metal cooling in thermal management of computer chips," *Frontiers of Energy and Power Engineering in China*, vol. 1, no. 4, pp. 384–402, Oct. 2007, doi: 10.1007/s11708-007-0057-3.
68. Y. Fukuoka and M. Ishizuka, "Thermal analysis of a new high density package cooling technology using low melting point alloys," *Japanese Journal of Applied Physics*, vol. 30, no. 6, pp. 1313–1319, Jun. 1991, doi: 10.1143/JJAP.30.1313.
69. X.-Q. Wang, C. Yap, and A. S. Mujumdar, "A parametric study of phase change material (PCM)-based heat sinks," *International Journal of Thermal Sciences*, vol. 47, no. 8, pp. 1055–1068, Aug. 2008, doi: 10.1016/j.ijthermalsci.2007.07.016.
70. E. M. Alawadhi and H. J. Alqallaf, "Building roof with conical holes containing PCM to reduce the cooling load: Numerical study," *Energy Conversion and Management*, vol. 52, no. 8-9, pp. 2958–2964, Aug. 2011, doi: 10.1016/j.enconman.2011.04.004.
71. A. Stupar, U. Drogenik, and J. W. Kolar, "Optimization of phase change material heat sinks for low duty cycle high peak load power supplies," *IEEE Transactions on Components, Packaging and Manufacturing Technology*, vol. 2, no. 1, pp. 102–115, Jan. 2012, doi: 10.1109/tcpmt.2011.2168957.
72. L. Shao, A. Raghavan, G-H. Kim, L. Emurian, J. Rosen, M. C. Papaefthymiou, T. F. Wenisch, M. M. K. Martin, and K. P. Pipe, "Figure-of-merit for phase-change materials used in thermal management," *International Journal of Heat and Mass Transfer*, vol. 101, pp. 764–771, Oct. 2016, doi: 10.1016/j.ijheatmasstransfer.2016.05.040.

73. P. J. Shamberger, "Cooling capacity figure of merit for phase change materials," *Journal of Heat Transfer*, vol. 138, no. 2, Sep. 2015, doi: 10.1115/1.4031252.
74. A. M. Khudhair and M. M. Farid, "A review on energy conservation in building applications with thermal storage by latent heat using phase change materials," *Energy Conversion and Management*, vol. 45, no. 2, pp. 263–275, Jan. 2004, doi: 10.1016/S0196-8904(03)00131-6.
75. D. Zhou, C. Y. Zhao, and Y. Tian, "Review on thermal energy storage with phase change materials (PCMs) in building applications," *Applied Energy*, vol. 92, pp. 593–605, Apr. 2012, doi: 10.1016/j.apenergy.2011.08.025.
76. Kaizawa A, Kamano H, Kawai A, Jozuka T, Senda T, Maruoka N, N. Okinaka and T. Akiyama, "Technical feasibility study of waste heat transportation system using phase change material from industry to city," *ISIJ International*, vol. 48, no. 4, pp. 540–548, Apr. 2008, doi: 10.2355/isijinternational.48.540.
77. A. Artoni, N. J. Hewitt, and F. Polonara, "State of the art of thermal storage for demand-side management," *Applied Energy*, vol. 93, pp. 371–389, May 2012, doi: 10.1016/j.apenergy.2011.12.045.
78. M. J. Vesligaj and C. H. Amon, "Transient thermal management of temperature fluctuations during time varying workloads on portable electronics," *IEEE Transactions on Components and Packaging Technologies*, vol. 22, no. 4, pp. 541–550, Dec. 1999, doi: 10.1109/6144.814970.
79. S. Krishnan, S. V. Garimella, and S. S. Kang, "A novel hybrid heat sink using phase change materials for transient thermal management of electronics," *IEEE Transactions on Components and Packaging Technologies*, vol. 28, no. 2, pp. 281–289, Jun. 2005, doi: 10.1109/TCAPT.2005.848534.
80. D.-w. Yoo and Y. K. Joshi, "Energy efficient thermal management of electronic components using solid-liquid phase change materials," *IEEE Transactions on Device and Materials Reliability*, vol. 4, no. 4, pp. 641–649, Dec. 2004, doi: 10.1109/TDMR.2004.840854.
81. R. W. Johnson, J. L. Evans, P. Jacobsen, J. R. Thompson, and M. Christopher, "The changing automotive environment: high-temperature electronics," *IEEE Transactions on Electronics Packaging Manufacturing*, vol. 27, no. 3, pp. 164–176, Jul. 2004, doi: 10.1109/TEPM.2004.843109.
82. J. Kwon, J. Kim, E. Fallas, S. Pagerit and A. Rousseau, "Impact of Drive Cycles on PHEV Component Requirements," SAE Technical Paper 2008-01-1337, presented at the 2008 World Congress, Detroit, MI, USA, Apr. 14-17, 2008, doi: 10.4271/2008-01-1337.
83. J.-Y. Favez, M. Weilenmann, and J. Stilli, "Cold start extra emissions as a function of engine stop time: Evolution over the last 10 years," *Atmospheric Environment*, vol. 43, no. 5, pp. 996–1007, Feb. 2009, doi: 10.1016/j.atmosenv.2008.03.037.
84. J. Lee, H. Ohn, J.-Y. Choi, S. J. Kim, and B. Min, "Development of effective exhaust gas heat recovery system for a hybrid electric vehicle," SAE Technical Paper 2011-01-1171, presented at the 2011 SAE World Congress & Exhibition, Detroit, MI, USA, Apr. 12-14, 2011, doi: 10.4271/2011-01-1171.
85. L. Chiew, M. W. Clegg, R. H. Willats, G. Delplanque, and E. Barrieu, "Waste heat energy harvesting for improving vehicle efficiency," *SAE International Journal of Materials and Manufacturing*, vol. 4, no. 1, pp. 1211–1220, Apr. 2011, doi: 10.4271/2011-01-1167.
86. M. Gumus, "Reducing cold-start emission from internal combustion engines by means of thermal energy storage system," *Applied Thermal Engineering*, vol. 29, no. 4, pp. 652–660, Mar. 2009, doi: 10.1016/j.applthermaleng.2008.03.044.

87. M. Gumus and A. Ugurlu, "Application of phase change materials to pre-heating of evaporator and pressure regulator of a gaseous sequential injection system," *Applied Energy*, vol. 88, no. 12, pp. 4803–4810, Dec. 2011, doi: 10.1016/j.apenergy.2011.06.053.
88. P. Claudy, J.-M. L  toff  , B. Neff, and B. Damin, "Diesel fuels: determination of onset crystallization temperature, pour point and filter plugging point by differential scanning calorimetry. Correlation with standard test methods," *Fuel*, vol. 65, no. 6, pp. 861–864, Jun. 1986, doi: 10.1016/0016-2361(86)90082-7.
89. J. V  zquez, R. Palacios, and M. A. Sanz-Bobi, "Thermoelectric device to allow diesel engine start-up at cold weather conditions," in *Proceedings of the 7th European Workshop on Thermoelectrics*, Pamplona, Spain, Oct. 3-4, 2002, pp. 1–4.
90. S. D. Stouffer, A. B. Lewis, T. J. Whitney, and M. L. Drake, "Diesel engine cold start improvement using thermal management techniques," University of Dayton Research Institute, Dayton, OH, USA, US Army Research Laboratory, Army Research Office, Contract No.: DAA55–9801-0035, Final Report, Oct. 1, 2000, DTIC Accession No.: ADA384223, Available: www.dtic.mil/docs/citations/ADA384223
91. A. P. Simard and M. Lacroix, "Study of the thermal behavior of a latent heat cold storage unit operating under frosting conditions," *Energy Conversion and Management*, vol. 44, no. 10, pp. 1605–1624, Jun. 2003, doi: 10.1016/s0196-8904(02)00183-8.
92. E. Or  , L. Mir  , M. M. Farid, and L. F. Cabeza, "Thermal analysis of a low temperature storage unit using phase change materials without refrigeration system," *International Journal of Refrigeration*, vol. 35, no. 6, pp. 1709–1714, Sep. 2012, doi: 10.1016/j.ijrefrig.2012.05.004.
93. M. Liu, W. Saman, and F. Bruno, "Development of a novel refrigeration system for refrigerated trucks incorporating phase change material," *Applied Energy*, vol. 92, pp. 336-342, Apr. 2012, doi: 10.1016/j.apenergy.2011.10.015.
94. M. K. Sharma and D. Buddhi, "Performance studies of refrigerated van having PCM for generating off site refrigeration effect," *Journal of Pure and Applied Science & Technology*, vol. 3, no. 1, pp. 1–12, Jan. 2013 [Online]. Available: nlss.org.in/wp-content/uploads/2013/01/JPAST-Vol.-3_1_-Jan-13-1.pdf
95. M. Ahmed, O. Meade, and M. A. Medina, "Reducing heat transfer across the insulated walls of refrigerated truck trailers by the application of phase change materials," *Energy Conversion and Management*, vol. 51, no. 3, pp. 383–392, Mar. 2010, doi: 10.1016/j.enconman.2009.09.003.
96. C. Walgama, S. Fackrell, M. Karimi, A. Fartaj, and G. W. Rankin, "Passenger thermal comfort in vehicles - A review," *Proceedings of the Institution of Mechanical Engineers, Part D: Journal of Automobile Engineering*, vol. 220, no. 5, pp. 543–562, May 2006, doi: 10.1243/09544070D00705.
97. *DoD Design Criteria Standard - Human Engineering*, MIL-STD-1472F. US Department of Defense, Aug. 23, 1999, DTIC Accession No.: ADA550244, Available: www.dtic.mil/docs/citations/ADA550244
98. M. A. Lambert and B. J. Jones, "Automotive Adsorption Air Conditioner Powered by Exhaust Heat. Part 1: Conceptual and Embodiment Design," *Proceedings of the Institution of Mechanical Engineers, Part D: Journal of Automobile Engineering*, vol. 220, no. 7, pp. 959–972, Jul. 2006, doi: 10.1243/09544070JAUTO221.
99. K. J. Chua, S. K. Chou, W. M. Yang, and J. Yan, "Achieving better energy-efficient air conditioning – A review of technologies and strategies," *Applied Energy*, vol. 104, pp. 87-104, Apr. 2013, doi: 10.1016/j.apenergy.2012.10.037.

100. A. A. Al-Abidi, S. B. Mat, K. Sopian, M. Y. Sulaiman, C. H. Lim, and A. Th, "Review of thermal energy storage for air conditioning systems," *Renewable and Sustainable Energy Reviews*, vol. 16, no. 8, pp. 5802–5819, Oct. 2012, doi: 10.1016/j.rser.2012.05.030.
101. L. F. Cabeza, C. Castellón, M. Nogués, M. Medrano, R. Leppers, and O. Zubillaga, "Use of microencapsulated PCM in concrete walls for energy savings," *Energy and Buildings*, vol. 39, no. 2, pp. 113–119, Feb. 2007, doi: 10.1016/j.enbuild.2006.03.030.
102. A. Castell, I. Martorell, M. Medrano, G. Pérez, and L. F. Cabeza, "Experimental study of using PCM in brick constructive solutions for passive cooling," *Energy and Buildings*, vol. 42, no. 4, pp. 534–540, Apr. 2010, doi: 10.1016/j.enbuild.2009.10.022.
103. V. V. Tyagi and D. Buddhi, "PCM thermal storage in buildings: A state of art," *Renewable and Sustainable Energy Reviews*, vol. 11, no. 6, pp. 1146–1166, Aug. 2007, doi: 10.1016/j.rser.2005.10.002.
104. S. Bilodeau, "Thermal storage to optimize passenger shuttle cooling systems operating in severe conditions," SAE Technical Paper 2005-01-3638, presented at the *SAE Commercial Vehicle Engineering Congress*, Rosemont, IL, USA, Nov. 1-3, 2005, doi: 10.4271/2005-01-3638.
105. T. Craig, J. O'Brien, D. Polisoto, and N. Wolfe, "Integrated air conditioning evaporator with phase change material for thermal storage," presented at the *SAE Automotive Refrigerant and System Efficiency Symposium*, Scottsdale, AZ, USA, Jul. 13-15, 2010.
106. C. Kowsky, E. Wolfe, S. Chowdhury, D. Ghosh, and M. Wang, "PCM evaporator with thermosiphon," SAE Technical Paper 2014-01-0634, in *Proceedings of the SAE 2014 World Congress & Exhibition*, Detroit, MI, USA, Apr. 8-10, 2014, doi: 10.4271/2014-01-0634.
107. S. Shahidinejad, E. Bibeau, and S. Filizadeh, "Design and simulation of a thermal management system for plug-in electric vehicles in cold climates," SAE Technical Paper 2012-01-0118, in *Proceedings of the SAE 2012 World Congress & Exhibition*, Detroit, MI, USA, Apr. 24-26, 2012, doi: 10.4271/2012-01-0118.
108. R. A. Barnitt, A. D. Brooker, L. Ramroth, J. Rugh, and K. A. Smith, "Analysis of off-board powered thermal preconditioning in electric drive vehicles," in *Proceedings of the 25th World Battery, Hybrid and Fuel Cell Electric Vehicle Symposium and Exposition*, Shenzhen, China, Nov. 5-9, 2010, [Online]. Available: www.osti.gov/biblio/1001443
109. A. A. Manzela, S. M. Hanriot, L. Cabezas-Gómez, and J. R. Sodré, "Using engine exhaust gas as energy source for an absorption refrigeration system," *Applied Energy*, vol. 87, no. 4, pp. 1141–1148, Apr. 2010, doi: 10.1016/j.apenergy.2009.07.018.
110. M. A. Lambert and B. J. Jones, "Automotive Adsorption Air Conditioner Powered by Exhaust Heat. Part 2: Detailed Design and Analysis," *Proceedings of the Institution of Mechanical Engineers, Part D: Journal of Automobile Engineering*, vol. 220, no. 7, pp. 973–989, Jul. 2006, doi: 10.1243/09544070JAUTO222.
111. V. Pandiyarajan, M. C. Pandian, E. Malan, R. Velraj, and R. V. Seeniraj, "Experimental investigation on heat recovery from diesel engine exhaust using finned shell and tube heat exchanger and thermal storage system," *Applied Energy*, vol. 88, no. 1, pp. 77–87, Jan. 2011, doi: 10.1016/j.apenergy.2010.07.023.
112. J. Conover, H. Husted, J. MacBain, and H. McKee, "Logistics and capability implications of a Bradley fighting vehicle with a fuel cell auxiliary power unit," in SAE Technical Paper 2004-01-1586, in *Proceedings of the SAE World Congress & Exposition*, Detroit, MI, USA, Mar. 8-11, 2004, doi: 10.4271/2004-01-1586.
113. D. G. Pahinkar and V. Kumar, "Analytical model for human thermal comfort in passenger vehicles," *SAE International Journal of Materials and Manufacturing*, vol. 4, no. 1, pp. 204-215, Apr. 2011, doi: 10.4271/2011-01-0130.

114. J. Finn, D. J. Ewing, L. Ma, and J. Wagner, "Thermal protection of vehicle payloads using phase change materials and liquid cooling," in *Proceedings of the 2010 American Control Conference*, Baltimore, MD, USA, Jun 30- Jul 2, 2010, pp. 1204–1210, doi: 10.1109/ACC.2010.5531025.
115. E. Meissner and G. Richter, "The challenge to the automotive battery industry: the battery has to become an increasingly integrated component within the vehicle electric power system," *Journal of Power Sources*, vol. 144, no. 2, pp. 438–460, Jun. 2005, doi: 10.1016/j.jpowsour.2004.10.031.
116. K. C. Divya and J. Østergaard, "Battery energy storage technology for power systems—An overview," *Electric Power Systems Research*, vol. 79, no. 4, pp. 511–520, Apr. 2009, doi: 10.1016/j.epr.2008.09.017.
117. M. Alamgir and A. M. Sastry, "Efficient batteries for transportation applications," SAE Technical Paper 2008-21-0017, in *Proceedings of Convergence 2008*, Detroit, MI, USA, Oct. 20-22, 2008, [Online]. Available: papers.sae.org/2008-21-0017
118. A. A. Pesaran, T. Markel, H. S. Tataria, and D. Howell, "Battery requirements for plug-in hybrid electric vehicles -- Analysis and rationale," in *Proceedings of the 23rd International Electric Vehicle Symposium*, Anaheim, CA, USA, Dec. 2-5, 2007, [Online]. Available: www.osti.gov/biblio/959145
119. A. A. Pesaran AA, "Choices and requirements of batteries for EVs, HEVs, PHEVs," presented at the *CALSTART Webinar*, Golden, CO, USA, Apr. 21, 2011, [Online]. Available: www.osti.gov/biblio/1018087
120. Y. Gao and M. Ehsani, "Investigation of battery technologies for the Army's hybrid vehicle application," in *Proceedings of the IEEE 56th Vehicular Technology Conference*, vol. 3, Vancouver, Canada, Sep. 24-28, 2002, pp. 1505–1509, doi: 10.1109/VETEFCF.2002.1040467.
121. J. K. Heuvers, "Energy storage commonality military vs. commercial trucks," presented at the *Hybrid Truck Users Forum National Conference*, Atlanta, GA, USA, Oct. 27-29, 2009, DTIC Accession No.:ADA510660, Available: www.dtic.mil/docs/citations/ADA510660
122. R. Matthe, L. Turner, and H. Mettlach, "VOLTEC Battery System for Electric Vehicle with Extended Range," *SAE International Journal of Engines*, vol. 4, no. 1, pp. 1944–1962, Apr. 2011, doi: 10.4271/2011-01-1373.
123. A. A. Pesaran, A. Vlahinos, and S. D. Burch, "Thermal performance of EV and HEV battery modules and packs," in *Proceedings of the 14th International Electric Vehicle Symposium*, Orlando, FL, USA, Dec. 15-17, 1997, [Online]. Available: www.nrel.gov/docs/legosti/old/23527.pdf
124. S. M. Lukic, J. Cao, R. C. Bansal, F. Rodriguez, and A. Emadi, "Energy storage systems for automotive applications," *IEEE Transactions on Industrial Electronics*, vol. 55, no. 6, pp. 2258–2267, Jun. 2008, doi: 10.1109/TIE.2008.918390.
125. G.-H. Kim and A. A. Pesaran, "Analysis of heat dissipation in Li-Ion cells & modules for modeling of thermal runaway," presented at the *3rd International Symposium on Large Lithium Ion Battery Technology and Application*, Long Beach, CA, USA, May 11-17, 2007, [Online]. Available: www.osti.gov/biblio/913594
126. D. Lisbona and T. Snee, "A review of hazards associated with primary lithium and lithium-ion batteries," *Process Safety and Environmental Protection*, vol. 89, no. 6, pp. 434–442, Nov. 2011, doi: 10.1016/j.psep.2011.06.022.
127. Z. Rao and S. Wang, "A review of power battery thermal energy management," *Renewable and Sustainable Energy Reviews*, vol. 15, no. 9, pp. 4554–4571, Dec. 2011, doi: 10.1016/j.rser.2011.07.096.

128. A. A. Pesaran, "Battery thermal management in EVs and HEVs: Issues and solutions," in *Proceedings of the Advanced Automotive Battery Conference*, Las Vegas, NV, Feb. 6-8, 2001.
129. K. J. Kelly, M. Mihalic, and M. Zolot, "Battery usage and thermal performance of the Toyota Prius and Honda Insight during chassis dynamometer testing," in *Proceedings of the Seventeenth Annual Battery Conference on Applications and Advances*, Long Beach, CA, USA, Jan 15-18, 2002, pp. 247–252, doi: 10.1109/BCAA.2002.986408.
130. "Chevrolet Volt's revolutionary Voltec electric drive system delivers efficiency with performance," *General Motors Corporation*, Press Release, Oct. 10, 2010, [Online]. Available: media.gm.com/content/dam/Media/documents/US/Word/101010_volt_launch/10_Chevrolet_Volt_Propulsion.doc
131. R. Sabbah, R. Kizilel, J. R. Selman, and S. Al-Hallaj, "Active (air-cooled) vs. passive (phase change material) thermal management of high power lithium-ion packs: Limitation of temperature rise and uniformity of temperature distribution," *Journal of Power Sources*, vol. 182, no. 2, pp. 630–638, Aug. 2008, doi: 10.1016/j.jpowsour.2008.03.082.
132. S. M. Lukic, S. A. Khateeb, S. Al-Hallaj, J. R. Selman, and A. Emadi, "On the suitability of a new high-power lithium ion battery for hybrid electric vehicle applications," SAE Technical Paper 2003-01-2289, in *Proceedings of the Future Transportation Technology Conference & Exhibition*, Costa Mesa, CA, Jun 23-25, 2003, doi: 10.4271/2003-01-2289.
133. G.-H. Kim, J. Gonder, J. Lustbader, and A. Pesaran, "Thermal management of batteries in advanced vehicles using phase-change materials," *World Electric Vehicle Journal*, vol. 2, no. 2, pp. 134–147, Jun. 2008, doi: 10.3390/wevj2020134.
134. O. Gross and S. Clark, "Optimizing electric vehicle battery life through battery thermal management," *SAE International Journal of Engines*, vol. 4, no. 1, pp. 1928–1943, Jun. 2011, doi: 10.4271/2011-01-1370.
135. W. Lin and B. Sunden, "Vehicle cooling systems for reducing fuel consumption and carbon dioxide: literature survey," SAE Technical Paper 2010-01-1509, in *Proceedings of the Powertrains, Fuels & Lubricants Meeting*, Rio de Janeiro, Brazil, May 5-7, 2010, doi: 10.4271/2010-01-1509.
136. J. Hitchcock, "Ground vehicle power and mobility overview," presented for the US Army, TACOM Research Development and Engineering Center, May 30, 2007. DTIC Accession No.: ADA470330. Available: www.dtic.mil/docs/citations/ADA470330.
137. J. Vetrovec, "Engine cooling system with a heat load averaging capability," SAE Technical Paper 2008-01-1168, in *Proceedings of Convergence 2008*, Detroit, MI, USA, Oct. 20-22, 2008, doi: 10.4271/2008-01-1168.
138. K.-b. Kim, K.-w. Choi, Y.-j. Kim, K.-h. Lee, and K.-s. Lee, "Feasibility study on a novel cooling technique using a phase change material in an automotive engine," *Energy*, vol. 35, no. 1, pp. 478–484, Jan. 2010, doi: 10.1016/j.energy.2009.10.015.
139. D. Urciuoli, R. Green, A. Lelis, and D. Ibitayo, "Performance of a dual, 1200 V, 400 A, silicon-carbide power MOSFET module," in *Proceedings of the IEEE Energy Conversion Congress and Exposition*, Atlanta, GA, USA, Sep. 12-16, 2010, pp. 3303-3310, doi: 10.1109/ecce.2010.5618324.
140. K. Kelly, T. Abraham, K. Bennion, D. Bharathan, S. Narumanchi, and M. O'Keefe, "Assessment of thermal control technologies for cooling electric vehicle power electronics," in *Proceedings of the 23rd International Electric Vehicle Symposium*, Anaheim, CA, USA, Dec. 2-5, 2007, [Online]. Available: www.osti.gov/biblio/922552
141. F. P. McCluskey, R. Grzybowski, and T. Podlesak, *High temperature electronics*. New York, NY: CRC Press, 1997.

142. L. D. Stevanovic, K. S. Matocha, P. A. Losee, J. S. Glaser, J. J. Nasadoski, and S. D. Arthur, "Recent advances in silicon carbide MOSFET power devices," in *Proceedings of the Twenty-Fifth Annual IEEE Applied Power Electronics Conference and Exposition*, Palm Springs, CA, USA, Feb. 21-25, 2010, pp. 401–407, doi: 10.1109/APEC.2010.5433640.
143. L. Boteler, D. Urciuoli, G. Ovrebo, D. Ibitayo, and R. Green, "Thermal performance of a dual 1.2 kV, 400A silicon-carbide MOSFET power module," in *Proceedings of the 26th Annual IEEE Semiconductor Thermal Measurement and Management Symposium*, Santa Clara, CA, USA, Feb 21-25, 2010, pp. 170–175, doi: 10.1109/stherm.2010.5444297.
144. N. R. Jankowski, L. Everhart, B. R. Geil, C. W. Tipton, J. Chaney, T. Heil, W. Zimbeck, "Stereolithographically fabricated aluminum nitride microchannel substrates for integrated power electronics cooling," in *Proceedings of the 11th Intersociety Conference on Thermal and Thermomechanical Phenomena in Electronic Systems*, Orlando, FL, USA, May 28-31, 2008, pp. 180-188, doi: 10.1109/ITHERM.2008.4544269.
145. D. J. Sharar, N. R. Jankowski, and B. Morgan, "Thermal performance of a direct-bond-copper aluminum nitride manifold-microchannel cooler," in *Proceedings of the Semiconductor Thermal Measurement and Management Symposium*, Santa Clara, CA, USA, Feb. 21-25, 2010, pp. 68–73, doi: 10.1109/STHERM.2010.5444313.
146. L. Boteler, N. Jankowski, B. Geil, and P. McCluskey, "A micromachined manifold microchannel cooler," in *Proceedings of the ASME International Mechanical Engineering Congress and Exposition, vol. 5: Electronics and Photonics*, Lake Buena Vista, FL, USA, Nov. 13-19, 2009, pp. 61–68, doi: 10.1115/IMECE2009-11780
147. N. R. Jankowski and F. P. McCluskey, "Modeling transient thermal response of pulsed power electronic packages," in *Proceedings of the IEEE Pulsed Power Conference*, Washington, DC, USA, Jun. 28-Jul. 2, 2009, pp. 820–825, doi: 10.1109/PPC.2009.5386368.
148. L. Meysenc, M. Jylhakallio, and P. Barbosa, "Power electronics cooling effectiveness versus thermal inertia," *IEEE Transactions on Power Electronics*, vol. 20, no. 3, pp. 687–693, May 2005, doi: 10.1109/TPEL.2005.846548.
149. M. L. Buller, "Thermal Transients in Electronic Packages," *IEEE Transactions on Components, Hybrids, and Manufacturing Technology*, vol. 3, no. 4, pp. 588–594, Dec. 1980, doi: 10.1109/TCHMT.1980.1135667.
150. A. G. Evans, M. Y. He, J. W. Hutchinson, and M. Shaw, "Temperature distribution in advanced power electronics systems and the effect of phase change materials on temperature suppression during power pulses," *Journal of Electronic Packaging*, vol. 123, no. 3, pp. 211–217, Sep. 2000, doi: 10.1115/1.1370376.
151. N. R. Jankowski, B. C. Morgan, and F. P. McCluskey, "Design and Fabrication of a Substrate Integrated Phase Change Thermal Buffer Heat Sink," in *Proceedings of the ASME International Mechanical Engineering Congress and Exposition, vol. 5: Electronics and Photonics*, Lake Buena Vista, FL, USA, Nov. 13-19, 2009, pp. 75–84, doi: 10.1115/IMECE2009-12713.
152. E. Korin, R. Reshef, D. Tshernichovesky, and E. Sher, "Improving cold-start functioning of catalytic converters by using phase-change materials," SAE Technical Paper 980671, in *Proceedings of the 1998 SAE International Congress & Exposition*, Detroit, MI, USA, Feb. 23-26, 1998, doi: 10.4271/980671.
153. P. M. Laing, "Development of an alternator-powered electrically-heated catalyst system," SAE Technical Paper 941042, in *Proceedings of the 1994 SAE International Congress & Exposition*, Detroit, MI, USA, Feb. 28-Mar 3, 1994, doi: 10.4271/941042.
154. S. D. Burch, T. F. Potter, M. A. Keyser, M. J. Brady, and K. F. Michaels, "Reducing cold-start emissions by catalytic converter thermal management," SAE Technical Paper 950409,

- in *Proceedings of the 1995 SAE International Congress and Exposition*, Detroit, MI, USA, Feb 27-Mar 2, 1995, doi: 10.4271/950409, Available: www.osti.gov/biblio/27052
155. S. D. Burch, M. A. Keyser, C. P. Colucci, T. F. Potter, D. K. Benson, and J. P. Biel, "Applications and benefits of catalytic converter thermal management," SAE Technical Paper 961134, in *Proceedings of the SAE International Spring Fuels & Lubricants Meeting*, Dearborn, MI, USA, May 6-8, 1996, doi: 10.2172/266686.
 156. "Federal test procedure review project: Preliminary technical report," US Environmental Protection Agency, Office of Air & Radiation, Technical Report No.: EPA/420-R-93-007, May 1993, [Online]. Available: nepis.epa.gov/Exe/ZyPURL.cgi?Dockey=00000G9Q.txt
 157. T. V. Johnson, "Diesel emission control in review," SAE Technical Paper 2006-01-0030, in *Proceedings of the 2006 SAE World Congress & Exposition*, Detroit, MI, USA, Apr. 3-6, 2006, doi: 10.4271/2006-01-0030
 158. T. J. Hendricks and J. A. Lustbader, "Advanced thermoelectric power system investigations for light-duty and heavy duty applications. I," in *Proceedings of the International Conference on Thermoelectrics*, Long Beach, CA, USA, Aug. 25-29, 2002, pp. 381–386, doi: 10.1109/ICT.2002.1190343.
 159. K. Smith and M. Thornton, "Feasibility of thermoelectrics for waste heat recovery in conventional vehicles," *United States Department of Energy, National Renewable Energy Laboratory*, Golden, CO, USA, Technical Report No.: NREL/TP-540-44247. Contract No.: AC36-99-GO10337, Apr 1, 2009, doi: 10.2172/951806.
 160. J. Fu, J. Liu, R. Feng, Y. Yang, L. Wang, and Y. Wang, "Energy and exergy analysis on gasoline engine based on mapping characteristics experiment," *Applied Energy*, vol. 102, pp. 622–630, Feb. 2013, doi: 10.1016/j.apenergy.2012.08.013.
 161. Z. Dashevsky, D. Kaftori, and D. Rabinovich, "High efficiency thermoelectric unit within an autonomous solar energy converter," in *Proceedings of the Seventeenth International Conference on Thermoelectrics*, Nagoya, Japan, May 24-28, 1998, pp. 531–534, doi: 10.1109/ICT.1998.740434.
 162. T. S. Saitoh and A. Hoshi, "Proposed solar Rankine cycle system with phase change steam accumulator and CPC solar collector," in *Proceedings of the 37th Intersociety Energy Conversion Engineering Conference*, Washington, DC, USA, Jul 29-31, 2002, pp. 725–730, doi: 10.1109/IECEC.2002.1392137.
 163. M. Medrano, A. Gil, I. Martorell, X. Potau, and L. F. Cabeza, "State of the art on high-temperature thermal energy storage for power generation. Part 2 - Case studies," *Renewable and Sustainable Energy Reviews*, vol. 14, no. 1, pp. 56–72, Jan. 2010, doi: 10.1016/j.rser.2009.07.036.
 164. D. T. Crane and J. W. LaGrandeur, "Progress Report on BSST-Led US Department of Energy Automotive Waste Heat Recovery Program," *Journal of Electronic Materials*, vol. 39, no. 9, pp. 2142–2148, Nov. 2009, doi: 10.1007/s11664-009-0991-0.
 165. C. B. Vining, "An inconvenient truth about thermoelectrics," *Nature Materials*, vol. 8, no. 2, pp. 83–85, Feb. 2009, doi: 10.1038/nmat2361.
 166. A. D. LaLonde, Y. Pei, H. Wang, and G. J. Snyder, "Lead telluride alloy thermoelectrics," *Materials Today*, vol. 14, no. 11, pp. 526–532, Nov. 2011, doi: 10.1016/S1369-7021(11)70278-4.
 167. W. M. S. R. Weerasinghe, R. K. Stobart, and S. M. Hounsham, "Thermal efficiency improvement in high output diesel engines a comparison of a Rankine cycle with turbo-compounding," *Applied Thermal Engineering*, vol. 30, no. 14-15, pp. 2253–2256, Oct. 2010, doi: 10.1016/j.applthermaleng.2010.04.028.

168. E. W. Miller, T. J. Hendricks, and R. B. Peterson, "Modeling energy recovery using thermoelectric conversion integrated with an organic Rankine bottoming cycle," *Journal of Electronic Materials*, vol. 38, no. 7, pp. 1206–1213, Mar. 2009, doi: 10.1007/s11664-009-0743-1.
169. T. A. Horst, H.-S. Rottengruber, M. Seifert, and J. Ringler, "Dynamic heat exchanger model for performance prediction and control system design of automotive waste heat recovery systems," *Applied Energy*, vol. 105, pp. 293–303, 2013-05, doi: 10.1016/j.apenergy.2012.12.060.
170. C. Sprouse and C. Depcik, "Review of organic Rankine cycles for internal combustion engine exhaust waste heat recovery," *Applied Thermal Engineering*, vol. 51, no. 1-2, pp. 711–722, 2013-03, doi: 10.1016/j.applthermaleng.2012.10.017.
171. N. Gopal, R. Subbarao, V. Pandiyarajan, and R. Velraj, "Thermodynamic analysis of a diesel engine integrated with a PCM based energy storage system," *International Journal of Thermodynamics*, vol. 13, no. 1, pp. 15–21, Mar. 2010 [Online]. Available: dergipark.org.tr/en/pub/ijot/issue/5775/76804
172. N. R. Jankowski, L. Everhart, B. Morgan, B. Geil, and P. McCluskey, "Comparing microchannel technologies to minimize the thermal stack and improve thermal performance in hybrid electric vehicles," in *Proceedings of the IEEE Vehicle Power and Propulsion Conference*, Arlington, TX, USA, Sep 9-12, 2007, pp. 124–130, doi: 10.1109/vppc.2007.4544111.
173. C. Buttay, "Cross section of a classical Vertical Diffused Power MOSFET (VDMOS)," (accessed Dec. 17, 2014), [Online]. Available: commons.wikimedia.org/wiki/User:CyrilB_commonswiki/Gallery
174. C. Buttay, "Contributions to the on-resistance of a power MOSFET," (accessed Dec. 17, 2014), [Online]. Available: commons.wikimedia.org/wiki/User:CyrilB_commonswiki/Gallery
175. C. Gillot, C. Schaeffer, C. Massit, and L. Meysenc, "Double-sided cooling for high power IGBT modules using flip chip technology," *IEEE Transactions on Components and Packaging Technologies*, vol. 24, no. 4, pp. 698–704, Dec. 2001, doi: 10.1109/6144.974963.
176. L. A. Pipes, "Matrix analysis of heat transfer problems," *Journal of the Franklin Institute*, vol. 263, no. 3, pp. 195–206, 1957, doi: 10.1016/0016-0032(57)90927-4.
177. P. R. Strickland, "The thermal equivalent circuit of a transistor," *IBM Journal of Research and Development*, vol. 3, no. 1, pp. 35–45, Jan. 1959, doi: 10.1147/rd.31.0035.
178. M. O'Keefe and K. Bennion, "A comparison of hybrid electric vehicle power electronics cooling options," in *Proceedings of the IEEE Vehicle Power and Propulsion Conference*, Arlington, TX, USA, Sep 9-12, 2007, pp. 116–123, doi: 10.1109/VPPC.2007.4544110
179. E. A. Browne, G. J. Michna, M. K. Jensen, and Y. Peles, "Experimental investigation of single-phase microjet array impingement cooling," in *Proceedings of the ASME Summer Heat Transfer Conference*, vol. 1, San Francisco, CA, USA, Jul. 19-23, 2009, doi: 10.1115/ht2009-88213.
180. S. G. Leslie, "Cooling options and challenges of high power semiconductor modules," *Electronics Cooling*, Nov. 2006, [Online]. Available: www.electronics-cooling.com/2006/11/cooling-options-and-challenges-of-high-power-semiconductor-modules/
181. J. M. Fusaro, G. L. Romero, P. Rodriguez, and J. L. Martinez, "Thermal characterization of DBC and MMC stacks for power modules," in *Conference Record of the 1996 IEEE Industry Applications Conference*, San Diego, CA, USA, Oct. 6-10, 1996, pp. 1411–1417, doi: 10.1109/ias.1996.559250.

182. D. B. Tuckerman and R. F. W. Pease, "High-performance heat sinking for VLSI," *IEEE Electron Device Letters*, vol. 2, no. 5, pp. 126–129, May 1981, doi: 10.1109/edl.1981.25367.
183. G. Hestroni, A. Mosyak, and Z. Segal, "Nonuniform temperature distribution in electronic devices cooled by flow in parallel microchannels," *IEEE Transactions on Components and Packaging Technologies*, vol. 24, no. 1, pp. 16–23, Mar. 2001, doi: 10.1109/6144.910797.
184. G. Hestroni, A. Mosyak, Z. Segal, and G. Ziskind, "A uniform temperature heat sink for cooling of electronic devices," *International Journal of Heat and Mass Transfer*, vol. 45, no. 16, pp. 3275–3286, Jul. 2002, doi: 10.1016/s0017-9310(02)00048-0.
185. E. G. Colgan et al., "A Practical Implementation of Silicon Microchannel Coolers for High Power Chips," *IEEE Transactions on Components and Packaging Technologies*, vol. 30, no. 2, pp. 218–225, Jun. 2007, doi: 10.1109/tcapt.2007.897977.
186. Y. Chen and P. Cheng, "Heat transfer and pressure drop in fractal tree-like microchannel nets," *International Journal of Heat and Mass Transfer*, vol. 45, no. 13, pp. 2643–2648, Jun. 2002, doi: 10.1016/s0017-9310(02)00013-3.
187. G. M. Harpole and J. E. Eninger, "Micro-channel heat exchanger optimization," in *Proceedings of the Seventh IEEE Semiconductor Thermal Measurement and Management Symposium*, Phoenix, AZ, USA, Feb. 12-14, 1991, pp. 59–63, doi: 10.1109/stherm.1991.152913.
188. D. Copeland, H. Takahira, W. Nakayama, and B.-C. Pak, "Manifold microchannel heat sinks: Theory and experiments," *Thermal Science & Engineering*, vol. 3, no. 2, pp. 9–15, 1995.
189. R. W. Knight, D. J. Hall, J. S. Goodling, and R. C. Jaeger, "Heat sink optimization with application to microchannels," *IEEE Transactions on Components, Hybrids, and Manufacturing Technology*, vol. 15, no. 5, pp. 832–842, Oct. 1992, doi: 10.1109/33.180049.
190. J. H. Ryu, D. H. Choi, and S. J. Kim, "Three-dimensional numerical optimization of a manifold microchannel heat sink," *International Journal of Heat and Mass Transfer*, vol. 46, no. 9, pp. 1553–1562, Apr. 2003, doi: 10.1016/s0017-9310(02)00443-x.
191. L. Boteler, N. Jankowski, P. McCluskey, and B. Morgan, "Numerical investigation and sensitivity analysis of manifold microchannel coolers," *International Journal of Heat and Mass Transfer*, vol. 55, no. 25-26, pp. 7698–7708, Dec. 2012, doi: 10.1016/j.ijheatmasstransfer.2012.07.073.
192. K. Sienski, R. Eden, and D. Schaefer, "3-D electronic interconnect packaging," in *Proceedings of the 1996 IEEE Aerospace Applications Conference*, Aspen, CO, USA, Feb. 02, 1996, doi: 10.1109/aero.1996.495896.
193. T. Ruemenapp and D. Peier, "Dielectric breakdown in aluminium nitride," in *Proceedings of the 11th International Symposium on High-Voltage Engineering*, vol. 4, London, UK, Aug. 23-27, 1999, pp. 373–376, doi: 10.1049/cp:19990870.
194. M. Pecht, R. Agarwal, F. P. McCluskey, T. J. Dishongh, S. Javadpour, and R. Mahajan, *Electronic packaging materials and their properties*, Boca Raton, FL, USA: CRC Press, 1998.
195. F. A. Khan, L. Zhou, V. Kumar, I. Adesida, and R. Okojie, "High rate etching of AlN using $\text{BCl}_3\text{Cl}_2\text{Ar}$ inductively coupled plasma," *Materials Science and Engineering: B*, vol. 95, no. 1, pp. 51–54, Jul. 2002, doi: 10.1016/s0921-5107(02)00160-5.
196. T. E. Salem, D. Ibitayo, and B. R. Geil, "Validation of infrared camera thermal measurements on high-voltage power electronic components," *IEEE Transactions on Instrumentation and Measurement*, vol. 56, no. 5, pp. 1973–1978, Oct. 2007, doi: 10.1109/tim.2007.903590.

197. P.J. Linstrom and W.G. Mallard, eds., *NIST Chemistry WebBook, NIST Standard Reference Database Number 69*, National Institute of Standards and Technology, Gaithersburg MD, USA, (accessed Jan. 19, 2015) [Online]. Available: webbook.nist.gov
198. R. K. Shah and A. L. London, *Laminar Flow Forced Convection in Ducts, Advanced Heat Transfer, Supplement 1*, New York, NY: Academic Press, 1978.
199. M. E. Steinke and S. G. Kandlikar, "Single-phase liquid friction factors in microchannels," *International Journal of Thermal Sciences*, vol. 45, no. 11, pp. 1073–1083, Nov. 2006, doi: 10.1016/j.ijthermalsci.2006.01.016.
200. Y. S. Muzychka and M. M. Yovanovich, "Pressure drop in laminar developing flow in noncircular ducts: A scaling and modeling approach," *Journal of Fluids Engineering*, vol. 131, no. 11, p. 111105, Nov. 2009, doi: 10.1115/1.4000377.
201. R. W. Miller and L. S. Han, "Pressure losses for laminar flow in the entrance region of ducts of rectangular and equilateral triangular cross section," *Journal of Applied Mechanics*, vol. 38, no. 4, pp. 1083–1087, Dec. 1971, doi: 10.1115/1.3408927.
202. S. Narumanchi, M. Mihalic, K. Kelly, and G. Eesley, "Thermal interface materials for power electronics applications," in *Proceedings of the 11th Intersociety Conference on Thermal and Thermomechanical Phenomena in Electronic Systems*, Orlando, FL, USA, May 28-31, 2008, pp. 395–404, doi: 10.1109/ITHERM.2008.4544297.
203. M. Kristiansen, "Pulsed power applications," in *Proceedings of the 9th IEEE International Pulsed Power Conference*, Albuquerque, NM, USA, 1993, pp. 6–10, doi: 10.1109/ppc.1993.512864.
204. H. Akiyama, S. Sakai, T. Sakugawa, and T. Namihira, "Environmental applications of repetitive pulsed power," *IEEE Transactions on Dielectrics and Electrical Insulation*, vol. 14, no. 4, pp. 825–833, Aug. 2007, doi: 10.1109/tdei.2007.4286513.
205. L. E. Kingsley, M. Weiner, A. Kim, R. Pastore, R. J. Youmans, and H. Singh, "Ultrafast switching at the U.S. Army Pulse Power Center," in *Ultra-Wideband, Short-Pulse Electromagnetics 2*, Boston, MA, USA: Springer, pp. 85–96, 1995.
206. I. R. McNab, "Developments in battlefield power technology," in *Digest of Technical Papers of the 12th IEEE International Pulsed Power Conference*, Monterey, CA, USA, Jun. 27-30, 1999, pp. 375–378, doi: 10.1109/ppc.1999.825485.
207. D. J. Lim and S. H. Pulko, "Characterisation of heat spreader materials for pulsed IGBT operation," *IET Circuits, Devices & Systems*, vol. 1, no. 2, pp. 126–136, Apr. 2007, doi: 10.1049/iet-cds:20050227.
208. P. Asimakopoulos, K. Papastergiou, T. Thiringer, and M. Bongiorno, "Heat sink design considerations in medium power electronic applications with long power cycles," in *Proceedings of the 17th European Conference on Power Electronics and Applications*, Geneva, Switzerland, Sep. 8-10, 2015, doi: 10.1109/epe.2015.730915.
209. Y. Wang, S. Jones, A. Dai, and G. Liu, "Reliability enhancement by integrated liquid cooling in power IGBT modules for hybrid and electric vehicles," *Microelectronics Reliability*, vol. 54, no. 9-10, pp. 1911-1915, Sep.-Oct. 2014, doi: 10.1016/j.microrel.2014.07.037.
210. X. Cao, G.-Q. Lu, and K. D. T. Ngo, "Planar Power Module With Low Thermal Impedance and Low Thermomechanical Stress," *IEEE Transactions on Components, Packaging and Manufacturing Technology*, vol. 2, no. 8, pp. 1247-1259, Aug. 2012, doi: 10.1109/tcpmt.2012.2196799.
211. C. Buttay, J. Rashid, C. M. Johnson, P. Ireland, F. Udrea, G. Amaratunga, and R. K. Malhan, "High performance cooling system for automotive inverters," in *Proceedings of the*

- 2007 *European Conference on Power Electronics and Applications*, Aalborg, Denmark, Sep. 2-5, 2007, doi: 10.1109/epe.2007.4417363.
212. L. P. Cao, J. P. Krusius, T. S. Fisher, and C. T. Avedisian, "Transient energy management strategies for portable systems," in *Proceedings of the 45th Electronic Components and Technology Conference*, Las Vegas, NV, USA, May 21-24, 1995, pp. 1161–1165, doi: 10.1109/ectc.1995.517837.
213. B. Yang, "A distributed transfer function method for heat conduction problems in multilayer composites," *Numerical Heat Transfer, Part B: Fundamentals*, vol. 54, no. 4, pp. 314–337, 2008, doi: 10.1080/10407790802359038.
214. M. Pedram and S. Nazarian, "Thermal modeling, analysis, and management in VLSI circuits: principles and methods," *Proceedings of the IEEE*, vol. 94, no. 8, pp. 1487–1501, Aug. 2006, doi: 10.1109/jproc.2006.879797.
215. S. V. Garimella, A. S. Fleischer, J. Y. Murthy, A. Keshavarzi, R. Prasher, C. Patel, S. H. Bhavnani, R. Venkatasubramanian, R. Mahajan, Y. Joshi, B. Sammakia, B. A. Myers, L. Chorosinski, M. Baelmans, P. Sathyamurthy, and P. E. Raad, "Thermal Challenges in Next-Generation Electronic Systems," *IEEE Transactions on Components and Packaging Technologies*, vol. 31, no. 4, pp. 801–815, Dec. 2008, doi: 10.1109/tcapt.2008.2001197.
216. S. Singh, A. Bansal, M. Meterelliyoz, J. H. Choi, K. Roy, and J. Y. Murthy, "Compact thermal models for thermally aware design of VLSI circuits," in *Proceedings of the 10th Intersociety Conference on Thermal and Thermomechanical Phenomena in Electronics Systems*, San Diego, CA, USA, May 30 – Jun 2, 2006, pp. 671–677, doi: 10.1109/itherm.2006.1645410.
217. A. Bar-Cohen, A. Srivastava, and B. Shi, "Thermo-electrical co-design of three-dimensional integrated circuits: Challenges and opportunities," *Computational Thermal Sciences*, vol. 5, no. 6, pp. 441–458, 2013, doi: 10.1615/computthermalsci.2013007643.
218. R. Azar, F. Udrea, W. T. Ng, F. Dawson, W. Findlay, P. Waing and G. Amaratunga, "Advanced electrothermal Spice modelling of large power IGBTs," *IEE Proceedings - Circuits, Devices and Systems*, vol. 151, no. 3, pp. 249–253, Jun. 2004, doi: 10.1049/ip-cds:20040448.
219. J. T. Hsu and L. Vu-Quoc, "A rational formulation of thermal circuit models for electrothermal simulation. II. Model reduction techniques [power electronic systems]," *IEEE Transactions on Circuits and Systems I: Fundamental Theory and Applications*, vol. 43, no. 9, pp. 733–744, Sep. 1996, doi: 10.1109/81.536743.
220. A. Ammous, S. Ghedira, B. Allard, H. Morel, and D. Renault, "Choosing a thermal model for electrothermal simulation of power semiconductor devices," *IEEE Transactions on Power Electronics*, vol. 14, no. 2, pp. 300–307, Mar. 1999, doi: 10.1109/63.750183.
221. J. N. Reddy, *Energy Principles and Variational Methods in Applied Mechanics, 3rd ed.* Hoboken, NJ, USA: John Wiley & Sons, Inc., 2002
222. J. T. Hsu and L. Vu-Quoc, "A rational formulation of thermal circuit models for electrothermal simulation. I. Finite element method [power electronic systems]," *IEEE Transactions on Circuits and Systems I: Fundamental Theory and Applications*, vol. 43, no. 9, pp. 721–732, Sep. 1996, doi: 10.1109/81.536742.
223. P. M. Gresho and R. L. Lee, "Don't suppress the wiggles – They're telling you something!" *Computers & Fluids*, vol. 9, no. 2, pp. 223–253, Jun. 1981, doi: 10.1016/0045-7930(81)90026-8.
224. "The NASTRAN Theoretical Manual," *National Aeronautics and Space Administration*, NASA Special Publication No: NASA-SP-221(06), Jan. 1981, hdl: 2060/19840010609.

225. I. Harari, "Stability of semidiscrete formulations for parabolic problems at small time steps," *Computer Methods in Applied Mechanics and Engineering*, vol. 193, no. 15-16, pp. 1491-1516, Apr. 2004, doi: 10.1016/j.cma.2003.12.035.
226. J. S. Archer, "Consistent matrix formulations for structural analysis using finite-element techniques," *AIAA Journal*, vol. 3, no. 10, pp. 1910-1918, Oct. 1965, doi: 10.2514/3.3279.
227. D. J. Benson, "Computational methods in Lagrangian and Eulerian hydrocodes," *Computer Methods in Applied Mechanics and Engineering*, vol. 99, no. 2-3, pp. 235-394, Sep. 1992, doi: 10.1016/0045-7825(92)90042-i.
228. E. Rank, C. Katz, and H. Werner, "On the importance of the discrete maximum principle in transient analysis using finite element methods," *International Journal for Numerical Methods in Engineering*, vol. 19, no. 12, pp. 1771-1782, Dec. 1983, doi: 10.1002/nme.1620191205.
229. H. R. Thomas and Z. Zhou, "Minimum time-step size for diffusion problem in FEM analysis," *International Journal for Numerical Methods in Engineering*, vol. 40, no. 20, pp. 3865-3880, Dec. 1998, doi: 10.1002/(sici)1097-0207(19971030)40:20<3865::aid-nme246>3.0.co;2-c.
230. R. Madoliat and A. Ghasemi, "Inverse finite element formulations for transient heat conduction problems," *Heat and Mass Transfer*, vol. 44, no. 5, pp. 569-577, Mar. 2008, doi: 10.1007/s00231-007-0270-7.
231. K.-o. Kim, "A review of mass matrices for eigenproblems," *Computers & Structures*, vol. 46, no. 6, pp. 1041-1048, Mar. 1993, doi: 10.1016/0045-7949(93)90090-z.
232. C. Stavrinidis, J. Clinckemaillie, and J. Dubois, "New concepts for finite-element mass matrix formulations," *AIAA Journal*, vol. 27, no. 9, pp. 1249-1255, Sep. 1989, doi: 10.2514/3.10252.
233. B. Okorn, S. Hrabar, and I. Krois, "Investigation of basic physics of non-Foster negative capacitance in time domain," in *Proceedings of ELMAR-2011*, Zadar, Croatia, Sep. 11-14, 2011, pp. 373-376 [Online]. Available: ieeexplore.ieee.org/document/6044254
234. V. Mowery, "On hypergeometric functions in iterated networks," *IEEE Transactions on Circuit Theory*, vol. 11, no. 2, pp. 232-247, Jun. 1964, doi: 10.1109/TCT.1964.1082275.
235. R. Madoliat and A. Ghasemi, "Operating Regions for Discrete Models Based on Physical Reality of Diffusion Problems," *Journal of Thermophysics and Heat Transfer*, vol. 21, no. 1, pp. 158-165, Jan.-Mar. 2007, doi: 10.2514/1.24658.
236. D. Duffy, *Transform methods for solving partial differential equations*. Boca Raton, FL, USA: CRC Press, 1994.
237. J. W. Nilsson and S. A. Riedel, *Electric Circuits, 5th Ed.* Boston, MA, USA: Addison-Wesley, 1996
238. W. C. Elmore, "The transient response of damped linear networks with particular regard to wideband amplifiers," *Journal of Applied Physics*, vol. 19, no. 1, pp. 55-63, Jan. 1948, doi: 10.1063/1.1697872.
239. R. Gupta, B. Tutuianu, and L. T. Pileggi, "The Elmore delay as a bound for RC trees with generalized input signals," *IEEE Transactions on Computer-Aided Design of Integrated Circuits and Systems*, vol. 16, no. 1, pp. 95-104, Jan. 1997, doi: 10.1109/43.559334.
240. C.-J. Shi, "Analysis, sensitivity and macromodelling of the Elmore delay in linear networks for performance-driven VLSI design," *International Journal of Electronics*, vol. 75, no. 3, pp. 467-484, Sep. 1993, doi: 10.1080/00207219308907125.

241. J. Rubinstein, P. Penfield, and M. A. Horowitz, "Signal delay in RC tree networks," *IEEE Transactions on Computer-Aided Design of Integrated Circuits and Systems*, vol. 2, no. 3, pp. 202–211, Jul. 1983, doi: 10.1109/tcad.1983.1270037.
242. *LTspice XVII* (software), Analog Devices, Inc., 2020, [Online] Available: www.analog.com/en/design-center/design-tools-and-calculators/ltspice-simulator.html
243. *Undocumented LTspice*, LTWiki.org (web site), Nov. 24, 2019. (accessed Jul. 24, 2020) [Online]. Available: ltwiki.org/index.php?title=Undocumented_LTspice&oldid=2124
244. P. McCluskey, "Reliability of power electronics under thermal loading," in *Proceedings of the 7th International Conference on Integrated Power Electronics Systems*, Nuremberg, Germany, 2102, pp. 1–8 [Online]. Available: ieeexplore.ieee.org/document/6170625.
245. B. Xie, W.-l. Cheng, and Z.-m. Xu, "Studies on the effect of shape-stabilized PCM filled aluminum honeycomb composite material on thermal control," *International Journal of Heat and Mass Transfer*, vol. 91, pp. 135–143, Dec. 2015, doi: 10.1016/j.ijheatmasstransfer.2015.07.108.
246. G. Setoh, F. L. Tan, and S. C. Fok, "Experimental studies on the use of a phase change material for cooling mobile phones," *International Communications in Heat and Mass Transfer*, vol. 37, no. 9, pp. 1403–1410, Nov. 2010, doi: 10.1016/j.icheatmasstransfer.2010.07.013.
247. C. Y. Zhao, W. Lu, and Y. Tian, "Heat transfer enhancement for thermal energy storage using metal foams embedded within phase change materials (PCMs)," *Solar Energy*, vol. 84, no. 8, pp. 1402–1412, Aug. 2010, doi: 10.1016/j.solener.2010.04.022.
248. S. P. Gurrum, Y. K. Joshi, and J. Kim, "Thermal management of high temperature pulsed electronics using metallic phase change materials," *Numerical Heat Transfer, Part A: Applications*, vol. 42, no. 8, pp. 777–790, Dec. 2002, doi: 10.1080/10407780290059800.
249. C. E. Green, A. G. Fedorov, and Y. K. Joshi, "Time scale matching of dynamically operated devices using composite thermal capacitors," *Microelectronics Journal*, vol. 45, no. 8, pp. 1069–1078, Aug. 2014, doi: 10.1016/j.mejo.2014.05.013.
250. D. Gonzalez-Nino, L. M. Boteler, D. Ibitayo, N. R. Jankowski, and P. O. Quintero, "Numerical evaluation of multiple phase change materials for pulsed electronics applications," in *Proceedings of the ASME Summer Heat Transfer Conference*, vol. 2, Washington, DC, USA, 2016, doi: 10.1115/ht2016-7223.
251. D. Gonzalez-Nino et al., "Experimental evaluation of metallic phase change materials for thermal transient mitigation," *International Journal of Heat and Mass Transfer*, vol. 116, pp. 512–519, Jan. 2018, doi: 10.1016/j.ijheatmasstransfer.2017.09.039.
252. N. R. Jankowski and F. P. McCluskey, "Numerical study on the thermal performance of a substrate integrated thermal buffer heat sink," in *Proceedings of the ASME International Mechanical Engineering Congress & Exposition*, vol. 10, Denver, CO, USA, Nov. 11–17, 2011, pp. 687–696, doi: 10.1115/IMECE2011-65590.
253. V. Alexiades, *Mathematical Modeling of Melting and Freezing Processes*. Boca Raton, FL, USA: CRC Press, Taylor & Francis Group, 1993, pp. 3–4.
254. H. Hu and S. A. Argyropoulos, "Mathematical modelling of solidification and melting: a review," *Modelling and Simulation in Materials Science and Engineering*, vol. 4, no. 4, pp. 371–396, Jul. 1996, doi: 10.1088/0965-0393/4/4/004.
255. B. B. Budkowska and I. Kreja, "Fixed finite element model of heat transfer with phase change - part I. Theoretical formulation and numerical algorithm," *International Journal of Offshore and Polar Engineering*, vol. 7, no. 2, p. 8, Jun. 1997 [Online]. Available: www.onepetro.org/journal-paper/ISOPE-97-07-2-127

256. N. Provatas, N. Goldenfeld, and J. Dantzig, "Efficient computation of dendritic microstructures using adaptive mesh refinement," *Physical Review Letters*, vol. 80, no. 15, pp. 3308–3311, Apr. 1998, doi: 10.1103/physrevlett.80.3308.
257. C. R. Swaminathan and V. R. Voller, "A general enthalpy method for modeling solidification processes," *Metallurgical Transactions B*, vol. 23, no. 5, pp. 651–664, Oct. 1992, doi: 10.1007/bf02649725.
258. S. Chen, B. Merriman, S. Osher, and P. Smereka, "A simple level set method for solving Stefan problems," *Journal of Computational Physics*, vol. 135, no. 1, pp. 8–29, Jul. 1997, doi: 10.1006/jcph.1997.5721.
259. M. Benes, "Mathematical and computational aspects of solidification of pure substances," *Acta Mathematica Universitatis Comenianae*, vol. 70, no. 1, pp. 123–151, 2001 [Online]. Available: www.iam.fmph.uniba.sk/amuc/_vol-70/_no_1/_benes/benes.html
260. H. T. Hashemi and C. M. Sliepcevich, "A numerical method for solving two-dimensional problems of heat conduction with change of phase," *Chemical Engineering Progress Symposium Series*, vol. 63, pp. 34–41, 1967.
261. C. Bonacina, G. Comini, A. Fasano, and M. Primicerio, "Numerical solution of phase-change problems," *International Journal of Heat and Mass Transfer*, vol. 16, no. 10, pp. 1825–1832, Oct. 1973, doi: 10.1016/0017-9310(73)90202-0
262. V. R. Voller, C. R. Swaminathan, and B. G. Thomas, "Fixed grid techniques for phase change problems: A review," *International Journal for Numerical Methods in Engineering*, vol. 30, no. 4, pp. 875–898, Sep. 1990, doi: 10.1002/nme.1620300419.
263. F. Civan and C. M. Sliepcevich, "Limitation in the apparent heat capacity formulation for heat transfer with phase change," *Proceedings of the Oklahoma Academy of Science*, vol. 67, pp. 83–88, 1987 [Online]. Available: ojs.library.okstate.edu/osu/index.php/OAS/article/view/5416/5043
264. M. Muhieddine, E. Canot, and R. March, "Various approaches for solving problems in heat conduction with phase change," *International Journal on Finite Volumes*, vol. 6, no. 1, pp. 1–20, Jan. 2009 [Online]. Available: ijfv.math.cnrs.fr/spip.php?article23
265. M. Yao and A. Chait, "Application of the homographic approximation in the enthalpy method for phase change problems," *International Journal of Numerical Methods for Heat & Fluid Flow*, vol. 3, no. 2, pp. 157–172, Feb. 1993, doi: 10.1108/eb017523.
266. J. S. Hsiao, "An efficient algorithm for finite-difference analyses of heat transfer with melting and solidification," *Numerical Heat Transfer*, vol. 8, no. 6, pp. 653–666, Jan. 1985, doi: 10.1080/01495728508961877.
267. P. Råback, M. Malinen, J. Ruokolainen, A. Pursula, and T. Zwinger, "Model 1: Heat Equation," in *Elmer Models Manual*, CSC Scientific Computing, Ltd., 2018 [Online]. Available: www.csc.fi/elmer
268. Z.-X. Gong and A. S. Mujumdar, "Non-convergence versus non-conservation in effective heat capacity methods for phase change problems," *International Journal of Numerical Methods for Heat & Fluid Flow*, vol. 7, no. 6, pp. 565–579, Sep. 1997, doi: 10.1108/09615539710170754.
269. K. T. Lowe, R. V. Arimilli, and C. W. Ayers, "Thermal buffer heat sink for time-averaged operating conditions," University of Tennessee, Knoxville, TN, USA, US Department of Energy, Oak Ridge National Laboratory, Subcontract Report, Sep. 1, 2007.
270. E. Puppo and D. Panozzo, "RGB Subdivision," *IEEE Transactions on Visualization and Computer Graphics*, vol. 15, no. 2, pp. 295–310, Mar. 2009, doi: 10.1109/tvcg.2008.87.

271. R. K. Shah and D. P. Sekuli, *Fundamentals of heat exchanger design*. Hoboken, NJ, USA: John Wiley & Sons, Inc., 2003.
272. L. W. Nagel and D. O. Pederson, "SPICE (Simulation Program with Integrated Circuit Emphasis)," EECS Department, University of California, Berkeley, UCB/ERL M382, Apr. 1973 [Online]. Available: www2.eecs.berkeley.edu/Pubs/TechRpts/1973/22871.html
273. B. Zivkovic and I. Fujii, "An analysis of isothermal phase change of phase change material within rectangular and cylindrical containers," *Solar Energy*, vol. 70, no. 1, pp. 51-61, 2001, doi: 10.1016/s0038-092x(00)00112-2.
274. T. Matsumoto and K. Nogi, "Wetting in soldering and microelectronics," *Annual Review of Materials Research*, vol. 38, no. 1, pp. 251-273, Aug. 2008, doi: 10.1146/annurev.matsci.38.060407.132448.
275. A. M. Khounsary, D. Chojnowski, L. Assoufid, and W. M. Worek, "Thermal contact resistance across a copper-silicon interface," in *High Heat Flux and Synchrotron Radiation Beamlines*, 1997, doi: 10.1117/12.294497.
276. Y. S. Choi and M. S. Kim, "Experiments on thermal contact conductance between metals below 100 K," *AIP Conference Proceedings*, vol. 1573, no. 1, pp. 1070-1077, Jan. 2014, doi: 10.1063/1.4860824.
277. Y. Gao and J. Liu, "Gallium-based thermal interface material with high compliance and wettability," *Applied Physics A*, vol. 107, no. 3, pp. 701-708, Mar. 2012, doi: 10.1007/s00339-012-6887-5.
278. "Parylene Thermal Properties," Para-Coat Technologies, Inc., Johnstown, PA, USA, (accessed Nov. 6, 2020), [Online]. Available: pctconformalcoating.com/parylene/parylene-thermal-properties
279. D. J. Sharar, B. F. Donovan, R. J. Warzoha, A. A. Wilson, A. C. Leff, and B. M. Hanrahan, "Solid-state thermal energy storage using reversible martensitic transformations," *Applied Physics Letters*, vol. 114, no. 14, p. 143902, Apr. 2019, doi: 10.1063/1.5087135.
280. T. Davin, B. Lefez, and A. Guillet, "Supercooling of phase change: A new modeling formulation using apparent specific heat capacity," *International Journal of Thermal Sciences*, vol. 147, p. 106121, Jan. 2020, doi: 10.1016/j.ijthermalsci.2019.106121.
281. E. K. Bigg, "The Supercooling of Water," *Proceedings of the Physical Society. Section B*, vol. 66, no. 8, pp. 688-694, Aug. 1953, doi: 10.1088/0370-1301/66/8/309.
282. J. Hallett, "Experimental studies of the crystallization of supercooled water," *Journal of the Atmospheric Sciences*, vol. 21, no. 6, pp. 671-682, Nov. 1964, doi: 10.1175/1520-0469(1964)021<0671:esotco>2.0.co;2.
283. D. Turnbull, "The undercooling of liquids," *Scientific American*, vol. 212, pp. 28-46, 1965 [Online]. Available: www.scientificamerican.com/article/the-undercooling-of-liquids/
284. W. Kauzmann, "The nature of the glassy state and the behavior of liquids at low temperatures," *Chemical Reviews*, vol. 43, no. 2, pp. 219-256, Oct. 1948, doi: 10.1021/cr60135a002.
285. V. Alexiades, A. D. Solomon, and D. G. Wilson, "The Formation of a Solid Nucleus in Supercooled Liquid, I," *Journal of Non-Equilibrium Thermodynamics*, vol. 13, no. 3, 1988, doi: 10.1515/jnet.1988.13.3.281.
286. D. Turnbull and B. Vonnegut, "Nucleation Catalysis.," *Industrial & Engineering Chemistry*, vol. 44, no. 6, pp. 1292-1298, Jun. 1952, doi: 10.1021/ie50510a031.
287. B. Vonnegut, "The Nucleation of Ice Formation by Silver Iodide," *Journal of Applied Physics*, vol. 18, no. 7, pp. 593-595, Jul. 1947, doi: 10.1063/1.1697813.

288. G. R. Edwards and L. F. Evans, "Ice nucleation by silver iodide: I. Freezing vs sublimation," *Journal of Meteorology*, vol. 17, no. 6, pp. 627–634, Dec. 1960, doi: 10.1175/1520-0469(1960)017<0627:inbsii>2.0.co;2.
289. A. Petersen, G. Rau, and B. Glasmacher, "Reduction of primary freeze-drying time by electric field induced ice nucleus formation," *Heat and Mass Transfer*, vol. 42, no. 10, pp. 929–938, Jun. 2006, doi: 10.1007/s00231-006-0153-3.
290. S. Hirano and T. S. Saitoh, "Influence of operating temperature on efficiency of supercooled thermal energy storage," in *Proceedings of the 37th Intersociety Energy Conversion Engineering Conference*, Washington, WA, USA, Jul. 29-31, 2002, doi: 10.1109/iecec.2002.1392129.
291. A. W. Brewer and H. P. Palmer, "Freezing of Supercooled Water," *Proceedings of the Physical Society. Section B*, vol. 64, no. 9, pp. 765–773, Sep. 1951, doi: 10.1088/0370-1301/64/9/306.
292. S. Akio, U. Yoshio, O. Seiji, M. Kazuyuki, and T. Atsushi, "Fundamental research on the supercooling phenomenon on heat transfer surfaces—investigation of an effect of characteristics of surface and cooling rate on a freezing temperature of supercooled water," *International Journal of Heat and Mass Transfer*, vol. 33, no. 8, pp. 1697–1709, Aug. 1990, doi: 10.1016/0017-9310(90)90025-p.
293. S. Okawa, A. Saito, and H. Suto, "The experimental study on freezing of supercooled water using metallic surface," *International Journal of Refrigeration*, vol. 25, no. 5, pp. 514–520, Aug. 2002, doi: 10.1016/s0140-7007(01)00038-x.
294. T. Hozumi, A. Saito, S. Okawa, and K. Watanabe, "Effects of electrode materials on freezing of supercooled water in electric freeze control," *International Journal of Refrigeration*, vol. 26, no. 5, pp. 537–542, Aug. 2003, doi: 10.1016/s0140-7007(03)00008-2.
295. T. Hozumi, A. Saito, S. Okawa, and Y. Eshita, "Effects of shapes of electrodes on freezing of supercooled water in electric freeze control," *International Journal of Refrigeration*, vol. 28, no. 3, pp. 389–395, May 2005, doi: 10.1016/j.ijrefrig.2004.08.009.
296. S. Okawa, A. Saito, and T. Matsui, "Nucleation of supercooled water on solid surfaces," *International Journal of Refrigeration*, vol. 29, no. 1, pp. 134–141, Jan. 2006, doi: 10.1016/j.ijrefrig.2005.05.010.
297. M. Faucheux, G. Muller, M. Havet, and A. LeBail, "Influence of surface roughness on the supercooling degree: Case of selected water/ethanol solutions frozen on aluminium surfaces," *International Journal of Refrigeration*, vol. 29, no. 7, pp. 1218–1224, Nov. 2006, doi: 10.1016/j.ijrefrig.2006.01.002.
298. V. J. Schaefer, "The production of ice crystals in a cloud of supercooled water droplets," *Science*, vol. 104, no. 2707, pp. 457–459, Nov. 1946, doi: 10.1126/science.104.2707.457.
299. S. Okawa, A. Saito, R. Minami, "The solidification phenomenon of the supercooled water containing solid particles," *International Journal of Refrigeration*, vol. 24, pp. 108-117, 2001.
300. D. Turnbull, "Principles of solidification," in *Thermodynamics in Physical Metallurgy*, Cleveland, OH, USA: American Society for Metals, Noveltly, 1950, pp. 282–306.
301. B. Chalmers, *Principles of Solidification*. Melbourne, FL, USA: R. E. Krieger Publishing Co., 1977.
302. W. Kurz and D. J. Fisher, *Fundamentals of Solidification*. Aedermannsdorf, Switzerland: Trans Tech Publications, 1984.

303. T. Inada, X. Zhang, A. Yabe, and Y. Kozawa, "Active control of phase change from supercooled water to ice by ultrasonic vibration 1. Control of freezing temperature," *International Journal of Heat and Mass Transfer*, vol. 44, no. 23, pp. 4523–4531, Dec. 2001, doi: 10.1016/s0017-9310(01)00057-6.
304. E. P. Ona, X. Zhang, S. Ozawa, H. Matsuda, H. Kakiuchi, M. Yabe, M. Yamazaki, and M. Sato, "Influence of Ultrasonic Irradiation on the Solidification Behavior of Erythritol as a PCM," *Journal of Chemical Engineering of Japan*, vol. 35, no. 3, pp. 290–298, 2002, doi: 10.1252/jcej.35.290.
305. X. Zhang, T. Inada, A. Yabe, S. Lu, and Y. Kozawa, "Active control of phase change from supercooled water to ice by ultrasonic vibration 2. Generation of ice slurries and effect of bubble nuclei," *International Journal of Heat and Mass Transfer*, vol. 44, no. 23, pp. 4533–4539, Dec. 2001, doi: 10.1016/s0017-9310(01)00058-8.
306. J. D. Hunt and K. A. Jackson, "Nucleation of solid in an undercooled liquid by cavitation," *Journal of Applied Physics*, vol. 37, no. 1, pp. 254–257, Jan. 1966, doi: 10.1063/1.1707821.
307. M. A. Abbas and J. Latham, "The Electrofreezing of Supercooled Water Drops," *Journal of the Meteorological Society of Japan. Ser. II*, vol. 47, no. 2, pp. 65–74, 1969, doi: 10.2151/jmsj1965.47.2_65.
308. H. R. Pruppacher, "Electrofreezing of supercooled water," *Pure and Applied Geophysics PAGEOPH*, vol. 104, pp. 623–634, Dec. 1973, doi: 10.1007/bf00875907.
309. W. Rau, "Eiskeimbildung durch dielektrische polarisation," (in German) *Zeitschrift für Naturforschung A*, vol. 6, no. 11, pp. 649–657, Nov. 1951, doi: 10.1515/zna-1951-1115.
310. R. W. Salt, "Effect of electrostatic field on freezing of supercooled water and insects," *Science*, vol. 133, no. 3451, pp. 458–459, Feb. 1961, doi: 10.1126/science.133.3451.458.
311. R. P. Hans, "The effect of an external electric field on the supercooling of water drops," *Journal of Geophysical Research*, vol. 68, no. 15, pp. 4463–4474, Aug. 1963, doi: 10.1029/jz068i015p04463.
312. L. B. Loeb, "A tentative explanation of the electrical field effect on the freezing of supercooled water drops," *Journal of Geophysical Research*, vol. 68, no. 15, pp. 4475–4476, Aug. 1963, doi: 10.1029/jz068i015p04475.
313. G. R. Edwards and L. F. Evans, "The mechanism of activation of ice nuclei," *Journal of the Atmospheric Sciences*, vol. 28, no. 8, pp. 1443–1447, Nov. 1971, doi: 10.1175/1520-0469(1971)028<1443:tmoaoi>2.0.co;2.
314. J. B. Doolittle and G. Vali, "Heterogeneous Freezing Nucleation in Electric Fields," *Journal of the Atmospheric Sciences*, vol. 32, no. 2, pp. 375–379, Feb. 1975, doi: 10.1175/1520-0469(1975)032<0375:hfnief>2.0.co;2.
315. I. M. Svishchev and P. G. Kusalik, "Electrofreezing of liquid water: A microscopic perspective," *Journal of the American Chemical Society*, vol. 118, no. 3, pp. 649–654, Jan. 1996, doi: 10.1021/ja951624l.
316. S. Wei, X. Xiaobin, Z. Hong, and X. Chuanxiang, "Effects of dipole polarization of water molecules on ice formation under an electrostatic field," *Cryobiology*, vol. 56, no. 1, pp. 93–99, Feb. 2008, doi: 10.1016/j.cryobiol.2007.10.173.
317. G. Mandal and P. P. Kumar, "A laboratory study of ice nucleation due to electrical discharge," *Atmospheric Research*, vol. 61, no. 2, pp. 115–123, Feb. 2002, doi: 10.1016/s0169-8095(01)00129-6.
318. T. Shichiri and T. Nagata, "Effect of electric currents on the nucleation of ice crystals in the melt," *Journal of Crystal Growth*, vol. 54, no. 2, pp. 207–210, Aug. 1981, doi: 10.1016/0022-0248(81)90461-9.

319. T. Shichiri and Y. Araki, "Nucleation mechanism of ice crystals under electrical effect," *Journal of Crystal Growth*, vol. 78, no. 3, pp. 502–508, Dec. 1986, doi: 10.1016/0022-0248(86)90152-1.
320. H. Matsuda, E. P. Ona, Y. Kojima, S. Ozawa, M. Yabe, H. Kakiuchi, S. Chihara, and M. Sato, "Enhancement of phase change of a high temperature PCM with the aid of ultrasonic energy," presented at the 3rd *Workshop for the International Energy Agency, Energy Conservation through Energy Storage Implementing Agreement, Annex 17*, Tokyo, Japan, Oct. 1-2, 2002.
321. A. Shukla, D. Buddhi, and R. L. Sawhney, "Thermal cycling test of few selected inorganic and organic phase change materials," *Renewable Energy*, vol. 33, no. 12, pp. 2606–2614, Dec. 2008, doi: 10.1016/j.renene.2008.02.026.
322. H. Hidaka, M. Yamazaki, M. Yabe, H. Kakiuchi, E. P. Ona, Y. Kojima, H. Matsuda, "New PCMs prepared from erythritol-polyalcohols mixtures for latent heat storage between 80 and 100°C," *Journal of Chemical Engineering of Japan*, vol. 37, no. 9, pp. 1155–1162, 2004, doi: 10.1252/jcej.37.1155.
323. D. Feldman, M. M. Shapiro, D. Banu, and C. J. Fuks, "Fatty acids and their mixtures as phase-change materials for thermal energy storage," *Solar Energy Materials*, vol. 18, no. 3-4, pp. 201–216, Mar. 1989, doi: 10.1016/0165-1633(89)90054-3.
324. K. Peippo, P. Kauranen, and P. D. Lund, "A multicomponent PCM wall optimized for passive solar heating," *Energy and Buildings*, vol. 17, no. 4, pp. 259–270, Jan. 1991, doi: 10.1016/0378-7788(91)90009-r.
325. V. N. Danilin and S. G. Shabalina, "Heat storage materials based on high molecular weight compounds," (in Russian), *Fiziko-khimicheskii Analiz Svoistv Mnogokomponentnykh System*, vol. 1, 2003 [Online]. Available: fh.kubstu.ru/fams/
326. "ClimSel Product Data Sheets," Climator Sweden AB, Skövde, Sweden, (accessed Sep. 24, 2020), [Online]. Available: www.climator.com/en/pcm-climsel/product-data-sheets